Characterization of Minerals, Metals, and Materials 2020

Edited by
Jian Li
Mingming Zhang
Bowen Li
Sergio Neves Monteiro
Shadia Ikhmayies
Yunus Eren Kalay
Jiann-Yang Hwang
Juan P. Escobedo-Diaz
John S. Carpenter
Andrew D. Brown

TMS
Springer

The Minerals, Metals & Materials Series

Jian Li · Mingming Zhang ·
Bowen Li · Sergio Neves Monteiro ·
Shadia Ikhmayies · Yunus Eren Kalay ·
Jiann-Yang Hwang · Juan P. Escobedo-Diaz ·
John S. Carpenter · Andrew D. Brown
Editors

Characterization of Minerals, Metals, and Materials 2020

TMS

Springer

Editors
Jian Li
CanmetMATERIALS
Hamilton, ON, Canada

Bowen Li
Michigan Technological University
Houghton, MI, USA

Shadia Ikhmayies
Al Isra University
Amman, Jordan

Jiann-Yang Hwang
Michigan Technological University
Houghton, MI, USA

John S. Carpenter
Los Alamos National Laboratory
Los Alamos, NM, USA

Mingming Zhang
ArcelorMittal Global R&D
Schererville, IN, USA

Sergio Neves Monteiro
Military Institute of Engineering
Rio de Janeiro, Brazil

Yunus Eren Kalay
Middle East Technical University
Ankara, Turkey

Juan P. Escobedo-Diaz
University of New South Wales
Canberra, BC, Australia

Andrew D. Brown
United States Army Research Laboratory
Adelphi, MD, USA

ISSN 2367-1181 ISSN 2367-1696 (electronic)
The Minerals, Metals & Materials Series
ISBN 978-3-030-36627-8 ISBN 978-3-030-36628-5 (eBook)
https://doi.org/10.1007/978-3-030-36628-5

Cover illustration: From Chapter "Study on the Separation of Zinc and Iron in Electric Arc Furnace Baghouse Dusts and Its Kinetics", Zhao-ran Wang et al, Fig. 1 Microscopic morphology of electric furnace bag. https://doi.org/10.1007/978-3-030-36628-5_70

This Springer imprint is published by the registered company Springer Nature Switzerland AG
The registered company address is: Gewerbestrasse 11, 6330 Cham, Switzerland

Preface

Developing and optimizing industrial processes to form materials to their desired size, shape, and microstructure are in turn deciding the products' properties. This composition–process–structure–property relationship is the key for any materials processing routine. Characterization of properties and microstructure is an important element in determining critical processing parameters. Recent advances in characterization instruments have contributed to an in-depth understanding of materials properties and structure that has enabled much precise process control.

The Characterization of Minerals, Metals and Materials Symposium is sponsored by the Materials Characterization Committee of The Minerals, Metals & Materials Society (TMS). The main focus of this symposium includes but is not limited to advanced characterization of extraction and processing of minerals and the process–microstructure–property relation of metal alloys, ceramics, polymers, composites, and electronic materials. New characterization methods, techniques, and instrumentations are also emphasized.

The Characterization of Minerals, Metals and Materials symposia are one of the largest at each TMS Annual Meeting and attract researchers in the field of materials, minerals, mechanical engineering, chemistry, and physics. At the TMS 2020 149th Annual Meeting & Exhibition held in San Diego, California, USA, this symposium received 222 abstract submissions, of which 122 submissions were accepted for oral presentation in 13 technical sessions, and 100 were accepted as poster presentations. This proceeding volume includes 72 peer-reviewed manuscripts of original research. The authors of the papers represent more than 24 countries from North America, South America, Asia, Europe, Australia, and Africa.

This proceeding publication is a valuable reference for academia and industry that includes advanced characterization methods and instrumentations that cover a wide range of research fields. Readers will enjoy the diversity of topics with novel approaches to process and characterize materials at various length scales.

The editors of this proceeding volume are very grateful to the authors for their contributions and willingness to share their research findings. The editors would also like to thank TMS for providing this valuable opportunity to publish this

stand-alone volume. Appreciations also extend to the Materials Characterization Committee and Extraction and Processing Division (EPD) for sponsoring the symposium. The editors also thank the publisher, Springer, for its timely publication of this book.

Jian Li
Lead Organizer

Contents

Part II Advances in Characterization Methods II

Part III Minerals Processing and Analysis II

Part IV Characterization of Mechanical Properties I

Part V Mineral Processing and Analysis III

Part VI Characterization of Corrosion Resistance

Part VII Characterization of Electronic and Magnetic Materials

About the Editors

Jian Li is a senior research scientist and program manager at CanmetMATERIALS in Natural Resources Canada. He obtained his B.Sc. in Mechanical Engineering from Beijing Polytechnique University, M.Sc. in Metallurgical Engineering from Technical University of Nova Scotia, and Ph.D. in Materials and Metallurgical Engineering from Queen's University, Kingston, Ontario, Canada. He has a broad experience in materials processing and characterization including alloys deformation, recrystallization, and micro-texture development. He has extensive experience in focused ion beam (FIB) microscope techniques. He is also an expert in various aspects of SEM-EDS and EPMA techniques. He has authored three chapters and published more than 160 papers in scientific journals and conference proceedings.

Mingming Zhang is a lead research engineer at ArcelorMittal Global R&D in East Chicago, Indiana. He has more than 15 years of research experience in the field of mineral processing, and metallurgical and materials engineering. He obtained his Ph.D. degree in Metallurgical Engineering from the University of Alabama and his master's degree in Mineral Processing from General Research Institute for Non-ferrous Metals in China. Prior to joining ArcelorMittal, he worked with Nucor Steel in Tuscaloosa, Alabama, where he was a metallurgical engineer leading the development of models for simulating slab solidification and secondary cooling processes. He has conducted a number of research projects involving mineral beneficiation,

thermodynamics and kinetics of metallurgical reactions, electrochemical processing of light metals, metal recycling, and energy efficient and environmentally cleaner technologies. He has published more than 50 peer-reviewed research papers and is the recipient of several US patents. He also serves as an editor or reviewer for a number of prestigious journals including *Metallurgical and Materials Transactions A* and *B*, *JOM*, *Journal of Phase Equilibria and Diffusion*, and *Mineral Processing and Extractive Metallurgy Review*. He has made more than 30 research presentations at national and international conferences including more than ten keynote presentations. He was the recipient of the 2015 TMS Young Leaders Professional Development Award. He has served as a conference/symposium organizer and technical committee chair in several international professional organizations including The Minerals, Metals & Materials Society (TMS), Association for Iron & Steel Technology (AIST), and the Society for Mining, Metallurgy & Exploration (SME).

Bowen Li is a research professor in the Department of Materials Science and Engineering and Institute of Materials Processing at Michigan Technological University. His research interests include materials characterization and analysis, metals extraction, ceramic process, antimicrobial additives and surface treatment, porous materials, applied mineralogy, and solid waste reuse. He has published more than 120 technical papers in peer-reviewed journals and conference proceedings, authored/co-authored three books, and edited/co-edited eight books. He also holds 15 patents and has delivered more than 30 invited technical talks.

He received a Ph.D. degree in Mineralogy and Petrology from China University of Geosciences Beijing in 1998 and a Ph.D. degree in Materials Science and Engineering from Michigan Technological University in 2008. He has been an active member in The Minerals, Metals & Materials Society (TMS), Society for Mining, Metallurgy & Exploration (SME), and China Ceramic Society. At TMS, he currently serves as the Past Chair of the Materials Characterization Committee and as a member of the Powder Materials Committee and Biomaterials

Committee. He also has served as an EPD Award Committee member, a *JOM* subject advisor, and a key reader for *Metallurgical and Materials Transactions A*. He has been organizer/co-organizer of a number of international symposia and sessions. He also served as an editorial board member of the *Journal of Minerals and Materials Characterization and Engineering, Reviews on Advanced Materials Science*, and *FUTO Journal Series*.

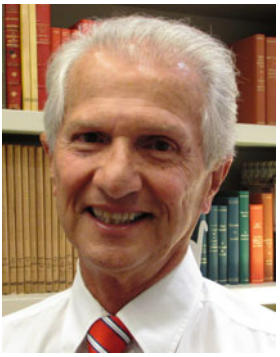

Sergio Neves Monteiro graduated as a metallurgical engineer (1966) at the Federal University of Rio de Janeiro (UFRJ). He received his M.Sc. (1967) and Ph. D. (1972) from the University of Florida, followed by a 1975 course in energy at the Brazilian War College, and a postdoctorate (1976) at the University of Stuttgart. In 1968, he joined the Metallurgy Department of UFRJ as full professor of the postgraduation program in engineering (COPPE). He was elected head of department (1978), coordinator of COPPE (1982), and UnderRector for Research (1983) and was invited as Under-Secretary of Science for the State of Rio de Janeiro (1985) and Under-Secretary of College Education for the Federal Government (1989). He retired in 1993 from the UFRJ and joined the State University of North Rio de Janeiro (UENF), from where he retired in 2012. He is now professor at the Military Institute of Engineering (IME), Rio de Janeiro, and has published more than 1,200 articles in journals and conference proceedings and has been honored with several awards including the ASM Fellowship. He is a top researcher (1A) of the Brazilian Council for Scientific and Technological Development (CNPq) and top scientist of State of Rio de Janeiro (FAPERJ). He was the president of the Superior Council of the State of Rio de Janeiro Research Foundation, FAPERJ (2012), and currently is the coordinator of the Engineering Area of this foundation. He also has served as the president of the Brazilian Association for Metallurgy, Materials and Mining (ABM, 2017–2019), a consultant for the main Brazilian R&D agencies, and a member of the editorial board of five international journals as well as associate editor of the *Journal of Materials Research and Technology*.

Shadia Ikhmayies received a B.Sc. and M.Sc. from the physics department at the University of Jordan in 1983 and 1987, respectively, and a Ph.D. in producing CdS/CdTe thin film solar cells from the same university in 2002. She now works at Isra University in Jordan as an associate professor. Her research is focused on producing and characterizing semiconductor thin films and thin film CdS/CdTe solar cells. She also works in characterizing quartz in Jordan for the extraction of silicon for solar cells and characterizing different materials by computation. She has published more than 50 research papers in international scientific journals, more than 70 research papers in conference proceedings, and three chapters in books. She is the editor of the books *Advances in II-VI Compounds Suitable for Solar Cells Applications* (Research Signpost) and *Advances in Silicon Solar Cells* (Springer), and the eBook series *Advances in Materials Research and Technology* (Springer). She has also served as editor for several TMS Annual Meeting proceedings publications.

She is a member of The Minerals, Metals & Materials Society (TMS) and the World Renewable Energy Network (WREN). She is a member of the international organizing committee and the international scientific committee of the European Conference on Renewable Energy Systems (ECRES2015-ECRES2020). She is a member of the editorial board of the *International Journal of Materials and Chemistry* and has served as guest editor or field editor for six topics published in *JOM* (2014, 2019, and 2020), topical collections published in the *Journal of Electronic Materials* (ECRES 2015–2018), the topical collection "Energy, Power, and Materials Modelling" (SN Applied Sciences), and the journal *Energy Systems*. She is a reviewer for 24 international journals and was the Chair of the TMS Materials Characterization Committee (2016–2017).

Yunus Eren Kalay is an associate professor in the Metallurgical and Materials Engineering Department and an Assistant to the President at Middle East Technical University (METU), Ankara, Turkey. He received his Ph.D. degree from Iowa State University in 2009. His Ph.D. topic was related to the metallic glass formation in Al-based metallic alloy systems. Following his Ph.D., he pursued postdoctoral research at Ames National Laboratory, where he practiced atom probe tomography. In 2011, He joined the Department of Metallurgical and Materials Engineering (METE) of METU as an assistant professor, and in 2014 he was promoted to associate professor. His research interests span microstructural evolution in metallic alloys, rapid solidification of metallic alloys, nanostructured and amorphous alloys, lead-free solders, electronic packaging, and advanced characterization techniques such as scanning and transmission electron microscopy, electron and X-ray spectroscopy, and application of synchrotron X-ray scattering in materials research. He was awarded the "METU Prof. Dr. Mustafa Parlar Foundation Research Incentive Award", which is a prestigious award that recognizes young scientists in Turkey with exceptional achievements and research productivity. He is also an active member of the TMS Materials Characterization Committee and Phase Transformations Committee and served on organizing committees of three international and one national congress including IMMC, MS&T, and TMS. He is a *JOM* guest editor (2019–2020). He also has been involved in many synergistic activities such as being founding editor of Turkey's first undergraduate research journal, *MATTER* (http://matter.mete.metu.edu.tr/) and organizing materials science camps for K-12 students.

Jiann-Yang Hwang is a professor in the Department of Materials Science and Engineering at Michigan Technological University. He is also the Chief Energy and Environment advisor at the Wuhan Iron and Steel Group Company, a Fortune Global 500 company. He has been the editor-in-chief of the *Journal of Minerals and Materials Characterization and Engineering* since 2002. He has founded several enterprises in areas including water desalination and treatment equipment, microwave steel production, chemicals, fly ash processing, antimicrobial materials, and plating wastes treatment. Several universities have honored him as a guest professor, including the Central South University, University of Science and Technology Beijing, Chongqing University, Kunming University of Science and Technology, and Hebei United University. He received his B.S. from National Cheng Kung University in 1974, and his M.S. in 1980 and Ph.D. in 1982, both from Purdue University. He joined Michigan Technological University in 1984 and served as its director of the Institute of Materials Processing from 1992 to 2011 and the Chair of Mining Engineering Department in 1995. He has been a TMS member since 1985. His research interests include the characterization and processing of materials and their applications. He has been actively involved in the areas of separation technologies, pyrometallurgy, microwaves, hydrogen storage, ceramics, recycling, water treatment, environmental protection, biomaterials, and energy and fuels. He has more than 28 patents and has published more than 200 papers. He has chaired the Materials Characterization Committee and the Pyrometallurgy Committee in TMS and has organized several symposia. He is the recipient of the TMS Technology Award and of Michigan Tech's Bhakta Rath Research Award.

Juan P. Escobedo-Diaz is a senior lecturer in the School of Engineering and Information Technology (SEIT) at UNSW Canberra. He obtained his doctoral degree in Mechanical Engineering at Washington State University. Prior to taking up this academic appointment, he held research positions at the Institute for Shock Physics at Los Alamos National Laboratory. His main research interests center on the dynamic behavior of materials under extreme conditions, in particular high pressure and high strain rate. His focus has been on investigating the effects of microstructural features on the dynamic fracture behavior of metals and metallic alloys. He has published primarily in the fields of shock physics and materials science. He has been a member of The Metals, Minerals & Materials Society (TMS) since 2011. During this time, he has co-organized more than five symposia at the Annual Meetings including the symposium on Characterization of Minerals, Metals and Materials since 2014. He was awarded a 2014 SMD Young Leaders Professional Development Award.

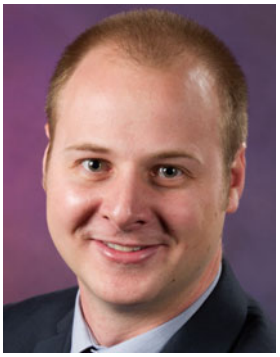

John S. Carpenter is a scientist within the manufacturing and metallurgy division at Los Alamos National Laboratory, USA. He received his Ph.D. in Materials Science and Engineering from The Ohio State University in 2010 after performing his undergraduate studies at Virginia Tech.

His research focus is on enabling advanced manufacturing concepts through experiments employing novel processing techniques, advanced characterization, and small-scale mechanical testing. Currently, he is working on projects related to the qualification of additively manufactured components and using high-energy X-rays to study phase transformations during solidification in MIG cladding. Throughout his career, he has utilized many characterization techniques including neutron scattering, X-ray synchrotron, XCT, PED, TEM, EBSD, and SEM.

He has more than 55 journal publications, one chapter, and 35 invited technical talks to his credit.

With regard to TMS service, he currently serves as the EPD representative on the Program Committee, SMD representative on the Content Development and Dissemination Committee, and EPD liaison on the

Additive Manufacturing Bridge Committee. He is a participating member of the Mechanical Behavior of Materials Committee and has served as Chair of both the Materials Characterization Committee and the Advanced Characterization, Testing, and Simulation Committee in the past. He serves as a Key Reader for *Metallurgical and Materials Transactions A* and has co-edited special sections in *JOM* related to neutron diffraction, coherent X-ray diffraction imaging methods, and modeling in additive manufacturing. He is the 2012 recipient of the TMS EPD Young Leaders Professional Development Award. He also received the 2018 Distinguished Mentor Award at Los Alamos National Laboratory.

Andrew D. Brown is a mechanical engineer with the Soldier Protection Sciences Branch (FCDD-RLW-PB) of the Weapons and Materials Research Directorate at the Army Research Laboratory (ARL), Aberdeen Proving Grounds, Maryland, USA. He obtained his B.S. in Mechanical Engineering at North Carolina State University (2009) and his doctoral degree in Mechanical Engineering at Arizona State University (2015). He spent three years (2015–2018) at UNSW Canberra as a postdoctoral researcher where he oversaw the daily operations of the Impact Dynamics Laboratory, mentored undergraduate and graduate student research projects, and performed teaching duties. His research expertise is understanding the microstructural effects on the mechanical performance and damage processes of materials subjected to high dynamic pressures (shock) and high strain rates. Since joining ARL in 2018, he has shifted focus to high-rate injury biomechanics research to improve injury outcome prediction and protect the US Warfighter. He has been an active member of TMS since 2011, was a co-organizer for the symposium on Characterization of Minerals, Metals, and Materials in 2018; and has been the symposium's EPD Award Representative from 2017–present. He has published more than 35 peer-reviewed articles in the fields of mechanical engineering, materials science, and biomedical engineering.

Part I
Mineral Processing and Analysis I

Characterization of Iron Ore Sinter Samples by Automated SEM

Mingming Zhang and Marcelo Andrade

Abstract This paper presents a new mineralogical and textural characterization solution for iron ore sinter samples using an automated single scanning electron microscope. It employs a motorized and computer-controlled multiple sample stage. Mosaic images covering large areas of polished sections are acquired to measure the volume/weight fraction of mineral compositions (phase fraction calculation is based on user-defined density per phase). Different classifiers discriminate hematite, calcium ferrite, calcium silico-ferrite, magnesioferrite, calcium silicate and glasses. The entire process is automatic and produces a full pdf report containing typical images and the quantification of mineral phases and grain size. This study represents a convenient method for analyzing mineral phase and grain size in iron ore sinter samples that can allow for quicker results in sintering process control and optimization.

Introduction

Iron ore sinter constitutes an important part of total ferrous burden in modern blast furnace ironmaking operations. Nowadays, most sinter plant operates with large amount of fine materials and reverts; the characteristics of available sintering feed and operation conditions of sinter plant vary from time to time, making it difficult to control and predict production rates as well as sinter quality. Characterization of mineral phases of sinter is a cost-effective and complementary tool to conventional physical and metallurgical testing of iron ore sinter in evaluating and predicting sinter quality. The understanding of sinter mineralogy also can help improve blast furnace operation stability and productivity [1]. This is because the porosity of sinter affects the reducibility of iron ore to pig iron, while its morphological characteristics affect the reducibility and strength of the iron-bearing material in blast furnaces.

Over the years, many schemes have been developed for characterizing iron ore sinter to classify primary sinter phases such as unreacted and partially reacted hematite

M. Zhang (✉) · M. Andrade
ArcelorMittal Global R&D, East Chicago, IN 46312, USA
e-mail: Mingming.Zhang@ArcelorMittal.com

J. Li et al. (eds.), *Characterization of Minerals, Metals, and Materials 2020*,
The Minerals, Metals & Materials Series,
https://doi.org/10.1007/978-3-030-36628-5_1

and magnetite and secondary phases, including prismatic high-temperature silico-ferrite of calcium and alumina (SFCA), secondary hematite and magnetite, glass, larnite (dicalcium silicate; Ca_2SiO_4) and remnant fluxes [2]. Quantification of these phases has traditionally been carried out by visual point counting method under a reflective light microscope; recently, new technologies based on automated optical image analysis, quantitative X-ray diffraction and scanning electron microscopy have been reported and made available for evaluation. Particularly, mineralogical quantification through automated SEM including QEMSCAN® can give consistent and reproducible phase recognition because of its automation and may be more robust than point counting reflective light microscopy because of its chemically and backscattered electron (BSE)-based identification [3].

For all SEM-based systems, potential difficulties in mineral phase analysis occur when phases of similar chemistry such as hematite and magnetite also have similar average atomic numbers (i.e., similar BSE intensities). It is therefore important to develop an automated SEM method to differentiate magnetite and hematite based on surface characteristics of the iron oxides being measured (gray scales, porosity, texture, etc.) and the degree of ionic substitution in the iron oxides (Mg, Ca, Al and Mn et al.).

This paper presents an automated SEM method based on stereology and point counting principle to discriminate and measure major phases and grain size in iron ore sinter samples. The automated SEM method makes use of software paradigm to differentiate iron oxide mineral phases with similar chemistry and atomic numbers. In addition, BSE stabilizers, gun alignment, and magnification field size, stage height (working distance) are optimized to determine gray scale of interested phases. The third point BSE calibration standards are adopted and beam dwell times on specific point can be increased to enhance identification to improve discrimination between similar phases. Image analysis and post-processing are also used to eliminate certain artifacts of analysis. Two sinter samples of different chemistry were prepared and characterized using the developed method, and the implication of the results obtained from this quantification method is also assessed. The method presented in this study can be an expedient way to analyze mineral phase and grain size in iron ore sinter samples that can allow for quicker results in sintering process control and optimization.

Materials and Methods

Sample Selection and Preparation

Two set of pot-grate sinter samples were selected as iron ore samples for this study. For each set of sinter samples, ten sinter pieces in the granulometric fraction of 10 to 15 mm were examined. All the samples were cold mounted with epoxy resin and subsequently ground and polished. After an initial examination under a reflective

Table 1 List of samples and their chemical composition

Sinter sample set	Total Fe	FeO	SiO_2	CaO	Al_2O_3	MgO	CaO/SiO_2
2-1	53.06	9.37	5.06	13.80	1.5	3.40	2.73
2-2	53.75	9.67	5.00	12.90	1.3	3.11	2.58

light microscope, the cross-section was covered by an evaporated carbon layer to make it conductive and suitable for SEM analysis (Table 1).

Mineral Phase Analysis Method by Automated SEM

A JEOL-JXA 50 scanning electron microscope (SEM) with a Bruker Quantax 200 Energy Dispersive X-ray Spectroscopy (EDS) system was used to acquire a backscattered electron image of each sample. The SEM is also equipped with a multiple sample holder, which makes it easy to analyze multiple samples in one session. The SEM investigation was carried out with 20 keV energy. The chemical analyses could, therefore, be used to determine the different types of mineral phases by comparing these compositions to those reported in the literature [4].

Stereology and point count method were used to correlate the two-dimensional (2D) SEM elemental analysis data with three-dimensional mineral phase volume fraction. The classical rules of stereology are a set of relationships that connect the various measures obtained with the different probes with the structural parameters. The most fundamental rule is that the volume fraction (VV) of a phase within the structure is measured by the area fraction (AA) on the image, or VV = AA [2]. Another way to describe the relationship is, <PP> = VV where VV is the volume fraction occupied by the phase being counted and the brackets around <PP> signify the expected value for this normalized count, in this case the point fraction. For example, if 100 points are sampled, and 50 are hematite, 35 are calcium ferrite and 15 are glasses, then the volume fraction is estimated at 50% hematite, 35% calcium ferrite and 15% glasses. A key aspect of point counting is in the sampling; this criterion is realized by using a rectangular grid of points with equivalent space between all adjacent rows and columns of points. The point count method is most efficient when the grid spacing is such that adjacent points rarely fall within the same feature, cell or region in the image (they are then said to be independent samples of the structure). An advantage of this method is that when the hits produced by the point grid are all independent, the number of hits can be used directly to estimate the measurement precision. After the volumetric fractions were obtained from point counting method, the mass fractions of the mineral phases were computed based on their theoretical densities as shown in Table 2.

During the automated SEM analysis, the grid points in each field are analyzed. Point counting method uses program logic for moving to a sample, subdividing sample surface into fields and moving to fields, collecting field images, collecting

Table 2 Mineral phase distinction in automated SEM [4]

Mineral phases	Formula	Density (g/cm^3)	Approx. chemical composition	Automated SEM
Magnetite	$FeO \cdot Fe_2O_3$	5.1–5.2	72% Fe, 28% O	Fe and O signals above threshold value
Magnesioferrite	$MgO \cdot Fe_2O_3$	4.8–5.0	56% Fe, 32% O, 12% Mg	Mg, Fe and O signals
Calciomagnetite	(Ca, Fe)O Fe_2O_3	5.2	68% Fe, 28% O, 4% Ca	Fe and O signals with low Ca signatures
Wustite	FeO	5.9	78% Fe, 22% O	Fe and O signals close to threshold value
Hematite	Fe_2O_3	5.2–5.3	70% Fe, 30% O	Fe and O signals below threshold value
Calcium ferrite	$CaO \cdot 2Fe_2O_3$	4.4–4.5	61% Fe, 30% O, 9% Ca	Fe and O signals with high Ca signatures
Calcium silico-ferrite	$3CaO \cdot SiO_2 \cdot 5Fe_2O_3$	4.0–4.3	56% Fe, 32% O, 9% Ca, 3% Si	Ca, Si, Fe and O signals that may contain Al
Calcium silicates	$xCaO \cdot ySiO_2$	2.8–3.3	34% Ca, 24% Si, 42% O	Ca, Si and O signals (may be different according to CaO/SiO_2 ratio)
Glass	SiO_2	2.7	47% Si, 53% O	Si and O signals

and processing EDS spectra, storing particle data, processing stopping criteria, etc. At each point, an EDS x-ray spectrum is first collected, then its elemental composition is quantified, and backscatter intensity is measured with long-term averaging and finally, its mineral species is determined via classification rules. The points can be excluded via thresholding (e.g., exclude sample mounting material). Pseudo-geometry is stored for each point to facilitate post-analysis computation of phase fractions, assay, deportment, etc.

Results and Discussion

Modal mineralogical results obtained by SEM-based image analysis for the two set of sinter samples are shown in Fig. 1 and Tables 3 and 4. The most common elements in iron ore sinter were analyzed including O, Mg, Al, Si, K, Ca, Mn and Fe.

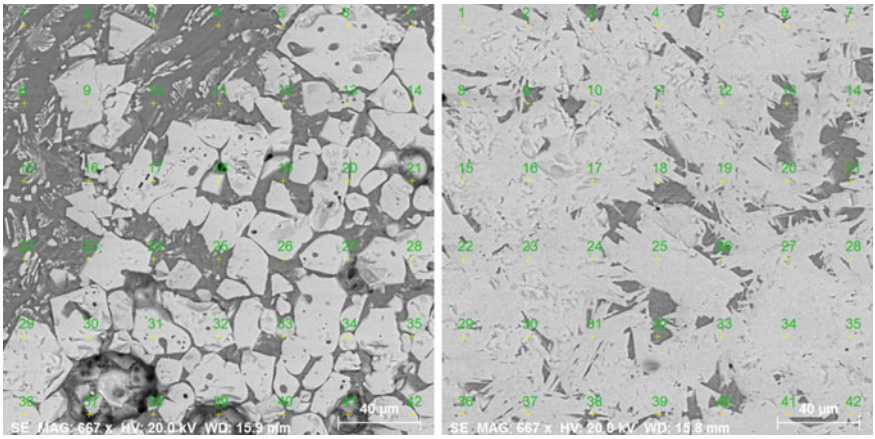

Fig. 1 SEM micrographs of two iron ore sinter samples with point spectrum analyses

Elemental results obtained from each grid point were recalculated to determine the compositions of the different phases present in the sinter samples. The results were clustered according to the elemental analyses and the results recalculated to fit the phases present (i.e., hematite, magnetite, calcium ferrites, calcium silicates, calcium silico-ferrite, calcium silicates and glasses et al.). The main phase composition and grain size of sinter samples are given in Table 5.

Most iron minerals in both sets of sinter samples are hematite/magnetite (47.10% and 48.40%, respectively), followed by calcium ferrite/SFCA (30.80% and 26.22%, respectively), calcium silico-ferrite (14.7% and 16.50%, respectively) and wustite (5.86% and 7.77%, respectively). Minor iron minerals are carried by magnesioferrite (0.05% and 0.01%, respectively), while other iron-bearing minerals are less than 1%.

The mineral phase analysis results based on the automated SEM method agreed well with chemical analysis results on the two sets of sinter samples. The higher mass fraction of hematite/magnetite and wustite in sample 2-2 is consistent with the higher iron content in chemical analysis results of sample 2-2. The higher basicity of sample 2-1 was also confirmed by more calcium ferrite/SFCA mineral phases in sample 2-1 comparting to that of sample 2-2. The differentiation between magnetite and hematite is primarily based on the surface characteristics of iron oxides being measured (gray scale values, porosity and texture) and the degree of ionic substitution being encountered in the iron oxides (Mg, Ca, Al and Mn). However, detailed calcium ferrites and SFCA classification were not easy because classifications of the two phases were based primarily on morphological schemes rather than chemical schemes in addition to inconsistent definitions reported on SFCAs and calcium ferrites [5, 6]. Particularly, the definition of SFCA and SFCA-I phases on the basis of chemical analysis was only partially successful, with uncertainty due to limited resolution of data for individual point analyses and problems in direct correlation with

Table 3 Semi-quantitative elemental analysis results on sample 2-1 (all values are given in wt%, normalized)

Spectrum	O	Na	Mg	Al	Si	P	K	Ca	Fe	Possible phases
1	37.48	0.49	1.25	1.13	17.63	0.16	1.18	34.82	5.86	Calcium silicates
2	36.91	0.98	0.67	2.28	19.01	0.34	3.25	26.52	10.04	SFCA
3	32.90	0.03	1.10	0.16	12.62	0.03	0.12	33.89	19.16	Calcium silico-ferrite
4	38.45	0.80	1.73	1.77	17.80	0.23	1.66	28.04	9.50	SFCA
5	36.78	0.55	0.59	0.67	9.00	0.13	0.52	18.89	32.87	Calcium ferrite
6	28.95	0.01	0.01	0.00	0.01	0.00	0.00	0.19	70.83	Hematite
7	32.43	0.22	0.37	0.24	9.97	0.02	0.20	24.66	31.89	Calcium ferrite
8	31.85	0.16	0.58	0.60	18.34	0.11	0.67	44.03	3.66	Calcium silicates
9	27.78	0.43	4.72	0.26	0.58	0.00	0.00	2.14	64.09	Magnesioferrite
10	34.18	0.09	0.34	0.26	17.15	0.03	0.41	45.89	1.63	Calcium silicates
17	36.35	0.38	0.59	1.17	4.95	0.04	0.23	11.32	44.96	Calcium silico-ferrite

Table 4 Semi-quantitative elemental analysis results on sample 2-2 (all values are given in wt%, normalized)

Spectrum	O	Na	Mg	Al	Si	P	K	Ca	Fe	Minerals
1	37.48	0.49	1.25	1.13	17.63	0.16	1.18	34.82	5.86	SFCA
2	36.91	0.98	0.67	2.28	19.01	0.34	3.25	26.52	10.04	SFCA
3	32.90	0.03	1.10	0.16	12.62	0.03	0.12	33.89	19.16	Calcium ferrite
5	36.78	0.55	0.59	0.67	9.00	0.13	0.52	18.89	32.87	Calcium silico-ferrite
6	28.95	0.01	0.01	0.00	0.01	0.00	0.00	0.19	70.83	Hematite
7	32.43	0.22	0.37	0.24	9.97	0.02	0.20	24.66	31.89	Calcium ferrite
9	27.78	0.43	4.72	0.26	0.58	0.00	0.00	2.14	64.09	Magnesioferrite
11	33.99	0.13	0.28	0.23	15.30	0.27	0.21	47.12	2.48	Calcium silicates
12	36.29	0.88	0.62	0.57	4.35	0.10	0.22	7.18	49.80	Calcium silico-ferrite
16	31.37	0.30	1.26	0.11	10.31	0.15	0.13	34.64	21.73	Calcium ferrite
18	27.65	0.17	0.00	0.08	0.05	0.00	0.01	0.23	71.81	Magnetite

Table 5 Modal mineral analysis results by automated SEM

Sample set		2-1	2-2
Size fraction		−300/+3 μm	−300/+3 μm
Calculated ESD particle size		28	28
Mineral mass (%)	Wustite	5.86	7.77
	Hematite/magnetite	42.00/5.10	42.20/6.20
	Calcium ferrite/SFCA	30.80	26.22
	Calcium silico-ferrite	14.70	16.50
	Calcium silicates	1.09	0.76
	Magnesioferrite	0.05	0.01
	Glasses/silicates	0.27	0.24
	Other	0.17	0.13
	Total	100.00	100.00
Mean grain size by frequency (μm)	Wustite	7	7
	Hematite/magnetite	10	9
	Calcium ferrite/SFCA	10	9
	Calcium silico-ferrite	9	10
	Calcium silicates	8	7
	Magnesioferrite	8	9
	Glasses/Silicates	9	9
	Other	5	5

the known relationship between SFCA (low Fe, high Si) and SFCA-I (high Fe) composition. Further work is recommended to resolve the resolution issues in terms of SFCA/SFCA-I phases, amorphous/glass concentration and overall magnetite/SFCA concentration. This work should include EPMA mapping of SFCA textures to better quantify their chemical compositions.

Conclusions

Two different sets of iron ore sinter samples were analyzed using automated SEM method.

The present study reveals that automated SEM-based image analysis can be used effectively to characterize major mineral phases in iron ore sinter. The results of SEM-based image analysis also provides access to tangible data on mineral grain size distribution, mineral association information that cannot be obtained by other analytical tools currently available.

Acknowledgements The authors would like to thank ArcelorMittal Global R&D management for their permission to publish this work.

References

1. Honeyands T et al (2019) Comparison of the mineralogy of iron ore sinters using a range of techniques. Minerals 9:333
2. Russ JC, Dehoff RT (1999) Practical stereology, 2nd edn. Plenum Press, New York. ISBN 0-306-46476-4
3. Sandmann D (2015) Method development in automated mineralogy. Dissertation, TU Bergakademie Freiberg, Institut für Mineralogie, pp 1–152
4. Tonžetić IŽ (2015) Quantitative analysis of iron ore using SEM-based technologies. Mineral Process Environ Sustain 161–189
5. Tonzetic I, Dippenaar A (2011) An alternative to traditional iron-ore sinter phase classification. Miner Eng 24(12):1258–1263
6. Nicol S et al (2018) A review of the chemistry, structure and formation conditions of silico-ferrite of calcium and aluminum ('SFCA') phases. ISIJ Int 58(12):2157–2172

Effects of Sintering Temperature and Time on Preparation of Refractory Materials from Ferronickel Slag Under Microwave Irradiation

Huimin Tang, Zhiwei Peng, Foquan Gu, Lei Yang, Ziming Liu, Quanle Leng, Weiguang Tian, Mingjun Rao, Guanghui Li and Tao Jiang

Abstract Ferronickel slag can be used for refractory material production by sintering it with the addition of sintered magnesia in the microwave field. In this study, the influence of microwave sintering temperature and time on the refractoriness and mechanical properties of refractory material was assessed based on determination of the phase transformations and microstructural evolutions of the materials obtained at different sintering temperatures and time. It was shown that a high-quality refractory material with refractoriness of 1730 °C was obtained when the sample was sintered at 1350 °C for 20 min. The findings can be used for developing an efficient approach for utilization of ferronickel slag and other related industrial wastes.

Keywords Microwave sintering · Ferronickel slag · Refractory material · Sintering time · Sintering temperature

Introduction

Ferronickel slag is a main waste in the production of ferronickel alloy. Currently, about 12–14 tons of ferronickel slag are obtained by smelting 1 ton of ferronickel alloy [1]. Recently, the discharge and accumulation of ferronickel slag have increased significantly due to the rapid development of ferronickel alloy production. Although the annual output of ferronickel slag has exceeded 30 million tons [2], the utilization percentage of the slag is only 8–15% [3]. The majority of ferronickel slag is still stocked in landfill, which not only occupies a lot of farmland, but also seriously pollutes soil and groundwater [4]. In order to address the problem, the authors'

H. Tang · Z. Peng (✉) · F. Gu · L. Yang · Z. Liu · Q. Leng · M. Rao · G. Li · T. Jiang
School of Minerals Processing and Bioengineering, Central South University, Changsha, Hunan 410083, China
e-mail: zwpeng@csu.edu.cn

National Engineering Laboratory for High Efficiency Recovery of Refractory Nonferrous Metals, Changsha, Hunan 410083, China

W. Tian
Guangdong Guangqing Metal Technology Co. Ltd, Yangjiang, Guangdong 529500, China

J. Li et al. (eds.), *Characterization of Minerals, Metals, and Materials 2020*,
The Minerals, Metals & Materials Series,
https://doi.org/10.1007/978-3-030-36628-5_2

team proposed a method converting ferronickel slag into refractory material using microwave energy as heating source [5]. Compared with conventional sintering, a refractory material with higher refractoriness and better mechanical properties was obtained by microwave sintering of ferronickel slag with the addition of sintered magnesia due to the unique characteristics of microwave sintering, including volumetric and selective heating as well as microwave non-thermal effect [5, 6]. In addition, the refractory material prepared by microwave sintering had better densification and low production cost [7] due to the shorter sintering (holding/dwell) time (3–5 h vs. 20 min) and lower sintering temperature (1500–1650 °C vs. 1350 °C) [8]. It is well known that the sintering temperature and time may have strong effects on the physical and mechanical properties of the resulting materials [9]. These factors must be optimized to obtain better-quality refractory material, realizing the value-added utilization of ferronickel slag.

The aim of this study was to determine the influence of sintering temperature and time on the phase transformation, microstructural evolution, and properties of the refractory material, including bulk density, compressive strength, apparent porosity, and refractoriness. The results demonstrated that appropriate sintering temperature and time are of significance for promoting densification and refractoriness of the refractory material.

Experimental

Materials

The ferronickel slag used in this study was a solid waste produced by smelting of laterite ore. Its main chemical components were SiO_2 (49 wt %), MgO (31 wt %), and FeO (7.4 wt %). According to the previous study [5], its main phase component was olivine ($Mg_{1.8}Fe_{0.2}SiO_4$). Sintered magnesia was used as an additive in sintering to promote the formation of spinel and forsterite for achieving high refractoriness of the resulting material [5]. It had 95 wt % MgO with the main phase of periclase.

Method

The ferronickel slag and sintered magnesia were, respectively, ground to obtain appropriate particle size (< 74 μm). The slag was then fully mixed and milled with a specified mass ratio of sintered magnesia (25 wt %). Subsequently, the mixture in the presence of 5 wt % magnesium chloride solution (1.3 g/m^3) was pressed into cylindrical briquettes at 200 MPa using a briquetting machine. The briquettes were then loaded and sintered in a vertical microwave furnace (Power: 2.5 kW, frequency: 2.45 GHz, Hunan Huae Microwave Technology Co., Ltd., Changsha, China) at different temperatures or for different periods of time. After cooling, the briquettes were collected for characterization of properties.

Characterizations

The thermal stability of ferronickel slag was determined using a thermal gravimetric analyzer (TG-DSC, TZSCH STA449C) by measuring the thermogravimetry and differential scanning calorimetry (TG-DSC) curves of the slag in air. The phase compositions of the resulting materials were determined using an X-ray diffraction spectrometer (XRD, BRUKER X'Pert PRO MPD). The microstructural changes of the materials were determined by using a scanning electron microscope (SEM; SIGMA Nova450) equipped with an energy-dispersive (EDS) detector. The values of bulk density/apparent porosity, compressive strength and refractoriness of the materials were measured according to the Chinese National Standard Test Methods GBT 2997-2000, GBT 5072-2008, and GBT 7322-2007, respectively.

Results and Discussion

TG-DSC Analysis

The thermal stability of ferronickel slag in the range 200–1400 °C was determined by the TG-DSC analysis, and the results are shown in Fig. 1. The TG curve presented a weight loss in 200–500 °C and a successive weight gain in the range 500–1400 °C, while the DSC curve showed two endothermic peaks. The first peak endothermic appeared at about 760 °C due to the decomposition of olivine ($Mg_{1.8}Fe_{0.2}SiO_4$) in the

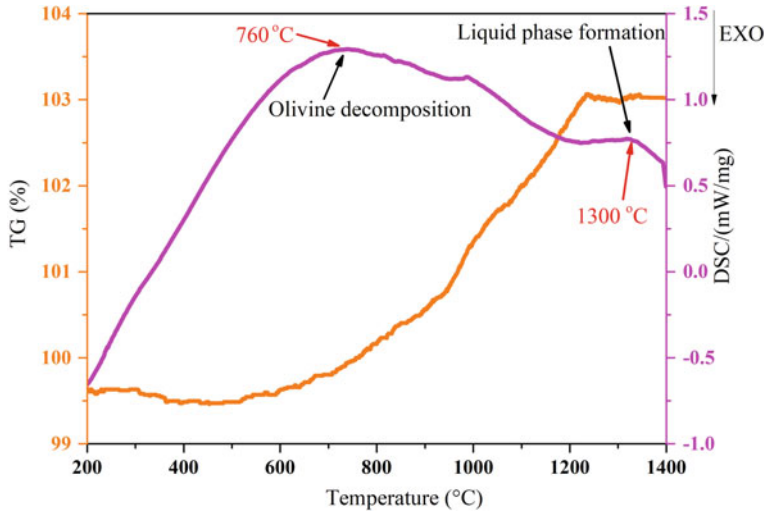

Fig. 1 TG-DSC curves of ferronickel slag in air

ferronickel slag into forsterite, FeO, and amorphous silica as well as to the oxidation of FeO to Fe_2O_3, which resulted in the weight gain in TG curve [5]. The second endothermic peak located at about 1300 °C, which was attributed to the formation of liquid phase derived from the low melting phase of the refractory material (calcium or aluminium or magnesium silicate) at high temperatures [10, 11].

X-Ray Diffraction Analysis

Figure 2 shows the XRD patterns of refractory materials obtained by microwave sintering of ferronickel slag with addition of 25 wt % sintered magnesia at 900–1400 °C for 20 min. When the sintering temperature reached 900 °C, the main phases were olivine, forsterite, and periclase. Increasing temperature did not change other phases except the presence of enstatite due to the reaction between part of silica and forsterite around 1000 °C [5]. As the temperature increased continuously to 1200 °C, donathite ($MgFe_{0.2}Cr_{1.8}O_4$) appeared due to the reaction between MgO, Cr_2O_3, and Fe_2O_3 in the refractory material under microwave irradiation, as also revealed by the weakening of diffraction peaks of periclase [12, 13]. When the temperature continued to rise, the diffraction peaks of forsterite became stronger while those of enstatite and periclase weakened. It indicated that elevating temperature in this stage was

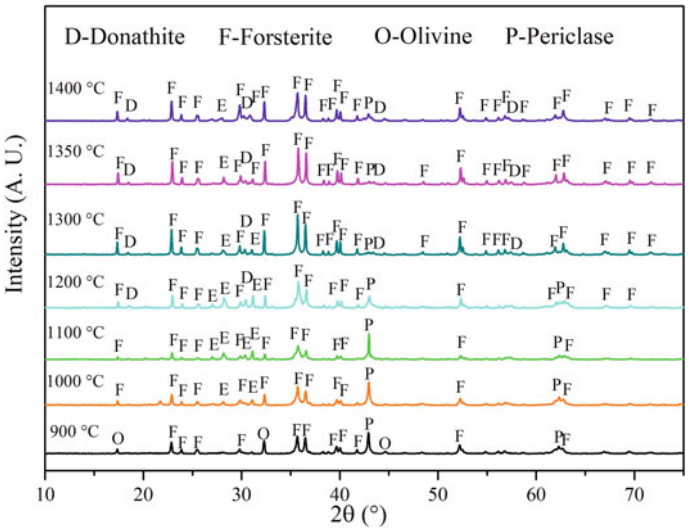

Fig. 2 XRD patterns of refractory materials obtained by microwave sintering of ferronickel slag with addition of 25 wt % sintered magnesia at 900-1400 °C for 20 min

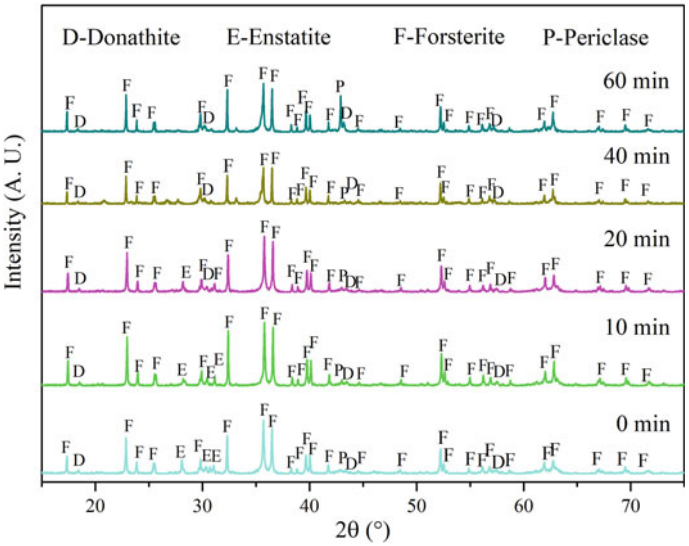

Fig. 3 XRD patterns of refractory materials obtained by microwave sintering of ferronickel slag with addition of 25 wt % sintered magnesia at 1350 °C for 0–60 min

conducive to the formation of forsterite by facilitating the reaction between enstatite and periclase [14]. When the temperature reached 1400 °C, the diffraction peaks of forsterite became weaker due to the grain growth caused by excessive temperature. Therefore, 1300–1350 °C was believed to be suitable for converting ferronickel slag to good-quality refractory material.

Figure 3 shows the XRD patterns of refractory materials obtained by microwave sintering for 0–60 min at 1350 °C. Initially (0 min), the main phases were forsterite, enstatite, and donathite. As the sintering time was prolonged, the main phase remained unchanged. However, the diffraction peaks of forsterite and donathite became intensified with simultaneous reduction of peak intensity of enstatite. It indicated that increasing sintering time was beneficial to further transformation of enstatite to forsterite as well as the formation of donathite due to the complete reaction between the raw materials. When the sintering time exceeded 20 min, the diffraction peaks of forsterite and donathite weakened. It was probably in association with abnormal growth of grain [15–17].

Properties of the Refractory Materials

Figure 4 shows the effect of sintering temperature on the physical and mechanical properties of the refractory material when the time was 20 min. It was found that the properties changed in three different stages. Firstly, the bulk density of the material

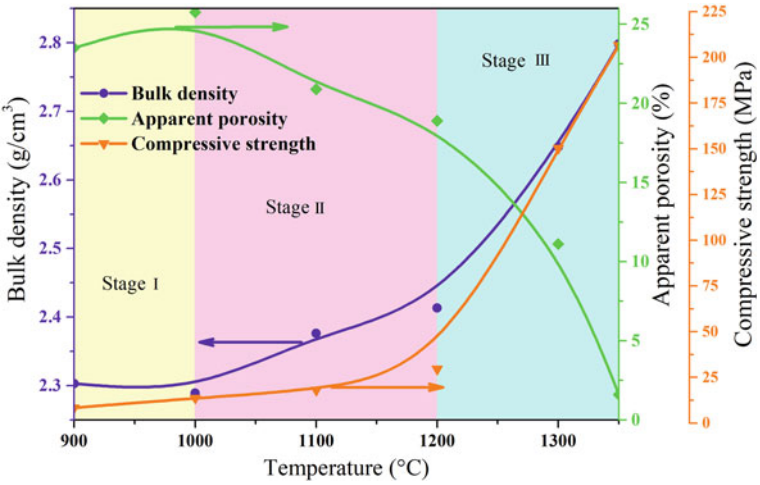

Fig. 4 Effect of temperature on the bulk density, apparent porosity, and compressive strength of the refractory material obtained by microwave sintering of ferronickel slag with addition of 25 wt % sintered magnesia

decreased from 2.30 g/cm^3 to 2.28 g/cm^3 in stage I due to the reaction between part of SiO_2 and forsterite which formed enstatite in the refractory material, inhibiting the densification of the refractory material [18]. As the temperature increased from 1000 °C to 1350 °C, the bulk density increased continuously. This was because increasing temperature was conducive to the further formation and development of forsterite, enhancing the densification and thereby increasing the bulk density of the refractory material. However, the increasing rates of bulk density of the refractory material in stages II and III were distinct. In stage II, the bulk density increased slowly. However, when the temperature exceeded 1200 °C (stage III), the bulk density increased considerably. This was because at temperatures above 1200 °C forsterite began to form and develop remarkably. Additionally, the change of compressive strength was consistent with that of bulk density, which was contrary to that of apparent porosity. When the temperature exceeded 1350 °C (not shown in the figure), the sample would melt, making measurement of the mechanical properties impossible. For this reason, too high temperature was not suitable for preparing the refractory material.

Figure 5 shows the influence of sintering time on the physical and mechanical properties of the refractory material when the sintering temperature was 1350 °C. The change of bulk density could also be divided into three stages. When the microwave sintering time increased from 0 min to 20 min (stage 1), the bulk density of the material increased from 2.44 g/cm^3 to 2.80 g/cm^3. It was because increasing sintering time facilitated the reaction between MgO in sintered magnesia and ferronickel slag to form forsterite, promoting the densification of the refractory material. When the time was prolonged to 40 min (stage 2), the bulk density of the refractory material

decreased. It was believed to be in association with two factors. Firstly, too long sintering time led to excessive increase of grain size, which was adverse to the mechanical performance of the refractory material. Secondly, excessive spinel was formed, leading to the volume expansion and thus poor densification of the material.

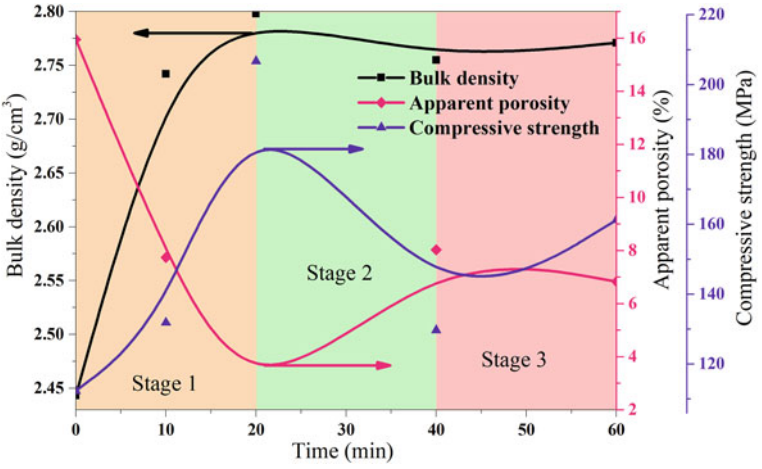

Fig. 5 Effect of time on the bulk density, apparent porosity, and compressive strength of the refractory material obtained by microwave sintering of ferronickel slag with addition of 25 wt % sintered magnesia

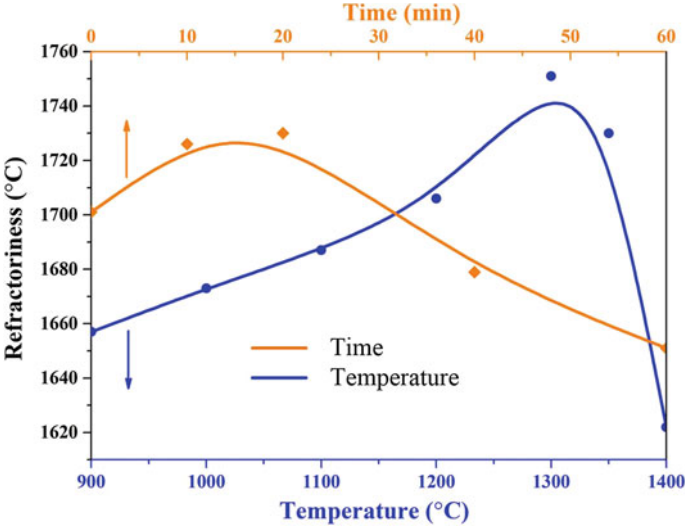

Fig. 6 Effects of temperature and time on the refractoriness of the refractory material obtained by microwave sintering of ferronickel slag with addition of 25 wt % sintered magnesia

As the sintering time extended further (stage 3), the bulk density increased due to increase of forsterite, which agreed with the XRD patterns in Fig. 3.

Figure 6 shows the effects of sintering temperature and time on the refractoriness of the refractory materials by fixing the time of 20 min and temperature of 1350 °C, respectively. It was found that as the temperature increased from 900 °C to 1400 °C, the refractoriness first increased and then declined. It had a maximum value of 1751 °C at sintering temperature of 1300 °C, which was due to the formation and development of high melting point forsterite and donathite, as well as to the reduction of low melting point enstatite. When the temperature increased further, the grain size of the material grew excessively, which was harmful to refractoriness [15–17]. For this reason, the refractoriness decreased slightly to 1730 °C when the sintering temperature was 1350 °C. As the sintering time increased from 0 min to 60 min, the refractoriness initially increased and then decreased and reached the highest value at 20 min. This was because prolonging sintering time properly promoted the reactions in refractory materials (such as the formation and development of forsterite and donathite), which improved the refractoriness of the refractory material. It should be pointed out that excessive exposure of the sample to microwave would lead to abnormal growth of grains, deteriorating the refractoriness of the material [15–17].

Conclusion

In this study, the effects of sintering temperature and time on the preparation of refractory materials from ferronickel slag were explored by microwave sintering of ferronickel slag in the presence of sintered magnesia. It demonstrated that appropriate sintering temperature and time were not only conducive to the transformation of low melting point enstatite into forsterite with high melting point, but also beneficial to the formation and development of high melting point donathite, contributing to excellent physical and mechanical properties of refractory materials. However, excessive sintering temperature and too long sintering time could lead to abnormal grain growth, deteriorating the performance of refractory material. When the slag was sintered at 1350 °C for 20 min, the refractory material with bulk density of 2.80 g/cm^3, apparent porosity of 1.6%, compressive strength of 206.6 MPa and refractoriness of 1730 °C was obtained.

Acknowledgements This work was partially supported by the National Natural Science Foundation of China under Grants 51774337, 51504297, and 51811530108, the Science and Technology Planning Project of Hunan Province, China, under Grant 2019RS2008, the Key Laboratory for Solid Waste Management and Environment Safety (Tsinghua University) Open Fund under Grant SWMES2017-04, the Project of State Key Laboratory Cultivation Base for Nonmetal Composites and Functional Materials under Grant 17kffk11, and the Fundamental Research Funds for the Central Universities of Central South University under Grants 2018zzts779 and 2018zzts220.

References

1. Kim H, Lee CH, Ann KY (2019) Feasibility of ferronickel slag powder for cementitious binder in concrete mix. Constr Build Mater 207:693–705
2. Huang Y, Wang Q, Shi M (2017) Characteristics and reactivity of ferronickel slag powder. Constr Build Mater 156:773–789
3. Gu F, Zhang Y, Peng Z, Su Z, Tang H, Tian W, Liang G, Lee J, Rao M, Li G, Tao Jiang T (2019) Selective recovery of chromium from ferronickel slag via alkaline roasting followed by water leaching. J Hazard Mater 374:83–91
4. Wang D, Wang Q, Zhuang S, Yang J (2018) Evaluation of alkali-activated blast furnace ferronickel slag as a cementitious material: reaction mechanism, engineering properties and leaching behaviors. Constr Build Mater 188:860–873
5. Peng Z, Tang H, Augustine R, Lee J, Tian W, Chen Y, Gu F, Zhang Y, Li G, Jiang T (2019) From ferronickel slag to value-added refractory materials: a microwave sintering strategy. Resour Conserv Recy 149:521–531
6. Peng Z, Hwang JY (2015) Microwave-assisted metallurgy. Int Mater Rev 60(1):30–63
7. Zuo F, Saunier S, Marinel S, Chanin-Lambert P, Peillon N, Goeurio D (2015) Investigation of the mechanism(s) controlling microwave sintering of α-alumina: influence of the powder parameters on the grain growth, thermodynamics and densification kinetics. J Eur Ceram Soc 35:959–970
8. Ganesha I, Bhattacharjee S, Saha BP, Johnson R, Rajeshwari K, Sengupta R, Ramana Rao MV, Mahajan YR (2002) An efficient $MgAl_2O_4$ spinel additive for improved slag erosion and penetration resistance of high-Al_2O_3 and MgO-C refractories. Ceram Int 28:245–253
9. Oghbaei M, Mirzaee O (2010) Microwave versus conventional sintering: a review of fundamentals, advantages and applications. J Alloy Compd 494:175–189
10. Zhao F, Ge T, Gao J, Chen L, Liu X (2018) Transient liquid phase diffusion process for porous mullite ceramics with excellent mechanical properties. Ceram Int 44:19123–19130
11. Douy A (2002) Aqueous synthesis of forsterite (Mg_2SiO_4) and enstatite ($MgSiO_3$). J Sol-Gel Sci Techn 24:221–228
12. Sabri K, Rais A, Taibi K, Moreau M, Ouddane B, Addou A (2016) Structural Rietveld refinement and vibrational study of $MgCr_xFe_{2-x}O_4$ spinel ferrites. Physica B 501:38–44
13. Zakaria AKM, Nesa F, Saeed KMA, Datta TK, Aktar S, Liba SI, Hossain S, Das AK, Kamal I, Yunus SM, Eriksson SG (2015) Cation distribution and crystallographic characterization of the spinel oxides $MgCr_xFe_{2-x}O_4$ by neutron diffraction. J Alloy Compd 633:115–119
14. Wilding MC, Benmore CJ, Tangeman JA, Sampath S (2004) Evidence of different structures in magnesium silicate liquids: coordination changes in forsterite to enstatite composition glasses. Chem Geol 213:281–291
15. Upadhyaya A, Tiwari SK, Mishra P (2007) Microwave sintering of W-Ni-Fe alloy. Scripta Mater 56(1):5–8
16. Panda SS, Singh V, Upadhyaya A, Agrawal D (2006) Sintering response of austenitic (316 L) and ferritic (434 L) stainless steel consolidated in conventional and microwave furnaces. Scripta Mater 54:2179–2183
17. Madhan M, Prabhakaran G (2019) Microwave versus conventional sintering:microstructure and mechanical properties ofAl_2O_3-SiC ceramic composites. Bol Soc Esp Ceram Vidrio 58:14–22
18. Zhao F, Zhang L, Ren Z, Gao J, Chen X, Liu X, Ge T (2019) A novel and green preparation of porous forsterite ceramics with excellent thermal isolation properties. Ceram Int 45:2953–2961

Non-isothermal Carbothermic Reduction Kinetics of Calcium Ferrite

Gang Li, Xuewei Lv, Xuangeng Zhou, Guishang Pei and Guibao Qiu

Abstract Calcium ferrite is recognized as the ideal bonding phase with superior strength and reducibility in the iron ore sintering process. In present study, the reduction behavior of $CaO \cdot Fe_2O_3$ with graphite was studied by a non-isothermal method using thermo-gravimetric analysis coupled with mass spectrometry. The Flynn-Wall-Ozawa method and the Škvára-Šesták method were adopted to analyze the 'kinetics triplet' (activation energy, pre-exponential factor, and model function). Results indicated that the reduction process did not start until 1090 K, and the reactions shifted toward a higher temperature with an increase of heating rate. The maximum reduction degree of $CaO \cdot Fe_2O_3$ could reach 0.93 at 1473 K. X-ray diffraction measurements indicated that $CaO \cdot Fe_2O_3$ was reduced to CaO and Fe with four steps (CF $\rightarrow$ CWF $\rightarrow$ $CW_3F \rightarrow C_2F \rightarrow$ Fe). The apparent activation energy of $CaO \cdot Fe_2O_3$ varied from 543.33 to 753.10 kJ/mol. The reduction in $CaO \cdot Fe_2O_3$ can be described by 2-D diffusion model with an integral form of $G(\alpha) = [1 - (1 - \alpha)^{1/2}]^2$.

Keywords Calcium ferrite · Carbothermic reduction · Non-isothermal kinetics · Activation energy · Model function

Introduction

Fluxed sinter is the main iron-containing material that charged into the blast furnace. Iron oxide and silico-ferrite of calcium and aluminum (SFCA), the dominant iron-containing phase and ideal bonding phase, considerably contribute to the reduction process of fluxed sinter. The reduction behavior of calcium ferrite (CF) with CO or H_2 has been widely studied in the previous literature. Taguchi [1] clarified the reduction process of $2CaO \cdot Fe_2O_3$ (C_2F), $CaO \cdot Fe_2O_3$ (CF), and $CaO \cdot 2Fe_2O_3$ (CF_2)

G. Li · X. Lv (✉) · X. Zhou · G. Pei · G. Qiu
College of Materials Science and Engineering, Chongqing University, Chongqing 400044, China
e-mail: lvxuewei@163.com

Chongqing Key Laboratory of Vanadium-Titanium Metallurgy and New Materials, Chongqing University, Chongqing 40044, China

J. Li et al. (eds.), *Characterization of Minerals, Metals, and Materials 2020*,
The Minerals, Metals & Materials Series,
https://doi.org/10.1007/978-3-030-36628-5_3

in $CO–CO_2$ mixed gas under isothermal conditions. Sato [2] analyzed the reduction behavior of four synthesized calcium ferrites, $3CaO \cdot FeO \cdot 7Fe_2O_3$ (C_3WF_7), $4CaO \cdot FeO \cdot 4Fe_2O_3$ (C_4WF_4), $CaO \cdot FeO \cdot Fe_2O_3$ (CWF), and $CaO \cdot 3FeO \cdot Fe_2O_3$ (CW_3F), with various $CO–CO_2$ gas mixtures. Recently, Ding and Lv [3, 4] investigated the isothermal reduction kinetics of powdered C_2F, CF, and CF_2 in 30% CO and 70% N_2 gas mixture, the reduction degree, phase transformation, and apparent activation energy were studied; a new kinetics model based on powder samples was also introduced for the reduction process. Similar kinetics investigations under H_2 atmosphere were also performed by Ding and Lv [5].

Obviously, these reduction investigations mainly focused on isothermal conditions for calcium ferrites samples, whereas rarely on non-isothermal conditions which are more in accordance with the actual temperature characteristics in a blast furnace. In addition, previous studies mainly paid attention to the reduction process of CF in a gaseous environment, and the coal-based reduction of CF remains poorly understood. Hence, the non-isothermal carbothermic reduction kinetics of CF with graphite was investigated in this study.

Experimental

Materials and Sample Preparation

The raw materials of $CaCO_3$ and Fe_2O_3 with molar ratio of 1:1 were pressed into a cylindrical-shaped block after a mixing process. The block was heated to 1173 K for 1 h and then roasted at 1473 K for 12 h allowing the complete formation of CF. The entire process was performed in the air atmosphere. The sample was ground into powder (<74 μm) for further investigations.

The purity of the sample was ensured by X-ray diffraction (XRD) [Model D/max2500/PC (Cu–K_α)] analysis. Scanning was performed at an angular range of 10° to 90° with a scan rate of 4°/min. The XRD patterns of sample CF and the standard CF are shown in Fig. 1. The results show that CF samples are pure enough.

The molar ratio between carbon in the graphite (≥99.9% purity, <74 μm in particle size) and transferable oxygen in CF sample was fixed at 1.2. Powder mixtures of CF and graphite were uniformly mixed.

Thermo-Gravimetric Analyzer and Mass Spectrometer

The reduction tests of CF with graphite were performed in a thermo-gravimetric analyzer (TGA, Setaram Evo TG-DTA 1750). Quadrupole mass spectrometer (TILON LC-D200, AMETEK LLC, USA) was used to detect the off gas engendered from the TG experiments. The mixed sample (30 mg) was heated from room temperature to

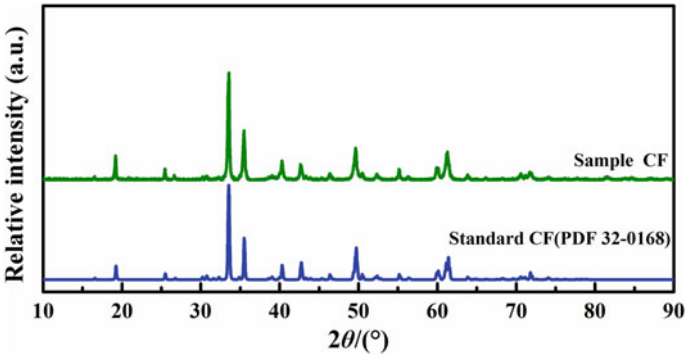

Fig. 1 XRD patterns of sample CF

1473 K with three different heating rates () of 10, 15, and 20 K min^{-1} in an alumina crucible. The mass loss was recorded until the end of the reduction.

Results and Discussion

TG and DTG Analysis

The TG and DTG curves of carbothermic reduction of CF at different heating rates are shown in Figs. 2 and 3. It can be seen that the reduction process did not start until 1090 K, and the weight loss was 27% when the temperature reached 1473 K. Four individual stages were gradually distinguished, and the characteristic temperatures of each reduction stage at different heating rates are shown in Table 1.

Fig. 2 TG curves of CF carbothermic reduction

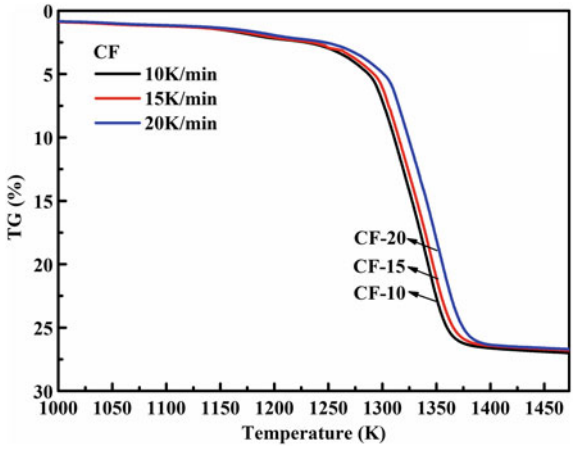

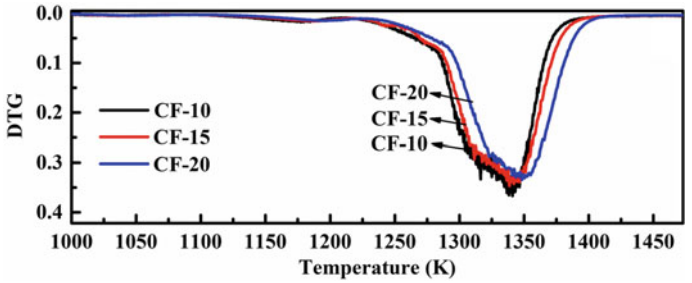

Fig. 3 DTG curves of CF carbothermic reduction

Table 1 Characteristic temperatures (K) of each CF reduction stage at different heating rates

β/(K min^{-1})	I: CF → CWF	II: CWF → CW_3F	III: CW_3F → C_2F	IV: C_2F → Fe
10	1090–1215	1215–1285	1285–1324	1324–1473
15	1091–1220	1220–1293	1293–1328	1328–1473
20	1092–1230	1230–1300	1300–1333	1333–1473

The off gas containing CO and CO_2 was detected by mass spectrometer, and the results are shown in Fig. 4. Before 1090 K corresponding to the initial temperature of stage I, CO_2 was not detected, whereafter, with the reduction process proceeding,

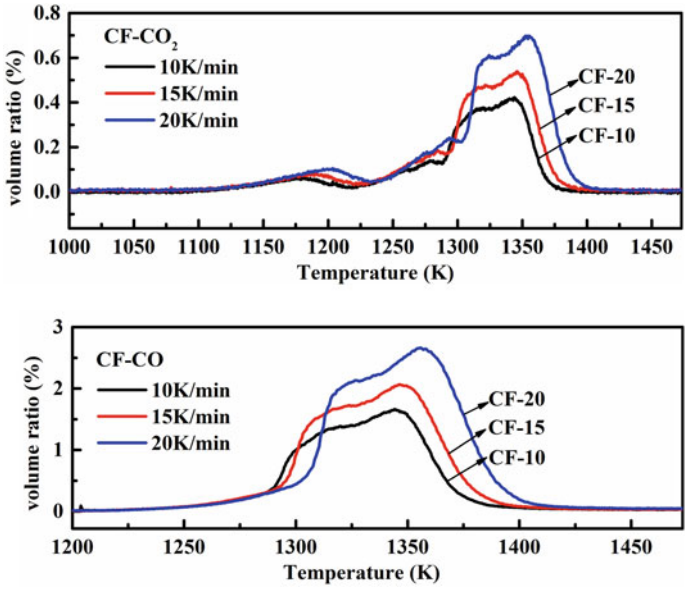

Fig. 4 CO_2 and CO volume ratio in the carbothermic reduction

the volume ratio of CO_2 gradually increased and reached the first extreme value at about 1190 K. Three heavily overlapped peaks can be seen in the second, broad, and high-temperature peak of CO_2, and the last peak had the highest volume ratio. Seeing from the curve profile of CO, the accumulation of CO only occurred at a high temperature. The volume ratio of CO gradually increased at around 1220 K and drastically increased at around 1290 K corresponding to the initial temperature of stage III. The dramatic increase of CO was caused by the accelerated carbon gasification reaction.

Reduction Degree

Reduction degree (α) is defined as the mass ratio of removed oxygen at a fixed time t to the theoretical removable oxygen combined with Fe in CF:

$$\alpha = \frac{\Delta m_{\mathrm{O}}}{\Delta m_{\mathrm{Omax}}} \tag{1}$$

where Δm_{O} is the mass ratio of removed oxygen at a fixed time t, and Δm_{Omax} is the mass ratio of theoretical removable oxygen combined with Fe in CF. The relationship between weight loss of the sample and the off gas is

$$\Delta m = \Delta m_{\mathrm{CO}} + \Delta m_{\mathrm{CO_2}} \tag{2}$$

$$\varphi(\mathrm{CO_2}) = \frac{44\,V_{\mathrm{CO_2}}}{44\,V_{\mathrm{CO_2}} + 28\,V_{\mathrm{CO}}} \times 100 \tag{3}$$

$$\varphi(\mathrm{CO}) = \frac{28\,V_{\mathrm{CO}}}{44\,V_{\mathrm{CO_2}} + 28 V_{\mathrm{CO}}} \times 100 \tag{4}$$

where Δm is the weight loss mass percent of sample, $\varphi(\mathrm{CO_2})$ and $\varphi(\mathrm{CO})$ are the mass percent of CO_2 and CO in the evolved gas, respectively, $\varphi(\mathrm{CO_2}) + \varphi(\mathrm{CO}) = 100\%$, $V_{\mathrm{CO_2}}$ and V_{CO} are the volume percentage of CO_2 and CO in the evolved gas. Thus, the reduction degree is calculated as follows:

$$\alpha = \frac{\Delta m_{\mathrm{O}}}{\Delta m_{\mathrm{Omax}}} = \frac{\frac{32}{44}\Delta m \times \varphi(\mathrm{CO_2})/100 + \frac{16}{28}\Delta m \times \varphi(\mathrm{CO})/100}{\Delta m_{\mathrm{Omax}}} \tag{5}$$

Figure 5 shows the reduction degree of CF at different heating rates. It can be seen that the value of reduction degree decreased with the increasing of the heating rate at a fixed temperature. The maximum reduction degree could reach 0.93 at 1473 K.

Figure 6 shows the reduction rates of CF with different heating rates. The reduction rates increased with the increasing of heating rates at a fixed temperature. According to the peak curves, the reduction in CF contained four stages, where reduction degree

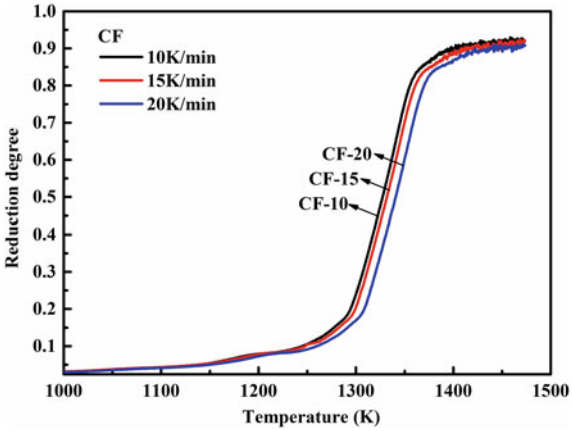

Fig. 5 Reduction degree of CF at different heating rates

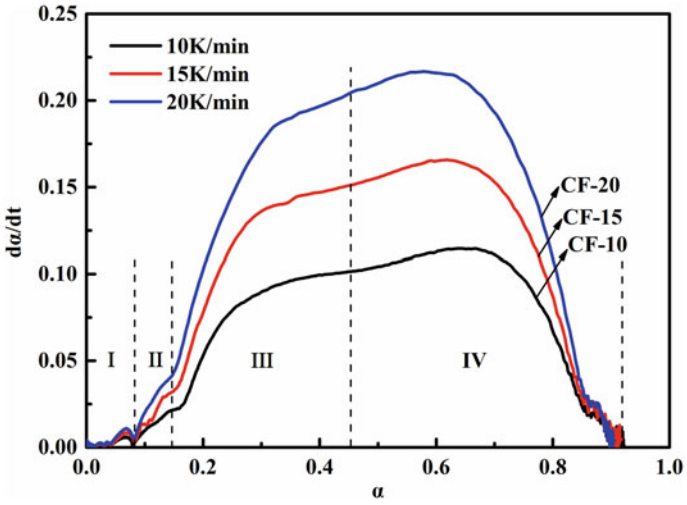

Fig. 6 Reduction rates of samples with different heating rates

lay in 0–0.08 for stage I, 0.08–0.15 for stage II, 0.15–0.45 for stage III, and 0.45–0.92 for stage IV. The phase transformation of CF reduction with a heating rate of 15 K/min was studied by XRD tests, and the results are shown in Fig. 7. The results show that the four progressive reduction stages of CF were CF → CWF → CW_3F → C_2F → Fe.

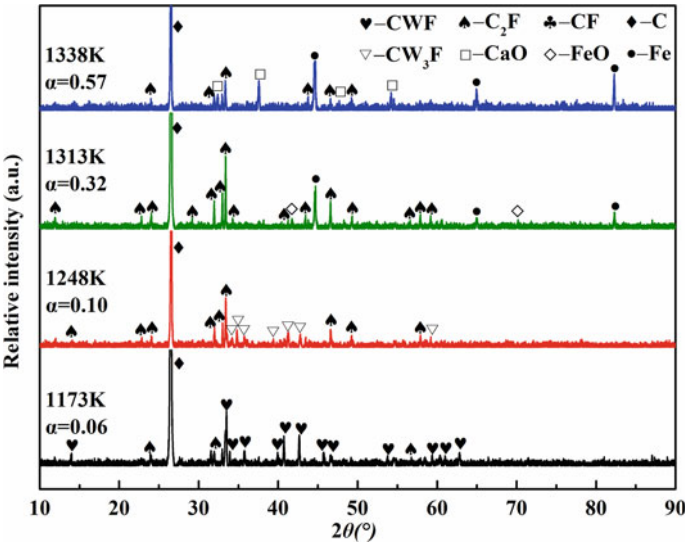

Fig. 7 XRD patterns of the reduced CF at fixed degrees

Apparent Activation Energy

In this study, the FWO method was adopted to calculate the activation energy. The ordinary kinetic equation is shown in Eq. (6):

$$\frac{\mathrm{d}\alpha}{\mathrm{d}t} = k(T)\,f(\alpha) \tag{6}$$

where $k(T)$ and $f(\alpha)$ are the rate constant (min^{-1}) and model function of the reduction reaction, respectively. $k(T)$ can be given by the Arrhenius equation:

$$k(T) = A\exp\left[\frac{-E}{RT}\right] \tag{7}$$

where A is the pre-exponential factor (min^{-1}), E is the apparent activation energy (kJ/mol), and R is the gas constant [8.314 J/(mol K)]. Considering the heating rate ($\mathrm{d}T/\mathrm{d}t$), Eq. (7) can be further expressed as follows:

$$\frac{\mathrm{d}\alpha}{\mathrm{d}T} = \frac{A}{\beta}\exp\left[\frac{-E}{RT}\right] f(\alpha) \tag{8}$$

When the value of reduction degree changes from 0 to α and the temperature changes from 0 to T, Eq. (8) can be transformed into the following formation:

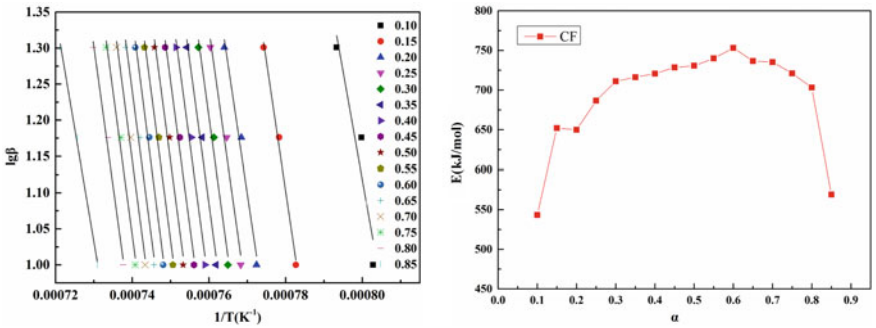

Fig. 8 Regression lines for various reduction degrees based on the FWO method

$$\int_0^{\alpha} \frac{\mathrm{d}\alpha}{f(\alpha)} = G(\alpha) = \frac{A}{\beta}\int_0^{T} \exp\left[\frac{-E}{RT}\right]\mathrm{d}T \tag{9}$$

Thus, combining the approximation expressed by Doyle [6], the FWO method will be obtained by the following function:

$$\lg \beta = \lg\left(\frac{AE}{RG(\alpha)}\right) - 2.315 - 0.4567\frac{E}{RT} \tag{10}$$

Therefore, the activation energy can be obtained from the linear fitting of lg() against $1/T$ based on least squares principle. Figure 8 shows the plots of lg() versus $1/T$ corresponding to the selected reduction degrees and the value of activation energy at different reduction degree. Evidently, there was a good linearity between lg (β) and $1/T$.

The activation energy of CF reduction by different reductants has been calculated in previous investigations (Table 2). Riley studied the reduction kinetics in CF by two different chars and found lower activation energy than this study. The study of

Table 2 Activation energy of CF reduction by other studies

E(kJ/mol)	Samples	Reductant	T/K	References
70–470	CF, 43–53 μm, powder	Illinois #6 char	1123–1223	Riley [7]
50–300		Wyodak char		
20.32–86.68	CF, <74 μm, powder	30% CO + 70% N_2	1123–1223	Ding [3]
27.83–52.57	CF, <74 μm, powder	30% H_2 + 70% N_2	1123–1223	Ding [5]
543.33–753.10	CF, <74 μm, powder	Graphite	10–20 K/min → 1473	Present study

Ding reflected the gas–solid reaction of CO/H_2–CF without the coupling of carbon solution loss reaction, which may be the reason for much lower activation energy than this study.

Model Function

Table 3 shows the most commonly used differential and integral expressions of mechanism functions. In present study, the Škvára-Šesták method [8] was adopted to determine the most probable mechanism function, which is given by

$$\lg G(\alpha) = \lg \frac{AE_S}{R\beta} - 2.315 - 0.4567\frac{E_S}{RT} \tag{11}$$

where E_s is the activation energy estimated by the linear least squares plot of $\lg G(\alpha)$ versus $1/T$. The model function can be determined by the linear relationship between $\lg G(\alpha)$ and $1/T$. If one $G(\alpha)$ gives the greatest linearity relationship of the straight

Table 3 Differential and integral expressions of common reaction mechanism functions [9, 10]

Symbol	Mechanism	$G(\alpha)$	$f(\alpha)$
D_1	1-D diffusion	α^2	$1/2\alpha^{-1}$
D_2	2-D diffusion (Valensi)	$\alpha + (1-\alpha)\ln(1-\alpha)$	$[-\ln(1-\alpha)]^{-1}$
D_3	2-D diffusion (Jander)	$[1-(1-\alpha)^{1/2}]^2$	$(1-\alpha)^{1/2}[1-(1-\alpha)^{1/2}]^{-1}$
D_4	3-D diffusion (G-B)	$1-2/3\alpha\ -(1-\alpha)^{2/3}$	$3/2[(1-\alpha)^{-1/3}\ -1]^{-1}$
D_5	3-D diffusion (Z-L-T)	$[(1-\alpha)^{-1/3}\ -1]^2$	$3/2(1-\alpha)^{4/3}[(1-\alpha)^{-1/3}\ -1]^{-1}$
A_2	Random nucleation and nuclei growth	$[-\ln(1-\alpha)]^{1/2}$	$2(1-\alpha)\ [-\ln(1-\alpha)]^{1/2}$
A_3	Random nucleation and nuclei growth	$[-\ln(1-\alpha)]^{1/3}$	$3(1-\alpha)\ [-\ln(1-\alpha)]^{1/3}$
A_4	Random nucleation and nuclei growth	$[-\ln(1-\alpha)]^{1/4}$	$4(1-\alpha)\ [-\ln(1-\alpha)]^{1/4}$
C_1	Reaction order (n = 2)	$(1-\alpha)^{-1}\ -1$	$(1-\alpha)^2$
C_2	Reaction order (n = 3/2)	$(1-\alpha)^{-1/2}$	$2(1-\alpha)^{3/2}$
C_3	Reaction order (n = 3)	$(1-\alpha)^{-2}$	$1/2(1-\alpha)^3$
R_2	2-D phase boundary reaction	$1-(1-\alpha)^{1/2}$	$2(1-\alpha)^{1/2}$
R_3	3-D phase boundary reaction	$1-(1-\alpha)^{1/3}$	$3(1-\alpha)^{2/3}$

Table 4 Calculated mechanism functions of CF reduction based on the Škvára-Šesták method

Heating rate (K/min)	D_2 model			D_3 model		
	E_s (kJ/mol)	lg$A$	R^2	E_s (kJ/mol)	lg$A$	R^2
10	593.31	22.15	0.974	624.94	23.19	0.973
15	585.09	21.87	0.967	616.46	22.89	0.967
20	600.36	22.48	0.969	632.83	23.54	0.970

line fitting, meanwhile the Es is approximately equal to the activation energy (E) obtained by the FWO method; this $G(\alpha)$ is exactly the model function which can describe the reaction process. Subsequently, the corresponding parameters of A can be calculated by the intercept of the linear fitting.

The mechanism function of CF at different heating rates is shown in Table 4. It can be distinguished that the value of E_s for D_3 model was closer to the value of E calculated by the FWO method compared with the D_2 model. Therefore, D_3 model with an equation of $f(\alpha) = (1-\alpha)^{1/2}[1-(1-\alpha)^{1/2}]^{-1}$ is the most suitable mechanism function to describe CF carbothermic reduction.

Conclusions

The non-isothermal reduction kinetics of CF with graphite heated from room temperature to 1473 K was investigated through TG-MS analysis. The conclusions are summarized as follows:

(1) The reduction process of CF initiated at 1090 K, and the weight loss was 27% when the temperature reached 1473 K.
(2) X-Ray diffraction measurements at various stages revealed that the reduction in CF can be divided into four steps that is CF → CWF → CW_3F → C_2F → Fe.
(3) The activation energy of CF obtained by the FWO method and the Škvára-Šesták method varied from 543.33 to 753.10 kJ/mol and 616.46 to 632.83 kJ/mol, respectively.
(4) Škvára-Šesták methods indicated that CF reduction was described by a 2-D diffusion model, with an integral form of $G(\alpha) = [1-(1-\alpha)^{1/2}]^2$.

Acknowledgements The authors are grateful to the financial support of the National Key Research and Development Program of the Ministry of Science and Technology (2018YFC1900501) and National Natural Science Foundation of China (Grant No. 51674055).

References

1. Taguchi N, Otomo T, Tasaka K (1983) Reduction process of CaO–Fe_2O_3 binary calcium ferrite and resultant expansion. Tetsu-to-Hagané 69(11):1409–1416
2. Sato S, Kikuchi T, Yoshii C (1971) Reduction tests of synthetic calcium ferrites: in ternary systems of CaO-FeO-Fe2O3. Bull Fac Eng Hokkaido Univ 61:39–43
3. Ding C, Lv X, Xuan S (2016) Isothermal reduction kinetics of powdered hematite and calcium ferrite with CO–N_2 gas mixtures. ISIJ Int ISIJINT-2016-238
4. Ding C, Lv X, Li G (2017) Reduction of CaO–Fe_2O_3 series compounds by CO. ISIJ Int 57(7):1181–1190
5. Ding C, Lv X, Li G (2018) Isothermal reduction of powdery 2CaO· Fe_2O_3 and CaO· Fe_2O_3 under H_2 atmosphere. Int J Hydrogen Energy 43(1):24–36
6. Doyle CD (1961) Kinetic analysis of thermogravimetric data. J Appl Polym Sci 5(15):285–292
7. Riley J, Siriwardane R, Tian H (2017) Kinetic analysis of the interactions between calcium ferrite and coal char for chemical looping gasification applications: identifying reduction routes and modes of oxygen transfer. Appl Energy 201:94–110
8. Škvára F, Šesták J (1975) Computer calculation of the mechanism and associated kinetic data using a non-isothermal integral method. J Therm Anal 8(3):477–489
9. Galwey AK, Brown ME (1999) Thermal decomposition of ionic solids: chemical properties and reactivities of ionic crystalline phases. Elsevier
10. Zhang T, Hu R, Li F (1994) A method to determine the non-isothermal kinetic parameters and select the most probable mechanism function using a single non-isothermal DSC curve. Thermochim Acta 244(3):177–184

Gasificating Dephosphorization During the Carbothermic Reduction of Medium Phosphorus Iron Ore Concentrate in the Presence of Na_2CO_3 and SiO_2

Jing Zhang, Guoping Luo, Yanbiao Chen, Wenbin Xin and Jianguo Zhu

Abstract To relieve the increasing lack of high-quality iron ore, the medium and high phosphorus refractory mineral resources are being developed worldwide due to the rich storage. The novel method of pre-reducing sinter process was applied to remove phosphorus, characterized by reduced atmosphere, high temperature, and negative pressure. For medium phosphorus Bayan Obo iron ore concentrate, the effect of the carbon mixing ratio, reduction temperature, and time on phosphorous gasification and iron metallization during carbothermic reduction was investigated using XRD, FESEM-EDS, and FactSage software, in the presence of Na_2CO_3 and SiO_2. The optimal carbothermic reduction is conducted at 1050 °C for 60 min with 20 wt% carbon mixing ratio. The corresponding gasificating dephosphorization and iron metallization are 31% and 96%, respectively. Moreover, the further increased carbon mixing ratio and reduction temperature causes the large absorption of reduced phosphorus gas into metallic iron. Notably, the above result provides data support for pre-reducing sinter process.

Keywords Bayan Obo iron ore concentrate · Carbothermic reduction · Phosphorus gasification · Carbon mixing ratio · Reduction temperature · Reduction time

J. Zhang · G. Luo (✉) · Y. Chen · W. Xin
School of Materials and Metallurgy, Inner Mongolia University of Science and Technology, Baotou 014010, China
e-mail: luoguoping3@126.com

J. Zhang
e-mail: lulu2910@126.com

Y. Chen
e-mail: 15540250739@163.com

W. Xin
e-mail: xwb2580zxc@163.com

J. Zhu
Engineering Training Center, Inner Mongolia University of Science and Technology, Baotou 014010, China
e-mail: 13947228242@163.com

J. Li et al. (eds.), *Characterization of Minerals, Metals, and Materials 2020*,
The Minerals, Metals & Materials Series,
https://doi.org/10.1007/978-3-030-36628-5_4

Introduction

As the lacking of high-quality iron ore is increasingly serious, the refractory mineral resources with medium and high content of phosphorus are progressively investigated due to the rich storage [1–3]. However, almost all the phosphorus will enter into hot metal during ironmaking process, which leads to the high phosphorus content in liquid iron and steelmaking slag. Therefore, it is essential to remove phosphorus of raw materials to decrease the dephosphorization burden in the production of iron and steel [4, 5].

The conventional physical and chemical methods of dephosphorization, such as magnetic separation [6], flotation separation [7], gravity separation [8], gas-based reduction [9], microwave [10], and leaching [11], tend to be out of large industrial application due to the unsatisfactory performance, great pollution, and high consumption. Besides, the carbothermic reduction process followed by mechanical grinding + screening or grinding + magnetic separation accounts for a better dephosphorization and iron metallization whereas the difficulty lies in controlling an appropriate intensity of grinding and magnetic field, coupled with the increased cost of external operation [12, 13]. In view of these issues, the novel method of pre-reducing sinter process characterized by reduced atmosphere, high temperature, and negative pressure was applied to remove phosphorus, providing beneficially thermodynamic and kinetic condition for gasificating dephosphorization. For this method, the phosphorus migration into gas phase is encouraged and the restriction factor that affects the phosphorus gasification is the large absorption of reduced phosphorus into metallic iron [14, 15]. Therefore, effects of the carbon mixing ratio, reduction temperature, and time on gasificating dephosphorization and iron metallization during carbothermic reduction process were conducted on the medium phosphorus iron ore concentrate to reveal the mechanism of phosphorus removal via gasification and to optimize the parameter of dephosphorization.

Materials and Experimental Methods

Materials

The medium phosphorus iron ore concentrate (hereafter referred as iron ore concentrate) used in this work was provided by the Bayan Obo iron ore in Baotou, China. The main chemical composition is listed in Table 1. According to our previous study

Table 1 Main chemical composition of iron ore concentrate (mass fraction, mass%)

Fe_{total}	CaO	SiO_2	MgO	Al_2O_3	K_2O	Na_2O	F	S	P
63.00	1.58	5.28	0.83	0.50	0.14	0.23	0.52	1.80	0.08

Table 2 Chemical composition of coke (mass fraction, mass%)

Fixed carbon	Ash	Volatile matter	S	CaO	SiO_2	Al_2O_3	P
86.84	11.90	1.21	0.96	0.74	6.77	2.67	0.097

on existing status of phosphorus and iron in Bayan Obo iron ore concentrate, the phosphorus containing minerals are mainly apatite including fluorapatite and the iron containing minerals is composed by magnetite and a small quantity of hematite.

Coke was used as the reductant and its composition is listed in Table 2.

The analytical reagent grade (>99.8 mass%) of sodium carbonate and silica were used as dephosphorization agent in the carbothermic reduction process.

Experimental Methods

The iron ore concentrate and coke were crushed and ground to pass through a 200 mesh screen and then mixed with 1 mass% Na_2CO_3, 3 mass% SiO_2, 8 mass% water. The 5 g mixture was compressed into tablet with a diameter of 20 mm, using a pressure of 5 MPa for 2 min. Tablets were dried in a drying oven at 105 °C for 4 h. The reduction roasting was conducted in a graphite tube resistance furnace under vacuum condition with a negative pressure of 0.9 atm. The prepared tablets were heated from room temperature to reaction temperature at 15 °C/min and then held for different reduction time. Finally, the roasted tablets were taken out from the furnace and cooled to room temperature.

FactSage software 7.0 was applied to calculate the phase composition at equilibrium under different condition of carbothermic reduction.

The powder of tablets after roasting reduction was prepared to measure phase composition by using X-ray diffraction (XRD, Rigaku, MiniFlex600, Japan) with a Cu Kα X-ray source. The scanning angle 2θ is in the range of 10°–90° and the step size is 0.02°. Besides, the used voltage and current were 40 kV and 15 mA, respectively.

The reduced tablets embedded in epoxy resin were prepared to observe the microstructure and analyze the composition of metallic iron and gangue minerals, using field emission scanning electron microscope in conjunction with energy dispersive spectroscope (FESEM-EDS, Zeiss Sigma 500, Germany; Bruker, Germany).

Evaluation Indexes

Gasificating dephosphorization and iron metallization of the reduced tablets were calculated using Eqs. (1) and (2).

$$\eta = (1 - \frac{m_1 p_1}{m_0 p_0}) \times 100\% \quad (1)$$

$$M = \frac{\delta}{\alpha} \times 100\% \quad (2)$$

where η is the gasificating dephosphorization of total reduction process, %; m_0 and m_1 are the weight of dried tablet and reduced tablet, respectively, g; p_0 and p_1 is the phosphorus content of dried tablet and reduced tablet, respectively, mass%; M is the iron metallization of reduced tablet, %; δ is the metallic iron content of reduced tablet, mass%; and α is the total iron grade of reduced tablet, mass%.

Results and Discussion

Effect of the Carbon Mixing Ratio on Gasificating Dephosphorization and Iron Metallization

The prepared tablets composed by different content of coke ranging from 5 mass% to 25 mass% with an interval of 5 mass%, 1 mass% sodium carbonate, 3 mass% silica, 8 mass% water, and the balanced iron ore concentrate were reduced at 1050 °C for 60 min. The effect of the carbon mixing ratio on gasificating dephosphorization and iron metallization is presented in Fig. 1a. As the carbon mixing ratio increases from 5 mass% to 25 mass%, the gasificating dephosphorization first increases from 1% to 31% and then decreases to 11%. For iron metallization, it also first increases from 82 to 96% and then decreases to 85%. The maximum value for the above items is obtained with the carbon mixing ratio of 20 mass%.

The phase composition of the carbothermic reduction at equilibrium with different carbon mixing ratio calculated by FactSage software is shown in Fig. 2. From Fig. 2a and d, it is evident that the iron oxides are mainly progressively reduced to FeO coupled with a small amount of metallic iron. The reduced FeO easily combines with SiO_2 and forms fayalite. Besides, the reduction of iron oxide is in preference to that of apatite and little apatite has been reduced with the carbon mixing ratio of 5 mass%. Thus, the formation of phosphorus gas and Fe_xP is really unobvious. When the carbon mixing ratio increases to 20 mass% (shown in Fig. 2b and e), the iron oxide is basically reduced to metallic iron which transformed to Fe_3C because of carburization. Meanwhile, the quantity of apatite is evidently decreased accompanying the formation of the phosphorus gas and Fe_xP. With the carbon mixing ratio increases to 25 mass%, the apatite is further reduced coupled with the remarkable decreased quantity of the phosphorus gas and the increased amount of Fe_xP, as shown in Figs. 2c and f. It should be noted that the reduced phosphorus gas tends to be absorbed into the metallic iron and promotes the formation of Fe_xP. Therefore, the larger amount of apatite is reduced as the carbon mixing ratio increases from 20 mass% to 25

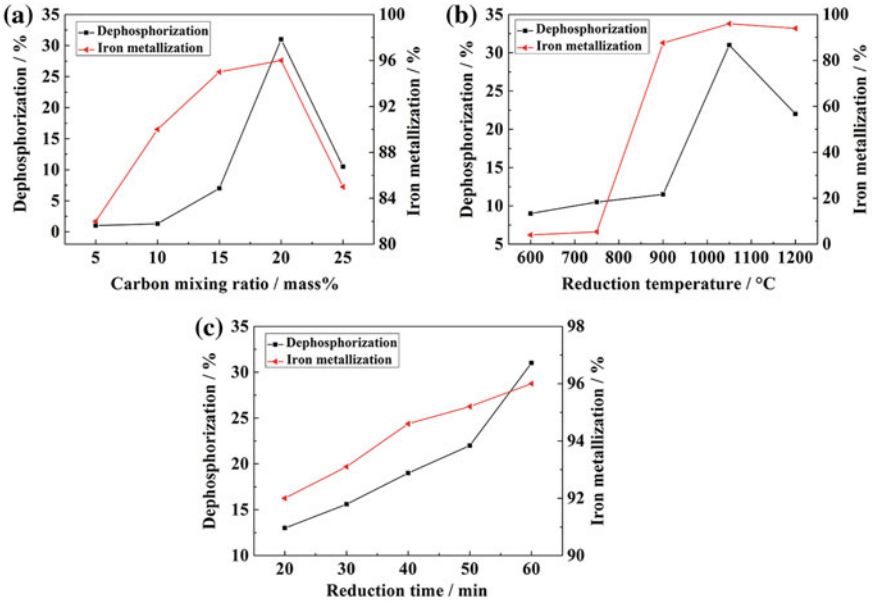

Fig. 1 Effect of the carbon mixing ratio (**a**), reduction temperature (**b**), and reduction time (**c**) on gasificating dephosphorization and iron metallization of iron ore concentrate

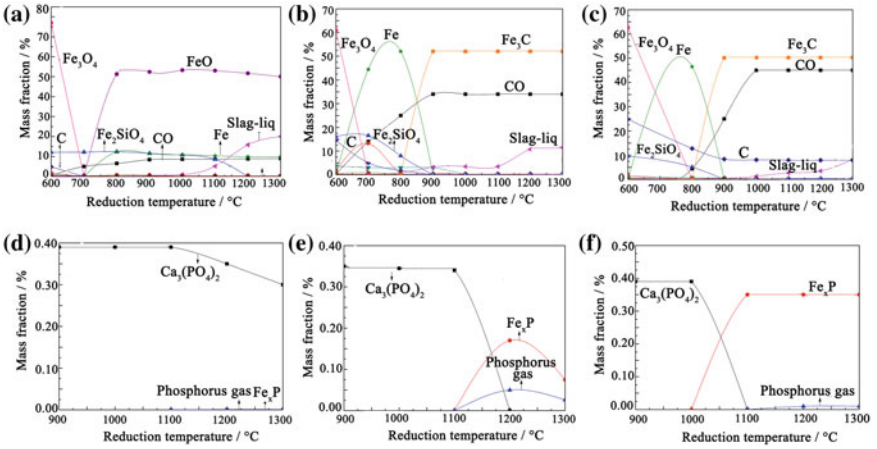

Fig. 2 Phase composition of carbothermic reduction at equilibrium with different carbon mixing ratio calculated by FactSage software: **a** and **d** 5 mass%; **b** and **e** 20 mass%; **c** and **f** 25 mass%

mass% whereas the quantity of phosphorus gas is decreased as well as the value of gasificating dephosphorization.

To further investigate the minerals evolution of iron ore concentrate during carbothermic reduction process, XRD patterns with different carbon mixing ratio are shown in Fig. 3a. It is obvious that apatite, wustitie, and metallic iron are observed in the reduced tablets with 5 mass% and 10 mass% carbon mixing ratio, which suggests that a portion of FeO and apatite has not been reduced. The diffraction peak of FeO and apatite is disappeared and the intensity of metallic iron is increased as the carbon mixing ratio increases to 15 mass%. When the carbon mixing ratio reaches 20 mass% and 25 mass%, the intensity of metallic iron is decreased and the peak of Fe_3C phase appears because of carburization.

As the phase of Fe_xP is not detected in XRD pattern due to the low content of phosphorus in iron ore concentrate, SEM-EDS analysis of the roasted tablets with different carbon mixing ratio has been conducted, as shown in Fig. 4. It is exhibited that the metallic iron with white grey contrast and gangue minerals in dark grey are associated closely. From Fig. 4a, the EDS maps of Ca and P are totally overlapped indicating that a rather large portion of apatite has not been reduced with carbon

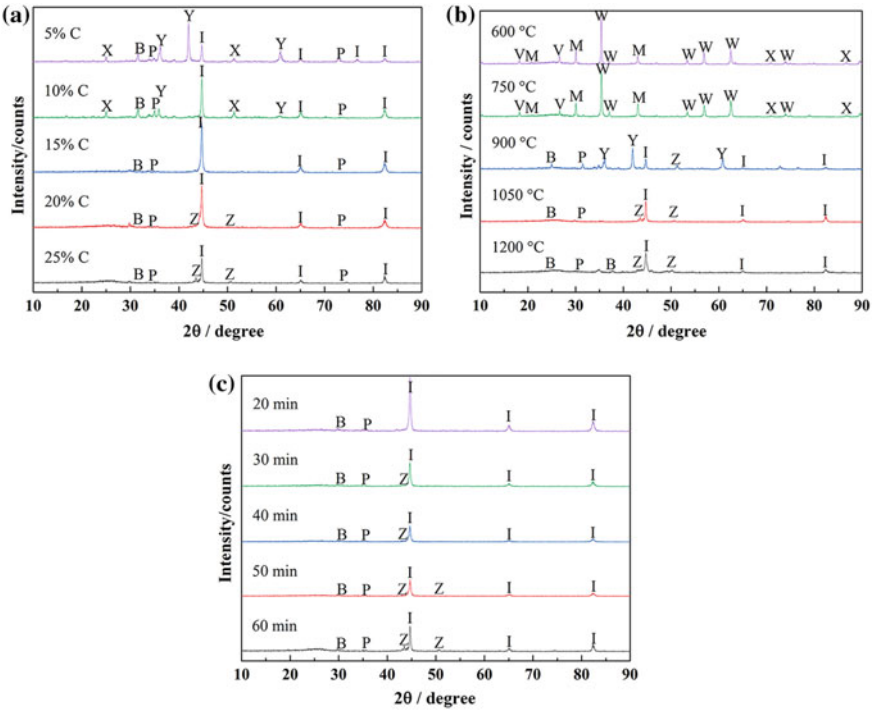

Fig. 3 XRD patterns of iron ore concentrate reduced with different carbon mixing ratio (**a**), reduction temperature (**b**), and reduction time (**c**) (B–Ca_2SiO_4; I–Fe; M–SiO_2; P–$Na_2CaSi_5O_{12}$; V-Carbon; W-Fe_3O_4; X-$Ca_3(PO_4)_2$; Y-FeO; Z-Fe_3C)

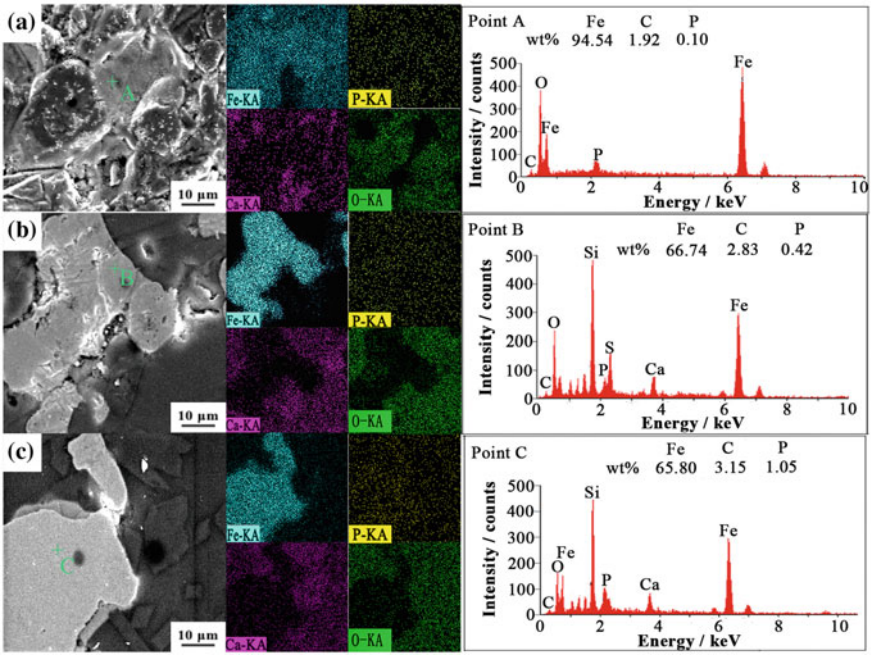

Fig. 4 Typical SEM images and EDS maps of iron concentrate ore reduced with different carbon mixing ratio at 1050 °C for 60 min: **a** 5 mass%; **b** 15 mass%; **c** 20 mass%

mixing ratio of 5 mass%. When it increases to 15 mass% and 20 mass% shown in Figs. 4b and c, the more and more areas of EDS map of P element are overlapped with that of Fe. The reason is that the apatite has been reduced under the condition of more carbon and a part of phosphorus gas has entered into the reduced iron phase, resulting in the formation of Fe_xP. According to the EDS analysis of Point A-C in metallic iron, the content of carbon and phosphorus in iron phase is increased as the carbon mixing ratio increases due to the carburization and absorption of phosphorus into metallic iron.

From the abovementioned analysis, the increased carbon mixing ratio varying from 5 mass% to 20 mass% brings about the reduction of apatite and enhances gasificating dephosphorization. As the carbon mixing ratio further increases to 25 mass%, the reduced phosphorus gas obviously migrates to metallic iron which is directly related to the accelerated carburization. Thus, the optimum carbon mixing ratio is chosen to be 20 mass%.

Effect of Reduction Temperature on Gasificating Dephosphorization and Iron Metallization

The prepared tablets composed by 20 mass% coke, 1 mass% sodium carbonate, 3 mass% silica, 8 mass% water, and the balanced iron ore concentrate were reduced at temperature ranging from 600 to 1200 °C with an interval of 150 °C for 60 min. The effect of reduction temperature on gasificating dephosphorization and iron metallization is presented in Fig. 1(b). As the reduction temperature elevates from 600 to 1200 °C, the dephosphorization first increases from 9 to 31% and then decreases to 22%. For iron metallization, it also first increases from 4 to 96% and then slightly decreases to 94%. It is evident that the optimal reduction temperature is 1050 °C.

Under the condition of different reduction temperature, the phase transformation of iron ore concentrate after reduction was analyzed and the XRD patterns, SEM images, and EDS maps are shown in Figs. 3b and 5.

As can be seen in Fig. 3b, magnetite, apatite, silica, and carbon are observed in the reduced tablets roasted at 600 and 750 °C. That is to say, the main reduction of iron and phosphorus containing minerals is not happened at the temperature lower than 750 °C. When the reduction temperature increases to 900 °C, the diffraction peak of wustitie, metallic iron, and cementite appears, indicating that FeO has not

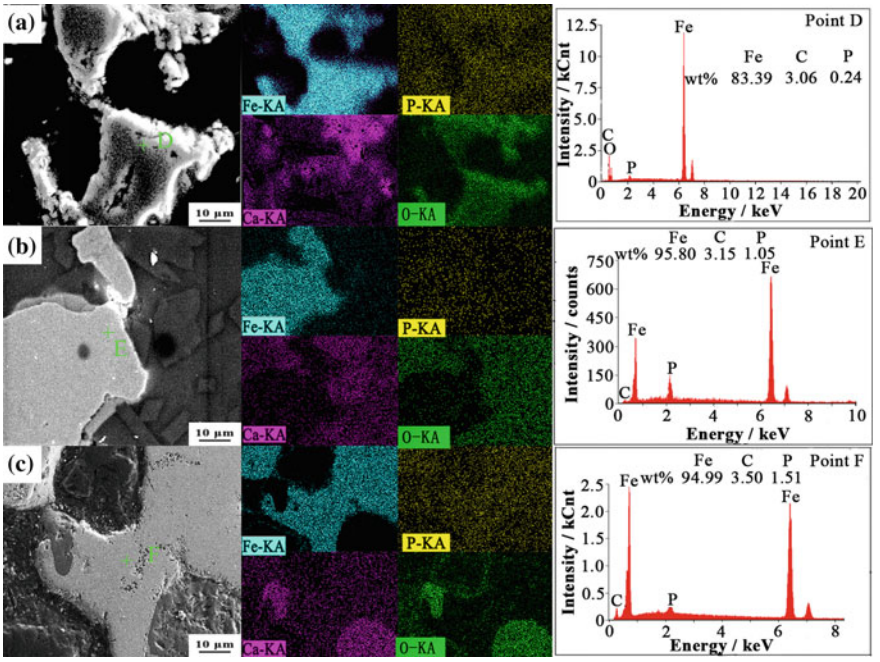

Fig. 5 Typical SEM images and EDS maps of iron ore concentrate reduced at different reaction temperature for 60 min: **a** 900 °C; **b** 1050 °C; **c** 1200 °C

been completely reduced and was existed in the single phase. With the reduction temperature further increasing to 1050 and 1200 °C, the diffraction intensity of metallic iron first increases and then decreases obviously caused by the aggravated carburization.

SEM images and EDS maps of the reduced tablets roasted at different temperature are illustrated in Fig. 5. As shown in Fig. 5a, the element P is distributed with elements Ca and Fe at 900 °C. Meanwhile, a portion of iron oxide is still existed as shown in EDS spectrum of Point D. When the temperature reaches 1050 and 1200 °C, the reduced iron phase is tightly surrounded by gangue minerals, which is shown in Figs. 5b and c. The overlapped area of P and Fe is remarkably increased with the elevated temperature. Moreover, the EDS maps of P and Fe have nearly the same distribution character at 1200 °C, suggesting that a large amount of the reduced phosphorus gas has been absorbed by metallic iron. In addition, the phosphorus content is obviously increased with the increase of reduction temperature from EDS spectrums of Point D, E, and F.

Above all, increasing the reduction temperature tends to accelerate the phosphorus gasification because the reduction of apatite is endothermic reaction. However, the absorption of the reduced phosphorus gas into metallic iron would also be strongly aggravated when the reduction temperature exceeds 1050 °C, which leads to the sharp decrease of dephosphorization.

Effect of Reduction Time on Gasificating Dephosphorization and Iron Metallization

The prepared tablets composed by 20 mass% coke, 1 mass% sodium carbonate, 3 mass% silica, 8 mass% water, and the balanced iron ore concentrate were reduced at 1050 °C for different time ranging from 20 min to 60 min with an interval of 10 min. The effect of reduction time on gasificating dephosphorization and iron metallization is presented in Fig. 1c. As reduction time extends from 20 min to 60 min, the gasificating dephosphorization and iron metallization increase from 13% to 31% and 92% to 96%, respectively. The maximum value is acquired when the time arrives to 60 min.

The XRD patterns showing phase composition of the reduced tablets with different reduction time are basically the similar, as seen in Fig. 3c. Meanwhile, the diffraction peak of Fe_3C appears when the reduction time exceeds 20 min and its intensity is continually strengthened as the reduction time increases.

As the reduction of iron oxides is prior to that of apatite, the longer reduction time promotes a larger amount of phosphorus containing minerals transforming into the reduced phosphorus gas, consequently enhancing the gasificating dephosphorization.

Conclusions

The gasificating dephosphorization during the carthermic reduction process of medium phosphorus iron ore concentrate in the presence of sodium carbonate and silica was investigated in this work. The main conclusions are as follows:

(1) Increasing the carbon mixing ratio from 5 mass% to 20 mass% results in phosphorus migrating from gangue minerals into gas phases and consequently improves dephosphorization. Whereas the carbon mixing ratio further increases, it will accelerate the reduced phosphorus gas being absorbed into iron phase, which yields the phosphorus gasification.
(2) When reduction temperature elevates from 600 to 1050 °C, the gasificating dephosphorization increases because the reduction of apatite is endothermic reaction. However, the reduced phosphorus gas easily moves into metallic iron as the reduction temperature is higher than 1050 °C, and finally, decreases the gasificating dephosphorization.
(3) An increase of reduction time from 20 to 60 min promotes a larger amount of phosphorus transforming into reduced gas and increases the dephosphorization.
(4) The optimal carbothermic reduction is carried out at 1050 °C for 60 min with 20 mass% carbon mixing ratio and the corresponding gasificating dephosphorization and iron metallization are 31% and 96%, respectively. The experimental result combined with the FactSage calculation would provide data support for pre-reducing sinter process.

Acknowledgements The authors gratefully acknowledge the financial supported from the National Nature Science Foundation of China (Grant No. 51664045, 51804170) and Nature Science Foundation of Inner Mongolia (Grant No. 2018BS05002).

References

1. Li GH, Zhang SH, Rao MJ et al (2013) Effects of sodium salts on reduction roasting and Fe–P separation of high-phosphorus oolitic hematite ore. Int J Miner Process 124:26–34
2. Wu J, Wen ZJ, Cen MJ (2011) Development of technologies for high phosphorus oolitic hematite utilization. Steel Res Int 82(5):494–500
3. Sun YS, Han YX, Gao P et al (2015) Thermogravimetric study of coal-based reduction of oolitic iron ore: kinetics and mechanisms. Int J Miner Process 143:87–97
4. Wang G, Liu J, Wang JS, Xue QG et al (2015) Dephosphorisation of high phosphorus oolitic hematite by carbon composite pre-reduction and fast melting separation. Ironmaking Steelmaking 42(9):689–697
5. Li GH, Rao MJ, Ouyang CZ et al (2015) Distribution characteristics of phosphorus in the metallic iron during solid-state reductive roasting of oolitic hematite ore. ISIJ Int 55(11):2304–2309
6. Ionkov K, Gaydardzhiev S, de Araujo AC et al (2013) Amenability for processing of oolitic iron ore concentrate for phosphorus removal. Miner Eng 46:119–127

7. Nunes APL, Pinto CLL, Valadão GES et al (2012) Floatability studies of wavellite and preliminary results on phosphorus removal from a Brazilian iron ore by froth flotation. Miner Eng 39:206–212
8. Ito M, Tsunekawa M, Yamaguchi E et al (2008) Estimation of degree of liberation in a coarse crushed product of cobalt-rich ferromanganese crust/nodules and its gravity separation. Int J Miner Process 87(3–4):100–105
9. Tang HQ, Guo ZC, Zhao ZL (2010) Phosphorus removal of high phosphorus iron ore by gas-based reduction and melt separation. J Iron Steel Res Int 17(9):1–6
10. Lei Y, Li Y, Chen W et al (2017) Microwave carbothermic reduction of oolitic hematite. ISIJ Int 57(5):791–794
11. Wang HH, Li GQ, Zhao D et al (2017) Dephosphorization of high phosphorus oolitic hematite by acid leaching and the leaching kinetics. Hydrometallurgy 171:61–68
12. Matinde E, Hino M (2011) Dephosphorization treatment of high phosphorus iron ore by pre-reduction, mechanical crushing and screening methods. ISIJ Int 51(2):220–227
13. Rao MJ, Ouyang CZ, Li GH et al (2015) Behavior of phosphorus during the carbothermic reduction of phosphorus-rich oolitic hematite ore in the presence of Na_2SO_4. Int J Miner Process 143:72–79
14. Sato H, Machida S, Nushiro K et al (2006) Development of production process for pre-reduced agglomerates and evaluation of its quality. Tetsu-to-Hagané 92(12):815–824
15. Zhang J, Luo GP, Zhao W et al (2019) Phosphorus gasification during the carbothermic reduction of medium phosphorus magnetite ore by adding Na_2CO_3. ISIJ Int 49(2):235–244

Trends in Characterization and Beneficiation of Non-ferrous Metallic Ores in Nigeria

Furqan Abdulfattah, Ibrahim A. Rafukka and Sunusi M. Manladan

Abstract Nigeria a nation adequate blessed with large deposit of non-ferrous metallic ores which are yet to be fully harnessed, characterized, and beneficiated due to lack of sufficient studies and technology. The non-ferrous metallic ores found in Nigeria include lead-zinc ore, tin ore (Cassiterite), niobium ore, uranium ore, and precious metals such as (Gold and Silver). This article focuses on trends in previous works on characterization and beneficiation of some non-ferrous metallic ores deposits, showing the mineral, elemental contents, and the amount present in a particular ore. Knowledge gap in the field of study was identified to enable further research on non-ferrous metallic ore characterization and beneficiation of yet to be characterized and beneficiated non-ferrous metallic ore which include; columbite, cassiterite, tantalite, chalcopyrite, gold, niobium ore, etc. Also, in-depth and further studies be done on lead-zinc ore, which is the most characterized and beneficiated non-ferrous metallic ore in Nigeria.

Keywords Lead-zinc ore · Tin ore · Characterization · Beneficiation · Non-ferrous · Metallic ores

Introduction

Nigeria is a country adequately blessed with solid minerals ranging from coal to iron ore, galena, cassiterite, chalcopyrite, gold, etc., which spread across all regions of the country harnessing these minerals adequately and properly will boost the nation's

F. Abdulfattah (✉) · I. A. Rafukka · S. M. Manladan
Department of Mechanical Engineering, Bayero University, Kano, Nigeria
e-mail: phurqoon93@gmail.com; fa1700001.mme@buk.edu.ng

F. Abdulfattah
Nigerian Institute of Mining and Geosciences (NIMG), Jos, Nigeria

S. M. Manladan
School of Materials Science and Engineering, Tianjin University, Tianjin 300072, China

J. Li et al. (eds.), *Characterization of Minerals, Metals, and Materials 2020*,
The Minerals, Metals & Materials Series,
https://doi.org/10.1007/978-3-030-36628-5_5

gross domestic product (GDP). A nation like Nigeria can overcome its present economic challenges if attention is directed towards the solid mineral industries. Most of the minerals found in Nigeria still remain unexploited or under explored due to inadequate knowledge on their status, economic viability, and requisite mining technologies. Importing non-ferrous metallic products such as lead, zinc, tin, columbite, manganese, copper, etc., from other countries is costly. Nigeria's potential of mineral resources could increase employment opportunity in the country.

This study is aimed at bringing together work done and literatures, on characterization of non-ferrous metallic ores deposits around the country. In order to identify possible gap in non-ferrous metallic ore characterization and beneficiation to give possible directions on further works and researches to be done in the area of study.

Lead-Zinc Ore

There are more than 60 known lead-containing minerals but the most important primary ore of the metal is the lead sulphide, galena [1]. Galena (PbS) often contains silver, zinc, copper, gold, cadmium, bismuth, arsenic, and antimony. Other commercially significant lead-containing minerals are cerussite ($PbCO_3$) and anglesite ($PbSO_4$). These are known as secondary minerals because they are derived from galena through natural actions, such as weathering [1].

Galena is very widely distributed, and has up to 86.6% Pb, with a specific gravity of 7.4–7.6. It occurs in veins, often with sphalerite, pyrite, chalcopyrite, tetrahedrite, and gangue minerals such as quartz, calcite, dolomite, barite, and fluoride. It is also found in pegmatites, and as replacement bodies in limestone and dolomite rocks, with garnets, feldspar, diopside, rhodonite, and biotide. Galena often contains up to 0.5% silver and is important source of the metal [1].

Lead-zinc ore deposits abound in Nigeria. It is estimated that, there are at least 30 lodes of lead-zinc with an aggregate length of about 6000 m [2]. The lodes cover over 560 km in a narrow belt from Adun in Cross River State through Ishiagu in Imo State and Abakaliki in Ebonyi State, to Arufu in Taraba State to Wase and Zurak in Plateau State and Gwona in Bauchi State [3]. Other deposits are located in Abia, Adamawa, Bauchi, Benue, Enugu, and Nassarawa. The total estimated reserve is 20,000 million tons has seen in Table 1 [4, 5].

Copper Ore

Copper occurs as native copper or in minerals such as the copper sulphides: chalcopyrite ($CuFeS_2$); and chalcocite (copper glance or copper sulphide) (Cu_2S); covellite (CuS); bornite (Cu_5FeS_4); enargite (Cu_3AsS_4); tetrahedrite [$(CuFe)_{12}Sb_4S_{13}$]; copper carbonates: azurite or basic copper carbonate ($Cu_2(OH)2CO_3$); and malachite (Cu_2CO_3); copper(I) oxide: mineral cuprite or copper oxide (Cu_2O); chrysocolla

Table 1 Lead-zinc ore deposits in Nigeria

S/No.	State	Location	LGA	Reserve (tons)
1.	Ebonyi	Ishiagu	Ivo	1,040,000
		Abakaliki	Abakaliki	450,000
		Ameri		
		Ameka		
2.	Enugu	Enyigba	Umulopa	Na
		Nyeba		
3.	Plateau	Wase	Wase	Na
		Zurak		
4.	Nasarawa	Akwanga	Akwanga	
5.	Cross River	Arufu zone	Akamkpa	150,000
		Adua		
		Oban		

Source RMRDC, 2004 in Technical Brief on Minerals in Nigeria-Lead/Zinc

Table 2 Nigerian copper ore deposits and their locations

S/No.	State	Location	Reserve (tons)
1.	Nasarawa	Akiri	Inferred
		Azara Rafin Gabas	Inferred Inferred
2.	Bauchi	Nahuta Yelwa Rishi	Inferred Inferred
3.	Zamfara	Anka	Inferred
4.	Kano State	Zarara Hill	Inferred
5.	Ebonyi State	Ishiagu	Inferred

($CuSiO_3$). Most copper is mined or extracted as copper sulphides from large open pit mines in porphyry copper deposits that contain 0.4 to 1.0% copper.

Chalcopyrite is the most common mineral found in porphyry-type deposits, while chalcocite occurs predominantly in hydrothermal veins [1, 6]. Chalcopyrite is the copper ore deposit of Falum, Sweden of Namagaland in South Africa. However, vast crystals or deposits occur in Ishiagu, Ebonyi State; South Eastern region of Nigeria. High great chalcopyrite deposit can also be found in Baluba, East of Lusaka, Zambia [7]. Nigerian copper ore is mostly found as complex ore alongside zinc and lead [6]. Copper ore deposit around Nigeria could be described in the Table 2 [8].

Cassiterite (Tin Ore)

Prior to the discovery of oil in Nigeria, the major revenue and source of foreign exchange for the country was from tin mining operation. From the geological evidence, there are extensive cassiterite deposits lies buried under basalt and volcanic flows particularly in Plateau, Bauchi, Nassarawa, FCT, Kano, Kaduna, Kwara, Kogi, Ondo, and Osun States. The most important tin mineral is cassiterite (SnO_2) [9]. Cassiterite is the only tin mineral that is in sufficient abundance in the earth's crust to have any commercial value. When chemically pure, which is rare, cassiterite contains 78.6 percent tin but, when contaminated with impurities such as quartz, muscovite, wolframite, tourmaline, topaz, fluorite, scheelite, lepidolite, arsenopyrite, bismuth, and molybdenite, the tin content varies between 73 and 75 percent [10]. It belongs to rutile group of minerals. Cassiterite is mainly found in two types of deposits. First type, it occurs as a primary accessory constituent of certain late-stage granitic intrusions, and is found in veins (In medium- to high-temperature hydrothermal) and fissures both in the granite (greisens) and surrounding country rock. The second type of deposit is of a secondary origin and occurs as alluvial or placer (granite pegmatite, rhyolite; rarely in contact metamorphic) and detrital deposits [11]. The principal ore of tin deposits are widespread across the world. It is obvious from the physical characteristics of cassiterite that its 22 high relative density in relation to its gangue constituents makes it an ideal mineral for the application of gravity-separation techniques. Unfortunately, it's relative hardness approximately equal to that of steel—is accompanied by the unfortunate quality of extreme brittleness.

Trends in Characterization and Beneficiation Non-ferrous Metallic Ores

Copper Ore

Damisa, examined Nahuta lead-zinc-Copper complex ore has 5.2% copper. Hence, there is need for the ore to be explored and beneficiated for its copper mineral [6]. Oyeladun et al. worked on the determination of chemical composition and work index of Rafin Gabas chalcopyrite ore. They reported that the ore contains 12.6% Cu and has a work index of 22.38 kWh/tonne [12]. Abubakre et al. worked on chemical and mineralogical analysis of Akiri copper ore and established that the ore contains 2.5% Cu in form of malachite [13]. Jatau et al. worked on the physico-chemical properties of Agwada chalcopyrite ore and established that the ore contains 4.62% Cu [14]. Ali et al. worked on the determination of liberation size of Agwada chalcopyrite ore and established that the liberation size of the ore to be 125 μm having the highest assay of 8.17% Cu [15]. Oyeladun worked on charaterization of azara Copper ore deposit and discovered that the ore contains 3.30% Cu [8]. However, from some of these works carried out on some Nigeria copper ore deposits, it is clear that some of the

Nigeria copper ore deposits with geochemical history are mineable and profitable as their percent copper cut-off grades are slightly above the specific cut-off grade of 0.4–1.0% Cu [8, 16].

Lead-Zinc Ore

Olanipekun worked on quantitative leaching of Abakaliki galena and discovered that it contains 85.20% Pb, 1.03% Zn, 0.48% Fe, 13.90% S, and 0.02% Cu [17]. Olubambi et al. worked on mineralogical characterization of Ishiagu sulphide ore and discovered that the ore contains siderite, sphalerite, galena, quartz, and traces of pyrite, and copper bearing minerals [18]. Damisa worked on the process design for the beneficiation of Nahuta lead deposit in Bauchi State. He concluded that the major economic minerals present in Nahuta deposit are lead and copper in the forms of galena (PbS) and covellite (CuS); that bulk floatation followed by differential floatation is best to achieve high recovery in the beneficiation of the ore [6]. Masok worked on characterization and beneficiation of Zurak lead-zinc ore deposit using X-ray fluorescence revealed that the run-of-mine ore contained 6.33% Pb and 4.65% Zn on the average, which meets the typical standard feed grades of 1–5% Pb and 1–10% Zn usually required for mining lead-zinc ore. While the mineralogical analysis using X-ray diffraction technique revealed that the ore contained 7.11% galena (PbS) and 7.51% sphalerite (ZnS) as the major valuable minerals; 3.04% magnetite (Fe_3O_4), 1.5% rutile (TiO_2) as minor minerals; and 65.65% quartz (SiO_2) as the main gangue [5]. Obassi et al. worked on liberation size and beneficiation of Enyigba lead ore, Ebonyi State [19]. Alabi et al. worked on Abuni galena-sphalerite-azurite complex ore by selective froth floatation. They discovered that the complex ore contains 18.17% PbO, 17.23% ZnO, and 4.46% CuO for the XRF result, while the XRD analysis showed that the complex ore contains galena 14.53%, sphalerite 13.82%, and azurite 3.58% by weight [20]. Alabi et al. worked on zinc ore from Gumau-Toro town and discovered that the ore contains 20.20% zinc, 66.72% SiO_2, 2.36% lead, 16.62% iron, and 0.001% Silver [21]. Alabi et al. worked on Lead in Sabon-Layi, Alkaleri local government, Bauchi State Lead-Zinc Ore deposit. Chemical analysis of the composition reveals that this crude ore contains 38.76% Lead and other related minerals such as 29% silica, 22.80% sulphur, 2.76% zinc, 4.17% CaO and others in traces; these related minerals are gangues that hinder the appreciation of the lead grade found in this ore [22]. Nnanwube et al. worked on a Nigerian galena and results of the elemental composition by X-ray fluorescence technique showed that the galena mineral exists mainly as PbS with metals such as Na, Mg, Al, Ca, Fe, and Zn occurring as minor elements, and K, Cr, and Sr as traces. The elemental analysis gave Pb (60.01%), S (14.66%), Fe (4.32%), Na (3.78%), Si (7.69%), Mg (1.21%), Al (1.94%), P (1.37%), Cl (1.19%), K (0.09%), Ca (1.99%), Cr (0.01%), Mn (0.49%), Zn (1.22%), and Sr (0.04%) [23].

Tin Ore

Kinniard et al. worked on mineralogy, geochemistry, and mineralization of Riruwai complex ore. Where the ore mineralogy confirms the paragenetic columbite (pyrochlore)-cassiterite-sphalerite evolution [24]. Ogwuegbu et al. worked on mineralogical characterization of Kuru cassiterite ore and discovered from the inductive coupled plasma–optical emission spectrometry the elemental analysis as follows; Sn (28.0%), Si (5.5%), Fe (5.16%), Ti (3.51%), Al (2.48%), Y (1.06%), and Nb (2.53%). The other trace elements found include Mn, K, Na, Mg, La, Ce, U, and Ca [25]. Thomas and Yaro worked on characterization of Haita-Vom Cassiterite deposit and discovered from the X-Ray Fluorescence (XRF) Analysis that the Ore contains 17.37% Sn, 10.42% Ca, 7.05% Ti, 3.71% Ti, as the major elements, 0.27% Cr and 0.10% Nb [26]. Abere et al. worked on comparative study of Kuru-Jantar cassiterite mining methods and discovered that the XRF analysis gave 66.462% Sn, 40.4% Nb; 26.5% Fe; 22.3% Ti; 2.5% Ta; 2.3% Sn; and 5.1% W for the paddock mining method and 68.69% Sn, 37.6% Nb; 24.8% Fe; 21.5% Ti; 2.3% Ta; 5.8% Sn; and 4.9% W for lotto mining method [27]. Abere et al. worked on upgrading of Kudedu cassiterite deposit. They discovered with ED-XRFS analysis of the crude ore that the ore contains 15.75% SnO_2 with other associated minerals in different proportions [28].

Gold

Ajayi worked on mineralogical studies of gold ore of Ilesha area discovered particle size analysis that most of the gold is contained in fine particles size of -600 μm $+300$ μm to -75 μm. The trend is that the gold content of the ore increases with decrease in particle size [29]. Danbatta et al. worked on geochemistry if gold deposit in Anka Schist belt (ASB) and submitted that the study has confirmed the gold occurrences of ASB, as well as their overall mineralogical and chemical characteristics [30]. The geochemical characterization of the ASB gold mineralization suggests a metamorphic origin for the gold mineralizing fluid which was generated and expelled during late brittle movements along the Anka fault, in line with those of [31–33]. A similar model was proposed by [34, 35] to explain the metamorphic origin of the Au-mineralizing fluids at Bin Yauri (Zuru schist Belt) and Tsofon Birnin Gwari (Kushaka Schist Belt). This is also similar to what has been reported from many other areas of gold mineralization in the country and the world [30]. Ramadan and Abdelfattah worked on characterization of gold mineralization in Garin Hawal area, the geochemical studies indicate that the gold content reaches 8 g/t in the alteration zones, while it reaches up to 35 g/t in the quartz veins. Mineralogical studies indicate that the alterations are strongly potassium enriched. Pyrophyllite, kaolinite, illite, gypsum, and quartz also occur. The main ore minerals are gold, chalcopyrite, arsenopyrite, pyrite, galena, and iron oxides [36]. Ogundare et al. worked on Itagunmodi gold ore and the SEM shows that the morphology of the particles of gold ore from Itagunmodi

deposit is in trihedron shapes, while the morphology of gold extracted from the gold ore is in tetrahedron and hexahedron shapes. The average particle size of the gold ore was evaluated statistically to be 106 μm, while that of the gold extracted was found to be 412 μm. The particles size distribution revealed that the gold extracted had better homogeneity than that of the gold ore [37]. Ayodele et al. carried out geochemical analysis (XRF) on the bedrocks of Okemesi (Ajindo), and the mineralization shows gold with concentration values of 10–0.05 ppm. This prompted the investigation for confirmation of gold mineralization on the bedrocks of Okemesi area (Ajindo) [38]. Akanmu et al. worked on mineralogical characterization of the gold bearing rock around Okemesi-Ijero area and discovered that, this study has actually confirmed the presence of gold mineral in the Precambrian basement rocks of Okemesi area. The XRD studies also revealed a strong affinity with the petrographic analysis and also indicated Au showings in Okemesi area (Ajindo Bedrock) which has now confirmed the phase of Au showings in the schistose quartzites [39].

Conclusion

This study has examined Nigerian non-ferrous metallic ores which include lead-zinc ores, cassiterite (Tin ore), gold ore, and copper ore deposits found in the country with the resources available. Although, the most of the minerals are not fully utilized for industrial improvement in Nigeria, also the mineral development is so slow due to lack of knowledge on the amount of mineral contents present in a particular ore. If this trend continues, then there is little hope of fully harnessing the mineral resources for industrial and technological development. This paper has reviewed previous works done on characterization and beneficiation of Nigerian metallic ores in order to motivate government, stakeholders, and investors to put more interest towards developing these important resources.

This review shows more work is needed to be done on characterization and beneficiation of metallic ores (such as Riruwai Cassiterite, Zarara Hill Copper Ore, Numan lead-zinc deposit, Nasarawa and Bauchi Zircon, Plateau Tantalite, Kaduna Tourmaline, etc.) in the countries has few works are done yet. From this research, the non-ferrous metallic ores that are yet to be adequately characterized and beneficiated include; columbite, cassiterite, tantalite, chalcopyrite, gold, Illmenite, wolframite, niobium ore, etc. Also, in-depth and further studies (such as upgrading the ore by beneficiating in several reagents) be done on iron ore and lead-zinc Ore. Metallic ores across the states in the countries be looked at especially states with more metallic ores such as Nassarawa, Plateau, Kogi, Niger, Bauchi, Taraba, Adamawa, Oyo, Ogun, Benue, Ebonyi, Cross River, Zamfara, Kwara, Kano, Kebbi, Kaduna, etc.

References

1. Britannica. Encyclopedia Brittanica (2014)
2. Wills BAM (2006) Mineral processing technology. Elsevier Science and Technology Books, New York
3. MSMD (2006) Lead-zinc exploration opportunities in Nigeria. Ministry of Solid Minerals Development, Abuja
4. RMRDC (2004) Technical brief on minerals in Nigeria, lead/zinc pamphlet. Raw Materials Research and Development Council, Abuja
5. RMRDC (2003) Multi-disciplinary committee report of the techno-economic survey on base metals, iron and steel and engineering sector. Raw Material Research and Development Council, Abuja
6. Damisa EOA (2008) Beneficiation potentials of Nahuta lead deposit, Bauchi State, Nigeria. Ph.D. Thesis, A.B.U., Zaria
7. Alafara AB, Kuranga IA, Folahan AA, Malay KG, Olushola SA, Rafiu BB, Abdul RS, Sangita RP (2012) A review on novel techniques for chalcopyrite ore processing. Int J Min Eng Min Process 1(1):1–16
8. Oyeladun OA (2015) Characterization of Azara copper ore deposit, Nasarawa State, Nigeria. M.Eng. Thesis submitted to Department of Materials and Metallurgical Engineering, Ahmadu Bello University, Zaria. Unpublished
9. Bamalli US, Moumouni A, Chaanda MS (2011) A review of Nigerian metallic minerals for technological development. Scientific research. Nat Res 2:87–91. https://doi.org/10.4236/nr.2011.22011, http://www.scirp.org/journal/nr
10. Holland-Batt AB (1998) Gravity separation: a revitalized technology. Society for Mining, Metallurgy and Exploration, Inc., Littlelton, Colorado (SME preprint), pp 45–98
11. Mineral Data Publishing. Cassiterite. 2001–2005, version 1
12. Oyeladun OAW, Thomas DG, Yaro SA (2012) Determination of the chemical composition and the work index of Rafin Gabas chalcopyrite ore. Niger Min J 10(1):37–44
13. Abubakre AO, Usaini MNS, Ali M (2014) Chemical and mineralogical analysis of Akiri copper ore. Niger Min J 12:P38–42
14. Jatau BS, Akindele UM, Aye AE (2014) Physico-chemical appraisal of Agwada chalcopyrite ore, Nasarawa State. Niger Min J 10(1):P46–50
15. Ali M, Aye AE, Akindele UM (2014) Determination of liberation size of Agwada chalcopyrite ore, Nasarawa State, Nigeria. J Min Res 1(2):84–87
16. Weiss NL (1985) Mineral processing handbook by American Institute of Mining Metallurgical and Petroleum Engineering Incorporation. Kings Port Press, United States of America
17. Olanipekun EO (2000) Quantitative leaching of Galena. Bull Chem Soc Ethiop 14:25–32. https://doi.org/10.4314/bcse.v14i1.71994
18. Olubambi PA, Ndlovu S, Potgieter JH, Borode JO (2008) Mineralogical characterization of Ishiagu (Nigeria) complex sulphide ore. Int J Miner Process 87:83–89. https://doi.org/10.1016/j.minpro.2008.02.008
19. Obassi E, Gundu DT, Akindele UM (2015) Liberation size and beneficiation of Enyigba lead ore, Ebonyi State, South-East Nigeria. J Min Mater Charact Eng 3:125–133. http://www.scirp.org/journal/jmmce, http://doi.org/10.4236/jmmce.2015.33015
20. Alabi OO, Araoye BO, Bala MB, Igbonwelundu MT, Abere DV, Dalhatu AA (2016) Influence of selective froth floatation on process mechanism of Abuni Galena. Nigerian Society of Mining Engineers, Niger Min J 14:45–50. ISBN 1117-4307
21. Oyelola AO, AbduDA, Victor AD, Igonwelundu MT, Bosan BM, Oyebode AB (2016) Extraction of a low grade zinc ore using gravity and froth flotation methods. J Appl Sci Environ Manage 20:903–908. http://doi.org/10.4314/jasem.v20i4.1
22. Alabi OO, Araoye BO, Bala MB, Igbonwelundu MT, Abere DV, Dalhatu AA (2016) Comparative test for the upgrading of lead in Sabon Layi Lead–Zinc ore (Alkaleri Local Government Area, Bauchi State). Using gravity and froth flotation beneficiation methods. Infogain Publication. Int J Adv Eng Manage Sci (IJAEMS) 2(6). ISSN: 2454-1311

23. Nnanwube IA, Onukwuli OD (2018) Hydrometallurgical processing of a Nigerian Galena ore in nitric acid: characterization and dissolution kinetics. J Min Mater Charact Eng 6:291–293
24. Kinnaird JA, Bowden P, Ixer RA, Odling NWA (1985) Mineralogy, geochemistry and mineralization of the Ririwai complex, Northern Nigeria. J Afr Earth Sci 3(1/2):185–222
25. Ogwuegbu M, Onyedika G, Hwang JY, Ayuk A, Peng Z, Li B, Ejike ENO, Andriese M (2011) Mineralogical characterization of Kuru Cassiterite ore by SEM-EDS, XRD and ICP techniques, USA. J Min Mater Charact Eng 10(9):855–863. jmmce.org
26. Thomas DG, Yaro SA (2016) Characterization of Haita-Vom cassiterite ore using X-ray flourescence (XRF) spectrometry and scanning electron microscope (SEM). Niger Soc Min Eng Niger Min J 14(1):27–31. ISSN 1117-4307
27. Abere DV, Oyatogun GM, Abioye AA, Rominiyi AL, Abioye OP, Yaskuma U, Onotu GO, Ogar MO, Oyatogun AO, Igbonwelundu MT, Filusi GF, Akinwole IE (2017) Comparative study of local mining methods and assay of cassiterite with other alluvial mineral deposits in Kuru-Jantar, Plateau State, Nigeria. Am J Min Metall 4(1):51–61. https://doi.org/10.12691/ajmm-4-1-5
28. Abere DV, Oyatogun GM, Ayodele TJ, Ogar MO, Ohwoekevwo JU, Adejo OH (2018) Upgrading of tin in Kudedu cassiterite (tin ore) deposit using air floating and 3D-magnetic beneficiations techniques. Open Sci J Anal Chem 3(3):28–32
29. Ajayi JA (2003) Mineralogical studies of the gold ore of Ilesha area, Southwestern Nigeria (Nigerian Mining and Geosciences Society (NMGS), Nigeria). J Min Geol 39(2):63–70
30. Danbatta UA, Abubakar YI, Ibrahim AA (2008) Geochemistry of gold deposits in Anka Schist Belt, Northwestern, Nigeria. Niger J Chem Res 13
31. Eisonlohr D, Groves DI, Partington GA (1989) Miner Deposita 24
32. Powell R, Will TM, Phillips GN (1991) J Metall Geol 12:141
33. Kerrich R, Fryer BJ (1979) Can J Earth Sci 16:440
34. Garba I (2000) J Afr Earth Sci 31:433
35. Koln RS (1982) Fortschr Miner 60(2):235
36. Ramadan TM, Fattah MFA (2010) Characterization of gold mineralization in Garin Hawal area, Kebbi State, Northwestern Nigeria, using remote sensing. Egypt J Remote Sens Space Sci 13:153–163 (National Authority for Remote Sensing and Space Sciences printing by Elsevier B.V.). https://doi.org/10.1016/j.ejrs.2009.08.001
37. Ogundare OD, Adeoye MO, Adetunji AR, Adewoye OO (2014) Beneficiation and characterization of gold from Itagunmodi gold ore by cyanidation. J Min Mater Charact Eng 2:300–307. https://doi.org/10.4236/jmmce.2014.24035
38. Ayodele OS, Oshin OO, Awokunmi EE (2017) Auriferous showings in the bedrocks and stream sediments of Okemesi-Ijero area, southwestern Nigeria. Am J Earth Sci 4:8–31
39. Akanmu T, Oshin OO, Ayodele OS (2019) Mineralogical characterization of the gold-bearing rocks around Okemesi-Ijero area, southwestern Nigeria. Glob Sci J 7. www.globalscientificjournal.com. ISSN 2320-9186

Kinetics of Coke Gasification Reaction Catalyzed by Alkali Carbonates

Yunpeng Fang, Shengfu Zhang, Cheng Yin, Yuhan Zhu, Rongjin Zhu and Yang Li

Abstract Coke is the main material of blast furnace (BF), and its reaction speed has an important influence on BF smooth operation. The coke reactivity is mainly affected by coke structure and mineral catalysis. The objective of the present work is to expand the catalytic mechanism of alkali carbonates on coke gasification reaction. Thermogravimetric equipment was used to carry out the non-isothermal analysis experiment and the isothermal analysis experiment. The software (FactSage 6.2) was used to carry out the thermodynamic calculation for gasification of alkali carbonates. Then, the interaction of surface activated oxygen species of C_6 clusters and alkali carbonates, the adsorption, and subsequent desorption behaviors of CO_2 on the oxygen vacant surface of Na_2O and K_2O were systematically studied by using the first-principle method based on density functional theory. The reaction path of carbon–oxygen catalytic gasification was theoretically analyzed to explain the reaction mechanism of catalytic gasification.

Keywords Coke · Alkali carbonates · Gasification reaction kinetics · First-principle method

Introduction

The gasification reactivity of coke is one of the main thermal properties in blast furnace production and the alkali metals, alkaline earth metals, and some transition metals of group VIII have certain catalytic effects on coal gasification and coke gasification, and the catalytic effects will cause the degradation of coke properties [1, 2]. Wang et al. [3] analyzed the coke with different potassium carbonate and sodium carbonate adsorption (with concentration of 5–15%) and found that Na_2CO_3 had good fluidity and poor volatility and was easy to interact with minerals in coke ash, leading to the catalytic activity of Na_2CO_3 stronger than K_2CO_3. Zhou et al. [4] studied the catalytic effect of KCl, NaCl, Na_2CO_3, and K_2CO_3 by loading them into

Y. Fang · S. Zhang (✉) · C. Yin · Y. Zhu · R. Zhu · Y. Li
College of Materials Science and Engineering, Chongqing University, Chongqing 400044, China
e-mail: zhangsf@cqu.edu.cn

J. Li et al. (eds.), *Characterization of Minerals, Metals, and Materials 2020*,
The Minerals, Metals & Materials Series,
https://doi.org/10.1007/978-3-030-36628-5_6

coke with dipping method and found that the catalytic effect was successively K_2CO_3 > Na_2CO_3 > KCl > NaCl. Fan et al. [5] also studied the influence of alkali metals on gasification activity and microcrystalline structure of coke by dipping method, the results showed that the catalytic effect of Na was stronger than that of K in the early stage of gasification reaction, and the effect was opposite in the late stage.

But the previous researches mainly focused on the macroscopic experimental phenomena to explain the mechanism of coke dissolution in blast furnace, but the systematic researches on the catalytic thermodynamics and dynamics of alkali metals reaction to coke gasification were few. In this study, the thermodynamic calculation software (FactSage 6.2) was carried out to calculate the thermodynamics of coke gasification reaction adding Na_2CO_3 and K_2CO_3 and then studied the catalytic process of Na_2CO_3 and K_2CO_3 on coke gasification reaction by thermogravimetric experiment, and analyzed the influence of Na_2CO_3 and K_2CO_3 on the characteristic temperature of coke gasification reaction. Then, the interaction of surface activated oxygen species of C_6 clusters and alkali carbonates, the adsorption, and subsequent desorption behaviors of CO_2 on the oxygen vacant surface of Na_2O and K_2O were systematically studied by using the first-principle method based on density functional theory, and the catalytic mechanism of Na_2CO_3 and K_2CO_3 on coke gasification reactions is clarified, providing theoretical support for the subsequent process research.

Experimental

Sample Preparation

The coke samples used in the experiment are self-made coke in the laboratory. The coal type and ratio refer to the production practice of a steel enterprise. The proximate analysis and ultimate analysis are described in Table 1, characterized by Chinese Standard Methods GB/T 212-2008, GB/T 31391-2015. And the ash analysis is shown in Table 2.

Table 1 Proximate and ultimate analysis of coke

Proximate analysis (wt%)				Ultimate analysis (wt%)			
M_{ad}	V_{ad}	A_{ad}	FC_{ad}	C_d	O_d	N_d	H_d
0.25	1.93	15.26	82.56	85.25	0.11	0.67	0.34

Table 2 Ash analysis of coke

SiO_2	Al_2O_3	Fe_2O_3	CaO	MgO	TiO_2	P_2O_5	K_2O	Na_2O
47.00	34.87	5.98	3.21	0.64	1.64	0.39	0.61	0.92

Non-Isothermal Kinetic Experiments and Isothermal Kinetic Experiments

The prepared coke samples were crushed to 150 ~ 200 microns and then dried to a constant mass at 105 (±5) °C. During the experiment, 10 g of dried coke powder was accurately weighed and mixed according to Table 3. The mixed samples were fully mixed in agate mortar for 30 min to ensure even mixing of the samples. After that, they were put into sample bags for marking and placed in dry and ventilated places for later use.

The experiment was carried out on thermogravimetric balance. Before the experiment, argon was injected into the thermal balance at a flow rate of 80 ml/min for 30 min to exhaust air, and then, a small amount of mixed coke powder (50 mg) was accurately weighed and placed in a corundum crucible for non-isothermal experiment. At this time, argon valve was closed, and CO_2 was injected at a flow rate of 60 ml/min. In this experiment, the temperature rise rate was set by the programmed temperature rise control system. Firstly, the temperature rose to 600 °C at the rate of 10 K/min, and then to 1200 °C at the rate of 5 K/min. After that, the temperature rise was stopped, and the sample was cooled to room temperature by argon gas.

Isothermal kinetics experiments were also carried out on the thermobalances. Before the experiment, argon was injected into the thermogravimetric balance at a flow rate of 80 ml/min for 30 min to exhaust air, and then, a small amount of mixed powder (50 mg) was accurately weighed and placed in the corundum crucible. In this experiment, the temperature rise rate was set through the programmed temperature rise control system. Firstly, argon gas was heated to 1100 °C at the rate of 100 K/min, and then, CO_2 was injected at the gas flow rate of 60 ml/min. Then, the sample was insulated at 1100 °C until the quality of the sample was no longer changed.

Table 3 Experimental scheme for the mixing of alkali carbonates with coke

The sample names	Ratio
Raw-coke	100%Coke
C–N1	1% Na_2CO_3 + 99%Coke
C–N2	2% Na_2CO_3 + 98%Coke
C–N3	3% Na_2CO_3 + 97%Coke
C–K1	1% K_2CO_3 + 99%Coke
C–K3	3% K_2CO_3 + 97%Coke
C–K5	5% K_2CO_3 + 95%Coke

Results and Discussion

Thermodynamic Calculation

After adding Na_2CO_3 and K_2CO_3, Na_2CO_3 and K_2CO_3 are reduced by fixed carbon or CO in coke during the process, and the possible reactions are shown in Eqs. (1)–(4) [6, 7].

$$K_2CO_3 + 2C = 2K + 3CO \tag{1}$$

$$Na_2CO_3 + 2C = 2Na + 3CO \tag{2}$$

$$Na_2CO_3 + CO = 2Na + 2CO_2 \tag{3}$$

$$K_2CO_3 + CO = 2K + 2CO_2 \tag{4}$$

Figure 1 is a schematic diagram of temperature variation of Gibbs free energy of coke added with Na_2CO_3 and K_2CO_3 in the gasification reaction process calculated by FactSage 6.2 software. It can be seen from Fig. 1 that the gasification reaction of coke may occur at 700 °C, but compared with the previous study, the gasification reaction obviously occurs when the temperature is higher than 900 °C.

For the gasification experiment with the coke added Na_2CO_3 and K_2CO_3, the critical temperature for the reduction was 1100 and 1160 °C [8], respectively, and at this temperature, the gasification reaction of coke in this experiment has basically ended, so the above reduction process can be ignored.

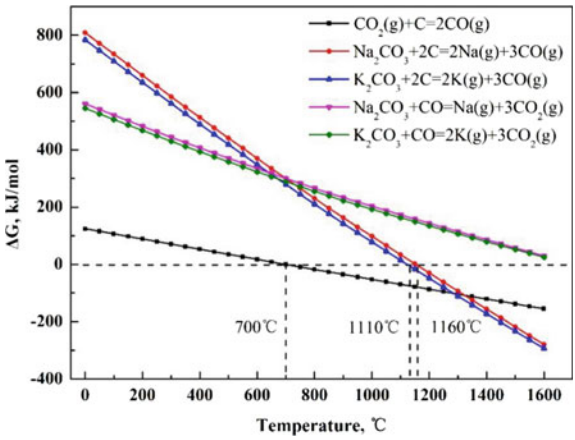

Fig. 1 Change of Gibbs energy of possible reduction reactions of sodium carbonate and potassium carbonate at different temperatures

Effects of Sodium Carbonates and Potassium Carbonates on Characteristic Temperature of Coke Gasification Reaction

The effects of Na_2CO_3 and K_2CO_3 on conversion rate and reaction rate of coke gasification reaction are shown in Fig. 2a and b. The effect of Na_2CO_3 on conversion rate and reaction rate of coke gasification reaction is similar to that of K_2CO_3. It can be seen from Fig. 2a and b that at the same temperature before the end of the reaction, coke conversion rate increases with the increase in Na_2CO_3 and K_2CO_3

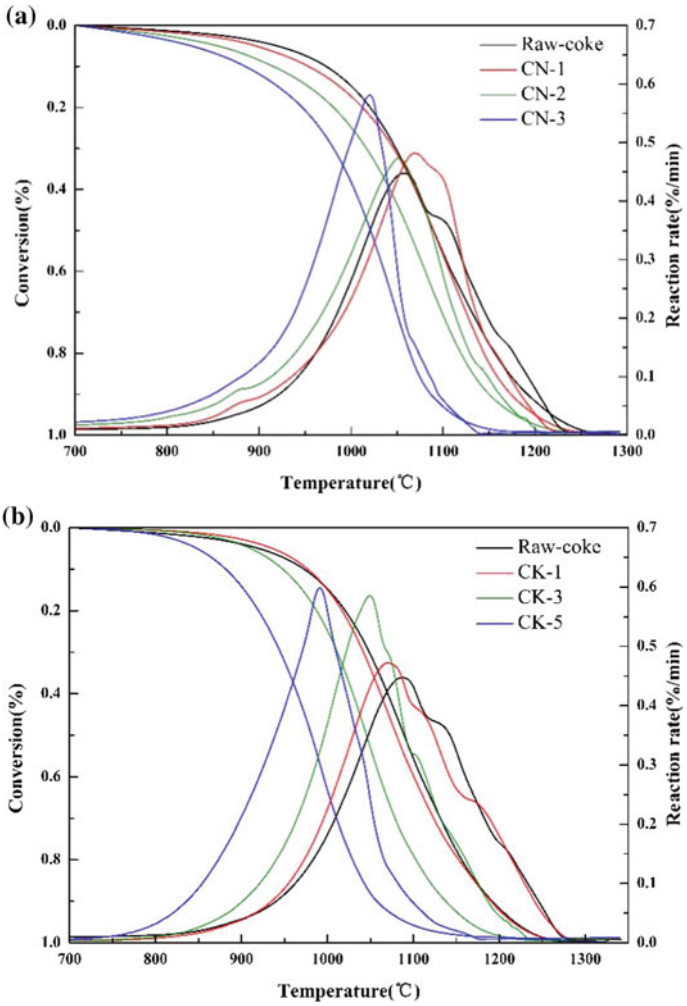

Fig. 2 Carbon conversion and normalized reaction rate versus temperature in gasification with different content of alkali carbonates ($\beta = 50$ °C/min)

Table 4 Influence of sodium carbonate and potassium carbonate on the characteristic temperatures of coke gasification

The sample names	Characteristic temperature (°C)		
	T_0	T_{max}	T_f
Raw-coke	991	1088	1190
C–N1	986	1098	1194
C–N2	959	1079	1166
C–N3	928	1047	1117
C–K1	981	1069	1181
C–K3	915	1049	1126
C–K5	879	991	1043

content. When the addition amount of Na_2CO_3 is 3% and the addition amount of K_2CO_3 is 5%, the coke prepared has the fastest complete reaction. Meanwhile, with the increase in Na_2CO_3 and K_2CO_3 content, the maximum reaction rate of coke gasification reaction also increases.

In order to better study the catalytic mechanism of alkali carbonates, the concept of characteristic temperature is introduced into this study by referring to the thermal analysis method proposed by Liu et al. [9]. Table 4 shows the characteristic temperature of coke gasification reaction after adsorption of Na_2CO_3 and K_2CO_3, from which it can be seen that both Na_2CO_3 and K_2CO_3 can reduce the initial reaction temperature and intense reaction temperature of coke gasification reaction, and with the increase in Na_2CO_3 and K_2CO_3 content, the initial reaction temperature and intense reaction temperature of coke gasification reaction gradually move to the low temperature zone. When the addition of K_2CO_3 reaches 3%, the initial reaction temperature, end reaction temperature, and intense reaction temperature of gasification reaction can be significantly reduced. Compared with the influence of K_2CO_3 on coke gasification reaction, the characteristic temperature of coke gasification reaction is not obvious after adding Na_2CO_3.

Gasification Kinetics of Coke with Alkali Metal Carbonates

Generally speaking, Coats-Redfern method and Metzger method are two integral methods for solving gas–solid reaction dynamics [10–12]. In this paper, Coats-Redfern method is adopted and the equation is as follows:

$$\ln\left[\frac{G(x)}{T^2}\right] = \ln\left(\frac{AR}{\beta E}\right) - \frac{E}{RT} \tag{5}$$

where $G(x)$ is the integral expression of gasification reaction mechanism function.

Ten different gas–solid reaction mechanism functions are selected to fit the data of coke gasification [13–15]. By comparing the correlation coefficient R^2 in the linear

fitting process, the model ($g(x) = 2(1-x)\,[-\ln(1-x)]^{1/2}$, $G(x) = [-\ln(1-x)]^{1/2}$) is determined to be the optimal model to describe the gasification reaction.

By linear fitting $\ln(\beta/T^2)$ and $1/T$, the apparent activation energy of the reaction can be calculated from the slope of the fitting curve, and the frequency factor A of the reaction can be calculated according to Eq. 5. The calculation results are shown in Table 5. Figure 3 shows the relationship between $\ln[G(x)/T^2]$ and 1/T in the gasification reaction of coke containing alkali carbonates. When the alkali carbonates content is low, the first-order reaction follows, while when the alkali carbonates content is high, the second-order reaction follows, indicating that chemical reaction is the restrictive link of coke gasification reaction. Combining with the kinetic parameters can be seen in Table 5, apparent activation energy and frequency factor, the original focus of the average apparent activation energy and frequency factor (average E_a = 172.9942 kJ/mol, average $\ln(A)$ = 45.187 s^{-1}) were higher than other samples corresponding numerical (average E_a = 129.3654–161.3654 kJ/mol, average $\ln(A)$ = 38116–42.231 s^{-1}). This shows the original reaction of coke is the most difficult of the sample decomposition and the most complicated. On the other hand, with the addition of Na_2CO_3 and K_2CO_3, the E_a and $\ln(A)$ of the samples showed a gradually decreasing trend, indicating that the coke gasification reaction was easier with the increase of alkali metal carbonate content, and the alkali metal carbonate promoted the coke gasification reaction. The results show that alkali carbonates can promote the gasification of coke in the gasification process, and the reactivity of coke gasification is reduced, so that the reaction is more favorable to gasification.

Table 5 Kinetic parameters of coke after gasification

Samples	Raw-coke	CN-1	CN-2	CN-3	CK-1	CK-3	CK-5
E (kJ/mol)	172.99	161.37	155.24	152.37	159.79	146.35	129.37
$\ln(A)$ (s^{-1})	45.19	42.23	41.27	41.65	42.36	40.62	38.12

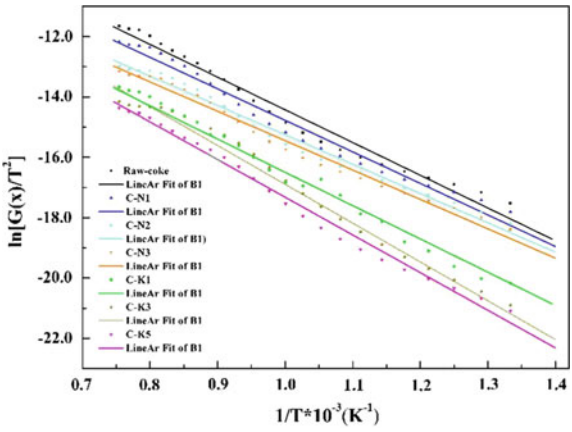

Fig. 3 Arrhenius plots of coke gasification by alkali carbonates with different contents

Catalytic Mechanism of Alkali Carbonates on Coke Gasification Reaction

For this section, mainly adopting the first-principle method based on density functional theory of the system studied the C_6 clusters and Na_2O and K_2O surface activated oxygen species interactions [16–18], CO_2 in Na_2O and K_2O adsorption on the surface of the oxygen vacancy and subsequent stripping behavior from the theoretical analysis of carbon–oxygen catalytic gasification reaction path, catalytic gasification reaction mechanism.

Figure 4 shows the coke gasification reaction path and the energy change, and the gasification reaction in initial stage is mainly for the CO_2 adsorption process of coke on the C_6 clusters. In the process, C–C bonds in C_6 clusters fracture, then the C bonds combined with C in the CO_2 generate new C–C bonds, and the structure energy after restructuring is 0.69 eV higher than unreacted structure, which shows that the process is the endothermic process. The process from P1 to P2 is the migration and transformation of oxygen in the C–O bonds, and then from P2 to P3 is the desorption process of CO from the carbon chain. In this process, two C–C bonds break and absorb a large amount of heat (2.91 eV), which is the limiting link of the reaction.

Figure 5a shows the reaction path and energy change of sodium carbonate-absorbed coke after gasification. During the gasification reaction, Na_2CO_3 is decomposed into oxide, so Na_2O is selected as the base catalyst in the simulation. C_6 clusters in the gasification reaction initial stage are mainly adsorbed on the Na_2O basement, the C_6 molecules absorbed activate, C–C bonds fracture, and absorb energy is 0.35 eV, the C bonds fractured damage Na–O bonds structure in Na_2O, and combined with O generate C–O bond, which compared with the original coke gasification of C–C bonds fracture in C_6 clusters, the lower energy (down from 0.69 to 0.35 eV) needed, shows that adding Na_2O can reduce the energy barrier of C6 fracture, promoting coke gasification reaction. In the process from P2 to P3, oxygen transfer is completed through the Na_2O matrix, and O in CO_2 is adsorbed by Na_2O with oxygen

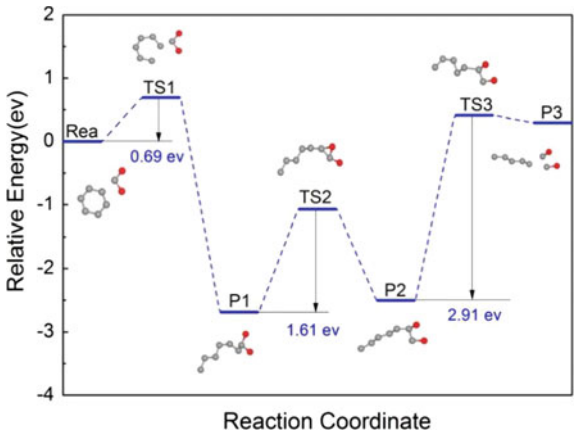

Fig. 4 Reaction path and energy change of coke gasification

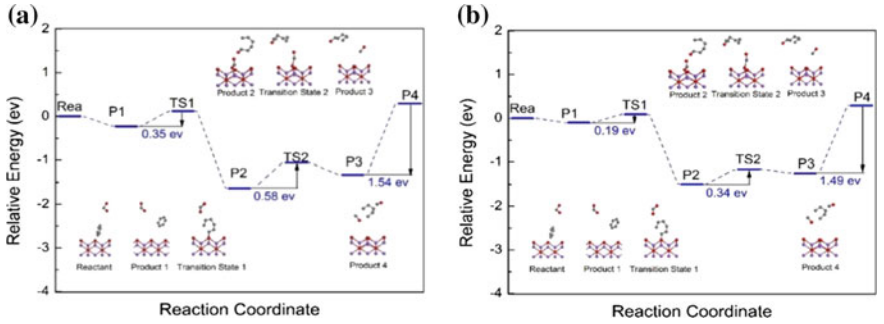

Fig. 5 Reaction path and energy change of sodium carbonate-absorbed coke after gasification

vacancy, which leads to the fracture of C–O bond in CO_2 and the formation of Na–O bond in Na_2O. In this step, the energy barrier is low (0.58 eV). In the end, the C–C bonds that connected with the C–O bonds in C_6O break and get CO, completing the whole catalytic process. As there is only one C–C bond break in this process, the energy barrier is greatly reduced (from 2.91 to 1.54 eV), and the reaction is promoted. Figure 5b shows reaction path and energy change of potassium carbonate-absorbed coke after gasification. Because during the gasification process, the change trend of reaction path and energy is similar to that of sodium carbonate-absorbed coke after gasification, we won't explore it in this article.

Conclusions

In the non-isothermal thermodynamic analysis experiment, the conversion rate of coke increases with the increase in alkali carbonates content, and the complete reaction is fastest when sodium carbonate content is 3% and potassium carbonate content is 5%. Meanwhile, with the increase in alkali carbonates content, the maximum reaction rate also increases. Both sodium carbonate and potassium carbonate can reduce the initial reaction temperature and intense reaction temperature, and with the increase in alkali carbonates content, the initial reaction temperature and intense reaction temperature gradually move to the low temperature zone. Compared with potassium carbonate, the influence of sodium carbonate on the characteristic temperature of coke gasification reaction is obviously strong.

In the kinetic analysis of coke gasification, first the optimal mechanism function was determined, then the effect law of different alkali carbonates content to reaction activation energy and pre-exponential factor was calculated. The results show that when the content of alkali carbonates is low, alkali carbonates can obviously reduce the activation energy, but when the content reaches a certain value, the effect of reducing the activation is not obvious. When the content of alkali carbonates is low,

the first reaction is followed; when the content is high, the second reaction is followed, indicating that the reaction is a restrictive link in coke gasification reaction.

Acknowledgements This work was supported by the National Natural Science Foundation of China (Grant No. 51774061) and Scientific Research Innovation Training Program for College Students in Chongqing (Grant No. S201910611300).

References

1. Veraa MJ, Bell AT (1978) Effect of alkali metal catalysts on gasification of coal char. Fuel 57(4):194–200
2. Matsukata M, Kikuchi E, Morita Y (1992) A new classification of alkali and alkaline earth catalysts for gasification of carbon. Fuel 71(7):819–823
3. Wang Y, Wang Z, Huang J et al (2015) Catalytic gasification activity of Na_2CO_3 and comparison with K_2CO_3 for a high-aluminum coal char. Energ Fuels 29(11):6988–6998
4. Zhou H, Liu R, Liu Z et al (2015) Effects of alkali metals on NO_X release during coke combustion. J China Coal Soc 40(5):1160–1164
5. Fan W, Cui T, Li H et al (2016) Influence of alkali metals and alkali earth metals on gasification activity of Shenfu coal coke. J Fuel Chem Technol 44(8):897–903
6. Li P, Liu W, Zhang H et al (2017) Impact of potassium on gasification reaction and post-reaction strength of ferro-coke. ISIJ Int 57(11):1947–1954
7. Mei Y, Wang Z, Fang H et al (2017) Na-containing mineral transformation behaviors during Na_2CO_3-catalyzed CO_2 gasification of high-alumina coal. Energ Fuels 31(2):1235–1242
8. Du X, Wang S, Li X et al (2016) Effects of alkali metal salts and elemental elements on the thermal properties of coke. Anhui Metall 47(6):28–30
9. Liu Z (2011) Thermal analysis and calorimeter and its application. Chemical Industry Press, Beijing
10. Wendlandt WW (1964) Thermal methods of analysis. Interscience Publishers
11. Cheng SZD, Li CY (2002) Structure and formation of polymer single crystal textures. Mater Sci Forum 408–412:25–38
12. Chen Y, Qi W (2007) Thermal oxidative degradation kinetics of flame-retarded polypropylene with intumescent flame-retardant master batches in situ prepared in twin-screw extruder. Polym Degrad Stab 92(2):280–291
13. Cheng SZD, Li CY, Calhoun BH et al (2000) Thermal analysis: the next two decades. Thermochim Acta 355(1):59–68
14. Yong P, Xiao CZ (2012) Investigating the structural evolution of thiolate protected gold clusters from first-principles. Nanoscale 4(14):4054–4072
15. Filatov M, Harris N, Shaik S (1999) A theoretical study of electronic factors affecting hydroxylation by model ferryl complexes of cytochrome P-450 and horseradish peroxidase. J Chem Soc Perkin Trans 2(3):399–410
16. Fujita S (2003) Oxidative destruction of hydrocarbons on a new zeolite-like crystal of $Ca1_2Al_{10}Si_4O_{35}$ including O_2^- and O_2^{2-} radicals. Cheminform 34(12):255–263
17. Xia W, Zhang D, Weng W et al (2013) Pathways between superoxide and peroxide species on small La-O clusters. Chin J Catal 34(11):2130–2137
18. Suzuki K, Li C (2015) Hydroxyl sodalite having combustion gas purification function. Appl Mech Mater 749:25–29

Part II
Advances in Characterization Methods II

Phase Transformation Characterization by Means of High Temperature Digital Image Correlation for Graded Thermo-Mechanical Processing of Steel Sheet Parts

A. Reitz, O. Grydin and M. Schaper

Abstract By locally adjusting the microstructure during the press hardening process, the production of load-tailored safety relevant parts is possible. The thermo-mechanical treatment of 22MnB5 steel at different austenitization temperatures, cooling, and forming conditions within a sheet leads to the development of mixed microstructures, which locally influence the material properties. A high number of experiments and specimens are necessary to determine the resulting phase composition in such graded parts. Within this study, a contactless characterization method to detect local phase transformations across an inhomogeneous treated flat steel specimen is developed. Digital image correlation and infrared thermography are used to identify transformation induced local straining during the inhomogeneous thermo-mechanical treatment. Flat steel specimens of 22MnB5 steel up to a thickness of 2 mm are tested. Coupling of temperature and strain fields enables the characterization of transformation kinetics for different austenitization temperatures, cooling rates, and hot deformation strains with a reduced number of samples.

Keywords Phase transformation · Steel · Sheet material · Flat specimens · Thermal imaging · Digital image correlation

Introduction

The increased demands related to environment protection, advancing technology, and occupant safety require the application of ultra-high strength steels in the automobile sector, which can be formed by press hardening [1]. Press hardening is a thermo-mechanical forming process with intended phase transformation [2]. The blank is formed in one single step that combines forming at high temperature with a subsequently fast quenching using cooled dies [3]. The boron-alloyed steel 22MnB5 is the most commonly used steel grade in press hardening processes [4]. If the cooling rate exceeds a minimum of approximately 27 K/s, at a temperature of around 400 °C,

A. Reitz (✉) · O. Grydin · M. Schaper
Department of Materials Science, Paderborn University, Paderborn, Germany
e-mail: reitz@lwk.upb.de

J. Li et al. (eds.), *Characterization of Minerals, Metals, and Materials 2020*,
The Minerals, Metals & Materials Series,
https://doi.org/10.1007/978-3-030-36628-5_7

a diffusionless martensitic transformation will be induced, which is responsible for the high strength of the press hardening part [3]. The resulting microstructure of the press hardening components is closely related to the thermo-mechanical process of the 22MnB5 sheets [5]. Several sheet metal parts manufactured by the conventional press hardening process would benefit of regions with a reduced strength but higher ductility in order to enhance their crashworthiness [6]. This can be achieved, for example, by specific austenitization, cooling, or annealing strategies [7]. One example is the B-pillar automotive component in which the bottom part should have higher energy absorption capacity than the one provided by a fully martensitic structure in order to enhance the side crash performance, whereas the upper part must retain the martensitic structure to show high intrusion resistance [6]. Investigations on the thermo-mechanical properties at different annealing temperatures have shown that for the applicability of lower annealing temperatures to achieve a lower ductility profile for components with tailored properties, a temperature lower than 825 °C has to be chosen to assure a significantly lower strength and hardness than that of commonly press hardened sheet metal [8]. Depending on the initial grain size, carbon content, austenitization temperature, dwell time, forming conditions, and the cooling rate, a various mixed microstructure can be reached.

Monitoring of phase transformations and the knowledge of continuous cooling transformation (CCT) diagrams are important to get a component with the above mentioned properties [9]. When steel undergoes a phase transformation, the lattice structure will become altered and, as a rule, produce a change in specific volume [10]. Phase transformations are exothermal, and when plotting the thermal data, they appear as small deviations from the otherwise smooth cooling curve [11]. Therefore, phase transformations can be observed by dilatometry, differential thermal analysis, or differential scanning calorimetry [9]. With dilatometer tests, phase transformations can be detected, and CCT diagrams can be developed. Results of these investigations often have to be confirmed by means of micrographs and hardness tests because phase transformations in multiphase steels are very complex [9]. Most of the phase transformation studies for ferritic or austenitic steels were based on isothermal treatments, which usually require a large number of specimens for a complete description of all transformations [12]. Using dilatometry to determine the resulting mixed microstructure for a graded component like a B-pillar would lead to both a high number of dilatometer tests and a high experimental effort.

The present study aims to investigate a contactless characterization method for the analysis of phase transformations for graded thermo-mechanical processed flat steel specimens made of 22MnB5. Therefore, high temperature digital image correlation (DIC) and thermal imaging were used for the investigations.

Experimental Procedure

For the high temperature DIC tests, uncoated 22MnB5 specimens with a thickness of 1, 1.5, and 2 mm were cut following the rolling direction of the sheets by wire-cut EDM. The chemical compositions of the steel sheets are presented in Table 1.

Figure 1 shows the experimental setup for the high temperature DIC tests. A medium frequency generator from Trumpf Hüttinger with a maximum power of 10 kW and a frequency of 250 kHz was used in this study, to heat the flat steel specimens with a frontal inductor. It allows fast heating of the specimens up to 1000 °C. Mechanical testing was conducted on an MTS Landmark universal testing machine. The frontal inductor was moved in front of the specimen until a coupling distance of about 2 mm between the specimen and the inductor was reached.

For the DIC tests, the specimens were painted with a black high temperature varnish, and the speckle pattern was sprayed using a white high temperature varnish of the same type. Temperatures within a range of 250–1000 °C were recorded with an FLIR thermal imaging camera. This was necessary to detect the martensite start

Table 1 Initial grain size and chemical composition of the investigated 22MnB5 flat steel sheets

Thickness (mm)	Initial grain size (μm)	C%	Si%	Mn%	Cr%	B%	Ti%	Fe%
1.0	5.84	0.230	0.180	1.191	0.191	0.0025	0.025	97.98
1.5	6.88	0.219	0.200	1.185	0.193	0.0020	0.027	97.95
2.0	7.65	0.236	0.218	1.188	0.181	0.0022	0.025	97.95

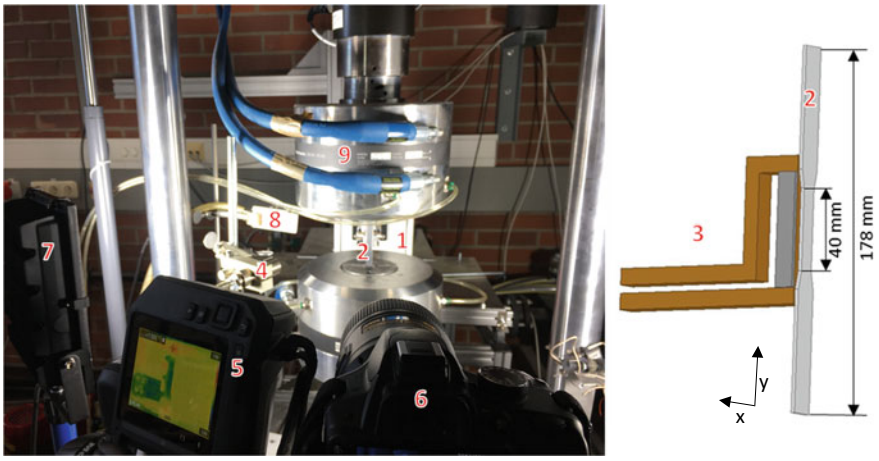

Fig. 1 Experimental setup for the characterization of phase transformations: (1) medium frequency oscillator, (2) specimen, (3) frontal inductor with magnetic flux concentrator, (4) ratio pyrometer 300–1500 °C, (5) thermal imaging camera 250–1200 °C, (6) digital camera, (7) LED spotlight, (8) air nozzle, and (9) servo-hydraulic testing machine

Table 2 Experimental plan for the thermal and thermo-mechanical treatment of the flat steel specimens

Specimen	Thickness (mm)	Austenitization temperature (°C)	Dwell time (s)	Cooling method	Treatment
P1	2	850	10	Ambient air	Thermal
P5	1.5	850	10	Air pressure	Thermal
P7	2	950	300	Ambient air	Thermo-mechanical

and finish (M_s and M_f) temperatures for an austenitization temperature of about 850–950 °C [13]. The emission coefficient for the thermal imaging camera was determined by a comparison measurement with a ratio pyrometer.

The geometry of each specimen was flat with a length of 178 mm as depicted in Fig. 1. In all tests, the specimens were heated up to a temperature of about 850 or 950 °C via induction heating and then cooled down by ambient air or quenched by compressed air (Table 2). GOM correlate was used to calculate the local strain during the cooling of the specimens. The influence of the surface radiation due to high temperature was significantly minimized by the camera settings in combination with two LED-spotlights. Pictures for the DIC-evaluation were done every second by automatic triggering. In the first test phase, the specimens were fixed on one side in front of the inductor, and only a thermal treatment was done, to proof the feasibility of the contactless characterization method. After that, the specimens were cut for hardness testing and metallographic analysis. The thermo-mechanical treatment was performed after a dwell time of 5 min with a test speed of 1 mm/s until a total elongation of 10% was reached. Then, the specimen was immediately cooled by means of ambient air.

Due to the heating principle and the shape of the inductor, the centre of the specimen was its hottest area (Fig. 2). An almost homogenous temperature field (±2.5 °C) existed only in an area of 25 mm^2 around the hottest temperature point. The possibility of investigating different austenitization temperatures with one specimen is a big benefit of this heating principle.

With the data from the GOM correlate system and the thermal analysis, it is possible to contrast the changes in strain and temperature for all specimens. Diagrams like Fig. 3 were constructed to graphically determine when the phase transformations start and end. This was done with a high magnification. The $D\varphi_y/DT$ curve shows the ratio of the change in strain and temperature as a function of time for an investigated area of the specimen. If this curve indicates a deviation from the usually horizontal course of the graph and if additionally small deviations from the otherwise smooth cooling curve are apparent, a phase transformation took place. Three characteristic areas were investigated for each specimen to verify the functionality of the method (Fig. 2). The cooling rate of each viewed area was calculated according to [14]:

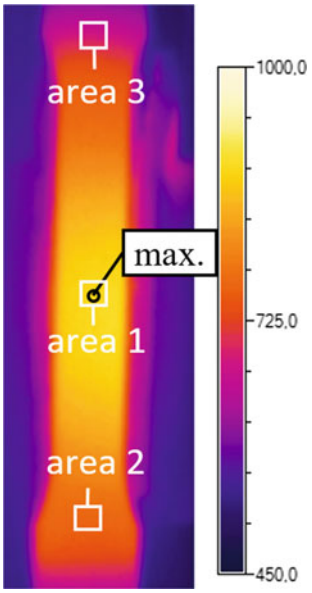

Fig. 2 Thermal image of a heated specimen

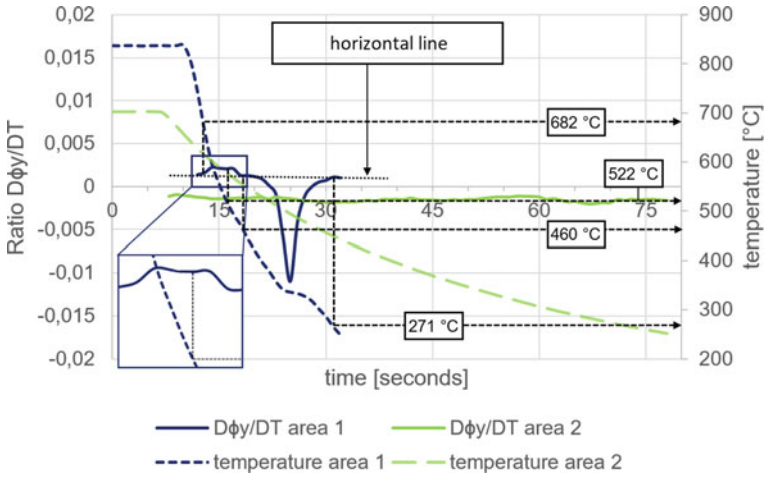

Fig. 3 Temperature-time curve and ratio of $D\varphi_y/DT$ for specimen P5 (area 1 plotted) with a cooling rate of about 52 K/s and specimen P1 (area 2 plotted) with a cooling rate of about 12 K/s

$$\text{cooling rate} = \frac{\text{temperature range from } 800 \text{ to } 500\,^{\circ}\text{C}}{\text{time taken from } 800 \text{ to } 500\,^{\circ}\text{C during cooling}}$$

To investigate the microstructure and hardness, optical light microscopy (Zeiss Axiophoto) and an automatic hardness tester (KB 30 FA) were utilized. To create micrographs, all specimens were etched with 2% Nital. The chemical composition of Table 1 was performed by spark spectroscopy.

The general experimental plan for the thermal and thermo-mechanical treatment of the flat steel specimens is presented in Table 2.

Results and Discussion

Phase Transformation Analysis

Figure 3 shows the results for the heat treatment of the flat steel specimens with a thickness of 2 and 1.5 mm. Area 2 of specimen P1 indicated no phase transformations. The cooling curve showed no jumps or deviations from its smooth course. In addition, the $D\varphi_y/DT$ curve did not significantly deviate from its horizontal course either. The temperature of area 2 was about 700 °C and according to [13] beneath the austenite start temperature (Ac_1) of 720 °C, which was determined for a heating rate of 5 K/s. With the used heating principle, higher heating rates were achieved. According to [15], a high heating rate above 500 K/s results in a longer-term transformation of ferrite to austenite. The Ac_1 temperature and the finish temperature of primary ferrite to austenite transformation (Ac_3) increased compared to the literature, which described lower heating rates.

In contrast to area 2 of specimen P1, the cooling curve for the investigated area 1 of specimen P5 shows deviations. Phase transformations could be detected via the $D\varphi_y/DT$ curve. The curve displays two larger peaks, which would indicate at least two phase transformations. If start and end point of the first peak were transferred to the cooling curve, a start temperature of about 682 °C and an end temperature of about 460 °C could be detected for the first phase transformation. This end temperature is also the beginning of the next phase transformation, which ends at about 270 °C. In compliance with the relative large deviation, the last transformation indicates that the last phase should have the highest proportion. In [16], the CCT diagram shows a ferritic transformation at a temperature of about 670 °C and a martensite finish temperature of about 270 °C for a cooling rate of about 12 K/s, which could be related to the results of the new characterization method in Fig. 3.

Figure 4 shows the temperature-time curve and ratio of $D\varphi_y/DT$ for specimen P7 for area 1 and area 3. No phase transformation could be detected in area 3, which correlates with the associated temperature-time curve. The $D\varphi_y/DT$ curve of area 1 indicates, with reference to the start temperature of 570 °C and end temperature of 400 °C, one phase transformation, which should be the bainitic transformation. According to [17], a hot plastic deformation increases the mean value of the B_s (bainite start temperature) from 580 to 600 °C, but the effect will be decreased by a reduction of the cooling rate. The M_s temperature was about 400 °C, while in

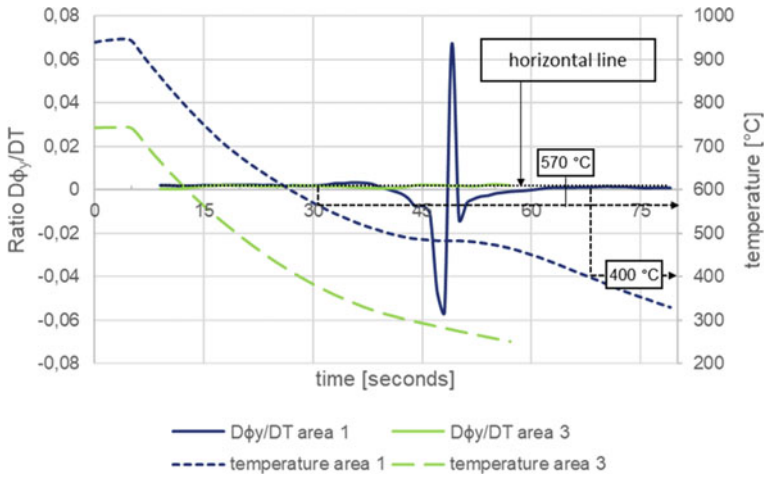

Fig. 4 Temperature-time curve and ratio of $D\varphi_y/DT$ for specimen P7 (10% elongation; area 1: cooling rate 11 K/s; area 3: cooling rate 17 K/s)

this study no martensite transformation could be detected with the method. Area 3 potentially had a higher cooling rate than area 1 since the clamping jaws of the MTS testing machine were water-cooled.

The thermo-mechanical treatment of specimen P7 showed that not the whole area of the sample could be analysed due to lower elongation of the high temperature coating. Because of the ceramic basis of the high temperature coating, cracks appear within the coating (Fig. 5a), which enhanced scaling on the surface of the specimen. This led to the occurrence of spalling and to not evaluable areas (Fig. 5b).

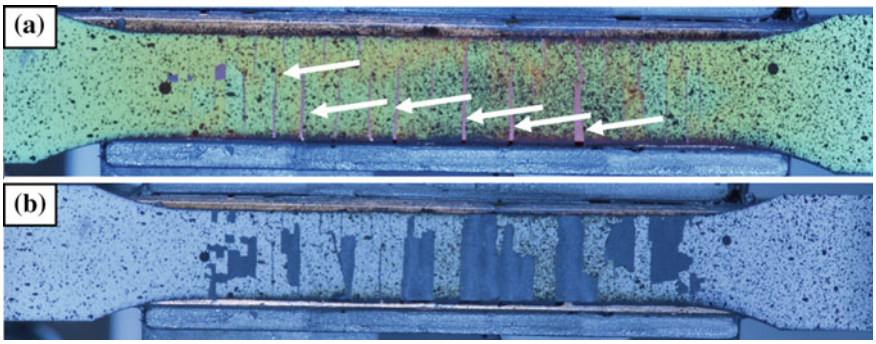

Fig. 5 **a** Cracks within the coating of specimen P7 after 10% elongation directly before cooling, **b** spalling of the coating after cooling

Microstructural and Hardness Analysis

Micrographs and hardness for the specific areas of the specimen P1, P5, and P7 are presented in Fig. 6. In comparison with the initial state, specimen P1 marginally changed in its microstructure and hardness (Fig. 6a and b). The lower hardness could be explained with a short soft annealing, within area 2 of P1. Järvinen et al. investigated different initial microstructures and their effect on the final material properties. Within their study an annealing process above the Ac_1 temperature produced a similar microstructure but with a higher hardness of about 210 HV [18]. An annealing for 5 min above the Ac_3 temperature combined with a subsequent cooling rate of 9 K/s leads to a mixed microstructure with ferrite, bainite, and martensite [16]. Since area 2 was heated beneath the Ac_1 temperature, no phase transformation could take place. In addition, Fig. 6b validates the result of the $D\varphi_y/DT$ curve, which indicated that no phase transformations took place.

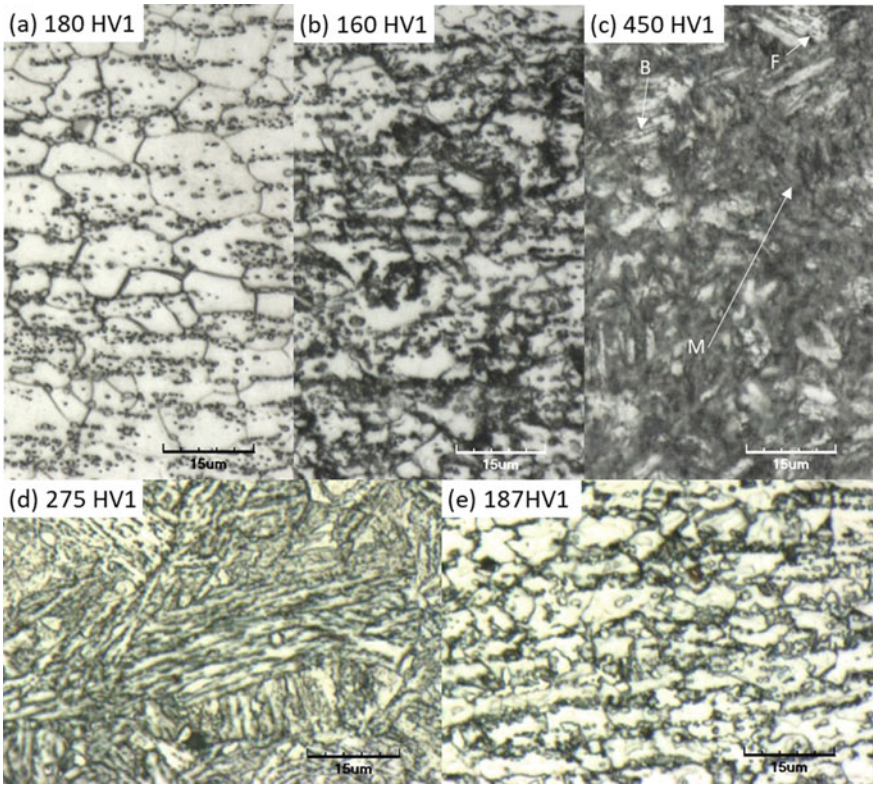

Fig. 6 Micrographs and average hardness of **a** initial state, **b** specimen P1 area 2, **c** specimen P5 area 1, **d** specimen P7 area 1, and **e** area 3 (F: ferrite, B: bainite, M: martensite)

In Fig. 4c, a mixed microstructure is visible within area 1 of specimen P5. It contains a high amount of martensite with small amounts of ferrite and bainite. According to Salzgitter Flachstahl [19], the hardness of 22MnB5 steel sheets after austenitization and immediate water quenching can reach about 500 HV1. The high hardness of 450 HV1 indicates a high amount of martensite. Figure 3 showed at least two phase transformations though the enlarged section reveals a second increase of the curve after a slight drop, which could indicate the beginning of a third phase transformation. Since three different microstructure constituents are visible in Fig. 6, this transformation must be the bainitic. Based on the results of [15], that high heating rates shift the Ac_1 and Ac_3 temperatures to higher temperatures and the short time austenitization was done below the Ac_3 temperature of 880 °C [13], and the start of quenching was realised within the inhomogeneous austenite area. This could explain why area 1 had a mixed microstructure although a high cooling rate of 40 K/s was reached. According to [13], a cooling rate above 25 K/s should have led to the formation of a fully martensitic microstructure.

Figure 6d shows a bainitic microstructure with a hardness of about 275 HV1. No martensitic microstructure could be found within this area, which supports the results of Fig. 4. The $D\varphi_y/DT$ curve illustrates that there only was a bainitic transformation, which could be verified by the micrograph. According to [13], a continuous cooling rate of about 11 K/s should have led to the formation of a mixed microstructure with ferrite, martensite, and a high amount of bainite. Since the deformed CCT diagram was developed for a strain of about 0.4, a complete comparison with this study was not possible. Further investigations by scanning electron microscopy are planned to specify exactly, which metallographic constituents exist within this area.

A ferritic-perlitic microstructure was detected in area 3 of specimen P7 (Fig. 6e). Since the microstructure consisted of finer grains compared to Fig. 6a and 6b, a recrystallization during the thermo-mechanical treatment could have taken place. This could explain a higher hardness in contrast to Fig. 6a and b.

Conclusions and Outlook

A new characterization method to determine phase transformations was studied based on a thermo-mechanical treatment of flat steel samples. The results can be summarized as follows:

- Phase transformations could be detected with a new contactless characterization method and validated with micrographs and hardness tests
- The dimensions of the peaks indicate the extend of a phase
- For thermo-mechanical treatments, the specimens should be painted with a high temperature coating, which could enable a higher elongation to guarantee a full analysis of the specimens.

In further studies, the accuracy of the characterization method should be verified with already determined CCT diagrams for 22MnB5. Furthermore, the same forming, heating, and cooling conditions should be applied for the treated specimens.

Acknowledgements The authors thank the German Research Foundation (DFG) for financial support of the project SCHA 1484/38-1.

References

1. Merklein M, Stöhr T, Svec T, Wieland M (2010) Funktionsoptimierte Strukturbauteile im Presshärtprozess. Lightweight Des 3(5):52–58
2. Karbasian H, Tekkaya AE (2010) A review on hot stamping. J Mater Process Technol 210(15):2103–2118
3. Venturato G, Novella M, Bruschi S, Ghiotti A, Shivpuri R (2017) Effects of phase transformation in hot stamping of 22MnB5 high strength steel. Procedia Eng 183:316–321
4. Naderi M, Ketabchi M, Abbasi M, Bleck W (2011) Analysis of microstructure and mechanical properties of different boron and non-boron alloyed steels after being hot stamped. Procedia Eng 10:460–465
5. Min J, Lin J, Min YA (2013) Effect of thermo-mechanical process on the microstructure and secondary-deformation behavior of 22MnB5 steels. J Mater Process Technol 213(6):818–825
6. Merklein M, Wieland M, Lechner M, Bruschi S, Ghiotti A (2016) Hot stamping of boron steel sheets with tailored properties: a review. J Mater Process Technol 228:11–24
7. Merklein M, Lechler J, Svec T (2009) Verformungsabhängiges Umwandlungsverhalten von presshärtbaren Bor-Mangan-Stählen. In: Proceedings of the 4th Erlanger workshop, pp 143–161
8. Stöhr T, Lechler J, Merklein M (2009) Investigations on different strategies for influencing the microstructural properties with respect to partial hot stamping. In: 2nd international conference on hot sheet metal forming of high-performance steel, pp 273–281
9. Grajcar A et al (2014) Dilatometric study of phase transformations in advanced high-strength bainitic steel. J Therm Anal Calorim 118(2):739–748
10. Gojić M, Sućeska M, Rajić M (2004) Thermal analysis of low alloy Cr–Mo steel. J Therm Anal Calorim 75(3):947–956. https://doi.org/10.1023/B:JTAN.0000027188.58396.03
11. Zachrisson J (2006) In situ detection and characterisation of phase transformations in weld metals
12. de Lima MSF, Santo AMDE (2012) Phase transformations in an AISI 410S stainless steel observed in directional and laser-induced cooling regimes. Mater Res 15(1):32–40
13. Naderi M, Saeed-Akbari A, Bleck W (2008) The effects of non-isothermal deformation on martensitic transformation in 22MnB5 steel. Mater Sci Eng A 487(1–2):445–455
14. Kumar R, Arya HK, RK S (2014) Experimental determination of cooling rate and its effect on microhardness in submerged arc welding of mild steel plate (grade c-25 as per IS 1570). J Mater Sci Eng 3(2):1–4. https://www.omicsonline.org/open-access/experimental-determination-of-cooling-rate-and-its-effect-on-microhardness-in-submerged-arc-welding-of-mild-steel-plate-grade-c-25-as-per-is-1570-2169-0022.1000138.pdf
15. Hordych I, Bild K, Boiarkin V, Rodman D, Nürnberger F (2018) Phase transformations in a boron-alloyed steel at high heating rates. Procedia Manuf 15:1062–1070
16. Nikravesh M, Naderi M, Akbari GH, Bleck W (2015) Phase transformations in a simulated hot stamping process of the boron bearing steel. Mater Des 84:18–24
17. Nikravesh M, Naderi M, Akbari GH (2012) Influence of hot plastic deformation and cooling rate on martensite and bainite start temperatures in 22MnB5 steel. Mater Sci Eng A 540:24–29

18. Järvinen H, Isakov M, Nyyssönen T, Järvenpää M, Peura P (2016) The effect of initial microstructure on the final properties of press hardened 22MnB5 steels. Mater Sci Eng A 676:109–120
19. Salzgitter Flachstahl 22MnB5—Boronalloyed quenched and tempered steel [Online]. Available https://www.salzgitter-flachstahl.de/fileadmin/footage/MEDIA/gesellschaften/szfg/informationsmaterial/produktinformationen/warmgewalzte_produkte/eng/22mnb5.pdf

Austenite Stability Under Focused Ion Beam Milling

Jian Li and Pei Liu

Abstract Artifacts from FIB milling can be of great concern. Aside from commonly known defects (e.g., Ga ion implantation, re-deposition, microstructure change due to specimen temperature increase, surface amorphization, etc.), FIB milling can even result in phase transformation in some metal alloys. Limited study has shown normal incident Ga ion beam milling which can transform austenite (FCC) to BCC structure in some stainless steels. This can be detrimental when austenite in stainless steels needs to be analyzed. However, one important question to answer is if milling in high glancing angle can result in such transformation. The susceptibility of austenite transformation to BCC structure is studied using EBSD on commercial stainless steels. When irradiated by normal incidence Ga ion beam, even with low dose, surface of SS304 and SS316 was transformed from austenite to BCC structure. However, irradiation from high glancing angle does not result in such transformation of relatively unstable austenite structure in SS304.

Keywords FCC · BCC · FIB · Phase transformation

Introduction

Precision focused ion beam (FIB) milling has become a well-established routine in microstructure characterization. Whether it is cross-sectioning, site-specific TEM specimen preparation and micro-deposition in FIB, and the high energy primary ion beam (Ga ion or Xe ion) interact with specimen and create certain degree of disturbance to the substrate material. In crystalline materials, various types of artifacts can be generated [1]. Among the commonly known artifacts, we already have very good idea on the surface amorphization, the development of short range dislocation especially on light weight metals (e.g. aluminum and magnesium alloys), formation of low melting point Ga phase [2], etc. Strategies to minimize these well-known artifacts during FIB milling are in place.

J. Li (✉) · P. Liu
CanmetMATERIALS, 183 Longwood Road South, Hamilton, ON L8P 0A5, Canada
e-mail: jlica@canada.ca

J. Li et al. (eds.), *Characterization of Minerals, Metals, and Materials 2020*,
The Minerals, Metals & Materials Series,
https://doi.org/10.1007/978-3-030-36628-5_8

Among the artifacts, there are few reports on FIB milling induced phase transformation. Knipling et al. [3] studied phase transformation of three austenitic stainless steels upon Ga ion beam milling. Among the three alloys, even when milling with very low dose, austenite (FCC) was found to transform to BCC in two ferrous alloys that have less stable austenite phase. The austenite phase in super-austenitic alloys, Al-6XN, remains un-affected by FIB milling. Upon low dose exposure in Knipling's experiment (less than 0.05 nC/μm^2), the FCC to BCC transformation was found to be crystallographic orientation dependant, among which (100) plane being the most stable orientation. Similar experiment carried out by Basa et al. [4] on a super-duplex stainless steel irradiated under much higher ion doses (1 nC/μm2). FCC to BCC phase transformation occurred even under low beam acceleration voltage (5 kV). The EBSD analysis suggested the FCC to BCC phase transformation is a result of changes in chemical composition by Ga ion implantation.

The Ga induced FCC to BCC phase transformation in steels is a great concern. FIB has been widely used to characterize various types of steels. The amount and distribution of austenite in steels is among one of the most important factors affecting their performance. For example, in weld heat affected zones, the appearance of MA phase plays a significant role in weld zone toughness. Characterizing weld zone microstructure and correlate with weld zone toughness is of critical importance in developing welding parameters for the construction of new pipelines using advanced pipeline steels (e.g. X80). MA phase is usually very small and frequently requires TEM to characterize its morphology, composition, and distribution. FIB has been the best tool to produce site-specific TEM specimens. It is of utmost importance to under the stability of austenite phase in commercial alloys upon FIB ion beam milling to provide knowledge and confidence that the microstructure in FIB prepared TEM foil is a true representation of the bulk material. Among previous reports [3.4], millings were performed using incident Ga ion beams, under which, the beam damage and implantation are at their worst. There has been no report on if FIB cross-sectioning will result in such phase transformation. This is very important as majority of post-FIB examinations are on FIB cross sections (e.g. serial sectioning for 3-D reconstruction and TEM specimen preparation).

In this study, we carried FIB milling experiments on three commercial austenitic alloys (SS304, SS316, and Alloy 800). Milling with incident Ga ion beam results in near complete phase transformation on SS304 and SS316 at low ion dose of 0.12 nC/μm^2. The transformation is found to be independent of crystallographic orientation. Austenite phase was completely stable for Alloy 800. On the ion beam cross-sectioned surface of SS304, no phase transformation was observed.

Experiment

Three samples from SS304, SS316, and Alloy-800 were prepared using standard metallurgical polish routine. Final polishing was carried out using colloidal silica

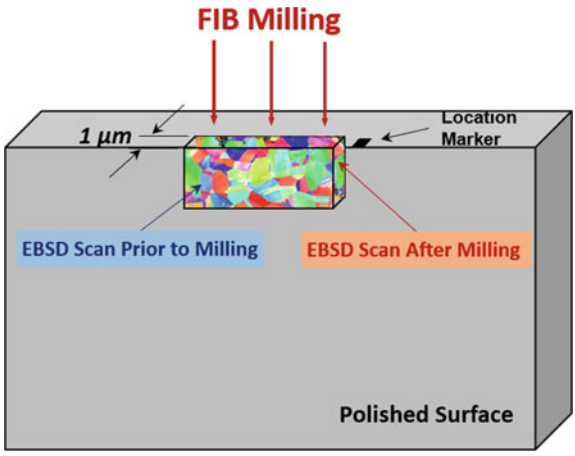

Fig. 1 FIB sectioning and EBSD scans of the SS304 sample

suspension. Small graphite markers were placed on each specimen for location identification purpose. Prior to FIB milling, SEM imaging and EBSD scans were performed using a FEI Nova NanoSEM-650 equipped with a Hikari EBSD system. FIB millings were performed using a FEI Helios NanoLab-650 dual beam system on identical areas to assess the status of phase transformations. Millings were performed in an area of about 200 × 200 µm with beam acceleration voltage of 30 kV, beam current 2.5 nA, and beam dwell time of 100 ns. Total milling dose was kept at 0.12 nC/µm^2. EBSD scans were performed on the FIB milled area. EDS spectra were also collected from the ion milled area to assess the degree of Ga ion implantation.

In addition to study the phase transformation induced by incident Ga ion beam, the polished surface of SS304 sample was FIB cross-sectioned. EBSD scans were carried out before and after the sectioning. Figure 1 is a schematic diagram showing the geometry of the FIB sectioning and EBSD scans.

Results and Discussion

Inverse pole figure (IPF) map in Fig. 2 shows the as-received SS304 has fully recrystallized equi-axed grains. The phase map shows the structure is predominantly austenite (FCC) except a few small patches of BCC structure. These small BCC islands within austenite grains are attributed to the FCC to BCC transformation due to mechanical polishing.

FIB milling was carried out using quite a low dose (0.12 nC/µm^2). This is primarily because higher ion dose can generate significant surface topography, this, when added to re-deposition, can significantly degrade diffraction pattern quality and reduce indexing confidence. Subsequent EBSD scan on the same area in Fig. 3 shows the milled area is completely transformed to BCC structure. Even with such low dose milling, the transformation is found to be independent of original crystallographic

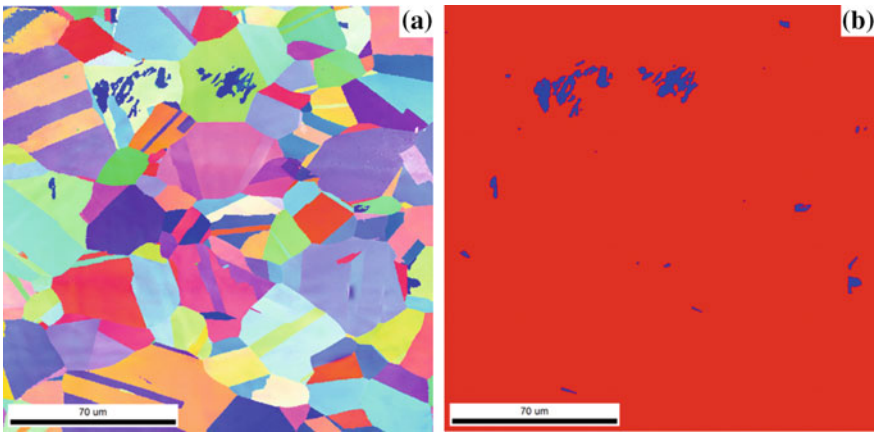

Fig. 2 EBSD scan of as-received SS304. **a** IPF map, **b** phase map (red: austenite, blue: BCC)

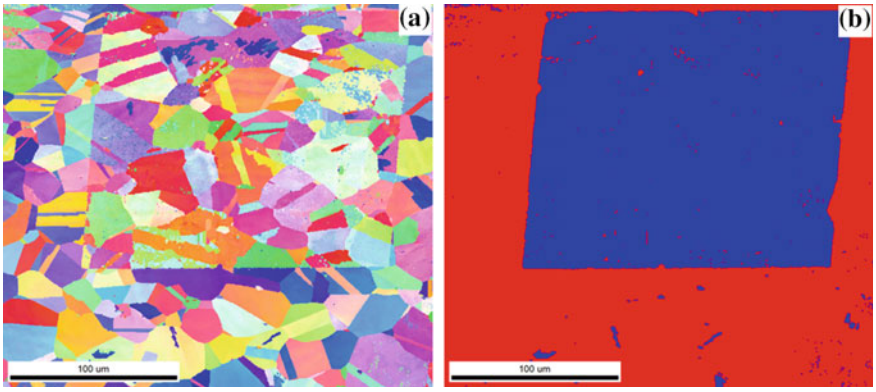

Fig. 3 EBSD scan of FIB milled area on SS304. **a** IPF map, **b** phase map (red: austenite, blue: BCC)

orientation of austenite grains. This is different to the previous report by Knipling et al. [3]. The IPF maps before and after FIB milling shows the close packed {111} plane in austenite (FCC) grains are parallel to {110} plane in transformed BCC grains, indicating the FCC-BCC transformation follows the traditional Kurdjumov-Sachs (K-S) orientation relationship.

As shown in Fig. 4, FIB milling of SS316 also result in near complete FCC to BCC transformation. For both stainless steels, FIB milling resulted degradation in diffraction pattern indexing quality. However, the confidences of indexing in both EBSD scans are still quite reasonable (0.34) after FIB milling.

In contrast to the two stainless steels, the austenite structure in Alloy-800 appeared to be very stable under the same FIB milling condition. EBSD scan in Fig. 5 shows no sign of FCC to BCC transformation.

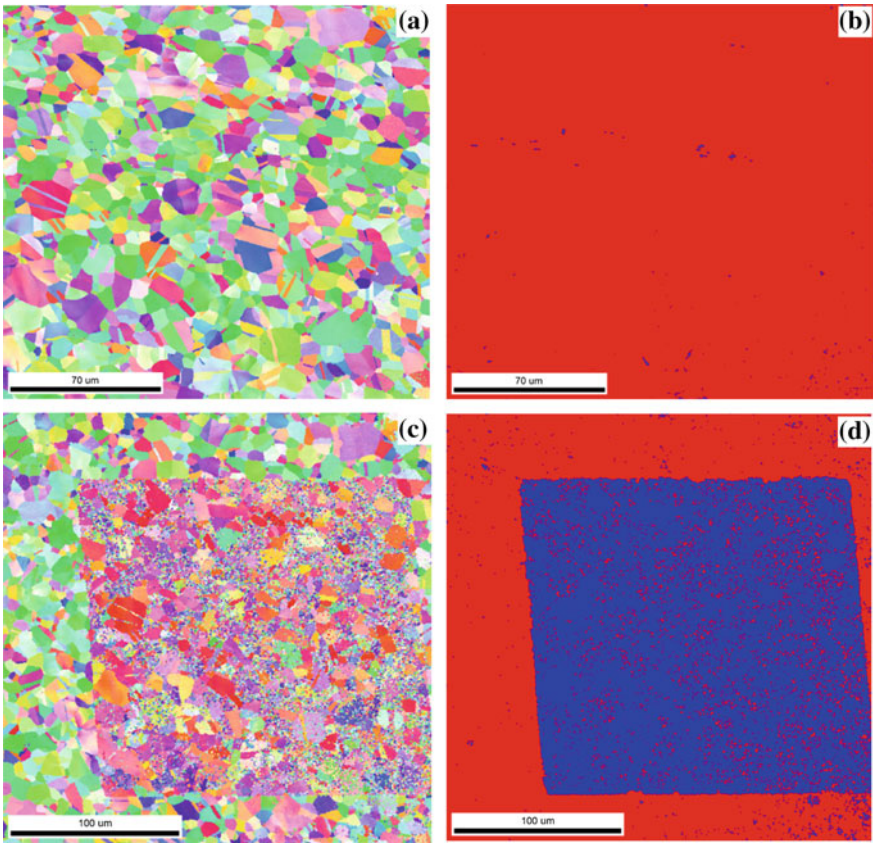

Fig. 4 EBSD scan SS316 before and after FIB milling. **a** As-received IPF map, **b** as-received phase map (red: austenite, blue: BCC), **c** after FIB milling IPF, **d** after FIB milling phase map

Basa et al. [4] suggested such phase transformation is neither a result of plastic deformation nor an increase in the dislocation density, as has been established for the metastable austenite to martensite phase transformation, but rather triggered by local change in the composition. In stainless steels, Ni, Carbon, Mn, and N stabilize austenite, while Cr, Si, Mo, and Nb stabilize ferrite phase. Eichelman and Hull [5] studied the effect of chemical composition on the austenite to martensite transformation temperature (M_s) in 304 type of stainless steel. They concluded the relative effectiveness of the alloying element to stabilize austenite decreases following the orders of nitrogen, carbon, nickel, chromium, manganese, and silicon. Based on the calculation of temperature at which 50% of the austenite transforms to martensite with 30% true strain [6], the austenite in SS304 is very unstable, followed by SS316. The high Ni content in Alloy 800 makes its austenite extremely stable. Kolman et al. [7] showed that gallium is a ferrite stabilizer and small addition of Ga to steels promotes austenite to ferrite phase transformation. Milling with incident Ga ion beam

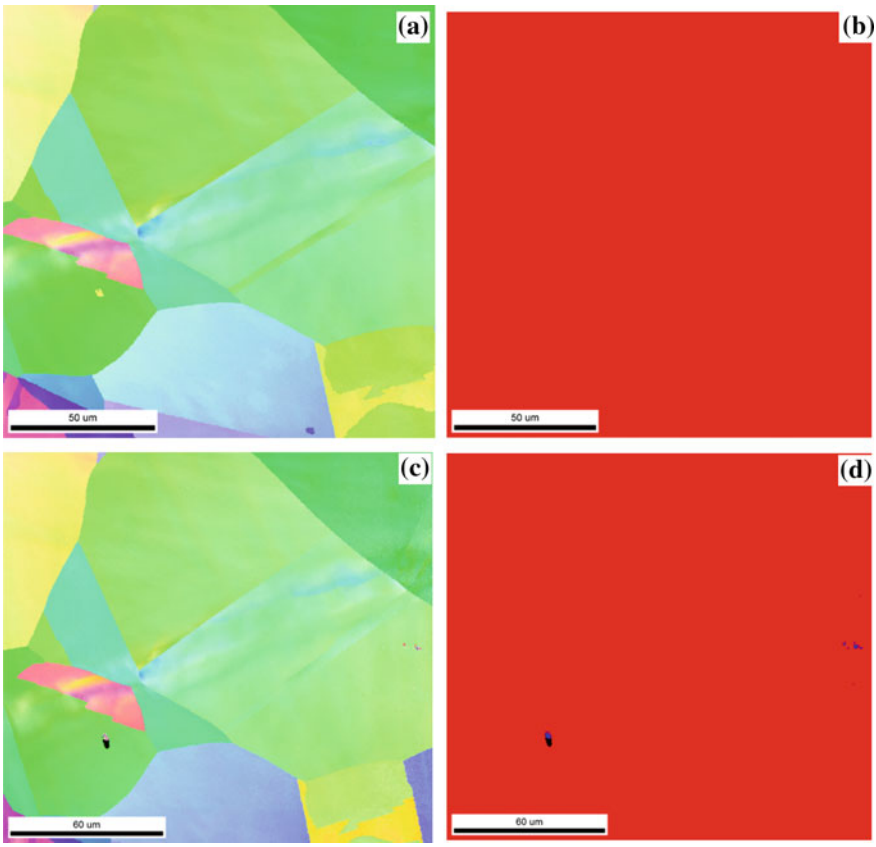

Fig. 5 EBSD scan Alloy 800 before and after FIB milling. **a** As-received IPF map, **b** as-received phase map (red: austenite, blue: BCC), **c** after FIB milling IPF, **d** after FIB milling phase map

implants significant amount of Ga into the substrate. This will promote the FCC to BCC phase transformation. The crystal structure super-stable austenite phase in Alloy-800 remains unchanged upon incident ion beam milling. EDS analyses on the milled surface of the three alloys show significant Ga peaks, and a crude semi-quantitative calculation yield about 4 wt% Ga in all three alloys. Unlike FIB milling of Cu [8] where low melting Cu_xGa_y phase can form, the Ga content in this study is not high enough to form Fe-Ga phases.

One important unanswered question is if this phase transformation can occur on FIB milled trenches where the Ga ion beam is nearly parallel to the surface of interest. If it does, one should be very concerned about the FIB sectioned surface and FIB-prepared TEM foils. We selected the SS304 that has the least stable austenite for this experiment. Sample geometry with respect to EBSD scans and FIB trenching is shown in Fig. 1. EBSD maps of the area of interest before and after FIB milling are shown in Fig. 6. Small patches of BCC phase can be found on post-FIB milled

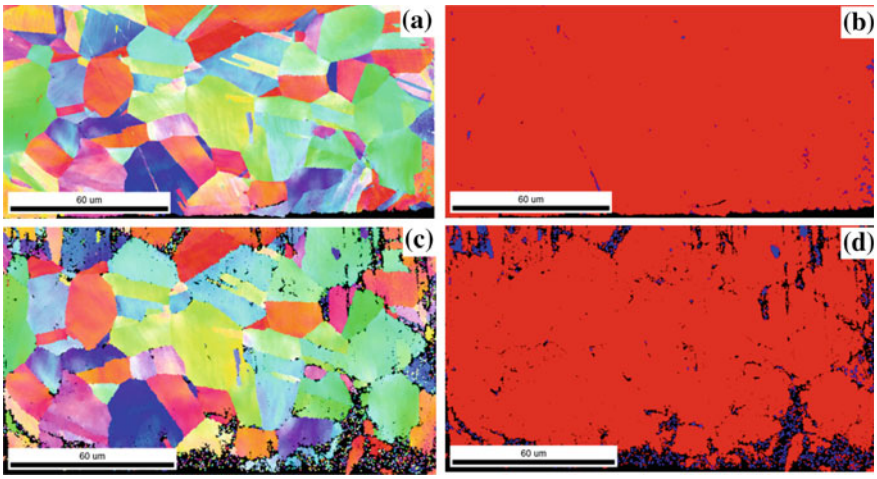

Fig. 6 EBSD scan on SS304 before and after FIB trenching. **a**, **b** Before sectioning IPF map, phase map (red: austenite, blue: BCC), **c**, **d** After FIB sectioning, phase map

surface (Fig. 6d). However, when looking into the corresponding IPF (Fig. 6c), these labelled BCC areas are very poorly indexed areas. This can be a result of a number of factors including FIB ion damage, local amorphization and re-deposition. Thus, one can argue that the BCC islands in Fig. 6d are artifact from poor EBSD indexing in these areas. The fact that at least the majority of the area (if not all) are not transformed is due to the milled surface is nearly parallel to the primary Ga ion beam, and the amount of ion beam damage and Ga ion implantation is minimal. Subsequent EDS spectrum collected from the milled surface indicate much lower level of Ga implantation (less than 0.8 wt%). This proved to be not enough to result in austenite to BCC transformation.

Conclusion

FIB milling by incident Ga ion beam, even at low dose, can transform austenite phase to BCC structure in both SS304 and SS316 alloys. The transformation is not a result of new intermetallic phase formation, but the change in local chemistry. For Alloy 800 that has much higher Ni content, the austenite is stable upon incident ion beam milling. Meanwhile, FIB sectioning does not result in noticeable phase transformation in cross-sectioned surface in SS304 in which the austenite is relatively unstable. The finding provided much needed confidence in FIB cross sections and lift out TEM specimens of ferrous metals.

References

1. Li J (2011) Advanced techniques in TEM specimen preparation. In: Maaz K (ed) The transmission electron microscope. ISBN: 979-953-307-311-7
2. Phaneuf MW, Li J, Shuman RF, Noll K, Casey JD (2003) Apparatus and method for reducing differential sputter rates, US patent #6,641,705. Issued 04 Nov 2003
3. Knipling KE, Rowenhorst DJ, Fonda RW, Spanos G (2010) Effects of focused ion beam milling on austenite stability in ferrous alloys. Mater Charact 61:1–6
4. Basa A, Thaulow C, Barnoush A (2014) Chemically induced phase transformation in austenite by focused ion beam. Metall Mater Trans A 3:1189–1198
5. Eichelman GH, Hull FC (1953) Trans Am Soc Met 45:77
6. McGuire MF Stainless steels for design engineers. ASM International. ISBN: 978-0-87170-717-8
7. Kolman DG, Bingert JF, Field RD (2004) Metall Mater Trans A 35:3445–3454
8. Casey JD et al (2002) Advanced sub 0.13 μm Cu devices—failure analysis and circuit edit with improved FIB chemical processes and beam characteristics. In: Proceedings of international symposium for testing and failure analysis, pp 553–557

Part III
Minerals Processing and Analysis II

Experimental Research on Pellet Production with Boron-Containing Concentrate

Yunqing Tian, Gele Qin, Yan Zhang, Luyao Zhao and Tao Yang

Abstract In this paper, the basic performance of boron-containing concentrate and the method of pellet production with boron-containing concentrate was studied. Research results show that the granularity of boron-containing concentrate was finer; it had a good performance in pelletizing, and the green ball ballability index was at a higher level. If the boron-containing concentrate was heated, there was an obvious endothermic reaction between 550 and 700 °C. This phenomenon had a negative effect on the compressive strength of preheated pellet. So the preheating temperature and preheating time of pellet should be increased in order to reduce the ring forming phenomenon of rotary kiln. The compressive strength of boron-bearing pellet decreased with the increase of the proportion of boron-bearing ore powder; the appropriate roasting system should be selected according to the proportion of boron-bearing concentrate. The metallurgical properties of boron-bearing pellets were similar to those of ordinary acid pellets.

Keywords Boron-containing concentrate · Particle size distribution · Metallurgical properties

Introduction

Our country has abundant boron iron ore resources. The reserves of boron iron ore resources in Liaoning province alone amount to 2.8 billion tons. Boron-containing concentrate is obtained from boron iron ore after mining which is mainly used to produce borax, boron fine chemical products, and magnesium deep processing products, etc. Because of the limited demand and low output value of these boron-containing concentrate powder cannot be well utilized comprehensively, and does not match the huge reserves, so it is urgent to develop new uses. With the deepening of the national supply-side structure adjustment, energy saving, and emission reduction,

Y. Tian (✉) · G. Qin · Y. Zhang · L. Zhao · T. Yang
Shougang Group Co Ltd Research Institute of Technology, Beijing 100043, China
e-mail: tianyunqing@126.com

J. Li et al. (eds.), *Characterization of Minerals, Metals, and Materials 2020*,
The Minerals, Metals & Materials Series,
https://doi.org/10.1007/978-3-030-36628-5_9

and environmental protection, the iron and steel industry needs to expand new high-quality resources, and the application of boron-containing concentrate in iron and steel industry is also a direction [1, 2].

The phase of boron-containing concentrate powder is different from that of ordinary magnetite powder. The phase of boron-containing concentrate powder contains magnetite, fibrous brucite, and calcium metaborate, as well as associated minerals such as dolomite, serpentine, and magnesite. The iron grade of boron-containing concentrate is low, only about 52%. It is uneconomical to use iron as raw material for iron making or sintering in iron and steel industry. Therefore, it is necessary to further process the boron-containing concentrate in order to give full play to the resource advantages of boron-containing concentrate and realize the resource utilization. According to the resource characteristics of boron iron ore, it is imperative to combine with other iron ore resources to produce magnesium pellets and enhance the value of magnesium, boron, and other elements in products. Therefore, through a series of experimental studies, the method of producing pellets with boron-containing concentrate was discussed in this paper [3, 4].

Experimental Methods and Analysis of Raw Material Performance

Experimental Methods

The equipment used for pelletizing is a disc pelletizer with a diameter of 800 mm. The rotational speed is controlled for 19 r/min, the inclination angle is 45°, and pelletizing time is 9 min. After the pelletizing experiment, the green ball with diameters of 10–12.5 mm was screened, and then, the performance index of green ball was measured such as drop number, compressive strength, moisture content, and burst temperature.

The equipment used for pellet roasting is pellet roast cup which can simulate the whole roasting process of belt roaster such as blast drying, exhaust drying, preheating, roasting, soaking, and cooling. The inner diameter of the roasting cup is 120 mm, and the height is 400 mm. After the roasting experiment, the compressive strength of pellet was measured and the metallurgical properties of pellets, such as reduction index (RI), reduction swelling index (RSI), and low-temperature reduction disintegration indices (RDI), were tested in accordance with relevant national standards.

Basic Properties of Raw Materials

Two kinds of iron concentrate powder (ordinary iron concentrate powder and boron-containing concentrate powder) and one kind of bentonite were used in this experiment. The chemical composition was shown in Table 1, and the particle size composition was shown in Table 2.

As can be seen from Table 1, the iron grade of ordinary iron concentrate powder is higher, 69.31%, and the content of SiO2 is 1.84%. The iron grade of boron-containing concentrate powder is 52.21%, the content of SiO2 is 5.29%, and the content of MgO is 10.75%. The particle size of the two kinds of iron concentrates is fine, and the content of −74 μm is both above 80%. The physical properties of bentonite were shown in Table 3. Its water absorption rate in 2 h is 375%, and its expansion index is 13 mL/2 g.

Analysis of Boron-Containing Concentrate Performance

Micro-morphology

The micro-morphology of boronite concentrate powder was observed by scanning electron microscopy (SEM), as shown in Fig. 1. According to the micro-morphology, the particles of boron-containing concentrate powder are gravel-like, and there are many fine particles in the coarse particles. The surface of the particles is rough. The morphology of the particles is relatively favorable for pelletizing.

XRD

The phase of boron-containing concentrate powder was analyzed by XRD, as shown in Table 4. The boron-containing concentrate contains 76.3% magnetite, 12% fibromagnesite, and 11.7% CaB_2O_4.

TG-DSC

The TG-DSC curve of boron-containing concentrate was shown in Fig. 2.

From the TG-DSC curve of boron-containing concentrate in Fig. 2, it can be seen that there is a weight gain between 300 and 580 °C, which should be the oxidative weight gain of magnetite; there is a relatively obvious endothermic reaction between 550 and 700 °C, which should be the dehydration and decomposition heat absorption of fibrous brucite and serpentine. There is a significant weight loss between 600 and 750 °C for boron-containing concentrate. There is little change between 750 and 1000 °C. The endothermic and weightlessness phenomena between 1000 and 1200 °C should be the re-decomposition of solid solution formed by dolomite decomposition.

Table 1 Chemical composition of raw materials/%

	TFe	FeO	SiO_2	CaO	Al_2O_3	MgO	P	S	K_2O	Na_2O	Loss
Ordinary iron concentrate	67.98	28.53	3.89	0.43	0.46	0.51	0.029	0.05	0.033	0.012	−2.57
Boron-containing concentrate	52.21	21.84	5.29	0.42	0.20	10.75	0.019	0.69	0.057	0.011	1.79
Bentonite	–	–	61.95	2.88	13.74	3.24	0.069	1.20	1.30	2.44	10.65

Table 2 Particle size composition/%

Granularity	+180 μm	180–120 μm	120–109 μm	109–96 μm	96–80 μm	80–74 μm	−74 μm
Iron concentrate	0.96	2.81	1.02	1.24	3.76	6.42	83.79
Boron-containing concentrate	0.68	2.63	3.23	2.65	4.68	5.57	80.56

Table 3 Physical properties of bentonite

	Colloidal value (mL/15 g)	Ethylene blue adsorbed (g/100 g)	Expanded ratio (mL/2 g)	Water absorption (%)	−74 μm (%)
Bentonite	375	30.78	13	380	98.50

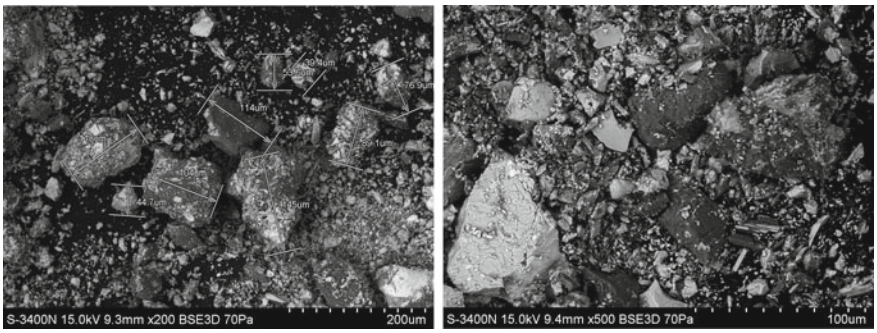

Fig. 1 Microscopic morphology of boron-containing concentrate powder

Table 4 Phase of boron-containing concentrate powder

Phase	Fe_3O_4	$MgBO_2(OH)$	CaB_2O_4
Proportion	76.3	12	11.7

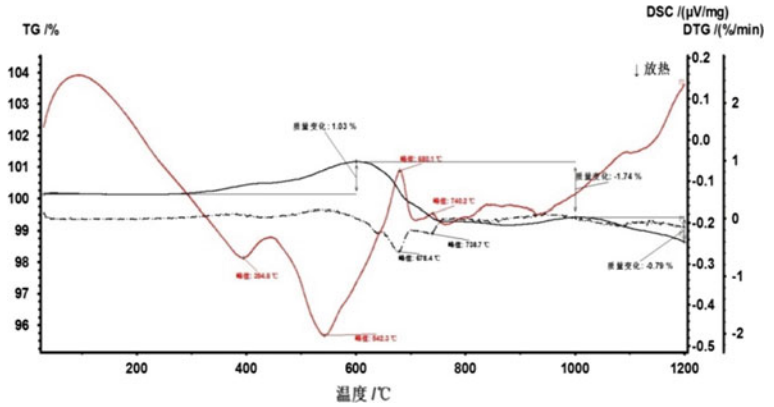

Fig. 2 TG-DSC curve of boron-containing concentrate

Experimental Results and Analysis

Results and Analysis of the Pelletizing Experiment

The pelletizing test was carried out by mixing ordinary iron concentrate with boron-containing concentrate, and the proportion of boron-containing concentrate was from 0, 20, 40, 60, 80, to 100%. The pelletizing experiment scheme and green ball performance index were shown in Table 5.

From Fig. 3, it can be seen that the drop number of green ball increases gradually with the increase of the proportion of boron-containing concentrate powder, while the compressive strength of green ball does not change much. When the proportion of boron-containing concentrate powder is 100%, the green ball drop number is 12.3, and the compressive strength is 10.01 N/P. The main reason for the improvement of drop number of green ball after adding boron-containing concentrate powder is that boron-containing concentrate powder is finer and the micro-morphology is beneficial to the formation of ball.

Results and Analysis of the Preheating Experiment

The compressive strength of preheated pellet is very important for the ring formatting and stable production of the rotary kiln. According to the analysis of TG-DSC, the boron-containing concentrate has obvious heat absorption between 550 and 700 °C, which may have a great influence on the compressive strength of preheated pellet. In order to study the compressive strength of the preheated pellet after adding boron-containing concentrate powder, drying and preheating experiment were carried out on the green ball. In the experiment, the maximum preheating temperature is 930 °C. The curve of preheating temperature was shown in Fig. 4. The relationship between the compressive strength of preheated pellet and the proportion of boron-containing concentrate was shown in Fig. 5.

From Fig. 5, it can be seen that the compressive strength of preheated pellet decreases with the increase of the proportion of boron-containing concentrate. When the proportion of boron-containing concentrate reaches 40%, the compressive strength of preheated pellet is 515 N/P. If the pellets with boron-containing concentrate are produced in the chain-castor-rotary kiln process, it is necessary to increase the temperature of the preheating section and prolong the preheating time to meet the decomposition endotherm of boron-containing concentrate, increase the strength of the preheated pellet, and reduce the ring formation problem of the rotary kiln caused by the fragility of the preheated pellet when it enters the rotary kiln due to its low strength.

Table 5 Pelletizing experiment scheme and green ball performance index

Serial number	Ordinary iron concentrate (%)	Boron-containing concentrate (%)	Bentonite (%)	Performance index of green ball			
				Drop number/0.5 m	Compressive strength N/P	Moisture (%)	Bursting temperature (°C)
1	100	0	2.0	6.5	11.0	9.3	>600
2	80	20	2.0	6.6	10.24	9.2	>600
3	60	40	2.0	7.3	10.85	10.2	>600
4	40	60	2.0	8.5	10.44	10.5	590
5	20	80	2.0	10.0	10.56	11.4	590
6	0	100	2.0	12.3	10.01	11.7	560

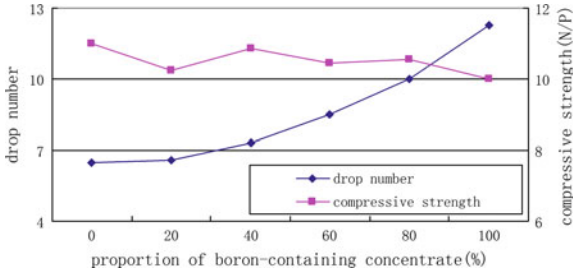

Fig. 3 Performance of green ball with different proportions of boron-containing concentrate

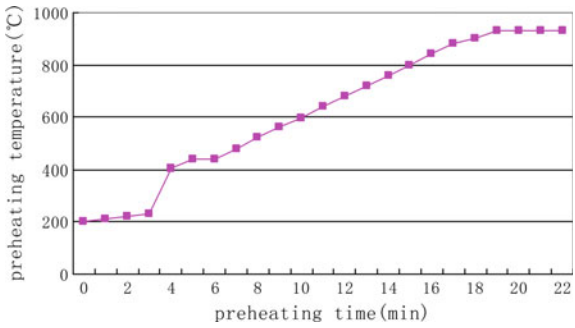

Fig. 4 Curve of preheating temperature

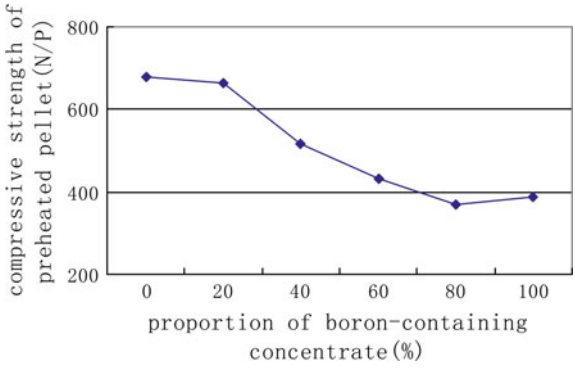

Fig. 5 Relationship between the compressive strength of preheated pellet and the proportion of boron-containing concentrate

Results and Analysis of the Roasting Experiment

The green ball with different proportions of boron-containing concentrate powder was roasted in pellet roasting cup. Three roasting experiments were carried out under different roasting temperatures and roasting time. The roasting temperature of experiment 1 was 1250 °C, the roasting time was 54 min (curve 1), the roasting temperature of experiment 2 was 1230 °C, the roasting time was 54 min (curve 2), the roasting temperature of experiment 3 was 1200 °C, and the roasting time was 56 min (curve 3). The roasting time curves were shown in Fig. 6.

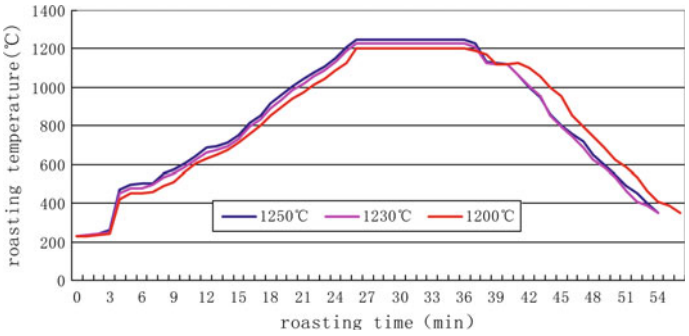

Fig. 6 Roasting curves

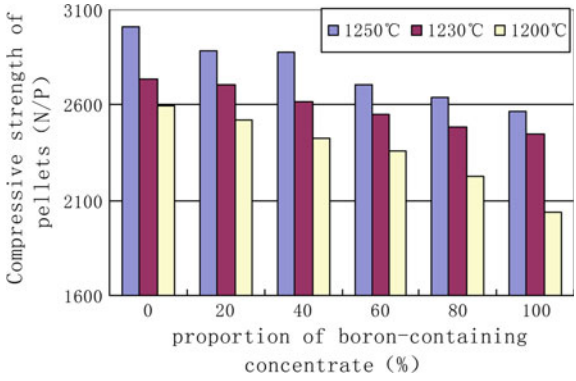

Fig. 7 Compressive strength of pellets at different roasting temperatures and different proportions of boron-containing concentrate

It can be seen from Fig. 7 and Table 6 that the compressive strength decreases with the increase of the ratio of boron-containing concentrate at different roasting temperatures. The compressive strength of pellet is above 2500 N/P, at 1250 °C; the compressive strength of pellet can reach above 2500 N/P, when the ratio of boron-containing concentrate is below 60% at 1230 °C; the compressive strength of pellet can reach above 2500 N/P, when the ratio of boron-containing concentrate is below 20% at 1200 °C. Generally speaking, the requirement of roasting temperature for boron-containing concentrate is not high, and the appropriate roasting temperature should be selected according to the proportion of boron-containing concentrate.

Metallurgical Properties of Pellets Containing Boron

The metallurgical properties and experiments of pellets containing boron were carried out, as shown in Table 7. The results of metallurgical properties experiment show that the reduction swelling index (RSI), reduction degree index (RI), and low-temperature

Table 6 Roasting scheme and compressive strength of pellet

Serial number	Ordinary iron concentrate (%)	Boron-containing concentrate (%)	Bentonite (%)	Compressive strength (N/P)		
				1250 °C	1230 °C	1200 °C
1	100	0	2.0	3012	2735	2597
2	80	20	2.0	2885	2704	2519
3	60	40	2.0	2879	2618	2424
4	40	60	2.0	2705	2552	2355
5	20	80	2.0	2637	2483	2223
6	0	100	2.0	2563	2450	2035

Table 7 Metallurgical properties of pellets containing boron

Iron concentrate	Boron-containing concentrate	Bentonite	RSI	RI	RDI Indices		
					$RDI_{+6.3}$	$RDI_{+3.15}$	$RDI_{-0.5}$
100	0	2.0	15.53	65.34	96.58	97.69	2.13
70	30	2.0	17.35	63.23	97.02	97.23	2.09
50	50	2.0	15.97	63.50	96.45	96.89	2.67
0	100	2.0	14.80	60.59	97.32	97.36	2.48

reduction disintegration indices (RDI) of pellets containing boron have little change compared with ordinary pellet.

Conclusion

(1) The particles of boron-containing concentrate powder are gravel-like, and there are many fine particles in the coarse particles. The surface of the particles is rough. The morphology of the particles is relatively favorable for pelletizing. The results of pelletizing experiment show that the pelletizing performance of boron-containing concentrate powder is better, and the performance index of green ball tends to increase with the increase of the proportion of boron-containing concentrate. When the proportion of boron-containing concentrate powder is below 60%, the bursting temperature of green ball can reach 600 °C under the condition of proper control of moisture content of green ball.

(2) The compressive strength of preheated pellet decreases with the increase of the proportion of boron-containing concentrate. This is related to the obvious endothermic reaction between 550 and 700 °C. If the pellets with boron-containing concentrate are produced in the chain-castor-rotary kiln process, it is necessary to increase the temperature of the preheating section and prolong the preheating time to meet the decomposition endotherm of boron-containing

concentrate, increase the strength of the preheated pellet, and reduce the ring formation problem of the rotary kiln caused by the fragility of the preheated pellet when it enters the rotary kiln due to its low strength.

(3) The compressive strength decreases with the increase of the ratio of boron-containing concentrate at different roasting temperatures. Generally speaking, the requirement of roasting temperature for boron-containing concentrate is not high; the appropriate roasting temperature should be selected according to the proportion of boron-containing concentrate.

(4) The reduction swelling index (RSI), reduction index (RI), and low-temperature reduction disintegration indices (RDI) of pellets containing boron have little change compared with ordinary pellet.

References

1. Zhao Q, Wang C (2001) Develop and application of paigeite. Liaoning Chem Ind 30(7):297–298
2. Liu R, Xue X, Jiang T et al (2006) Comprehensive utilization of ludwigite and its prospect. Multipurpose Utilization Min Res 2:33–37
3. Zhou L (2002) Process mineralogy. Metallrugical Industry Press, Beijing, pp 163–164
4. Zhu D, Zhou W, Pan J et al (2014) Improving pelletization of Brazilian hematite by adding boron-containing magnetite. J Central South Univ Sci Technol 45(2):351–352

Leaching of Platinum Group Metals from Automobile Spent Catalyst

Sujun Lu, Dalin Chen, Peng Zhang, Guoju Chen, Yan Zhang, Yujun Pan, Ruikang Wang, Jinxi Qiao, Xintao Sun and Ailiang Chen

Abstract Automobile spent catalyst is leached for recovering platinum group metals using oxidizing acid leaching. Hydrogen peroxide is regarded as oxidant and hydrochloric acid as leaching reagent. The experimental results show that the best conditions are as follows: the concentration of hydrochloric acid is 6 mol/l, the liquid-solid ratio is 10:1, the reaction temperature is 9 5 °C, the volume ratio of hydrogen peroxide to raw material is 5 ml/g, and the reaction time is 2 h. Under the above conditions, the leaching ratio of platinum, palladium, and rhodium are 93.9%, 99.8%, and 86.9%, respectively. In this study, the platinum group metal is directly recovered from the automobile spent catalyst, achieving a good leaching effect. This provides a feasible method for the effective treatment of the automobile spent catalyst.

Keywords Automobile spent catalyst · Platinum group metals · Hydrogen peroxide · Acid leaching

Introduction

Platinum group metals play an extremely important role in science and technology, new energy resources, and other fields as non-renewable. They are also indispensable strategic resources for the sustainable development of national economy [1]. What's

S. Lu · D. Chen · P. Zhang · G. Chen · Y. Zhang (✉)
State Key Laboratory of Nickel and Cobalt Resources Comprehensive Utilization, Jinchang, Gansu 737104, China
e-mail: Qiaojinxi@csu.edu.cn

Y. Pan · R. Wang · J. Qiao · X. Sun · A. Chen
School of Metallurgy and Environment, Central South University, Changsha 410083, China

J. Li et al. (eds.), *Characterization of Minerals, Metals, and Materials 2020*,
The Minerals, Metals & Materials Series,
https://doi.org/10.1007/978-3-030-36628-5_10

more, platinum group metals have unique ability to purify automobile exhaust, more than 60% of them are used as catalysts for automobile exhaust purifiers each year [2, 3]. It is investigated that a light gasoline vehicle needs about 3–5 g of platinum group metal. The higher the amount of platinum group metal used, the less exhaust gas is usually emit [4]. The catalysts for automobile exhaust purifier are always composed of the carrier of cordierite ($2MgO{\cdot}2Al_2O_3{\cdot}5SiO_2$), the coating of Al_2O_3 (γ-Al_2O_3), the active component of platinum group metals, and auxiliary agent (CeO_2). It can effectively remove pollutants from automobile exhaust and the removal rate can achieve 99% [5]. Therefore, a large number of catalysts for automobile exhaust purifier have been put into use since the 1970s in order to reduce the impact of automobile exhaust on air pollution. However, this catalyst does not last too long because of the inactivation of one component or the discarding of the vehicle. With the large use of catalyst of automobile exhaust purifier, a lot of waste catalyst will be produced every year. The demand of automotive exhaust gas purification catalyst in 2018 is very high [6].

At present, the two most common technique removing platinum group metals from waste catalysts were pyrometallurgy and hydrometallurgy [7]. The recovery of Pt, Pd, and Rh from waste catalyst by the copper capture method was studied. The result showed that the capture rates of Pt, Pd, and Rh were 98.2, 99.2, and 97.6% [8]. Pyrometallurgical processes require high energy consumption, and its technological process is more complex. At the same time, this method has more serious environmental pollution. Liu Gongzhao studied the recovery of Pd from Pd-Al_2O_3 waste automobile exhaust gas catalyst using H_2SO_4 and the recovery rate was over 97% [9]. Hydrometallurgy processes are more simple and effective. And the recovery rate of platinum group metals is higher. The Kunming Institute of Precious Metals [10, 11] also achieved a good leaching rate by using the pyrometallurgy and hydrometallurgy.

Therefore, hydrometallurgy process is chosen to conduct the optimum condition of the leaching of the platinum group metals. And it is also useful for subsequent metal recovery. According to the composition of the cordierite carrier, platinum is wrapped in the coating of Al_2O_3. In the experiment, hydrochloric acid is used to leach the metals, and hydrogen peroxide is added as an oxidant. In this way, a complex of platinum group metal is dissolved in the solution, which will improve the leaching rate of platinum group metals.

Experimental

Materials

The raw material, waste catalysts for automobile exhaust purifier, is provided by a Chinese company. Its composition is listed in Table 1. The raw material was ground to obtain a powdery sample having a particle size about of 20 μm.

Table 1 Main content of elements in waste catalyst

Elements	PGM's (g/t)			Other metal (%)				
	Pd	Pt	Rh	Al_2O_3	SiO_2	MgO	Ce	Zr
Content	1310	712	162	39.06	31.66	4.6	3.53	3.83
Elements				Fe	Mn	Ba	La	
Content				1.37	1.18	0.76	0.61	

Method

10 g of the raw material was added to a certain concentration of hydrochloric acid. The reaction was stirred at a certain temperature. After the reaction time was reached, filtration was carried out to obtain a filtrate rich in copper, cobalt, nickel, and zinc. The contents of platinum, palladium, and rhodium in the filtrate were determined by ICP (Thermo Scientific ICAP 7200 Radial, Thermo Fisher Science, USA). The leaching ratio was calculated from the content of elements in the filtrate. The specific calculation formula is:

$$\eta = \frac{c \times V \times n}{M \times m} \times 100\% \tag{1}$$

where

c is the concentration of the element in the sample measured by ICP, ppm;
V is the volume of leaching solution, ml;
n is the dilution factor;
M is the mass of the element in each gram of raw material, mg;
m is the mass of the raw material before the experiment, g.

Results and Discussion

The platinum group metals usually exist in automobile spent catalyst in the form of the elementary substance. Platinum group metals are generally poorly soluble in acids. They only form complexes in the presence of strong acids and oxidants [12]. As a result, the leaching process needs the oxidizing reagents, which can confirm a certain amount of potential, except for the chloridoid and hydron supplying the acidity to effectively leach. Sodium chlorite and hydrogen peroxide were commonly used as oxidizing reagents. This section also uses the hydrogen peroxide to extract the platinum, palladium, and rhodium in the automobile spent catalyst.

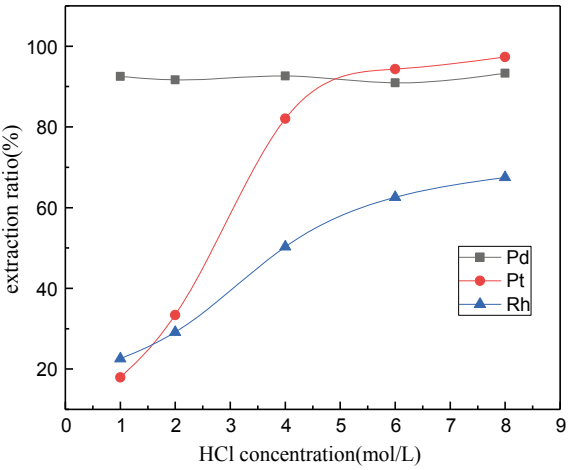

Fig. 1 Effect of hydrochloric acid on leaching ratio

Effect of Hydrochloric Acid Concentration

Figure 1 shows the effect of hydrochloric acid concentration on leaching ratio of platinum, palladium, and rhodium under the condition of the liquid-solid ratio of 10:1, the reaction temperature of 80 °C, the volume ratio of hydrogen peroxide to raw material 100 ml/L, and the reaction time of 1 h.

According to Fig. 1, the leaching ratio of platinum, palladium, and rhodium only can up to 18%, 92%, and 22%, respectively, at the concentration of the hydrochloric acid was 1 mol/L. The reason is that a part of palladium metal was already oxidized to palladium oxide, which was in dissolvable in this system. H_2O_2 is added for leaching platinum group metals. Palladium is oxidized to palladium oxide as time increases. But palladium oxide is insoluble in acid solution [13]. As the concentration of hydrochloric acid increases, the leaching ratio of palladium is almost stable while that of platinum and rhodium go up constantly. When the concentration of the hydrochloric acid comes to 6 mol/L, the leaching ratio of platinum and rhodium go up to 94.31% and 62.51%, respectively. When the concentration of the hydrochloric acid comes to 8 mol/L, the leaching ratio of platinum and rhodium only climb 3.00% and 4.89%, respectively. As a result, considering the severe corrosion to the facility with the acid concentration increases. We chose the optimum condition for leaching when the concentration of sulfuric acid is 6 mol/L.

Effect of the Ratio of Liquid to Solid

The experimental conditions are controlled at the condition as follows: the reaction temperature is 80 °C, the concentration of the hydrochloric acid is 6 mol/L, the volume ratio of hydrogen peroxide to raw material is 100 ml/L, and the reaction time

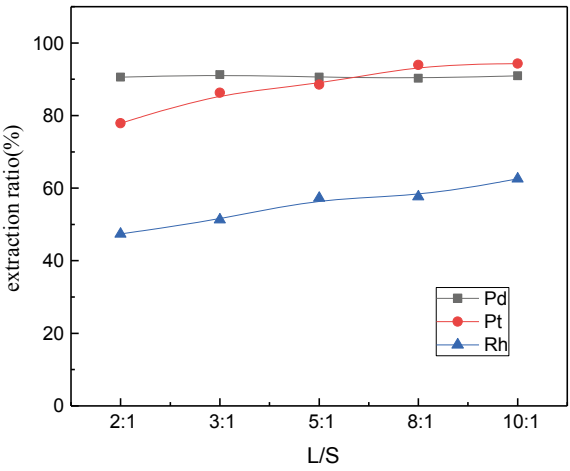

Fig. 2 Effect of liquid to solid ratio on leaching ratio

is 1 h. This mainly considers the effect of the liquid-solid ratio on the leaching ratio of the platinum group metals. And the experimental results are shown in Fig. 2.

According to Fig. 2, with the liquid-solid ratio increasing, the leaching ratio of palladium is nearly stable, whereas that of platinum and rhodium is growing continuously. Such as, when the liquid-solid ratio increases from 2:1 to 10:1, the leaching ratio of platinum and rhodium goes up more than 10%. This means the increasing concentration of the reactants can strengthen the leaching process of those two metals. It decreases the potential of the leaching process and increases the leaching ratio. This verifies the thermodynamic calculation. As a result, it shows that the best leaching liquid-solid ratio is 10:1. Zheng xiangjiang's study also showed that the leaching rate of palladium was the highest when the liquid-solid ratio was 10:1 [14].

Effect of Hydrogen Peroxide Consumption

Figure 3 shows the effect of hydrogen peroxide ranging to 10 M on leaching ratio of platinum group metals at the temperature of 80 °C, the HCl concentration of 6 M, the reaction time of 1 h and 10:1 of liquid-solid ratio.

As can be seen from Fig. 3, the leaching ratio of Pt and Rh is only about 38 and 40%. That of Pd is about 82% when hydrogen peroxide is not added. With the increase of hydrogen peroxide, the leaching ratio of Pt, Pd, and Rh also increases. At the dosage of 5 ml hydrogen peroxide, the leaching ratio of Pt, Pd, and Rh has the maximum value of about 99, 90, and 68%. The leaching ratio of Pt, Pd, and Rh will decrease slowly if hydrogen peroxide exceeds 5 ml. The leaching potential of the whole system has increased with the increase of hydrogen peroxide, which prompts the balance of the leaching reaction to the positive direction. However, excess hydrogen peroxide will react with Cl^- in the solution to form hypochlorous acid. It

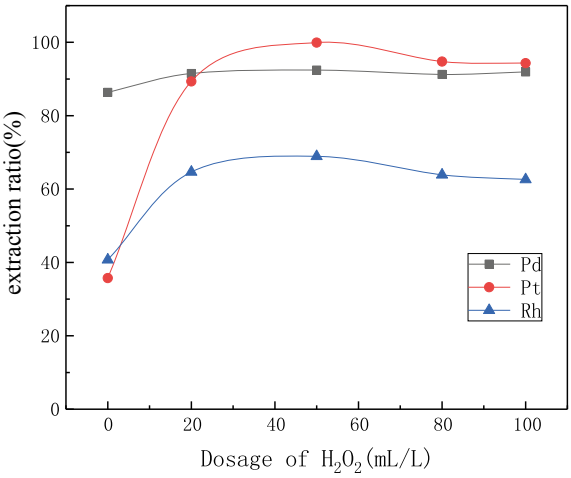

Fig. 3 Effect of hydrogen peroxide consumption on leaching ratio

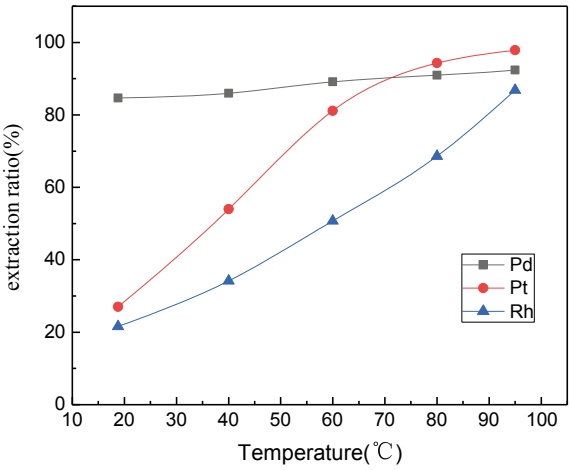

Fig. 4 Effect of reaction temperature on leaching ratio

makes some metal ion oxidized, leading to the ratio decrease. Therefore, hydrogen peroxide needs to be added slowly during the leaching process. If added at one time, Cl^- in the leaching system will be definitely reduced and hydrogen peroxide will be wasted.

Effect of Reaction Temperature

Figure 4 shows the effect of reaction temperature on the leaching ratio of platinum group metals under the condition as follows: HCl concentration is 6 M, the liquid-solid ratio is 10:1, the reaction time is 1 h, and the hydrogen peroxide is 5 ml.

It can be seen that the leaching ratio of Pt, Pd, and Rh increases with increasing temperature. The leaching ratio of Pt, Pd and Rh increases to 7%, 71%, 63%, respectively, when the reaction temperature rises from 18.8 to 95 °C. According to the Arrhenius formula, reaction rate constant $K = A \exp[-\mathrm{Ea}/(\mathrm{RT})]$ (Ea is activation energy and A is pre-exponential factor; R is the molar gas constant; and T is thermodynamic temperature). With the increase of temperature, the rate of reaction speeds up, the activation energy of the reaction reduces, and the proportion of active molecules increases. It enhances the leaching reaction [15]. However, the water solution begins to boil and the saturated vapor pressure increases when the temperature rises to 100 °C. A large number of hydrochloric acid, hydrogen peroxide, and chlorine and oxygen generated by hydrogen peroxide will also spill out of the solution quickly. Therefore, 95 °C is regarded as the most appropriate reaction temperature.

Effect of Reaction Time

Under the condition of HCl of 6 M, liquid-solid ratio of 10:1, 5 ml hydrogen peroxide and the reaction temperature of 95 °C, the effect of the reaction time (0.5, 1, 2, 4, 6 h) on leaching ratio of platinum group metals is shown in Fig. 5.

The platinum group metals have been leached mostly during the first 30 min, and the leaching ratio of Pt, Pd, and Rh are basically stable at 99.8%, 93.9%, and 86.87%, respectively, when reacting is 1 h. With the extension of reaction time, the capacity

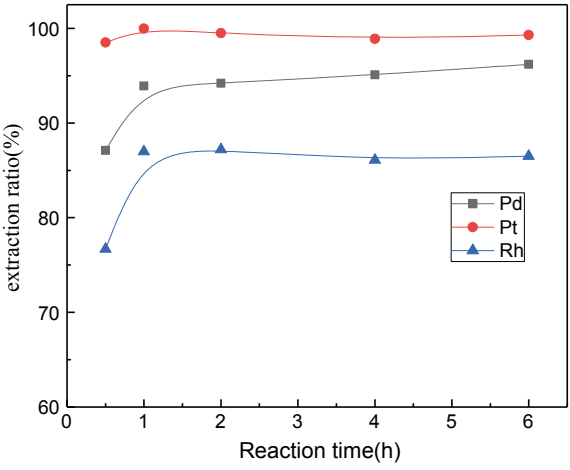

Fig. 5 Effect of reaction time on leaching ratio

of leach decreased, and the increase of leaching ratio is not obvious in the late. In terms of energy consumption, 1 h may be the best leaching time.

Conclusion

The experimental conditions for the leaching of platinum group metals with hydrogen peroxide are as follows: hydrochloric acid concentration is 6 mol/l, liquid-solid ratio is 10:1, reaction temperature is 95 °C, hydrogen peroxide is used as raw material, 5 ml, reaction time is hour. The leaching ratio of platinum, palladium, and rhodium are 93.9%, 99.8%, and 86.9%, respectively.

Acknowledgements Financial support from the Hunan Natural Science Foundation Project (No. 2019JJ40379), the Opening Project of State Key Laboratory of Nickel and Cobalt Resources Comprehensive Utilization and the Research Fund Program of State Key Laboratory of Rare Metals Separation and Comprehensive Utilization (No. GK-201805) is gratefully acknowledged.

References

1. Song W, Li G, Han X (2011) Theoretical mechanism and system explanation of lack of rare earth pricing power. Chin Ind Econ 10:46–55
2. Bernardis FL, Grant RA, Sherrington DC (2005) A review of methods of separation of the platinum group metals through the irchloro complexes. React Funct Polym 65(3):205–217
3. Han S, Wu X, Wang H (2010) Research progress in recovery of platinum group metals from spent catalysts for automobile exhaust. Min Metall 19(2):80–83
4. Jo D, Lie L, Brooks D (2018) Substitution of platinum for palladium in the automotive sector—a case of 'WHEN', Not 'IF'. Precious Met 39(S1):132–140
5. Zhang M, Ke Z (2004) Heavy metals, phosphorus and some other elements in urban soils of Hangzhou City, China. Pedo Sphere 14(2):177–185
6. Bao D, Cheng T (2018) Platinum group metal supply and demand and market price outlook. Precious Met 39(2):82–86
7. Yang H (2005). Process and technology of recovery of platinum group metals from waste carrier catalyst. Shanghai Nonferrous Met (02)
8. Zhao J, Cui H, Bao S (2018) Study on recovery of platinum, palladium and rhodium from waste automotive catalysts by copper trapping. Precious Met 39(1):56–59
9. Liu G, Huo W (2006) Study on extraction of palladium from deactivated catalysts. Compr Utilization Min 1:47–49
10. Xiaofeng W, Wang Y, Tong W (2010) Study on new technology of extracting platinum group metal from waste automobile exhaust gas catalyst by pyrometallurgy and hydrometallurgy. Precious Met 31(4):24–31
11. Kunming Institute of Precious Metals (2009) Method for extracting precious metal from waste automobile exhaust gas catalyst by pyrometallurgy and hydrometallurgy. China, CN, 200910094317.5, 2009-09-02
12. De Aberasturi DJ, Pinedo R, de Larramendi IR et al (2011) Recovery by hydrometallurgical extraction of the platinum-group metals from car catalytic converters. Min Eng 24(6):505–513
13. Greenwood NN, Earnshaw A (1996) Chemistry of Element. In: Zengjun Wet al (Trans), vol 367. Higher Education Press, Beijing

14. Zheng X (2007) Preparation of single palladium automobile exhaust gas purification catalyst and waste palladium recovery. Beijing University of Chemical Technology
15. Barakat MA, Mahmoud MHH (2004) Recovery of platinum from spent catalyst. Hydrometallurgy 72:179–184

Characterization on the Behaviors of Ca and Si Constituents During the Consolidation of Ferruginous Manganese Ores

Bingbing Liu, Ruijie Li, Shengpeng Su and Yuanbo Zhang

Abstract Consolidation of the ferruginous manganese ore fines is of vital importance for manganese extraction in the smelting process. The main impurities in the Fe–Mn ores are Ca and Si constituents and they have a significant effect on the consolidation of iron and manganese oxides. In this study, characterization on the behaviors of Ca and Si constituents during the roasting process of Fe–Mn ores were investigated by thermodynamic, fusion temperatures, and phase identification analyses. The results showed that the Ca and Si constituents can decrease the fusion temperature of the MnO_2–Fe_2O_3 binary system dramatically due to the formation of low-melting complicate silicates from the CaO, SiO_2, and partial manganese and iron oxides. The high-melting solid manganese ferrites phase generated from the remaining manganese and iron oxides were bonded and solidified by the liquid phase. This provided favorable mineralization conditions for the consolidation of Fe–Mn ore.

Keywords Consolidation · Elemental behaviors · Ferruginous manganese ores · Mineralization

Introduction

As rich manganese ores are used up gradually, much attention is paid to extract and recover manganese from Fe–Mn ores to satisfy the developing requirement of manganese industry [1, 2]. Ferruginous manganese ore (Fe–Mn ore) fines are one kind of important manganese resources for manganese extraction by pyrometallurgical beneficiation process in blast furnace [3–7]. However, in order to achieve ideal smelting effect in the blast furnace, Fe–Mn ore fines or concentrates must be agglomerated before being charged into blast furnace [8, 9].

B. Liu · R. Li · S. Su
School of Chemical Engineering, Zhengzhou University, Zhengzhou, Henan 450001, China

B. Liu · Y. Zhang (✉)
School of Minerals Processing & Bioengineering, Central South University, Changsha, Hunan 410083, China
e-mail: zybcsu@126.com

J. Li et al. (eds.), *Characterization of Minerals, Metals, and Materials 2020*,
The Minerals, Metals & Materials Series,
https://doi.org/10.1007/978-3-030-36628-5_11

Sintering is considered as the most efficient process to supply qualified furnace burden with superior chemical and physical properties. Efficient mineralization of Fe–Mn ore fines promotes the energy saving and reduction of consumption for the manganese industry. As well known, the appropriate amount of liquid phase generation during the sintering process is beneficial to the consolidation of the sinters. Manganese oxides and iron oxides are the main minerals of the Fe–Mn ores. The sintering behaviors of the MnO_2–Fe_2O_3 binary system have been systematically investigated in our previous works [10–14]. However, it is found that the main phase after high-temperature roasting is high-melting solid manganese ferrite, and the coke breeze consumption for the sintering process is as high as 8–10% [8]. For the high-carbon ferromanganese alloy production, flux method with basicity of m(CaO)/m(SiO_2) (m(CaO)/m(SiO_2) refers to the mass ratio of CaO and SiO_2) in range of 1.3–1.5 was adopted in blast furnace and extra raw alkaline fluxes must be added into the smelting furnace if the Fe–Mn sinters with natural basicity was used as burdens [1].

In consideration of above-mentioned situation, alkaline fluxes were added in advance into the sintering process of the Fe–Mn ore fines to intensify the liquid phase generation and realize the reduction of solid fuel consumption. In this work, the characterization on the behaviors of Ca and Si constituents during the roasting processing of Fe–Mn ores were investigated to determine the suitable m(CaO)/m(SiO_2) for the efficient mineralization of Fe–Mn ore fines.

Experimental

Materials

Fe–Mn ore used in the present work are with 14.2%Mn metal, 30.6%Fe metal, 18.63%SiO_2, and 0.22%CaO, respectively. The Mn/Fe mass ratio is 0.46 and this ore is characterized as a typical Fe–Mn ore. The main phases of the Fe–Mn ores are goethite, pyrolusite, and quartz. In order to study the effect of different basicity on the consolidation behaviors of Fe–Mn ores, the chemically pure SiO_2, and CaO powders were used as the additives.

Roasting Process

Before roasting, the Fe–Mn ore powders with and without additives were evenly mixed and then the mixture was briquetted by a mold into cylindrical briquette with a diameter of 10 mm and height of 15 mm at a pressure of 10 MPa, and then the cylindrical briquettes were dried at 110 °C for 4 h. The dried briquettes were roasted in a horizontal resistance furnace with air atmosphere and then cooled for the phase analysis.

Characterization

FactSage 7.4 thermodynamic software was used to analyze the liquid phase formation of the MnO_2–Fe_2O_3–CaO–SiO_2 system. The "Equlib" module was adopted and the used databases were "FToxid" and "FactPS".

As for the characteristic fusion temperatures of the Fe–Mn ore with and without additives, the powders mixtures were shaped by a mold into pyramids with bottom side length of 5 mm and vertical height of 12 mm. After that, the pyramids were roasted in a horizontal resistance furnace. The external shape change of the sample was continuously recorded by a camera every 10 s during the preheating process with a heating rate of 10 °C/s. Three characteristic temperatures were distinguished to determine the soft and fusion characteristics. The characteristic temperatures were estimated according to: (1) deformation temperature (T_D), determined by the temperature at which the tip of the pyramid becomes spherical or curved; (2) sphere temperature (T_S), determined by the temperature at which the whole pyramid deforms to be hemispheric; (3) flow temperature (T_F): determined by the temperature at which the pyramid melts until the vertical height is less than 1.5 mm.

Liquid Phase Formation of the MnO_2–Fe_2O_3–CaO–SiO_2 System

Effect of SiO_2 Content

MnO_2, Fe_2O_3, and SiO_2 are the main components of the Fe–Mn ores. MnO_2–Fe_2O_3–SiO_2 system is the main ternary system and is also the benchmark for the comparative study. Based on the characteristic of the Fe–Mn ore described in this work, the molar ratio of MnO_2 and Fe_2O_3 is fixed as 1:1. Liquid phase formation of the MnO_2–Fe_2O_3–SiO_2 system is calculated and listed in Fig. 1. The SiO_2 content is in the range of 0–35% and the temperature range is 1250–1600 °C.

As shown in Fig. 1, under the same temperature, the mass percentage of liquid phase of the MnO_2–Fe_2O_3–SiO_2 system is increased with the increase of SiO_2 content. As the temperature increased from 1250 to 1600 °C under the constant SiO_2 content, the mass percentage of liquid phase of the MnO_2–Fe_2O_3–SiO_2 system is increased rapidly to a maximum and then kept at a steady state when the temperature is further increased to 1600 °C. In special, when the SiO_2 content is 0, the liquid phase of the MnO_2–Fe_2O_3 system is scarcely generated. In other words, the fusion point of the MnO_2–Fe_2O_3 system is over 1600 °C. This result indicates that the solid fuel consumption is very high to guarantee the mineralization of Fe–Mn ores with lower SiO_2 content.

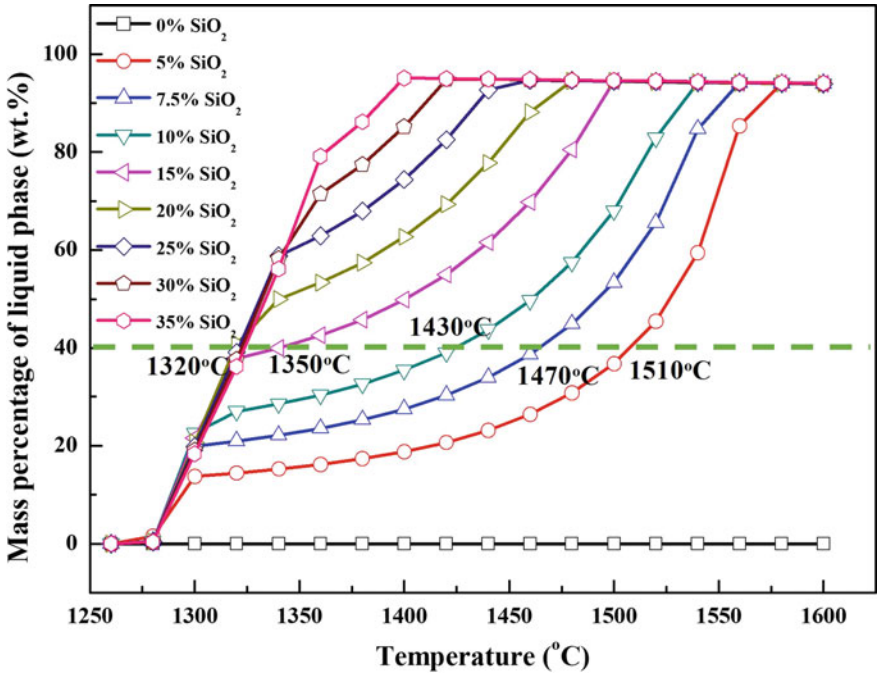

Fig. 1 Effect of SiO_2 content and temperature on the mass percentage of liquid phase in MnO_2–Fe_2O_3–SiO_2 system

On the other hand, it is also found that the temperatures for 40% liquid phase formation of the MnO_2–Fe_2O_3–SiO_2 system with different SiO_2 contents decrease from 1510 to 1350 °C with the SiO_2 content increase from 5 to 15%. It is demonstrated the presence of the SiO_2 can accelerate the formation of the liquid phase.

Effect of CaO Content

The CaO content of the Fe–Mn ore is less than 1%. In order to determine the effect of CaO/SiO_2 on the liquid phase formation of MnO_2–Fe_2O_3 system, the MnO_2–Fe_2O_3–CaO system was also investigated for comparison. The molar ratio of MnO_2 and Fe_2O_3 is also fixed as 1:1. The liquid phase formation of the MnO_2–Fe_2O_3–CaO system was shown in Fig. 2.

As displayed, the mass percentage of liquid phase of the MnO_2–Fe_2O_3–CaO system increased with the increase of CaO content. The presence of the CaO can also facilitate the formation of the liquid phase. For the MnO_2–Fe_2O_3–SiO_2 system, the initial temperatures for liquid phase formation is about 1250–1275 °C. However, the initial temperatures for liquid phase formation of the MnO_2–Fe_2O_3–CaO system

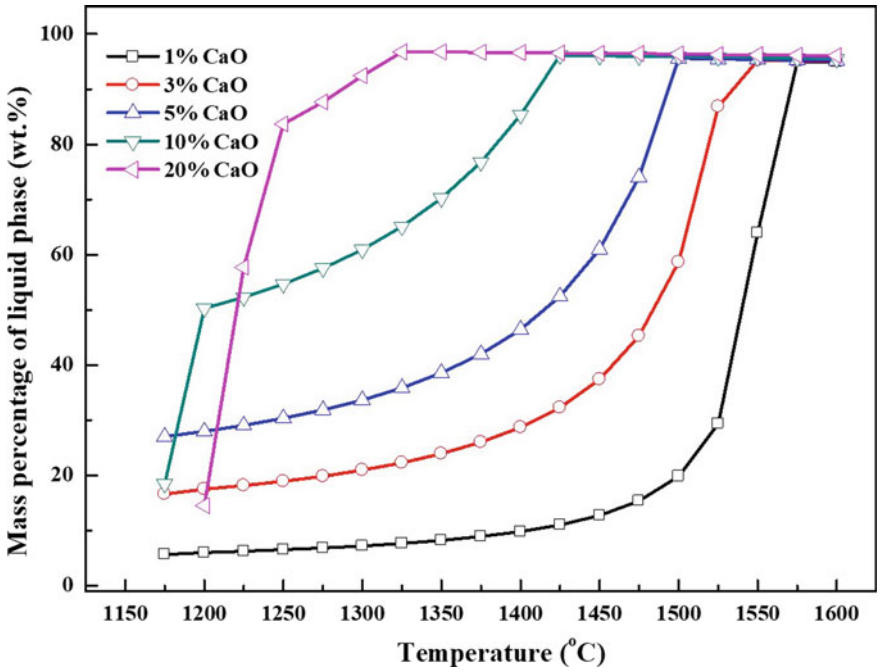

Fig. 2 Effect of CaO content and temperature on the mass percentage of liquid phase in MnO_2–Fe_2O_3–CaO system

decrease to 1150–1200 °C. The above results indicated that CaO addition was able to decrease the fusion temperature and conducive to mineralization of the Fe–Mn ore.

Effect of CaO/SiO₂

Effect of CaO/SiO_2 and temperature on the mass percentage of liquid phase in MnO_2–Fe_2O_3–CaO–SiO_2 system with 5% SiO_2 is drawn in Fig. 3. The $m(CaO)/m(SiO_2)$ is in the scope of 0–1.2. As shown in Fig. 3a, the mass percentage of liquid phase is increased continuously with the increase of temperature. Compared with the effects of SiO_2 and CaO, the initial temperatures for liquid phase formation decrease to 1140–1180 °C. This indicates combined addition of CaO and SiO_2 can further decrease the fusion temperature of the MnO_2–Fe_2O_3–CaO–SiO_2 system.

As shown in Fig. 3b, below 1260 °C, the mass percentage of liquid phase is increased firstly and then decreased with the increase of $m(CaO)/m(SiO_2)$ from 0 to 1.2. When the temperature is increased over 1280 °C, the mass percentage of liquid phase is increased sequentially with the increase of $m(CaO)/m(SiO_2)$ from 0 to 1.2.

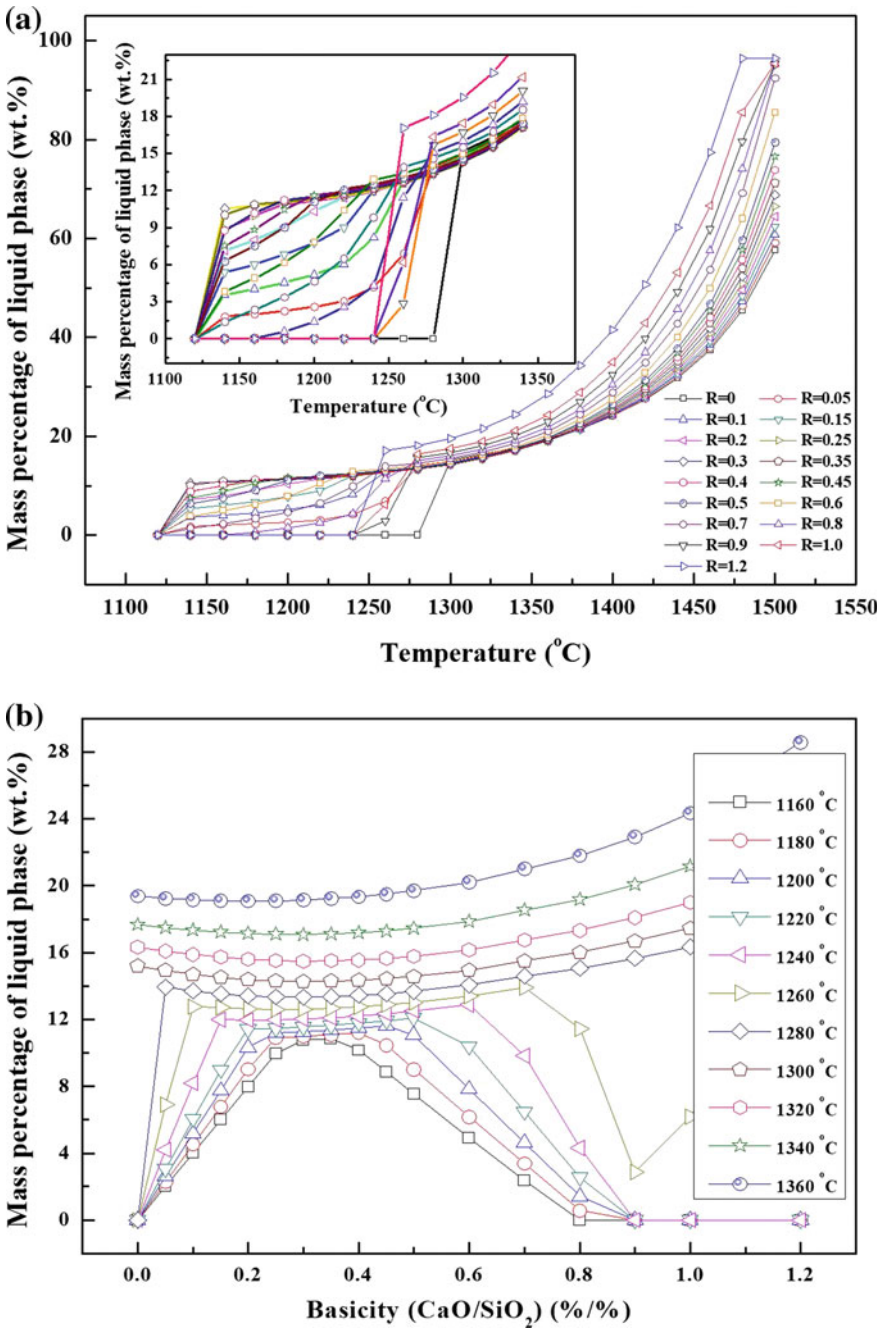

Fig. 3 Effect of m(CaO)/m(SiO_2) and temperature on the mass percentage of liquid phase in MnO_2–Fe_2O_3–CaO-SiO_2 system with 5% SiO_2

Effect of m(CaO)/m(SiO_2) and temperature on the compositions of liquid phase in MnO_2–Fe_2O_3–CaO–SiO_2 system with 5% SiO_2 is presented in Fig. 4. In the ternary system of MnO_2–Fe_2O_3–SiO_2, the main compositions in the liquid phase are SiO_2, FeO, Fe_2O_3, MnO, and Mn_2O_3. With the increase of temperature, the Fe_2O_3 and Mn_2O_3 contents increase while the SiO_2 content decreases. In the quaternary system of MnO_2–Fe_2O_3–CaO–SiO_2, the main compositions in the liquid phase are CaO, SiO_2, FeO, Fe_2O_3, MnO, and Mn_2O_3. The CaO and SiO_2 contents decrease with

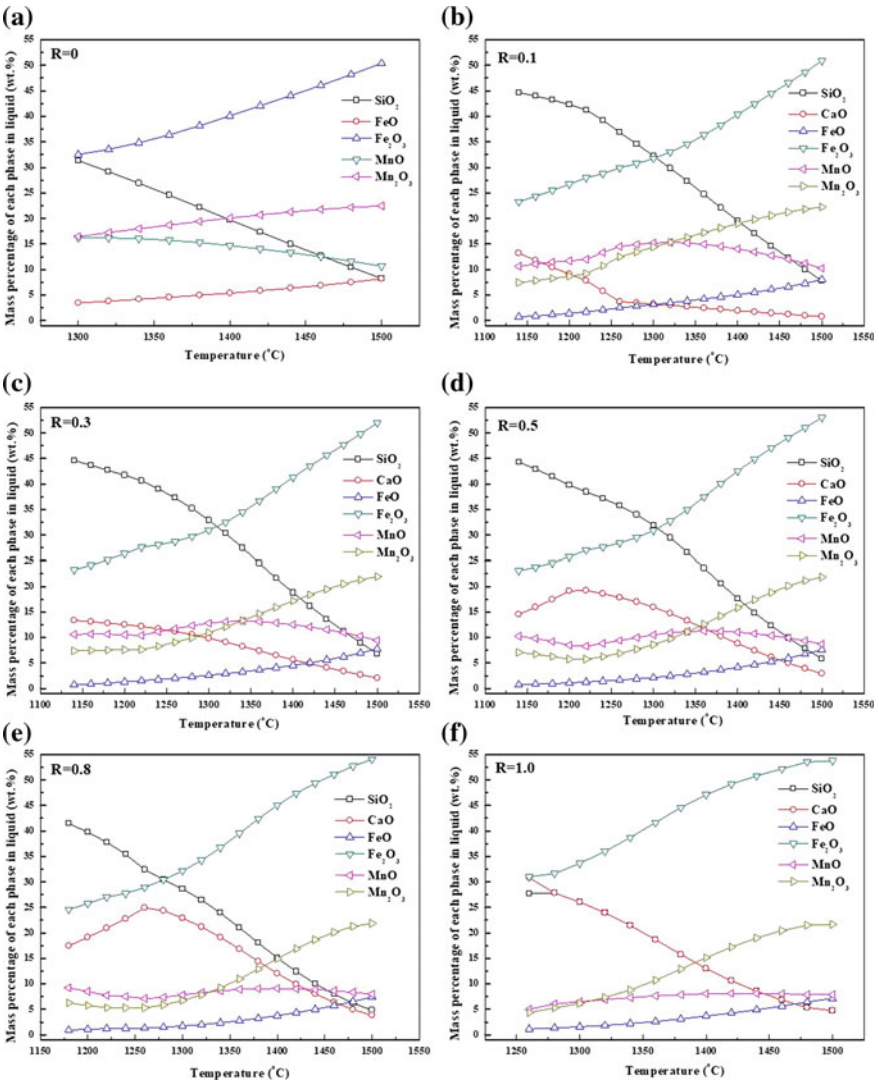

Fig. 4 Effect of m(CaO)/m(SiO_2) and temperature on the compositions of liquid phase in MnO_2–Fe_2O_3–CaO–SiO_2 system with 5% SiO_2

the increase of temperature. Note that, when the m(CaO)/m(SiO_2) is 1, the changing curves of CaO and SiO_2 are overlapping. The decreasing phenomenon is ascribed to the strong chemical bonding ability of CaO and SiO_2 to form the high-melting calcium silicate, and the solid phase is separated out from the liquid phase.

Effect of CaO/SiO_2 on Melting Performance

The fusion characteristic temperatures of Fe–Mn ore roasted under air atmosphere are shown in Fig. 5. As presented in Fig. 6, the deformation, sphere, and flow temperatures decrease with the increase of SiO_2 content and m(CaO)/m(SiO_2). The flow temperature decreases form over 1600 to 1375 °C as the SiO_2 content increases from 0 to 30% (Fig. 6a). In special, the flow temperature of the raw material with 18% SiO_2

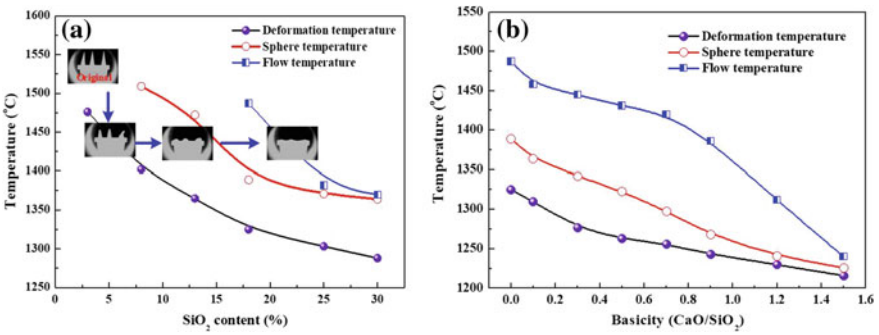

Fig. 5 Fusion characteristic temperatures of Fe–Mn ore roasted under air atmosphere **a** effect of SiO_2 content, **b** effect of CaO/SiO_2

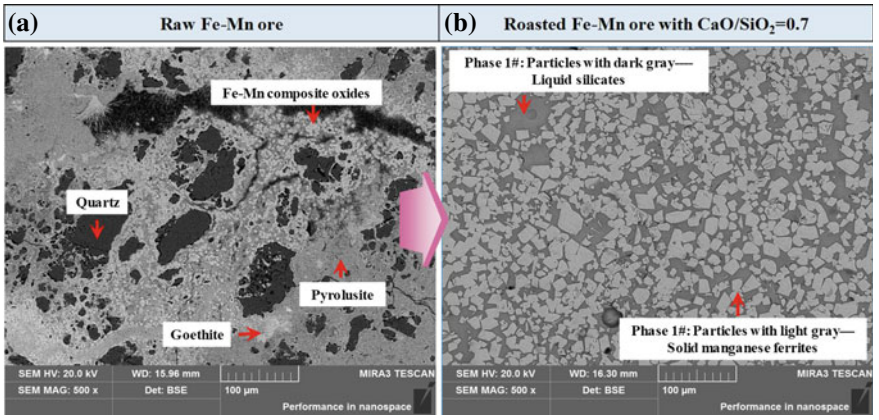

Fig. 6 SEM image of the Fe–Mn ore **a** with CaO/SiO_2 of 0.7 roasted at 1300 °C **b**

is 1487 °C. As shown in Fig. 6b, the flow temperature of the Fe–Mn ore decreases form over 1487 to 1240 °C as the m(CaO)/m(SiO_2) increases from natural basicity to 1.5. It's economically and technologically reasonable to add the CaO to the sintering process of Fe–Mn ore for the high-carbon ferromanganese alloy production due to the addition of CaO can decrease the fusion temperature the Fe–Mn ore and also reduce the extra addition of CaO flux in the blast furnace operation.

Discussion on the Ca and Si Behaviors

The SEM image of the Fe–Mn ore with m(CaO)/m(SiO_2) of 0.7 roasted at 1300 °C is shown in Fig. 6. It can be seen from Fig. 6a that the microstructure of the raw Fe–Mn ore is complicated and the quartz particles are distributed in the pyrolusite and goethite. After roasting with addition of CaO, the mineral phases in the Fe–Mn ore are reconstructed. As observed from Fig. 6b, two main phase of manganese ferrites and silicates are observed. The solid manganese ferrites with melting temperature over 1600 °C are scattered in the low-melting complicate silicates. During the roasting process, the CaO, SiO_2, and partial manganese and iron oxides (FeO, Fe_2O_3, MnO, and Mn_2O_3) are formed the low-melting complicate silicates. The solid manganese ferrites phase is bonded and solidified by the liquid phase. Under this favorable mineralization conditions, the Fe–Mn ore sinter has good mechanical strength.

Conclusions

In this study, characterization on the behaviors of Ca and Si constituents during the consolidation of ferruginous manganese ores was investigated by thermodynamic, fusion temperatures, and phase identification analyses. The thermodynamic results showed that the melting temperature of the MnO_2–Fe_2O_3 system was over 1600 °C, while the Ca and Si constituents can decrease the melting temperature of the MnO_2–Fe_2O_3 system dramatically due to the formation of liquid phase. The initial temperatures for liquid phase formation of the MnO_2–Fe_2O_3 system with SiO_2, CaO, and SiO_2 + CaO addition decreased to 1250 °C–1275 °C, 1150 °C–1200 °C, and 1140 °C–1180 °C, respectively. When the Fe–Mn ore with m(CaO)/m(SiO_2) of 0.7 was roasted at 1300 °C, CaO, SiO_2, and partial manganese and iron oxides (FeO, Fe_2O_3, MnO, and Mn_2O_3) were formed to the low-melting complicate silicates. The solid manganese ferrites phase generated from the remaining manganese and iron oxides are bonded and solidified by the liquid phase. This provided favorable mineralization conditions for the consolidation of Fe–Mn ore.

Acknowledgements The authors wish to express their thanks to the National Natural Science Foundation of China (No. 51904273), the Hunan Provincial Innovation Foundation for Postgraduate (No. CX2016B053) and the Postdoctoral Science Foundation of China (No. 2019TQ0289).

References

1. Tan ZZ, Mei GG, Li WJ, Zeng KX, Liang RT, Zeng XB (2004) Metallurgy of manganese. Central South University Press, Changsha, China
2. Fan D, Yang P (1999) Introduction to and classification of manganese deposits of China. Ore Geol Rev 15:1–13
3. Eriç RH (1995) An overview on manganese alloy production and related fundamental research in South Africa. Min Proc Ext Met Rev 15(1–4):191–200
4. Ahmed A, Ghali S, El-Fawakhry MK, El-Faramawy H, Eissa M (2014) Silicomanganese production utilising local manganese ores and manganese rich slag. Ironmaking Steelmaking 41(4):310–320
5. Eissa M, Fathy A, Ahmed A, El-Mohammady A, El-Fawakhry K (2004) Factors affecting silicomanganese production using manganese rich slag in the charge. In: Tenth international ferroalloys congress, pp 245–253
6. El-Faramawy H, Mattar T, Eissa M, El-Fawakhry K, Ahmed AM (2004) Demanganisation of high manganese pig iron to produce high manganese slag. Ironmaking Steelmaking 31(1):23–30
7. El-Faramawy H, Mattar T, Fathy A, Eissa M, Ahmed AM (2004) Silicomanganese production from manganese rich slag. Ironmaking Steelmaking 31(1):31–36
8. Zhang YB, Liu BB, You ZX, Su ZJ, Luo W, Li GH, Jiang T (2016) Consolidation behavior of high-Fe manganese ore sinters with natural basicity. Min Proc Ext Met Rev 37:333–341
9. Liu BB, Zhang YB, Lu MM, Su ZJ, Li GH, Jiang T (2019) Extraction and separation of manganese and iron from ferruginous manganese ores: a review. Miner Eng 131(2019):286–303
10. Liu BB, Zhang YB, Wang J, Wang J, Su ZJ, Li GH, Jiang T (2018) New understanding on separation of Mn and Fe from ferruginous manganese ores by the magnetic reduction roasting process. Appl Surf Sci 444:133–144
11. Liu BB, Zhang YB, Wang J, Wang J, Su ZJ, Li GH, Jiang T (2018) A further investigation on the MnO_2–Fe_2O_3 system roasted under CO–CO_2 atmosphere. Adv Powder Technol 30(2019):302–310
12. Liu BB, Zhang YB, Su ZJ, Li GH, Jiang T (2017) Phase transformation of MnO_2 and Fe_2O_3 mixture roasted under CO–CO_2 atmospheres. In: TMS characterization of minerals metals and materials, pp 311–319
13. Liu BB, Zhang YB, Su ZJ, Lu MM, Peng ZW, Li GH, Jiang T (2017) Formation mechanism of $Mn_xFe_{3-x}O_4$ by solid-state reaction of MnO_2 and Fe_2O_3 in air atmosphere: morphologies and properties evolution. Powder Technol 313:201–209
14. Liu BB, Zhang YB, Wang J, Lu MM, Peng ZW, Li GH, Jiang T (2017) Investigations on the MnO_2–Fe_2O_3 system roasted in air atmosphere. Adv Powder Technol 28:2167–2176

Microscopic Appearance Transformation of Bornite During Acid Leaching and Bioleaching

Hao Lin, Jun Wang, Yuling Liu and Yi Zhou

Abstract The microscopic appearance transformation of bornite during leaching and bioleaching was investigated in this article. Leaching experiments, X-ray diffraction (XRD), scanning electron microscope (SEM), and energy dispersive spectrometer (EDS) were conducted to investigate the microscopic appearance of bornite in the presence of *Leptospirillum ferriphilum* (*L. ferriphilum*) and sterile condition. The leaching and bioleaching experimental results showed that the recovery of acid leaching was 29.117% while the recovery of bioleaching was 51.328%, which means that the presence of *L. ferriphilum* significantly improved recovery of copper. The SEM imaging revealed that the bioleaching sample surface is rougher than sterile leaching sample due to surface roughness of the bornite increased with oxidation potential.

Keywords Scanning electron microscope · Bornite · Bioleaching · *Leptospirillum ferriphilum*

H. Lin (✉) · J. Wang · Y. Liu · Y. Zhou
School of Minerals Processing & Bioengineering, Central South University, Changsha 410083, Hunan, China
e-mail: mrlinhaoxi@csu.edu.cn

J. Wang
e-mail: wjwq2000@126.com

Y. Liu
e-mail: 1348302685@qq.com

Y. Zhou
e-mail: 1837678526@qq.com

Key Lab of Biohydrometallurgy of Ministry of Education, Changsha 410083, Hunan, China

J. Li et al. (eds.), *Characterization of Minerals, Metals, and Materials 2020*,
The Minerals, Metals & Materials Series,
https://doi.org/10.1007/978-3-030-36628-5_12

Introduction

Nowadays, the grades of copper ores are falling continuously as the higher grade resources are extensively exploited and progressively depleted [1, 2], the consumption of energy and emission of greenhouse gas in the production of copper by traditional industrial methods increase significantly, which leads to the increase of economic and environmental cost [3]. Hydrometallurgy and biohydrometallurgy are considered as important mineral processing techniques in processing low grade ores as it is simple, low cost, and eco-friendly [4], but most studies focused on chalcopyrite [5–7] and few reports about bornite bioleaching have been published. As a secondary copper sulfide, bornite is an important source of copper. Therefore, the development of porphyry processing can bring great returns, from the perspective of economic and social development. As a result, the oxidation of bornite has been the subject of extensive research in recent years. Most of these works were focused on studying bornite dissolution mechanisms during leaching because it is still ambiguous, but only few researchers studied on microscopic appearance transformation of bornite during leaching[8, 9]. Surface oxidation of bornite is a very important part of extracting copper and is critical to understanding and controlling microscopic surface changes of secondary copper sulfide in leaching. As a powerful surface analysis method, scanning electron microscope (SEM) has been widely applied in various fields such as material processing, mineral processing, and battery manufacturing [10–12].

The present work seeks to contribute to a better understanding of microscopic appearance transformation of bornite during acid leaching and bioleaching by identifying bornite surface oxidation microscopic appearance.

Materials and Methods

Minerals

Bornite samples were purchased from Meizhou, Guangdong Province, China. Chemical analysis showed that the bornite sample contained (w/w) 60.62% Cu, 11.74% Fe, and 23.83% S. XRD result indicated that bornite used in the study was of high purity (Fig. 1).

Microorganisms and Bioleaching Experiments

The domestication of *L. ferriphilum* was conducted in 1000 mL flasks that include 12 g mineral and 600 mL iron-free 9 K basic salt medium. All basic solutions were

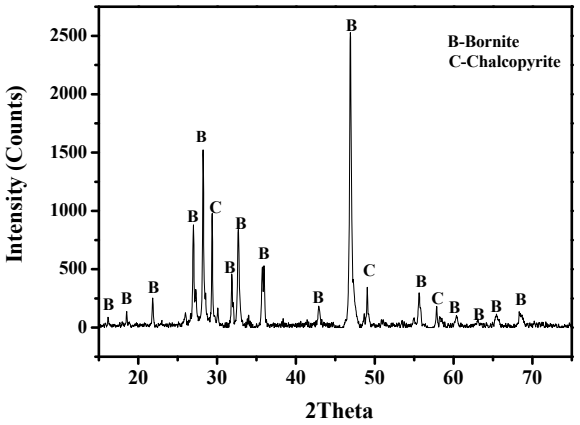

Fig. 1 X-ray powder diffraction analysis of bornite

autoclaved at 121 °C for 20 min. Planktonic cells were collected from bacteria solution in logarithmic phase by centrifugation, and then the collected bacteria are used for bioleaching experiments. Bioleaching experiments were conducted in 250 mL flasks containing 100 mL sterilized basal medium. 1 mL of a bacteria culture as well as 1 g bornite was added to each flask, which were then incubated at 45 °C and 170 rpm on a rotary shaker. The initial cell concentration was higher than 1.0×10^7 cells/mL. Evaporation loss was compensated periodically by adding distilled water, and the pH was adjusted to 1.50 ± 0.03 with sulfuric acid on the first day. During the bioleaching process, the variation of pH value, redox potential, and the concentrations of ferric, ferrous, and copper were measured. Leaching characteristics of pH value, redox potential, concentrations of total copper, total iron and Fe(II) were measured every day. Evaporation loss was compensated with distilled water. The sampling loss was supplemented with the same volume of sulfuric acid or iron-free 9 K medium (pH = 1.5). In the end of leaching tests, the residues were filtered from leaching solution through qualitative filter papers (medium speed), rinsed with pH = 1.5 sulfuric acid and distilled water, and then air dried to send for XRD analysis and SEM observations.

Analysis Methods

The solution pH values were measured by PHS-3C type pH meter. And redox potential was measured in the potential profile of PHS-3C type pH meter by using a platinum electrode with an $Hg/HgCl_2$ reference electrode (SCE). Chemical analysis was conducted by X-ray fluorescence, using an X-ray fluorescence S4 Explorer spectrometer (Bruker AXS, Germany). The X-ray tube (Rh tube with a 75 μm window) was set at 40 kV and 15 mA and the sample powder was scanned over the range

of 5°–85°. The concentration of copper ion and iron was determined by BCO spectrophotometry and o-phenanthroline spectrophotography, respectively (their correlation coefficient of standard curve-r is greater or equal to 0.999). The XRD analysis of mineral samples was performed by a Bruker D8 Advance X-Ray diffractometer (Cu Kα, $\lambda = 1.5406$ Å) with an operating voltage of 40 kV, temperature of 25 °C, current of 40 mA, steps of 0.004°, and a step time of 28.5 s in the range of 2θ from 10° to 80°. MDI Jade 6 software was used for the assignment of all diffraction peaks by reference to PDF-2004 standard cards. SEM observations were performed with a Nova NanoSEM 230 scanning electron microscope coupled with EDS (FEI Electron Optics B.V, Czech).

Results and Discussion

Leaching Test

The variations of solution pH, ORP, copper extractions and cell concentration during leaching test of bornite were shown in Fig. 2. It was shown that the dissolution of

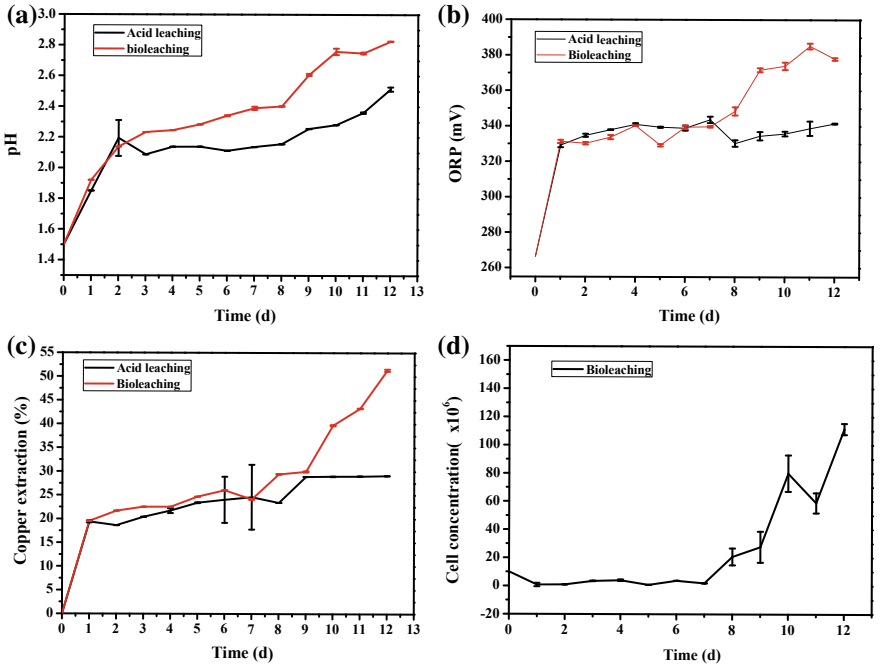

Fig. 2 Variations of solution pH **(a)**, ORP **(b)** copper extractions **(c),** and cell concentration **(d)** during leaching test

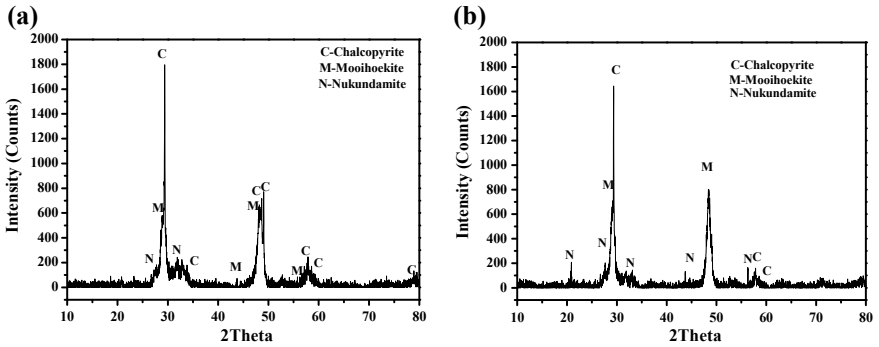

Fig. 3 XRD patterns of residues after leaching for 13 days. **a**Acid leaching, **b** Bioleaching

bornite was an acid-consuming process [13] and the solution pH increased faster in bioleaching which means that bioleaching consumed more acid than acid leaching in this test. The solution ORP increased slowly in the first eight days, and then successively increased from 339.75 to 371.75 mV in bioleaching due to bacterial activity such as oxidation of ferrous to ferric iron [14] while the ORP of acid leaching contained a stable region the next few days. The copper extractions of both test increased rapidly in the first days, then it went smoothly. And at ninth day, the copper extractions of bioleaching increased slowly while acid leaching stopped at 29.117%, and it stopped at 51.328% finally. As shown in Fig. 2b, c, copper concentration was related to solution ORP.

The Characterization of Leaching Residues

As shown in Fig. 3a, b, many distinct diffraction peaks of chalcopyrite ($CuFeS_2$), mooihoekite ($Cu_9Fe_9S_{16}$), and nukundamite ($Cu_{3.38}Fe_{0.62}S_4$) were detected in the residues. Some researchers [3, 13] also obtained a similar conclusion when studying phase transformation of bornite during acid leaching and bioleaching. The intensity of chalcopyrite peaks for bioleaching had a decline as compared with acid leaching, and a broad diffraction bump appeared in the 2θ range of 25°–50°, implying the occurrence of amorphous copper ferric and sulfur. These results indicated that the presence of *L. ferriphilum* promotes phase transition in bornite dissolution and improved copper extraction which was connected with leaching test.

Figure 4 shows the SEM images of bornite leached by 9 K medium in the presence and absence of *L. ferriphilum*. As presented in Fig. 4b, c, some new products with high crystallinity were almost completely covered on the surface of bornite during acid leaching and bioleaching, which proved to be mooihoekite and nukundamite by the method of XRD shown in Fig. 3. In leaching test, a considerable amount of precipitates containing mooihoekite and amorphous copper ferric and sulfur were

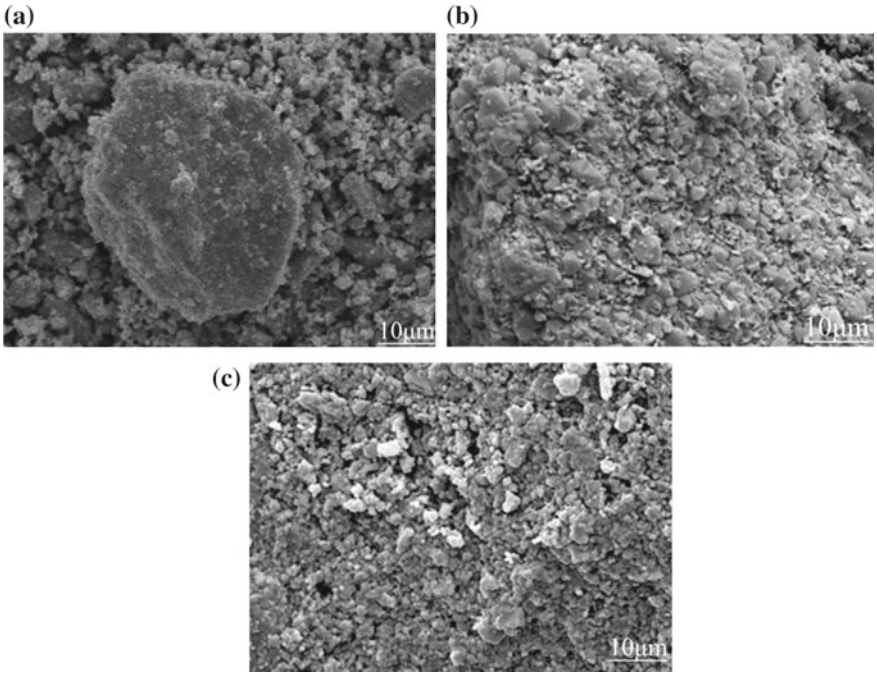

Fig. 4 SEM micrographs of bornite sample (**a**), after acid leaching for 13 days (**b**), and after bioleaching for 13 days (**c**)

coated on the sample surface (Fig. 4b, c). And the products were loose and even some have fallen off from the sample particles. Based on the results of XRD, the product was confirmed to be amorphous copper ferric and sulfur.

It is notable that the presence of *L. ferriphilum* further damaged the bornite surface compared with acid leaching which provided more surface area to make bornite furthermore dissolution. And as shown in SEM pattern (Fig. 4b, c), sample surface was much rougher in bioleaching than acid leaching. In EDS analysis (Table 1), we have found there were more element oxygen, ferric, and less element copper in sample surface during bioleaching compared with acid leaching due to bacterial

Table 1 EDS analysis results (wt%)

Sample	Cu	Fe	S	O	K	Ag
a	61.97	13.91	23.71			0.41
b	70.59	13.64	11.03	4.77		
c	31.68	29.4	16.22	18.17	4.52	

[a]bornite
[b]acid leaching 13 days
[c]bioleaching 13 days

oxidated of ferrous to ferric iron to reproduction and other activities which provided higher ORP [15, 16]. In a word, sample surface in bioleaching is rougher than sterile leaching sample due to surface roughness of the bornite increased with oxidation potential.

Conclusion

The microscopic appearance transformation of bornite during acid leaching and bioleaching was investigated by leaching experiments, scanning electron microscope(SEM), and energy dispersive spectrometer (EDS). The leaching results showed that the presence of *Leptospirillum ferriphilum* significantly promoted copper concentration and consumed more acid during leaching test. The SEM and EDS imaging revealed that the bioleaching sample surface is rougher than sterile leaching sample due to surface roughness of the bornite increased with oxidation potential.

References

1. Zhao H et al (2015) Cooperative bioleaching of chalcopyrite and silver-bearing tailing by mixed moderately thermophilic culture: an emphasis on the chalcopyrite dissolution with XPS and electrochemical analysis. Miner Eng 81:29–39
2. Norgate T, Jahanshahi S (2010) Low grade ores—smelt, leach or concentrate? Miner Eng 23(2):65–73
3. Wang X et al (2018) Synergetic effect of pyrite on strengthening bornite bioleaching by *Leptospirillum ferriphilum*. Hydrometallurgy 176:9–16
4. Zhao H et al (2015) Effects of pyrite and bornite on bioleaching of two different types of chalcopyrite in the presence of *Leptospirillum ferriphilum*. Biores Technol 194:28–35
5. Ai C et al (2019) Increased chalcopyrite bioleaching capabilities of extremely thermoacidophilic *Metallosphaera sedula* inocula by mixotrophic propagation. J Ind Microbiol Biotechnol 46(8):1113–1127
6. Panda S et al (2015) Current scenario of chalcopyrite bioleaching: a review on the recent advances to its heap-leach technology. Biores Technol 196:694–706
7. Zhu J et al (2015) Insights into the relation between adhesion force and chalcopyrite-bioleaching by *Acidithiobacillus ferrooxidans*. Colloids Surf B 126:351–357
8. Pratesi G, Cipriani C (2000) Selective depth analyses of the alteration products of bornite, chalcopyrite and pyrite performed by XPS, AES, RBS. Eur J Mineral 12(2):397–409
9. Zhao H et al (2018) Insights into the surface transformation and electrochemical dissolution process of bornite in bioleaching. Minerals 8(4)
10. Deng S et al (2018) Catalytic effect of pyrite on the leaching of arsenopyrite in sulfuric acid and acid culture medium. Electrochim Acta 263:8–16
11. Smith ME, Finke EH (1972) Critical point drying of soft biological material for the scanning electron microscope. Invest Ophthalmol 11(3):127–132
12. Liu LJ et al (2002) Al_2O_3-coated $LiCoO_2$ as cathode material for lithium ion batteries. Solid State Ion 152:341–346
13. Hong M et al (2019) Intermediates transformation of bornite bioleaching by *Leptospirillum ferriphilum* and *Acidithiobacillus caldus*. Minerals 9(3)

14. Zhang Y et al (2019) Interactions between marmatite and bornite during the oxidative dissolution process in abiotic and biotic systems. RSC Adv 9(46):26609–26618
15. Zhao H et al (2016) Role of pyrite in sulfuric acid leaching of chalcopyrite: an elimination of polysulfide by controlling redox potential. Hydrometallurgy 164:159–165
16. Zhao H-B et al (2015) Surface species of chalcopyrite during bioleaching by moderately thermophilic bacteria. Trans Nonferrous Met Soc China 25(8):2725–2733

Pb(II) Removal from Acidic Wastewater by Magnetic Manganese Ferrites Synthesized from Ferromanganese Ores

Jia Wang, Zijian Su, Manman Lu, Juan Wang and Yuanbo Zhang

Abstract Pb(II) is a typical toxin in industrial wastewater, which has significant pollution risk for drinking water sources. Magnetic manganese ferrites are a proven recyclable adsorption material on account of their excellent ferromagnetism. In this study, manganese ferrites adsorbent synthesized from ferromanganese ore were used for Pb(II) removal from acid wastewater. Thermodynamic calculation and adsorption tests were conducted. Under optimal conditions, the removal ratio of Pb(II) reached 99.4% when initial Pb(II) concentration was 10 mg/L (pH = 5), and the residual Pb(II) concentration was reduced to lower than 0.1 mg/L. The results indicated that the synthetic manganese ferrites were an excellent magnetic adsorbent, which was easy to be separated and recycled. The adsorption mechanism was explored by isothermal adsorption analysis using φ-pH and ICP.

Keywords Manganese ferrites · Pb(II) removal · Magnetic adsorbent

Introduction

Heavy metals (Cu, Pb, Zn, Cr, etc.) are the main pollutants in effluents discharged from the battery, smelting, printing, and dyeing industries [1]. Among these metal ions, Pb(II) is the most common and typical contaminant in industrial wastewater. Due to the non-biodegradability and bioaccumulation of lead ions, it has been reported that Pb(II) concentrations in drinking water exceeding the acceptable limit (0.1 mg/L) can cause great harm to humans [2]. Therefore, removing Pb(II) from wastewater is an important and urgent task for protecting human health and the environment. Many effective heavy metal removal methods have been developed, such as chemical precipitation, ion exchange, membrane filtration, electrochemical

J. Wang · Z. Su (✉) · M. Lu · J. Wang · Y. Zhang
School of Mineral Processing and Bioengineering, Central South University, Changsha 410083, Hunan, China
e-mail: szjcsu@163.com

National Engineering Laboratory for High Efficiency Recovery of Refractory Nonferrous Metals, Changsha 410083, Hunan, China

J. Li et al. (eds.), *Characterization of Minerals, Metals, and Materials 2020*,
The Minerals, Metals & Materials Series,
https://doi.org/10.1007/978-3-030-36628-5_13

treatment and adsorption [3]. Adsorption is one of the most effective water purification methods due to its flexibility, low cost, high efficiency, and environmental friendliness. Therefore, studying various adsorbents for water treatment has become a research hotspot.

Spinel magnetic ferrites MFe_2O_4 (M=Mn, Ni, Co, etc.) have recently been reported to be effective adsorbents for Pb(II) removal because of their obtainability, high magnetic permeability and easy separation from water [4]. Among the different types of spinel ferrites, magnetic manganese ferrite $MnFe_2O_4$ was a promising adsorbent because it was easily functionalized with chemical groups to increase its affinity for heavy metals. In addition, $MnFe_2O_4$ has a very stable structure, wherein the Mn^{2+} and Fe^{3+} occupy tetrahedral and octahedral cation sites in the spinel lattice, respectively, which ensures high chemical stability in acidic conditions. To date, conventional magnetic $MnFe_2O_4$ preparation techniques have been reported, such as co-precipitation, hydrothermal, sol-gel, and solid-state reactions [5, 6]. However, the need for pure synthetic materials and the complex experimental conditions of these methods substantially increase the cost of producing $MnFe_2O_4$ and obviously limit its practical application, especially for industrial production. Therefore, there is great demand for an effective and inexpensive method for the preparation of $MnFe_2O_4$.

Ferromanganese ores are a common, inexpensive resource, and comprehensive research on the utilization of these ores shows that iron-manganese spinel is easily formed at high temperature during roasting, resulting in incomplete separation and recovery of manganese and iron [7]. In previous studies, high purity magnetic spinel manganese ferrite $MnFe_2O_4$ was successfully synthesized by high temperature calcination using ferromanganese ore as a raw material [8]. This synthetic method has many advantages, such as low cost, high yield, and easy operation.

Numerous reports were available describing the action of $MnFe_2O_4$ for Pb(II) removal from aqueous solutions, but the adsorption efficiency of $MnFe_2O_4$ products prepared from ferromanganese ores has not been studied. In this study, we used magnetic $MnFe_2O_4$ synthesized from ferromanganese ores to remove Pb(II) from acidic wastewater and selected an acceptable Pb(II) concentration limit (0.1 mg/L) as an evaluation index for adsorption results. Thermodynamic calculations and adsorption tests were conducted, and the adsorption behavior (adsorbent dosage, pH), thermodynamic calculation, and kinetics were presented. The adsorption mechanism was investigated by isothermal adsorption analysis using φ-pH and ICP.

Experimental

Materials

The ferromanganese ores used in this study contained 44.2 wt% Fe and 15.4 wt% Mn and were acquired from the Jiangxi Province of China. The chemical reagents ($Pb(NO_3)_2$, HNO_3, NaOH) were obtained from Aladdin Reagent (China). All of the

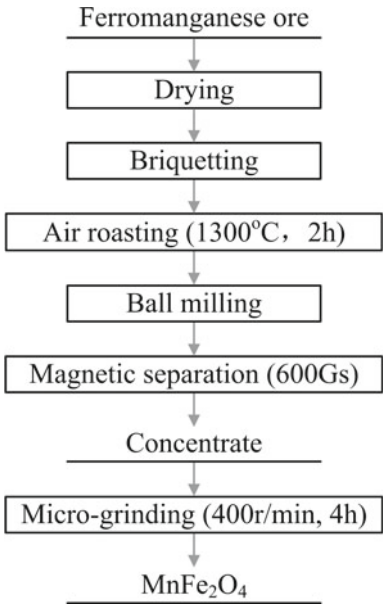

Fig. 1 Synthesis process of manganese ferrites

solutions were prepared using ultrapure water for the experiments. The synthesis process is shown in Fig. 1.

Adsorption Experiments

Adsorption experiments were conducted in batches under isothermal conditions. 50 ml of solutions containing different concentrations of Pb(II) were added to Erlenmeyer flasks. After ultrasonic dispersion, the manganese ferrite was accurately weighed and added to a conical flask. The mixture was then shaken at a constant temperature of 308 K for 24 h to achieve adsorption equilibrium. Next, the suspension was treated with a 0.44 μm membrane filter. The concentration of equilibrium Pb(II) in the solution was determined by ICP. The adsorption capacity of $MnFe_2O_4$ for Pb(II) can be obtained by the following formulas [9]:

$$R = \frac{(C_0 - C_e) \cdot 100\%}{C_0} \tag{1}$$

$$q_e = \frac{(C_0 - C_e) \cdot V}{m} \tag{2}$$

where R is the removal ratio of solution Pb(II) by $MnFe_2O_4$ (%); q_e is the adsorption amount (mg/g); C_0 and C_e are the initial and equilibrium concentrations of Pb(II) (mg/L), respectively; V is the volume of the Pb(II) solution in the experiment (L); and m is the mass of the $MnFe_2O_4$ adsorbent (g).

The same experimental procedures were also used to test the effect of pH (4.5–7.0) on Pb(II) adsorption. The adsorption kinetics was studied using different adsorption times. Different isothermal adsorption experiments were conducted at 298, 308, and 313 K.

Characterization

An inductively coupled plasma-optical emission spectrometer (ICAP7400 Radial) was used to measure the ion concentration in solution. Nitrogen adsorption experiments (BET, Micro-ASAP 2020) and X-ray diffraction experiments (XRD, Bruker D8) were performed to determine the specific surface area and phase composition of synthesized products, respectively. A Malvern laser particle size analyzer (Mastersizer 2000, Britain) was used to measure the particle size distributions of the samples. The pH_{pzc} was detected using the powder addition method.

Results and Discussion

Characterization of the Synthesized Products

XRD analysis of the synthesized materials is shown in Fig. 2, and the standard PDF pattern of $MnFe_2O_4$ is presented as well. The results indicated that the product matched well with the characteristic peaks of spinel $MnFe_2O_4$, which shows that spinel $MnFe_2O_4$ can be successfully prepared by this method. The median particle

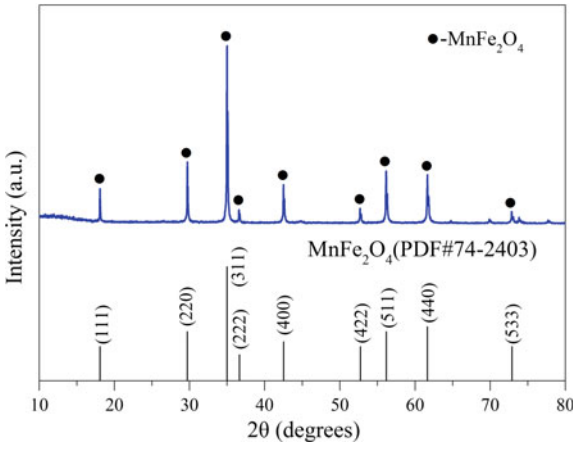

Fig. 2 XRD pattern of the products synthesized from ferromanganese ores

diameter (D50) of the $MnFe_2O_4$ powders was 1.326 μm, with a specific surface area of 32.0 m^2/g.

Effect of Adsorbent Dosages and pH

Isothermal adsorption tests were conducted to investigate the effect of the adsorbent dosage and solution pH, and the results are shown in Fig. 3. It was clear in Fig. 3a that at the equilibrium of adsorption, the adsorption amount and concentration of Pb(II) decreased with increasing amounts of $MnFe_2O_4$. In particular, at a $MnFe_2O_4$ concentration of 0.6 g/L, the equilibrium concentration (C_e) of Pb(II) rapidly decreased to less than 0.1 mg/L from the initial 10 mg/L, which was with a removal of 99%. This $MnFe_2O_4$ concentration was used as the optimal dose for the following adsorption experiments.

Figure 3b showed that the removal ratio and equilibrium concentrations of Pb(II) were closely related to the pH. When pH < 3.0, $MnFe_2O_4$ had poor adsorption capacity for Pb(II). By increasing the solution pH > 3.0, the removal ratio was significantly improved. The Pb(II) removal ratio and equilibrium concentration at pH = 5 were 99.4% and 0.07 mg/L, respectively. At pH > 6.0, the removal ratio reached its maximum value, which was negligible (below 1%) for heavy metal adsorption. The effect of pH on the adsorption behavior can be explained by the change in the degree of deprotonation of the adsorbent surface in solution [10]. The decrease of H^+ concentration in the solution led to an increase in the degree of deprotonation of the surface of $MnFe_2O_4$, thereby promoting the absorption of Pb(II). Accordingly, the Pb(II) adsorption tests were conducted at pH 5.0. It was worth noting that when the pH = 4.5, the removal ratio reached 98%, which indicated that $MnFe_2O_4$ has promising adsorption performance for removing Pb(II) from acidic solutions (4.5 < pH < 7.0).

The above results proved that $MnFe_2O_4$ prepared from ferromanganese ores has good performance for the removal of Pb(II) from acidic solutions. The adsorption

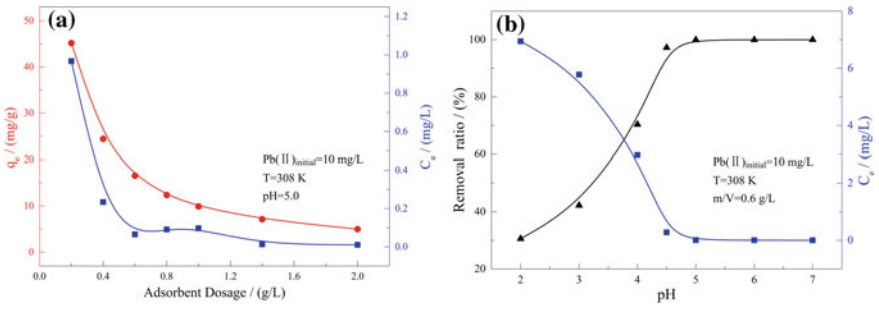

Fig. 3 Effect of the adsorbent dosages and pH on the removal of the Pb(II)

kinetics and adsorption isotherms will be also measured to further investigate the adsorption behavior of $MnFe_2O_4$.

Adsorption Kinetics

Adsorption kinetic analysis is commonly used to estimate the rate of adsorption of heavy metals by adsorbents. Figure 4 shows the amount of Pb(II) adsorbed as a function of contact time. The adsorption process was simulated by using two equations, including the pseudo-first-order Eq. (3) and the pseudo-second-order formula (4) [9]:

$$\log(q_e - q_t) = \log(q_e) - \frac{k_1 t}{2.303} \tag{3}$$

$$\frac{t}{q_t} = \frac{1}{k_2 q_e^2} + \frac{t}{q_e} \tag{4}$$

where q_e and q_t (mg/g) are the capacities of the Pb(II) adsorbed at the equilibrium state and at time (t, min), respectively, and k_1 (min^{-1}), k_2 (g/mg min^{-1}) and n are the adsorption rate constants. The results in Fig. 4 indicated that $MnFe_2O_4$ has a faster adsorption of Pb(II). Approximately 90% of Pb(II) was adsorbed during the first 50 min and then reached equilibrium after 6 h. The pseudo-second-order kinetic model was suitable for explaining the adsorption behavior, illustrating that

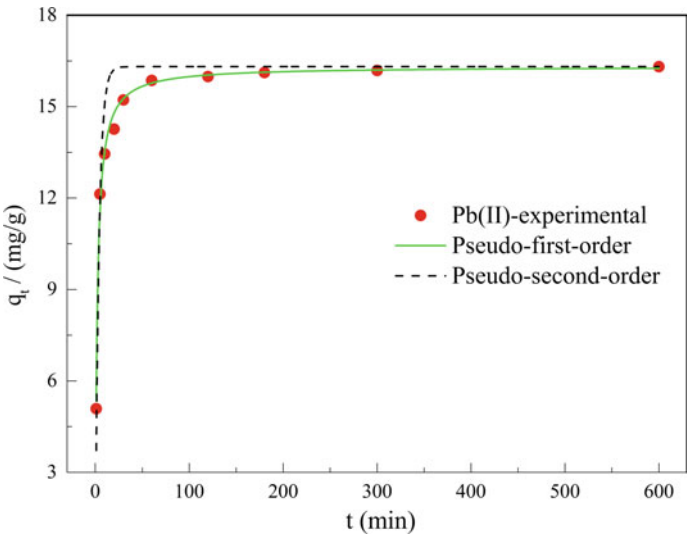

Fig. 4 Relationship between adsorption capacity of Pb(II) and the adsorption time ($Pb(II)_{initial}$ = 10 mg/L, pH = 5.0, m/V = 0.6 g/L and T = 308 K)

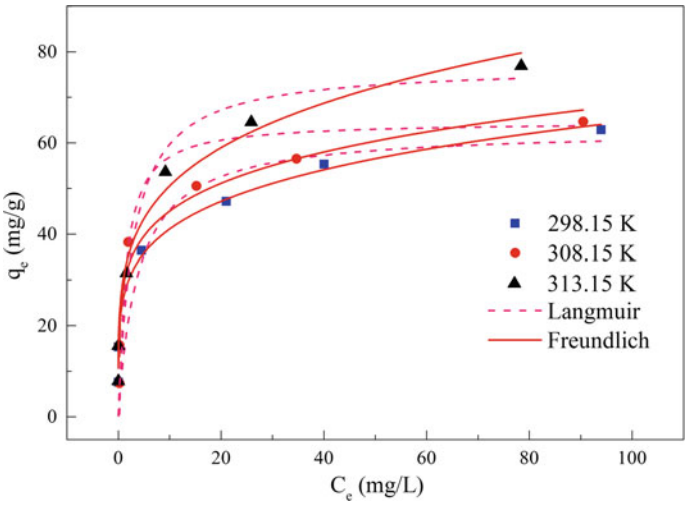

Fig. 5 Adsorption isotherms of Pb(II) at 298, 308 and 313 K ($Pb(II)_{initial}$ = 0–100 mg/L, pH = 5.0, m/V = 0.6 g/L)

the adsorption follows a chemical adsorption process [9]. Decreases in the amount of active sites for adsorption could explain the slower rate of adsorption [11]. Therefore, t = 600 min is an appropriate time for the adsorption isotherm experiments.

Adsorption Isotherms

Figure 5 shows the adsorption isotherms at different temperatures (298, 308, and 313 K) for determining the adsorption capacity. The Langmuir (Eq. 5) and Freundlich models (Eq. 6) used for thermodynamic analysis are shown in the following formulas [12]:

$$q_e = \frac{q_m k_3 C_e}{1 + k_3 C_e} \tag{5}$$

$$q_e = k_4 C_e^{\frac{1}{n}} \tag{6}$$

where C_e (mg/L) and q_m (mg/g) are the concentration and adsorption amount of Pb(II) at adsorption equilibrium, respectively; q_e (mg/g) is the sorption capacity at time t; and k_3 (L/mg), k_4 ((mg L^{-1})$^{1/n}$ (mg g^{-1})) and n are adsorption isotherm constants. From Fig. 5, the temperature played a key role in the adsorption behavior, and the adsorption capacity noticeably increased as the temperature increased from 298 to 313 K.

Table 1 Parameters for adsorption models of Pb(II) on $MnFe_2O_4$

T/K	Langmuir			Freundlich		
	q_m (mg/g)	k_3 (L/mg)	R^2	n	k_4 (L/mg)	R^2
298	64.065	0.256	0.869	0.199	26.064	0.992
308	69.726	0.750	0.869	0.181	29.823	0.965
313	66.812	0.346	0.913	0.221	30.327	0.985

Table 1 lists the isotherm specific parameters of the two models at the three temperatures tested. The fitting results of the two models and the correlation coefficients ($R_L^2 < R_F^2$) demonstrated that the adsorption behavior was more consistent with the Freundlich model, which revealed that Pb(II) was intermittently adsorbed on $MnFe_2O_4$ in the single-molecule form [2, 13]. Additionally, the Freundlich constant (n) value indicated that the Pb(II) was easily adsorbed on $MnFe_2O_4$ in the solution.

The φ-pH analysis is typically used to predict the morphology and condition of elements that are stable in aqueous solutions at a particular potential and pH. Figure 6 shows φ-pH tests of the Pb–H–O system at different temperatures that were calculated using FactSage 7.2.

It should be noted that lead existed in different forms at different solution pH conditions, including Pb(II), $Pb_4(OH)_4^{4+}$, and $Pb_6(OH_{)8}^{4+}$. When pH < 4.8, the lead in the solution was almost all Pb(II), resulting in weak adsorption capacity at lower pH values, which can be attributed to the competition of H^+ and Pb(II) at the surface active sites of $MnFe_2O_4$. The removal of lead in the solution in this range is dominated by the adsorption reaction. When the solution pH was in the range of 4.7–7.0, the Pb(II) in the solution was converted to $Pb_4(OH)_4^{4+}$, which was easily hydroxylated with the

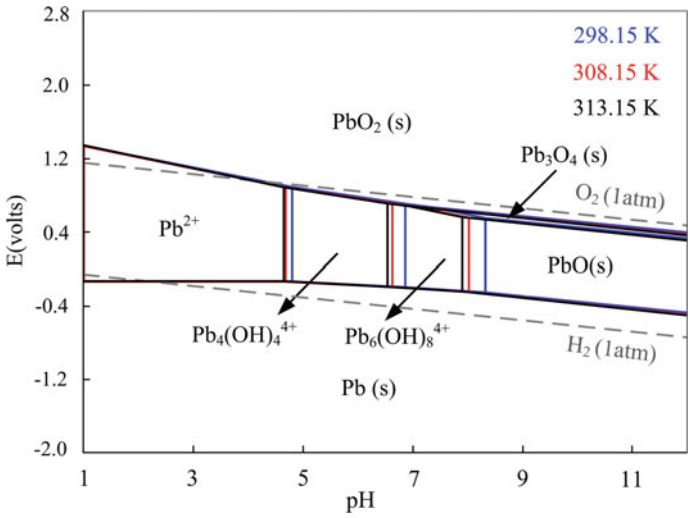

Fig. 6 φ-pH figure of the Pb–H–O system at 298, 308, and 313 K

chemical components of the surface of the $MnFe_2O_4$ adsorbent, thereby facilitating the adsorption reaction. The results of these analyses demonstrated that elevated temperatures lead to the easier conversion of Pb(II) to $Pb_4(OH)_4^{4+}$, meaning that it was beneficial for the adsorption experiment to be performed at a higher temperature. The φ-pH result corresponded to the above experimental data, confirming the adsorption performance of manganese ferrite for removing lead ions from acidic solutions.

Under the condition that the concentration of $MnFe_2O_4$ synthesized by ferromanganese ore was 0.6 g/L and the solution pH was 5.0, the effective removal of Pb(II) can be achieved in less than an hour. The increase in temperature promoted the conversion of Pb(II) to $Pb_4(OH)_4^{4+}$, thereby enhancing the adsorption capacity of $MnFe_2O_4$ for Pb(II).

Conclusion

In this study, magnetic spinel $MnFe_2O_4$ was successfully prepared by the solid phase reaction of ferromanganese ore. The removal of Pb(II) from acid wastewater clearly proved that the synthetic product $MnFe_2O_4$ has a strong adsorption affinity for lead ions. More than 98% of Pb(II) was removed when 0.6 g/L of ferromanganese was added to an acidic solution ($4.5 < pH < 7.0$) at 308 K. Under optimal conditions ($pH = 5$, 308 K), the removal ratio reached 99.4%, which was a significant reduction in the concentration of Pb(II) from the initial 10 mg/L to less than 0.1 mg/L. The adsorption kinetics and adsorption isotherm analysis indicated that the adsorption of Pb(II) by $MnFe_2O_4$ in acidic solutions occurs via a rapid single-molecule chemisorption process. φ-pH analysis further showed that Pb was mainly adsorbed on the surface of manganese ferrite in the form of $Pb_4(OH)_4^{4+}$.

Acknowledgements We sincerely appreciate the supports of Central South University Innovation Foundation for Postgraduate (No. 2018zzts780), the Open Sharing Fund for the Large-scale Instruments and Equipments of Central South University (No. CSUZC201907) and National Natural Science Foundation of China (No. 51574283 and No. U1960114).

References

1. Kumar S, Nair RR, Pillai PB, Gupta SN, Iyengar MAR, Sood AK (2014) Graphene oxide-$MnFe_2O_4$ magnetic nanohybrids for efficient removal of lead and arsenic from water. ACS Appl Mater Interf 6(20):17426–17436
2. Jung KW, Lee SY, Lee YJ (2018) Facile one-pot hydrothermal synthesis of cubic spinel-type manganese ferrite/biochar composites for environmental remediation of heavy metals from aqueous solutions. Bioresour Technol 261:1–9
3. Ren Y, Li N, Feng J, Luan T, Wen Q, Li Z, Zhang M (2012) Adsorption of Pb(II) and Cu(II) from aqueous solution on magnetic porous ferrospinel $MnFe_2O_4$. J Colloid Interf Sci 367(1):415–421

4. Bateer B, Tian C, Qu Y, Du S, Yang Y, Ren Z, Fu H (2014) Synthesis, size and magnetic properties of controllable $MnFe_2O_4$ nanoparticles with versatile surface functionalities. Dalton Trans 43(26):9885–9891
5. Zhang L, Wu Y (2013) Sol-Gel synthesized magnetic $MnFe_2O_4$ spinel ferrite nanoparticles as novel catalyst for oxidative degradation of methyl orange. J Nanomater 2013:2
6. Casbeer E, Sharma VK, Li XZ (2012) Synthesis and photocatalytic activity of ferrites under visible light: a review. Sep Purif Technol 87:1–14
7. Liu B, Zhang Y, Wang J, Wang J, Su Z, Li G, Jiang T (2018) New understanding on separation of Mn and Fe from ferruginous manganese ores by the magnetic reduction roasting process. Appl Surf Sci 444:133–144
8. Liu B, Zhang Y, Lu M, Su Z, Li G, Jiang T (2019) Extraction and separation of manganese and iron from ferruginous manganese ores: a review. Miner Eng 131:286–303
9. Lu M, Zhang Y, Zhou Y, Su Z, Liu B, Li G, Jiang T (2019) Adsorption-desorption characteristics and mechanisms of Pb (II) on natural vanadium, titanium-bearing magnetite-humic acid magnetic adsorbent. Powder Technol 344:947–958
10. Li N, Zhang L, Chen Y, Tian Y, Wang H (2011) Adsorption behavior of Cu(II) onto titanate nanofibers prepared by alkali treatment. J Hazard Mater 189(1–2):265–272
11. Hou X, Feng J, Ren Y, Fan Z, Zhang M (2010) Synthesis and adsorption properties of sponge like porous $MnFe_2O_4$. Colloid Surf A-Physicochem Eng Asp 363(1–3):1–7
12. Hu Q, Liu Y, Gu X, Zhao Y (2017) Adsorption behavior and mechanism of different arsenic species on mesoporous $MnFe_2O_4$ magnetic nanoparticles. Chemosphere 181:328–336
13. Deng J, Liu Y, Liu S, Zeng G, Tan X, Huang B, Tang X, Wang S, Hua Q, Yan Z (2017) Competitive adsorption of Pb(II), Cd(II) and Cu(II) onto chitosan-pyromellitic dianhydride modified biochar. J Colloid Interf Sci 506:355–364

Recovery of Valuable Metals from the Leaching Tailings from the Arsenic/Nickel/Cobalt Residue

Jinxi Qiao, Ailiang Chen, Xintao Sun, Zhen Qian, Yan Zhang, Yutian Ma and Yalin Ma

Abstract The leaching residue after extracting arsenic from the arsenic/nickel/cobalt residue is treated to recover copper, cobalt, nickel, and other valuable metals. The experimental results show that the best conditions are as follows: the liquid–solid ratio is 10:1, the ratio of oxidant to raw material is 0.6 ml/g, the sulfuric acid concentration is 20%, the temperature is 40 °C, and the leaching time is 2 h. Under the above conditions, the leaching ratio of copper, cobalt, nickel, zinc, and arsenic reached 96.31%, 97.23%, 98.56%, 98.46%, and 93.84%, respectively. The leaching kinetics of copper, cobalt, and nickel were further studied. The activation energy of copper, cobalt, nickel is 47.22 kJ/mol, 37.91 kJ/mol, and 44.93 kJ/mol, respectively, and the reaction grades are 1.88, 1.94, and 1.92, respectively. The above valuable metals may be further recovered in the leaching residue. This technique is beneficial for the efficient use of resources, reducing resource waste in the metallurgical process.

Keywords Recovery · Nickel · Cobalt · Copper · Arsenic residue

J. Qiao · A. Chen · X. Sun · Y. Ma (✉)
School of Metallurgy and Environment, Central South University, Changsha 410083, China
e-mail: 13707316399@163.com

J. Qiao
e-mail: Qiaojinxi@csu.edu.cn

Y. Zhang · Y. Ma
State Key Laboratory of Nickel and Cobalt Resources Comprehensive Utilization, Jinchang 737104, Gansu, China

Z. Qian
Changsha Research Institute of Mining Metallurgy Co. Ltd, Changsha 410012, China

Y. Zhang · Y. Ma
Jinchuan Group Co. Ltd, Jinchang 737104, Gansu, China

J. Li et al. (eds.), *Characterization of Minerals, Metals, and Materials 2020*,
The Minerals, Metals & Materials Series,
https://doi.org/10.1007/978-3-030-36628-5_14

Introduction

The demand for minerals in China is greatly increased in the past years along with the development of the metallurgical industry. Zinc of hydrometallurgy has accounted for more than 80% of the total zinc smelting in the world [1]. And it has become the development direction of world zinc smelting production. In the traditional leaching process, the cobalt in the zinc sulfate solution can be removed by using an arsenic salt to form a cobalt residue [2–5]. The cobalt residue contains many valuable metals such as copper, nickel, cobalt, and so on, but there are also harmful element arsenic, which will become a serious environmental pollution. So in order to make full of the resources in the residue and reduce the environmental pollution, the smelting company usually further processes the leaching residue [6–8]. But to reduce production costs, companies usually recycle arsenic from cobalt residue. In this study, the leaching residue from arsenic extraction process was further processed and valuable metals such as copper are recycled.

Experiment

Materials

The raw materials used in this experiment are the tailings after arsenic extraction process from the arsenic/nickel/cobalt residue. Its composition is listed in Table 1. The raw material mainly contained 66.24 wt% copper, 3.40 wt% zinc, 3.04 wt% cobalt, and 0.87 wt% nickel. Figure 1 shows the XRD pattern of the residue, which mainly presents in the form of copper oxide, cuprous oxide, and cobalt oxide.

Method and Analysis

5g of the raw material is added to a certain concentration of sulfuric acid solution, and the reaction is stirred at a certain temperature in the presence of an oxidizing agent; after the reaction time is reached, filtration is carried out to obtain a filtrate rich in copper, cobalt, nickel, and zinc. The contents of copper, cobalt, nickel, and zinc in the filtrate were determined by ICP (Thermo Scientific ICAP 7200 Radial, Thermo Fisher Science, USA), and the leaching ratio was calculated from the content

Table 1 Raw material main content analysis table (wt%)

Ingredient	Co	Cu	Ni	Zn
Content	3.04	66.24	0.87	3.40

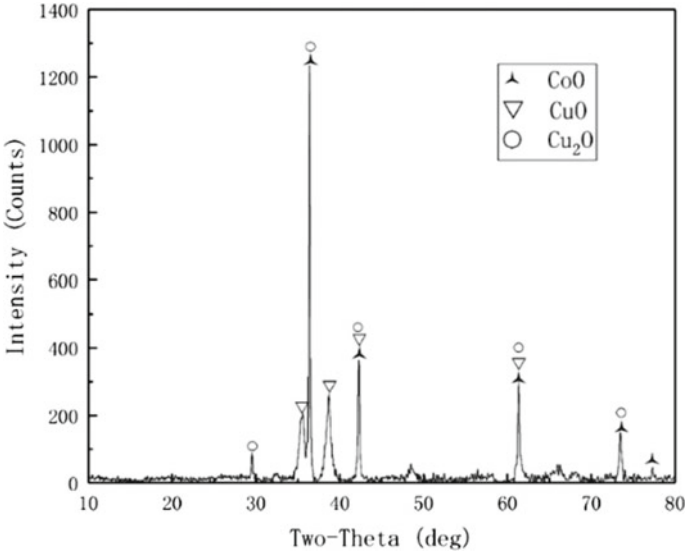

Fig. 1 XRD pattern of raw material

of elements such as copper in the filtrate. The specific calculation formula is:

$$\eta = \frac{c \times 0.1 \times 500}{M \times m} \times 100\% \tag{1}$$

where c is the concentration of the element in the sample measured by ICP, ppm;
M is the mass of the element in each gram of raw material, mg;
m is the mass of the raw material before the experiment, g.

Results and Discussion

Effect of Reaction Time

Figure 2 shows the effect of time on leaching ratio of Co, Cu, Ni, and Zn under the condition of the reaction the liquid–solid ratio of 10:1, the temperature of 80 °C, the acid concentration of 50%.

It can be seen from Fig. 2 that with the reaction progresses, the leaching ratio of each elements in the raw material is continuously increased, reaches a peak after 2 h. The leaching ratio of copper reaches 84.86%, and then tends to be gentle. The leaching ratio of other elements decreased after reaching the peak value. Considering the small content in the raw material, the error may be large. So it can be determined that all the elements reached the maximum leaching ratio after 2 h of reaction.

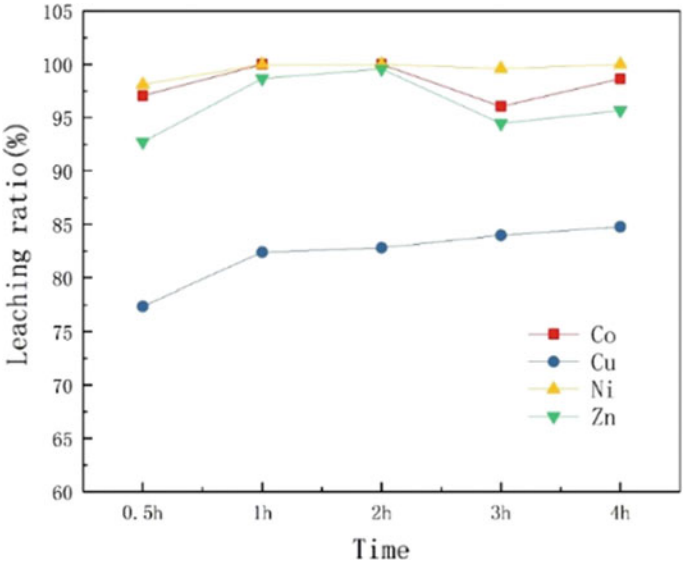

Fig. 2 Effect of leaching time

In addition, the leaching ratio of copper is always below 90%. Combined with the analysis of the XRD component of the raw material, the cuprous oxide in the raw material undergoes a disproportionation reaction under acidic conditions. The divalent copper ion and the elemental copper are formed. The elemental copper does not dissolve in the sulfuric acid, resulting in a low copper leaching ratio. Therefore, the addition of an oxidizing agent during the leaching process facilitates copper leaching.

Effect of Oxidant

The experimental conditions were controlled at the condition as follows: The temperature is 80 °C, the acid concentration is 50%, the reaction time is 2 h, and the liquid–solid ratio is 10:1. The leaching ratio of copper leaching ratio was studied when the oxidant H_2O_2 was added in 1 ml, 2 ml, 3 ml, 4 ml, and 5 ml, respectively. The results are shown in Fig. 3.

It can be seen from the figure that the addition of oxidant has a great influence on the leaching of copper. When the oxidant was 3–5 ml, the leaching ratio of copper reaches over 96%, and the leaching ratio is increased by about 10%. Before the amount of oxidant added was less than 3 ml, the leaching ratio of copper was linearly related to the amount of oxidant, indicating that cuprous oxide in the raw material reacted with H_2O_2 to form divalent copper ions. When the amount of oxidant reached 3 ml, the cuprous copper is completely converted into Cu^{2+}.

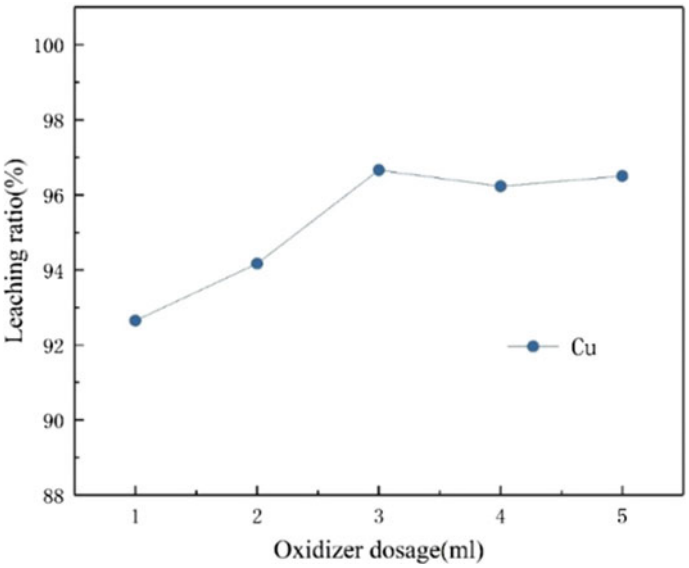

Fig. 3 Effect of oxidant on copper leaching ratio

Effect of Liquid–Solid Ratio

Figure 4 shows the effect of the liquid–solid ratio of the system on the leaching ratio which was studied when the temperature was 80 °C, the acid concentration was 50%, and the reaction time was 2 h.

When the liquid–solid ratio is less than 10:1, the leaching ratios increase with the increase of liquid–solid ratio. The leaching ratios is the highest when the liquid–solid ratio reached 10:1. Combined with the leaching effect and cost factor, the optimum leaching condition of the raw material when the liquid-solid ratio of the reaction is 10:1.

Effect of Sulfuric Acid Concentration

The experimental conditions were controlled at temperature of 80 ° C, reaction time of 2 h, liquid–solid ratio of 10:1, and oxidant addition of 3 ml. The effect of acid concentration on the leaching rate was investigated. The results were shown in Fig. 5.

After analyzing Fig. 5, it can be found that when the concentration of sulfuric acid does not reach 20%, the leaching ratios are significantly lower. As the concentration of sulfuric acid increases, the leaching ratios gradually increase. The leaching ratio of copper is increased from about 65 to 95% at the concentration of sulfuric acid from 5 to 50%. When the sulfuric acid concentration reaches 20%, the leaching ratios reach

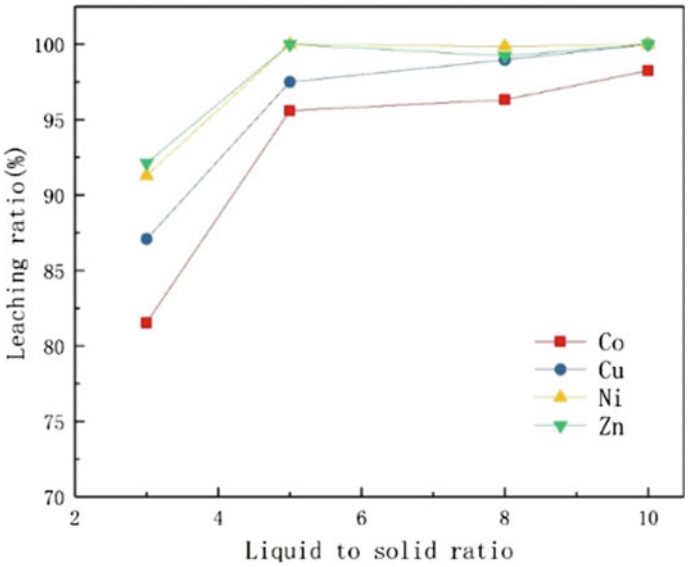

Fig. 4 Effect of liquid–solid ratio

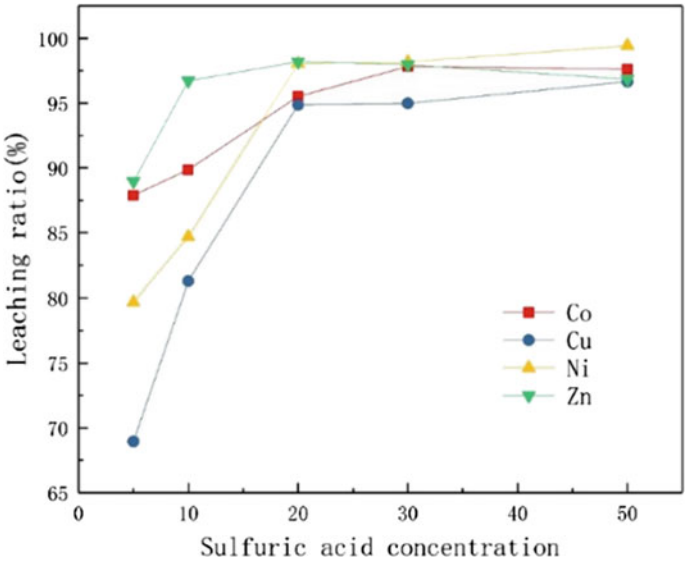

Fig. 5 Effect of acid concentration

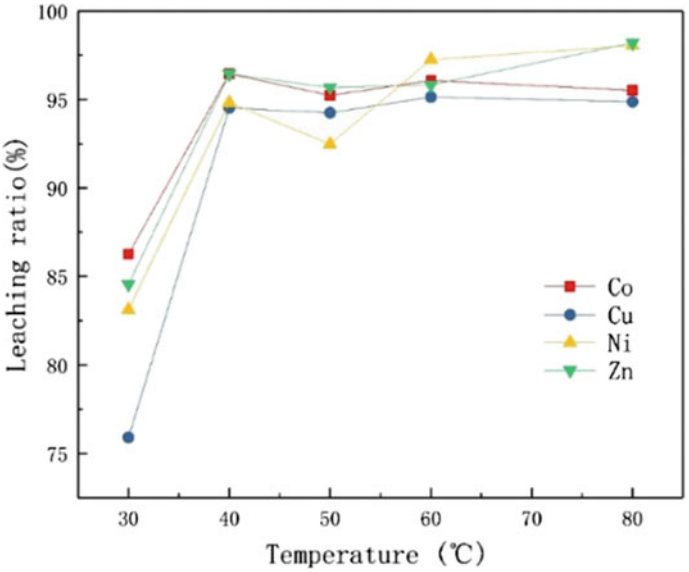

Fig. 6 Effect of reaction temperature on leaching ratio

the highest level, and without any increasement as the acid concentration continue to rise. It indicates that the solution has reached saturation. Therefore, the optimum leaching acid concentration condition of the raw material is 20%.

Effect of Temperature

Figure 6 shows the effect of temperature on the leaching ratio. The experiment was at the condition of reaction time of 2 h, a liquid–solid ratio of 10:1, an oxidant addition amount of 3 ml, and an acid concentration of 20%.

When the reaction temperature is raised to 40 °C, the leaching ratios are remarkably improved. When the temperature is 40 °C, the reactants have almost completely reacted, and the substances in the solution have been completely stabilization, which is regarded as the best condition for the reaction.

Leaching Reaction Optimal Condition Verification Experiment

Based on the above results, the optimal leaching conditions of the cobalt/nickel residue were obtained as follows: The reaction time was 2 h, the liquid–solid ratio was 10:1, the amount of the oxidizing agent was 3 ml, the acid concentration was

Table 2 Leach ratio table for each element under optimal conditions

Experiment no.	Leaching ratio (%)				
	As	Co	Cu	Ni	Zn
1	92.56	96.98	94.27	98.08	97.23
2	93.37	97.23	95.48	98.17	98.46
3	92.12	96.38	96.31	97.58	96.69
4	93.84	94.72	95.45	98.56	97.35
5	92.57	96.19	95.83	97.44	97.5

20%, and the temperature was 40 °C. To verify the optimal conditions, eight sets of verification experiments were performed under the same conditions. The results were shown in Table 2.

The results showed that the average leaching ratio of each element was calculated as: Cobalt was 96.30%; copper was 95.47%; nickel was 97.97%; zinc was 97.45% under the optimal leaching conditions.

Leaching Kinetics

Leaching Reaction Series

The equivalent leaching ratio method was used to determine the reaction order [9–11]. During the reaction, the sample was taken at a certain time interval. The leaching ratio of each element at each time point was obtained by ICP detection. The relationship between the leaching ratio and time under the five groups of sulfuric acid concentration was analyzed.

The relationship between the leaching ratio of cobalt in the raw material and the reaction time was shown in Fig. 7.

From Fig. 7, the time taken to reach the same leaching ratio at different concentrations can be obtained, and the time of t_1, t_2, and t_3 used was obtained when the leaching rate of cobalt reaches 75%, 80%, and 85%, respectively (Table 3).

According to the data in the table, the values of lnt and lnC were calculated, respectively, and made a lnt-lnC graph as Fig. 8.

It can be seen from the calculation of Fig. 8 that when the leaching ratio is 75%, 80%, 85%, the reaction order n is 2.14, 2.07, 1.60, respectively, and the average reaction order is 1.94, which is greater than 1. This indicates the reaction may occur from the kinetic zone to the diffusion zone.

The average reaction order of copper and nickel obtained by the same method was 1.88 and 1.92, respectively.

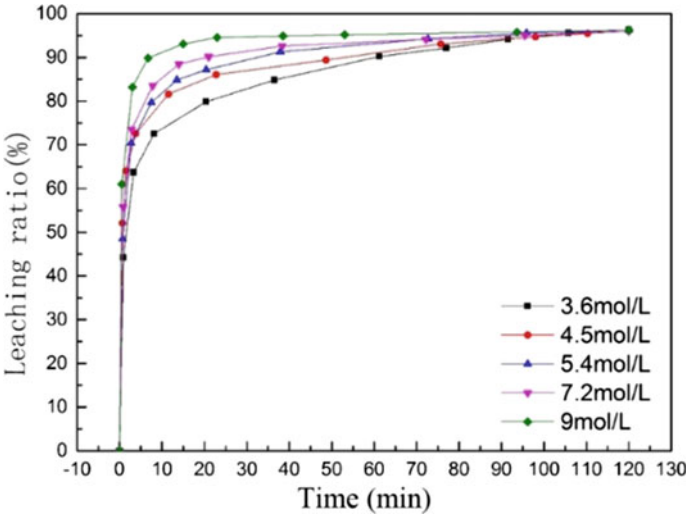

Fig. 7 Effect of different acid concentrations on cobalt leaching ratio

Table 3 Time required to reaching the same leaching ratio at different acid concentrations

Sulfuric acid concentration (mol/L)	t_1	t_2	t_3
3.6	13.2	20.8	37.2
4.5	7.8	10.3	23.6
5.4	5.9	7.6	19.5
7.2	3.1	5.1	12.7
9	1.8	2.7	7.9

Leaching Reaction Activation Energy

During the reaction, the sample was taken at a certain time interval. The leaching ratio of each element at each time point was obtained by ICP detection. The relationship between the leaching ratio and time under the four temperature conditions was analyzed.

The relationship between the leaching ratio of cobalt in the raw material and the reaction time is shown in Fig. 9.

From Fig. 9, the time taken to reach the same leaching ratio at different temperatures can be obtained, and the time of t_1, t_2, and t_3 used is obtained when the leaching ratio of cobalt reaches 65%, 70%, and 75%, respectively.

According to the data in Table 4, calculate the values of lnt and $1/T$, respectively, and make a lnt-$1/T$ map.

It can be seen from the calculation of Fig. 10 that the apparent activation energies E were 39.07 kJ/mol, 35.14 kJ/mol, 39.53 kJ/mol respectively, when the leaching

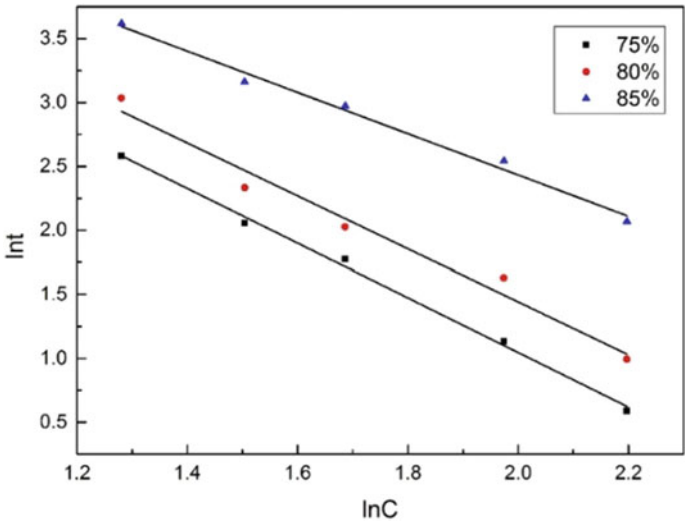

Fig. 8 lnt–lnC pattern under different leaching ratios

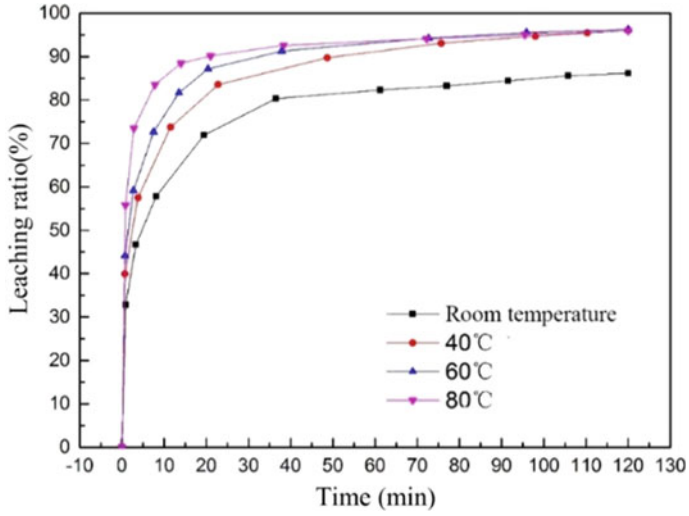

Fig. 9 Effect of different temperatures on cobalt leaching ratio

Table 4 Time required to reaching the same leaching ratio at different temperatures

Temperature (°C)	t_1	t_2	t_3
25	12.5	17	25
40	7.5	9	13
60	5	7	9.5
80	2	3	5

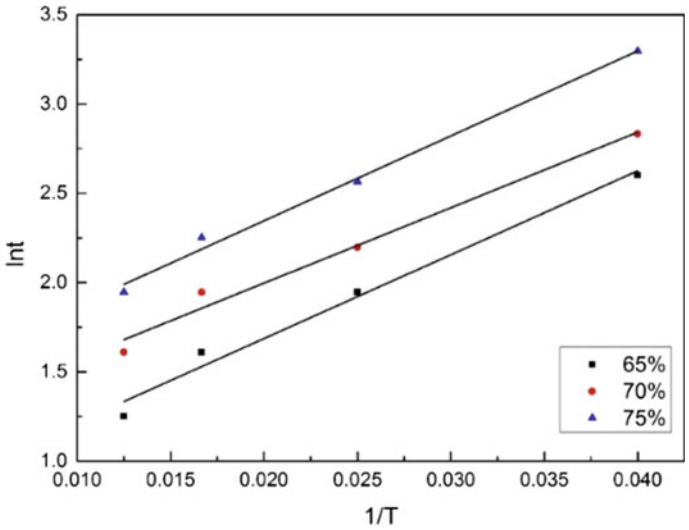

Fig. 10 lnt-1/*T* pattern under different leaching ratios

ratios are 65%, 70%, 75%. The average activation energy was 37.91 kJ/ Mol. The cobalt leaching in arsenic/copper/cobalt residue is mainly controlled by chemical reaction. Increasing the temperature is beneficial to cobalt leaching.

The average activation energies of copper and nickel leaching in the same way were 47.22 kJ/mol and 44.93 kJ/mol, respectively, indicating that copper and nickel leaching were mainly controlled by chemical reactions.

Conclusion

(1) The arsenic-containing waste was the residue after arsenic removal of arsenic-containing copper/cobalt residue, mainly containing 66.24% of copper, 3.04% of cobalt, 0.87% of nickel, 3.4% of zinc and 1.64% of arsenic, accounting for 75.19%.

(2) The optimal leaching conditions of the cobalt/nickel residue were obtained as follows: The reaction time was 2 h, the liquid–solid ratio was 10:1, the amount of the oxidizing agent was 3 ml, the acid concentration was 20%, and the temperature was 40 °C. Finally, the leaching ratio of copper, cobalt, nickel and zinc was 96.31%, 97.23%, 98.56%, and 98.46%, respectively.

(3) The activation energies of copper, cobalt, nickel leaching reaction are 47.22 kJ/mol, 37.91 kJ/mol, and 44.93 kJ/mol, respectively; and the reaction grades are 1.88, 1.94, and 1.92, respectively.

Acknowledgements Financial support from the Opening Project of State Key Laboratory of Nickel and Cobalt Resources Comprehensive Utilization, the Hunan Natural Science Foundation Project (No. 2019JJ40379), and the Research Fund Program of State Key Laboratory of Rare Metals Separation and Comprehensive Utilization (No. GK-201805) is gratefully acknowledged.

References

1. Qi J (2002) Recovery and utilization of arsenic in heavy ferrous metal smelting. Kunming University of Science and Technology
2. Qiao J, Long S, Ma Y, Qiu Y, Chen J, Miao H, Chen A (2018) Air oxidizing alkali leaching arsenic, cobalt and nickel residue. Chin J Nonferrous Met 28(11):2358–2365
3. Zeng G, Xie G, Yang D, Wang J (2006) The effect of cadmium ion on cobalt removal from zinc sulfate solution. Miner Eng 19(2):197–200
4. Yu G, Zhang Y, Zheng S (2014) Extraction of arsenic from arsenic-containing cobalt and nickel slag and preparation of arsenic-bearing compounds. Trans Nonferrous Met Soc China 24(6):1918–1927
5. Krause B, Sandenbergh RF (2015) Optimization of cobalt removal from an aqueous sulfate zinc leach solution for zinc electrowinning. Hydrometallurgy 155:132–140
6. Wu T, Yang C, Li Y, Zhu H, Gui W, Wang Y (2013) Study on the control of waste acid addition in the process of cobalt removal from zinc arsenic salt in wet process. J Central South Univ: Sci Technol 44(12):4881–4886
7. Cao W (2001) Discussion on removal of cobalt by arsenic salt and barium salt. Hunan Nonferrous Met (S1):17–18+22
8. Li L (2009) Determination of metal recovery in cobalt slag by wet zinc method. Sci Technol Innov Rev 36:99–100
9. Zhang W, Wang C, Ma B (2019) Leaching kinetics of calcium molybdate with hydrochloric acid in presence of phosphoric acid. Trans Nonferrous Met Soc China 29(4):859–867
10. Ajiboye EA, Panda PK, Adebayo AO (2019) Leaching kinetics of Cu, Ni and Zn from waste silica rich integrated circuits using mild nitric acid. Hydrometallurgy 188:161–168
11. Zhu X, Liu X, Zhao Z (2019) Leaching kinetics of scheelite with sodium phytate. Hydrometallurgy 186:83–90

Part IV
Characterization of Mechanical Properties I

Effect of Microstructure on Cleavage Fracture of Thick-Section Quenched and Tempered S690 High-Strength Steel

V. M. Bertolo, Q. Jiang, C. L. Walters and V. A. Popovich

Abstract One of the main challenges in applying thick-section high-strength steels (HSS) at arctic condition in offshore and maritime industry is to maintain a sufficient level of toughness to prevent brittle failure. An aspect that requires special attention is the through-thickness microstructural variation which may result in different local mechanical responses affecting the overall material's fracture behaviour. This paper presents an experimental study combining microstructural investigation and sub-sized fracture toughness testing at −100 °C of different sections of 80 mm S690QL steel aimed to evaluate the effect of microstructure on cleavage fracture. In addition, different crack depth to width ratios (a/W) were used to investigate the constraint effect, while different notch orientations were applied to assess the effect of rolling orientation. Results show lower fracture toughness for the middle of the plate, which was attributed to the presence of large Nb-rich inclusions which may feature pre-existing cracks and/or defects in the inclusion/matrix interface and also often distributed as clusters. It was also observed that a/W ratio plays an important role in fracture toughness showing shallow-notched specimens with substantially higher fracture toughness than deep cracked specimens. Moreover, microstructural features such as inclusions aligned parallel to the pre-crack can ease the crack propagation and contribute to a reduction in fracture toughness.

Keywords Fracture toughness · Microstructure · Cleavage fracture · Multiphase high-strength steel

V. M. Bertolo (✉) · Q. Jiang · V. A. Popovich
Department of Materials Science and Engineering, Delft University of Technology, Delft, The Netherlands
e-mail: v.moretebarbosabertolo@tudelft.nl

C. L. Walters
Structural Dynamics, TNO, Delft, The Netherlands

J. Li et al. (eds.), *Characterization of Minerals, Metals, and Materials 2020*,
The Minerals, Metals & Materials Series,
https://doi.org/10.1007/978-3-030-36628-5_15

Introduction

As a consequence of severe service conditions and the trend towards design for higher loads in offshore and maritime industry, thick-section high- strength steels such as quenched and tempered S690 have been increasingly used in the last few decades as their favourable combination of high strength and toughness allow for lighter structures and good performance [1]. However, due to the expansion of exploration areas into low-temperature regions such as the Arctic, these activities have been facing material-related challenges.

High-strength steels (HSS) are known to transition from ductile-to-brittle with the decrease of temperature and, consequently, at low operating temperatures, their fracture process is dominated by cleavage, which may cause sudden and catastrophic failure without any warning [2]. Cleavage fracture exhibits strong sensitivity to material microstructure and, hence, microstructural investigation is of paramount importance in order to ensure the ability to meet minimum operating requirements and, consequently, guarantee safety of the structural components.

HSS are multiphase materials and thick-section high-strength steels (above 60 mm) exhibit a through-thickness microstructural variation exhibiting coarse and fine microstructures, as well as a combination of multiple phases, variation owing to through-thickness gradient of cooling rates and deformation levels during the processing route. Such inhomogeneous and multiphase microstructures lead to a large variation of properties through the thickness, which makes it increasingly difficult to predict and control cleavage fracture [3, 4].

Therefore, the aim of this work is to provide a better understanding of the effects of microstructural features on cleavage fracture initiation through the thickness. For this purpose, the through-thickness microstructure and fracture toughness of 80 mm S690QL HSS plate were investigated via crack tip opening displacement (CTOD) testing at −100 °C, where, based on the ductile-to-brittle transition curve, the material is in the lower-shelf region (failure by cleavage). In addition, extensive investigation of the fracture surface was made to identify cleavage initiation sites.

This study also includes an investigation of the effect of two variables on fracture toughness: (1) Specimen orientation with respect to the rolling direction and (2) Crack depth to width ratio (a/W) as crack-like flaws found in structural components are often shallow defects rather than deep cracks as the ones found in standard fracture toughness specimens [5].

Experimental Conditions

Material

A commercially available 80 mm thick quenched and tempered S690 high-strength steel plate (designated as S690QL in accordance to EN 10025-6 [6]) was used in this

work. The chemical composition of top quarter (further referred to as top) and middle sections of the steel plate was studied by X-ray fluorescence (XRF) and LECO combustion analysis. The through-thickness microstructure of the steel plate was etched with 5% Nital and analysed by means of optical microscopy and scanning electron microscopy (SEM). For the prior austenite grain (PAG) investigation, samples were swab etched with 100 ml saturated aqueous picric acid solution and 0.5 g of sodium dodecyl benzene sulfonate etching for 5 min and the PAG size measurements were carried out by ImageJ software according to the ASTM E112-10 standard [7]. SEM with Energy-dispersive X-ray spectroscopy (EDS) was used to study morphology and chemical composition of inclusions, while quantification was performed by Keyence optical microscope according to the ASTM E1245-03:2016 standard [8].

Mechanical Testing

Fracture toughness tests were performed according to ISO 12135 [9] at −100 °C using sub-sized single edge-notched bending (SENB) specimens, where dimensions are given in Fig. 1a, with a/W ratios of 0.5 and 0.1 and on both T-L (Fig. 1b) and L-T (Fig. 1c) notch orientations. All fracture specimens were tested in three-point bending at a deformation rate of 2 mm/s using a MTS 858 servo hydraulic.

The CTOD results for low-constraint condition ($a/W = 0.1$) were also calculated according to the ISO 12135 standard [9]. However, the plastic rotational factor value ($r_p = 0.4$ for high-constraint specimens) was set to 0.24. This value was found through finite element analysis where the specimen was modelled in three dimensions with appropriate boundary conditions according to the experimental set-up. The total initial crack length used was 2 mm, which includes a 0.6 mm long notch and an 1.4 mm long pre-fatigued crack, reproducing conditions for the low-constraint specimens used experimentally in this study. The crack tip was modelled with an initial blunted opening with a radius of 0.005 mm. The finite element model was loaded by displacement ramp imposed on the loading point through a rigid roller.

The plastic rotational factor, r_p, is calculated from its relationship with CTOD and crack mouth opening displacement (CMOD):

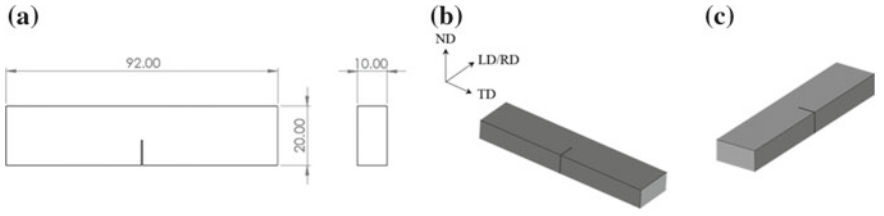

Fig. 1 Schematic illustration of SENB specimens showing **a** the dimensions and **b** T-L and **c** L-T notch orientations, where ND is the normal direction, LD/RD are the longitudinal and rolling direction and TD the transverse direction

$$\delta p = \frac{r_p(W-a)V_p}{r_p(W-a)+a} \quad (1)$$

where δp is the plastic CTOD component and V_p is the plastic CMOD measured from the finite element model.

Examination of fracture surfaces was performed using SEM with EDS to characterize the mode of failure and to locate and identify microstructural features contributing to the cleavage.

Results and Discussion

Microstructural Characterisation

The through-thickness chemical composition for S690QL steel is given in Table 1. As can be seen, there is a concentration gradient through the thickness for C, which is higher in the top section.

Representative microstructures of top and middle sections of the plate are shown in Fig. 2. The top section of the plate presents a tempered martensitic structure, while the middle section exhibits a mixed microstructure of tempered martensite and tempered bainite. This microstructural inhomogeneity, found throughout the

Table 1 Through-thickness chemical composition of S690QL (measured by XRF and LECO)

wt (%)	Fe	C	Si	Al	Mo	Other
Top	Bal.	0.17 ± 0.001	0.29 ± 0.022	0.07 ± 0.005	0.30 ± 0.007	Mn, Ni, Cr, Nb
Middle	Bal.	0.16 ± 0.001	0.30 ± 0.03	0.08 ± 0.011	0.29 ± 0.02	

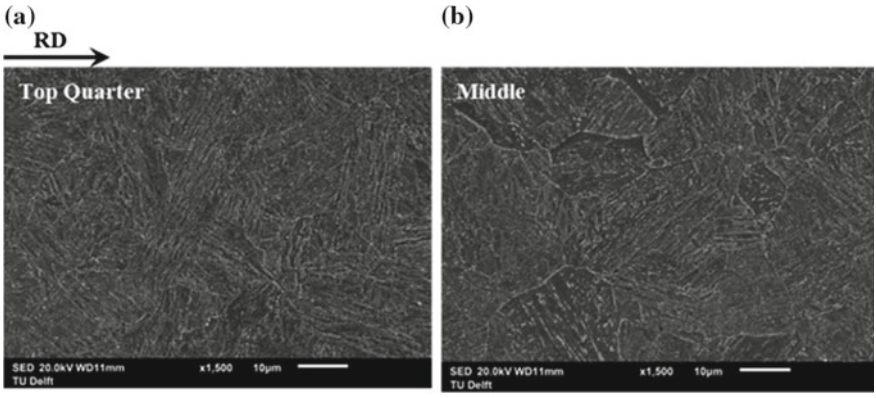

Fig. 2 Microstructure of the S690QL steel plate at **a** top and **b** middle sections

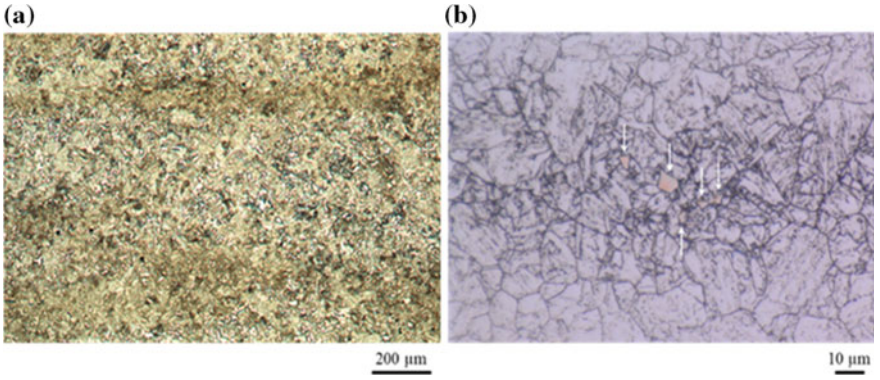

Fig. 3 Images showing **a** centreline segregation bands and **b** inclusions present in these bands (indicated by arrows) found in the middle section of S690QL steel plate

thickness of the plate, is a result of through-thickness gradient of cooling rates during quenching where cooling rates are approximately 4 and 6 °C/s for top and middle sections, respectively. The as-quenched microstructure varies from fully martensitic at areas closer to the surface, where it cools quickly, to mixed martensite and bainite towards the centre, where heat takes longer to dissipate [4, 10]. Afterwards, these microstructures are tempered.

Moreover, clear centreline segregation bands aligned in the rolling direction (Fig. 3a) as well as inclusions associated to these bands (Fig. 3b) were observed in the central part of the plate.

In addition to the already presented microstructural distinctions, variations in the prior austenite grain (PAG) size and distribution were also observed and found to be influenced by the centreline segregation bands. The top thickness position was found to have a rather uniform PAG distribution with an average PAG size of 21 µm (ASTM grain size equal to 7.9). The middle section, which contains centreline segregation bands (Fig. 3), has a larger PAG with an average size of 22 µm (ASTM grain size equal to 7.7) and exhibits a bimodal distribution with distinctly smaller grains in the segregation band (Fig. 4).

The variation of PAG size between the outer and central parts of the steel plate is a result of non-uniform deformation strain during the hot rolling process. High strain values are reached in the surface and decrease through the thickness. Consequently, more energy for recrystallization is stored by the material close to the surface than in the middle of the plate. Hence, the recrystallization of the austenite during hot rolling leads to a finer austenite grain structure in the outside part of the slab.

It should be noted that the PAG size difference between these two sections of the plate would have been larger if not for the presence of centreline segregation bands in the middle section. Figure 4a, b show the PAG distribution in the middle section of the steel plate in the absence and presence of the segregation bands, respectively. In the absence of segregation bands, there is a relatively uniform grain size distribution with an average PAG size of 23 µm (ASTM grain size equal to 7.6). In contrast, in the

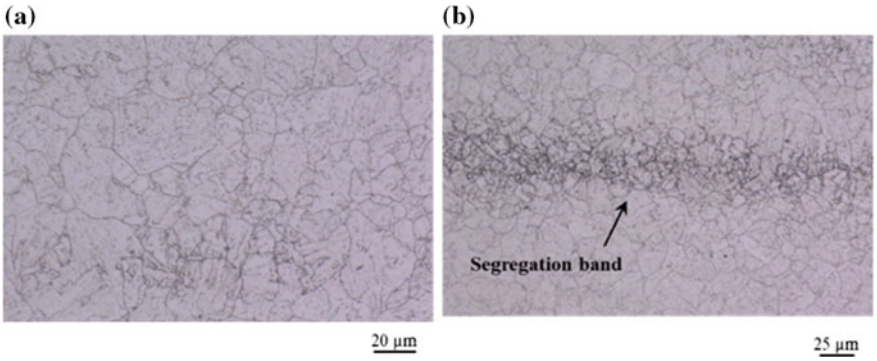

Fig. 4 Prior austenite grain (PAG) distribution in the middle of the plate **a** without the segregation band and **b** with the segregation band showing a reduction in PAG size in the region of the band

presence of segregation bands, the PAG distribution is bimodal with smaller grains size in the banded area. The fine-grained segregation band present a PAG grain size equal to 11 µm (ASTM grain size equal to 9.7) and, consequently, the overall PAG (Fig. 4b) size is reduced to 22 µm. Pallaspuro (2018) observed the same behaviour for a 0.13 wt% carbon steel [11]. EBSD analysis will be carried out in order to further validate the observed grain size distribution.

Figures 5 and 6 illustrate the most common types of inclusions observed in top and central parts of the plate, respectively. In the top position of the plate, spherical, and cubic inclusions with dimensions ranging from 1 to 5 µm (Fig. 5) were observed. Inclusions included rather complex chemical composition of oxides, nitrides, and carbonitrides such as spherical (Mg,Ti)(O,N), (Mg,Al,Ca)(O,N) and (Mg,Al,Ca,Ti)(O,N), and cubic (B,Ti,Nb)(N,C).

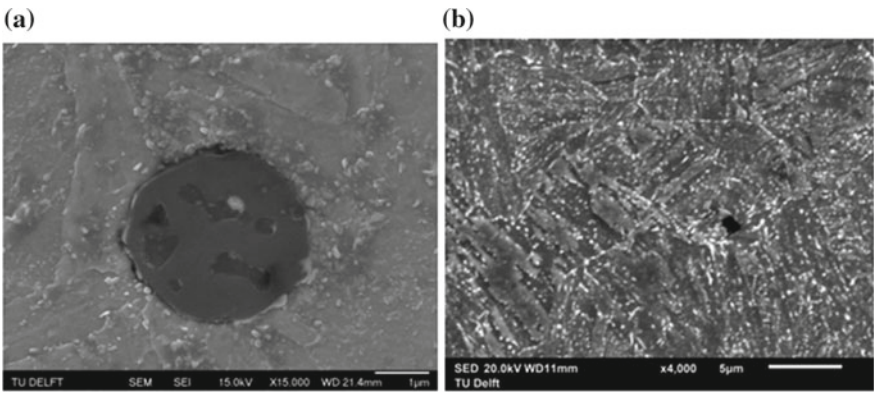

Fig. 5 SEM micrographs of inclusions in the top position of the S690QL steel plate: **a** (Mg,Al,Ca)(O,N) and **b** (B,Ti,Nb)(N,C)

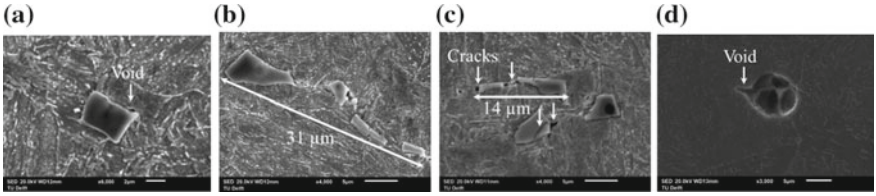

Fig. 6 SEM micrographs of inclusions in the middle position of the S690QL steel plate, found prior to fracture toughness testing: **a** (Ti,Nb)(N), **b** Nb(C), **c** Nb(C) and (Nb,Ti)(N) and **d** (Mg,Al,Ca)(O)

In the middle position, large cubic, elongated, and spherical inclusions with dimensions ranging from 1 to 11 μm were observed. Inclusions included oxides and niobium-rich carbides and nitrides such as spherical (Mg,Al,Ca)(O) and cubic (Ti,Nb)(N), (Ti,Nb)(C), Nb(C), and (Nb,Ti)(C,N) (Fig. 6).

Moreover, inclusions in the middle section were sometimes associated with defects and often distributed as clusters, such as voids and cracking of both matrix/inclusion interface and inclusions cracking (see Fig. 6 shows defects pointed out by arrows). These cracks might have been caused by deformation during the rolling process. However, the sample preparation procedure can also influence the formation of these cracks. The behaviour of various inclusions when steels are deformed under hot rolling was recently reported by da Costa e Silva [12].

In general, inclusions that are brittle and less deformable are likely to crack and/or break under rolling pressure. Besides that, the interfacial strength inclusion/matrix is low and the interface is a source of microvoid and crack formation [13]. This effect can be pronounced in case of coarse and irregular-shaped inclusions, as the carbide and/or nitride inclusions found in the S690QL steel, as high stress concentration can be generated at sharp interfacial points and micro-cracks can grow from inclusion interfaces under rolling load, even when the steel has enough ductility [13]. Inclusions distributed as clusters should be considered as a line of collinear inclusions and therefore represent a single large crack (Fig. 6b). It is important to note that taking this into consideration, instead of considering an initial crack size equal to the inclusion size (between 1 and 11 μm), larger crack sizes apply, as shown in Fig. 6b where the initial defect size is approximately 30 μm. The same consideration should be given to inclusions associated to cracks which propagate to the matrix (Fig. 6c).

These inclusions were quantified for both thickness positions and it was found that the mean area fraction through the thickness of the plate is higher for the middle section ($7.0 \times 10^{-4} \pm 2.7 \times 10^{-4}$) than for the top ($5.4 \times 10^{-4} \pm 2.8 \times 10^{-4}$).

Therefore, middle section is apparently more critical than top as, besides the larger mean area fraction of inclusions, it presents larger inclusions, that were found to be sometimes associated to defects and often distributed as clusters, being considered as large cracks of 30 μm, which, according to with Griffith [14], leads to lower stresses to fracture.

Fracture Toughness

Table 2 presents CTOD results at −100 °C for top and middle thickness positions at T-L and L-T orientations and high- and low-constraint conditions. It is important to mention that sub-size specimens are shown to be suitable only for fracture toughness investigation in the lower shelf which means CTOD values below 0.2 mm and only in cleavage failure mode [15]. Hence, CTOD values greater than 0.2 mm (e.g. top section specimens under low constraint) will not be considered in this study as sub-size specimens are not suitable, and plastic collapse is outside of the scope of this project. Note that for the low constraint, top, T-L condition, only 4 out of 10 specimens showed reasonable CTOD results and the result in Table 2 is based on these samples.

It is worth mentioning that the steel used in this study fully satisfies the design requirements for offshore and maritime applications. However, the temperature condition applied in this work (−100 °C) is much stricter in order to operate in the lower-shelf region and ensure the material to fail by cleavage. Consequently, the S690QL steel exhibits weaknesses under these more severe test conditions which impact its performance.

Top versus Middle

Table 2 shows that CTOD values for the top section are greater than for the middle. Popovich and Richardson (2015) observed the same behaviour between top and middle sections for a similar steel [4]. Fracture surface analysis was performed to understand the microstructural differences between the outer and central plate regions that lead to such different fracture performance. Preliminary fractographic examination results for high-constraint specimens are shown in Figs. 7, 8, 9, and 10 for top quarter and middle thickness positions, respectively.

Table 2 CTOD results for high- and low-constraint conditions, top and middle thickness positions and, T-L and L-T orientations

Constraint	Thickness position	Orientation	Minimum CTOD (mm)	Maximum CTOD (mm)	Average CTOD (mm)
High constraint ($a/W = 0.5$)	Top quarter	T-L	0.026	0.082	0.05 ± 0.02
		L-T	0.010	0.077	0.04 ± 0.03
	Middle	T-L	0.012	0.013	0.012 ± 0.001
		L-T	0.018	0.033	0.025 ± 0.008
Low constraint ($a/W = 0.1$)	Top quarter	T-L	0.131	0.179	0.16 ± 0.02
		L-T	0.221	0.379	0.30 ± 0.08
	Middle	T-L	0.016	0.062	0.03 ± 0.02
		L-T	0.012	0.069	0.04 ± 0.03

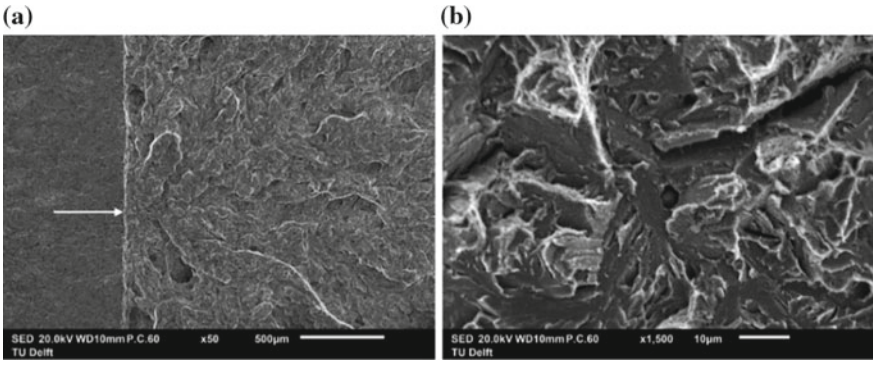

Fig. 7 **a** River lines indicating the cleavage initiation site in high constraint, top, T-L specimen fractured at −100 °C and **b** a (Mg,Al,Ca)(O,S) as a likely initiation site

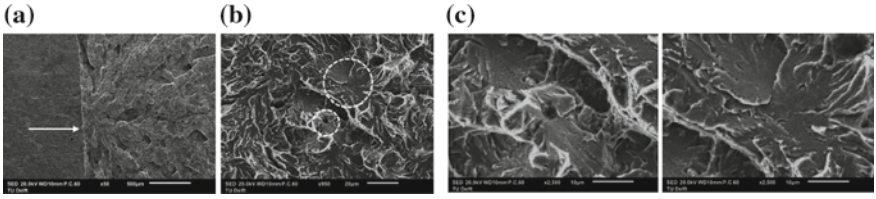

Fig. 8 **a** River lines indicating the cleavage initiation site in high constraint, top, L-T specimen fractured at −100 °C, **b** higher-magnification image of an area with two initiation sites presented separately in (**c**)

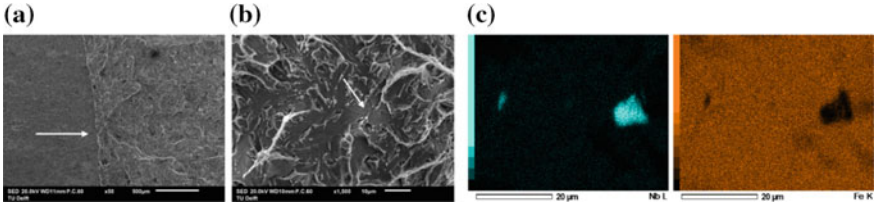

Fig. 9 **a** River lines indicating the cleavage initiation site in high constraint, middle, T-L specimen fractured at −100 °C and **b** Nb-rich inclusion (indicated by white arrow) acting as cleavage initiation site **c** EDS mapping of Fig. 8b showing Nb and Fe maps for the matrix and Nb-rich inclusion

Fractographic examinations reveal that distinct microstructural features can play a role in top quarter specimens. Figure 7a shows clear river lines indicating an (Mg,Al,Ca)(O,S) inclusion as the cleavage initiation site in a high constraint, top quarter, T-L specimen.

On the other hand, Fig. 8 shows that two probable initiation sites can be identified for a high constraint, top quarter, L-T specimen. The first one is a (Mg,Al)(O,N) inclusion located in a cleavage facet and the second refers to cleavage facets arranged

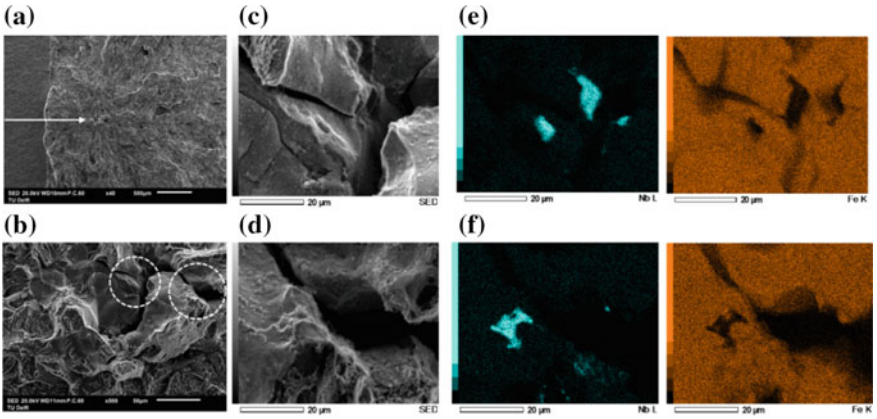

Fig. 10 **a** River lines indicating the cleavage initiation site in high constraint, middle, L-T specimen fractured at −100 °C, **b** cleavage initiation site composed of several cleavage facets and cracks indicating extremely embrittled region, **c**, **d** higher-magnification image of two regions of the cleavage origin from **b** to **f** EDS mapping images showing Nb and Fe maps for the matrix and Nb-rich inclusions in both regions

at the initiation site without a clear triggering microstructural feature. For the latter initiation site, a carbide particle was assumed as the triggering point. Higher-magnification analysis is required to confirm this assumption. It should be noted that cleavage initiation from carbides was also observed in Ref. [16].

In specimens manufactured from the central region of the steel plate, Nb-rich inclusions were identified as a trigger in the cleavage fracture process for both T-L and L-T orientations (Figs. 9 and 10, respectively). As can be seen in Fig. 9, a single coarse (around 8 µm) Nb-rich inclusion was present in the cleavage initiation facet. On the other hand, Fig. 10 shows that a cluster of niobium-rich inclusions (ranging from 8 to 13 µm in size) triggered the fracture process, thus significantly weakening the material as indicated by several smooth cleavage facets and cracks. Unlike inclusions commonly reported as initiation sites where they are torn off by one of the halves of the fractured specimen leaving a cavity in the cleavage facet [4], the inclusion indicated by the white arrow in Fig. 9 appears as a flat surface, which is rather difficult to distinguish using common fractography.

Cleavage fracture comprises two critical sequential steps. First, the nucleation of cracks in a hard particle takes place for which the criterion is a critical plastic strain. Second, the unstable propagation of cracks across the particle/matrix and matrix/matrix interfaces occurs, for which the criterion is a critical tensile stress [17]. However, when the inclusions present ahead of the crack tip are associated with cracks such as carbides and nitrides found in the middle section of the plate as shown in Fig. 6, these cracks serve as Griffith cracks and the nucleation stage is no longer necessary in the fracture process [18]. Moreover, at low-temperature and high-constraint conditions, as in these specimens, the critical cleavage event is the propagation through the particle/matrix boundaries and the size of inclusion is

a critical parameter where a higher inclusion size lowers the stress to failure [18]. Therefore, the middle section is more susceptible to cleavage fracture than the top quarter and exhibits lower CTOD values, since the latter still needs to meet both the nucleation and crack propagation criteria for fracture to occur and the former presents larger inclusions which can be associated with cracks that consequently increase the initial crack length.

High-constraint versus Low-constraint

The investigation of constraint effects on fracture toughness is relevant as the crack depth to width ratio (a/W) was reported to have important effects on fracture toughness and crack-like defects often observed in structural components are surface (shallow) cracks, which leads to a low-constraint state, rather than deep cracks, which results in a high-constraint state, commonly found in standard specimens [5, 19, 20].

CTOD fracture toughness tests are based on the plastic hinge model and some studies observed that the value of plastic rotation factor (r_p) significantly affects the calculated CTOD result [19, 20]. In case of shallow-notched specimens, where there is a significant reduction of the a/W ratio compared to deep-notched standard specimens ($0.45 < a/W < 0.55$), the plastic hinge point location in the unnotched ligament ahead of the crack tip can be shifted. Through experimental analysis, it was shown that r_p can be much lower than 0.4 (used in the most common standards for fracture toughness measurement) for shallow-notched specimens. It was estimated at 0.2 for $a/W = 0.1$ [19, 20]. Hence, the determination of r_p values for low-constraint specimens is of paramount importance as the standard procedure can provide a conservative assessment of these defects.

The value of r_p obtained in this study by (finite element analysis (FEA) simulation specifically for the notch/pre-crack configuration and specimen type used in this work was 0.24, which is in agreement with the value found in the literature [20, 21]. The CTOD results for shallow cracked specimens calculated using the new value of r_p show a reduction of about 15% for top, which has more expressive plastic behaviour, and 10% for middle compared to the results calculated with the value of r_p equal to 0.4 used in the standard for deeply cracked specimens. Hence, analysis of the fracture behaviour of shallow defects using the procedure provided in the standards with deep-notched specimens may lead to conservative results, especially for cases where the plastic portion of CTOD is more significant. Therefore, a correction of the plastic rotation factor must be made.

As can be seen in Table 2, specimens in low-constraint condition exhibit much higher CTOD values than those of high constraint. Shallow cracked components display low hydrostatic stresses at the crack tip and less-restrained plastic flow fields (low crack-tip stress triaxiality), which contrast neatly to conditions present in deeply cracked specimens [5]. As a result, shallow-notched specimens have a greater ability to resist crack propagation compared to deep-notched specimens. In addition, Smith and Rolfe (1994) observed a shift in the ductile-to-brittle transition curve to lower temperatures for carbon steels and ferritic steels due to the reduction of a/W ratio [22].

In this case, the temperature of −100 °C may have been transferred from the lower shelf to the ductile–brittle transition region; thus, increasing the fracture toughness of the material.

Notch Orientation: T-L versus L-T

The notch orientation effect is clear for high constraint, middle specimens where direction L-T displays higher fracture toughness than direction T-L. This behaviour can be primarily attributed to cracks associated with inclusions that are oriented parallel to the rolling direction and the crack propagation direction, which eases the fracture of the material.

Therefore, the energy required to propagate a crack in L-T oriented specimens due to this microstructural characteristic is higher than in T-L oriented specimen resulting in higher fracture toughness. However, more in-depth fracture surface investigation, EBSD analysis, and tensile tests in different orientations to the rolling direction will be performed in order to provide further information on cleavage crack propagation micromechanisms, crystallographic features, and effect of orientation to the material's strength to enrich the discussion on the impact of specimen orientation on the fracture toughness of the material.

Conclusions

The microstructure across the thickness of an 80 mm thick quenched and tempered S690 high-strength steel plate was characterized, and its effects on cleavage fracture toughness at −100 °C was investigated. Furthermore, an analysis on constraint and notch orientation effects on cleavage fracture toughness was made. The following conclusions were drawn:

1. The steel plate shows through-thickness variation in terms of microstructural composition (phase composition; prior austenite grain size; inclusion's characteristics such as chemical composition, morphology, and size; and cleavage fracture toughness) and this was observed to have a clear effect on fracture toughness of the thick-section high-strength steel being studied in this work.
2. The lower CTOD fracture toughness results for the middle section of the plate is attributed to large Nb-rich inclusions, which may be distributed as clusters and may be associated with cracks, acting as weakest links for the second (and only) step of crack propagation since the pre-existing crack serve as a Griffith crack for the first step. For the identification of these inclusions as cleavage initiation sites, it was necessary to combine SEM fractographic analysis and EDS maps as it was rather difficult to distinguish using only common fractography examination.

3. Low-constraint specimens, which contain shallow cracks similar to the ones observed in real structures, have greater fracture toughness compared to high-constraint specimens due to low hydrostatic stresses at the crack tip and less-restrained plastic flow fields. In addition, the ductile-to-brittle transition curve expected for deeply cracked specimens may shift to lower temperatures when evaluating shallow-notched specimens and it is likely that at −100 °C low-constraint specimens are not being evaluated at the lower shelf, as for high-constraint specimens, but rather in the ductile–brittle transition region showing greater fracture toughness.
4. High constraint, middle specimens show an explicit effect of notch orientation on fracture toughness. In this case, the difference is related to the parallel alignment of cracks associated to inclusions to the pre-crack. This characteristic contributes to a lower resistance to crack propagation and ease the final fracture of the material.

Acknowledgements The authors of this work are grateful to our sponsors, which include Allseas Engineering, Dillinger, the Dutch Ministry of Defence, Lloyd's Register and TNO. This work was carried out under the Micro-Tough research project number 16350, which is (partly) financed by the Netherlands Organization for Scientific Research (NWO).

References

1. Billingham J et al (2003) Review of the performance of high strength steels used offshore. http://www.hse.gov.uk/research/rrpdf/rr105.pdf
2. Morris Jr JW (1993) Steels: for low temperature applications. In: McPherson HD (ed) Encyclopedia of advanced materials. Pergamon Press, Oxford
3. Liu H, Zhang H, Li J (2018) Thickness dependence of toughness in ultra-heavy low-alloyed steel plate after quenching and tempering. Metals 8(628)
4. Popovich V, Richardson IM (2015) Fracture toughness of welded thick section high strength steels. Paper presented at the 144th TMS annual meeting, Orlando, Florida, 15–19 March 2015
5. Donato GHB, Ruggieri C (2006) Estimation procedure for J and CTOD fracture parameters using three-point bend specimens. Paper presented at the 6th international pipeline conference, Calgary, Alberta, 25–29 September 2006
6. NEN (2019) EN 10025-6: hot rolled products of structural steels—Part 6: technical delivery conditions for flat products of high yield strength structural steels in the quenched and tempered condition
7. ASTM International. ASTM E112-13: standard test methods for determining average grain size
8. ASTM International (2016) ASTM E1245-03: standard practice for determining the inclusion or second-phase constituent content of metals by automatic image analysis
9. International Standard (2015) ISO 12135: metallic materials—unified method of test for the determination of quasistatic fracture toughness
10. Vieira I, De Moor E (2017) Tempering response of bainitic and martensitic microstructures. Paper presented at 3rd Pan American Materials Congress, San Diego, California, 26–2 February/March 2017
11. Pallaspuro S (2018) On the factors affecting the ductile-brittle transition in as-quenched fully and partially martensitic low-carbon steels. Ph.D. thesis, University of Oulu

12. da Costa e Silva ALV (2019) The effects of non-metallic inclusions on properties relevant to the performance of steel in structural and mechanical applications. J Mater Res Technol 8(2):2408–2422
13. Mandal SK (2014) Steel metallurgy—properties, specifications, applications. McGraw-Hill Education, India
14. Griffith AA, Ingram TG (1920) The phenomena of rupture and flow in solids. Philos Trans R Soc London, A
15. Walters CL et al (2013) Validation of the acceptability of 10 × 20 mm specimens for fracture toughness determination of high-strength steels. Paper presented at 32nd international conference on ocean, offshore and arctic engineering, Nantes, France, 9–14 June 2013
16. Namewaga T et al (2019) Effect of carbon content on toughness of tempered martensitic steels analysed by toughness prediction model. ISIJ Int 59(7):1337–1343
17. Chen JH, Cao R (2015) Micromechanism of cleavage fracture of metals. Elsevier
18. Yan W, Shan YY, Yang K (2007) Influence of TiN inclusions on the cleavage fracture behaviour of low-carbon microalloyed steels. Metall Mater Trans A 38A:1211–1222
19. Dawes MG, Cho G (1992) Shallow crack fracture mechanics toughness tests and applications: first international conference. Woodhead Publishing
20. Rak I (2016) CTOD toughness evaluation of hyperbaric repair welds made under severe conditions. Struct Integrity Life 16(3):171–178
21. Kirk MT, Doods RH (1993) *J* and CTOD estimation equations for shallow cracks in Si edge notch bend specimens. J Test Eval 21(4):228–238
22. Smith JA, Rolfe ST (1994) The effect of crack depth (a) and crack depth to width ratio (a/W) on the fracture toughness of A553-B steel. J Press Vessel Technol, 115–121

Effect of Thermal Aging on Impact Toughness of Electron Beam-Welded AISI 316 Stainless Steel

Arun Kumar, Sandeep Singh Sandhu and Beant Singh

Abstract Thick section of cold-rolled austenite stainless steel AISI 316 is widely used in heat exchangers, jet engines, furnace parts, exhaust manifolds, fast breeder test rector, etc., because of its high strength, corrosion, and pitting resistance properties at high working temperature 400–550 °C approximately. Electron beam welding is considered as highly efficient welding process in order to achieve high-quality welds with low heat-affected zone. In this paper, single-pass narrow gap square butt welding of 18-mm-thick plates using electron beam welding at constant accelerating voltage 150 kV, beam current 90 mA, welding travel speed 600 mm/min, and beam oscillation in circular pattern was investigated. The impact toughness and metallurgical properties in as-welded condition and after imparting post-weld thermal aging (PWTA) at 750 °C for 24 h were also investigated in this piece of work. The full penetration had been achieved in single pass by optimizing the relationship between welding parameters (beam accelerating voltage, beam current, welding travel speed, and beam oscillation). The results showed that welding of plates without filler metal leads to defect-free welds. The average impact toughness conducted by Charpy impact test at cryogenic temperature (−40 °C) in as-welded samples was recorded as 284 J, and after aged at 750 °C for 24 h it reduced to 180 J.

Keywords AISI 316 SS · Electron beam welding · Microstructure · Microhardness · Cryogenic impact toughness

A. Kumar · S. S. Sandhu (✉)
Department of Mechanical Engineering, Quest Infosys Foundation Group of Institutions, Jhanjeri, Mohali, Punjab 140307, India
e-mail: ersandeepsandhu@gmail.com

A. Kumar
e-mail: arunjaito@gmail.com.com

B. Singh
Department of Mechanical Engineering, Punjab College of Engineering and Technology, Lalru, Punjab, India
e-mail: beantsingh7@yahoo.co.in

J. Li et al. (eds.), *Characterization of Minerals, Metals, and Materials 2020*,
The Minerals, Metals & Materials Series,
https://doi.org/10.1007/978-3-030-36628-5_16

Introduction

AISI 316 austenitic stainless steel (SS) is widely used in nuclear power plants, heat exchangers, and fast breeder test reactors [1] as structural materials. The preference of this alloy is due to its high-temperature tensile strength, fatigue strength along with excellent fracture toughness in combination with excellent weldability and fabricability. The joining of 316-type austenitic stainless steel by welding processes and its exposure to harsh environment can be the cause of the formation of various phases which can affect its properties significantly. Raghunathan et al. [2] reported that AISI 316 SS when heat-treated between the temperature range of 900 and 1100 °C, the ferrite content of the weld decreases with increase in aging time. Moreover, the dendritic morphology of ferrite phase tried to break up and spheroidize. Kar et al. [3] investigated that electron beam (EB)-welded joints possessed similar tensile properties at room temperature and at 700 °C irrespective of being prepared with beam oscillation or non-oscillating beam. Dutt et al. [4] concluded that resistance to crack initiation of 316(N) welds decreased when aged at 370, 475, and 550 °C for 20,000 h. The Charpy energy values decreased when aged at 475 °C for 20,000 h. The embrittlement of the welds occurred at 370–550 °C for long durations leads to decline in mechanical properties.

Xia et al. [5] concluded that beam oscillation in electron beam welding leads to uniform weld morphology and increased the weld width. The ferrite morphology changed from lathy/skeletal grains in the top layer to equiaxed grains at bottom of the bead. Further, they also claimed that the solidification of fusion zone (FZ) changed due to beam oscillation. However, beam oscillation had a very little impact on microstructure. Alali et al. [6] concluded that finer dendritic structure was noticed at the bottom of the weld zone. The weld centerline contained a microstructural boundary is called parting. The yield strength of bottom section of the weld metal was 14–52 MPa higher than top section. The tensile testing specimens extracted from the bottom of the weld had 4% higher UTS than the specimens extracted from top of the weld. The entire lot of tensile specimen failed at the center of the fusion zone usually at the parting region.

Zumelzu et al. [7] concluded that the thermal contribution was directly proportional to the ferrite content and tensile strength in 316 L SS weld joints. Joseph et al. [8] varied the electron beam power from 3 to 4.2 kW while welding and concluded that by increasing Q/V ratio the hardness and toughness of the material decreased which is due to the variation in the cooling rate. Kim et al. [9] concluded that heat-treating 316 SS at 600 °C for 10 h resulted in a very little change in the microstructure. The heat treatment for 650 and 700 °C reduced the mechanical properties. Further, when HAZ of 316 was heat-treated for 600 °C for 10 h the tensile strength reduces marginally but was still higher than base metal. Kozuh et al. [10] concluded that tensile strength of the weld metal was higher than the parent metal and the impact toughness decreased with increase in annealing temperature. Further, post-weld heat treatment decreased the value of microhardness for both the base and HAZ. The increase in annealing temperature led to decrease in delta ferrite

content. Xia et al. [11] after conducting the microstructure analysis concluded that weld metal was composed of austenitic matrix along with dendritic ferrite. As the thickness increased, the morphology of delta ferrite changed to columnar equiaxed ferrite from skeletal, lacy, and lathy ferrite. The fusion zone had lower hardness as compared to base metal due to the presence of coarse columnar grains and increasing delta ferrite content. Balaji et al. [12] concluded that thermal aging has an adverse affect on the mechanical properties of 316 steel as it gets embrittled. Embrittlement is mainly due to precipitation of $M_{23}C_6$ carbides on the grain boundaries.

Kar et al. [13] stated that electron beam oscillation resulted in better mechanical properties as compared to non-beam oscillation. Due to the higher cooling rate, the width of fusion zone in beam oscillation EB welds was less than non-beam oscillating EB welds. The microstructure revealed that EB welds contain similar content of δ ferrite with skeletal and lathy morphology with non-beam oscillation and beam oscillation, respectively. Tjong et al. [14] investigated that the microstructure study showed that high cooling and under-cooling associated with electron beam and laser welding caused formation of cellular and equiaxed dendrites in both EB and laser welds. The hardness in both the cases was higher in HAZ and weld metals than the base metal.

Shaikh et al. [15] concluded that aging of 316 L SS weld metal at 600 °C for 20 h resulted in precipitations of carbides. On the contrary when aged at 20,000 h resulted in the formation of sigma phase. They also found that matrix softening had a significant effect on yield strength whereas UTS was influenced by matrix hardening.

Chen and Gan [16] observed that the formation of carbides in the grain boundaries caused cracking and shearing which destabilized the grain boundaries. These alterations in grain boundaries reduced the ductility leading to the reduction in tensile elongation and also reduced the impact strength of the material. Further, they concluded that the reduction in impact strength mainly depended on the ageing time. The carbides were fine and denser in the specimens thermally aged at 650 and 750 °C with normal aging time and at 550 °C after long aging time and lead to the high reduction in tensile elongation and impact strength. High-temperature thermally aged specimens (900 °C) had large size carbides at the grain boundaries causing reduction in elongation. The present work aimed at fabrication of completely penetrated electron beam welds of 18-mm thick AISI 316 SS plates, confirming to sound industrial quality. Further, the welds were examined for impact toughness and metallurgical properties in the as-welded state and after aging at 750 °C for 24 h, in order to study the effect of precipitating phase on the performance of AISI 315 SS welds.

Experimental Procedure

In this study, the rolled and annealed AISI 316 austenitic stainless steel workpieces of 400 mm × 75 mm × 18 mm were used. The length was transverse to rolling direction. The chemical composition obtained by spectroscopic analysis is shown in Table 1.

Table 1 Chemical composition of the base material AISI 316 SS (wt%)

Element	C	Si	Mn	S	P	Cr	Ni	Mo	Cu	Ti	V	Co	Nb	W	Fe
AISI 316	0.064	0.538	0.948	0.025	0.023	16.146	10.441	2.178	0.191	0.009	0.061	0.025	0.041	0.007	Balance

Table 2 Welding parameters employed in the present work

Beam voltage, V (kV)	Beam current, I (mA)	Welding speed (mm/min), S	Oscillation pattern	Oscillation frequency	Heat input (KJ/mm)
150	90	600	Circle	800 Hz	1.28

Heat input per unit length of weld $= \eta\ (V \times I)/S.$, whereas η denotes heat source efficiency (taken as 0.95), V is beam voltage, I is beam current, and S is beam travel speed

Electron beam welding (EBW) in autogenous mode, i.e. welding without filler metal, was used to achieve single-pass, full penetration square butt joint. Before welding, edges of the plates were carefully machined by using milling machine to obtain perfect square and were cleaned by acetone to remove dust, rust, etc. The vacuum pressure in the working chamber of EBW machine was approximately 5×10^{-6} mbar, and the gun pressure was approximately 2×10^{-6} mbar. The welding parameters used in this study are shown in Table 2.

The metallographic specimens were cut precisely by wire-cut EDM for microstructure analysis by using optical microscope. To reveal the microstructure, the specimens were polished using emery paper of 80–3000 grit size and the specimens were chemically etched by aqua regia solution (1 part of HNO_3 and 3 parts of HCl) for 15–20 s. The specimens prepared were thermally aged at 750 °C for 24 h followed by air cooling to facilitate the precipitation of the carbides. The microhardness values (approximately 5 readings per point) were taken across (from left to right with a spacing of 0.15 mm) and along the weld bead centerline (from top to bottom with 0.5 mm spacing) as indicated in Fig. 1. Vickers microhardness testing of weld bead was carried using a load of 1 kg for a dwell time of 20 s. The Charpy V-notch impact test specimens from welded joint were cut according to the ASTM E23 standard from three locations (top, middle, and bottom). Charpy impact tests were carried out at cryogenic temperature (−40 °C) on specimens of 55 mm × 10 mm × 6 mm dimensions. To measure the error in readings, three specimens were tested from one location.

Results and Discussion

Morphology of the Welds

The cross-sectional view of the weld joint fabricated using EBW process is shown in Fig. 1. The macrostructure shows the regions of base metal, HAZ and FZ. The through weld was obtained along 18 mm thickness of the weld plates, and it penetrated 1/4 of the backing plate. The macrostructure shows dagger-shaped weld bead (wide top and narrow bottom regions) obtained without any weld defects. The total welding heat input per unit length was 1.28 kJ/mm. During the EBW, the molten metal deposits

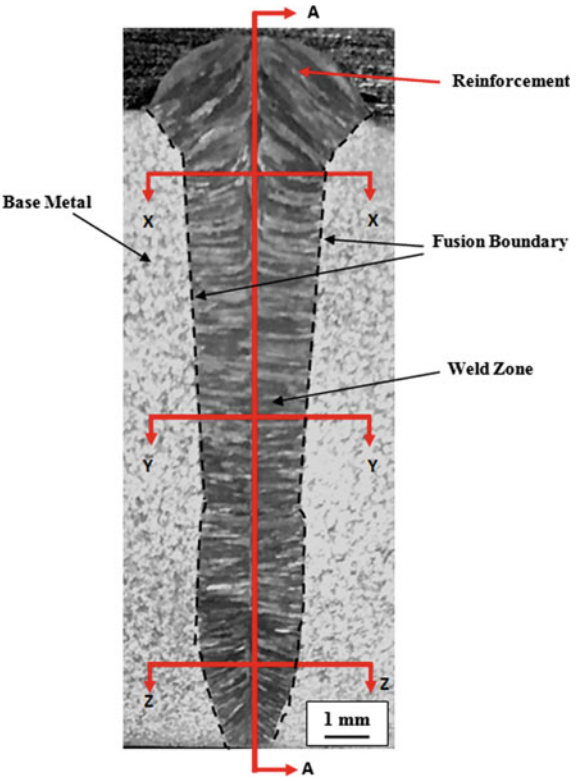

Fig. 1 Macrostructure of EB welds; *X–X-*, *Y–Y-*, and *Z–Z-*axes represent the location across the weld centerline, and *A–A* represents along the weld centerline

at the top side (keyhole mode welding), and the total heat accumulation was more on the top of the weld due to large weld volume accumulation which further leads to slower cooling rates and vice versa on the middle and bottom weld bead. The optical microstructures of the welds in the as-welded and after post-weld thermal aging treatment (750 °C for 24 h) are shown in Figs. 2 and 3 respectively. The weld microstructure consists of austenite matrix along with dendritic δ ferrite grains. The EBW increases the cooling rate of the molten metal which results in non-uniform solidification, hence incomplete ferrite to austenite transformation [17]. Figure 2b depicts the microstructure of the fusion zone at the top of the weld bead, which shows the presence of columnar grains growing perpendicular to the parting line. The vermicular structure of ferrite dendrites was visible within the parting line.

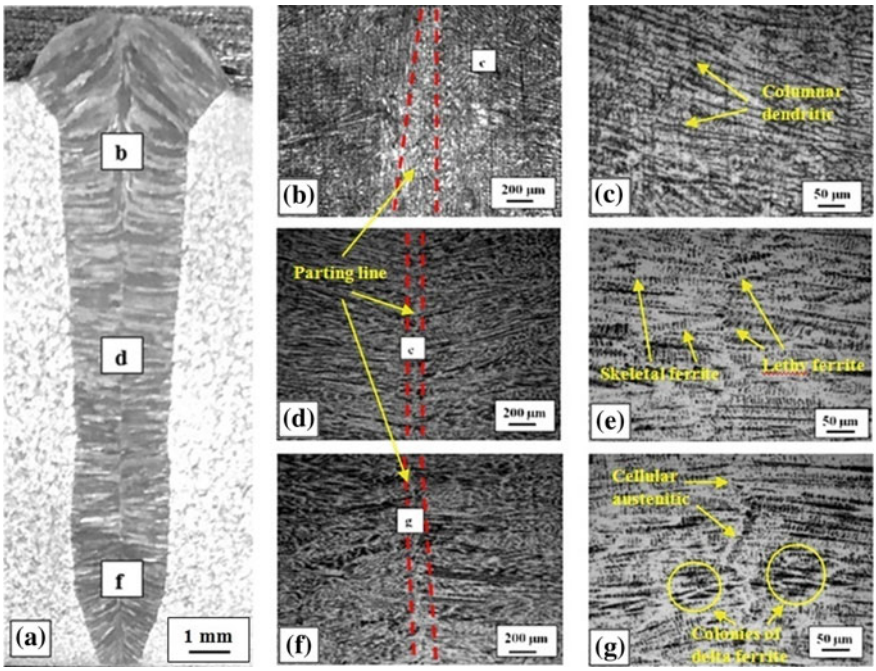

Fig. 2 Macrostructure and microstructure of EB as-welded joint. **a** Macrostructure of FZ, **b** columnar structure at top part of weld bead at 50×, **c** top part of weld bead at higher magnification, 200×, **d** columnar and equiaxed delta ferrite at middle of weld bead, 50×, **e** lathy structure at middle of weld bead, 200×, **f** delta ferrite formation at bottom of the FZ, 50×, **g** primary austenitic structure at bottom of the FZ, 200×

Figure 2c shows higher magnification of columnar grains growing towards the parting line. Figure 2d depicts the microstructure of the middle zone of the weld bead. The microstructure in this area consists of both equiaxed and columnar delta ferrites, and this may be due to higher cooling rates at the center than the top of the weld bead. Figure 2e shows the magnified view of the grains at the centerline, which shows the formation of lathy ferrite at the weld centerline and skeletal ferrite at weld zone. Figure 2f shows microstructure of fusion zone at the bottom of the weld. The microstructure consists of colonies of delta ferrite forming from the parting line, growing outwards. The weld centerline had cellular austenitic structure, which could be due to higher cooling rates at the bottom of the weld bead [18, 19].

Figure 3 shows the macrostructure and microstructure of weld bead after PWTA (750 °C for 24 h). After aging, the microstructures at top, middle, and bottom show the precipitation of carbides in the austenitic network.

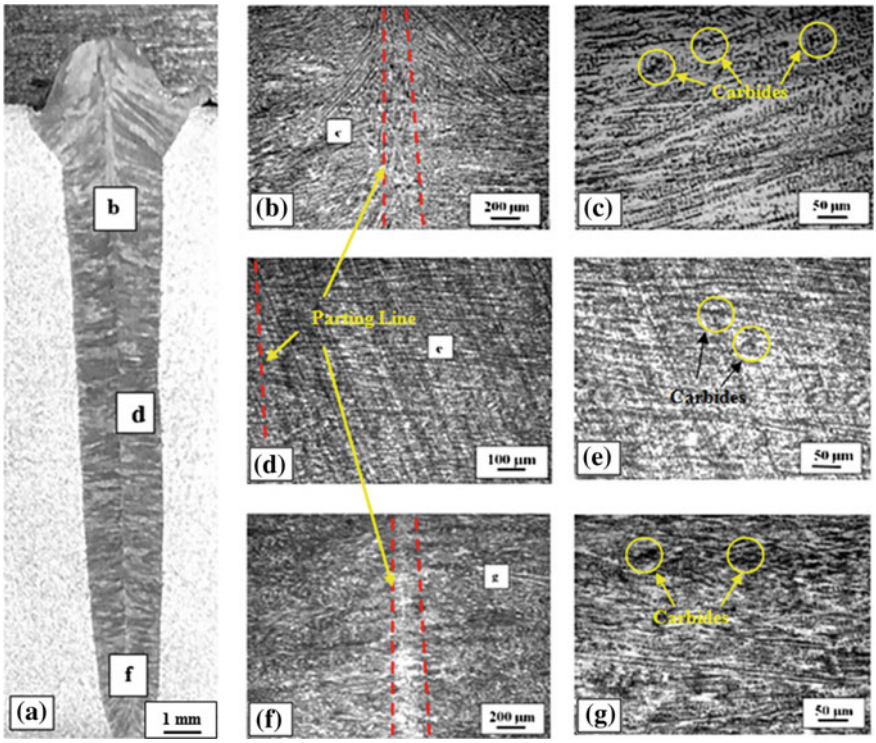

Fig. 3 Macrostructure and microstructure of PWTA specimen. **a** Macrostructure of FZ, **b**, **c** microstructure shows carbide precipitation at top part of weld bead at 50× and 200×, respectively, **d**, **e** microstructure shows carbide precipitation at middle part of weld bead at 100× and 200×, respectively, **f**, **g** microstructure shows carbide precipitation at bottom part of weld bead at 50× and 200×, respectively

Microhardness Properties

Figure 4a, b shows the microhardness variations across and along different zones of the weld. Figure 4a shows the microhardness along the weld bead, and the microhardness in the as-welded conditions increased from top (192.3 VHN) to bottom (226.8 VHN) of the weld. The reason behind this could be the finer grain structure at the bottom of the weld as compared to top and middle as reported by [20]. On the contrary, the microhardness values decreased after the aging treatment (750 °C for 24 h) by approximately 11% throughout the weld bead. This is due to the precipitation of secondary phases along the grain boundaries. While measuring the microhardness

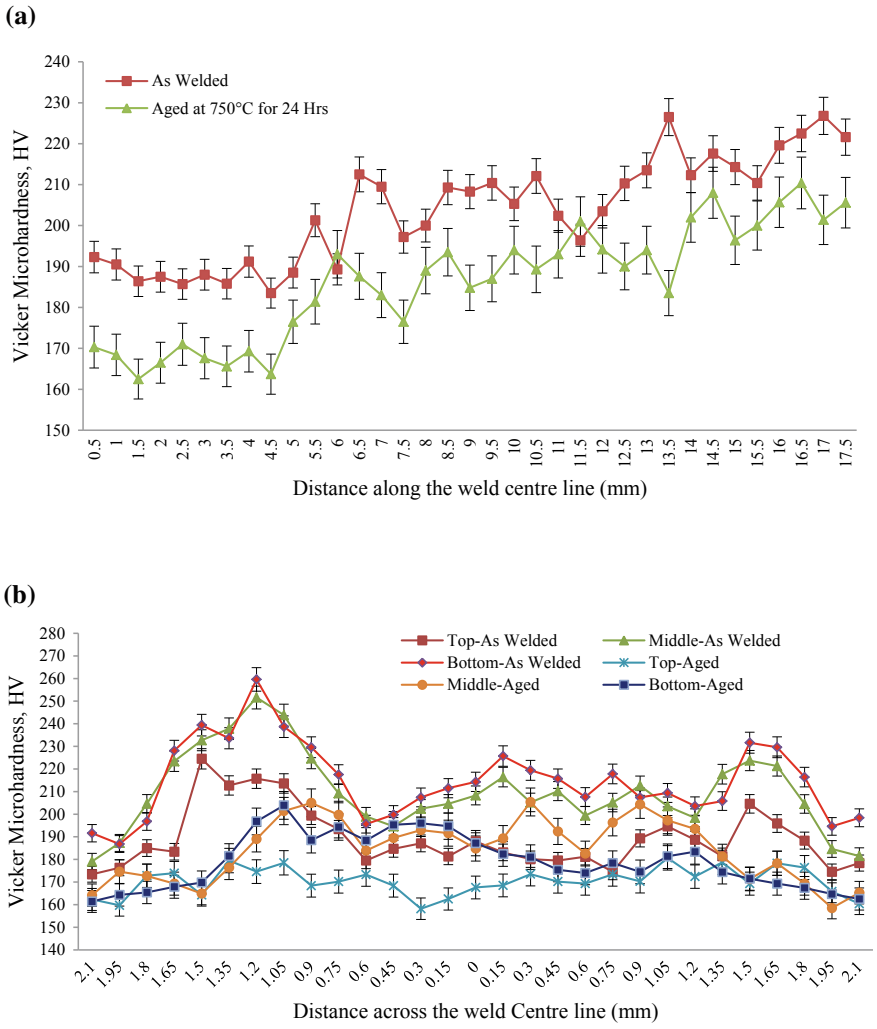

Fig. 4 Vickers microhardness. **a** Along the weld centerline and **b** across the weld centerline

across the weld bead (Fig. 4b), the maximum microhardness obtained was 259.6 VHN at the bottom near the fusion line region in as-welded condition. This could be due to the presence of finer grain structure. The minimum microhardness reported was 158.2 VHN at the top of the weld bead on the parting line after thermal aging. The percentage error in as-welded specimens was 4%, whereas after aging the error increases to 6%. This may be attributed to the formation of precipitates.

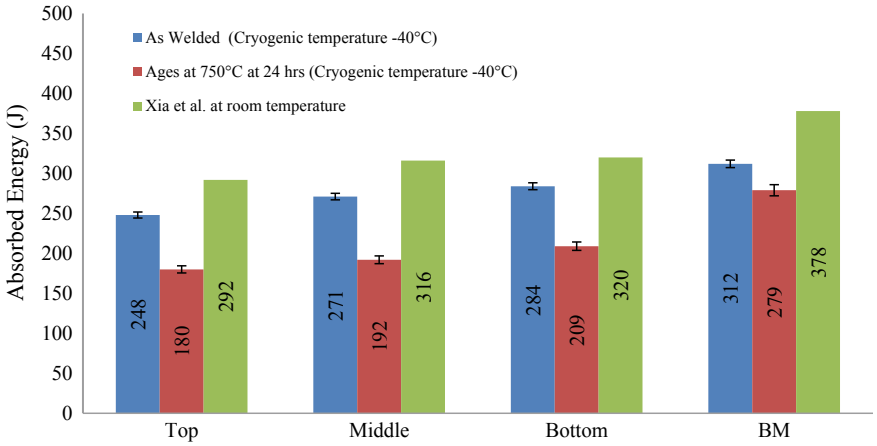

Fig. 5 Impact toughness tested at cryogenic temperature (−40 °C) in as-welded and after aging at 750 °C for 24 h

Impact Toughness Properties

The results of impact test at cryogenic temperature (−40 °C) are presented in Fig. 5. The maximum impact energy of 312 J was absorbed by the base metal in the as-welded condition. It was followed by the impact specimens extracted from bottom and middle of the weld bead in the as-welded condition with average values equal to 284 J and 271 J, respectively. The similar pattern was depicted by Xia et al. [11] while testing at the room temperature. The aging treatment reduced the impact toughness of all the specimens as compared to as-welded specimens. Singh and Shahi [20] observed the same pattern. The percentage error in as-welded specimens was 3%, whereas after aging the error increases to 5%.

Conclusions

The present work reported about the metallurgical and impact toughness of EBW joints of 18-mm-thick AISI 316 SS in as-welded and aged (750 °C for 24 h) condition. The following conclusions could be drawn based on the results.

1. Single-pass, fully penetrated EB welds, with full sidewall fusion, were achieved in 18-mm-thick AISI 316 SS plates with heat input of 1.28 kJ/mm.
2. The weld zone near the fusion boundary of the weld joint had relatively higher microhardness. The aging treatment reduced the microhardness by approximately 11%.

3. The impact toughness of the specimens extracted from the bottom of the weld bead is highest in as-welded condition. However, the base metal had the maximum impact toughness.
4. The aging treatment reduced the impact toughness approximately by 26% due to the precipitation of carbides at the grain boundaries.

Acknowledgements The authors wish to acknowledge the experimental support/facilities extended by the Welding Metallurgy Laboratory, Mechanical Engineering Department, Sant Longowal Institute of Engineering and Technology, Longowal, Sangrur (Deemed University), Punjab, India.

References

1. Karthik V et al (2013) Characterization of mechanical properties and microstructure of highly irradiated SS 316. J Nucl Mater 439(1–3):224–231
2. Raghunathan VS, Seetharaman V, Venkadesan S, Rodriguez P (1979) The influence of post weld heat treatments on the structure, composition and the amount of ferrite in type 316 stainless steel welds. 10(November):1683–1689
3. Kar J, Roy SK, Roy GG (2016) Effect of beam oscillation on electron beam welding of copper with AISI-304 stainless steel. J Mater Process Technol
4. Dutt BS, Sasikala G, Shanthi G, Venugopal S, Babu MN (2011) Mechanical behaviour of SS 316 (N) weld after long term exposure to service temperatures. 0–5
5. Xia X, Wu J, Liu Z, Shen X, Ma J, Liu Z (2019) Study of microstructure difference properties of electron beam welds with beam oscillation of 50 mm 316 L in CFETR. Fusion Eng Des 138(December 2018):339–346
6. Alali M, Todd I, Wynne BP (2017) Through-thickness microstructure and mechanical properties of electron beam welded 20 mm thick AISI 316 L austenitic stainless steel. Mater Des
7. Zumelzu E, Sepu J (1999) Influence of microstructure on the mechanical behaviour of welded 316 L SS joints. 94:36–40
8. Joseph B, Katherasan D, Sathiya P, Murthy CVS (2012) Weld metal characterization of 316 L (N) austenitic stainless steel by electron beam welding process. 4(2):169–176
9. Kim HS et al (2019) Effects of heat treatment on mechanical properties and sensitization behavior of materials in dissimilar metal weld. Int J Press Vessel Pip 172(March):17–27
10. Kozuh S, Gojic M, Kose L (2009) Mechanical properties and microstructure of austenitic stainless steel after welding and post-weld heat treatment. Kov Mater 47(4):253–262
11. Xia X et al. (2019) Correlation between microstructure evolution and mechanical properties of 50 mm 316 L electron beam welds. Fusion Eng Des 147(June):111245
12. Balaji C, Kumar SVA, Kumar SA, Sathish R, Nadu T (2012) Evaluation of mechanical properties of SS 316 L weldments using tungsten inert gas welding. 4(5):2053–2057
13. Kar J, Roy SK, Roy GG (2017) Effect of beam oscillation on microstructure and mechanical properties of AISI 316 L electron beam welds. Metall Mater Trans A Phys Metall Mater Sci 48(4):1759–1770
14. Tjong SC, Zhu SM, Ho NJ, Ku JS (1995) Microstructural characteristics and creep rupture behavior of electron beam and laser welded AISI 316L stainless steel. 227:24–31
15. Shaikh H, Khatak HS, Seshadri SK, Gnanamoorthy JB, Rodriguez P (1995) Effect of ferrite transformation on the tensile and stress corrosion properties of type 316 L stainless steel weld metal thermally aged at 873 K. Metall Mater Trans A 26(7):1859–1868
16. Chen SY, Gan D (1988) Effects of grain boundary carbides on the tensile and impact properties of type 316 stainless steel. Mater Sci Eng 102(2):193–199

17. Zhang M, Chen G, Zhou Y, Liao S (2014) Optimization of deep penetration laser welding of thick stainless steel with a 10 kW fiber laser. Mater Des 53:568–576
18. Elmer JW, Allen SM, Eagar TW (1989) Microstructural development during solidification of stainless steel alloys. Metall Trans A 20(10):2117–2131
19. Brooks JA, Thompsom AW Microstructural development and solidification cracking susceptibility of austenitic stainless steel welds (1)
20. Singh J, Shahi AS (2019) Metallurgical, impact and fatigue performance of electron beam welded duplex stainless steel joints. J Mater Process Technol 272(May):137–148

Part V
Mineral Processing and Analysis III

Preparation and Photocatalytic Properties of Mo-Doped TiO_2@Fly Ash Cenospheres for Degradation of Methylene Blue

Yongfeng Cai, Bin Xu, Min Li, Pengxu Cao, Jun Luo, Mingjun Rao, Zhiwei Peng and Guanghui Li

Abstract Mo-doped titanium dioxide (TiO_2)-coated fly ash cenosphere (FAC) was synthesized by the sol-gel method. The novel photocatalysts were characterized by X-ray diffraction (XRD), scanning electron microscopy (SEM), ultraviolet–visible diffuse reflectance spectroscopy (UV–Vis DRS), and X-ray photoelectron spectra (XPS). The results showed that the catalyst maintains the structure of anatase (TiO_2), and the majority of doped Mo ions existed as Mo^{6+} substitution in anatase lattice, which caused redshift of TiO_2 light absorption wavelength, broadening the light absorption range and making more effective use of solar energy. The photocatalytic activity of Mo-TiO_2@FAC sample for the degradation of methylene blue (MB) under visible light irradiation was investigated. The photocatalyst that was calcined at 550 °C with Mo/Ti molar ratio of 0.3% and concentration of 2 g/L exhibited the optimal photodecomposition property.

Keywords Mo-doped TiO_2 · Fly ash cenospheres · Visible light · Photodegradation · Sol-gel

Introduction

Environmental photocatalysts have attracted much attention in recent years. Titanium dioxide (TiO_2) is commonly used as a photocatalyst because of its low toxicity, easy reforming, long-term stability, and simple production [1, 2]. However, its low photo-efficiency under visible light irradiation and limitations of powder size restrict its commercial application. At present, modification of TiO_2 has been extensively studied to overcome the limitation of pure TiO_2 which has wide energy band gap and low quantum yields. Many groups have been involved in depositing transition

Y. Cai · B. Xu · M. Li · P. Cao · J. Luo · M. Rao · Z. Peng · G. Li (✉)
School of Minerals Processing and Bioengineering, Central South University, Changsha, Hunan 410083, China
e-mail: liguangh@csu.edu.cn

National Engineering Laboratory for High Efficiency Recovery of Refractory Nonferrous Metals, Changsha, Hunan 410083, China

J. Li et al. (eds.), *Characterization of Minerals, Metals, and Materials 2020*,
The Minerals, Metals & Materials Series,
https://doi.org/10.1007/978-3-030-36628-5_17

metal ions, such as Fe, Au, Ag, V, Cr, and Ni, onto the surface of titania to improve the separation of electrons and holes [3, 4]. But these modified photocatalysts cannot be easily retrieved after the reaction on account of their nanometer scales. Hence, numerous researchers have paid attention to the formation of TiO_2 films on different substrates.

The applications of MCM-41 [5], silica [6], clays [7], zeolite [8], and activated carbon [9] as substrate materials to increase the efficiency and immobility of the catalysts have been reported in recent years. However, the costs of substrate materials should be considered in practical applications. Coal fly ash cenospheres (CFACs) are the largest industrial solid waste in China and have initiated environmental issues owing to considerable amount and inappropriate disposal [10]. CFAC utilization could essentially provide desirable waste management solution to increasing disposal issues. It is noticed that the CFACs have a range of advantageous properties such as nontoxicity, low cost, and stable chemical properties [11]. In addition, it has low density and high specific surface because of the spherical porous and hollow solid structure [12]. Therefore, CFACs have been used as promising substrates in catalysis.

In this work, to recover and reuse catalysts from treated water, FACs were served as substrates for the preparation of fly ash cenosphere with molybdenum-doped TiO_2 (Mo-TiO_2@FAC) photocatalysts by using a simple sol-gel method. Catalysts floating in water can be easily illuminated by light in the laboratory, and solar irradiation is used as the light source in industry. In this study, the effect of calcination temperatures, molybdenum doping contents, and addition of catalyst on photocatalytic degradation of MB under visible light irradiation were investigated.

Experimental

Materials

FACs were collected from Borun Foundry Material Corporation, Henan, China. Titanium butoxide ($Ti(OC_4H_9)_4$) was obtained from Shanghai Aladdin Biochemical Technology Co., Ltd. (China). Absolute ethyl alcohol (CH_3CH_2OH) was obtained from Tianjin Hengxing Chemical Preparation Co., Ltd. (China). Ammonium molybdate ($(NH_4)_6Mo_7O_{24}{\cdot}4H_2O$) was obtained from Kaida Technology Development Corporation, Tianjin, China.. Nitric acid (HNO_3) was obtained from Huihong Chemical Corporation Hunan, China. Glacial acetic acid ($C_2H_4O_2$) was obtained from Sinopsin Group Chemical Reagent Co., Ltd. (China). Polyethylene glycol ($H(OCH_2CH_2)_nOH$) was obtained from Sinopsin Group Chemical Reagent Co., Ltd. (China). All reagents were of analytical grade. Deionized water was used for all the experiments.

Synthesis of Photocatalysts

The FACs were activated in 10% dilute nitric acid and stirred at room temperature for 12 h to cleanse the solid oxides on the surface. Then, they were filtered by a vacuum filter and washed repeatedly with deionized water until the pH of the suspension was 6–7. After pretreatment, the FACs were dried at 105 °C for 2 h. The Mo-TiO_2@FAC photocatalysts were mainly prepared by the sol-gel method; 20 ml titanium butoxide was mixed with 70 ml absolute ethanol, which was named solution A. Different amounts of ammonium molybdate were added to a mixture of 9 mL of glacial acetic acid, 20 ml of deionized water, and 70 mL of ethanol under continuous stirring, which was named solution B, adjusting pH of solution B to about 3 by 67% HNO_3 under stirring. Then, solution B was slowly added dropwise into the solution A; 1.2 g polyethylene glycol was added into the homogeneous solution as the surfactant with magnetic stirring at room temperature. 5 g FACs were added into the gel with stirring for 1 h in constant water bath at 40 °C. Subsequently, the gels were placed at 25 °C for 24 h and dried at 80 °C until a dry gel was obtained. In the end, the dry gel was calcinated for 2 h in a muffle furnace at 350, 450, 550, and 650 °C, respectively. For comparison, TiO_2 and Mo-TiO_2 were prepared by the same method. The molar ratios of Mo to Ti were 0, 0.1%, 0.3%, 0.5%, and 1.0%, respectively. According to the molybdenum content, the final powders were denoted as Mo_x-TiO_2@FAC (x = 0.1, 0.3, 0.5, 1.0).

Degradation Experiment

The photocatalytic experiment was carried out in a self-made reactor using a Xe lamp with 500 W as visible light source. At adsorption experiment, the 100 ml of MB (10 mol/L) solution and appropriate catalyst were mixed up in the reactor and stirred for 45 min in the dark to get adsorption equilibrium. The following photodecomposition of MB experiment was achieved under visible light irradiation. The 5 mL intermixtures were taken from it each 30 min interval (30–180 min), then the upper layer of intermixtures was filtered by 0.22 μm filter membrane, and the residual content of MB was measured at 664 nm with UV–visible spectrophotometer.

Characterizations

X-ray diffraction (XRD) patterns were recorded by a Bruker D8 Advance X-ray diffractometer using Cu-Kα radiation. The surface morphology was investigated using a scanning electron microscope (SEM; PhenomPro, USA). X-ray photoelectron spectra (XPS) were conducted by Thermo Fisher-VG Scientific ESCALAB 250

XPS system with Al Kα X-ray radiation. UV–Vis spectra were characterized by a Shimadzu UV2550 UV–Vis spectrophotometer.

Results and Discussion

XRD patterns of TiO_2@FAC and Mo-TiO_2@FAC with different Mo doping amounts are shown in Fig. 1a. Obviously, the peak of anatase in Mo-TiO_2@FAC is higher than that of TiO_2@FAC and no rutile phase or brookite phase is detected, suggesting doping Mo element promotes the formation of anatase phase. Different doping Mo amount samples have similar diffraction patterns and the major peaks of anatase phase at 2θ of 25.32°, 37.86°, 48.06°, 53.97°, and 55.09° for the (1 0 1), (0 0 4), (2 0 0), (1 0 5), and (2 1 1) diffraction planes, respectively [13]. No peak of MoO_3 phases is observed even in the 1.0% Mo/Ti molar ratio sample, indicating the incorporation of Mo^{6+} ion into the TiO_2 lattice. The ionic radius of Mo^{6+} and Ti^{4+} is 0.062 nm and 0.068 nm, respectively [14]. The close ion radius creates a condition for incorporating molybdenum into titanium dioxide lattice, resulting in a narrower energy gap, which could be observed in the following UV–Vis spectroscopy.

Figure 1b reveals XRD patterns of samples calcined at different temperatures. Results show that calcined temperature has a significant influence on crystalline forms of photocatalysts. The character peaks of anatase became sharper and stronger with calcination temperature increasing. However, new rutile phase is observed with temperature a further increase to 650 °C whose major peaks are at 27.44°, 36.09°, and 54.34°.

SEM images in Fig. 2 show morphologies of photocatalysts. As shown in Fig. 2a, b, the pure FAC is a hollow spherical particle with a diameter of 120 μm and wall thickness of 5 μm. Figure 2c, d presents SEM images of TiO_2@FAC at different magnifications. This confirms that TiO_2 was successfully coated on the surface of

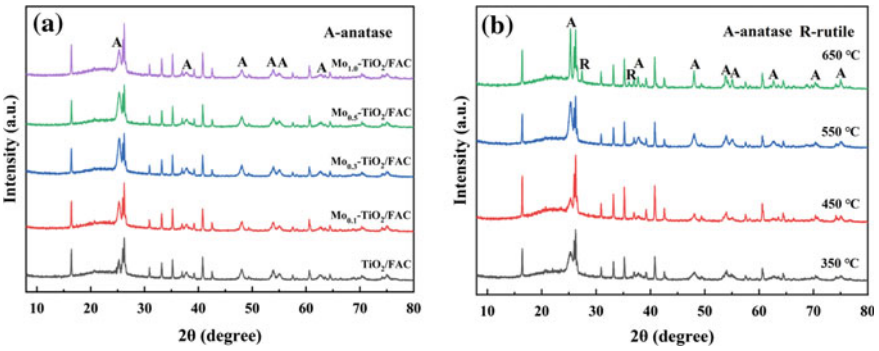

Fig. 1 XRD patterns. **a** With different Mo doping amount photocatalysts calcinated at 550 °C and **b** $Mo_{0.3}$-TiO_2@FAC calcined at different temperatures

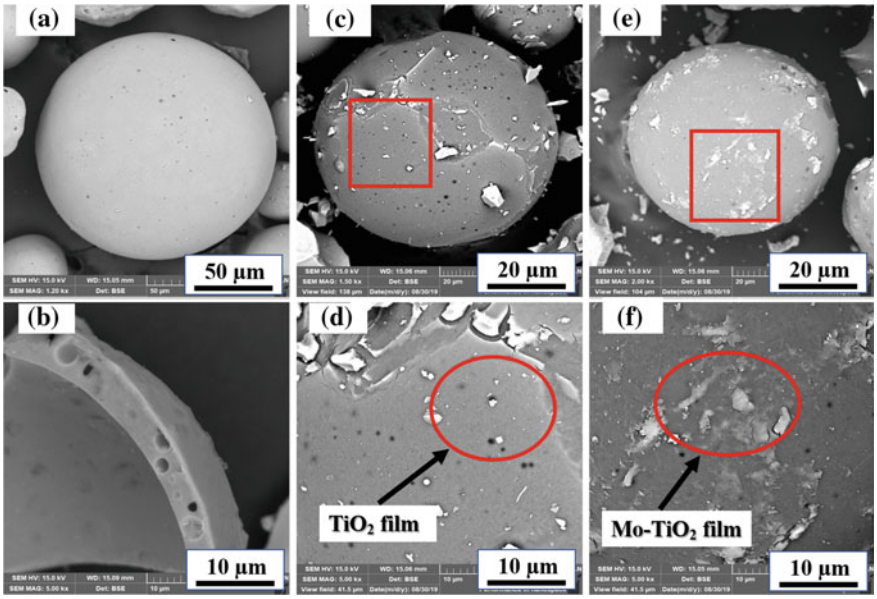

Fig. 2 SEM images of **a** a pretreated FAC, **b** a broken FAC, **c**, **d** TiO_2@FAC-550 °C, and **e**, **f** $Mo_{0.3}$-TiO_2@FAC-550 °C at low and high magnification

the FAC with some little grains being observed merely in small regions. The surface of Mo-TiO_2@FAC has an obviously uneven and rough appearance owing to shrinkage in the drying and calcination process after molybdenum doping(Fig. 2e, f).

The UV–visible spectra of Mo-TiO_2@FAC photocatalysts calcined at 550 °C with different molybdenum contents are illustrated in Fig. 3a. Doping Mo in photocatalyst occurs redshifts of the absorption edge and increases light absorption in the range 400–500 nm. The absorbance increased with the increase of molybdenum content in

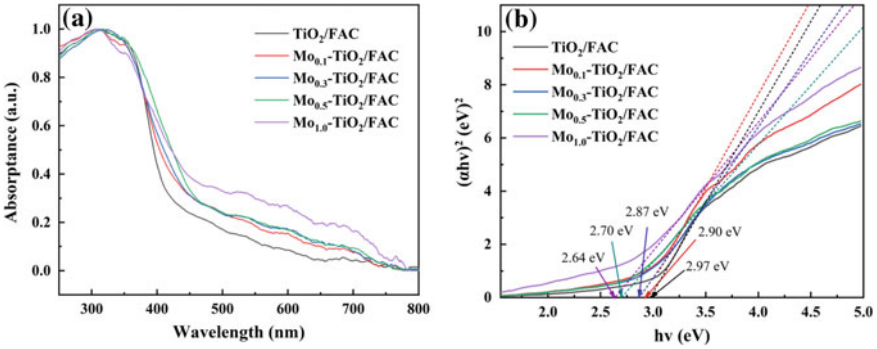

Fig. 3 **a** UV–Vis absorption spectra and **b** plot of $(\alpha h\nu)^2$ versus energy $(h\nu)$ of Mo-TiO_2@FAC photocatalysts (calcined at 550 °C) with different molybdenum doping contents

Mo-doped TiO_2, but inhibited with too much doping content of Mo. In comparison with all Mo-TiO_2@FAC, $Mo_{0.3}$-TiO_2@FAC showed the highest photo-absorption in the visible light region. Above results suggest that the doping elements were inserted into the lattice of TiO_2 and its electronic structures were changed. The energy band gaps of samples were calculated by the following equation:

$$\alpha h\nu = A(h\nu - Eg)^{n/2} \tag{1}$$

where α, ν, A, Eg, and n are the absorption coefficient, incident light frequency, constant, band gap and an integer, respectively. The n value represents the type of optical transition of a semiconductor ($n = 1$ for direct transition and $n = 4$ for indirect transition). The n values of 4 are reasonable for all the samples according to the existing literatures [15]. Figure 3b shows the samples' corresponding plots of $(\alpha h\nu)^2$ versus $h\nu$ to determine the direct band gap by extrapolation of the linear part of the graphics to the axis of the abscissa. The band gaps of TiO_2@FAC and 0.1, 0.3, 0.5, and 1.0% Mo-TiO_2@FAC were calculated to be 2.97, 2.90, 2.87, 2.70, and 2.64 eV, respectively. The band gap of molybdenum-doped TiO_2@FAC photocatalyst is lower compared to the Mo-undoped TiO_2@FAC photocatalyst, which attributes to the shift of the optical absorption edges to the lower energy regions and keeps higher photocatalytic activities. According to the previous literatures, below the conduction band of TiO_2 was introduced by the means of the doping of transition metal ions in TiO_2 [16]. Hence, the visible light absorption leads to the excitation of Mo^{6+} 3d electrons to the conduction band of TiO_2. In this way, the doping of Mo can decrease the band gap of TiO_2 and broaden the photocatalyst scope of illumination response.

XPS analyses were conducted to investigate the surface composition and the chemical state of elements in the photocatalyst. The overall XPS of TiO_2@FAC and $Mo_{0.3}$-TiO_2@FAC photocatalysts are shown in Fig. 4a, b, respectively. The photocatalysts are mainly composed of Ti, O, Mo, C, Si, and Al elements. The Si and Al originated from the FAC substrate, while Mo was from the doping solution.

As shown in Fig. 4c, it was found that the values of the peaks of Ti^{4+} in TiO_2 lattice located at binding energy of 458.4 and 463.9 eV corresponded to $Ti2p_{3/2}$ and $Ti2p_{1/2}$, respectively [17]. However, the binding energies of $Ti2p_{3/2}$ and $Ti2p_{1/2}$ in $Mo_{0.3}$-TiO_2@FAC were 458.55 eV and 464.25 eV, respectively. A few right shifts were caused by Mo doping. This result provides further evidence that molybdenum atoms indeed substituted titanium atoms in the lattice.

$Mo3d_{5/2}$ and $Mo3d_{3/2}$ peaks of $Mo_{0.3}$-TiO_2@FAC are shown in Fig. 4d. The peaks at 232.2 eV and 234.8 eV corresponded to the feature of Mo^{6+}, while peaks at 230.8 eV corresponded to Mo^{5+}. No Mo^{4+} peak was present, indicating that the main valances of molybdenum in the samples were +6 and +5. It can be believed that the major doped Mo ions existed as Mo^{6+} in TiO_2 lattice, and at the same time a small part of Mo ions existed as Mo^{5+}.

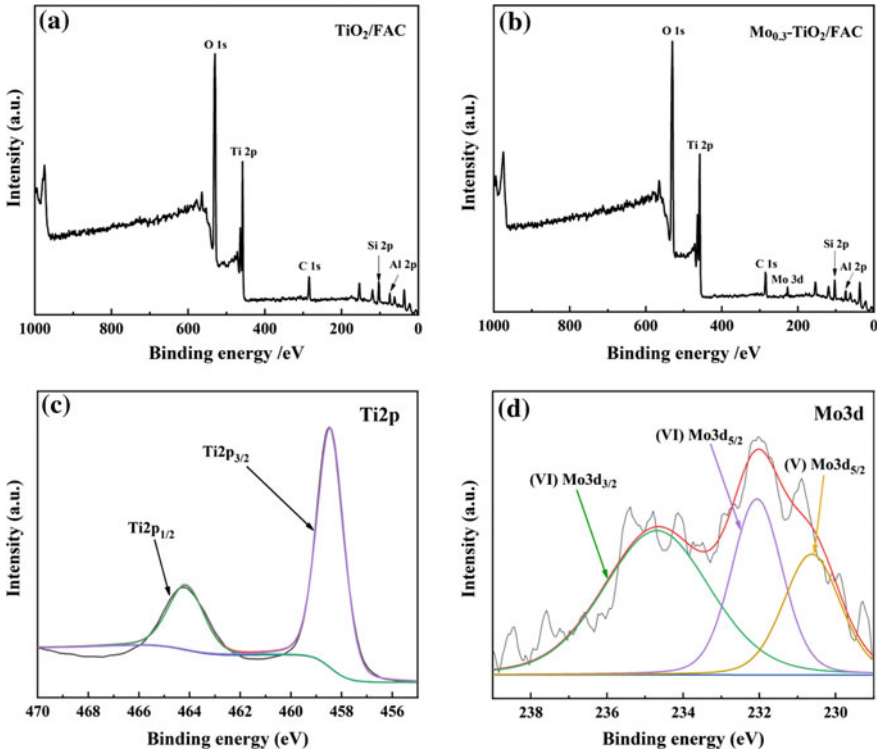

Fig. 4 XPS of **a** TiO_2@FAC and **b** $Mo_{0.3}$-TiO_2@FAC (calcined at 550 °C), and corresponding high-resolution XPS spectra of **c** Ti2p and **d** Mo3d

Photocatalytic Activity

Figure 5a displays the photocatalytic degradation ratio of MB using different Mo doping amounts. The photocatalytic degradation ratio increased markedly as doping Mo content from 0 to 0.3%, which can be attributed to the transform in optical absorption threshold of catalysts into visible region. However, the doping Mo content exceeds 0.3%, and the degradation ratio significantly decreased. It may be that excessive Mo^{6+} ions would cause the carrier recombination. As a result, the recombination of generated electron/hole pair exceeded the carrier transition to the surface of photocatalysts. Once the concentration of Mo was beyond an optimum quantity, Mo^{6+} role as a carrier recombination center would counteract its role of trapping carriers and prolonging carrier lifetime [18]. A decrease of photocatalytic activity was observed.

Figure 5b shows the relationship between the photocatalytic degradation ratio and the calcination temperatures. As the calcination temperature increased, the photocatalytic degradation ratio improves and reaches a maximum at 550 °C. The main reason may be that amorphous TiO_2 gradually turned into anatase when the calcined

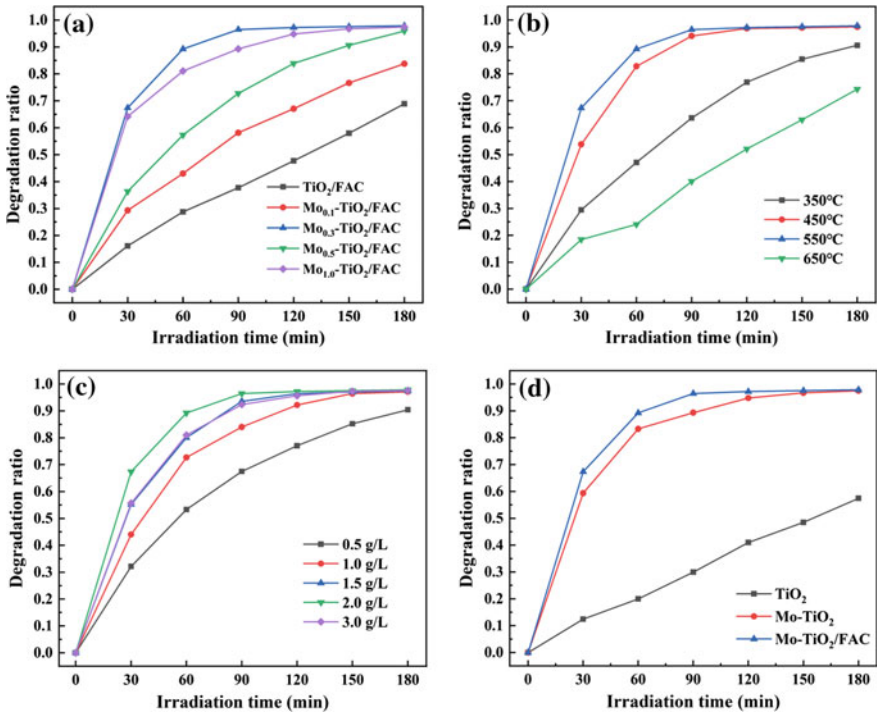

Fig. 5 Photocatalytic degradation ratio of composites with different **a** Mo doping amounts, **b** calcination temperatures, **c** catalyst dosages, and **d** TiO_2, TiO_2@FAC and $Mo_{0.3}$-TiO_2@FAC (550 °C)

temperature increased from 350 to 550 °C, resulting in promotion of the photocatalytic ability of photocatalyst [19]. However, the photocatalytic degradation ratio reduced with temperature a further increase to 650 °C because the appearance of rutile phase induces wide energy gap and large particle size. It can be concluded that the Mo doping amount of 0.3% and the calcination temperature of 550 °C were optimum.

The effect of catalyst dosage on degradation efficiency was studied using 10 mg/L of MB and 0.5, 1, 1.5, 2, and 3 g/L of $Mo_{0.3}$-TiO_2@FAC. As shown in Fig. 5c, the degradation rate increased with the increase of the dosage and reached a peak of 98% when the dosage was 2 g/L, but then decreased with a further increase of the dosage. The main reason is that the appropriate amount of catalyst increases the contact area and generates more photoelectron–hole pairs, contributing to sufficient carriers captured by the methylene blue and thorough oxidation and decomposition of the MB. As the dosage of the catalyst in the reactor increases, the turbidity of the reaction solution causes the light transmittance to deteriorate, eventually resulting in a decrease in photocatalytic efficiency. Therefore, the optimal addition amount is 2 g/L.

The MB concentration was no significant decrease using pristine FAC decomposition MB for 1 h, suggesting that FAC itself has no photocatalytic activity. As seen in Fig. 5d, the degradation ratio of Mo-TiO_2 is 8% less than that of Mo-TiO_2@FAC (0.3%, 550 °C) and extremely higher than that of pure titanium dioxide particles. FAC used as substrates in the Mo-TiO_2@FAC composite has two vital functions. Firstly, the adsorption capacity of FAC based on pore structure can improve the adsorption capacity of MB on the substrate surface. Second, as a dispersing carrier, it can inhibit grain growth, which is helpful to make full use of light for photocatalysis. Because of the synergistic effect of Mo-titanium dioxide and FAC, Mo-TiO_2@FAC composite has high photocatalytic activity.

Conclusions

Mo-TiO_2 films are deposited successfully on FAC by the sol-gel method, and the synthesized Mo-TiO_2@FAC photocatalysts can take advantage of solar light in comparison with TiO_2@FAC and pure TiO_2 particles and can be easily separated from water after the reaction due to their buoyant property. The results of photocatalytic activity of the samples for degradation of MB showed that 2 g/L of the $Mo_{0.3}$-TiO_2@FAC photocatalyst calcined at 550 °C has higher photocatalytic activity than the other samples under visible light irradiation, and the introduction of FAC in photocatalysts can contribute to the degradation of MB in water. In the future, the influence of catalyst preparation conditions on the degradation of other dyes will be studied.

References

1. Deng BN, Si PX, Bauman L, Luo J, Rao MJ, Peng ZW, Jiang T, Li GH, Zhao BX (2019) Photocatalytic activity of $CaTiO_3$ derived from roasting process of bauxite residue. J Cleaner Prod. https://doi.org/10.1016/j.jclepro.2019.118598
2. Fujishima A, Zhang X, Tryk DA (2008) TiO_2 photocatalysis and related surface phenomena. Surf Sci Rep 63(12):515–582
3. Yu J, Xiang Q, Zhou M (2009) Preparation, characterization and visible-light-driven photocatalytic activity of Fe-doped titania nanorods and first-principles study for electronic structures. Appl Catal B: Environ 90(3–4):595–602
4. Choi J, Park H, Hoffmann MR (2010) Effects of single metal-ion doping on the visible-light photoreactivity of TiO_2. J Phys Chem C 114(2):783–792
5. Liu S, You K, Song J, Deng R, Zhao F, Liu P (2018) Supported TiO_2/MCM-41 as an efficient and eco-friendly catalyst for highly selective preparation of cyclohexanone oxime from solvent-free liquid phase oxidation of cyclohexylamine with molecular oxygen. Appl Catal A: Gene 568:76–85
6. Ren XL, Liu ZW, Dong L, Miao G, Liao N, Li Z, Xiao J (2018) Dynamic catalytic adsorptive desulfurization of real diesel over ultra-stable and low-cost silica gel-supported TiO_2. AlChE J 64(6):2146–2159

7. Ruiz-Hitzky E, Aranda P, Akkari M, Khaorapapong N, Ogawa M (2019) Photoactive nanoarchitectures based on clays incorporating TiO_2 and ZnO nanoparticles. Beilstein J Nanotechnol 10:1140–1156
8. Zhang GX, Song AK, Duan YW, Zhang SL (2018) Enhanced photocatalytic activity of TiO_2/zeolite composite for abatement of pollutants. Microporous Mesoporous Mater 255:61–68
9. Pereira LD, Sales IM, Zampiere LP, Vieira SS, Guimaraes I D, Magalhaes F (2019) Preparation of magnetic photocatalysts from TiO_2, activated carbon and iron nitrate for environmental remediation. J Photochem Photobiol A: Chem 382
10. Yao ZT, Xia MS, Sarker PK, Chen T (2014) A review of the alumina recovery from coal fly ash, with a focus in china. Fuel 120:74–85
11. Song J, Wang X, Bu Y, Zhang J, Wang X, Huang J (2016) Preparation, characterization, and photocatalytic activity evaluation of Fe–N-codoped TiO_2/fly ash cenospheres floating photocatalyst. Environ Sci Pollut Res 23(22):22793–22802
12. Ahmaruzzaman M (2010) A review on the utilization of fly ash. Prog Energy Combust Sci 36(3):327–363
13. Khan M, Xu J, Chen N, Cao W (2012) First principle calculations of the electronic and optical properties of pure and (Mo, N) co-doped anatase TiO_2. J Alloys Compd 513(none):0–545
14. Delekar SD, Yadav HM, Achary SN, Meena SS, Pawar SH (2012) Structural refinement and photocatalytic activity of Fe-doped anatase TiO_2 nanoparticles. Appl Surf Sci 263(Complete):536–545
15. Yan Y, Zhou X, Lan J, Li Z, Zheng T, Cao W, Liu W (2018) Efficient photocatalytic disinfection of *Escherichia coli* by N-doped TiO_2 coated on coal fly ash cenospheres. J Photochem Photobiol A: Chem 367:355–364
16. Wang B, Yang Z, An H, Zhai J, Li Q, Cui H (2015) Photocatalytic activity of Pt-TiO_2, films supported on hydroxylated fly ash cenospheres under visible light. Appl Surf Sci 324:817–824
17. Huang JG, Guo XT, Wang B, Li LY, Zhao MX, Dong LL, Huang YT (2015) Synthesis and photocatalytic activity of Mo-doped TiO_2 nanoparticles. J Spectro 2015:1–8
18. Pang YL, Abdullah AZ (2012) Effect of low Fe^{3+} doping on characteristics, sonocatalytic activity and reusability of TiO_2 nanotubes catalysts for removal of rhodamine B from water. J Hazard Mater 235–236(none):326–335
19. Soon-Kil J, Takashi A, Masayuki M, Kiminori I (2010) Mechanistic studies of the photocatalytic oxidation of trichloroethylene with visible-light-driven N-doped TiO_2 photocatalysts. Chem Eur J 12(21):5526–5534

Removing Arsenic from the $NiSO_4$ Solution Using Modified D301 Resin

Ailiang Chen, Xintao Sun, Jinxi Qiao, Zhen Qian, Yan Zhang, Yutian Ma, Zhiqiang Liu and Lixue Shi

Abstract Arsenic is removed from the $NiSO_4$ solution using modified D301 resin. The modification is based on the fact that WO_4^{2-} react with AsO_4^{3-} in the $NiSO_4$ solution to form arsenotungstic ions. This study grafted WO_4^{2-} onto the resin to remove arsenic in the $NiSO_4$ solution and avoided the loss of tungsten. The effects of reaction time, temperature, and the pH of solution on arsenic removal efficiency were investigated. When the reaction time is 4 h and the pH value of solution is 3.06, arsenic is removed using WO_4^{2-}-loaded D301 in the $NiSO_4$ solution at normal temperature. Results show that the concentration of As (V) from 50 mg/L fell to below 5 mg/L in the $NiSO_4$ solution. There is no impurities were brought in the process of arsenic removal, achieving higher ratio of arsenic removal in the industry.

Keywords Arsenic removal · $NiSO_4$ solution · D301 · Ratio of arsenic removal

A. Chen · X. Sun · J. Qiao (✉) · Z. Qian
School of Metallurgy and Environment, Central South University, Changsha 410083, China
e-mail: Qiaojinxi@csu.edu.cn; 1258374979@qq.com

Z. Liu
Guangdong Research Institute of Rare Metals, Guangzhou 510665, China

State Key Laboratory of Rare Metals Separation and Comprehensive Utilization, Guangzhou 510665, China

Y. Zhang · Y. Ma
State Key Laboratory of Nickel and Cobalt Resources Comprehensive Utilization, Jinchang 737104, China

Y. Ma
Jinchuan Group Co. Ltd., Jinchang 737104, Gansu, China

L. Shi
School of Aeronautics and Astronautics, Central South University, Changsha 410083, China

J. Li et al. (eds.), *Characterization of Minerals, Metals, and Materials 2020*,
The Minerals, Metals & Materials Series,
https://doi.org/10.1007/978-3-030-36628-5_18

Introduction

Arsenic oxides and their compounds are harmful to human's health due to their toxicity. Arsenic always enters into acidic nickel sulfate solution together during the process of nickel metallurgy. It is easy to form hydrogen arsenide gas (AsH_3) with greater toxicity than arsenic oxide. Arsenic has also been regarded as a harmful element in the production of nickel products [1]. In the recent years, the changeable arsenic-containing raw materials increase the difficulty of producing nickel products. Thus, it is necessary to remove arsenic from $NiSO_4$ solution.

In the pyrometallurgical process, arsenic can be removed through forming As_2O_3 by roasting before the technology of nickel electrolysis [2]. The hydrometallurgical process generally refers to arsenic removal in the solution. Some common technologies, like precipitation, biological, adsorption, extraction, and ion exchange have been used to remove arsenic from nickel solution [3]. Huang et al. [4] found $Ca(OH)_2$ added as precipitant to form insoluble arsenic-containing compounds in the solution. The arsenic removal ratio can reach 99.05% in the wastewater with low arsenic concentration. Iron and manganese oxides were used as adsorbents for removing arsenic from aqueous solution in an experimental study of Chang et al. [5]. Its saturated adsorption capacity for arsenic reached 326 mg g^{-1}. Liao et al. [6] treated with algae to form a symbiotic organism with bacteria and acclimated it in the arsenic-containing wastewater. It can remove arsenic and nutrients in the wastewater. It is still in the stage of laboratory research. TBP (Tributyl phosphate) and N_{235} (N, N-dioctyl-1-Octanamine) were used as extraction solvent for arsenic removal in the copper electrolyte. It can eventually remove 72.82% of arsenic [7]. But the organic reagents easily enter into the $NiSO_4$ solution, which affects the quality of electrolytic nickel. Korngold et al. [8] used two strong alkaline resins to remove arsenic. However, arsenic removal in the $NiSO_4$ solution would be affected by the concentration of SO_4^{2-}. It is difficult to deeply remove arsenic from the $NiSO_4$ solution.

In order to deeply remove arsenic in the process of nickel product, a method of molecular design was used to transform AsO_4^{3-} into macromolecular groups like $[AsW_{12}O_{40}]^{3-}$, $[AsW_9O_{34}]^{9-}$. This improves the difference between SO_4^{2-} and arsenic-containing groups, achieving deep remove arsenic from the $NiSO_4$ solution. In this work, experiments were carried out to determine the most suitable ion exchange resin. And then conditional experiments were done to verify the optimal reaction temperature, the pH value of solution, reaction time, and initial arsenic concentration.

Experimental

Materials

$NiSO_4$ solution containing arsenic comes from a nickel factory in China. The concentration of SO_4^{2-}, Ni^{2+}, and arsenic is 100 g/L, 60 g/L, and 50 mg/L, respectively. D301 resin (produced by Jiangsu Suqing Water Treatment Engineering Group Co., Ltd.) and extraction solvent (sulfonated kerosene and N_{235}) are industrial products. Other analytical reagents, including NaCl, Na_2WO_4, NaOH, hydrochloric acid, sulfuric acid, and Na_3AsO_4.

Method and Analysis

Extraction: Sulfonated kerosene and N_{235} were mixed as extraction solvent. The volume ratio of N_{235} to sulfonated kerosene was 3:7, and O:A = 1:1. 100 ml $NiSO_4$ solution was mixed with the extraction solvent to oscillate for a period at a certain temperature. The mixture stands for several minutes after the reaction was completed, separating the $NiSO_4$ solution from the organic phase.

Ion exchange: Na_2WO_4 and SO_4^{2-}-loaded D301 was added in the $NiSO_4$ solution at a certain temperature, and it reacted for a period with magnetic stirring. Then the D301 resin adsorbing arsenic in the solution was filtered out for desorption.

The equations for calculating some parameters are as follows:

$$\beta = \frac{1 - c_a}{c_b} \tag{1}$$

where β is the arsenic removal ratio of D301 resin. c_a is the arsenic concentration after removing arsenic with D301 resin. c_b is the initial arsenic concentration in the $NiSO_4$ solution.

$$\gamma = \frac{m_a}{m_c} \tag{2}$$

where γ is the amount the arsenic removed per gram of D301 resin. m_a is the amount of arsenic removed with the D301 resin, and m_c is the amount of the D301 resin in the $NiSO_4$ solution.

Results and Discussion

Selection of Removal Reagents

Table 1 shows the effect of removing arsenic with N_{235}, SO_4^{2-}-loaded D301 and WO_4^{2-}-loaded D301. It can be seen that the removal ratio of arsenic is 55.77% with SO_4^{2-}-loaded D301, 57.72% with N_{235} and 93.05% with WO_4^{2-}-loaded D301. It can be found that the arsenic removal ratio of WO_4^{2-}-loaded D301 is the highest among the three methods. The WO_4^{2-}-loaded D301 is transformed as follows:

$$\overline{R-Cl} + OH^- \rightarrow \overline{R-OH} + Cl^- \tag{3}$$

$$2\overline{R-OH} + WO_4^{2-} \rightarrow \overline{R_2-WO_4} + 2OH^- \tag{4}$$

The tungstate radical $\left(WO_4^{2-}\right)$ loaded in the resin will form insoluble nickel tungstate ($NiWO_4$) with Ni^{2+} of the solution as follows:

$$WO_4^{2-} + Ni^{2+} = NiWO_4 \tag{5}$$

It prevents the loss of WO_4^{2-} at high concentration of $SO_4^{2-} \cdot AsO_4^{3-}$ reacts with WO_4^{2-} in the resin under acidic condition. They can form macromolecular groups ($[AsW_{12}O_{40}]^{3-}$, $[AsW_9O_{34}]^{9-}$) improving the resin selectivity to remove arsenic. The reaction equations are as follows:

$$AsO_4^{3-} + 12NiWO_4 + 24H^+ \rightarrow [AsW_{12}O_{40}]^{3-} + 12H_2O + 12Ni^{2+} \tag{6}$$

$$AsO_4^{3-} + 9NiWO_4 + 12H^+ \rightarrow [AsW_9O_{34}]^{9-} + 6H_2O + 9Ni^{2+} \tag{7}$$

Figure 1a shows IR spectra of D301 at each stage. Compared with spectrum①, the weak absorption peak at 989 cm^{-1} of spectrum② is caused by ν_{as}(W=O). It proves that WO_4^{2-} as been loaded in the D301. There are three characteristic vibration patterns at 887, 912, and 945 cm^{-1}, which correspond to ν_{as}(As−O_a), ν_{as}(W–O_b–W), ν_{as}(W–O_d) of spectrum③, respectively. The characteristic peak at 989 cm^{-1} is attributed to W=O stretching vibration. This infers that AsO_4^{3-} of the $NiSO_4$ solution

Table 1 Effect of three methods for arsenic removal

	Extraction	SO_4^{2-}-loaded D301	WO_4^{2-}-loaded D301
c_a after removed/(mg/L)	21.66	22.66	3.56
β/%	57.72	55.77	93.05

Note c_a before removing arsenic is 51.23 mg/L

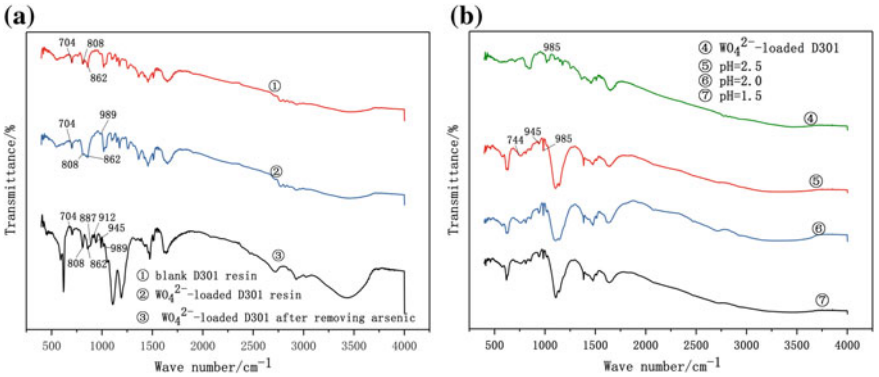

Fig. 1 IR spectra of D301 at each stage (**a**), and WO_4^{2-}-loaded D301 at different pH (**b**)

is removed with WO_4^{2-}-loaded D301 and form arsenotungstic acid like $[AsW_9O_{34}]^{-9}$ or $[AsW_{12}O_{40}]^{3-}$ [9].

Figure 1b is the infrared analysis diagram of WO_4^{2-}-loaded D301 at different pH. As can be seen from spectrum④, the weak absorption peak at 985 cm^{-1} was caused by ν_{as}(W=O). This implies that the resin has been transformed successfully. Spectrum⑥ shows characteristic vibration patterns at 744 and 985 cm^{-1}, which correspond to ν_{as}(W–O–As) and ν_{as} (W–O_d). The weak absorption peak at 985 cm^{-1} is also caused by ν_{as}(W=O). Compared with spectrum⑥ and spectrum⑦, it has a better effect of removing arsenic at pH value of 2.5.

Based on the above, arsenic of the $NiSO_4$ solution can be removed with WO_4^{2-}-loaded D301.

Effect of pH Value of the Solution

Table 2 gives the effect of removing arsenic with WO_4^{2-}-loaded D301 at different pH values. The arsenic concentration after removed is reduced to 4.77 mg/L when

Table 2 Effect of removing arsenic with WO_4^{2-}-loaded D301 at different pH value

pH	0.1	0.26	0.5	1.01	1.45	2.27	2.5	3.06	4.13	5.73
c_a after removing arsenic (mg/L)	38.48	36.54	30.37	21.09	14.11	6.10	5.45	4.77	10.17	36.99

Note Reaction temperature is 20 °C, reaction time is 4 h, initial arsenic concentration in the $NiSO_4$ solution is about 50 mg/L, and the concentrations of Ni^{2+} and SO_4^{2-} are 60 g/L, 100 g/L, respectively

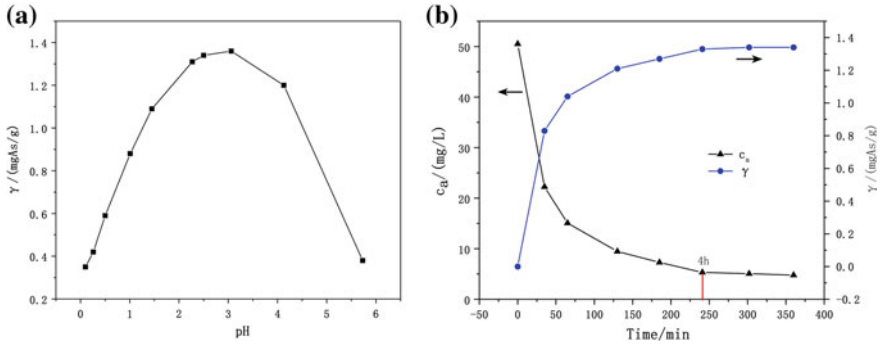

Fig. 2 Effect of the value of pH (**a**), and time (**b**) on arsenic removal. *Note* Reaction time for (**a**) is 4 h, the pH value of the solution for (**b**) is 2.27, reaction temperature is 20 °C, initial arsenic concentration in the $NiSO_4$ solution is about 50 mg/L, and the concentrations of Ni^{2+} and SO_4^{2-} are 60 g/L, 100 g/L

the pH value was 3.06. As the pH value rises to 5.73, the arsenic concentration rises to 36.99 mg/L. This is because AsO_4^{3-} can form various arsenotungstic acids with WO_4^{2-} low pH value. The molar ratio of arsenic to tungsten is 1:12, 1:11, 1:9, 1:6, 1:9, 1:8.5 [10].

Figure 2a shows the effect of the value of pH on arsenic removal. The arsenic removal capacity of D301 first increases and then decreases with the increase of pH value. The maximum amount of arsenic removed is at the pH value of 3.06. The arsenotungstic acid exists in the form of $[AsW_{12}O_{40}]^{3-}$ at pH value of 1.01 as shown in Eq. (6). When the pH value is 2.27, it includes $[AsW_{12}O_{40}]^{3-}$, $[As_2W_{21}O_{71}]^{6-}$, and $[AsW_{11}O_{39}]^{7-}$. The equations may be as follows:

$$2AsO_4^{3-} + 21NiWO_4 + 42H^+ = [As_2W_{21}O_{71}]^{6-} + 21H_2O + 21Ni^{2+} \quad (8)$$

$$AsO_4^{3-} + 11NiWO_4 + 18H^+ = [AsW_{11}O_{39}]^{7-} + 9H_2O + 11Ni^{2+} \quad (9)$$

At the pH value of 3.06, it also generates new arsenotungstic acid, such as $[As_2W_{18}O_{62}]^{6-}$, $[As_2W_{19}O_{67}]^{10-}$. The equations are as follows:

$$2AsO_4^{3-} + 18NiWO_4 + 36H^+ = [As_2W_{18}O_{62}]^{6-} + 18H_2O + 18Ni^{2+} \quad (10)$$

$$2AsO_4^{3-} + 19NiWO_4 + 34H^+ = [As_2W_{19}O_{67}]^{10-} + 17H_2O + 19Ni^{2+} \quad (11)$$

There are some arsenotungstic acids at the value of pH is 5.73, such as $[As_2W_{21}O_{71}]^{6-}$, $[AsW_{11}O_{39}]^{7-}$, and $[As_2W_{18}O_{62}]^{6-}$.

Figure 2b gives the arsenic concentration in the $NiSO_4$ solution and arsenic removal amount of WO_4^{2-}-loaded D301 at different reaction times. It can be seen that the arsenic concentration drops rapidly from 50.5 mg/L to about 15 mg/L within

60 min. The arsenic removal ratio reached 75%. The arsenic concentration keeps about 5 mg/L. It can remove 99% of arsenic in the $NiSO_4$ solution.

Reaction Time and Kinetics Analysis

According to Fig. 2b, the optimal reaction time is 4 h. Generally, the models of quasi-first-order and quasi-second-order kinetics are selected. Their linear equations are as follows:

$$\ln(Q_e - Q_t) = \ln Q_e - k_1 \tag{12}$$

$$\frac{t}{Q_t} = \frac{1}{k_2 Q_e^2} + \frac{t}{Q_e} \tag{13}$$

where Q_t is the arsenic removal amount of resin at a certain time, Q_e is the arsenic removal amount of resin under saturation, k_1 is the constant of quasi-first-order rate, and k_2 is the constant of quasi-second-order rate.

Figure 3a shows the correlation coefficient of the quasi-first-order kinetic model for fitting the arsenic removal process is 0.9965. That of quasi-second-order kinetic model is 0.9853. It is indicated that the quasi-secondary kinetic model can better explain the arsenic removal process with WO_4^{2-}-loaded D301.

Figure 3b shows the relationship of $1 + 2(1 - \alpha) - 3(1 - \alpha)^{\frac{2}{3}}$ and time. The relevant parameters were obtained by linear fitting. It can be seen that the correlation coefficient of the diffusion equation for the arsenic removal process is 0.9803. This can explain that the process of removing arsenic is mainly controlled by the diffusion of arsenic in the resin [12].

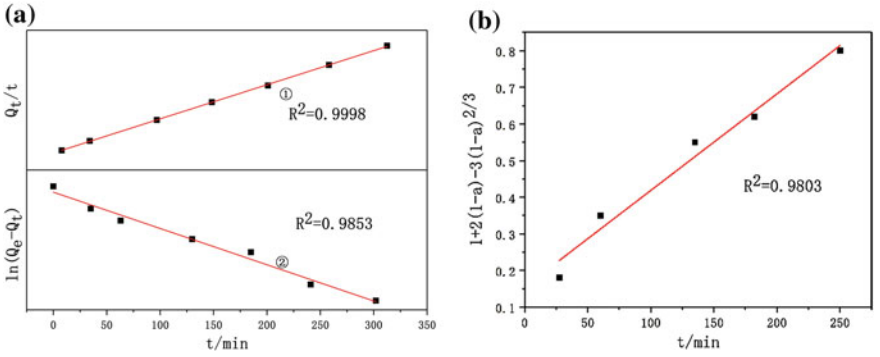

Fig. 3 Quasi-first-order (line①) and quasi-secondary-order (line②) kinetic models (**a**), and fitting the diffusion equation of removing arsenic with WO_4^{2-}-loaded D301 (**b**)

The process of removing arsenic can be regarded as the liquid–solid reaction. The D301 resin is a uniform sphere. The model of shrinking core can better describe the reaction mechanism of removing arsenic with WO_4^{2-}-loaded D301 [11]. Finally, Eq. (14) is obtained after formula derivation.

$$\frac{6nDC_A}{\rho_B R^2} \times t = \left[1 + 2(1-\alpha) - 3(1-\alpha)^{\frac{2}{3}}\right] \tag{14}$$

Reaction Temperature

Figure 4 expresses the effect of reaction temperature on the arsenic removal process. The arsenic removal amount is approximately unchanged below 25 °C. The higher the temperature, the more arsenic removal amount of resin. The reasons may be as follows:

(1) The process of removing arsenic with WO_4^{2-}-loaded D301 is endothermic reaction.
(2) The rise of temperature increases D301 resin's activity and diffusion rate of AsO_4^{3-} in the $NiSO_4$ solution. It makes the D301 resin fully contact and react with arsenic in the solution.

From the point of view of industrialization, the economic cost of rising the temperature to 50 °C is much greater than 20 °C. In addition, D301 resin belongs to organic substance. When the temperature is above 50 °C, it will be destroyed. Therefore, the optimum temperature of removing arsenic is 20 °C with WO_4^{2-}-loaded D301.

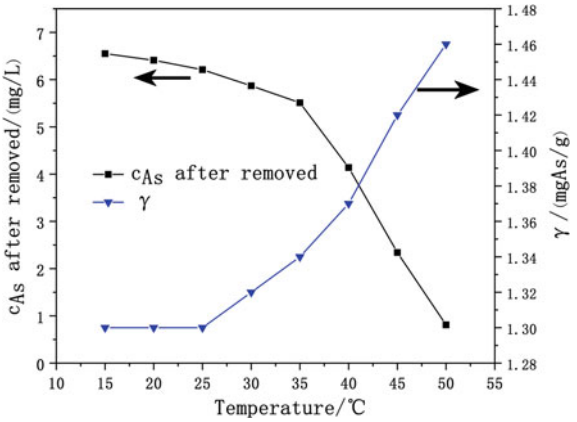

Fig. 4 Effect of reaction temperature on the arsenic removal process. *Note* The pH value of the solution is 3.0, reaction time is 4 h, initial concentration of arsenic in the $NiSO_4$ solution is about 50 mg/L, and the concentrations of Ni^{2+} and SO_4^{2-} are 60 g/L, 100 g/L, respectively

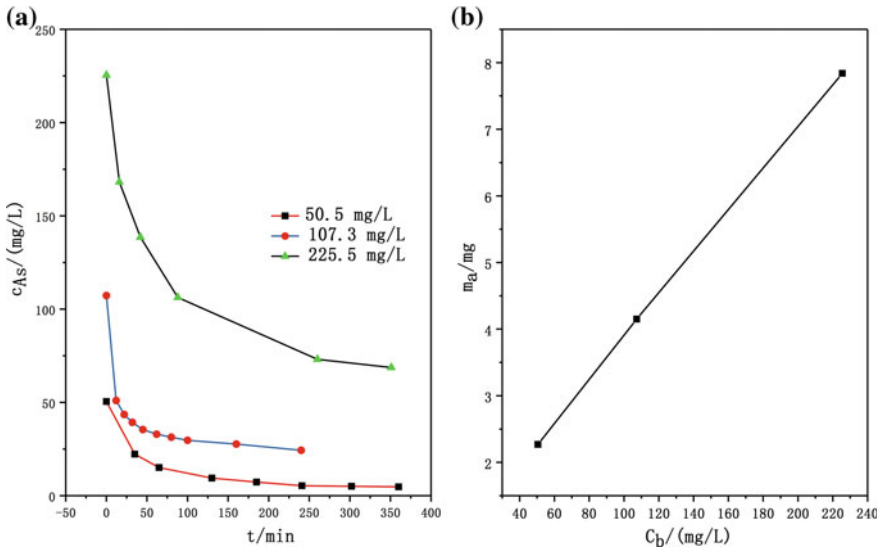

Fig. 5 Effect of initial concentration of arsenic on arsenic removal (**a**), and the relationship between the initial arsenic concentration and arsenic removal amount (**b**). *Note* Reaction temperature is 20 °C, the pH value of the solution is 3.0, reaction time is 4 h, and the concentrations of Ni^{2+} and SO_4^{2-} in the $NiSO_4$ solution are 60 g/L, 100 g/L, respectively

Initial Concentration of Arsenic

The effect of initial concentration of arsenic on arsenic removal is shown in Fig. 5a. It can be seen that the initial arsenic concentration is 225.5, 107.3 and 50.5 mg/L in the $NiSO_4$ solution. As time goes on, the arsenic concentration decreases to a stable level. Within the first hour, the concentration of arsenic decreased rapidly. In the later stage of reaction, the arsenic removal rate of the resin tends to be flat.

Figure 5b shows the relationship between the initial arsenic concentration and arsenic removal amount. It described that the higher initial concentration of arsenic in the $NiSO_4$ solution, the higher concentration of arsenic removed with WO_4^{2-}-loaded D301. When arsenic concentration of the reactants is moderate, resin can reach the highest removal ratio of arsenic.

Considering comprehensively, 100 mg/L is the optimal initial concentration of arsenic in the process of arsenic removal.

Conclusions

(1) By comparing the performance of three arsenic removal reagents (sulfonated kerosene and $N_{235,}$ SO_4^{2-}-loaded D301 resin, WO_4^{2-}-loaded D301 resin), WO_4^{2-}-loaded D301 has the best removal ratio of arsenic in the $NiSO_4$ solution. When the WO_4^{2-}-loaded D301 was used, arsenic can form the arsenotungstic acid with WO_4^{2-} in the resin. The formation of arsenotungstic acid makes arsenic remove thoroughly.
(2) Four conditional experiments are carried out, like pH value of the solution, reaction time, temperature, and initial concentration of arsenic. The results shown that the most significant factors affecting arsenic removal with WO_4^{2-}-loaded D301 are pH value of the solution and reaction time.
(3) The optimum conditions for industrialization are as follows: reaction temperature is 20 °C, reaction time is 4 h, pH value of solution is 3.0, and the initial concentration of arsenic is about 100 mg/L.

Acknowledgements Financial support from the Hunan Natural Science Foundation Project (No. 2019JJ40379), the Opening Project of State Key Laboratory of Nickel and Cobalt Resources Comprehensive Utilization, and the Research Fund Program of State Key Laboratory of Rare Metals Separation and Comprehensive Utilization (No. GK-201805) are gratefully acknowledged.

References

1. Banerji T, Kalawapudi K, Salana S, Vijay R (2019) Review of processes controlling arsenic retention and release in soils and sediments of Bengal basin and suitable iron based technologies for its removal. Groundw Sustain Dev 8:358–367
2. Gu K, Li W, Han J, Liu W, Qin W, Cai L (2019) Arsenic removal from lead-zinc smelter ash by NaOH–H_2O_2 leaching. Sep Purif Technol 209:128–135
3. Nazari A, Radzinski R, Ghahreman A (2017) Review of arsenic metallurgy treatment of arsenical minerals and the immobilization of arsenic. Hydrometallurgy 174:258–281
4. Huang Z, Liu Y, Tao Q, Geng C, He T (2012) Influencing factors of arsenic removal by lime precipitation. J Environ Sci 6(03):734–738
5. Chang F, Qu J, Liu R (2006) Preparation of ferromanganese composite oxides and their adsorptive performance for arsenic removal. J Environ Sci 26(11):1769–1774
6. Liao M, Xie Z, Wang R (1997) Preliminary study on the removal of arsenic from wastewater by bacterial algae. J Environ Pollut Prev 02:38–45
7. Wang R, Luo T (2015) TBP and N235 synergistically extract arsenic from copper electrolyte. Min Metall Eng 35(06):89–92
8. Korngold E, Belayev N, Aronov L (2001) Removal of arsenic from drinking water by anion exchangers. Desalination 141(1):81–84
9. Wang D, He H, Li T, Qi B, Wang S (2015) Electrochemical properties of novel saturated arsenic tungsten heteropoly acid modified electrode. Chin J Mol Sci 31:47–52
10. Li H, Yang J, Li K (2010) Tungsten metallurgy. Central South University Press, Changsha, pp 26–28

11. Zhao Z, Xu X, Chen X, Huo G, Chen A, Liu X, Xu H (2012) Thermodynamics and kinetics of adsorption of molybdenum blue with D301 ion exchange resin. Trans Nonferrous Met Soc China 22(3):686–693
12. An F, Wang Y, Xue X, Hu T, Gao J, Gao B (2018) Design and application of thiourea modified D301 resin for the effective removal of toxic heavy metal ions. Chem Eng Res Des 130:78–86

Activated Carbon Prepared from Bituminous Coal/Poplar Blends by Direct KOH Activation

Xiaohu Zhou, Shengfu Zhang, Yuyang Wei, Xiong Xiao and Weiyi Chen

Abstract Columnar activated carbons (ACs) were prepared from the bituminous coal/poplar blends using KOH as an activation agent by varying the mass ratio (bituminous coal/poplar and KOH/carbon materials). The specific 2D-NLDFT surface area and total pore volume of the prepared ACs are in the range of 436–825 m^2/g and of 0.193–0.360 cm^3/g, respectively. The pore size distribution of ACs shows that most of the pores are in the range from large micropores to small mesopores and their distribution can be controlled by both mass ratios. While the obvious differences in surface morphology between the wood and coal phase, as expected from the intrinsic property of the two materials, were observed from SEM images, the former was irregular, heterogeneous, and highly porous, while the latter showed a smooth and regular surface.

Keywords Bituminous coal · Poplar · Activated carbon · Specific area · Microcrystalline structure

Introduction

As we know, activated carbons have an excellent adsorption capacity because of their internal structure which consists of a large number of interconnecting fine pores [1]. And activated carbon (AC) has been widely used in many separation, purification, and adsorption chemical industries [1, 2]. They are usually made from various carbon materials (such as coal, wood, and other biomass) through physical or chemical activation processes [3, 4]. So the properties of activated carbon are largely determined by the carbon materials and preparation process [5].

Coal and lignocellulosic materials are the major sources for the production of commercial activated carbons. The literature shows that activated carbon made from hard materials with small internal pores, such as anthracite, bituminous coal, and nut shell, is characterized by lots of micropores, small pore openings, long internal

X. Zhou · S. Zhang (✉) · Y. Wei · X. Xiao · W. Chen
College of Materials Science and Engineering, Chongqing University, Chongqing 400044, China
e-mail: zhangsf@cqu.edu.cn

J. Li et al. (eds.), *Characterization of Minerals, Metals, and Materials 2020*,
The Minerals, Metals & Materials Series,
https://doi.org/10.1007/978-3-030-36628-5_19

pores, and highly adsorption potential, which is suitable for gas phase adsorption. And activated carbon prepared from lignite and sawdust with large original internal pores shows more transition pores (mesopore), and the internal pores are short and thick, which is suitable for liquid phase adsorption [6]. At present, because of the large production, abundant reserves, and plentiful microporous structure, coal is widely used as a feedstock for the production of activated carbons. Thus, coal-based activated carbon has been extensively used in flue gas treatment [7, 8]. However, coal is nonrenewable as it is used it is also used up, raising prices, and limiting further increases in productivity. Whereas, in the wood processing nearly twenty percent of the total input mass residues, comprised of sawdust, slabs, off-cuts, shavings, and chips, are usually disposed of either by burning or disposal in landfills [9]. Hence, it is meaningful to prepare activated carbon by combining coal with sawdust, which could both reduce coal resource consumption and maintain reasonable pore structure.

The main objective of this work is to produce promising ACs from bituminous coal and poplar by chemical activation. The 1/3 coking coal and poplar blends were activated using KOH as a chemical activating agent. We concentrated on the evaluation of these different variables: the effect of coal/wood and carbon materials/KOH ratio. The textural characteristics, surface morphology and surface chemical properties of the prepared ACs were also studied in detail.

Experimental

Materials

In this study, 1/3 coking coal and poplar as raw carbon materials, starch as binder, and KOH as activating agent were used to prepare the columnar activated carbon. The two types of raw carbon materials were powdered and sieved to get the powder with the particle size less than 150 μm. The approximate elemental analysis of the two types of raw carbon materials was listed in Table 1.

Preparation of Activated Carbons

A chemical activation method was employed to prepare ACs from 1/3 coking coal and poplar. The raw carbon materials were first dried and then mixed in different proportions (1/3 coking coal to poplar by 1, 3/1, or 3/2). The different mass ratio of activating agent to powdered raw materials (1/2, 1/1, or 3/2) was taken and mixed by dipping. The mixture was heated at 1073 K for 2 h in a horizontal tube furnace under the N_2 atmosphere to remove volatile and activate the samples. The activated carbons were washed out firstly with deionized water, then with 0.5 M HCl, and finally with deionized water again until the pH of the rinse reaches around 7. Subsequently, the

Table 1 Main ingredients of raw materials (%)

Samples	Proximate analysis				Elemental analysis				
	Moisture	Ash	Volatile	Fixed carbon	C	H	O	N	S
1/3coking coal	2.21	11.75	33.64	52.4	78.30	5.25	8.24	0.94	0.15
poplar	6.56	0.64	84.9	7.9	45.95	6.30	41.92	0.18	0.13

Table 2 Experimental design

Entry	CWm-r	M_{coal}/M_{wood}	M_{KOH}/M_{rm}	Temperature (°C)
1	CW10-1	1:0	1:1	800
2	CW31-0.5	3:1	0.5:1	800
3	CW31-1	3:1	1:1	800
4	CW31-1.5	3:1	1.5:1	800
5	CW32-1	3:2	1:1	800

Nomenclature = m-r, where m is mass amount of coal and poplar, r is the ratio of KOH to raw materials

ACs powder, starch, and deionized water were mixed at 353 K, and then columnar coke (∅ 10 mm) was obtained through a vacuum hydraulic extruder. Finally, the columnar AC was carbonized at 523 K for 1 h in N_2 atmosphere to remove the volatile substance of starch. The heating rate of the whole process was 10 K/min.

Five groups of samples, under different conditions, were prepared, and the parameters of each sample are listed in Table 2. Meanwhile, the ACs were named according to the mass ratio of the two types of raw carbon materials and the activating agent.

Characterization of Activated Carbon

Nitrogen adsorption capacity of ACs was measured using Quadrasorb 2MP (Quantachrome, USA) at 77 K. The samples were degassed at 573 K for 15 h under vacuum condition before analysis. The specific surface area, pore size distribution (PSD), and pore volume of the samples were calculated according to the non-local density functional theory (2D-NLDFT) using the nitrogen adsorption isotherm [10, 11]. Raman spectroscopy (Laser Raman Spectrophotometer, NRS5100, JASCO) study was carried out to understand the graphitic planar crystalline size and disordered region of the prepared ACs. The morphology of ACs samples has been observed by SEM (JEOL JSM-7800F FEG SEM) instrument. The SEM images were taken in secondary electrons; the acceleration voltage was equal to 15 kV, and the emission current was 20 pA.

Iodine number is widely used to evaluate the adsorption capacity of activated carbon, higher number indicates higher degree of activation, because of its simplicity and a rapid assessment of activated carbon quality. The iodine number is defined as the amount of iodine adsorbed by 1 g of carbon at the mg level, which indicates the porosity of activated carbon [12]. And in this study, the standard GB/T 7702.7-2008 was adapted.

Results and Discussion

Specific Surface Area and Porosity

The adsorption and desorption studies of nitrogen on ACs were conducted to characterize the prepared ACs. The nitrogen adsorption and desorption isotherm curves of ACs at 77 K are shown in Fig. 1. The nitrogen adsorption isotherms show typical three steps with the increase in relative pressure. The first step is a steeply increasing region at low relative pressures less than 0.02, which stands for the adsorption or condensation in small microspores. Then the adsorption amount slowly increases with relative pressure with notable hysteresis which indicating the existence of mesoporous. Finally, the adsorption amount increases abruptly at near the saturation pressure of nitrogen because of active capillary condensation. The ACs prepared in the study show the compound isotherms of type I and type IV according to the IUPAC classification, which shows that ACs have a large number of microporous and mesoporous structures at the same time.

The pore texture properties, including the specific surface areas, pore volume, and pore distribution, calculated by 2D-NLDFT method are listed in Table 3 and depicted in Fig. 2, respectively. The ACs show a wide range of well-developed pores (approximately from 0.5 to 5 nm) with a narrow peak at a pore width around 0.5–1.5 nm and properly developed small mesoporous in the range of 2–5 nm (Fig. 3). Meanwhile, the effect of the mass ratio of coal/wood and KOH/carbon-precursor could be observed clearly.

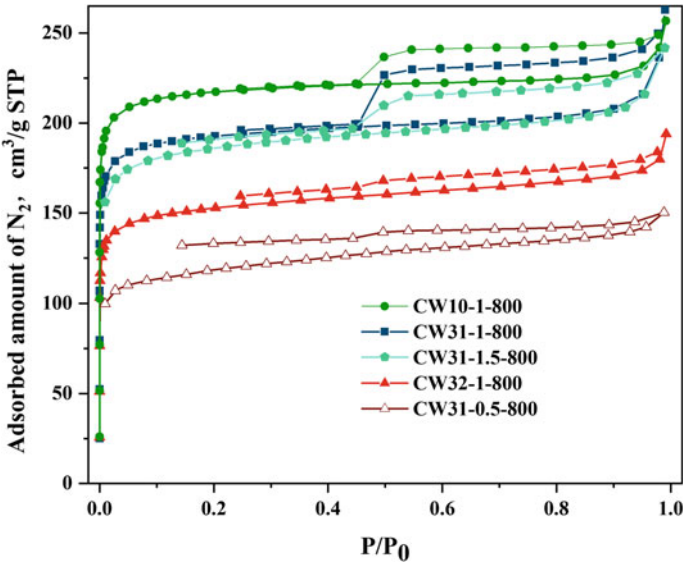

Fig. 1 Nitrogen adsorption/desorption isotherms of ACs at 77 K

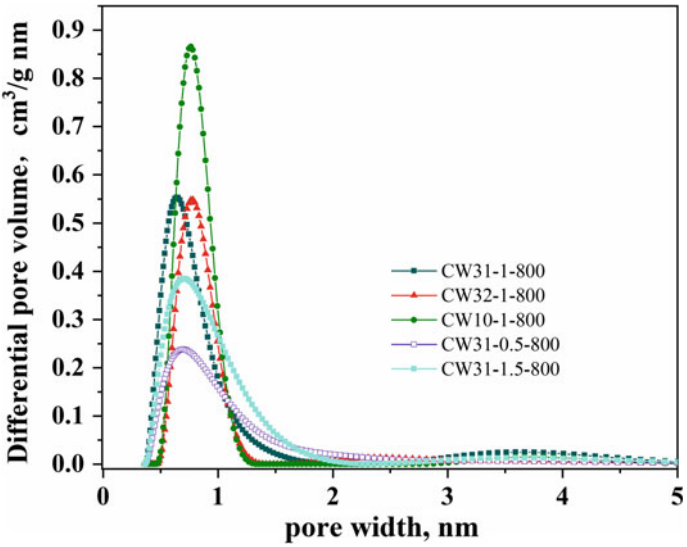

Fig. 2 NL-DFT pore size distribution of ACs

Table 3 Yield and textual properties of the ACs

Samples	Surface area (m^2/g)	Pore volume (cm^3/g)		Yield, %	Iodine number (mg/g)
		Micro	Meso		
CW10-1-800	815	0.312	0.039	68.2	922
CW31-1-800	832	0.277	0.083	52.3	893
CW32-1-800	556	0.214	0.050	42.4	795
CW31-0.5-800	436	0.172	0.021	57.9	383
CW31-1.5-800	683	0.270	0.022	51.2	873

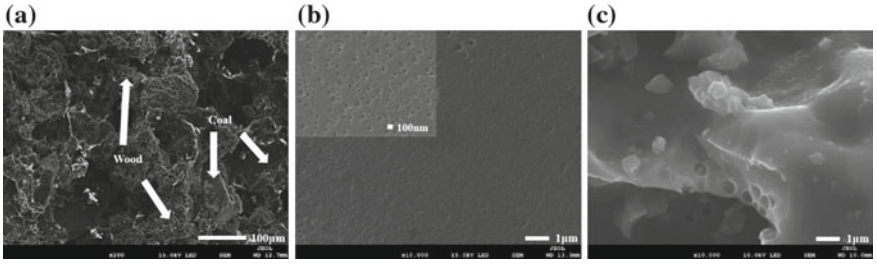

Fig. 3 SEM images of CW31-1. (a) ×200; (b) wood phase in 10,000 times; (c) coal phase in 10,000 times

The mass ratio of carbon to KOH caused some changes in the pore textural properties of the activated carbon. Compared with CW31-0.5-800, CW31-1-800, CW31-1.5-800, the surface areas, and pore volume of activated carbon were 436, 832, 683 m^2/g, and 0.193, 0.36, and 0.292 cm^3/g, respectively. It can be found here that, with the increased mass ratio of KOH to carbon, both parameters increased first and then decreased. The evolution mechanism is, with the increased burn-off, the pore is formed first then the adjacent wall structures between the micropores was collapsed induced the enlargement of the pore diameter [13]. With the increased mass ratio of wood in the carbon-precursor, the micropore volume of the prepared activated carbon shown a decreased trend, which was supported by CW10-1, CW31-1, and CW32-1 (Table 3). These results could be connected to the difference between coal and wood, as stated previously. The activated carbon prepared from coal contains much micropore, while the one from wood shows more mesopore and macropore. And it should be noted here that the specific surface increased slightly first, from 815 to 832 cm^2/g, and then decreased obviously, from to 832 to 556 cm^2/g. This is, to a great extent, caused by the change of pore structure. Even though the micropore volume decreased at a certain extent, from 0.312 to 0.277 m^3/g, while the mesopore volume goes through a rise at a greater extent, from 0.039 to 0.083 m^3/g. However, when the mass ratio of coal to wood come to 3:2, both the micropore and mesopore pore volume show a decreased trend, from 0.277 m^3/g to 0.214 m^3/g and 0.083 m^3/g to 0.050 m^3/g, respectively. This is induced by the augment of pore diameter, as the pore size distribution shown in Fig. 3, due to the higher relative content of wood decreased the content of fixed carbon so the mass ratio of KOH to fixed carbon was increased during the activation process in another form. What is more, the yield of carbon-precursor also decreased with the increase of wood because of the low fixed carbon content of wood.

The iodine number of activated carbon prepared at different conditions was also illustrated in Table 3. And there were good correlation between the iodine number and micropore volume, as described in the literature [14], due to the adsorption of iodine manly take place in the micropore. In this study, CW31-1 have the highest specific surface area, 832 m^2/g to be exact, and CW10-1 have the highest yield, namely 68.2%, at the same time, the iodine number and specific surface area were also high, that was 922 mg/g and 815 m^2/g, respectively. So CW10-1 has the best comprehensive performance. However, for the purpose of utilizing saw dust resource and save high-quality coal resource, the CW31-1 was chosen as the optimum activated carbon in this work.

SEM

The surface morphology of CW31-1 was recorded and shown in Fig. 3. As can be observed, there are obvious difference between the coal phase and wood phase. The wood phase shows an irregular, heterogeneous, and highly porous surface. And it should be noted here that many mesopore could be observed on the wood surface

(Fig. 3b). However, the coal phase has a distinctly different surface morphology (Fig. 3c), which is still granular, without any of the porosity. This difference reveals that the pore structure of activated carbon is greatly influenced by the properties of raw materials. The fixed carbon content of wood is about 10%. Therefore, the wood phase has a loose pore structure with more mesoporous and macroporous. On the contrary, the fixed carbon content of coal, especially bituminous and anthracite is high, which is associated with dense aromatic ring structure. And the pore structure is a slit between graphite microcrystalline lamellae, so it is generally a microporous.

Raman Spectra Analysis

Raman spectroscopy is a conventional non-destructive structural analysis method, which is often used to analyze the fine structure of diamond, graphite, carbon nanotubes, coke, and other materials [15, 16]. The Raman spectra of the activated carbon are shown in Fig. 4. The ACs represent two main broad peaks (G and D). The G band located at 1576.1 cm^{-1} suggests the presence of graphitic crystalline structure which corresponds to the stretching vibration of the sp2 carbon atoms in the aromatic hexagonal sheet. The Raman shift at 1250–1450 cm^{-1}, peak D (generally termed disorder band), refers to dual resonance Raman scattering mode, mainly reflecting information on defects in lattice structures and vacancies in aromatic ring lamellae [17, 18]. Therefore, the value of ID/IG is often used to characterize the ordering degree of carbon materials. At the same time, the characteristic size of microchip layer (La) can be calculated by Tuinstra-Koenig (TK) formula.

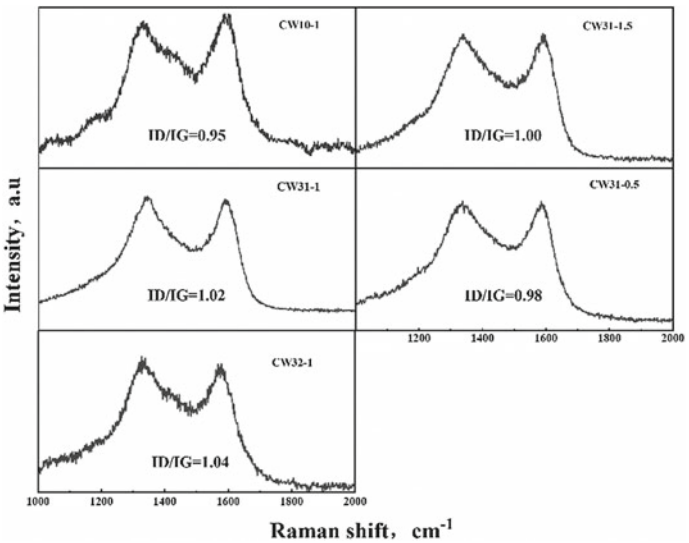

Fig. 4 Raman spectra of activated carbon

Table 4 Raman test results

Carbons	G band (cm^{-1})	Intensity (I_G)	D band (cm^{-1})	Intensity (I_D)	Aromatic sheet diameter La (nm)	I_D/I_G
CW10-1	1585	1635	1329	1559	4.63	0.95
CW31-1.5	1590	1290	1340	1329	4.27	1.03
CW31-1	1587	1622	1342	1660	4.31	1.02
CW31-0.5	1585	1635	1333	1604	4.49	0.98
CW32-1	1577	848	1326	884	4.23	1.04

$$\frac{\mathrm{I(D)}}{\mathrm{I(G)}} = (C(\lambda))/\mathrm{La}$$

$$\mathrm{C}(\lambda) = 2.4 \times 10^{-10} * \lambda^4$$

λ The Raman excitation wavelength
La Aromatic sheet diameter.

In this study, the intensity ratios (ID/IG) for ACs are in the ranges of 0.95–1.04 as given in Table 4. With the increased of the mass ratio of poplar to coal, the value of I_D/I_G was also increased, which means the rise of the disordered regions in the graphitic cluster. And this phenomenon may be relevant to the size of graphitic crystalline structure from lignocellulose is smaller and has more edges. Meanwhile, the higher mass ratio of KOH to material also lead to the growth of the disordered regions in the graphitic cluster, which could attributed to the ablative intensity increased. It has reported that some defective area may be the activity adsorption site for some molecule, such as the sulfur dioxide [19]. Therefore, it is helpful, to a certain extent, to improve the adsorption performance for some matters by increase the disordered regions in the graphitic cluster.

Conclusions

In this study, an activated carbon was prepared from 1/3 coking coal and poplar, using KOH as a chemical agent. The effect of the mass ratio of coal/wood and KOH/carbon-precursor on the properties of activated carbons were examined. Adsorption/desorption of N_2, SEM, Raman were applied to characterize the texture, morphology, and microcrystalline structure. The activated carbons were predominantly microporous adsorbents. With the increased of the mass ratio of poplar to 1/3 coking coal, the volume of micropore was decreased. This phenomenon could attribute to the structural difference between the coal and wood phase in AC, which was evaluated by SEM. The wood phase is loosely structured and a large number

of mesoporous and macropore structures can be observed, while the coal phase is densely structured. Based on the results, it is suggested the activated carbon with excellent properties could be manufactured using the mixture of bituminous coal and poplar under appropriate conditions, which could be used for flue gas treatment, requiring abundant microstructure.

Acknowledgements This work was supported by the Natural Science Foundation of China (Project 51774061) and the Fundamental Research Funds for the Central Universities (Project No.06112017CDJQJ138801).

References

1. Zondlo JW, Velez MR (2007) Development of surface area and pore structure for activation of anthracite coal. Fuel Process Technol 88(4):369–374
2. Dias JM, Alvimferraz MC, Almeida MF et al (2007) Waste materials for activated carbon preparation and its use in aqueous-phase treatment: a review. J Environ Manage 85(4):833–846
3. Ahmadpour A, Do DD (1996) The preparation of active carbons from coal by chemical and physical activation. Carbon 34(4):471–479
4. Yan L, Sorial GA (2011) Chemical activation of bituminous coal for hampering oligomerization of organic contaminants. J Hazard Mater 197(none):311–319
5. Wang J, Kaskel S (2012) KOH activation of carbon-based materials for energy storage. J Mater Chem 22(45):23710–23725
6. Guo MK, Xie ZL, Ye ZH et al (2017) Adsorption technology by activated carbon & its application in environment engineering, 2nd edn. Chemistry Industry Press, Beijing
7. Yang L, Jiang X, Jiang W et al (2017) Cyclic regeneration of pyrolusite-modified activated coke by blending method for flue gas desulfurization. Energy Fuels 31(4):4556–4564
8. Lin Y, Li Y, Xu Z et al (2018) Transformation of functional groups in the reduction of NO with NH_3 over nitrogen-enriched activated carbons. Fuel 223(none):312–323
9. Puziy AM, Poddubnaya OI, Martínez-Alonso Amelia (2007) Oxygen and phosphorus enriched carbons from lignocellulosic material. Carbon 45(10):1941–1950
10. Puziy AM, Poddubnaya OI, Gawdzik B et al (2016) Comparison of heterogeneous pore models QSDFT and 2D-NLDFT and computer programs ASIQwin and saieus for calculation of pore size distribution. Adsorption 22(4–6):459–464
11. Jagiello J, Olivier JP (2013) 2D-NLDFT adsorption models for carbon slit-shaped pores with surface energetical heterogeneity and geometrical corrugation. Carbon 55(Complete):70–80
12. ASTM (2006) Standard test method for determination of iodine number of activated carbon. ASTM Committee on Standards, ASTM D 4607-94, ASTM, Philadelphia, PA, USA
13. Foo KY, Hameed BH (2012) Potential of jackfruit peel as precursor for activated carbon prepared by microwave induced NaOH activation. Bioresour Technol 112(none):143–150
14. Ceyhan AA (2013) Surface and porous characterization of activated carbon prepared from pyrolysis of biomass by two-stage procedure at low activation temperature and it's the adsorption of iodine. J Anal Appl Pyrol 104:378–383
15. Tuinstra F, Koenig JL (1970) Raman spectrum of graphite. J Chem Phys 53(3):1126–1130
16. Mallet-Ladeira Philippe (2014) A Raman study to obtain crystallite size of carbon materials: a better alternative to the Tuinstra-Koenig law. Carbon 80:629–639
17. Mallet-Ladeira P, Puech P, Weisbecker P et al (2014) Behavior of Raman D band for pyrocarbons with crystallite size in the 2–5 nm range. Appl Phys A 114(3):759–763

18. Wang J, Kaskel S (2012) KOH activation of carbon-based materials for energy storage. Mater Chem 22(45):23710–23725
19. Jiang WJ (2003) Study on the desulfurization characteristics of activated carbon modified by microwave. Sichuan University

Preparation of Thermal Insulation Materials from Ferronickel Slag with Addition of Fly Ash Cenosphere

Lei Yang, Zhiwei Peng, Yawen Huang, Liancheng Wang, Leixia Zheng, Mingjun Rao, Guanghui Li and Tao Jiang

Abstract Ferronickel slag is the fourth largest industrial waste in China, in urgent need of efficient treatment. In this study, a facile route for preparing thermal insulation materials from ferronickel slag with the addition of fly ash cenosphere (FAC) was developed based on thermodynamic calculation and experimental exploration. The experimental results showed that a high-quality insulation material with thermal conductivity of 0.4752 W/(m K), bulk density of 1.36 g/cm^3, compressive strength of 49.13 MPa, water absorption of 16%, and linear shrinkage of 14.7% could be obtained when the ferronickel slag was sintered with the addition of 25 wt % FAC at 1200 °C for 2 h. The method is expected to provide a useful guide for value-added treatment of ferronickel slag.

Keywords Ferronickel slag · Fly ash cenosphere · Phase transformation · Thermal conductivity

Introduction

The rapid development of metallurgical industry has led to a large number of industrial solid wastes. Ferronickel slag is currently the fourth largest industrial waste in China, which poses a serious threat to the ecosystem [1]. In view of the physicochemical characteristics of ferronickel slag, many studies and industrial practices have been carried out. Up to now, the total generation of ferronickel slag is more

L. Yang · Z. Peng (✉) · L. Wang · L. Zheng · M. Rao · G. Li · T. Jiang
School of Minerals Processing and Bioengineering, Changsha, Hunan 410083, China
e-mail: zwpeng@csu.edu.cn

National Engineering Laboratory for High Efficiency Recovery of Refractory Nonferrous Metals, Changsha, Hunan 410083, China

Y. Huang
State Key Laboratory Cultivation Base for Nonmetal Composites and Functional Materials, Mianyang, Sichuan 621010, China

School of Materials Science and Engineering, Southwest University of Science and Technology, Mianyang, Sichuan 621010, China

J. Li et al. (eds.), *Characterization of Minerals, Metals, and Materials 2020*,
The Minerals, Metals & Materials Series,
https://doi.org/10.1007/978-3-030-36628-5_20

than 0.2 billion tons in China, among which only 8% is utilized for producing building materials [2–7], geopolymer [8, –10], concrete [11], and for recovering valuable metals [12, 13]. Its use in producing building and refractory materials had good mechanical and thermal properties which can meet the general production requirements [14]. In particular, its application in the preparation of refractory materials was mainly attributed to the conversion of the olivine phase in the slag to high melting point phases after sintering, including forsterite and various spinels [15]. As forsterite and spinels are also components with low thermal conductivity, ferronickel slag may be used as a material for producing high-quality thermal insulation materials if its density can be further reduced.

Fly ash cenosphere (FAC) is the by-product of coal-fired power plants and is formed by melting, pelletizing, and condensation of ash in pulverized coal in the high temperature flame. Improper disposal of FAC leads to environmental problems. Because FAC is constituted by a number of hollow glassy microspheres with density less than 1.0 g/cm^3 [16], it is widely used as pore former. For the same reason, its combined use with ferronickel slag may contribute to a very low thermal conductivity of the resulting material [17, 18].

In the present study, the feasibility of preparing insulation materials from ferronickel slag in the presence of FAC by sintering was assessed based on the thermodynamic analysis and experimental exploration. The findings are expected to provide a novel and economic guide for utilization of both wastes.

Experimental

Materials

The main raw materials were ferronickel slag and FAC. The ferronickel slag sample was obtained from a ferronickel smelting plant. The X-ray diffraction (XRD) pattern of ferronickel slag (Fig. 1a) shows that the olivine was its main phase component. The XRD pattern of FAC (Fig. 1b) shows that it was mainly composed of mullite and quartz. For preparing the thermal insulation materials through briquetting, an organic binder, sodium carboxymethyl cellulose (CMC), was also used.

Experimental Procedure

According to the chemical compositions of ferronickel slag and FAC, the addition of FAC was varied from 15 to 35 wt %. Initially, the grounded ferronickel slag (particles passing 74 μm sieve) and FAC (particles passing 74 μm sieve) were mixed in a planetary ball mill for 30 min. It was then used for producing briquettes of 20 mm in diameter and 15 mm in height by uniaxial pressing at 6 MPa with addition

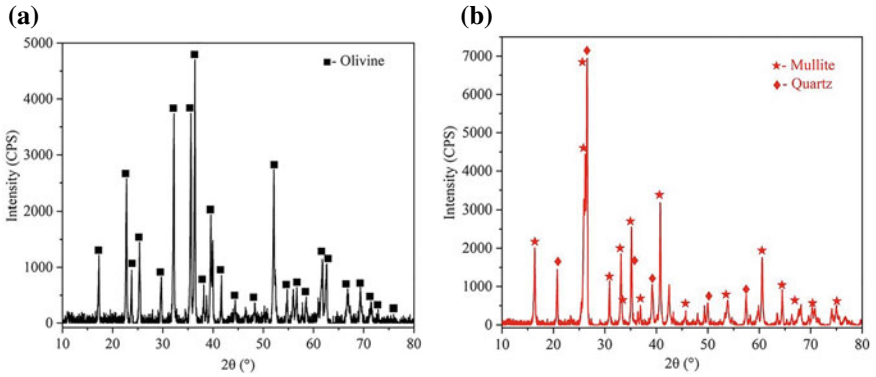

Fig. 1 XRD patterns of **a** ferronickel slag and **b** FAC

of 0.5 wt % CMC (0.6 g/cm^3) as the binder. The briquettes were then dried in a vacuum drying oven at 105 °C for 3 h. After drying, the briquettes were placed in a muffle furnace for sintering at designated temperatures for given periods of time. The sintered briquettes were cooled to room temperature as thermal insulation materials for subsequent characterization tests.

Characterizations

The phase constituents of the samples were identified using an X-ray diffraction spectrometer (XRD, D/max 2550PC, Japan Rigaku Co., Ltd). The morphological changes of the sintered samples were characterized using an electron scanning electron microscope (SEM; FEI QUANTA 200; FEI, Eindhoven, The Netherlands) equipped with an EDAX energy dispersive X-ray spectroscopy (EDS) detector (EDAX Inc., Mahwah, NJ, USA). The values of thermal conductivity of the samples were determined using a thermal constant analyzer (Hot Disk TPS2500S, Sweden). The values of bulk density, linear shrinkage, water absorption, and compressive strength of the insulation materials were measured according to the Chinese National Standard Test Methods (GBT 1966-1996, GBT 5998-2007 and GBT 5072-2008).

Result and Discussion

Thermodynamic Analysis

Theoretically, the effect of FAC addition on the preparation of thermal insulation materials from ferronickel slag can be predicted by the variations of contents of thermodynamic equilibrium phases of the slag in the presence of FAC at high temperature (e.g., 1200 °C), as shown by the ternary phase diagram of MgO–SiO_2–Al_2O_3 system in Fig. 2, which was calculated by the software FactSage 7.0. The main components of the ferronickel slag were SiO_2 and MgO, whose reactions produce relatively high melting point phases with low thermal conductivity, such as enstatite, cordierite, sapphirine, and cristobalite. The shaded area in Fig. 2 shows the potential phase transformation in the presence of FAC. The green point in Fig. 2 indicates the composition of ferronickel slag, and the dotted arrow indicates the possibility of altering its chemical composition by FAC addition. The phase diagram reveals that the primary phases (Mg_2SiO_3, Mg_2SiO_4, and $Mg_2Al_4Si_5O_{18}$) are transformed into the new phases (Mg_2SiO_3, $Mg_2Al_4Si_5O_{18}$, and SiO_2) because of the addition of FAC (15–35 wt %). The amount of each phase produced can also be calculated by FactSage 7.0 (Fig. 3) when the ferronickel slag system was added with FAC at 1200 °C. The enstatite decreased gradually, but the cordierite and cristobalite increased simultaneously because increasing SiO_2 and Al_2O_3 in the system will induce a few chemical reactions which produce new phases. It is obvious that the phase composition of the ferronickel slag can be changed by adding FAC. The main reactions can be given as follows:

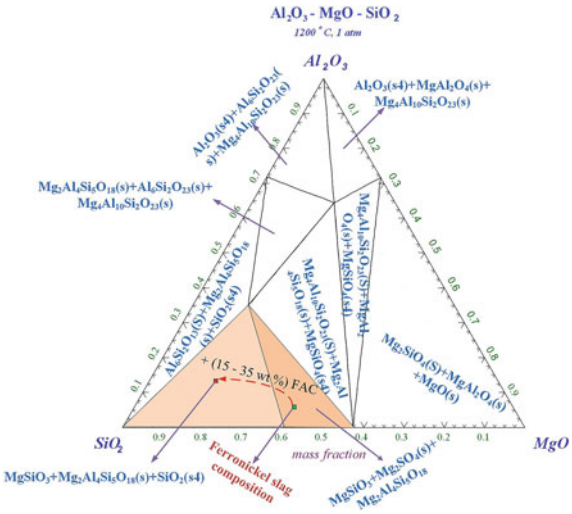

Fig. 2 Phase diagram of the MgO–SiO_2–Al_2O_3 system

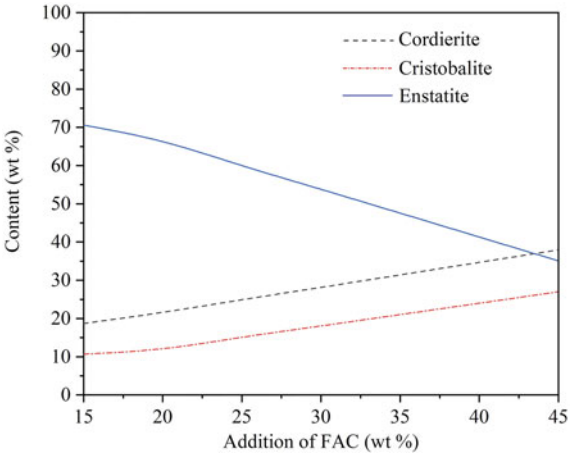

Fig. 3 Calculated contents of thermodynamic equilibrium phases in the ferronickel slag system with addition of FAC at 1200 °C

$$2[(Mg \cdot Fe)O \cdot SiO_2] + 3/2O_2 = 2MgO \cdot SiO_2 + Fe_2O_3 + SiO_2 \quad (1)$$

$$2MgO \cdot SiO_2 + SiO_2 = 2(MgO \cdot SiO_2) \quad (2)$$

$$MgO \cdot SiO_2 + MgO = 2MgO \cdot SiO_2 \quad (3)$$

$$14MgO + 2Al_2O_3 + 17SiO_2 = Mg_2Al_4Si_5O_{18} + 12MgSiO_3 \quad (4)$$

X-Ray Diffraction Analysis

According to the ternary phase diagram of $MgO–SiO_2–Al_2O_3$, with the addition of FAC between 15 and 35 wt %, the main phases of the product after sintering are enstatite, cordierite, and cristobalite. The contents of cordierite and cristobalite gradually increase with increasing addition of FAC, but the content of enstatite decreases gradually. The phase composition was consistent with the XRD patterns shown in Fig. 4, which shows the main phases were enstatite, cordierite, and cristobalite. The content of enstatite decreased gradually, while those of cordierite and cristobalite increased. Figure 5 shows the conversions of olivine and mullite, and quartz to enstatite (relatively high bulk density and high refractoriness), cordierite (low thermal conductivity and good corrosion resistance), and cristobalite (low thermal conductivity), contributing to the high quality of the resulting insulation materials.

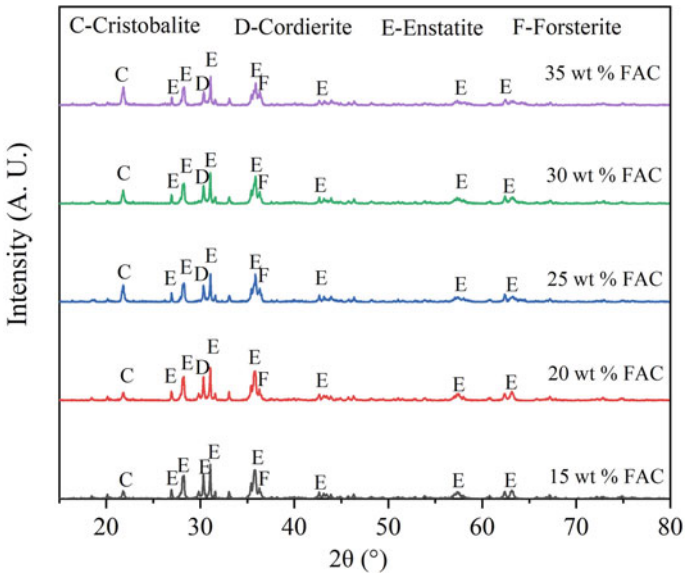

Fig. 4 XRD patterns of thermal insulation materials obtained by sintering with different additions of FAC at 1200 °C for 3 h

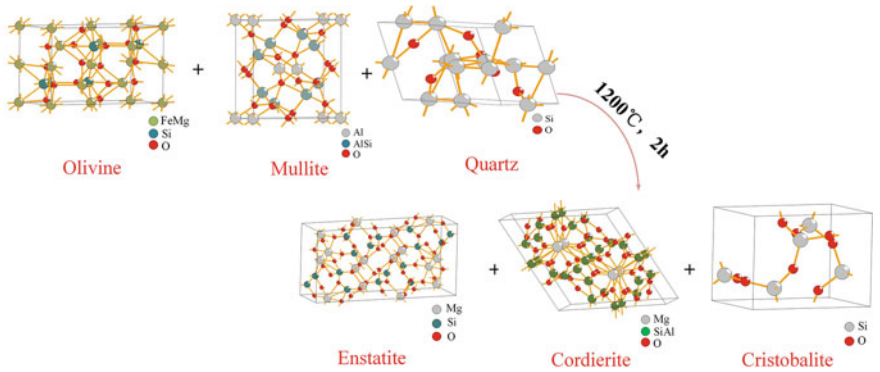

Fig. 5 Phase transformations during preparation of thermal insulation materials obtaining by sintering with addition of FAC

Properties of the Insulating Refractory Materials

The effect of FAC addition on the properties of the thermal insulation material was investigated when the slag was sintered with variable additions of FAC at 1200 °C for 2 h. As shown in Fig. 6, in the presence of 15 wt % FAC, forsterite and enstatite remained as the dominant phases, producing a thermal insulation material with relatively high thermal conductivity and low compressive strength. In the addition range

of 15–25 wt % FAC, the amounts of cordierite and cristobalite increased continuously, causing lower thermal conductivity and higher compressive strength of the thermal insulation material. In particular, with the addition of 25 wt % FAC, the thermal conductivity and compressive strength were 0.4752 W/(m K) and 49.13 MPa, respectively. When the addition of FAC increased to 35 wt %, the cristobalite and cordierite phases increased gradually, reducing compressive strength.

The effect of FAC addition on the bulk density of the insulation material was also evaluated under the same sintering conditions, as shown in Fig. 6. When the FAC addition increased from 15 to 25 wt %, the bulk density of thermal insulation material decreased from 1.67 to 1.36 g/cm^3. As the FAC addition was further increased, the bulk density of thermal insulation material decreased slowly. Obviously, the changes were closely associated with the phase transformations of the sample during sintering. Figure 7 shows the effect of FAC addition on the linear shrinkage and water absorption of thermal insulation material. It is obvious that they had opposite changing tendencies to that of bulk density.

According to the Chinese National Refractory Material Production Standard (GBT 2275-2007), a qualified thermal insulation material must meet the standard as follows: thermal conductivity less than 1.0 W/(m K), the bulk density must less than 1.5 g/cm^3, and the compressive strength higher than 1.0 MPa. Evidently, a good thermal insulation material with thermal conductivity of 0.4752 W/(m K), bulk density of 1.36 g/cm^3, water absorption of 16%, linear shrinkage of 14.7%, and compressive strength of 49.13 MPa was obtained when the ferronickel slag was sintered with addition of 25 wt % FAC at 1200 °C for 2 h. The insulation material is also superior

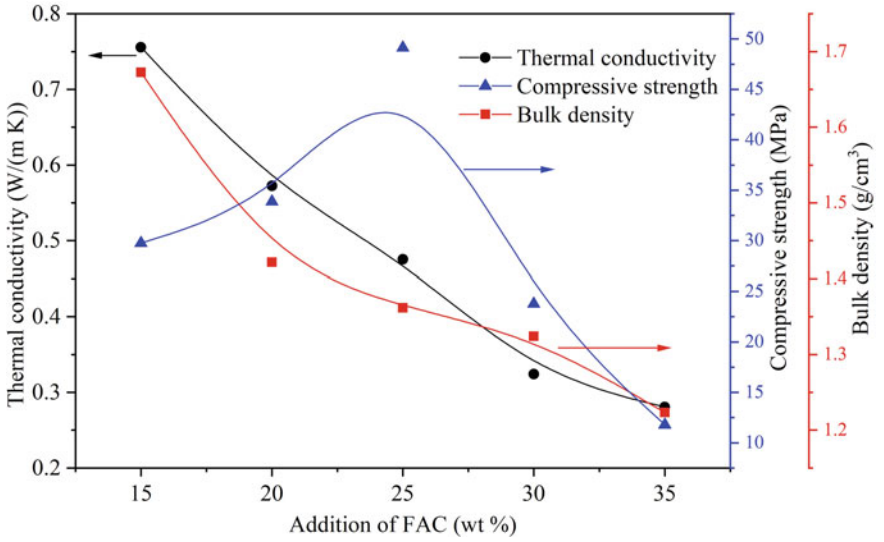

Fig. 6 Effect of FAC addition on the thermal conductivity, compressive strength, and bulk density

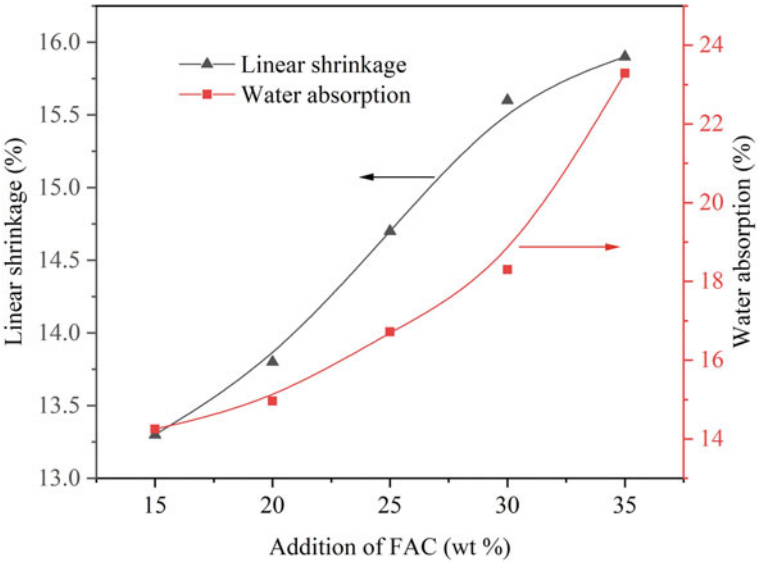

Fig. 7 Effect of FAC addition on the linear shrinkage and water absorption of thermal insulation material

to commercial counterparts because of its higher compressive strength and other improved properties.

Conclusions

The feasibility of a facile route for preparing thermal insulation materials from ferronickel slag with addition of FAC was examined from both thermodynamic and experimental perspectives. The thermodynamic equilibrium phases in ferronickel slag with addition of FAC at 1200 °C were determined. The X-ray diffraction patterns revealed that the main phases of the sintered product were enstatite, cordierite, and cristobalite, which contributed to superior properties (e.g., low thermal conductivity and high compressive strength) of the resulting thermal insulation material. The experimental results showed that under the conditions of addition of 25 wt % FAC, sintering temperature of 1200 °C, and sintering time of 2 h, a good insulation material with thermal conductivity of 0.345 W/(m K), bulk density of 1.36 g/cm^3, water absorption of 16%, linear shrinkage of 14.7%, and compressive strength of 49.13 MPa could be obtained.

Acknowledgements This work was partially supported by the National Natural Science Foundation of China under Grants 51774337, 51504297, and 51811530108, the Science and Technology Planning Project of Hunan Province, China, under Grant 2019RS2008, the Project of State Key Laboratory Cultivation Base for Nonmetal Composites and Functional Materials under Grant 17kffk11,

and the Fundamental Research Funds for the Central Universities of Central South University under Grants 2019zzts706.

References

1. Tiwari A, Singh S, Nagar R (2016) Feasibility assessment for partial replacement of fine aggregate to attain cleaner production perspective in concrete: a review. J Clean Prod 135:490–507
2. Owolabi OB, Adeosun SO, Aduloju SC, Metu CS, Onyedum O (2016) Review on novel application of slag fluxes and salts in metallurgical industry. Am J Chem Mater Sci 3(1):1–5
3. Katsiotis NS, Tsakiridis PE, Velissariou D, Katsiotis MS, Alhassan SM, Beazi M (2015) Utilization of ferronickel slag as additive in Portland cement: a hydration leaching study. Waste Biomass Valori 6(2):177–189
4. Saha AK, Sarker PK (2016) Expansion due to alkali-silica reaction of ferronickel slag fine aggregate in OPC and blended cement mortars. Constr Build Mater 123:135–142
5. Rahman MA, Sarker PK, Shaikh FUA, Saha AK (2017) Soundness and compressive strength of Portland cement blended with ground granulated ferronickel slag. Constr Build Mater 140:194–202
6. Wang Z, Ni W, Jia Y, Zhu LP, Huang XY (2010) Crystallization behavior of glass ceramics prepared from the mixture of nickel slag, blast furnace slag and quartz sand. J Non-Cryst Solids 356(31–32):1554–1558
7. Lemonis N, Tsakiridis PE, Katsiotis NS, Antiohos S, Papageorgiou D, Katsiotis MS, Beazi-Katsioti M (2015) Hydration study of ternary blended cements containing ferronickel slag and natural pozzolan. Constr Build Mater 81:130–139
8. Yang T, Yao X, Zhang X (2014) Geopolymer prepared with high-magnesium nickel slag: characterization of properties and microstructure. Constr Build Mater 59:188–194
9. Aba M, Sakoi Y, Shoya M, Tsukinaga Y, Nagataki S (2010) Properties of concrete incorporating ferronickel slag as coarse aggregates. Concr Res Technol 21(3):63–75
10. Zhang Z, Zhu Y, Yang T, Li L, Zhu H, Wang H (2017) Conversion of local industrial wastes into greener cement through geopolymer technology: a case study of high-magnesium nickel slag. J Clean Prod 141:463–471
11. Li B, Huo B, Cao R, Wang S, Zhang Y (2019) Sulfate resistance of steam cured ferronickel slag blended cement mortar. Cem Concrete Comp 96:204–211
12. Ettler V, Kvapil J, Šebek O, Johan Z, Mihaljevič M, Ratié G, Quantin C (2016) Leaching behaviour of slag and fly ash from laterite nickel ore smelting (Niquelândia, Brazil). Appl Geochem 64:118–127
13. Shen H, Forssberg E (2003) An overview of recovery of metals from slags. Waste Manage 23(10):933–949
14. Sakkas K, Nomikos P, Sofianos A, Panias D (2014) Utilisation of FeNi-slag for the production of inorganic polymeric materials for construction or for passive fire protection. Waste Biomass Valori 5(3):403–410
15. Peng Z, Tang H, Augustine R, Lee J, TianW Chen Y, Jiang T (2019) From ferronickel slag to value-added refractory materials: a microwave sintering strategy. Resour Conserv Recy 149:521–531
16. Ghosal S, Self SA (1995) Particle size-density relation and cenosphere content of coal fly ash. Fuel 74(4):522–529

17. Deepthi MV, Sharma M, Sailaja RRN, Anantha P, Sampathkumaran P, Seetharamu S (2010) Mechanical and thermal characteristics of high density polyethylene–fly ash cenospheres composites. Master Des 31(4):2051–2060
18. Sukkae R, Suebthawilkul S, Cherdhirunkorn B (2018) Utilization of coal fly ash as a raw material for refractory production. J Met Mater Miner 28(1):116–123

Leaching of Copper, Cobalt, and Nickel from Complex Ore

Yotamu R. S. Hara, Golden Kaluba, Douglas Musowoya, Kennedy Chikontwe, Choolwe Muchindu, Haggai Simfukwe, Tina Phiri Chanda and Stephen Parirenyatwa

Abstract The paper focuses on leaching of complex copper–cobalt–nickel ore from Mwinilunga district in Zambia, containing 0.6% Cu, 0.21% Co, 2.6% Fe, and 0.13% Ni. Mineralogical examination of the ore using scanning electron microscope (SEM) showed that copper, cobalt, and nickel exist in fine particles of heterogenite and limonite mineral phases. The effects of leaching temperature, pH, and sodium metabisulphate (SMBS) addition were studied. The optimal conditions were found as follows: leaching temperature of 65–75 °C, leaching time of 1 h, and SMBS addition at 0.6 wt%. Copper, cobalt, and nickel were recovered from the leach solution via precipitation with sodium sulphide and magnesium oxide. Sodium sulphide was more selective than magnesium oxide.

Keywords Heterogenite · Copper · Cobalt · Nickel and leaching

Introduction

Copper, cobalt, and nickel have wider applications [1–3]. Worldwide demand for these metallic components is increasing with the rising demand for high temperature applications, digital devices, and built environment and increasing focus on decarbonisation of the global economy [1–3]. Nickel and cobalt are used for production of high temperature super alloys. Nickel is used in batteries, including rechargeable nickel–cadmium batteries and nickel–metal hydride batteries used in hybrid vehicles [4]. On the other hand, cobalt is used for making strong magnets, energy storage devices, e.g. lithium–cobalt oxide batteries [5, 6].

The copper–cobalt ore deposits in Mwinilunga district of the North Western province of Zambia contain nickel in the range of 0.05–0.3 wt%. Owing to the high demand for nickel, it is important to recover it alongside copper and cobalt.

Y. R. S. Hara (✉) · G. Kaluba · D. Musowoya · K. Chikontwe · C. Muchindu · H. Simfukwe · T. P. Chanda · S. Parirenyatwa
The Copperbelt University, P.O. Box 21692 Kitwe, Zambia
e-mail: yotamuhara@gmail.com

J. Li et al. (eds.), *Characterization of Minerals, Metals, and Materials 2020*,
The Minerals, Metals & Materials Series,
https://doi.org/10.1007/978-3-030-36628-5_21

The common method of treating low grade oxide ores is via leaching in which the base metal(s) is selectively dissolved in acidic media [7]. The dissolution of the base metal requires that the matrix of host phase is broken during leaching. For example, leaching of copper and cobalt which is chemically combined with nickel, iron, manganese, will lead to dissolution of all these elements in solution. Copper and cobalt are chemically combined with nickel, manganese, aluminium, and silica, in the Mwinilunga deposits. Therefore, two problems might be encountered during hydrometallurgical treatment of this ore:

i. High acid consumption owing to dissolution of other elements (Ni, Fe, Mn, Al, and Mg) which are chemically combined with copper and cobalt.
ii. Produces a contaminated leach solution due to the presence of other dissolved elements.

Recovery of Cu, Co, and Ni from Leach Solution

Precipitation is the cheapest method of recovering copper, cobalt, and nickel from the leach solution. At commercial scale, selective precipitation is achieved by controlling pH as the respective compounds precipitate out at different pH values. The common reagents which are used to precipitate out copper, cobalt, and nickel are alkaline salts (MgO, CaO, NaOH, Na_2CO_3) [1, 2]. In essence, iron is first removed from the leach solution as it precipitates out at a lower pH than copper, cobalt, and nickel, and hence, it could contaminate these elements. Nonetheless, some cobalt is lost out as it co-precipitates with iron [8]. In addition to loss of cobalt via co-precipitation with iron, more serious problems might be encountered when the leach solution contains aluminium and magnesium sulphate, such as (i) high consumption of alkaline salts and, (ii) contamination of copper precipitate with aluminium as they precipitate in the similar pH range.

Precipitation with Sodium Sulphide

Sodium sulphate (Na_2SO_4) is more stable than copper, cobalt, nickel, and iron sulphates. On the other hand, copper, cobalt, nickel, and iron sulphides are more stable than sodium sulphide (Na_2S). This means that when sodium sulphide is reacted with copper, cobalt, nickel, and iron sulphates, an exchange reaction will occur as represented by Eq. 1 where M represents Cu, Co, Ni, Fe, etc.

$$MSO_4 + Na_2S = MS + Na_2SO_4 \tag{1}$$

The plot of Gibbs free energy changes against temperature for the precipitation of Cu, Co, Ni, Fe, and Mn with sodium sulphide via Eq. 1 shown in Fig. 1. One

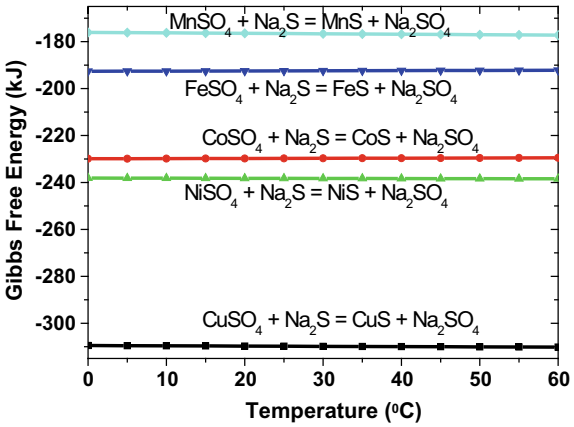

Fig. 1 Plot of Gibbs free energy against temperature for the precipitation of Cu, Co, Ni, Fe, and Mn with sodium sulphide [9]

important feature which can be observed from Fig. 1 is that selective precipitation can be achieved owing to the difference in the stability of the respective sulphides. The following observations can be made from Fig. 1:

1. There is a wide window between the precipitation of CuS and NiS, and hence, the former can be selectively precipitated.
2. There is a narrow window between the precipitation of CoS and NiS such that a mixture of CoS and NiS can be obtained during precipitation.
3. There is a wide window between the precipitation of CoS and FeS such that it is possible to selectively precipitate out CuS, CoS, and NiS, and hence, the former can easily be selectively precipitated.

There are no studies that have been carried out on Mwinilunga copper–cobalt ore, and hence, this paper focuses on processing of this ore.

Experimental Procedure

The sample was collected from Mwinilunga district of the North Western province of Zambia. The as-received sample was crushed in a laboratory jaw crusher and ground down to particle size of less than 150 μm. The full analysis of the sample is shown in Table 1 from which it can be observed that the sample contains 0.57 wt% copper,

Table 1 Analysis of the as-received sample

Cu	Co	Fe	Mn	Ni	Ca	Si	Mg	Al	F
0.57	0.20	2.41	0.42	0.13	1.39	23.48	14.94	4.99	0.89

0.2 wt% cobalt, and 0.13 wt% nickel. It is worth noting that no studies have been conducted on such material.

Leaching Experiments

A representative portion of the sample was collected and placed in a Pyrex glass. The weight of the sample in each experiment was 500 g. All samples were leached at 33% solids. The following parameters were varied during experiments in order to study their effects: temperature, pH, and quantities of sodium metabisulphite (SMBS). SMBS was added in powder form after the experiment had reached the set pH. A constant pH of the solution was maintained throughout the experiment.

Precipitation of Copper, Cobalt, and Nickel

Copper, cobalt, and iron were precipitated with magnesium oxide or sodium sulphide (Na_2S). Both magnesium oxide and sodium sulphide were added in slurry form at strength of 10% in order to minimise localised precipitation. The precipitation of copper, cobalt, and nickel hydroxide is dependent on pH, and hence, these experiments were carried out at fixed pH for a period of 1.5 h. Precipitation of copper was carried out at pH of 5.5, whereas cobalt and nickel were precipitated at pH of 8.5. Iron has a tendency of precipitating alongside cobalt and nickel, and hence, iron removal stage prior to precipitation of copper was carried out. For precipitation of copper, cobalt, and nickel with sodium sulphide, a stoichiometric amount was added by following Eq. 1.

Analysis of the Sample

As-received and reacted (after experiments) were all analysed and examined by atomic absorption spectroscope (AAS) and scanning electron microscope, respectively. The SEM machine is equipped with energy dispersive X-ray fluorescence spectroscopy (EDX) which allows both overall and phase quantification of the sample.

Results and Discussion

Scanning electron microscope image of the as-received sample is shown in Fig. 2. The phases were examined by analysing the individual particles in the sample. The

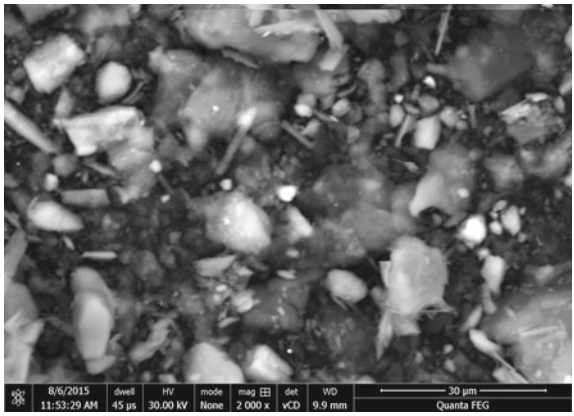

Fig. 2 Scanning electron microscope image under backscattered electron imaging of the as-received sample. The bright areas are the Cu–Co bearing particles

main gangue minerals were enstatite ($MgSiO_3$), pyrope ($Mg_3Al_2(SiO_4)_3$), and humite group ($(Mg,Fe)_7(SiO_4)_3(F,OH)_2$). On the other hand, the major Cu–Co–Ni bearing minerals are malachite, heterogenite, limonite, and complex magnesium aluminium silicate.

Leaching

The results showing effects of leaching pH and temperature are shown in Table 2 from which the following can be observed:

Table 2 Leach test results showing effect of pH and temperature on % recovery. Samples leached at 70 °C in (a) and at 25 °C in (b)

pH	SMBS (wt%)	% Recovery				Acid consumption (kg/ton ore)
		Cu	Co	Fe	Ni	
(a)						
pH = 1.4	1.0	81.58	88.57	36.10	70.00	138
pH = 1.6	1.0	74.91	88.57	20.75	58.46	106
pH = 1.8	1.0	70.18	81.90	14.11	58.46	67
pH = 2.0	1.0	74.21	81.90	17.84	61.54	40
(b)						
pH = 1.4	1.0	55.92	71.82	1.754	29.23	74
pH = 1.6	1.0	58.78	73.00	0.439	31.54	72
pH = 1.8	1.0	53.06	77.27	4.825	30.77	69
pH = 2.0	1.0	51.84	85.91	0.877	34.62	39

i. The recoveries of Cu, Co, Fe, and Ni are decreasing with increase in pH for the sample that was leached out at 70 °C.
ii. The consumption of sulphuric acid was decreasing with increase in pH for the sample that was leached out at 70 °C.
iii. There was minimal change in the recoveries of Cu and Ni, whereas that of co increased with increase in pH for the sample that leached out at 25 °C.
iv. The recovery of iron is lower at all pH range for the samples that were leached out at 25 °C compared to 70 °C.
v. Acid consumption is much higher at pH of 1.4 and 1.6 for the samples that were leached out 70 °C than at ambient temperature. However, acid consumptions were similar at pH of 1.8 and 2.0.

From the above observations, it can be concluded that high recoveries can be achieved when the sample is leached out at high temperature (70 °C). Nonetheless, pH should be 1.8 and above in order to have less acid consumption. High recoveries were obtained at high temperature because the complex copper–cobalt–nickel–magnesium–silicate matrix is broken down.

The results showing effect of SMBS addition and quantities is shown in Table 3 from which it can be observed that the recoveries of Cu, Co, and Ni were extremely poor in the absence of SMBS at both 25 and 70 °C. On the other hand, recoveries of Cu, Co, and Ni all increased when 0.6 wt% SMBS was added. However, there was minimal increase in recoveries of Cu, Co, and Ni when SMBS was added beyond 0.6%. Based on the results in Table 3, it can be concluded that the optimum SMBS addition is 0.6 weight %. By comparison, better recoveries were obtained at 70 °C than at 25 °C.

Table 3 Leach test results showing the effect of SMBS addition. Samples leached at 70 °C in (a) and at 25 °C in (b)

pH	SMBS wt%	% Recovery				Acid consumption (kg/ton ore)
		Cu	Co	Fe	Ni	
(a)						
pH = 1.8	0	27.52	16.32	6.93	12.04	36
pH = 1.8	0.6	74.74	80.48	15.77	65.38	84
pH = 1.8	1.0	70.18	81.90	14.11	58.46	67
pH = 1.8	1.5	77.89	87.62	30.29	63.85	69
pH = 1.8	2.0	76.32	86.67	34.44	66.15	74
(b)						
pH = 1.8	0	21.83	13.29	0.94	8.34	18
pH = 1.8	0.6	56.33	61.82	1.75	38.46	32
pH = 1.8	1.0	53.06	77.27	4.82	30.77	69
pH = 1.8	1.5	56.33	70.45	4.83	43.08	44
pH = 1.8	2.0	59.18	78.64	7.02	36.92	32

Analysis of the Leach Solution

The contents of the leach solution were determined by analysing the dried solids which were obtained by evaporating leach liquor, and the results are shown in Table 4. Apart from the usual Cu, Co, Ni, Fe, and Mn, the leach solutions contain Al, Mg, Si, and Na. The presence of Al, Mg, and Si is due to dissolution of complex nickel silicate phases. The dissolution of Al, Mg, and Si explains why acid consumption is extremely high for the material.

Precipitation of Copper, Cobalt, and Nickel with Magnesium Oxide

The results in Table 3 have shown high recoveries for the sample that was leached at 70 °C, and hence, precipitation test works were carried out on this material. pH of the solution was slowly raised to 3.8, 5.5, and 8.5 in order to allow selective precipitation of iron, copper, and cobalt hydroxide, respectively. The first precipitate at pH of 3.8 had 30.9 wt% Fe and very less Cu, Co, and Ni as shown in Table 5. The high selectivity in the precipitation of iron is because Cu, Co, and Ni are highly soluble at pH of 3.8.

The precipitate at pH of 5.5 only had 10.6 wt% Cu, and this was due to co-precipitation of aluminium and silica. In other words, precipitated aluminium hydroxide and silica decreased the grade of Cu in the precipitate. In addition, part of Co and Ni, co-precipitate such that the precipitate had 2 wt% Co and 1 wt% Ni. As such, it can be concluded that the co-precipitation of Co, Ni, silica, and aluminium hydroxide adversely affects the quality of copper precipitate at pH of 5.5.

The pH of the solution was further increased to 8.5, and the final precipitate had 3.42 wt% Co and 2.4 wt% Ni. In fact, the final precipitate demonstrates a possibility of producing a Co–Ni alloy which has wider applications.

Precipitation of Copper, Cobalt, and Nickel with Sodium Sulphide

The results showing the precipitation of copper, cobalt, and nickel with sodium sulphide are presented in Table 6. The first precipitate which was produced with 1.1 times stoichiometric amount for the formation of CuS has 58.13 wt% copper. A small amount of cobalt, iron, and nickel were also precipitated, and this might be due to the excess addition of sodium sulphide. In the second experiment (experiment B), only the stoichiometric amount of sodium sulphide was added and the grade of copper increased to 63 wt%.

Table 4 Chemical analysis in weight % of the dry solids obtained by evaporating the leach liquor

Conditions	Cu	Co	Fe	Ni	Mn	Al	S	Ca	Si	Mg	Na
pH = 1.4, 25 °C, 1% SMBS	2.49	0.67	1.14	0.23	1.32	1.95	16.9	0.02	1.85	2.22	8.52
pH = 1.4, 70 °C, 1% SMBS	2.08	0.39	3.03	0.41	0.96	2.54	22.3	0.03	0.55	1.74	2.80
pH = 2.0, 70 °C, 1.0% SMBS	3.85	1.67	3.22	0.69	2.91	3.55	16.9	0.08	1.53	1.92	3.98
pH = 2.0, 70 °C, 1.5% SMBS	2.83	1.19	3.53	0.52	1.97	3.24	16.2		0.98	1.72	5.22

Table 5 Chemical analysis in weight % for the precipitate that was obtained via precipitation with magnesium oxide

Conditions	Cu	Co	Fe	Ni	Mn
Precipitated at pH 3.8	0.21	0.13	30.88	0.01	0.02
Precipitated at pH 3.8 then 5.6	10.63	2.08	13.69	1.00	0.29
Precipitated at pH = 3.8, secondly at pH = 5.6, and finally ay pH = 8.5	0.76	3.42	0.67	2.40	1.93

Table 6 Chemical analysis in weight % for the precipitate that was obtained via precipitation with sodium sulphide

Addition of Na_2S	Cu	Co	Fe	Ni	Mn
Experiment A					
1.1 Times stoichiometric amount of Na_2S for formation of CuS	58.13	1.31	1.41	0.53	0.33
1.2 Times stoichiometric amount of Na_2S for formation of CoS, NiS, and FeS	0.10	9.59	14.91	4.58	0.58
Experiment B					
1.1 Stoichiometric amount of Na_2S for formation of CuS	63.01	1.08	0.55	0.55	–
1.2 Stoichiometric amount of Na_2S for formation of CoS, NiS, and FeS	2.78	12.18	5.37	7.42	–

Even though the amount of iron decreased to 0.55 wt%, the first precipitate had 1.01 wt% cobalt. The presence of a smaller amount cobalt and nickel might be due to localised precipitation. Thermodynamically, nickel, cobalt, and iron can only precipitate out when all copper is depleted but localised concentration might occur as the sodium sulphide solution comes in contact with the leach liquor.

The fact that the first precipitates are mainly rich in copper whereas the second precipitates are rich in cobalt and nickel confirms that there is broad agreement between the experimental results and thermodynamic prediction.

Conclusions

1. Addition of SMBS is important for dissolution of Cu, Co, and Ni during leaching as shown in Table 2. However, increasing the quantity of SMBS above 0.6% weight is not necessary as the recovery does not improve further as shown in Table 3.
2. There is broad agreement between the experimental results and thermodynamic prediction. Preferential precipitation of copper sulphide was achieved where a

solution containing copper, cobalt, nickel, iron, manganese, aluminium, silica, and magnesium was reacted with sodium sulphide.
3. The material must be leached out at a higher temperature (70 °C) for high recoveries for Cu, Co, and Ni. Nonetheless, pH should be 1.8 and above in order to have less acid consumption.
4. Some cobalt and nickel co-precipitate with copper during precipitation with magnesium oxide (MgO) at pH of 5.5 (see Table 5).
5. Use of Na_2S resulted in selective precipitation of a high-grade Cu_2S precipitate and second precipitate rich in cobalt and nickel sulphides.

References

1. Cobalt Monograph (1960) Cobalt monograph. Centre d'Information du Cobalt, Brussels, Belgium, p 515
2. Betteridge W (ed) (1982) Cobalt and its alloys. In: Industrial metals, 1st edn. Chichester, Ellis Horwood, pp 43–48
3. Davis JR (2001) Copper and copper alloys. ASM specialty handbook. A.S.M. International
4. Schmidt T et al (2016) Investigation of the primary production routes of nickel and cobalt products used for Li-ion batteries. Resour Conserv Recycl 112:107–122
5. Vijayakumar G et al (2011) Development and testing of PM flowmeter with samarium cobalt magnet assembly. Energy Procedia 7:630–637
6. Zhou X et al (2019) Validated model of thermochemical energy storage based on cobalt oxides. Appl Therm Eng 159
7. Davenport WGL et al (2002) Extractive metallurgy of copper. In: Chemical, petrochemical & process, 4th edn. Elsevier, pp 1–452
8. Dyer L et al (2012) Cobalt loss due to iron precipitation in ammoniacal carbonate solutions. Hydrometallurgy 125–126:144–147
9. Roine A (2002) HSC Chemistry 5.1. Outokumpu research oy, Finland
10. Li J et al (2009) Effect of pre-roasting on leaching of laterite. Hydrometallurgy 99:84–88. https://doi.org/10.1016/j.hydromet.2009.07.00

Part VI
Characterization of Corrosion Resistance

Corrosion Inhibition Effect of Clove Essential Oil Extract with Basil and Atlas Cedar Oil on Mild Steel in Dilute Acid Environment

Roland Tolulope Loto, Tiwa Olukeye and Eugene Okorie

Abstract The corrosion inhibition effect of clove, atlas cedar, and basil essential oil extracts on mild steel was studied. Clove essential oil was separately admixed with basil oil extract (CBO) and atlas cedar oil extract (CAO) in 0.5 M H_2SO_4 and HCl solutions. Weight loss measurement, potentiodynamic polarization technique, and optical microscopy were used to evaluate their performance. The two admixed inhibitor compounds performed effectively at most concentrations with highest inhibition performance of 95.48 and 95.32% in H_2SO_4 solution. In HCl solution, the inhibition performance of CBO and CAO inhibitor compounds are 92.7 and 97.98%. CBO and CAO displayed mixed inhibiting properties with dominant cathodic inhibition effect. Severe surface degradation was visible on the non-inhibited steels in H_2SO_4 while extensive localized degradation was visible on the non-inhibited steel from HCl solution. The presence of CBO and CAO inhibitor significantly improved the surface of the mild steel.

Keywords Mild steel · Corrosion · Oil · Inhibitor

Introduction

Steel has been the essential base material of construction for industrial parts, components, and equipment for over a century. Carbon steel production and application are the important indicators of the state of the global economy [1]. Steel has universal application across most industries and engineering applications [2]. This is due to their good balance of strength and ductility, relatively low cost, ready availability, ease of fabrication, and recyclability. However, they are vulnerable to corrosion due to the porosity of the oxide that forms on their surface when exposed to corrosive agents. Application of essential oil extracts for corrosion inhibition have been very promising; however, their inhibition performance is heavily concentration dependent

R. T. Loto (✉) · T. Olukeye · E. Okorie
Department of Mechanical Engineering, Covenant University, Ota, Ogun State, Nigeria
e-mail: tolu.loto@gmail.com

J. Li et al. (eds.), *Characterization of Minerals, Metals, and Materials 2020*,
The Minerals, Metals & Materials Series,
https://doi.org/10.1007/978-3-030-36628-5_22

which can be dangerous when there are fluctuations in the physical state and properties of the corrosive environment [3–9]. Synergistic combination effects of essential oil extracts have proven effective at all concentrations studies, giving additional advantage to the use of these oils for corrosion inhibition [10, 11]. In contribution to research on naturally occurring compounds for effective corrosion inhibition and their synergistic combination effect for improved performance, this research focuses on the synergistic combination effect of clove oil with basil oil, and clove oil with atlas cedar oil.

Experimental Methods

Materials and Preparation

Cylinders (thickness, 6 mm and diameter, 12 mm) of mild steel (MS) were purchased from Steel Works Lagos, Nigeria. The steel has nominal weight composition (wt%) of 0.8% Mn, 0.04% P, 0.05% S, 0.16% C, and 98.95% Fe, and was cut into 28 individual specimens with 6 mm thickness. Clove, atlas cedar, and basil oil extracts were purchased from NOW Foods, USA. Synergistic inhibition properties of the oil extracts were studied through admixture of clove oil with basil oil (CBO), and clove oil with atlas cedar oil (CAO) in 1:1 ratios. Their combined admixtures (CBO) and (CAO) were prepared in volumetric concentrations of 0.5, 1, 1.5, 2, and 2.5% in 200 mL of 0.5 M H_2SO_4 and HCl solution. MS specimens were individually immersed in 200 mL of 0.5 M H_2SO_4 and HCl solutions for 504 h and weighed at every 24 h through weigh loss measurement. Corrosion rate, weight loss, and inhibition efficiency were determined from the test. Potentiodynamic polarization of MS was performed at 30 °C ambient temperature. A triple electrode system (Pt rod counter electrode, Ag/AgCl reference electrode, and cylindrical MS working electrodes) within a glass cell containing 200 mL of acid (H_2SO_4, HCl)-inhibitor (CBO, CAO) solution was linked to Digi-Ivy 2311 potentiostat to perform the polarization test. Polarization plots were obtained at scan rates of 0.0015 V/s at potentials of −0.75 to +1.5 V. Optical micrographs of MS morphology from control acid solutions were analysed and compared to CBO and CAO inhibited MS morphology with Omax trinocular metallurgical microscope using ToupCam software.

Results and Discussion

Weight Loss Measurement

Tables 1 and 2 show the weight loss and corrosion rate, and CBO and CAO inhibition efficiency in H_2SO_4 and HCl solution at 504 h. The corrosion rate values of MS at 0%

Table 1 Results of MS corrosion inhibition in H_2SO_4 solution at 0–2.5% CBO and CAO concentrations from coupon analysis at 504 h

CBO inhibitor					CAO inhibitor				
Samples	CBO conc. (%)	CBO weight loss (g)	MS corrosion rate (mm/year)	CBO inhibition efficiency (%)	Samples	CAO conc. (%)	CAO weight loss (g)	MS Corrosion rate (mm/year)	CAO inhibition efficiency (%)
A	0	7.794	0.029	–	A	0	8.909	0.033	–
B	0.5	6.198	0.023	20.48	B	0.5	1.308	0.005	85.32
C	1	0.352	0.001	95.48	C	1	0.807	0.003	90.94
D	1.5	0.693	0.003	91.11	D	1.5	0.812	0.003	90.89
E	2	0.677	0.002	91.32	E	2	0.788	0.003	91.16
F	2.5	0.650	0.002	91.66	F	2.5	0.417	0.002	95.32

Table 2 Results of MS corrosion inhibition in HCl solution at 0–2.5% CBO and CAO concentrations from coupon analysis at 504 h

CBO inhibitor					CAO inhibitor				
Samples	CBO conc. (%)	CBO weight loss (g)	MS Corrosion rate (mm/year)	CBO inhibition efficiency (%)	Samples	CAO conc. (%)	CAO weight loss (g)	MS Corrosion rate (mm/year)	CAO inhibition efficiency (%)
A	0	2.807	0.010	–	A	0	2.330	0.009	–
B	0.5	1.276	0.005	54.54	B	0.5	1.342	0.005	42.40
C	1	0.716	0.003	74.47	C	1	1.136	0.004	51.26
D	1.5	0.614	0.002	78.12	D	1.5	0.054	0.0002	97.69
E	2	0.484	0.002	82.74	E	2	0.038	0.0001	98.35
F	2.5	0.205	0.001	92.70	F	2.5	0.047	0.0002	97.98

CBO and CAO concentration in both acid solutions significantly contrast the values obtained at higher CBO and CAO concentrations. The observation is due to the oxidation of MS in the presence of SO_4^{2-} and Cl^- anions [8]. The presence of CBO and CAO oil extracts (corrosion inhibitor) in the acid media significantly changed the dynamics of the redox electrochemical processes resulting in visible reduction in MS corrosion rate values. The corrosion inhibition performance of CBO and CAO above 0.5% concentration tends to be independent of concentration in H_2SO_4 solution compared to HCl media where slight dependence on concentration was observed. Comparison of the final inhibition efficiency values in Table 1 shows CBO and CAO inhibitor performed excellently with optimal inhibition values of 95.48% and 95.32% at 1% CBO and 2.5% CAO in H_2SO_4 solution, while in HCl solution (Table 2) the optimal values are 92.7% at 2.5% CBO and 98.35% at 2% CAO.

Potentiodynamic Polarization Studies

Tables 3 and 4 show the data obtained from the polarization test. Similar to the observation from weight loss, the corrosion rates of the control MS (0% CBO and CAO inhibitor) significantly differs from the inhibited steel due to suppression of the corrosion reaction mechanisms. The 0.5% inhibitor concentration of CAO (59.61%) slightly outperforms CBO at 32.52% inhibition efficiency in H_2SO_4 solution which corresponds to corrosion rate values of 6.20 and 3.71 mm/year. Increase in inhibitor concentration from 1 to 2.5% significantly improved the inhibition performance of CBO and CAO inhibitor to values above 80% with peak value of 87.16% (2.5% CBO) and 92.1% (1.5% CAO). Observation of the variation of MS corrosion potential with respect to CBO and CAO concentration after 0% concentration shows higher tendency for cathodic inhibition. However, shift in potential shows CBO and CAO compound has mixed inhibition properties. The anodic Tafel slope values after 0% CBO and CAO is due to inhibition of anodic dissolution of the steel resulting in higher anodic exchange current density. Changes in the Tafel values after 0% inhibitor concentration also shows surface coverage of MS by both inhibitors suppressed the electrochemical action of SO_4^{2-} thus hindering them from oxidizing the steel surface [12]. The extent of MS corrosion damage in HCl solution (0% inhibitor concentration) was slightly lower at corrosion rate of 5.94 mm/year. Addition of CBO inhibitor to HCl solution from 0.5 to 2.5% CBO concentration results in inhibition efficiency value generally above 80%. Effective inhibition of MS by CAO occurred after 0.5% CAO concentration.

Optical Microscopy Analysis

Optical images (mag. $\times 40$ and $\times 100$) of MS before corrosion, after corrosion in H_2SO_4 and HCl solution with inhibitor, and after corrosion in both acids at 0.5% and

Table 3 Potentiodynamic polarization data for MS corrosion in H_2SO_4 solution at 0–2.5% CBO and CAO inhibitor concentration

H_2SO_4-CBO									
Sample	CBO conc. (%)	MS corrosion rate (mm/year)	CBO inhibition efficiency (%)	Corrosion current (A)	Corrosion current density (A/cm^2)	Corrosion potential (V)	Polarization resistance, R_p (Ω)	Cathodic Tafel slope, B_c (V/dec)	Anodic Tafel slope, B_a (V/dec)
A	0	9.19	0	8.95E−04	7.92E−04	−0.432	9.46	−7.243	7.900
B	0.5	6.20	32.52	6.04E−04	5.35E−04	−0.438	178.40	−8.115	10.210
C	1	1.45	84.23	1.41E−04	1.25E−04	−0.466	184.40	−8.355	19.160
D	1.5	1.29	85.97	1.26E−04	1.11E−04	−0.486	192.15	−8.434	21.830
E	2	1.56	83.02	1.52E−04	1.35E−04	−0.467	178.17	−6.362	16.656
F	2.5	1.18	87.16	1.15E−04	1.02E−04	−0.448	223.70	−7.043	24.620
H_2SO_4-CAO									
Sample	CAO conc. (%)	MS corrosion rate (mm/year)	CAO inhibition efficiency (%)	Corrosion current (A)	Corrosion current density (A/cm^2)	Corrosion potential (V)	Polarization resistance, R_p (Ω)	Cathodic Tafel slope, B_c (V/dec)	Anodic Tafel slope, B_a (V/dec)
A	0	9.19	0	8.95E−04	7.92E−04	−0.432	9.46	−7.243	7.900
B	0.5	3.71	59.61	3.62E−04	3.20E−04	−0.463	71.08	−6.778	11.840
C	1	1.45	84.23	1.41E−04	1.25E−04	−0.456	246.30	−5.022	16.412
D	1.5	0.73	92.10	7.07E−05	6.26E−05	−0.433	363.40	−5.245	20.550
E	2	0.76	91.73	7.40E−05	6.55E−05	−0.462	348.64	−6.252	19.500
F	2.5	1.09	88.13	1.06E−04	9.40E−05	−0.461	287.90	−8.702	20.020

Table 4 Potentiodynamic polarization data for MS corrosion in HCl solution at 0–2.5% CBO and CAO inhibitor concentration

HCl-CBO									
Sample	CBO conc. (%)	MS corrosion rate (mm/year)	CBO inhibition efficiency (%)	Corrosion current (A)	Corrosion current density (A/cm^2)	Corrosion potential (V)	Polarization resistance, R_p (Ω)	Cathodic Tafel slope, B_c (V/dec)	Anodic Tafel slope, B_a (V/dec)
A	0	5.94	0	5.78E−04	5.12E−04	−0.471	44.43	−6.883	12.000
B	0.5	1.05	82.30	1.02E−04	9.06E−05	−0.475	250.90	−8.990	14.500
C	1	1.09	81.63	1.06E−04	9.41E−05	−0.482	264.40	−9.469	21.850
D	1.5	1.09	81.67	1.06E−04	9.38E−05	−0.488	260.20	−9.381	17.910
E	2	1.08	81.78	1.05E−04	9.33E−05	−0.496	257.30	−8.474	16.300
F	2.5	1.05	82.32	1.02E−04	9.05E−05	−0.478	251.10	−8.892	18.720
HCl-CAO									
Sample	CAO conc. (%)	MS corrosion rate (mm/year)	CAO inhibition efficiency (%)	Corrosion current (A)	Corrosion current density (A/cm^2)	Corrosion potential (V)	Polarization resistance, R_p (Ω)	Cathodic Tafel slope, B_c (V/dec)	Anodic Tafel slope, B_a (V/dec)
A	0	5.94	0	5.78E−04	5.12E−04	−0.471	44.43	−6.883	12.000
B	0.5	3.31	44.34	3.22E−04	2.85E−04	−0.480	79.79	−7.940	11.980
C	1	1.61	72.95	1.57E−04	1.38E−04	−0.506	164.10	−9.254	19.310
D	1.5	0.96	83.79	9.38E−05	8.30E−05	−0.467	273.90	−7.850	17.910
E	2	1.13	80.98	1.10E−04	9.74E−05	−0.470	225.58	−6.354	15.070
F	2.5	1.16	80.56	1.13E−04	9.96E−05	−0.486	228.50	−10.080	13.540

2.5% CBO and CAO concentrations are shown from Figs. 1, 2, 3, 4, 5, and 6b. Figure 1 shows the images of MS before corrosion test. Figure 2a, b shows the images of MS after corrosion in H_2SO_4 and HCl solution without the inhibitors. Figures 3a and 4b show the images of MS after corrosion in H_2SO_4 solution at 0.5% and 2.5% CBO and CAO concentrations, while Figs. 5a and 6b show the images of MS after corrosion in HCl solution at 0.5% and 2.5% CBO and CAO concentrations, respectively. The image of MS after corrosion in H_2SO_4 and HCl solution without CBO and CAO inhibitor (Fig. 2a, b) are generally similar. Severe deterioration of the steel surfaces is clearly visible on both figures; however, the corrosion pits and deep grooves on Fig. 2b is due to the electrochemical action of Cl^- anions whose actions tend to be

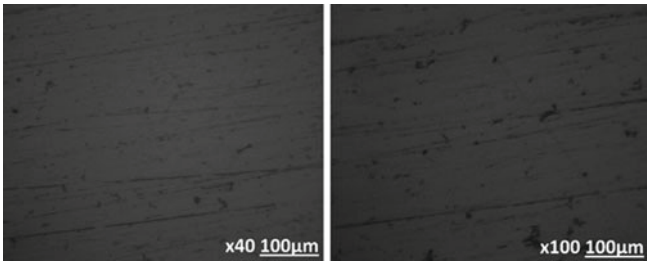

Fig. 1 Optical image of MS before corrosion test

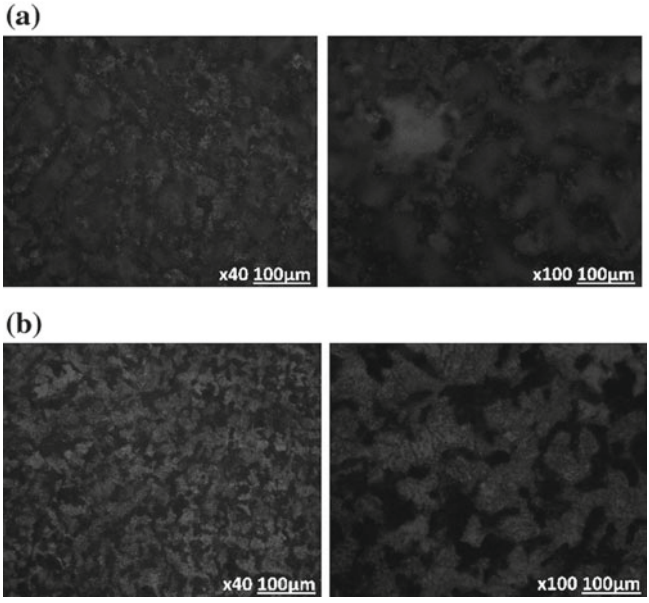

Fig. 2 Optical images of MS after corrosion without inhibitor **a** from H_2SO_4 and **b** from HCl solution

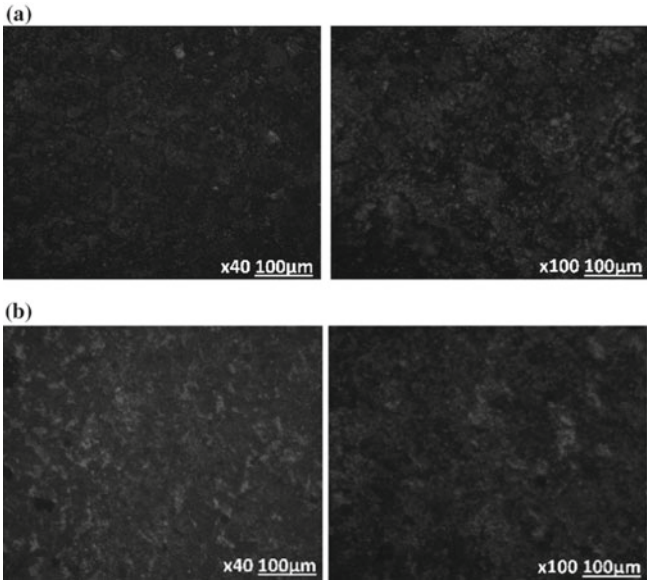

Fig. 3 Optical images of MS after corrosion in H_2SO_4 solution with inhibitor **a** CBO and **b** CAO at 0.5% concentration

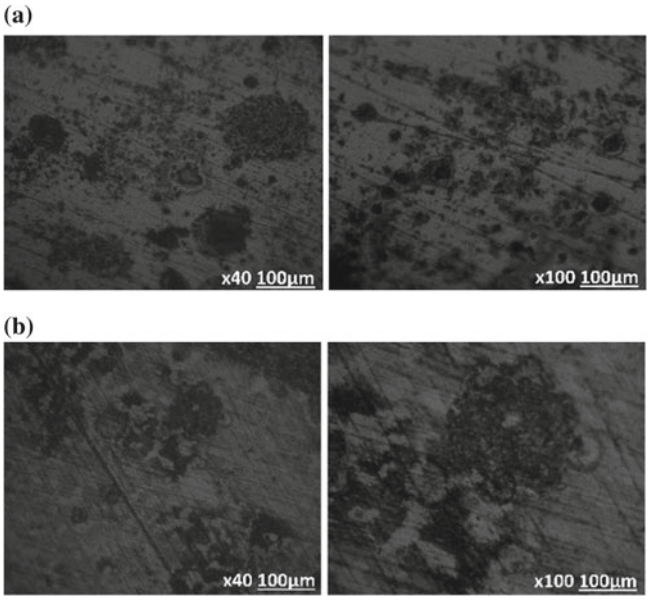

Fig. 4 Optical images of MS after corrosion in H_2SO_4 solution with inhibitor **a** CBO and **b** CAO at 2.5% concentration

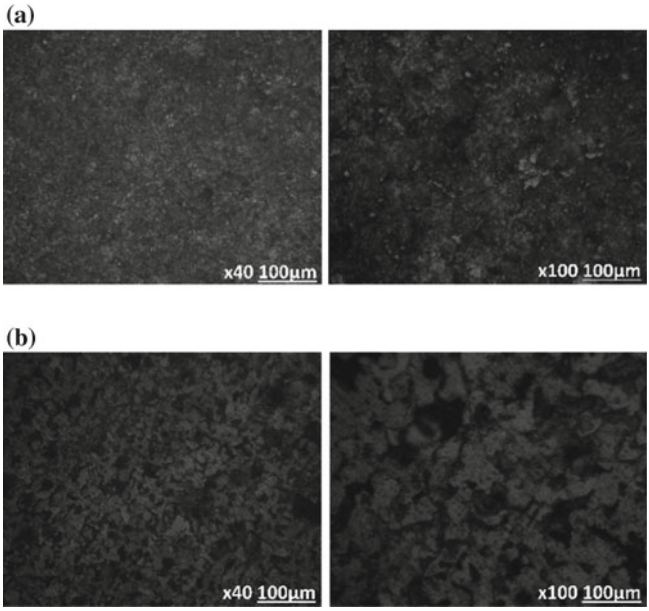

Fig. 5 Optical images of MS after corrosion in HCl solution with inhibitor **a** CBO and **b** CAO at 0.5% concentration

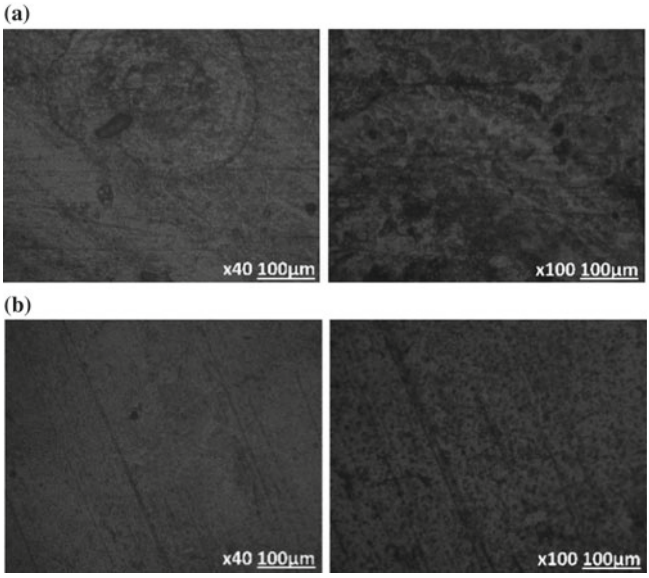

Fig. 6 Optical images of MS after corrosion in HCl solution with inhibitor **a** CBO and **b** CAO at 2.5% concentration

localized compared to Fig. 2b where the action SO_4^{2-} anions generally deteriorates the entire steel surface [13, 14]. Visual observation of the images from Figs. 3a and 4b shows marginal improvement in morphology of MS in H_2SO_4. However, CAO inhibitor slightly protects MS surface more than CBO at 0.5 and 2.5% concentration as the extent of deterioration is lower in the presence of CAO. Comparison of Figs. 3 and 4 with Figs. 5 and 6 shows the electrochemical action of CBO and CAO inhibitor on MS corrosion inhibition differs from their action in H_2SO_4. The morphology in Figs. 3 and 4 shows general surface deterioration compared to localized corrosion in Figs. 5 and 6. CBO seems to outperform CAO in hindering the deterioration of MS surface. Corrosion pits are visible in Figs. 5b and 6b, though the pits are drastically reduced in size in Fig. 6b due to higher concentration of CAO molecules. Comparing this observation to Figs. 5a and 6a, the extent of deterioration is lower in the presence of CBO inhibitor.

Conclusion

Admixture of clove essential oil extract with basil oil, and with atlas cedar oil produced a compound that effectively suppressed the corrosion of mild steel in 0.5 M H_2SO_4 and HCl solution. The corrosion inhibition performances of both admixed compounds were generally above 80% at most inhibitor concentrations in both acids. The admixed inhibitor compounds demonstrated mixed inhibiting properties with dominant cathodic influence. Significant morphological improvement of the carbon steel in the presence of both inhibiting compounds occurred in H_2SO_4. However, marginal deterioration of the steel occurred which visibly contrast the corroded steel without inhibitor in HCl solution.

Acknowledgements The author acknowledges Covenant University Ota, Ogun State, Nigeria for the sponsorship and provision of research facilities for this project.

References

1. Ocheri C, Ajani OO, Daniel A, Agbo N (2017) The steel industry: a stimulus to national development. J Powder Metall Min 6(1):156. https://doi.org/10.4172/2168-9806.1000156
2. Winnik S (2008) Design for the prevention of corrosion-under-insulation. In: Corrosion under insulation (CUI) guidelines
3. Narayanasamy P, Ramachanderen T, Natesan M, Murugavel SC (2009) Corrosion inhibition of mild steel by essential oils in an HCl environment. Mater Perform 48(9):52–56
4. Afia L, Benali O, Salghi R, Ebenso EE, Jodeh S, Zougagh M, Hammouti B (2014) Steel corrosion inhibition by acid garlic essential oil as a green corrosion inhibitor and sorption behaviour. Int J Electrochem Sci 9:8392–8406
5. Rekkab S, Zarrok H, Salghi R, Zarrouk A, Bazzi Lh, Hammouti B, Kabouche Z, Touzani R, Zougagh M (2012) Green corrosion inhibitor from essential oil of *Eucalyptus globulus* (myrtaceae) for c38 steel in sulfuric acid solution. J Mater Environ Sci 3(4):613–627

6. Dahmani K, Galai, M, Cherkaoui M, El hasnaoui A, El Hessni A (2012) Cinnamon essential oil as a novel eco-friendly corrosion inhibitor of copper in 0.5 M sulfuric acid medium. J Mater Environ Sci 8(9):1676–1689
7. Loto RT (2018) Electrochemical analysis of the corrosion inhibition effect of trypsin complex on the pitting corrosion of 420 martensitic stainless steel in 2M H_2SO_4 solution. PLoS ONE 13(4):e0195870. https://doi.org/10.1371/journal.pone.0195870
8. Loto RT (2018) Surface coverage and corrosion inhibition effect of *Rosmarinus officinalis* and zinc oxide on the electrochemical performance of low carbon steel in dilute acid solutions. Results Phys 8:172–179. https://doi.org/10.1016/j.rinp.2017.12.003
9. Loto RT (2019) Electrochemical analysis of the pitting corrosion inhibition performance of essential oil extracts on P4 low alloy steel in H_2SO_4 solution. Mater Res Express 6:026542. https://doi.org/10.1088/2053-1591/aaeec8
10. Loto RT, Olowoyo OO (2018) Corrosion inhibition properties of the combined admixture of essential oil extracts on mild steel in the presence of SO_4^{2-} anions. S Afr J Chem 26:35–41. https://doi.org/10.1016/j.sajce.2018.09.002
11. Loto RT, Leramo R, Oyebade B (2018) Synergistic combination effect of salvia officinalis and *Lavandula officinalis* on the corrosion inhibition of low-carbon steel in the presence of SO_4^{2-} and Cl^- containing aqueous environment. J Fail Anal Prev 18:1429–1438. https://doi.org/10.1007/s11668-018-0535-0
12. Kumari PP, Shetty P, Rao SA (2017) Electrochemical measurements for the corrosion inhibition of mild steel in 1 M hydrochloric acid by using an aromatic hydrazide derivative. Arab J Chem 10(5):653–663
13. Loto RT (2013) Pitting corrosion evaluation of austenitic stainless steel type 304 in acid chloride media. J Mater Environ Sci 4(4):448–459
14. Laitinen T (2000) Localized corrosion of stainless steel in chloride, sulfate and thiosulfate containing environments. Corros Sci 42(3):421–441

Effect of Dual Phase Stabilization via Varying Ti/Nb Ratios on the Pitting Behavior of AISI 347 Welds

A. S. Shahi and Dikshant Malhotra

Abstract The aim of the present work was to study the role of Ti additions made to Nb contained stabilized austenitic stainless steel grade AISI 347 welds for improving their metallurgical stability and pitting corrosion resistance. For achieving this, gas tungsten arc welding process (GTAW) was used to fabricate multi-pass and multi-layer weld pads comprising of 28 weld passes; and using AISI 347 (Nb based) and AISI 321 (Ti based) solid fillers in a systematic combination, so as to obtain different weld metals' surfaces with varying Ti/Nb ratios of 0.45, 0.66, and 1.57. These surfaces were examined for their pitting behavior using electrochemical method, an electron probe microanalyzer (EPMA) equipped with a wavelength dispersive X-ray spectrometer (WDS) for chemical composition analysis, and X-ray photoelectron spectroscopy (XPS) depth profiling of passive films. Austenitic stainless steel welds with Ti/Nb ratio of 0.45 exhibited maximum pitting potential of 380.5 mV_{SCE} as compared to sole Nb weld with 270.7 mV_{SCE}. The atomic concentration profiles of oxygen across different weld surfaces indicate that estimated passive film thickness values for sole Nb (347 weld metal) and Nb weld stabilized with Ti/Nb ratio of 0.45 were calculate to be 8.43 nm and 7.11 nm, respectively. Ti addition suppressed the carbide formation tendencies resulting in higher levels of Ni in the matrix as well as different dendritic regions of 347 weld metal. Thus, this study establishes that Ti additions of 0.21 wt% in Nb weld can significantly enhance its pitting resistance.

Keywords Stabilized stainless steel · Weld alloying · Pitting corrosion · Passive film

A. S. Shahi (✉) · D. Malhotra
Department of Mechanical Engineering, Sant Longowal Institute of Engineering and Technology, Longowal, Sangrur, Punjab 148106, India
e-mail: ashahisliet@yahoo.co.in; ashahi@sliet.ac.in

D. Malhotra
e-mail: dikshant.malhotra7@gmail.com

J. Li et al. (eds.), *Characterization of Minerals, Metals, and Materials 2020*,
The Minerals, Metals & Materials Series,
https://doi.org/10.1007/978-3-030-36628-5_23

Introduction

AISI 347 Nb stabilized austenitic stainless steel (γ-SS) welded structures are widely used in high temperature applications such as in boilers, nuclear reactors, superheaters, heat exchangers, and chemical reactors owing to their greater resistance to sensitization at elevated temperatures [1, 2]. Nb as a stabilizing addition is a strong carbide former than Cr and hence used to prohibit sensitization in ASS. Addition of Nb forms NbC that reduces the grain boundary precipitation of $Cr_{23}C_{6,}$ thereby restricting the chromium depletion, which ultimately improves the corrosion resistance of the material [3]. Despite having excellent resistance to sensitization, Nb stabilized weld metals exhibit inferior corrosion resistance than AISI 347 base material owing to subsequent heating and cooling thermal cycles during welding, which can lead to precipitation of chromium carbides. These chromium carbide precipitates are preferential sites for localized pitting corrosion attack [4], and pitting corrosion failures of stabilized AISI 347 ASS are also reported [5, 6]. Minor additions of titanium improve the corrosion resistivity of ferritic stainless steels by stabilizing the passive film [7]. Keeping in mind the literature reviewed so far, it is observed that no work has been reported on the influence of titanium additions to improve the pitting corrosion performance of Nb stabilized 347 ASS welds. Therefore, the present work aims at enhancing the pitting corrosion resistance of AISI 347 welds by improving metallurgical stability via using varying additions of Ti/Nb to AISI 347 welds.

Experimental Details

ASME section IX weld overlaying procedure was adopted for fabricating weld pad over AISI 347 substrate using gas tungsten arc welding process and fillers combination of ER 347 (Nb based) and ER 321 (Ti based). A multi-pass and multi-layer weld pad comprising of four overlays and seven passes in each overlay was specified to accomplish the objectives of the present work. Table 1 shows the chemical compositions of the substrate and the filler used. These filler wires' compositions were selected as per *AWS 5.9 standard* [8] and chemically compatible with AISI 347 substrate. The schematic view of a fabricated weld pad is presented in Fig. 1. In

Table 1 Chemical composition of base and filler material used (wt%)

Material	Code	Alloy element										
		C	Si	Mn	P	S	Ni	Cr	Mo	Nb	Ti	Fe
Base	AISI 347	0.058	0.52	1.78	0.02	0.02	10.65	17.36	0.37	0.55	–	Bal
Filler	ER 347	0.055	0.43	1.62	0.01	0.03	9.86	19.52	0.08	0.60	–	Bal
	ER 321	0.038	0.48	1.60	0.01	0.009	9.78	19.55	0.39	–	0.44	Bal

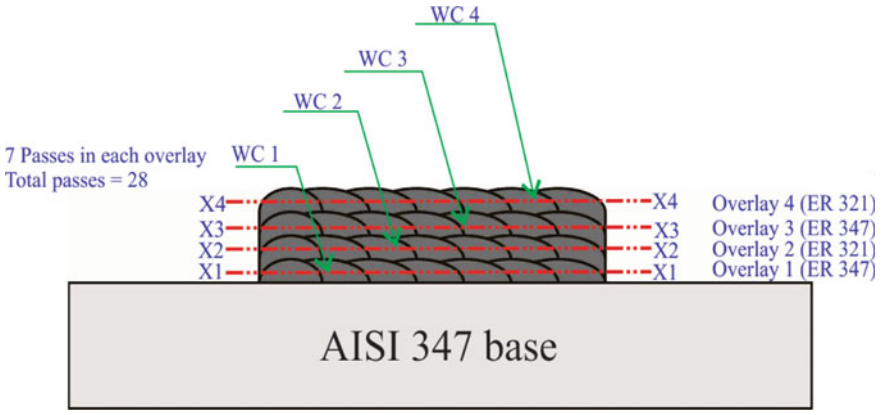

Fig. 1 Schematic view of weld multi-pass and multi-layer overlaying using different fillers combination

addition to following precautions of inter-pass cleaning, an inter-pass temperature of 150–175 °C was maintained after each pass so as to reduce the thermal cycling effects produced by the subsequent passes. Average heat input for second, third, and fourth weld overlays was lower as compared to the first overlay in the weld pad to minimize the thermal effects. Weld surfaces from each overlay were extracted using wire cut electrode discharge machining processes for obtaining different weld compositions. These weld surfaces were represented by specimens' notations as WC1 (X1-X1), WC2 (X2-X2), WC3 (X3-X3), and WC4 (X4-X4) as shown in Fig. 1.

Further, the chemical composition of the extracted weld surfaces as mentioned above was examined using OES (optical emission spectrometer). As per *ASTM standard G-5* [9], potentiodynamic anodic polarization (PAP) technique was used for evaluation of breakdown pitting potentials for different weld surfaces using potentiostat (Make: Gamry, Model: Reference 600) supported with Gamry framework software. The breakdown pitting potential indicates the pitting corrosion susceptibility of materials where stable pitting initiates. Several authors have stated the importance of pitting potential evaluation to determine the pitting corrosion resistance of different materials [10–12]. The weld sample was used as the working electrode, a graphite electrode as the counter electrode, and saturated calomel electrode (SCE) as the reference electrode in the paracell. The sample surfaces were polished through 3000 grit size, and 6 mm diameter of surface area (0.2826 mm^2) was exposed to acidic chloride electrolytic solution of [0.5 M H_2SO_4 (sulfuric acid) + 0.5 M NaCl (sodium chloride)]. The scan rate used for polarization in the positive direction was 1.67 mV/s, up to a potential of 1500 mV_{SCE}.

Point chemical compositions at different locations in the weld metal matrix were analyzed using electron probe microanalyzer (EPMA) equipped with WDS (wavelength X-ray spectrometer) system. The probe current and accelerating voltage used in EPMA analysis were 5.008×10^{-8} A and 25 kV, respectively. In order to determine the depth concentration of O and Cr in the passive film of weld surfaces, primary

XPS regions of O1s and Cr2p3 were scanned to obtain the depth profiles using monochromatic Al-kα X-ray source ($h\upsilon = 1486.6$ eV). The sputtering of Ar^+ ions was performed to determine the passive film thickness over weld surfaces by taking Ta_2O_5 as the reference standard [13]. All the samples were potentiodynamically polarized up to ending potentials within the passive potential range where growth of passive film occurred. After the polarization, samples were cleaned and dried before carrying out XPS analysis.

Results and Discussion

Chemical Composition and Pitting Potential Evaluation of Welds

Table 2 shows chemical compositions with varying Ti/Nb ratios for different welds. The highest and lowest Ti/Nb ratios were noticed in the weld surfaces extracted from overlay '2' and '3,' respectively. The Ti/Nb ratio of different weld surfaces was observed to be 0.45, 0.66, and 1.57. The weld surface taken from weld overlay 1 contained solely Nb and was used as the reference surface against which comparative studies were performed. Further, evaluation of the breakdown pitting potential (Epit) of these varying composition weld surfaces possessing different weld compositions indicate significant variation in Epit with composition. Figure 2a, b shows potentiodynamic anodic polarization (PAP) plots and pitting potential values for weld surfaces with different weld compositions. Among all the welds, WC3 weld (Ti/Nb = 0.45) exhibited maximum pitting potential (Epit = 380.5 mV_{SCE}) followed by sole Nb containing WC1 weld (Epit = 270.7 mV_{SCE}). It was also observed that as Ti/Nb ratio of welds increased, pitting potential values decreased indicating early breakdown of passive film and thus resulting in subsequent pitting initiation and propagation. The lowest pitting potential value was noticed for weld WC2 (Epit = 128.5 mV_{SCE}) with Ti/Nb ratio of 1.57 while WC4 weld (Ti/Nb ratio = 0.66) possessed pitting potential (Epit = 246.5 mV_{SCE}) which was close to sole Nb contained WC1 weld. Therefore, pitting potential evaluation of different weld surfaces indicated that higher titanium contents in Nb stabilized ASS welds were detrimental for their pitting corrosion resistance. An earlier study reported that higher titanium contents in commercial stainless steels form titanium rich inclusions which acted as preferential sites for pitting attack [14].

EPMA Point Chemical Composition Analysis of Welds

Figure 3a, b shows points across different locations (viz. matrix and different dendritic regions) for WC1 (Nb) and WC3 (Ti/Nb = 0.29) welds in the as welded condition

Table 2 Weld compositions obtained using optical emission spectrometer (wt%)

Material	Code	Alloy element										
		C	Si	Mn	P	S	Ni	Cr	Mo	Nb	Ti	Fe
Weld metal	WC1 (Nb)	0.074	0.44	1.92	0.03	0.012	9.48	19.08	0.43	0.53	–	Bal
	WC3 (Ti/Nb = 0.45)	0.067	0.41	1.91	0.03	0.011	9.60	19.58	0.41	0.47	0.21	Bal
	WC4 (Ti/Nb = 0.66)	0.076	0.43	1.94	0.03	0.012	9.22	18.82	0.46	0.39	0.26	Bal
	WC2 (Ti/Nb = 1.57)	0.079	0.49	1.88	0.02	0.01	9.12	18.68	0.52	0.21	0.33	Bal

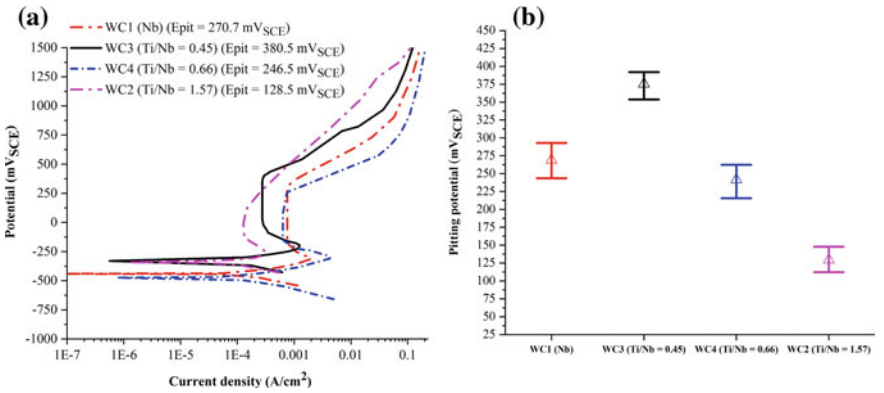

Fig. 2 **a** Potentiodynamic anodic polarization (PAP) plots for weld surfaces with different weld composition; and **b** pitting potential values for welds

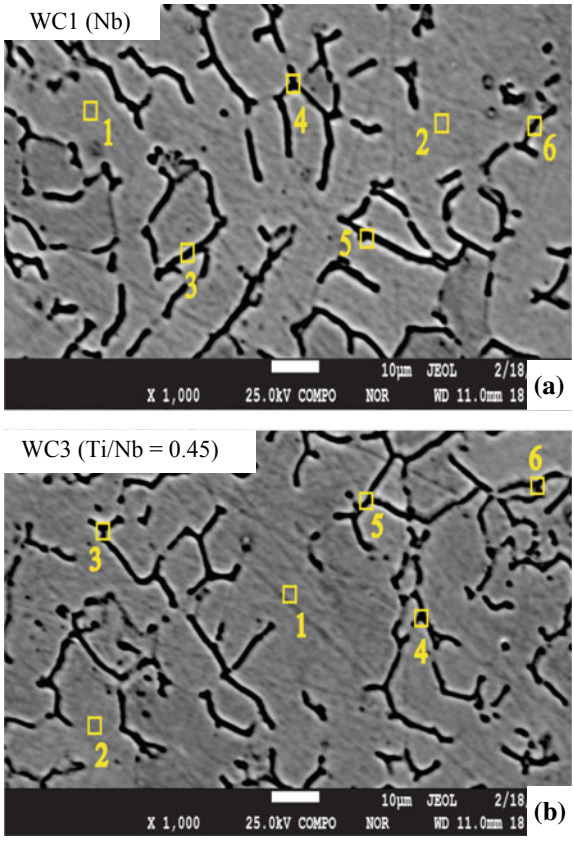

Fig. 3 EPMA-WDS point compositional analysis for welds at different locations: **a** WC1 (Nb); and **b** WC3 (Ti/Nb = 0.45)

Table 3 WDS results of WC1 (Nb)

WDS	Cr	Fe	Ni	Mo	C	Nb
1 (MX)	19.79	68.83	9.18	0.39	0.52	0.47
2 (MX)	19.82	68.66	9.23	0.42	0.49	0.52
3 (DT1)	21.53	68.19	7.25	0.51	0.92	0.72
4 (DT2)	21.68	68.04	7.75	0.48	0.85	0.81
5 (DT3)	22.73	67.83	6.59	0.53	0.88	0.85
6 (DT4)	23.38	67.69	6.28	0.55	1.10	0.88

MX Matrix region, *DT* dendritic region

Table 4 WDS results of WC3 (Ti/Nb = 0.45)

WDS	Cr	Fe	Ni	Mo	C	Nb	Ti
1 (MX)	19.92	68.97	9.62	0.39	0.33	0.45	0.21
2 (MX)	19.56	69.12	9.42	0.33	0.41	0.51	0.19
3 (DT1)	20.53	68.33	8.34	0.48	0.53	0.63	0.33
4 (DT2)	20.44	68.16	8.19	0.51	0.59	0.67	0.35
5 (DT3)	21.72	68.14	7.22	0.54	0.62	0.71	0.42
6 (DT4)	21.98	68.09	7.14	0.53	0.69	0.75	0.44

MX Matrix region, *DT* dendritic region

where chemical composition of desired elements was evaluated using EPMA-WDS technique.

Tables 3 and 4 show WDS point elemental compositions (mass %) at the matrix (MX1 and MX2) and dendritic regions (DT1, DT2, DT3, and DT4) of welds. In WC1 (Nb) weld, significant rise in Cr, C, and Mo contents was observed at the dendrites that indicated higher rate of depletion of these contents at γ/δ interfacial regions. An appreciable loss of Ni was observed at the dendritic regions of sole Nb containing welds. In contrast to a matrix free from heterogeneity, a drastic decrease in Ni content to almost 30% (6.28% at DT4 as listed in Table 3) of its corresponding matrix value was noticed at the dendritic regions. This severe degree of precipitation at the dendritic regions indicates significant chemical heterogeneity in these welds. On the contrary, rise in Cr, Mo, and C was less in WC3 weld as compared to WC1. Moreover, higher Ni content was observed at the dendritic regions in WC3 weld, thereby indicating lesser degree of chemical heterogeneity as compared to WC1 weld.

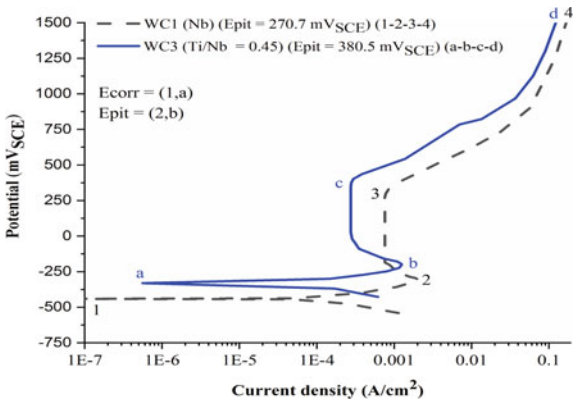

Fig. 4 PAP plots for sole Nb and Nb weld stabilized with Ti/Nb ratio of 0.45 in the as welded condition

Pitting Corrosion and XPS Studies of Welds

The PAP plots as shown in Fig. 4 depicts pitting potential, corrosion potential and passive current density values for WC1 (Nb) and WC3 (Ti/Nb = 0.45) welds in the as welded condition. Higher corrosion and pitting potential values besides lower passive current density were noticed for WC3 weld as compared to WC1. This indicates more stable passive film formation in case of weld with Ti/Nb ratio of 0.45. Higher pitting potential values as discussed previously exhibited a more stable passive film which enhances the pitting corrosion resistance of the material. Moreover, it is already reported that higher corrosion potential and lower passive current density values indicate increased thermodynamic stability of the metal/solution interface and lower dissolution of the passive film, respectively [15]. Further, O and Cr depth concentration profiles for passive film of WC1 (Nb) and WC3 (Ti/Nb = 0.45) welds showed considerable variation in O and Cr content in the passive film of these welds as shown in Fig. 5a, b. As the analysis depth increases, the O content gradually decreases as it approaches the film/matrix interface whereas Cr content increases. In WC3 weld, higher O concentration was noticed at the surface (0 nm) as compared to WC1 weld besides possessing higher Cr concentration (Fig. 5b). Moreover, passive film thickness values for welds could be estimated from the oxygen profile (Fig. 5a) by taking 50% value of the maximum oxygen concentration [16]. The passive film thickness values for WC1 and WC3 welds were estimated to be 8.43 and 7.11 nm, respectively, which show thinner passive film formation in (Nb + Ti) stabilized WC3 weld. With chromium enriched surface as observed in WC3 weld, the oxygen may react more readily with chromium which consequently forms a denser passive film which retards the inward diffusion of oxygen, resulting in decreasing film thickness and enhanced corrosion resistance [17].

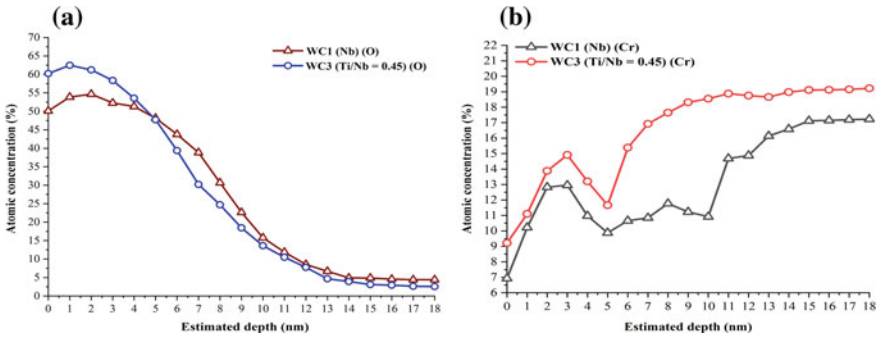

Fig. 5 XPS depth concentration profiles of desired elements in the passivated layers of weld surfaces with different weld compositions: **a** O; and **b** Cr

Conclusions

1. Nb weld stabilized with Ti/Nb ratio of 0.45 exhibited maximum pitting potential. However, as Ti/Nb ratio increases to 1.57, pitting potential value decreased and was lower than the solely Nb containing weld.
2. Lesser carbides formation tendencies and relatively higher nickel retention characteristics were observed in the weld metal matrix of weld with Ti/Nb ratio of 0.45, whereas significant nickel loss was observed in the dendritic regions of Nb contained weld which consequently improved the pitting performance of dual stabilized weld.
3. Inter-dendritic regions exhibited a relatively higher degree of chemical heterogeneity than the weld matrix indicating they are potential regions for precipitation and thus sites for pitting corrosion attack.
4. Higher O and Cr content in the passive film of dual stabilized weld resulted in thinner and densely packed passive film in the (Nb + Ti) stabilized weld with Ti/Nb ratio of 0.45 which improved the pitting corrosion resistance of AISI 347 weld metal significantly.
5. Generally, Ti additions within certain range can stabilize AISI 347 weld metal by improved pitting resistance. Hence, the concept of dual phase stabilization (Nb + Ti) can be beneficially used in exploiting the engineering potential of austenitic stainless steels welded structures used for extremely harsh corrosion conditions.

References

1. Guan K, Xu X, Xu H, Wang Z (2005) Effect of aging at 700 °C on precipitation and toughness of AISI 321 and AISI 347 austenitic stainless steel welds. Nucl Eng Des 235(23):2485–2494
2. Kallqvist J, Andren HO (1999) Microanalysis of stabilized austenitic stainless steel after long term ageing. Mater Sci Eng A 270(1):27–32

3. Thorvaldsson T, Dunlop GL (1982) Effect of stabilizing additions on precipitation reactions in austenitic stainless steel. Met Sci 16(4):184–190
4. Aquino JM, Della CA, Kuri SE (2009) Intergranular corrosion susceptibility in supermartensitic stainless steel weldments. Corros Sci 51(10):2316–2323
5. Schweinsberg DP, Sun B, Oteino-Alego V (1994) Corrosion and inhibition of aged 347 grade stainless steel boiler tubes. J Appl Electrochem 24:803–807
6. Chandra K, Kain V, Tewari R (2013) Microstructural and electrochemical characterisation of heat treated 347 stainless steel with different phases. Corros Sci 67:118–129
7. Seo M, Hultquist G, Leygraf C, Sato N (1986) The influence of minor alloying elements (Nb, Ti and Cu) on the corrosion resistivity of ferritic stainless steels in sulfuric acid solution. Corros Sci 26(11):949–960
8. AWS 5.9/A5.9M (2012) Specification for bare stainless steel welding electrodes and rods. American Welding Society, Miami
9. ASTM G5-14e1 (2014) Standard reference test method for making potentiodynamic anodic polarization measurements. ASTM International, West Conshohocken, PA
10. Revie RW, Uhlig HH (2008) Corrosion and corrosion control. Wiley, New Jersey
11. Moayed MH, Newman RC (2006) Evolution of current transients and morphology of metastable and stable pitting on stainless steel near the critical pitting temperature. Corros Sci 48(4):1004–1018
12. Hoar TP, Mears DC, Rothwell GP (1965) The relationships between anodic passivity, brightening and pitting. Corros Sci 5(4):279–289
13. Keller P, Strehblow HH (2004) XPS investigations of electrochemically formed passive layers on Fe/Cr alloys in 0.5 M H_2SO_4. Corros Sci 46(8):1939–1952
14. Srivastava SC, Ives MB (1989) The role of titanium in the pitting corrosion of commercial stainless steels. Corros J 45(6):488–493
15. Bonagani SK, Bathula V, Kain V (2018) Influence of tempering treatment on microstructure and pitting corrosion 13 wt.% Cr martensitic stainless steel. Corros Sci 131:340–354
16. Mischler S, Vogel A, Matheiu HJ, Landolt D (1991) The chemical composition of the passive film on Fe-24Cr and Fe-24Cr-11Mo studied by AES, XPS and SIMS. Corros Sci 32(9):925–944
17. Lothongkum G, Chaikittisilp S, Lothongkum AW (2003) XPS investigation of surface films on high Cr-Ni ferritic and austenitic stainless steels. Appl Surf Sci 218(1–4):203–210

Corrosion Resistance of GX4CrNiMo16-5-1 Martensitic, 316L Austenitic, and 904L Austenitic Stainless Steels Subjected to High Temperature Variation

Roland Tolulope Loto, Cleophas Akintoye Loto and Muyiwa Fajobi

Abstract Study of the effect of high temperature at 1000 °C on the corrosion resistance of GX4CrNiMo16-5-1 martensitic, 316L austenitic, and 904L austenitic stainless steels in 2 M H_2SO_4/3.5% NaCl solution was done through potentiodynamic polarization technique, potentiostatic method, and optical microscopy analysis. Untreated GX4CrNiMo16-5-1 steel displayed the highest corrosion rate of 4.775 mm/year while untreated 904L steel showed the lowest corrosion rate of 1.043 mm/year. Alteration of the microstructural properties of the steels due to high temperature exposure significantly decreased the corrosion rates of the stainless steels to 2.167, 1.396, and 0.519 mm/year. 904L steel exhibited the least significant metastable pitting activity among the untreated steels due to higher resistance to transient pit formation. Heat treated GX4CrNiMo16-5-1 steel lost its ability to passivate after anodic polarization. The heat treated steels were more resistant to pitting corrosion from observation of pitting potential values. The optical image of untreated and heat treated EN-1.4404 and EN-1.4539 steels was generally similar while the images for EN-1.4405 significantly contrast each other.

Keywords Corrosion · Pitting · Steel · Chloride · Passivation

Introduction

Stainless steels are universally applied worldwide due to their superior physical, mechanical, and corrosion resistance when compared to low alloys and carbon steels [1]. Corrosion resistance of stainless steels strongly influences their chemical properties in industrial conditions and consequentially impacts their lifespan during application [2–4]. Alteration of the microstructural configuration and metallurgical structure of stainless steels by heat treatment can either enhance or weaken their resistance to corrosion [5, 6]. Application of stainless steels in high temperature conditions such as in energy conversion plants, chemical and petrochemical industry, steam

R. T. Loto (✉) · C. A. Loto · M. Fajobi
Department of Mechanical Engineering, Covenant University, Ota, Ogun State, Nigeria
e-mail: tolu.loto@gmail.com

J. Li et al. (eds.), *Characterization of Minerals, Metals, and Materials 2020*,
The Minerals, Metals & Materials Series,
https://doi.org/10.1007/978-3-030-36628-5_24

boilers, and heat exchangers has become more prevalent due to the weak corrosion resistance of carbon and low-alloyed steels [7]. Lu et al. [8] studied the effect of heat treatment on the microstructural properties of plastic mold steel in chloride solution and determined the corrosion resistance of the steels increased with austenitizing temperature but decreased after tempering. Choi et al. [9] studied the effect of austenitizing temperature on the electrochemical performance 0.3C–14Cr–3Mo stainless steel in neutral chloride solutions and observed that increase in austenitizing temperature caused a proportionate increase in pitting corrosion of the steel due to the precipitation of carbides within the steel matrix. This article focuses on the effect of high temperature variation between 1000 and 37 °C on the corrosion resistance behaviour of GX4CrNiMo16-5-1 martensitic, 316L austenitic, and 904L austenitic stainless steels in 2 M H_2SO_4/3.5% NaCl solution.

Experimental Methods

Untreated GX4CrNiMo16-5-1 martensitic, 316L austenitic, and 904L austenitic stainless steels specimens (UN-GX4, UN-316 and UN-904) and their heat treated counterparts (HT-GX4, HT-316, and HT-904) were machined and subsequently embedded in resin mounts with exposed surface areas of 1 cm^2 and metallographically prepared with silicon carbide papers. 800 mL of 0.05 M H_2SO_4 solution at 3.5% NaCl concentration were prepared from standard grade reagent of the acid (98% purity) and NaCl (recrystallized). The stainless steels for heat treatment were subjected to repetitive heat treatment process in a muffle furnace at 1000 °C, sustained at the temperature for about 30 min, and naturally cooled to room temperature. The temperature was maintained with a regulator at an accuracy ±10 °C linked with a thermocouple (K-Type) to achieve the required temperature. Electrochemical test of the stainless steels was performed with Digi-Ivy potentiostat which consists of triple electrode configuration (embedded stainless steel electrode), Ag/AgCl reference electrode, and platinum wire counter electrode. Polarization curves were plotted at scan rate of 0.0015 V/s from −1.5 to +1.5 V. Morphological characterization of the untreated and heat treated stainless steel specimens was done before and after corrosion test with Omax trinocular metallurgical microscope for comparative analysis.

Results and Discussion

Potentiodynamic Polarization Studies

Table 1 shows the data obtained from the polarization test. Among the untreated steels UN-GX4 displayed the highest corrosion rate value at 4.775 mm/year corresponding to corrosion current density of 4.44×10^{-4} A/cm^2 and polarization resistance

Table 1 Potentiodynamic polarization data of untreated and heat treated GX4CrNiMo16-5-1 martensitic, 316L austenitic, and 904L austenitic stainless steels in 2 M H_2SO_4/3.5% NaCl

Untreated steels

Steel	Corrosion rate (mm/year)	Corrosion current (A)	Corrosion current density (A/cm^2)	Corrosion potential (V)	Polarization resistance, R_p (Ω)	Cathodic potential, B_c (V/dec)	Anodic potential, B_a (V/dec)
UN-GX4	4.775	4.44E−04	4.44E−04	−0.311	57.82	−8.814	3.272
UN-316L	1.934	1.80E−04	1.80E−04	−0.283	142.8	−8.458	1.232
UN-904L	1.043	9.96E−05	9.96E−05	−0.216	258.0	−4.732	−3.893

Heat treated steels

Steel	Corrosion rate (mm/year)	Corrosion current (A)	Corrosion current density (A/cm^2)	Corrosion potential (V)	Polarization resistance, R_p (Ω)	Cathodic potential, B_c (V/dec)	Anodic potential, B_a (V/dec)	% Change in Corrosion rate
HT-GX4	2.167	2.02E−04	2.02E−04	−0.362	127.4	−5.995	6.687	54.61
HT-316L	1.396	1.30E−04	1.30E−04	−0.269	198.7	−5.794	1.094	27.83
HT-904L	0.519	4.95E−05	4.95E−05	−0.235	518.9	−8.231	7.117	50.28

of 57.82 Ω. The corrosion rate of UN-904L was the lowest at 1.043 mm/year due to higher corrosion resistance compared to the other steels. The value and trend in corrosion potential values of the steels studied show anodic tendency associated with vulnerability to surface oxidation. These values align with the corrosion rate results obtained. Heat treatment significantly enhanced the corrosion resistance of the steels studied. The corrosion rate of HT-GX4, HT-316L, and HT-904L steels reduced by 54.61, 27.83, and 50.28% to 2.167 mm/year, 1.396 mm/year, and 0.519 mm/year. Changes in the microstructure and metallurgical properties of UN-GX4 (HT-1.4404) occurred due to heat treatment. The changes suppressed the H_2 evolution and O_2 reduction reactions on the steel surface. The corrosion potential of the heat treated steels (HT-GX4, HT-316L, and HT-904L) shifted to −0.362 V, −0.269 V, and −0.235 V. HT-GX4 and HT-904L exhibited cathodic shift due to reasons earlier stated while HT-316L shifted in the anodic direction due to decrease in the dominant oxidation reactions on its surface.

Passivation and Pitting Resistance Studies

Table 2 shows the potentiostatic data (metastable pitting, stable pitting, and passivation range) for the localized corrosion resistance of the untreated and heat treated steels studied in 2 M H_2SO_4/3.5% NaCl solution. UN-904L exhibited the shortest metastable pitting activity among the untreated steels following anodic polarization due to higher resistance of the steel to transient pit formation. Metastable pits initiated at −0.156 V (7.95×10^{-3} A) and ceased at 0.035 V (1.03×10^{-5} A). The

Table 2 Potentiostic data for the corrosion resistance of untreated and heat treated GX4CrNiMo16-5-1 martensitic, 316L austenitic, and 904L austenitic stainless steels in 2 M H_2SO_4/3.5% NaCl solution

Untreated Steel							
Steel	Metastable pitting potential (V)	Metastable pitting current (A)	Passivation potential (V)	Passivation current (A)	Pitting potential (V)	Pitting current (A)	Passivation range (V)
UN-GX4	−0.156	7.95E−03	0.035	1.03E−05	1.014	1.40E−04	0.979
UN-316L	−0.177	5.05E−03	0.010	2.90E−05	1.001	8.05E−05	0.991
UN-904L	−0.157	8.45E−04	0.030	9.49E−06	1.011	1.33E−04	0.981
Heat treated steel							
Steel	Metastable pitting potential (V)		Passivation potential (V)	Passivation current (A)	Pitting potential (V)	Pitting current (A)	Passivation range (V)
HT-GX4	–	–	–	–	–	–	–
HT-316L	−0.179	3.80E−03	−0.115	1.43E−02	1.014	4.77E−04	1.129
HT-904L	−0.159	6.90E−04	−0.093	2.40E−04	1.008	1.42E−04	1.101

metastable activity of UN-GX4 was the widest due to relatively weak resistance to transient pit formation. The activity extended from 7.95×10^{-3} to 1.03×10^{-5} A. HT-GX4 was unable to passivate after anodic polarization as a result the changes in the microstructural configuration of the steel. The metastable pitting activity of HT-316L and HT-904L initiated at −0.179 V and −0.159 V and stopped at −0.115 V and −0.093 V due to passivation as earlier mentioned. The pitting potential of the untreated steels is closely similar at 1.014, 1.001, and 1.011 V. Observation of the pitting current value shows UN-316L and UN-904L steels are more resistance to stable pit formation due to the higher pitting current values. The pitting current of the heat treated steels is generally higher than the untreated steels signifying increased pitting resistance. Comparison of the passivation range of the untreated and heat treated steels shows heat treatment extended the passivation range value of UN-1.4404 and UN-1.4539 steels at 0.991 V and 0.981 V to 1.129 V and 1.101 V (HT-316L and HT-904L).

Optical Microscopy Studies

Optical images of untreated and heat treated GX4CrNiMo16-5-1 martensitic, 316L austenitic, and 904L austenitic stainless before corrosion and after corrosion are shown from Figs. 1a, 2, and 3c. Figure 1a–c shows the optical images of UN-GX4, UN-316L, and 904L stainless steels before corrosion. Figure 2a–c shows the optical images of UN-GX4, UN-316L, and UN-904L stainless steels after corrosion while Fig. 3a–c shows the optical images of HT-GX4, HT-316L, and HT-904L stainless steels after corrosion. The optical image of UN-GX4 after corrosion (Fig. 2a) significantly differs from its un-corroded counterpart (Fig. 1a). Deep contoured grain boundaries are clearly visible in Fig. 1a with a minor pitted surface. The morphology of UN-316L (Fig. 2b) is less corroded with larger grain sizes and thinner grain

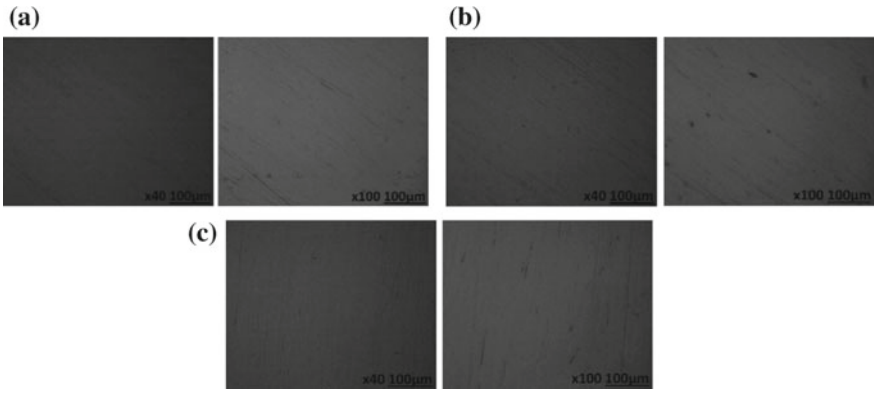

Fig. 1 Morphology of **a** UN-GX4, **b** UN-316L, and **c** UN-904L stainless steels before corrosion

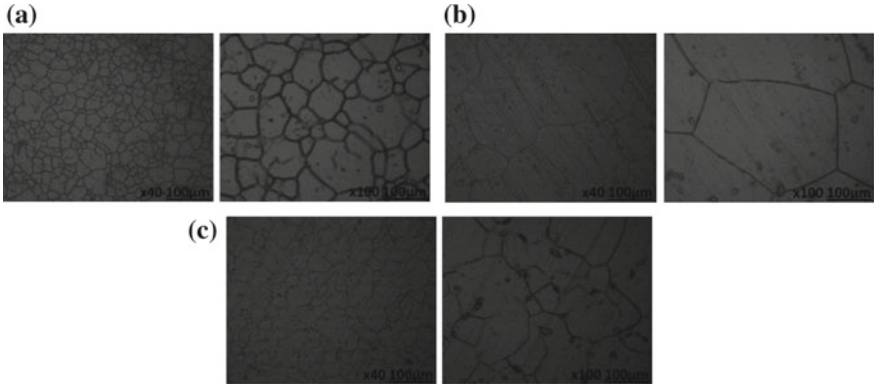

Fig. 2 Morphology of **a** UN-GX4, **b** UN-316L, and **c** UN-904L after corrosion in 2 M H_2SO_4/3.5% NaCl solution

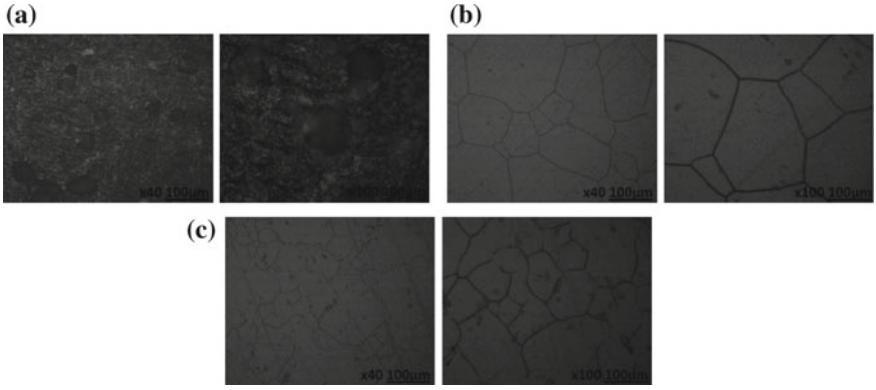

Fig. 3 Morphology of **a** HT-GX4, **b** HT-316L, and **c** HT-904L after corrosion in 2 M H_2SO_4/3.5% NaCl solution

boundary. This observation is due to its microstructural constituent which differs from UN-GX4 steel. The morphologies in Fig. 2a–c shows the steels are resistant to pitting corrosion, but somewhat more vulnerable to intergranular corrosion with UN-GX4 (Fig. 2a). Heat treatment had no significant effect on the morphological configuration of HT-316L and HT-904L stainless steels (Fig. 3a, b). However, the morphology of HT-GX4 was significantly influenced by changes in its microstructure, resulting in badly corroded morphology and corrosion pits.

Conclusion

High temperature variation on GX4CrNiMo16-5-1 martensitic, 316L austenitic, and 904L austenitic stainless steels significantly improved their general and localized corrosion resistance in dilute chloride/sulphate solution. The pitting current of the heat treated steels was generally higher than the untreated steels signifying increased pitting resistance. The passive film characteristics of 316L and 904L austenitic stainless steels were more resistant to corrosion after heat treatment compared to the untreated steels. Untreated and heat treated GX4CrNiMo16-5-1 steel displayed the lowest corrosion resistance compared to 904L austenitic steel which showed the highest resistance. The effect of heat treatment on the morphology on 316L and 904L austenitic stainless steels was insignificant compared to the morphology of GX4CrNiMo16-5-1 which was significantly altered and corroded after heat treatment.

Acknowledgements The authors appreciate Covenant University for their support for the research.

Conflict of Interest The author declares no conflict of interest.

References

1. Chan KW, Tjong SC (2014) Effect of secondary phase precipitation on the corrosion behavior of duplex stainless steels. Materials 7(7):5268–5304
2. Loto RT, Loto CA (2018) Corrosion behaviour of S43035 ferritic stainless steel in hot sulphate/chloride solution. J Mater Res Technol 7(3):231–239
3. Loto RT (2018) Effect of elevated temperature on the corrosion polarization of NO7718 and NO7208 nickel alloys in hot acid chloride solution. J Bio Tribo Corros 4(71). https://doi.org/10.1007/s40735-018-0190-8
4. Loto RT (2017) Study of the corrosion behaviour of S32101 duplex and 410 martensitic stainless steel for application in oil refinery distillation systems. J Mater Res Technol 6(3):203–212
5. Rajan A (1998) Heat treatment principles and techniques. Prentice Hall of India, New Delhi, pp 1–6
6. Loto RT, Aiguwurhuo O, Evana U (2016) Corrosion resistance study of heat treated 420 martensitic stainless steel and 316 austenitic stainless steel in dilute acid concentrations. Rev Téc Ing Univ Zulia 39(7):35–40
7. Stainless steel—high temperature resistance. Available at http://www.azom.com/article.aspx?ArticlEID=1175. Accessed 02:03:19
8. Lu S, Yao K, Chen Y, Wang M, Ge X (2015) Influence of heat treatment on the microstructure and corrosion resistance of 13 Wt %Cr-type martensitic stainless steel. Metall Mater Trans A 46A:6090–6102
9. Choi YS, Kim JG, Park YS, Park JY (2007) Austenitizing treatment influence on the electrochemical corrosion behavior of 0.3C–14Cr–3Mo martensitic stainless steel. Mater Lett 61(1):244–247

Part VII
Characterization of Electronic and Magnetic Materials

Influence on the Structural and Magnetic Properties of the Pre-alloyed Gas-Atomized Maraging Steel Powder During Mechanical Milling

G. V. Thotakura, R. Goswami and T. V. Jayaraman

Abstract We investigated the influence on the structural and magnetic properties of gas-atomized maraging steel powder during mechanical milling. The as-received powder comprised, primarily, martensite phase (α) and traces of retained austenite (γ); the saturation magnetization (M_S) and intrinsic coercivity (H_{CI}), at 300 K, were ~176 Am^2/kg and ~3 kA/m, respectively. Powders milled from 3 to 8 h comprised nanocrystalline α; the M_S and H_{CI} ranged from ~164 to 169 Am^2/kg and ~4.9 to 6.7 kA/m, respectively. Milling above 8 h formed austenite and extraneous intermetallic phases, reduced M_S, and increased H_{CI}. The M_S increased with the decrease in the temperature from 300 to 60 K, for both the as-received and milled powders. The thermomagnetic behavior of the as-received and the milled powders from 300 to 900 K was fairly reversible. The magnetic properties of as-received and powder milled for 5 h were comparatively better than the powder milled for 56 h.

Keywords Maraging steel powders · Mechanical milling · Nanocrystalline · Magnetic properties

Introduction and Background

Maraging steels are a class of high-strength steels known for low carbon content (~0.01 wt%) and weighty alloying additions Ni, Co, and Mo [1]. The strengthening effect is because of the intermetallic precipitate during the aging process [1–6]. The term "maraging" is the combination of "mar" (from martensite) and "aging" (from age hardening). There are several grades of maraging steels, which are 18 Ni (200), 18 Ni (250), 18 Ni (300), and 18 Ni (350) that typically constitute ~18 wt% Ni and varying wt% of Co, Mo, and Ti and have yield strength 200 ksi, 250 ksi, 300 ksi, and

G. V. Thotakura · T. V. Jayaraman (✉)
Department of Mechanical Engineering, University of Michigan, Dearborn 48128, USA
e-mail: tvjraman@umich.edu

R. Goswami
Naval Research Laboratory, Materials Science and Technology Division, Washington, DC 20375, USA

J. Li et al. (eds.), *Characterization of Minerals, Metals, and Materials 2020*,
The Minerals, Metals & Materials Series,
https://doi.org/10.1007/978-3-030-36628-5_25

350 ksi, respectively. The hardening in maraging steels is due to the formation of precipitates of the intermetallic compounds between Ni and Mo, Ni and Ti or among other alloying elements. The age hardening improves the properties, characterized by high tensile strength combined with high toughness, good weldability, and decent corrosion resistance compared to conventional high-strength steels [1–8].

Several research investigations have been carried out on the effects on the properties of maraging steels due to various synthesis techniques and processing variables such as aging duration, aging temperatures, changes in the composition, and so forth [1–16]. These steels find a wide range of applications in aerospace, hydrospace, tooling, and the rest [1–11]. The maraging steels in the bulk form are known to exhibit decent magnetic properties [12–16], while in the powder form their magnetic properties have not yet been characterized. The grain size and the phase distribution significantly affect the magnetic properties in materials [17]. Mechanical milling is known to reduce particle size, grain size, and induce phase transformations [18]. Hence, it is essential to investigate the phase evolution and associated changes in the magnetic properties during mechanical milling.

We investigated the influence on the structural and magnetic properties of the pre-alloyed gas-atomized maraging steel powder during mechanical milling at ambient and pressure. Magnetic characterization of the pre-alloyed gas-atomized maraging steel powder and the milled powders was performed at sub-ambient temperatures, as low as ~60 K. The thermomagnetic behavior of the powders was also investigated.

Materials and Methods

Material Synthesis

Pre-alloyed maraging steel powder, produced by inert gas atomization technique, was procured from an original manufacturer (EOS North America Inc.). The composition of the procured pre-alloyed gas-atomized maraging steel (as-received) powder was 18.5 wt% Ni, 8.7 wt% Co, 4.9 wt% Mo, 0.7 wt% Ti, 0.1 wt% Al, 0.1 wt% Cr, 0.07 wt% Mn, 0.03 wt% Cu, 0.02 wt% Si, 0.01 wt% C. 0.01 wt% S, <0.01 wt% P, balance Fe [19]. The composition is atypical to 18 wt% Ni (300) maraging steel [4, 5]. For milling, a high energy ball mill (SPEX SamplePrep 8000D mill) was used. Hardened steel vial and hardened steel balls (SPEX 8001) were the milling media. The ball-to-powder ratio adopted during the milling was 8:1. Stearic acid was the process control agent (PCA) during the milling process to avert any cold welding between the balls and with the vial walls. All the material handling—loading, sealing, and unloading of the powder particles, along with the balls and PCA, into the vial, were performed at ambient temperature and pressure conditions. Mechanical milling was performed as a cycle of 3 h of milling. A small amount of sample was removed from the vial at certain hours of milling and stored in glass vials as a representative of the hours of milling. Intermittent stoppages for ~½ h (cooldown period) were provided to rest the mill motor to prevent damage due to excessive heating.

Characterization

For structural characterization, the powders were analyzed in a Rigaku MiniFlex 600 diffractometer and JOEL IT500 Scanning electron microscope. The phase identification and the phase evolution in the powders were identified from the X-ray diffraction (XRD) patterns recorded. The source of X-ray was Cu K_α radiation (with wavelengths of $K_{\alpha 1}$ ~0.15406 nm and $K_{\alpha 2}$ ~0.15444 nm) at a voltage and current of 40 kV and 15 mA, respectively. The ($\theta - 2\theta$) scans were recorded between the 2θ angles 20°–100° with a step size of 0.02°. Structural characteristics such as lattice parameter and grain size/lattice strain of the powders were estimated from XRD patterns by using Bragg's equation and Williamson–Hall method, respectively [18]. The morphology of the powders and the powder particle size was evaluated from the SEM micrographs in an image processing software ImageJ 1.8. The statistical analysis of the particle size distribution is performed using a commercially available statistical analysis software MINITAB®. Magnetic characterization was performed in a vibrating sample magnetometer (VSM)–Quantum Design VersaLab 3-T Vibrating Sample Magnetometer. The magnetic properties—saturation magnetization (M_S) and intrinsic coercivity (H_{CI}) of the powders—were approximated from the magnetization (M) versus applied magnetic field (H) curves (hysteresis loops) at ambient temperature (300 K), at sub-ambient temperatures (as low as ~60 K). Thermomagnetic curves, magnetization (M) versus temperature (T), from ~300 to 900 K were generated to understand the nature of the milled powders, reversible, irreversible, or possible occurrence of phase changes upon exposure to elevated temperature.

Results and Discussions

Structure and Magnetic Properties at Ambient Temperature

Figure 1a shows the X-ray diffraction (XRD) patterns at the ambient temperature of the as-received powders (AR) and milled powders (milled for 3, 5, 8, 14, 20, 23, 35, 47, and 56 h). The evolution and the presence of different phases during milling show three different regions. Region 1 corresponds to the as-received powder, which consists of predominantly martensite (α) phase and traces of retained austenite (γ) phase. Region 2 corresponds to milling the as-received powder up to 8 h and shows the presence of predominantly the α phase having broadened peaks indicating the probable presence of nanocrystalline grains, or lattice strain, or both. With continued milling, 14 h and beyond (Region 3), the peak broadening further increased coupled with the evolution of some extraneous phases (probably the precipitates of Ni_3(Mo, Ti) and Fe_2Mo), present along with α and γ phase.

Figure 1b, c presents the estimated lattice parameter and lattice strain/average grain size, respectively, of the α phase in the as-received and milled (3, 5, and 8 h) powders. In the powders milled for more than 8 h, it was arduous to deconvolute

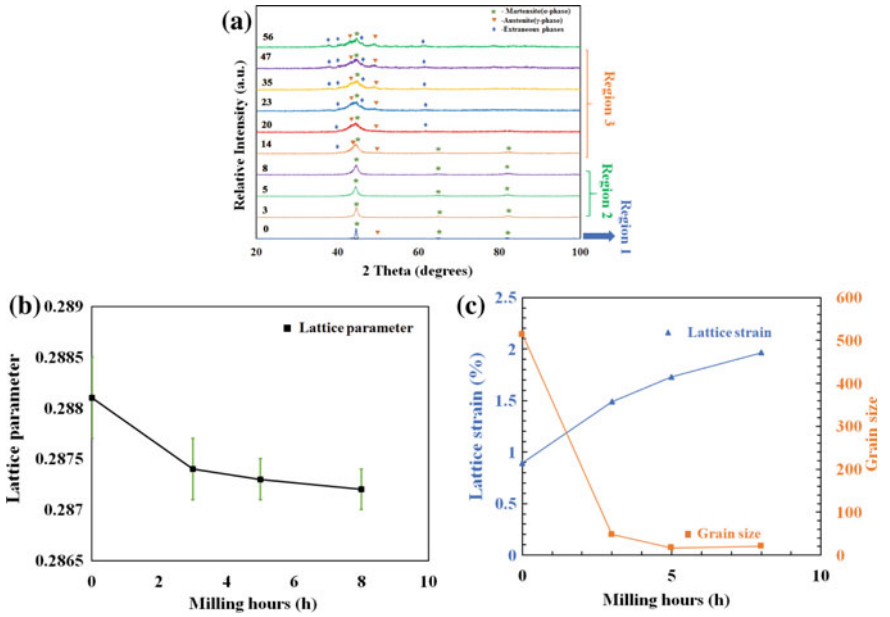

Fig. 1 **a** X-ray diffraction spectra of the milled powders (3, 5, 8, 14, 20, 23, 35, 47, and 56 h) and the as-received (AR) powder. The **b** lattice parameter and **c** lattice strain and grain size of the as-received and milled (3, 5, and 8 h) powders estimated from their respective XRD spectra, at ambient temperature

the high-intensity peaks (broadened) of the α phase that overlapped with the high-intensity peaks of the precipitates (extraneous phases). Hence, the grain size, lattice parameter, and the lattice strain of the milled powders in Region 3 are not reported in this investigation. The lattice parameter of the α phase in as-received powder was estimated to be ~0.2881 $\pm$ 0.0004 nm which is close to the lattice parameter of the α phase in maraging 300 steel (~0.2886 nm) [10]. The lattice parameter of the α phase in milled (3, 5, and 8 h) powders decreased compared to the as-received powder and maintained quite a constant value of ~0.2873 $\pm$ 0.0004 nm. This decrease in the milled powders is due to the high energy ball milling of that led to the combined effect of the presence of nanocrystalline grains and lattice distortion (due to lattice strain). While the grain size and lattice strain of the as-received powder and the milled powders were estimated to be ~513 nm and 0.89% (AR), ~48 nm and 1.49% (3 h), ~17 nm and 1.73% (5 h), ~21 nm and 1.96% (8 h), respectively. Lattice strain increased and the grain size reduced with the increase in milling time due to the repeated fracturing and cold welding of the powders during the milling. Thus, the maraging steel milled for 3, 5, and 8 h (Region 2) is in the nanocrystalline regime. The grain size and lattice strain reported in this investigation are preliminary results, and further analysis, including transmission electron microscopy, is currently underway. The presence of nanocrystalline grains facilitates diffusion paths for phase transformation; hence, milling above 8 h resulted in phase changes leading to extraneous phases.

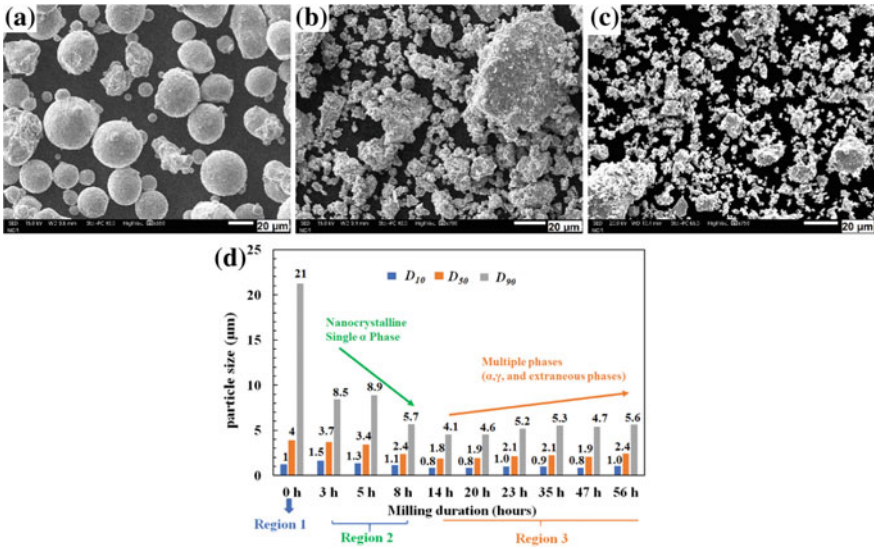

Fig. 2 Scanning electron micrographs of the **a** as-received powder (0 h) and milled powders **b** 5 h, and **c** 56 h, at ~750 X as a representative for each of the regions (1, 2, and 3); **d** D_{10}, D_{50}, and D_{90} of the as-received and the milled powders

Figure 2a–c shows the scanning electron micrographs of the as-received powder, powders milled for 5 and 56 h, as a representative of the three regions (1, 2, and 3). The morphology of the as-received powder was predominantly spherical, having minuscule levels of deformed particles. The milled powders were irregularly shaped, and the size distribution of the powders particles was somewhat inhomogeneous, consisting of predominantly finer particles coupled with a fair number of coarser particles probably due to the agglomeration of the particles due to excessive cold welding. The powder particle size characteristics D_{10} (the particle size equals to or less than 10% of the powder particles by population), D_{50}, and D_{90} of the as-received and milled powders were estimated from the SEM images, shown in Fig. 2d. The D_{90} of the as-received powder was ~21 μm. Powder particle size reduced with the milling duration in the Region 2. The D_{90} of the nanocrystalline maraging steel powders (in Region 2), milled for 3 h, 5 h, and 8 h is ~8.5 μm, ~8.9 μm, and ~5.7 μm, respectively. Subsequently, in Region 3, the particle size increased with an increase in milling duration. The increase in the particle size is most likely due to the increase in cold welding which results in the agglomeration of the powder and forming coarser particles.

Figure 3 presents the magnetization (M) versus the applied magnetic field (H) curves of the as-received and milled powders at ambient temperature. The saturation magnetization (M_S) decreased with the increase in milling duration. The M_S of the as-received powder is estimated as 176 ± 2 Am^2/kg. The M_S of maraging 300 steel sheet specimen at ambient temperature was reported ~188 Am^2/kg [16]. The decrease

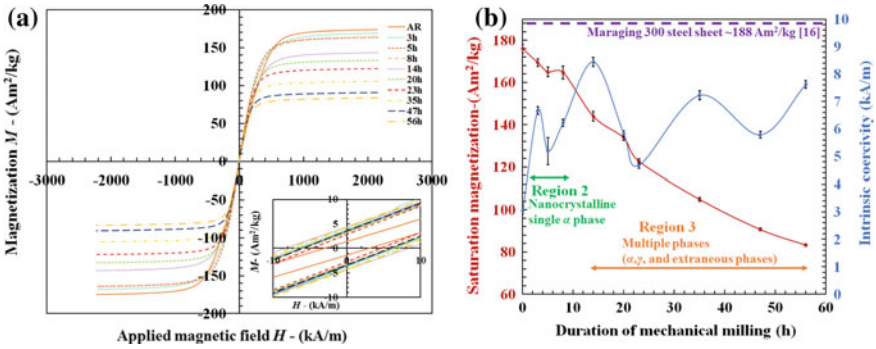

Fig. 3 **a** Magnetization (M) versus applied magnetic field (H) curves; inset shows the M–H curves at low magnetic field region (±10 kA/m), and the variation of **b** saturation magnetization (M_S) and intrinsic coercivity (H_{CI}) of the as-received and milled maraging steel powders

in M_S, by ~6%, is probably due to the increased surface area in powders, which results in a relatively higher degree of magnetic disorder in powders. The M_S of the milled powders for a duration of 3 h, 5 h, and 8 h decreased to 169.3 ± 1.8 Am^2/kg, 165.5 ± 1.5 Am^2/kg, and 164.7 ± 3.1 Am^2/kg, respectively. The decrease in M_S in the milled powders till 8 h could be due to the combined effect of reduced grain size and particle size when compared with the as-received powder. The increase in the grain boundary area and surface area typically results in a higher degree of magnetic disorder in the grain boundary region and particle surface compared to the grain interior and particle core, respectively [17]. The observed trend of M_S with milling time is shown in Fig. 3b. The M_S of maraging steel in sheet form [16] is included in the figure (dashed line) to compare with the M_S of as-received and milled maraging steel powders, in the present investigation. With further milling, the M_S decreased at a steeper rate which is accommodated just not only due to the reduction in the grain size and the particle size but also the combined effect of the presence of extraneous phases-austenite and probably the precipitates of Ni_3(Mo, Ti) and Fe_2Mo [12–16]. Formation of austenite associated with the precipitates started to occur after aging at high temperatures and which resulted in a decrease in the M_S [16]. The increase in the content of precipitates and the austenite in the milled powders reduce the M [13]; thus, M_S decreased. *I*ntrinsic coercivity (H_{CI}) changed irregularly with an increase in the duration of milling following a similar trend, shown in Fig. 3b. H_{CI} of the as-received powder was estimated to be ~3.0 ± 0.1 kA/m. The H_{CI} of the milled powders fluctuated between ~4.7 ± 0.1 and 8.4 ± 0.1 kA/m. The fluctuation of H_{CI} in the milled powders is probably due to the influence of a myriad of factors. The H_{CI} is a structure-sensitive property, and it is strongly influenced by the magnetocrystalline anisotropy, grain size, particle size, lattice strain, and the phase(s) present. H_{CI} increased in the milled powders when compared with the as-received powders which can be attributed as the effect of the decrement in the grain size, particle size, and increment in the lattice strain during the milling process, also the evolution of new phases due to milling for a longer duration.

Magnetic Properties at Sub-ambient Temperatures

The M versus H curves of as-received powder as well as the milled powders (5 and 56 h) at sub-ambient temperatures (as low as ~60 K) are shown in Fig. 4a–c. The variation of M_S with temperature T is shown in Fig. 4d. The M_S increased with decrease in temperature irrespective of milling duration, which was expected, as an increase in temperature decreases magnetic ordering [17]. The decrease in the M_S from ~300 to 60 K followed two different rates. The as-received and the nanocrystalline (milled for 5 h) maraging steel powder showed a decrease with the increase in temperature by ~5–7%, while the powder milled for 56 h showed a substantial decline ranging from ~8 to 16%. For ferromagnetic materials, the dependence of M_S on T in the region of low temperatures is given by Bloch's law [17]:

$$M_S(T) = M_S(0)\left[1 - AT^{3/2}\right] \tag{1}$$

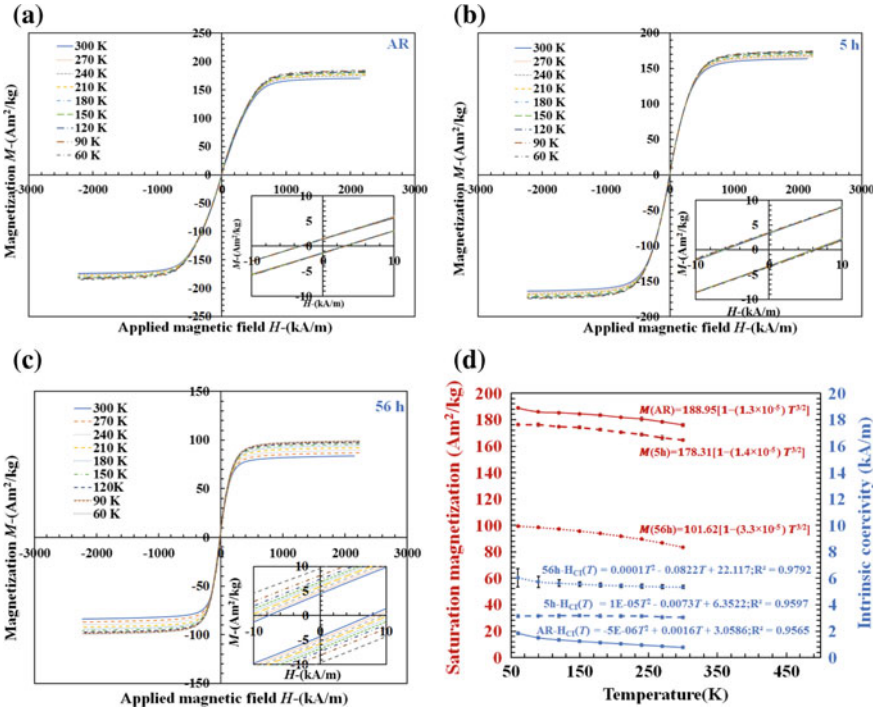

Fig. 4 Magnetization (M) versus applied magnetic field (H) curves of the **a** as-received powder and the milled powders for **b** 5 h, **c** 56 h from temperatures of 300–60 K, respectively. The inset in each figure shows the M versus H curves in a low magnetic field region of ±10 kA/m. Variation of **d** saturation magnetization (M_S) and intrinsic coercivity (H_{CI}) of the as-received and milled maraging steel powders

where M_S (0) is the saturation magnetization at absolute zero (0 K), and A is a constant [17]. By fitting the experimental results in Eq. 1, from the sub-ambient runs, M_S (0) and A of the samples were estimated and are plotted next to their respective M_S in Fig. 4d. M_S (0) reduced and A increased with the increase in milling duration. The M_S (0) and A of as-received, 5 h, and 56 h are ~188.9 Am^2/kg and ~1.3 × 10^{-5} $K^{-3/2}$, ~178.3 Am^2/kg and ~1.4 × 10^{-5} $K^{-3/2}$, and ~101.6 Am^2/kg and ~3.3 × 10^{-5} $K^{-3/2}$, respectively. Variation of H_{CI} was estimated (see Fig. 4d). It can be observed that the as-received powder showed a negligible change with temperature, while the nanocrystalline milled maraging steel powder (milled for 5 h) shows a minimal change of ~5% with the as-milled powders at 300 K. Powder milled for 56 h showed a higher rate of increase by ~1.8 times in H_{CI} with the decrease in temperature from 300 to 60 K. The observed decrease in the powders could be due to the decrease in the anisotropy field with an increase in temperature. These trends fit (quadratic), and their values at absolute 0 K were obtained by extrapolating their respective curves to absolute 0 K. Overall, the as-received powder and the milled powder for 5 h showed better magnetic properties compared to the powders milled for 56 h, even at the sub-ambient temperatures.

The Thermomagnetic Behavior

The thermomagnetic curves (M vs. T) were plotted for the as-received (Region 1) and the milled powders for 5 h (Region 2), 56 h (from Region 3). The magnetic field was set to ~79.6 kA/m, and the magnetization was measured from temperatures 300–900 K at a sweep rate of ~5 K/min in two different cycles: (1) heating (300–900 K) and (2) cooling (900–300 K). Two consecutive M versus T runs were performed on these powders, Fig. 5a–c. The as-received powder and milled powders showed a reversible behavior in both the M versus T runs. During the heating cycle, with the increase in temperature results decrease in M due to the thermal effect on magnetic ordering [17]. Thus, the decrease in the M of the as-received during the heating cycle in the 1st M versus T run could be attributed as due to this effect. In the case

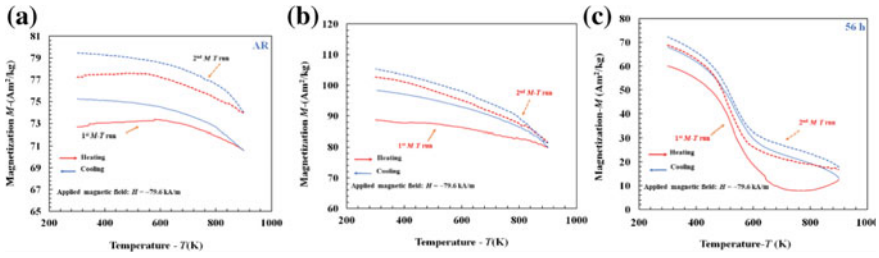

Fig. 5 Thermomagnetic curves (M vs. T) of the **a** as-received powder and the as-milled powders of **b** 3 h, and **c** 56 h; from 300 to 900 K and return, at ~5 K/min, and at an applied magnetic field (H) ~79.6 kA/m

of milled powder for 5 h, the decline is due to the decrease in magnetic ordering. Similarly, during the cooling cycle, the M value increased gradually with the decrease in temperature. The M of the as-received increased by ~4% at the end of the 1st M versus T run (when compared with the M at the end and the start of M at 300 K of the 1st M vs. T run), while the increase in M was by ~3% after the 2nd M versus T run. In the case of milled powder for 5 h, there was a significant increase in M by ~12% in these samples after the 1st M versus T run, while the increase in M was by ~3% after the 2nd M versus T run. On the other hand, milled powder for 56 h showed a different trend in the M versus T runs. In the heating cycle, M gradually decreased with the increase in temperature until ~400 K followed with a steep decrease in M till ~650 K and reaching a minimum value of ~8 Am^2/kg (~750 K). After that, the M started to increase gradually and reached ~12 Am^2/kg at ~900 K, which could be probably due to the phase transformation (extraneous phase) results in the fluctuation of M at that regime.

While in the cooling cycle, M followed a similar trend as 1st M versus T run showing the reversible behavior. The as-received powder and the milled powder for 5 h are stable up to ~900 K and possessed better magnetic properties. Thus, it is important to study the magnetic properties at elevated temperatures and also that if annealing could improve the magnetic properties of the powder. Further investigation at elevated temperatures is in progress.

In this work, the influence on the structural and magnetic properties of the pre-alloyed gas-atomized maraging steel powder during mechanical milling was investigated. Magnetic characterization of the as-received powders and the milled powders was performed at sub-ambient temperatures and elevated temperatures. The magnetic properties of as-received and powder milled for 5 h were comparatively better than powder milled for 56 h. Future work includes transmission electron microscopy characterization of the milled powders at ambient temperature to identify the intermetallic precipitates. Also, the effect of structural and magnetic properties of the powders is at elevated temperatures, annealing studies, and the thermally treated powders.

Summary and Conclusions

The influence on the structural and magnetic properties of the pre-alloyed gas-atomized maraging steel powder during mechanical milling was investigated. The as-received maraging steel powder was comprised of the martensite (α) and traces of retained austenite (γ). The saturation magnetization (M_S) and intrinsic coercivity (H_{CI}) of the as-received powder at ambient temperature was ~176 Am^2/kg and ~3 kA/m, respectively. Mechanical milling of the as-received powder till 8 h formed nanocrystalline α phase, grain size <50 nm. The lattice parameter was estimated to be ~0.2873 nm. D_{90} for the nanocrystalline milled powders (milled for 3, 5, and 8 h) was estimated as ~8.5 μm, ~8.9 μm, and ~5.7 μm, respectively, while milling for more than 8 h resulted in the formation of austenite and other extraneous phases of

precipitates. The M_S decreased with the increase in the milling duration, while the H_{CI} showed no specific trend. The M_S and H_{CI} of the nanocrystalline milled powders (3, 5, and 8 h) ranged from ~164 Am^2/kg to ~169 Am^2/kg, ~4.9 kA/m to ~6.7 kA/m, and ~3.4 Am^2/kg to 3.9 Am^2/kg, respectively. M_S increased with the decrease in the temperature from 300 to 60 K, for both the as-received and milled powders. Also, the thermomagnetic behavior of the as-received and the milled powders (5 and 56 h) from 300 to 900 K showed a fairly reversible nature. Overall, the magnetic properties of as-received and powder milled for 5 h were comparatively better than the powder milled for 56 h.

Acknowledgements The authors would like to thank the College of Engineering and Computer Science and the Institute of Advanced Vehicle Systems at the University of Michigan in Dearborn for the financial and infrastructural support to conduct the experimental work.

References

1. Floreen S (1968) The physical metallurgy of maraging steels. Metall Rev 13(1):115–128. https://doi.org/10.1179/mtlr.1968.13.1.115
2. Detert K (1967) The influence of small cold deformation preceding aging in 15% and 18% nickel maraging steel. Trans Metall Soc AIME 239:553–556
3. Antisiferov VN, Kolbenev YM (1972) A maraging steel produced by powder metallurgy method. Poroshk Metall 4(112):40–43
4. Schmidt ML (1988) Maraging steels: recent developments and applications. The Minerals, Metals & Materials Society, pp 213–235
5. Rohrbach K, Schmidt ML (1990) Maraging steels. In: ASM handbook, vol 1: Properties and selection: irons, steels, and high-performance alloys, pp 793–800
6. Viswanathan UK, Dey GK, Asundi MK (1993) Precipitation hardening in 350-grade maraging steel. Metall Trans A 24A:2429–2442
7. Habiby F, Siddiqui TN, Hussain H, Haq AUL, Khan AQ (1996) Lattice changes in the martensitic phase due to ageing in 18 wt% nickel maraging steel grade 350. J Mater Sci 31:305–309
8. Kempen K, Yasa E, Thijs L, Kruth JP, Van Humbeeck J (2011) Microstructure and mechanical properties of selective laser melted 18Ni-300 steel. Phys Procedia 12:255–263
9. Pardal JM, Tavares SSM, Fonseca MPC, Abreu HFG, Silva JJM (2006) Study of the austenite quantification by X-ray diffraction in the 18Ni-Co-Mo-Ti maraging 300 steel. J Mater Sci 41:2301–2307
10. Zhu F, Yin YF, Faulkner RG (2011) Microstructural control of maraging steel C300. Mater Sci Technol 27(1):395–405. https://doi.org/10.1179/026708309X12506933873503
11. Castro Guiza GM, Oliveira CAS (2016) Microstructural changes produced by hot forging in a C300 maraging steel. Mater Sci Eng A 655:142–151
12. Ahmed M, Ali A, Hasnain SK, Hashmi FH, Khan AQ (1994) Magnetic properties of maraging steel in relation to deformation and structural phase transformations. Acta Mater 42(3):631–638
13. Ahmed M, Hasnain SK, Nasim I, Ayub H (1995) Magnetic properties of maraging steels about nickel concentration. Metall Mater Trans A 26:1869–1876
14. Tavares SSM, Abreu HFG, Neto JM, da Silva MR, Popa I (2003) A thermomagnetic study of the martensite–austenite phase transition in the maraging 350 steel. J Alloy Compd 358:152–156
15. Tavares SSM, da Silva MR, Neto JM, Pardal JM, Cindra Fonseca MP, Abreu HFG (2004) Magnetic properties of a Ni–Co–Mo–Ti maraging 350 steel. J Alloy Compd 373:304–311

16. Tavares SSM, da Silva MR, Neto JM, Pardal JM, Cindra Fonseca MP, Abreu HFG (2007) Influence of temperature and aging time on hardness and magnetic properties of the maraging steel grade 300. J Mater Sci 42:2276–2281
17. Bozorth RM (1993) Ferromagnetism, 3rd edn. IEEE Press, New York, pp 190–209
18. Suryanarayana C (2001) Mechanical alloying and milling. Prog Mater Sci 46:1–184
19. Metal powder EOS maraging steel MS1 (2018) Mill test certificate/material safety data sheet. EOS Finland

Phase Diagram of the InP Binary System

Shadia J. Ikhmayies

Abstract Indium phosphide is the only compound in the InP binary system, and it is a semiconducting material used in optoelectronics, microelectronics, and solar cells. Understanding the thermodynamic properties of this material is important for these applications. Phase diagram of the InP binary system was determined at 1 bar pressure and temperature range 200–1400 K using Thermo-Calc 2019b software and compared with experimental and calculated ones found in the literature. There are four phases and six fields of which are four mixed (double phase) fields. The melting points of In and P elements and InP compound were determined and all reactions are determined too.

Keywords Phase diagram · InP · Solar cells · CALPHAD · Thermo-Calc 2019b software

Introduction

Indium Phosphide (InP) is III-V compound semiconductor, which is the only compound that forms from indium–phosphorus (InP) system. It has a zincblende structure with lattice constants $a = 5.8697$ Å [1] and space group $F\bar{4}3m$ [2]. It has potential use in solar cells, electro-optic devices, high speed, and high power devices.

The knowledge of the phase diagram and thermodynamic properties of materials is essential for the development and improvement of preparation techniques [3]. There are few experimental data and studies about phase diagram and thermodynamic properties of the InP system [3]. All of these are old, where the most recent work is that of Yamaguchi et al. [4] in 1989. The objective of this work is to reproduce the phase diagram of the InP system using Thermo-Calc software 2019b and the most recent database embedded in it. The results are discussed and compared with previous works.

S. J. Ikhmayies (✉)
Physics Department, Faculty of Science, Isra University, Amman 11622, Jordan
e-mail: shadia_ikhmayies@yahoo.com

J. Li et al. (eds.), *Characterization of Minerals, Metals, and Materials 2020*,
The Minerals, Metals & Materials Series,
https://doi.org/10.1007/978-3-030-36628-5_26

Methodology

Thermo-Calc software was used in this work to perform the phase diagram of InP binary system. It is a powerful software package for the calculation of thermodynamic and phase equilibria. In conjunction with suitable thermodynamic databases, assessed using the CALPHAD approach, Thermo-Calc can be used for a wide variety of applications [5]. The CALPHAD method is based on the fact that a phase diagram is a representation of the thermodynamic properties of a system. Hence, if the thermodynamic properties are known, it will be possible to calculate the multi-component phase diagrams [6].

The template "Binary Calculation" with the type of calculation "phase diagram" was chosen to calculate the equilibrium phase diagram of the InP binary system in this work. The total pressure is 1 bar, and the temperature range was automatically selected 200–1400 K. The used database is the TCBIN: TC Binary Solutions v1.1 database and just stable phases were credited.

Results and Discussion

Figure 1 shows the phase diagram of the InP binary system obtained in this work using Thermo-Calc software 2019b using the template "Binary Calculation" of type "phase diagram". It shows four phases; the two pure components In (TETRAGONAL_A6) and P (RED P) at the terminals, the semiconducting compound InP (B_3_ZINCBLENDE) at 50 P mole percent, and the liquid phase. The semiconducting compound InP is treated as a stoichiometric (or line) compound. The liquid in the In-rich side is indium melt, in the P-rich side is P melt, and after the melting point of InP, the liquid consists of nonstoichiometric InP melt.

Figure 1 also shows six fields, two of them are one phase fields which are the liquid phase, which extends on the whole P mole percent, and stoichiometric indium phosphide (InP) at 50 P mole percent and temperature range 300–1326.73 K. The other four fields are mixed, double phase fields which are: First, B3_ZINCBLENDE + TETRAGONAL_A6 which consists of solid indium and solid In-rich InP, and this field covers the region in the range 0–50 P mole percent, and temperature range 300–429.75 K. Second, B3_ZINCBLENDE + RED_P which consists of solid P-rich InP and red P in the P mole percent range 50–100 and temperature range 300–852.54 K. Third, LIQUID + B3_ZINCBLENDE which consists of liquid indium and solid In-rich InP, and this field extends from 0 to 50 P mole percent range and temperature range between melting points of In and InP. Fourth, LIQUID + B3_ZINCBLENDE which consists of liquid P and P-rich InP, and this field covers the range 50–100 P mole percent, and temperature range between melting temperatures of InP and P.

From Fig. 1 the melting points of In and P are 429.75 ± 0.025 K or (156.60 ± 0.025 °C) and 852.54 ± 0.025 K or (579.39 ± 0.025 °C), respectively. The melting point of InP is 1326.73 ± 0.025 K or (1053.58 ± 0.025 °C).

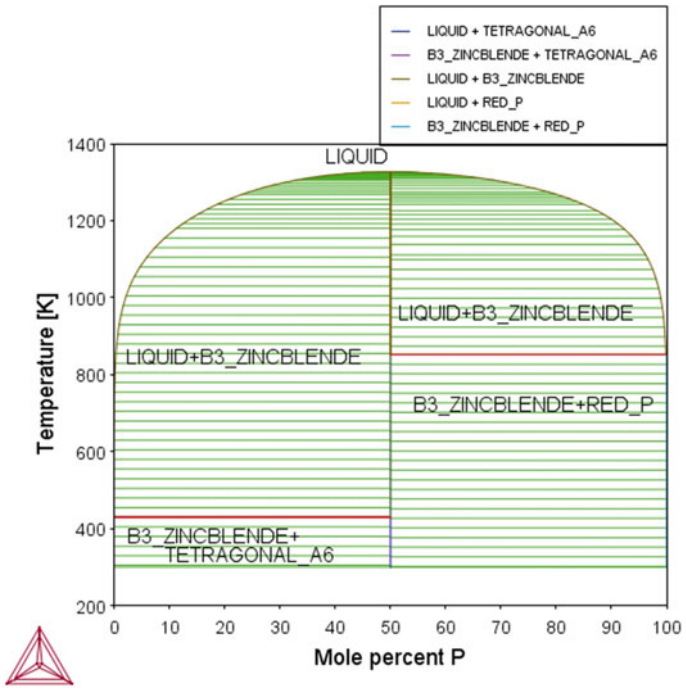

Fig. 1 The phase diagram of the InP binary system obtained in this work

Figure 2 shows the calculated and experimental phase diagrams of InP binary system given in Ref. [4]. The shapes of InP phase diagram in both of Figs. 1 and 2 are the same, but there are differences in melting points of P and InP, but good agreement in In melting point. From Fig. 2, the melting points of In and P are 430 and 851 K, respectively, while the calculated melting temperature of InP from Fig. 2 is 1341 K, but the experimental value is 1340 K [4]. There is a large discrepancy between the melting point of InP determined in this work and that in Fig. 2. The discrepancy between Figs. 1 and 2 is mainly due to the database used, where Fig. 2 was obtained in 1989, and the accuracy of experimental data or database is less than that in 2019, where more revolution and more development took place in all devices and softwares used in collecting and analyzing data.

There are two degenerate reactions and one congruent reaction [7]. Enlarged parts of Fig. 1 are shown in Fig. 3 to display the positions of these reactions. The first degenerate reaction is

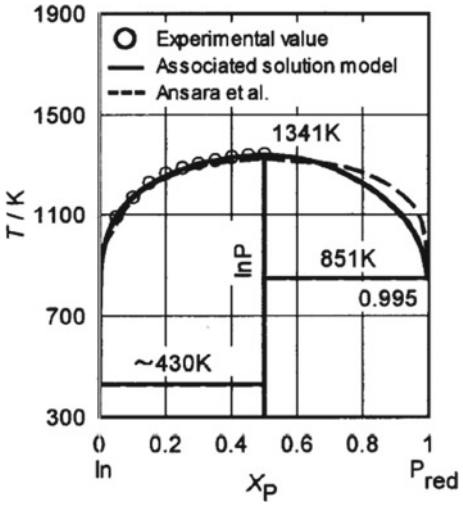

Fig. 2 Calculated phase diagram for InP system with experimental values. Reprinted after K. Yamaguchi et al. [3]. Copyright © 1997 by Elsevier Ltd.

$$\text{Liquid} \leftrightarrow \text{InP}_{(s)} + \text{In}_{(s)} \tag{1}$$

From Fig. 3a, this reaction takes place at 9.52×10^{-7} P mole percent and $T = 429.75 \pm 0.025$ K. But according to Yamaguchi et al. [3], this reaction takes place at $<6 \times 10^{-6}$ P mole percent and $T = 429.8$ K. The second degenerate reactions are

$$\text{Liquid} = \text{InP}_{(s)} + \text{P}_{\text{red}(s)} \tag{2}$$

From Fig. 3b, this reaction occurs at 99.6876 P mole percent and $T = 851.94$ K. According to Ref. [3], this reaction takes place at 0.995 P mole percent and $T = 851$ K.

The congruent reaction is

$$\text{InP}_{(s)} = \text{InP}_{(1)} \tag{3}$$

and it occurs at 0.50 and P mole percent and $T = 1326.73$ K as seen in Fig. 3c. But in Ref. [3], it occurs at 0.5 P mole percent and $T = 1341$ K.

As it can be seen in Fig. 1, there are no solid or liquid solutions in the phase diagram; hence, the solubility of InP in In, InP in P, P in InP, and In in InP are considered approximately zero.

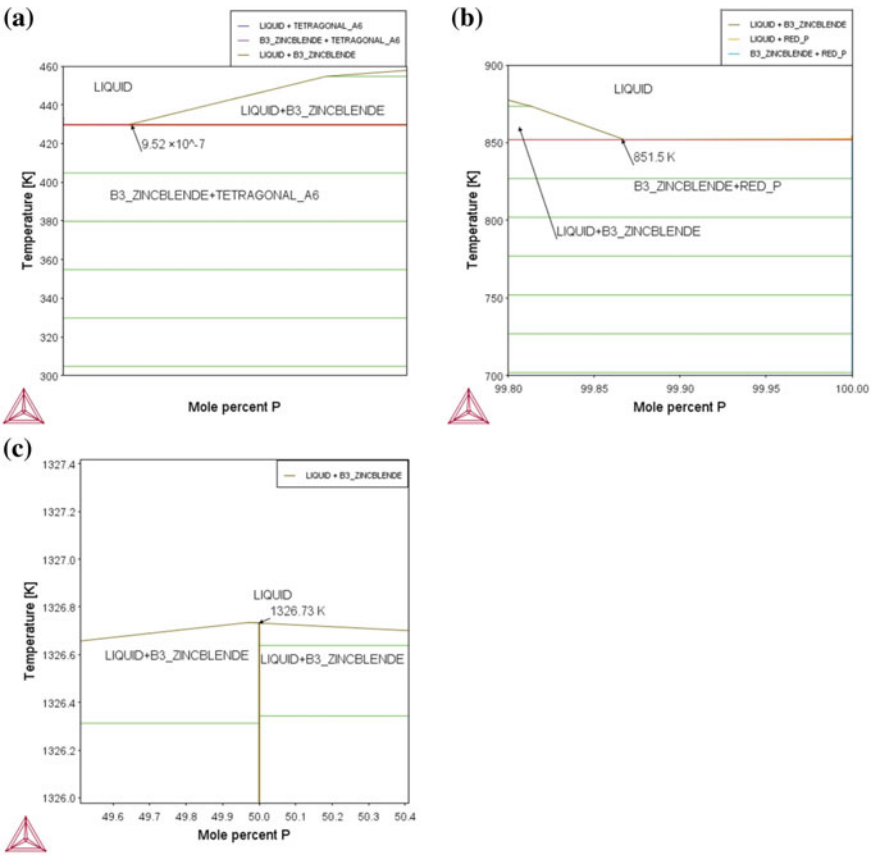

Fig. 3 Enlarged parts of Fig. 1 to show the positions of the reactions. **a** Position of reaction (1). **b** Position of reaction (2). **c** Position of reaction (3)

Conclusions

The phase diagram of InP binary system was reproduced using Thermo-Calc 2019b software and compared with the experimental and computed ones. Four phases were found; pure elements In, and P at the terminals, the compound semiconductor InP at 50 P mole percent, and the liquid phase. Six fields were found in the phase diagram of which are two single phase fields and four mixed double phases fields. The single phase fields are stoichiometric InP at 50 P mole percent and the liquid. The four mixed double phase fields are In + In-rich InP, P + P-rich InP, liquid In + In-rich InP, liquid P + P-rich InP. Melting points of In, P, and InP were determined, and some discrepancies from experimental values were found and discussed. Two degenerate

reactions and one congruent reaction were found in the phase diagram obtained in this work. These results are important for the use of InP in electronic industries, in solar cells, and for the development of preparation techniques of the material.

References

1. Faria PE Jr, Sipahi GM (2012) Band structure calculations of InP wurtzite/zinc-blende quantum wells. J Appl Phys 112:103716. https://doi.org/10.1063/1.4767511
2. Crystal lattice structures: the zincblende (B3) structure. https://homepage.univie.ac.at/michael.leitner/lattice/struk/b3.html. Accessed at 12 Oct 2019
3. Yamaguchi K, Itagaki K, Chang YA (1996) Thermodynamic analysis of the In-P, Ga-As, In-As and Al-Sb systems. Calphad 20(4):439–446
4. Yamaguchi K, Itagaki K, Yazawa A (1989) Thermodynamic investigation of liquid In-P and Ga-P systems by the use of drop-calorimeter. J Jpn Inst Met 53(11):1140–1147
5. Thermo-Calc. https://www.thermocalc.com/media/29198/thermo-calc_a4_web.pdf. Accessed at 12 Oct 2019
6. Computational thermodynamics. Calculation of phase diagrams using the CALPHAD method. Available at: http://www.calphad.com/calphad_method.html. Accessed at 16 Aug 2019
7. Ansara I, Chatillon C, Lukas HL, Nishizawa T, Ohtani H, Ishida K, Hillert M, Sundman B, Argent BB, Watson A, Chart TG, Anderson T (1994) A binary database for III–V compound semiconductor systems. Calphad 18(2):177–222

Part VIII
Characterization of Mechanical Properties II

Formation of the Carbon-Enriched Zone and Its Evolution During the Long-Term Aging Process for 9% Cr-CrMoV Dissimilar Welded Joint

Kai Ding, Bingge Zhao, Yuanheng Zhang, Tao Wei, Guanzhi Wu, Yuanfang Wang and Yulai Gao

Abstract The appearance of carbon migration in the 9% Cr-CrMoV dissimilar welded joint was resulted from the sharp content transition of the strong carbide-forming element Cr between the weld (~2.3 wt%) and the base metal (~10.6 wt%). The width of the carbon-enriched zone (CEZ) under original state was about 46 μm, and the width of CEZ increased and then kept in 65 μm during the 10,000 h aging treatment. The microhardness test showed that the carbon-depleted zone (CDZ) exhibited low hardness value (~220 HV) compared with that (~340 HV) in CEZ. The significant difference in carbide content was the crucial factor in the sharp change of hardness adjacent to the fusion line. Thus, it is important to understand the evolution of the CEZ to experience a long-term aging to avoid its negative influence on the impact toughness and fatigue performance.

Keywords Carbon migration · Long-term aging · Dissimilar welded joint · Carbides · Carbon-enriched zone

Introduction

Dissimilar welded joints are widely put into applications and generally regarded as a great industrial significance in the field like automobile manufacture [1] and power plant [2–5] attributing to their characteristics to make full use of the advantages for materials with different mechanical properties [6, 7]. Liu et al. [8] considered that welding magnesium alloys to copper could simultaneously achieve excellent properties for the both materials. Ramachandran et al. [9] illustrated that the motivation for efficient joining of Al alloy and steel was mainly attributed to the need for weight

K. Ding · B. Zhao (✉) · Y. Zhang · T. Wei · G. Wu · Y. Wang · Y. Gao (✉)
School of Materials Science and Engineering, Center for Advanced Solidification Technology (CAST), Shanghai University, Shanghai 200444, People's Republic of China
e-mail: binggezhao@shu.edu.cn

Y. Gao
e-mail: ylgao@shu.edu.cn

J. Li et al. (eds.), *Characterization of Minerals, Metals, and Materials 2020*,
The Minerals, Metals & Materials Series,
https://doi.org/10.1007/978-3-030-36628-5_27

reduction in view of enhancing energy efficiency and reducing the adverse impact on environment in automotive and marine sectors.

However, due to the different compositions and physical properties of various base metals (BMs), several issues including inhomogeneous microstructure, macro-segregation, and formation of intermetallic compounds would seriously affect the mechanical properties of the dissimilar welded joints. For instance, Hosseini et al. [10] reported grain growth occurred due to the heat input and the presence of precipitates could deteriorate the mechanical properties (hardness, yield, and ultimate strengths) of the Inconel 617/310 alloy dissimilar joint. The formation of brittle intermetallic compounds (IMCs) became the major metallurgical problem of joining aluminum alloys with steels [11, 12]. Wang et al. [13] suggested the difference in element mixing during welding process could lead to the macro-segregation with island-like and peninsula-like structure.

The present investigation focused on the 9% Cr-CrMoV welded by the narrow gap submerged arc welding. In our previous study [14], CDZ and CEZ were formed adjacent to the fusion line mainly due to the difference of Cr content between the WM and 9% Cr steel. In addition, the CrMoV-BM was the weak zone at the temperature lower than 470 °C, while the specimen fractured at the CDZ with the applied temperature of 470 °C during the high cycle fatigue test [15]. However, the microstructure evolution of CDZ or CEZ during long-term aging treatment at high temperature was still little involved.

Experimental Procedures

The 9% Cr and CrMoV steels were used as the BMs to fabricate the 9% Cr-CrMoV dissimilar welded joint. The composition of the BMs and the corresponding filler metal is listed in Table 1. Clearly, the content of Cr element in 9% Cr steel was about four times higher than that in CrMoV steel and filler metal. To some extent, the creep strength of heat-resistant steels could be enhanced by increased Cr content [16]. The BMs were joined by narrow gap submerged arc welding accompanied with the multi-layer and multi-pass technique. The welding current and voltage were 400 A and 30 V, respectively. Subsequently, the 9% Cr-CrMoV dissimilar welded joint was heat-treated at 660 °C for 20 h to release the residual stress and increase the structure stability [17, 18].

The schematic of the welded joint is shown in Fig. 1. The specimen for the microstructure observation containing all the characteristic zones was ground and polished after being cut from the whole 9% Cr-CrMoV dissimilar welded joint. The etchant of $HCl + HNO_3 + H_2O$ with the volume proportion of 3:3:5 was applied to reveal the microstructure of each characteristic zone. Optical microscopy (OM) and scanning electron microscopy (SEM) were used to analyze the microstructure evolution during series aging heat treatment processes.

Table 1 Chemical composition of 9% Cr-BM, CrMoV-BM, and the filler metal (wt%)

Elements	C	Si	Mn	Cr	Mo	Ni	V	Al	S	P	Fe
9% Cr	0.13	0.08	0.40	10.57	1.02	0.78	0.18	0.04	0.016	0.006	Bal.
CrMoV	0.26	0.31	0.76	2.28	0.97	0.62	0.21	0.04	0.014	0.011	Bal.
Filler metal	0.11	0.12	0.51	2.67	1.02	0.13	0.27	–	0.001	0.003	Bal.

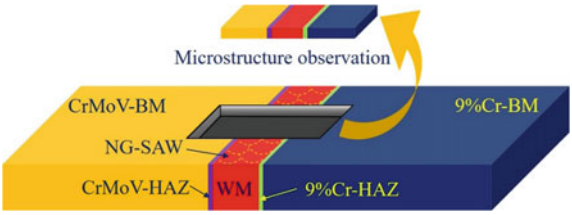

Fig. 1 Schematic of the microstructure observation for 9% Cr-CrMoV dissimilar welded joint

Results and Discussion

The optical images of the microstructure for each characteristic zone are shown in Fig. 2. The macrostructure of the 9% Cr-CrMoV dissimilar welded joint is shown in Fig. 2a, and the results showed that there existed seven characteristic zones containing base metal of 9% Cr steel (9% Cr-BM), heat-affected zone of 9% Cr steel (9% Cr-HAZ), weld metal (WM), CEZ, CDZ, CrMoV-HAZ, and CrMoV-BM. The width of WM was about 20 mm, and columnar and equiaxed zones formed by the SAW technique could be detected. The structure of 9% Cr-BM is shown in Fig. 2b, c, and the lath martensite could be observed. Tempered martensite was the main structure for CrMoV-BM, 9% Cr-HAZ, WM, and CrMoV-HAZ, which are displayed in Fig. 2c, d, f, g, respectively. In addition, much more details of the CDZ and CEZ are displayed in Fig. 2e. It should be noted that the CDZ and CEZ, which were formed adjacent to the fusion line, were owing to the carbon migration from the WM to 9% Cr steel during the welding process. Thus, the dark region in 9% Cr-HAZ represented CEZ, while CEZ displayed bright region.

In our previous study, the formation of CDZ and CEZ was resulted from the quite difference of alloy elements especially for the strong carbide-forming element Cr [14] and could therefore extremely decrease the chemical potential of carbon diffusion [19]. Highly decreasing of chemical potential of carbon diffusion in 9% Cr steel triggered the carbon to migrate from WM to 9% Cr steel. The schematic of the CDZ formation is exhibited in Fig. 3a, b. During the welding and the later heat treatment processes, the carbon content in WM adjacent to the fusion line gradually decreased. Correspondingly, the carbides were tended to be dissolved to compensate the migrated carbon when the carbon content decreased to the level lower than that of thermodynamic equilibrium for carbides [20, 21]. Figure 3c, d clearly reflects the above-mentioned process that the size and the amount of the carbides gradually reduced to cause the formation of CDZ in WM. The formation schematic of CEZ, which is displayed in Fig. 3e, f, was related to the nucleation and growth of the carbides in 9% Cr-HAZ near the fusion line with the process of carbon migration. SEM images of the WM, CDZ, CEZ, and the 9% Cr-HAZ are shown in Fig. 3c, d, g, h. The particles in Fig. 3c, g were identified as carbides by energy-dispersive

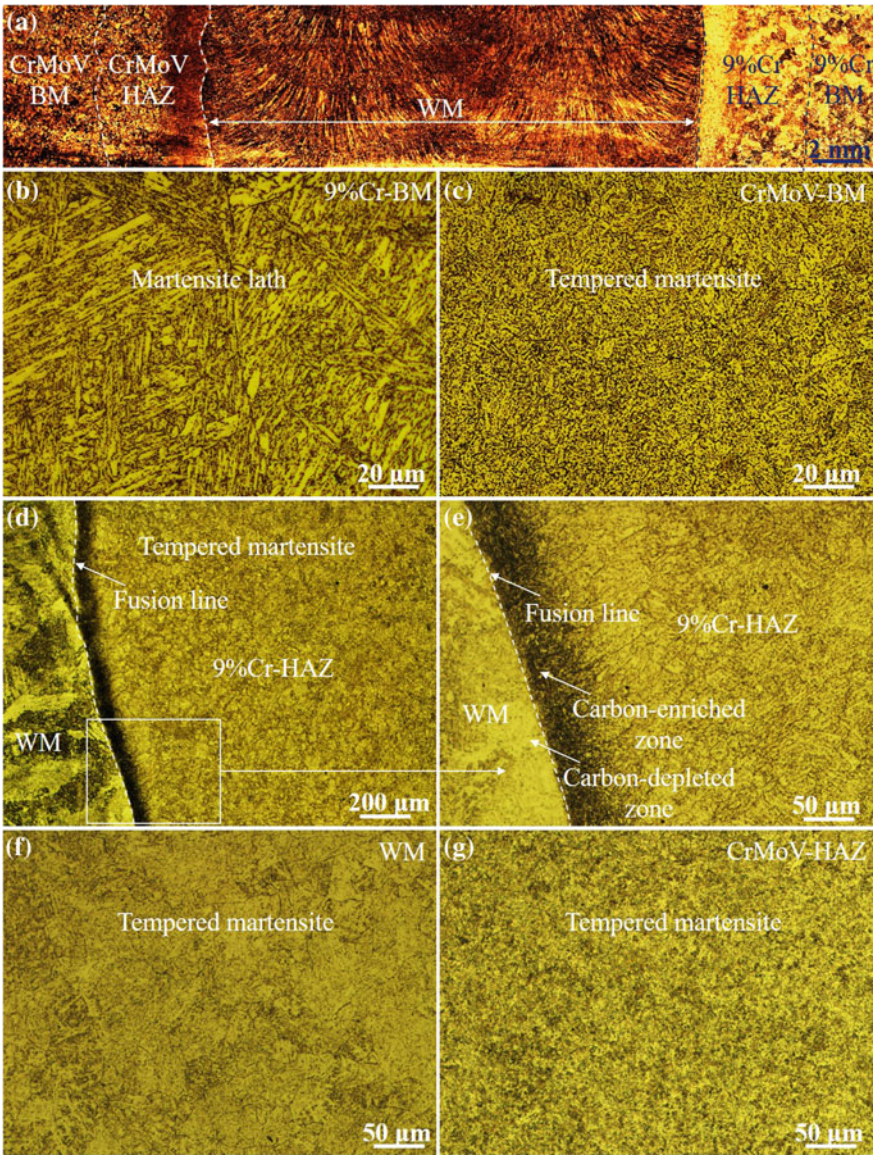

Fig. 2 Microstructure of the characteristic zone for 9% Cr-CrMoV dissimilar welded joint: **a** the macrostructure of the welded joint, **b** 9% Cr-BM, **c** CrMoV-BM, **d**, **e** the microstructure of CDZ and CEZ, **f** WM, and **g** CrMoV-HAZ

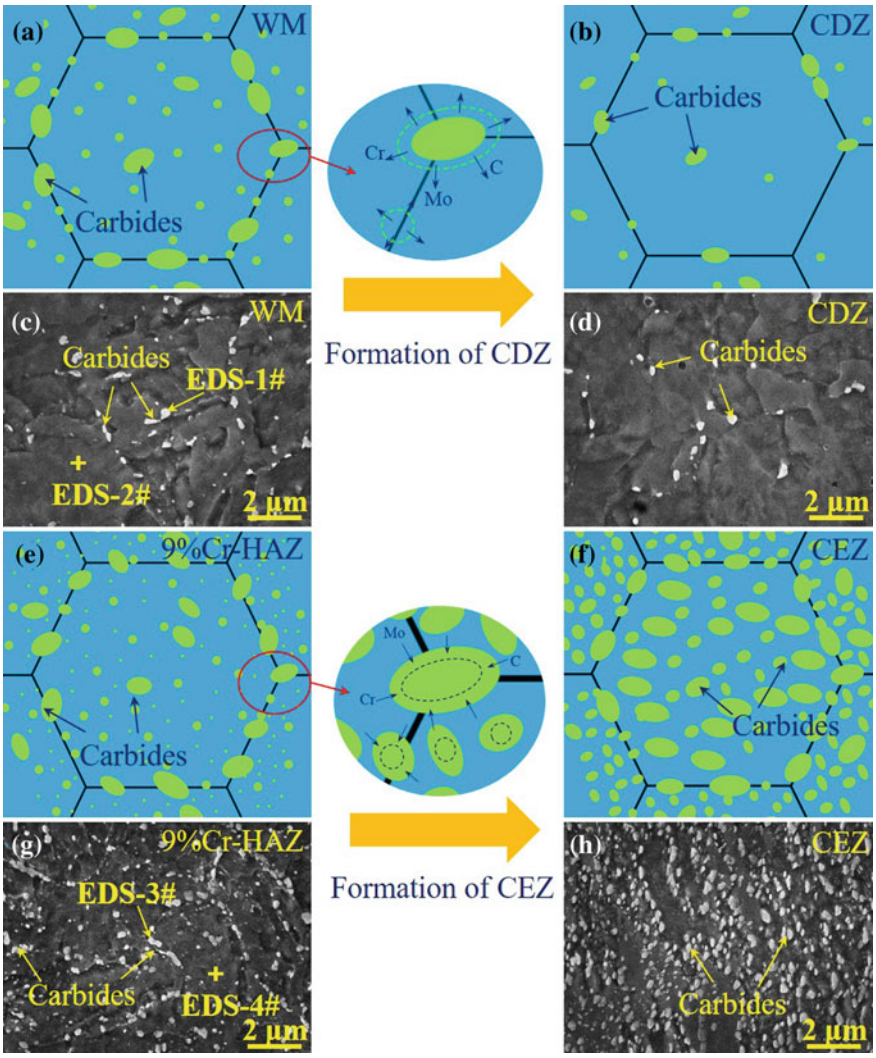

Fig. 3 Schematic of the carbon migration process: **a**, **b** the formation of CDZ, **c**, **d** details of carbides in WM and CDZ, **e**, **f** the formation of CEZ, and **g**, **h** details of carbides in 9% Cr-HAZ and CEZ

spectrum (EDS) results, which are displayed in Table 2. Lin et al. [22] investigated the microstructure and toughness of 9% Cr-CrMoV dissimilar welded joint and considered that such carbides participating in formation would reduce the toughness. Wen et al. [23] illustrated that high content of dispersive carbides distributed in the

Table 2 EDS results of particles in Fig. 3

Elements	Cr		Mo		Fe		C	
	wt%	at.%	wt%	at.%	wt%	at.%	wt%	at.%
EDS-1#	17.48	6.13	4.19	3.34	58.60	35.30	19.73	55.23
EDS-2#	2.97	2.55	1.09	0.49	87.70	67.49	8.24	29.47
EDS-3#	19.86	12.12	1.83	0.66	61.10	37.77	17.21	49.45
EDS-4#	2.84	2.38	0.36	0.19	89.01	69.19	7.78	28.24

matrix was a benefit to improve the strength and hardness, while degrading fracture toughness.

To shed much light on the role of carbon migration in the mechanical properties for 9% Cr-CrMoV dissimilar welded joint, microhardness distribution is displayed in Fig. 4a. It could be found that the microhardness of CrMoV-BM, WM, and 9% Cr-BM was 220 HV, 250 HV, and 280 HV, respectively. The higher hardness of 9% Cr-BM was attributed to the presence of martensite. Obvious fluctuation in hardness could be detected in HAZs due to the heterogeneous microstructure affected by heat input [24]. In addition, quite difference in microhardness at the fusion line was found, and the microhardness in CDZ and CEZ was 220 HV and 340 HV. The optical image of indentations around the fusion line is displayed in Fig. 4b, revealing smaller indentation in CEZ than that in CDZ. Undoubtedly, the carbon migration and resultant seriously different carbide contents were the crucial factor to form the microhardness change in the region near the fusion line.

As mentioned above, the CDZ was formed simultaneously combined with the CEZ due to the carbon migration. The width evolution of CEZ was enough to illustrate

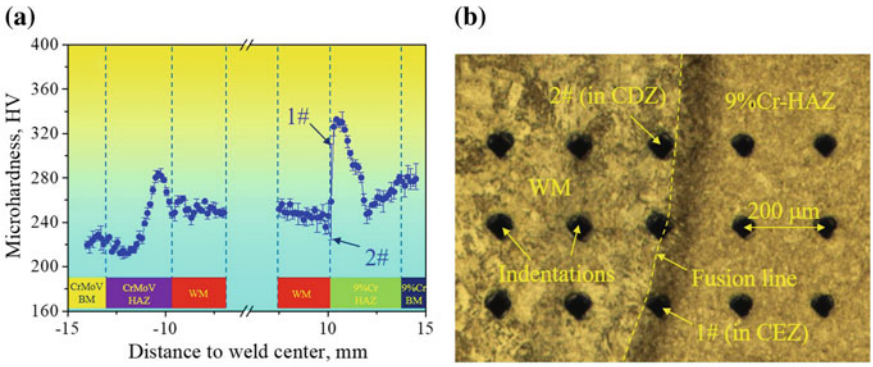

Fig. 4 Microhardness test results of 9% Cr-CrMoV dissimilar welded joint: **a** the whole microhardness distribution and **b** the optical image of indentation adjacent to the fusion line

the whole carbon migration during the long-term aging treatment. In order to better reflect the width of CEZ, optical and SEM analyses were both performed, which are shown in Fig. 5a, b. The width of the CEZ was about 46 μm. Figure 5c, d shows the width change of CEZ during the aging treatment with various aging parameters. The results showed that there contained increasing and stable stages of the CEZ width. When the aging time is below 5000 h, the width of CEZ increased with the increase of aging time and then kept at 65 μm with the aging time exceeded 5000 h.

The width of CEZ was mainly related to the evolution of carbides. Figure 6 displays the carbide details in CEZs with various aging times at 538 °C. It could be found that both the size and amount of the carbides increased with the aging time below 5000 h, and the amount of the carbides increased with the aging time exceeded 5000 h. Combining the results of the CEZ width during aging process, it could be concluded that the increasing stage was highly related to the nucleation and growth of carbides, and the stable stage was primarily relevant to the growth of carbides.

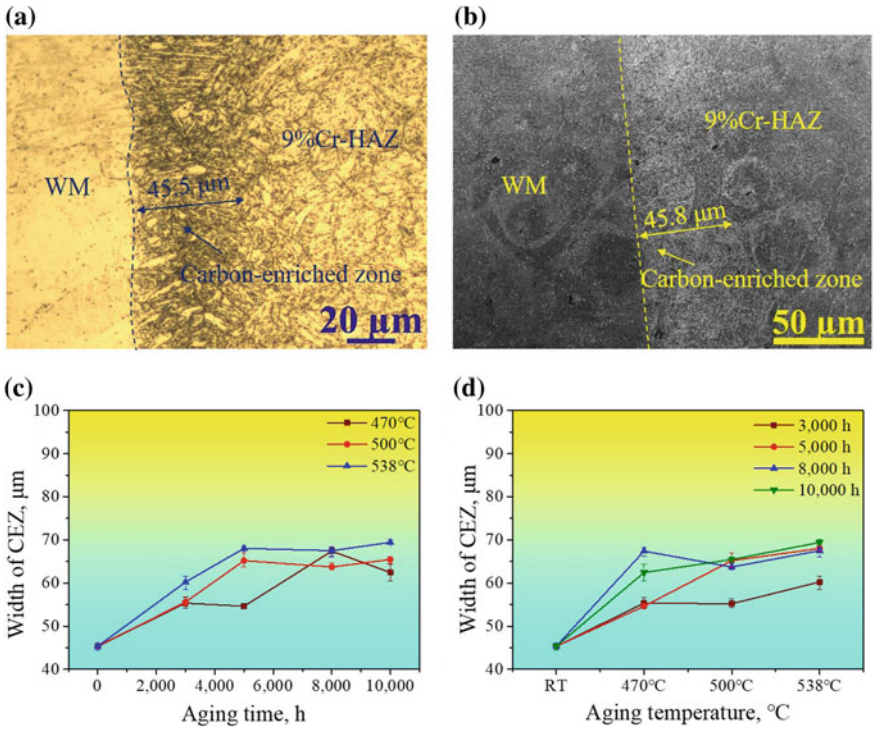

Fig. 5 Evolution of the CEZ during various aging treatments: **a**, **b** microstructure observation of CEZ and **c**, **d** the width evolution of CEZ with a different aging temperature and time

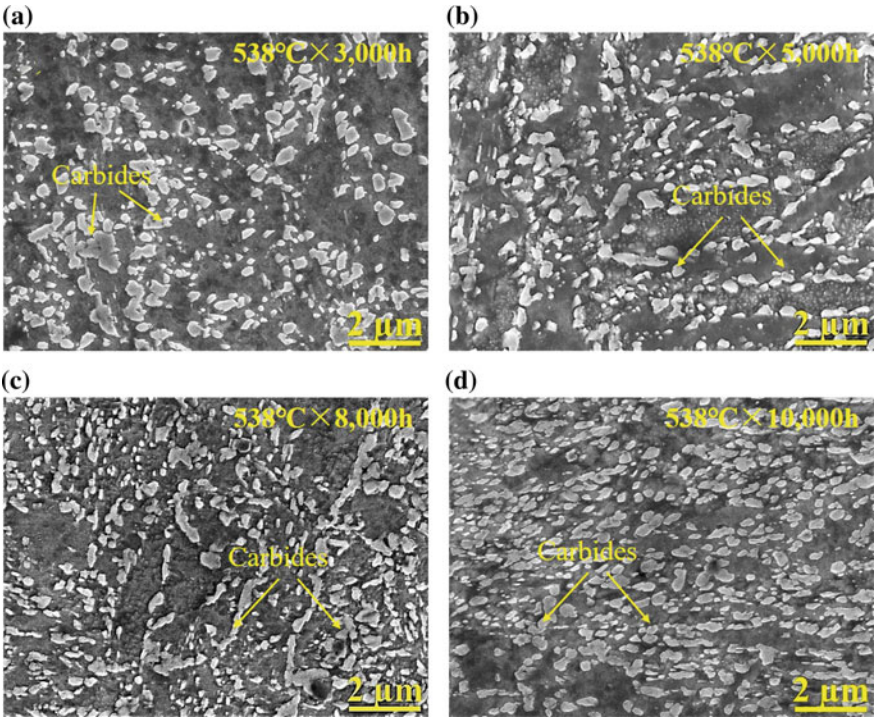

Fig. 6 Carbide details in CEZs for the specimens with various aging time at 538 °C: **a** 3000 h, **b** 5000 h, **c** 8000 h, and **d** 10,000 h

Conclusions

Seven characteristic zones were detected in the whole 9% Cr-CrMoV dissimilar welded joint. The structure of 9% Cr-BM was lath martensite, and the tempered martensite was the main structure for 9% Cr-HAZ, WM, CrMoV-HAZ, and CrMoV-BM. CDZ and CEZ were, respectively, formed in WM adjacent to the fusion line and 9% Cr-HAZ due to the composition difference in Cr content. Based on the results obtained by the OM and SEM, the formation of CDZ and CEZ was due to the carbon migration from the WM to 9% Cr steel. The width of the CEZ for the specimen without aging was about 46 μm, compared to ~65 μm for the specimen experiencing 10,000 h aging treatment. The microhardness test showed that the CDZ exhibited low hardness (~220 HV) compared with that (~340 HV) in CEZ. The significant difference in the content of the carbides was the main cause to result in the hardness change adjacent to the fusion line.

Acknowledgements The authors gratefully acknowledge the National Natural Science Foundation of China (Grant no. U1760102) and the financial support by the Program for Professor of Special

Appointment (Eastern Scholar) at Shanghai Institutions of Higher Learning and Shanghai Science and Technology Committee (Grant no. 13DZ1101502).

References

1. Gupta SK, Pandey KN, Kumar R (2015) Comparison of ANN and regression modeling for predicting the responses of friction stir welded dissimilar AA5083-AA6063 aluminum alloys joint. Appl Mech Mater 813–814:415–419
2. Shang YB, Shi HJ, Wang ZX, Zhang GD (2015) In-situ SEM study of short fatigue crack propagation behavior in a dissimilar metal welded joint of nuclear power plant. Mater Des 88:598–609
3. Ding K, Wang P, Liu X, Li XH, Zhao BG, Gao YL (2018) Formation of lamellar carbides in alloy 617-HAZ and their role in the impact toughness of alloy 617/9%Cr dissimilar welded joint. J Mater Eng Perform 27(11):6027–6039
4. Ding K, Zhao BG, Huo X, Fan MJ, Li XH, Zhang YH, Wei T, Wu GZ, Gao YL (2019) Failure transition mechanism of stress rupture performance of the Inconel 625/9 pct Cr steel dissimilar welded joint. Metall Mater Trans A. https://doi.org/10.1007/s11661-019-05372-0
5. Dehaghi EM, Moshayedi H, Sattari-Far I, Arezoodar A (2017) Residual stresses due to cladding, buttering and dissimilar welding of the main feed water nozzle in a power plant reactor. Int J Press Vessels Pip 152:56–64
6. Guo Q, Lu FG, Liu X, Yang RJ, Cui HC, Gao YL (2015) Correlation of microstructure and fracture toughness of advanced 9Cr/CrMoV dissimilarly welded joint. Mater Sci Eng A 638:240–250
7. Rahmani M, Eghlimi A, Shamanian M (2014) Evaluation of microstructure and mechanical properties in dissimilar austenitic/super duplex stainless steel joint. J Mater Eng Perform 23(10):3746–3753
8. Liu LM, Wang SX, Zhao LM (2008) Study on the dissimilar magnesium alloy and copper lap joint by TIG welding. Mater Sci Eng A 476(1–2):206–209
9. Ramachandran KK, Murugan N, Shashi Kumar S (2015) Effect of tool axis offset and geometry of tool pin profile on the characteristics of friction stir welded dissimilar joints of aluminum alloy AA5052 and HSLA steel. Mater Sci Eng A 639:219–233
10. Hosseini HS, Alishahi M, Shamanian M (2012) Zonular evaluation of inconel 617/310 SS dissimilar joint by shear punch test. Mater Lett 67(1):259–262
11. Bouché K, Barbier F, Coulet A (1998) Intermetallic compound layer growth between solid iron and molten aluminium. Mater Sci Eng A 249(1–2):167–175
12. Chen SH, Huang JH, Ma K, Zhang HQ, Zhao XK (2012) Influence of a Ni-foil interlayer on Fe/Al dissimilar joint by laser penetration welding. Mater Lett 79:296–299
13. Wang YQ, Cui HC, Fan MJ, Chen YX, Lu FG (2019) Characterization on the gradient microstructure near the fusion interface of dissimilar metal between high Cr heat-resistant steel and Ni-based Alloy 617. Mater Charact 151:227–236
14. Ding K, Ji HJ, Liu X, Wang P, Zhang QL, Li XH, Gao YL (2018) Prevention of carbon migration in 9% Cr/CrMoV dissimilar welded joint by adding tungsten inert gas overlaying layer. J Iron Steel Res Int 25:847–853
15. Wu QJ, Lu FG, Cui HC, Liu X, Wang P, Gao YL (2015) Soft zone formation by carbon migration and its effect on the high-cycle fatigue in 9% Cr-CrMoV dissimilar welded joint. Mater Lett 141:242–244
16. Abe F (2008) Precipitate design for creep strengthening of 9% Cr tempered martensitic steel for ultra-supercritical power plants. Sci Technol Adv Mater 9(1):1–15
17. Wei YH, Qiao SF, Lu FG, Liu W (2016) Failure transition mechanism in creep rupture of modified casting 9Cr-1.5Mo-1Co welded joint. Mater Des 97:268–278

18. Liu X, Cai ZP, Deng XL, Lu FG (2017) Investigation on the weakest zone in toughness of 9Cr/NiCrMoV dissimilar welded joint and its enhancement. J Mater Res 32(16):3117–3127
19. Rahman S, Priyadarshan G, Raja KS, Nesbitt C, Misra M (2008) Investigation of the secondary phases of alloy 617 by scanning kelvin probe force microscope. Mater Lett 62(15):2263–2266
20. Kang JH, Rivera-Díaz-Del-Castillo PEJ (2013) Carbide dissolution in bearing steels. Comput Mater Sci 67:364–372
21. Sandberg N, Henriksson KOE, Wallenius J (2008) Carbon impurity dissolution and migration in bcc Fe-Cr: first-principles calculations. Phys Rev B 78(9):1–7
22. Lin RQ, Cui HC, Lu FG, Huo X, Wang P (2016) Study on the microstructure and toughness of dissimilarly welded joints of advanced 9Cr/CrMoV. J Mater Res 31(22):3597–3609
23. Wen T, Hu XF, Song YY, Yan DS, Rong LJ (2013) Carbides and mechanical properties in a Fe–Cr–Ni–Mo high-strength steel with different V contents. Mater Sci Eng A 588:201–207
24. Liu W, Liu X, Lu FG, Tang XH, Cui HC, Gao YL (2015) Creep behavior and microstructure evaluation of welded joint in dissimilar modified 9Cr-1Mo steels. Mater Sci Eng A 644:337–346

The Evolution of Precipitates in a Novel Heat-Resistant Martensitic Steel During Creep

Pengyu Wen, Zhengzong Chen, Zhengdong Liu and Haiwen Luo

Abstract In the past decades, several 9–12 wt% Cr-containing martensitic steels have been researched for the application in ultra-supercritical power plants at 650 °C, which is still a worldwide challenge. Among them, G115 martensitic steel, which was developed in China, is one of promising candidates. It has the basic composition of 9% Cr-3% W-3% Co and contains 1% Cu (all in wt%) and the optimized contents of B and N, leading to much better creep strength and creep ductility than P92 steel. Both $M_{23}C_6$ carbides and ε-Cu particles were found during the tempering of G115 steel, and the former have finer size than those in P92 steel, which results in Laves phase to form with the refined size too during the latter creep stage. All these formed precipitates shall contribute to improved creep rupture strength of G115 steel.

Keywords Precipitate · Coarsening kinetics · Heat-resistant steel · Creep

Introduction

The demand to improve the steam parameters under advanced ultra-supercritical (A-USC) circumstances for higher thermal efficiency, lower emissions of harmful gases, and economically feasibility is imperative in fossil-fired steam power plants [1]. Compared to austenitic stainless steels or superalloys, the martensitic heat-resistant steels (MHRSs) are more competitive due to their superior physical properties, like high thermal efficiency and low thermal expansion, at a relatively low manufacturing cost. Nevertheless, the increase of permissible service temperature to 650 °C is still a worldwide challenge.

P. Wen · H. Luo (✉)
School of Metallurgical and Ecological Engineering, University of Science and Technology Beijing, 30# Xue Yuan Lu, Haidian District, Beijing 100083, People's Republic of China
e-mail: hawenluo@126.com

Z. Chen · Z. Liu (✉)
China Irons and Steel Research Institute Group, 76# Xue Yuan Nan Lu, Haidian District, Beijing 100081, People's Republic of China
e-mail: Liu_zhengdong@263.net

J. Li et al. (eds.), *Characterization of Minerals, Metals, and Materials 2020*,
The Minerals, Metals & Materials Series,
https://doi.org/10.1007/978-3-030-36628-5_28

The control of dislocation movement is the decisive factor for creep behavior of MHRS [1]. This means that the optimization of spatial distribution, size, number density, and volume fraction of the second particles shall benefit the creep performance. Precipitates in 9–12% Cr-containing MHRS include the nano-sized MX carbonitrides that could pin dislocations, $M_{23}C_6$, and Laves phase that often precipitate at grain boundaries or modified Z phase in the size of micrometers [2]. It is now well known that the enhanced recovery occurring at grain boundaries is the main cause of the premature behavior and the loss of the rupture strength [3]. The precipitates that pin both dislocations and boundaries could sufficiently stabilize the tempered martensitic lath structure (TMLS) with high dislocation density [4].

Nevertheless, the joint precipitation of Laves and $M_{23}C_6$ has been widely reported in MHRS; in particular, $M_{23}C_6$ was swallowed by the coarsening Laves phase in a 10Cr1W1MoNiVNb steel during creep [5]. Agglomeration and anomaly coarsening of precipitates are certainly harmful to the creep performance; thus, the new design of second-phase particles and their optimization of coupling effect are of predominant importance. In this research, Cu was added into the new type of MHRS, G115, in which both B and N contents were also optimized. The evolution of precipitates including $M_{23}C_6$, MX, Laves, and ε-Cu phase during creep was studied using SEM, STEM, and TEM on the creep ruptured specimens up to 14,000 h.

Experimental

The raw materials of G115 steel were melted in a vacuum induction furnace and then cast to ingots. Followed by forging and hot extruding into pipes, they were normalized at 1100 °C for 1 h to guarantee the re-dissolution of precipitates and appropriate prior austenite grain sizes [6], and then tempered at 780 °C for 3 h to achieve good toughness, thus meeting the fabrication requirements of thick section boiler components in A-USC plants [7]. The raw materials of P92 were normalized at 1100 °C for 0.5 h and tempered at 760 °C for 2 h. The chemical compositions of P92 and G115 steels are given in Table 1.

The specimens were machined with a gauge length of 25 mm and gauge diameter of 5 mm and underwent creep rupture tests. In specific, G115 steel was crept under applied stress of 200 and 130 MPa for up to 14,000 h at 650 °C. For comparison, P92 steel was tested under the applied stress of 175 and 100 MPa for up to 14,000 h at its highest service temperature 630 °C.

Equipment including TEM and STEM (JEM-2200) was employed to analyze the precipitate evolution of the uniform deformation parts (without necking) within gauge. The SEM samples were mechanically polished by emery paper, diamond sprayed buff, and colloidal silica, and then etched with 4% nitric acid for 10 s. The thin foils for TEM and STEM studies were prepared by electropolishing in a twin-jet apparatus using 7% perchloric acid in glacial acetic acid solution.

Table 1 Chemical composition (wt%) of investigated P92 and G115 MHRS

	C	Cr	W	Mo	Co	Cu	V	Nb	Mn	Si	B	N
P92	0.08–0.10	8.5–9.5	1.5–2.0	0.40–0.55	–	–	0.15–0.25	0.01–0.05	0.2–0.6	0.1–0.5	0.001–0.005	0.03–0.07
G115	0.08–0.10	8.5–9.5	2.5–3.0	–	2.50–3.50	0.5–1.5	0.15–0.25	0.01–0.05	0.2–0.6	0.1–0.5	0.005–0.015	0.005–0.015

Results and Discussion

The typical tempered martensite lath structure of G115 martensitic heat-resistant steel is illustrated in Fig. 1. It is clear in Fig. 1a that densely distributed $M_{23}C_6$ particles could sufficiently pin the lath boundaries and avoiding the significant recovery of lath boundaries happened due to the lack of pinning pressure from $M_{23}C_6$ particles. Two types of particles containing $M_{23}C_6$ and MX could precipitate out abundantly, whilst fewer ε-Cu particles could be formed due to the high solution of Cu atoms in matrix at such a high tempering temperature of 780 °C. It is also worth noted that all the above precipitates were in FCC structure. Figure 1b shows the SAED patterns of $M_{23}C_6$ particles, and Fe, Cr, and C enrichment in carbides was revealed by EDS; nevertheless, the B content was not detected due to its low concentration.

A STEM dark-field image and the corresponding EDX maps of G115 steel creeping under 130 MPa for 14,000 h are given in Fig. 2. The enrichment of Cu, W, and Cr represents ε-Cu, Laves phase, and $M_{23}C_6$ particles, respectively. It can be illustrated that most of $M_{23}C_6$ particles were located along the (sub)grain boundaries in small sizes whilst significant coarsening of Laves phase had taken place. These intermetallic compounds, with sizes between ~100 and 1000 nm, could be either independently formed or jointly precipitated with $M_{23}C_6$ and/or ε-Cu particles. It seems that partial $M_{23}C_6$ particles were swallowed by these significantly coarsened Laves phase (marked by yellow square) particles. This phenomenon has also been discovered in recent researches on martensitic heat-resistant steel [5]. In addition, partial Cu atoms were conspicuously diffused towards Laves phase, especially in those with coarser sizes, as displayed in Fig. 2b, c. It is noted here that there had never been any reports on Cu atoms being diffused into Laves phase before. Moreover, two types of ε-Cu particles in varied diameters could be observed. The small ε-Cu particles in nanometer sizes are mainly found in subgrain interior, whilst the sub-micrometer ones are distributed along the grain boundaries. It is also seen that ε-Cu particles offer extra nucleation sites for Laves phase along the (sub)grain boundaries.

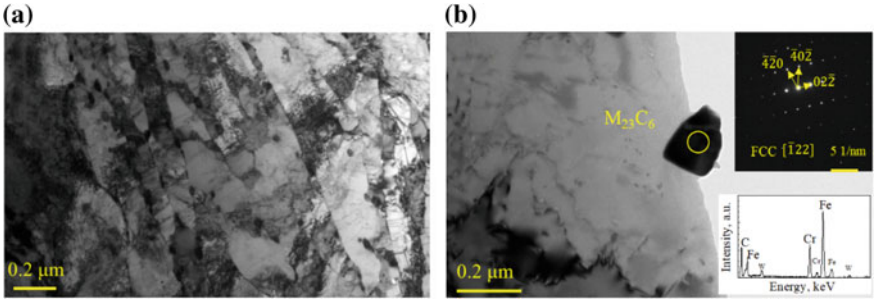

Fig. 1 TEM micrographs of tempered G115 steel: **a** tempered martensitic lath structure and **b** precipitate distribution and SAED pattern and EDS analysis of $M_{23}C_6$ particle

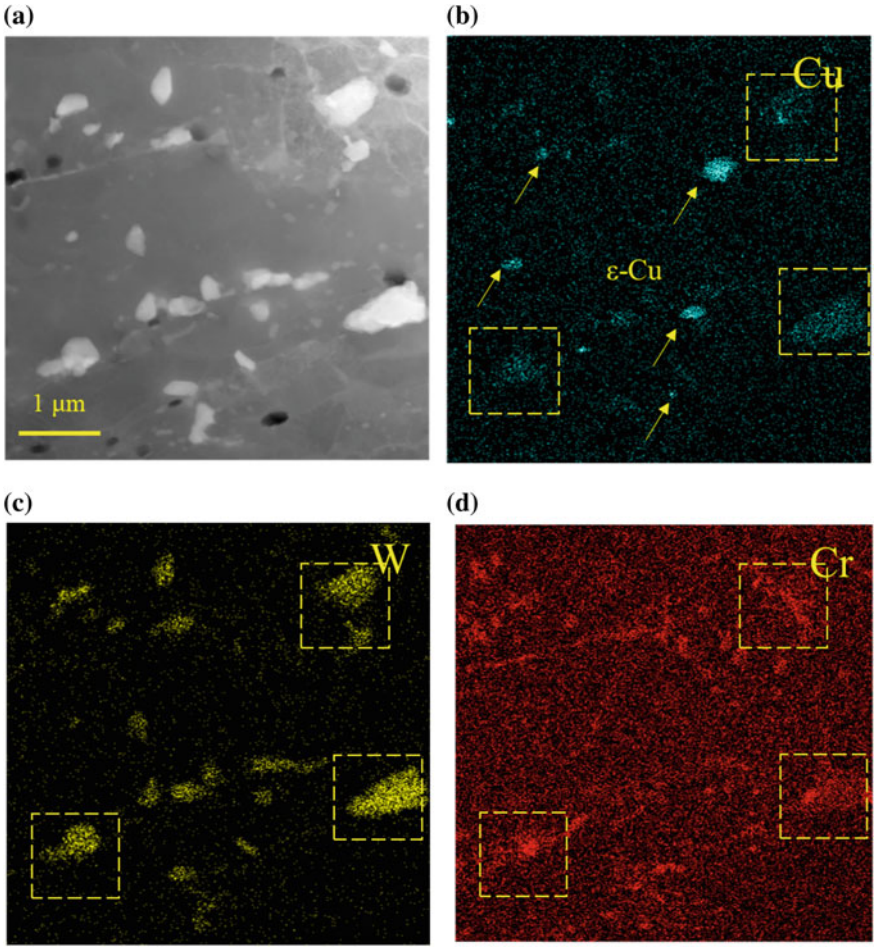

Fig. 2 STEM dark-field images of precipitate morphology and the relevant Cu, W, and Cr element distribution by area scanning in G115 steel samples crept under 130 MPa for 14,000 h

The coarsening kinetics of precipitates was measured from numerous TEM images, and at least 40 particles were counted for each type of precipitate in a certain creeping condition. It was found that the precipitate sizes of both $M_{23}C_6$ and Laves were smaller in G115 steel, despite that the creep temperature of P92 is lower. After creeping for 14,000 h, the size difference between two types of ε-Cu particles that formed within lath interior or along (sub)grain boundaries is about 90 nm.

It is reported that coarsening of the second particles in martensitic heat-resistant steel obeys the classical Ostwald ripening model, which can be simplified as the following form [8].

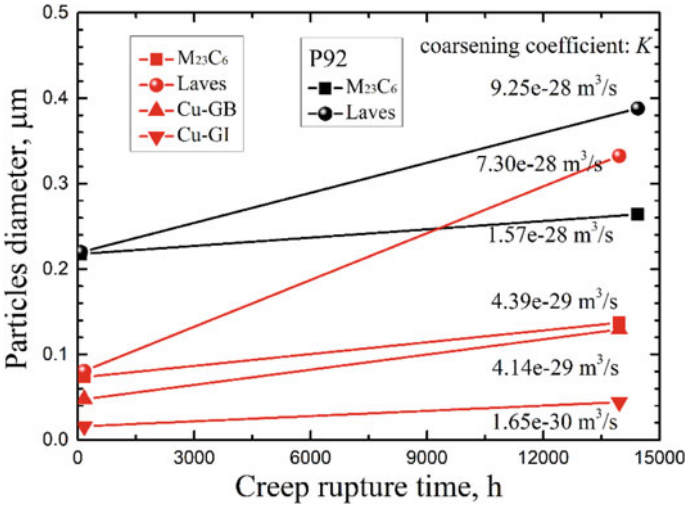

Fig. 3 Diameter evolution as a function of time for $M_{23}C_6$, Laves and ε-Cu particles in the investigated G115 and P92 steels (GB: grain boundary, GI; (sub)grain interior)

$$r_t^m - r_0^m = Kt \tag{1}$$

where r_0 and r_t are the average radii of particles at initial time and time t during creep, respectively. K is the coarsening coefficient. The values of exponent m are ~3 for particle growth controlled by lattice diffusion and ~4 that controlled by grain boundary diffusion.

The calculated coarsening coefficient of varied particles is also listed in Fig. 3 by assuming the value of exponent m is 3. It is obvious that coarsening rate of all phases is much smaller in G115 steel than those in P92 steel, and Laves phase particles exhibited highest coarsening rate due to their incoherence with BCC matrix. Moreover, the rapid coarsening of ε-Cu phase that formed along grain boundary might be ascribed to the Cu segregation along the grain boundaries as indicated by its high grain boundary enrichment factor reported in Ref. [9]. This might also lead to more ε-Cu particles formed along the grain boundaries instead of matrix as shown in Fig. 2.

Conclusion

(1) In comparison with P92 steel, both $M_{23}C_6$ and Laves phase were significantly refined in G115 steel, which depends on the contents of boron and tungsten.
(2) There are two types of ε-Cu phase precipitating in G115 steel during creeping after the creeping for 14,000 h. One was formed within martensite lath in

nanometer sizes and the other along the grain boundaries in sub-micrometer sizes.

(3) Both ε-Cu and $M_{23}C_6$ particles can precipitate during tempering and the early creep stage, which could promote the fine dispersive precipitation of Laves phase afterwards. The extensive measurements on precipitates using STEM reveal the diffusion of Cu atoms into Laves phase, which requires more researches in future.

Acknowledgements This work was financially supported by the National Key Research and Development Program of China under the Grant No. 2017YFB0305202 and Innovation Talent Cultivation Fund of University of Science and Technology Beijing.

References

1. Zhao JF, Gong JD, Saboo A, Dunand DC, Olson GB (2018) Dislocation-based modeling of long-term creep behaviors of Grade 91 steels. Acta Mater 149:19–28
2. Liu F, Rashidi M, Johansson L, Hald J, Andrén HO (2016) A new 12% chromium steel strengthened by Z-phase precipitates. Scripta Mater 113:93–96
3. Maruyama K, Sawada K, Koike JI (2001) Strengthening mechanisms of creep resistant tempered martensitic steel. ISIJ Int 41(6):641–653
4. Mishnev R, Dudova N, Kaibyshev R (2018) On the origin of the superior long-term creep resistance of a 10% Cr steel. Mater Sci Eng A 713:161–173
5. Xu YT, Nie YH, Wang MJ, Li W, Jin XJ (2017) The effect of microstructure evolution on the mechanical properties of martensite ferritic steel during long-term aging. Acta Mater 131:110–122
6. Yan P, Liu ZD, Bao HS, Weng YQ, Liu W (2014) Effect of normalizing temperature on the strength of 9Cr–3W–3Co martensitic heat resistant steel. Mater Sci Eng A 597:148–156
7. Yan P, Liu ZD, Bao HS, Weng YQ, Liu W (2014) Effect of tempering temperature on the toughness of 9Cr–3W–3Co martensitic heat resistant steel. Mater Des 54:874–879
8. Liu Z, Liu ZD, Wang XT, Chen ZZ (2019) Investigation of the microstructure and strength in G115 steel with the different concentration of tungsten during creep test. Mater Charact 149:95–104
9. Raabe D, Herbig M, Sandlöbes S, Li YJ, Tytko D, Kuzmina M, Ponge D, Choi P (2014) Grain boundary segregation engineering in metallic alloys: a pathway to the design of interfaces. Curr Opin Solid State Mater Sci 18(4):253–261

Part IX
Characterization of Polymers and Composites I

Synthesis and Characterization of Ultra-Hard Ceramic $AlMgB_{14}$-Based Materials Obtained from Al_xMg_y Intermetallic Powder and Boron Powder by the Spark Plasma Sintering

Ilya Zhukov, Pavel Nikitin, Alexander Vorozhtsov and Maxim Boldin

Abstract In this work, $AlMgB_{14}$-based materials were produced from the intermetallic Al_xMg_y powder and boron powder using mechanical treatment with a planetary mill and subsequent spark plasma sintering (SPS). Phase composition and structure of obtained materials were examined. Phase composition of sintered material is represented by the $AlMgB_{14}$ phase (~95 wt%) and the spinel phase $MgAl_2O_4$ (~5 wt%). The sintered bulk sample has a non-porous structure. The formation of the spinel phase is explained by the presence of oxygen in the raw boron powder.

Keywords $AlMgB_{14}$ · Aluminum-magnesium boride · Spark plasma sintering · XRD

Introduction

Aluminum magnesium boride—$AlMgB_{14}$ (so called BAM)—was first reported by Matkovich and Economy in 1970 [1], but interest in the study of this material increased significantly after obtaining of polycrystalline $AlMgB_{14}$, which possess an extreme hardness (28–32 GPa), low density (2.59 g/cm^3), and high thermal stability [1]. Further studies have shown a low friction coefficient (COF, 0.08–0.02) [2, 3]. The unique combination of these properties makes it possible to use $AlMgB_{14}$-based materials as wear-resistant coatings for cutting tools [4] and bearing parts of machines, where tribological behavior plays a crucial role, as well as structural materials in engineering.

I. Zhukov · P. Nikitin (✉) · A. Vorozhtsov
Tomsk State University, Tomsk 634050, Russia
e-mail: upavelru@yandex.ru

M. Boldin
Lobachevsky State University of Nizhny Novgorod, Nizhniy Novgorod 603950, Russia

J. Li et al. (eds.), *Characterization of Minerals, Metals, and Materials 2020*,
The Minerals, Metals & Materials Series,
https://doi.org/10.1007/978-3-030-36628-5_29

Typically, to produce $AlMgB_{14}$, elemental powders of aluminum, magnesium, and boron are mixed in an atomic ratio of 1:1:14 and then sintered by hot pressing [5–7], spark plasma sintering (SPS) [8], or high-temperature vacuum sintering [9, 10]. Mechanical treatment of Al–Mg–B powder mixture with a planetary mill can increase the reactivity of the powder mixture during sintering. The effect of mechanical activation time and dispersity of the Al–Mg–B powder mixture on the phase composition of sintered materials was described in [11, 12]. It was found that a change in the dispersion of the raw aluminum powder and the duration of mechanical activation of the Al–Mg–B powder mixtures significantly affects the phase composition of $AlMgB_{14}$-based materials sintered by high-temperature vacuum sintering, including the formation of the spinel phase $MgAl_2O_4$, which has a negative effect on the properties of $AlMgB_{14}$-based materials.

The SPS method is the simultaneous heating and consolidation of the powder mixture. The mixture is heated due to the transition of electric current to Joule heat, while electric current is passed directly through the graphite die and the powder mixture. This can significantly reduce the sintering time of the powder mixture. The SPS method is successfully used to obtain $AlMgB_{14}$-based materials [8, 13]. It should be noted that elemental powders of aluminum, magnesium, and boron are used as raw powders.

As an alternative method of obtaining $AlMgB_{14}$-based materials, instead of the elemental powders of aluminum, magnesium, and boron, powders of AlB_2, AlB_{12}, MgB_2 can be used [13, 14]. In this work, mixtures of intermetallic Al_xMg_y and boron powders were sintered, using SPS method, to obtain $AlMgB_{14}$-based materials.

Methods and Materials

Intermetallic Al_xMg_y powder (average particle size $<d>$ ~30 μm) and amorphous black boron powder ($<d>$ ~ 1–2 μm) were mixed in an atomic ratio of 2:14. Intermetallic Al_xMg_y powder was obtained from Al–Mg alloy. The process of obtaining aluminum–magnesium alloy is described in [15]. The obtained powder mixture was mechanically activated with a planetary mill in argon atmosphere. The rotation frequency was 14 Hz. The mass ratio of the powder mixture to milling balls was 1:2. The time of mechanical treatment was an hour. After mechanical treatment, obtained powder mixture was sintered in situ by spark plasma sintering at a temperature of 1400 °C, and a pressure of 70 MPa. XRD-analysis was performed using a Shimadzu XRD 7000 diffractometer with Cu-Kα radiation. The microstructure of sintered materials was characterized using a Joel JSM-640 microscope. To determine the amount of oxygen in the raw boron powder, a LECO N/O/H analyzer was used.

Results and Discussion

Figure 1a shows XRD-pattern of Al_xMg_y powder. It was found that the main phase in the obtained intermetallic powder is the $Al_{12}Mg_{17}$ phase. A small Al content was also found. Figure 1b shows XRD-pattern of the $AlMgB_{14}$-based material sintered by the SPS method from the $Al_{12}Mg_{17}$–B powder mixture. The phase composition of the obtained sample is represented by the phases $AlMgB_{14}$ (refined formula $Al_{0.75}Mg_{0.78}B_{14}$) and $MgAl_2O_4$. From the reflection, intensity ratio between the $AlMgB_{14}$ and the $MgAl_2O_4$ revealed in XRD-pattern was possible to calculate a preliminary content of $AlMgB_{14}$. It was found that the $AlMgB_{14}$ phase content in the sintered sample is ~95 mass%. According to the results of N/O/H analysis, the formation of the spinel phase is due to the presence of oxygen in the initial boron powder (oxygen mass fraction ~1.1%), which reacts with Al and Mg during sintering, forming the spinel phase $MgAl_2O_4$. The SEM-image is shown in Fig. 2. The sintered sample has a non-porous structure, while EDS analysis showed that O, Al, and Mg (probably $MgAl_2O_4$ spinel) are contained in bright regions. Al, Mg, and B are contained in dark regions, which correspond to the $AlMgB_{14}$ phase.

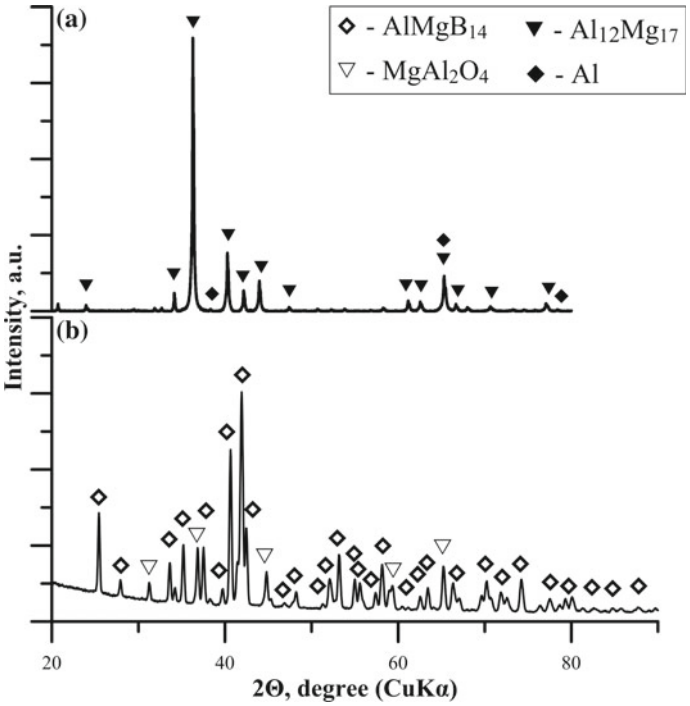

Fig. 1 XRD-patterns of: **a** Al_xMg_y powder; **b** material obtained by the spark plasma sintering from the Al_xMg_y–B powder mixture

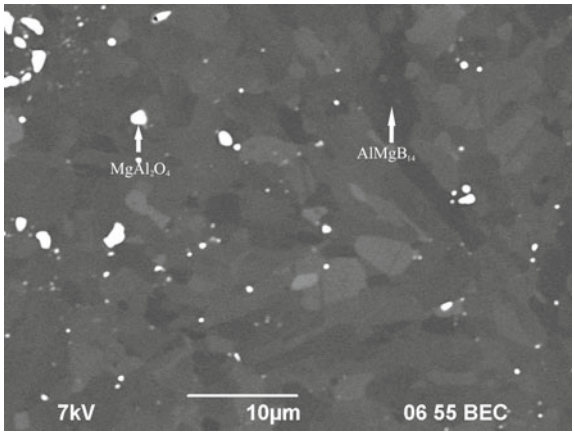

Fig. 2 SEM micrograph of the sintered $AlMgB_{14}$ sample

Conclusions

The phase composition and structure of $AlMgB_{14}$-based materials obtained by mechanical activation and subsequent spark plasma sintering was determined. The sintered sample has a non-porous structure, and according to the XRD results, is represented by the $AlMgB_{14}$ phase and the spinel phase $MgAl_2O_4$. The formation of the spinel phase is due to the presence of oxygen in the raw boron powder. To reduce the amount of $MgAl_2O_4$ in sintered materials, preliminary high-temperature annealing of boron is required.

Acknowledgements Studies were funded by Russia Science Foundation (project No. 19-79-10042).

References

1. Cook B et al (2000) New class of ultra-hard materials based on $AlMgB_{14}$. Scripta Mater 42:597–602
2. Ahmed A, Bahadur S, Cook BA, Peters J (2006) Mechanical properties and scratch test studies of new ultra-hard $AlMgB_{14}$ modified by TiB_2. Tribol Int 39:129–137. https://doi.org/10.1016/j.triboint.2005.04.012
3. Lu X, Yao K, Ouyang J, Tian Y (2015) Tribological characteristics and tribo-chemical mechanisms of Al–Mg–Ti–B coatings under water–glycol lubrication. Wear 326:68–73. https://doi.org/10.1016/j.wear.2014.12.034
4. Ahmed A, Bahadur S, Russell AM, Cook BA (2009) Belt abrasion resistance and cutting tool studies on new ultra-hard boride materials. Tribol Int 42:706–713. https://doi.org/10.1016/j.triboint.2008.10.013
5. Zhukov I, Nikitin P, Vorozhtsov A (2019) Structure, phase composition, and properties of ceramics based on $AlMgB_{14}$, obtained from various powders. In: Characterization of minerals, metals, and materials. Springer, Cham, pp 45–49. https://doi.org/10.1007/978-3-030-05749-7

6. Liu W, Miao Y, Meng Q, Chen S (2013) Structural characterization of $AlMgB_{14}$ prepared by field-activated, pressure-assisted synthesis. J Mater Sci Technol 29(1):77–81. https://doi.org/10.1016/j.jmst.2012.12.008
7. Zhukov IA, Nikitin PY, Grigoriev MV, Vorozhtsov AB. (2019) Phase composition and hardness of $AlMgB_{14}$-based polycrystalline materials. Russ Phys J 1–4. https://doi.org/10.1007/s11182-019-01791-z
8. Roberts DJ, Zhao J, Munir ZA (2009) Mechanism of reactive sintering of $MgAlB_{14}$ by pulse electric current. Int J Refract Metal Hard Mater 27(3):556–563. https://doi.org/10.1016/j.ijrmhm.2008.07.009
9. Li CS, Yang F, Yan G, Xiong XM, Liu GQ, Sun YY, Feng JQ (2014) $AlMgB_{14}$–TiB_2 synthesized by a two-step heat-treatment method. J Alloy Compd 587:790–793. https://doi.org/10.1016/j.jallcom.2013.11.013
10. Nesmelov DD, Danilovich DP, Perevislov SN, Ordan'yan SS (2019) Synthesis temperature influence on the $AlMgB_{14}$ phase composition. Glass Ceram 1–4. https://doi.org/10.1007/s10717-019-00122-5
11. Zhukov IA, Ziatdinov MK, Dubkova YA, Nikitin PY (2018) Synthesis of $AlMgB_{14}$: influence of mechanical activation of Al–Mg–B powder mixture on phase composition of sintered materials. Russ Phys J 61(8):1466–1471. https://doi.org/10.1007/s11182-018-1557-5
12. Nikitin P, Zhukov I, Vorozhtsov A, Zhukov A, Dubkova Y (2018) Effect of dispersity of powder system Al-Mg-B on the phase composition of sintered ceramics $AlMgB_{14}$. In: MATEC web of conferences, vol 243. EDP Sciences, p 00009. https://doi.org/10.1051/matecconf/201824300009
13. Xie Z, DeLucca V, Haber RA, Restrepo DT, Todd J, Blair RG, Orlovskaya N (2017) Aluminum magnesium boride: synthesis, sintering and microstructure. Adv Appl Ceram 116(6):341–347. https://doi.org/10.1080/17436753.2017.1317116
14. Kevorkijan V, Škapin SD, Suvorov D (2015) Synthesis and characterisation of ultra-hard and lightweight $AlMgB_{14}$–$xTiB_2$ composites for wear-resistance and ballistic protection. Metall Mater Eng 21(1):45–56
15. Sokolov S, Dubkova Y, Vorozhtsov A, Kuznetsov V, Promakhov V, Zhukov I (2018) Effect of mechanical activation duration on combustion parameters of Al-Mg-based high-energy systems. In: MATEC web of conferences, vol 243. EDP Sciences, p 00013. https://doi.org/10.1051/matecconf/201824300013

Microstructure Evolution of Additively Manufactured TiC Reinforced Graded Metal Matrix Composite

Jianshen Wang, Juan P. Escobedo-Diaz, Daniel East, Evgeny V. Morozov and Kun Yang

Abstract Ceramic reinforced metal matrix composites (MMCs) have advantages over traditional metallic materials, such as higher hardness, strength, and fracture toughness, which make them suitable for ballistic and defence applications. In this research, an in situ synthetized TiC reinforced Ti–Ni matrix sample was additively manufactured with Ti64 powders and Ni coated graphite powders. Input of Ni coated graphite powders increases from bottom to top of the sample to create a chemical gradient. Microstructure of the graded sample was examined using optical and scanning electron microscopy. The characterization results show that TiC dendrites are in situ synthesized within the metal matrix that contains α-Ti and Ti_2Ni. Morphologies and proportions of these phases change with the variation of chemical composition. Mechanisms of the evolution of microstructure are further analysed. The gradual variation of microstructures indicates that 3D printed graded MMC can provide gradient properties that are preferable for ballistic applications.

Keywords Microstructures characterization · Additive manufacturing · Metal matrix composites

Introduction

Metal matrix composites (MMCs) reinforced with ceramic particles, combining hardness and thermal resistance of ceramic with ductility and toughness of metal, have promising prospects in defence applications [1]. It has also been noticed that graded armour plates with mechanical properties changing from one surface to another show better ballistic performance than homogeneous plates [2]. The hard ceramic rich front surface can wear and split the projectile, and the ductile metal back plate can absorb

J. Wang (✉) · J. P. Escobedo-Diaz · E. V. Morozov
School of Engineering and Information Technology, University of New South Wales, Canberra, Australia
e-mail: jianshen.wang@student.unsw.edu.au

J. Wang · D. East · K. Yang
Lab 22, CSIRO Manufacturing, Melbourne, Australia

J. Li et al. (eds.), *Characterization of Minerals, Metals, and Materials 2020*,
The Minerals, Metals & Materials Series,
https://doi.org/10.1007/978-3-030-36628-5_30

energy. Furthermore, gradually varying properties can avoid lamination and improve spalling resistance.

Titanium alloys, characterized with high specific strength, good ductility, and corrosion resistance, are widely used in aerospace, automobile, and chemical industry [3, 4]. However, low hardness and poor wear resistance limit their ballistic applications. Ceramics such as TiB [5], TiC [6, 7], TiN [8], SiC, [9] and Al_2O_3 [10] are applied as reinforcements for improving tribology properties of Ti alloys. Among these reinforcements, TiC is preferable because of its low density, high melting point, high elastic modulus, high hardness, and especially good compatibility with Ti alloys [1].

Different methods are used for the fabrication of graded composites such as plasma spraying, powder metallurgy and self-propagating high-temperature synthesis (SHS) [11–13], and additive manufacturing (AM) [7]. Among all these methods, AM is preferable because its flexibility of changing manufacturing parameters at different positions of a component. Multi material 3D printing technologies such as Laser Engineered Net Shaping (LENS) are able to fabricate components from two or more different raw materials and enable the controlled varying of fractions of input materials, which is ideal for the manufacturing of graded composites. TiC–Ti functionally graded materials are manufactured using LENS with Ti and TiC particles.

For a ceramic reinforced MMC, its mechanical properties are closely connected with its microstructures such as grain size, ceramic volumes, size, and morphology of ceramic reinforcements [14–18]. For additively manufactured materials, microstructures are greatly influenced by manufacturing parameters [19, 20]. Thus, microstructure characterization is especially crucial for 3D printed MMCs because knowledge of how a microstructure is formed and how it affects the material properties is the bridge between the preferable properties and appropriate manufacturing parameters. In MMCs, in situ synthesized ceramic reinforcements have clean interfaces and strong interfacial bonding with metal matrix, which lead to better properties comparing with ex situ ceramic reinforced MMCs [21, 22].

In this research, MMCs with graded Ti–Ni matrix and in situ synthesized TiC reinforcements are additively manufactured with LENS system. Its microstructures are characterized with optical and scanning electron microscopy, and the formation mechanisms of different microstructures are analysed based on binary phase diagrams and Scheil solidification simulations performed with Thermo-Calc software.

Materials and Experimental Methods

In this work, a 10 mm cubic graded MMC sample was fabricated using an Optomec LENS™ MR-7 additive manufacturing system. The LENS system consists of a 1070 nm wavelength fibre laser, a controlled four hopper powder feed system, a motion control system, and a manufacturing chamber filled with argon protective atmosphere (Fig. 1a). The fibre laser, whose power can be changed between 0 and

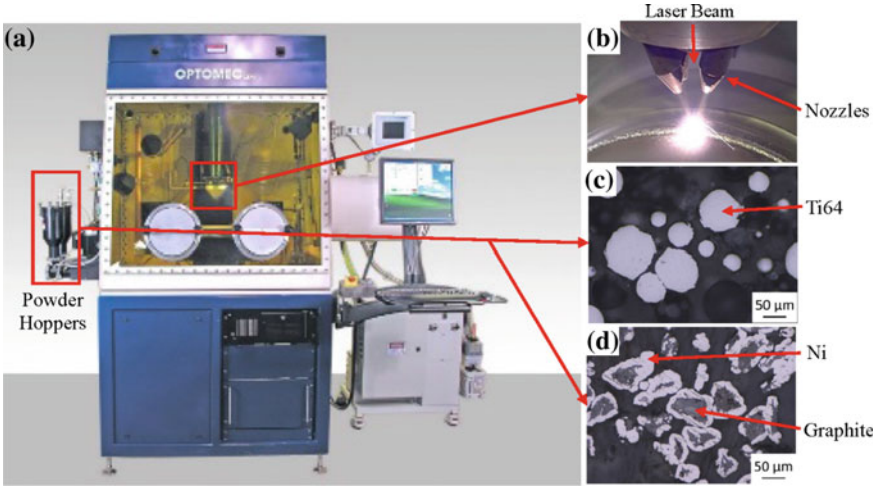

Fig. 1 **a** LENS™ MR-7 additive manufacturing system, **b** deposition head, **c** Ti64 powders, **d** Ni coated graphite powders

500 W, is focused to an approximately 600 μm size spot at the surface of work piece creating a melt pool to absorb the powder flow fed through nozzles (Fig. 1b). Ti64 powders and Ni coated graphite powders (Ni takes 75 wt%) are used as raw materials for manufacturing of this graded MMC sample. The Ti64 powders are in spherical shape, the Ni coated graphite powders are irregular in shape, and their particle size ranges are, respectively, 45–106 and 45–150 μm (Fig. 1c, d). Ti64 powders and Ni coated graphite powders are stored in different hoppers and can be fed separately with controlled feed rates. During 3D printing, Ti64 and Ni coated graphite powders are carried by argon flows to a chamber to be mixed before being delivered to the melt pool.

The graded cubic sample is built on a 6 mm thick Ti64 plate with 210 W laser power, 8.5 mm/s scanning speed, and 0.3 mm layer thickness. The first five layers (1.5 mm) at the bottom of sample are built with only Ti64 powders to get good bonding to the substrate. From the fifth layer to the top of sample, the weight percentage of Ni coated graphite powders linearly increases from 0 to 40%.

This graded sample is cut off from the substrate and further cut through the building direction (vertical) to present the graded properties. This interested section is grinded with 9 μm diamond suspension and chemical polished to mirror-like surface and then etched with Kroll's reagent for microstructure examination with optical microscopy (OM) and scanning electron microscopy (SEM) coupled with X-ray energy dispersive spectrum (EDS).

Results and Discussion

Based on the images obtained from OM, microstructures vary from bottom to top of graded sample (Fig. 2) with different Ni coated graphite inputs. After etching, the section shows different colours gradually varying with the chemical gradient, which indicates that phases and fractions of these phases also change from bottom to top. The phase variation will be further discussed in the following paragraphs with the SEM images. In Fig. 2, white round powders and black irregular shaped particles can be observed embedded in the colourful background. These particles are, respectively, Ti64 and graphite powders which are not completely melted into melt pools during the 3D printing process. At the bottom part of sample, where Ni coated graphite inputs are relatively low ($\leq$10 wt%), unmelted Ti64 powders can be found distributing horizontally between layers. This non-uniformly distribution of unmelted Ti64 powders is caused by the changing thermal status of melt pools at different layers. When depositing one layer of materials, some Ti64 powders will attach to the upper surfaces of solidifying melt pools and be covered by the next layer of deposition. If the temperature of melt pools in the second layer is high enough, the unmelted Ti64 powders left by the first layer will be completely melted into new melt pools. The amount of Ni coated graphite input will affect the

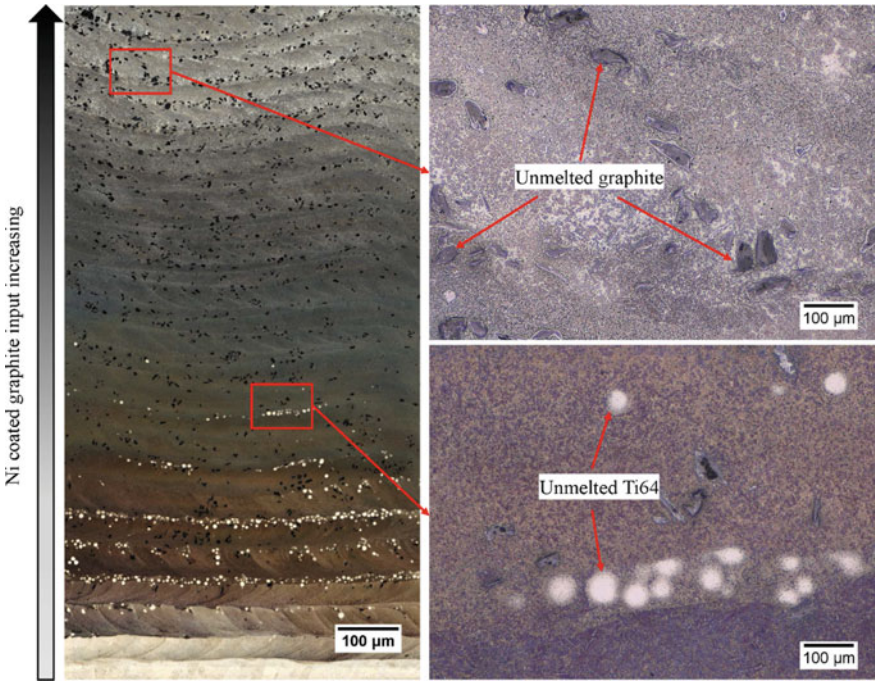

Fig. 2 Optical microscopy image of graded MMC

thermal condition of a melt pool in two different ways. First, laser energy absorption rate of a melt pool will be decreased by Ni coated graphite input, which in result has a negative influence to a melt pool for gaining energy. On the other hand, the synthesis of TiC and Ti_2Ni will generate extra heat to the melt pool. Considering both above influences, small amount of Ni coated graphite inputs will decrease the temperature of a melt pool, which leaves more unmelted Ti64 powders. When the Ni coated graphite input is higher, temperature of a melt pool will be kept high enough to eliminate all unmelted powders because of the reactive heat. Unmelted graphite particles are observed existing through all the background and more densely distributed among the layers having high Ni coated graphite inputs. The reason of the existence of graphite particles is similar to that of Ti64 powders. But graphite fraction increases with more Ni coated graphite input and graphite can survive at melt pools having high temperature, which explains why unmelted graphite tends to distribute at upper parts of the sample.

With a SEM, microstructures at smaller scales can be investigated. At bottom of the samples where no Ni coated graphite is added, 3D printed Ti64 shows a typical martensite microstructure because of high cooling rate (Fig. 3a). When small amount of Ni coated graphite (3 wt%) is added into powder supply, small granular size TiC precipitates appear in the composite, and the metallic matrix shows a basket-weave structure (Fig. 3b). Based on the Scheil solidification diagram (Fig. 4a), solidification sequence of a melt pool containing 3 wt% Ni coated graphite can be expressed as formulas (1) and (2). In such a melt pool, small amount of primary TiC_p (subscript p for primary) first precipitates from the liquid, and then, β-Ti and TiC_{ec} (subscript ec for eutectic) are generated through a eutectic reaction until the melt pool solidifies completely. Because the C% is low in L_2, β-Ti phase takes most volume of the eutectic structure. Based on Ti–Ni binary phase diagram [23], β-Ti will turn into eutectoid α-Ti and Ti_2Ni (formula 3), and α-Ti phase is far more than Ti_2Ni because of the low Ni composition in β-Ti. This typical microstructure can be described as small size TiC particles (about 0.53 μm^2 average size) embed in α-Ti dominating matrix, which is the microstructure we see in Fig. 3b.

$$L_1\left(\text{Liquid}_1\right) \rightarrow TiC_p + L_2 \tag{1}$$

$$L_2 \rightarrow TiC_{ec} + \beta\text{−Ti} \tag{2}$$

$$\beta\text{−Ti} \rightarrow \alpha\text{−Ti} + Ti_2Ni \tag{3}$$

With more Ni coated graphite added into powder supply (approximately 6 wt%), larger sized TiC phase dendrites and white Ti_2Ni phase can be clearly observed embedded in grey Ti phase in microstructure (Fig. 3c). The solidification simulation diagram is shown in Fig. 4b, and the solidification sequence can be expressed by formulas (4)–(6). Still, primary TiC_p precipitates first from liquid and then acts as nucleus for the following eutectic reaction (5). Afterwards, at grain boundaries of these eutectic phases, the Ni rich liquid (L_3) solidifies via another eutectic reaction

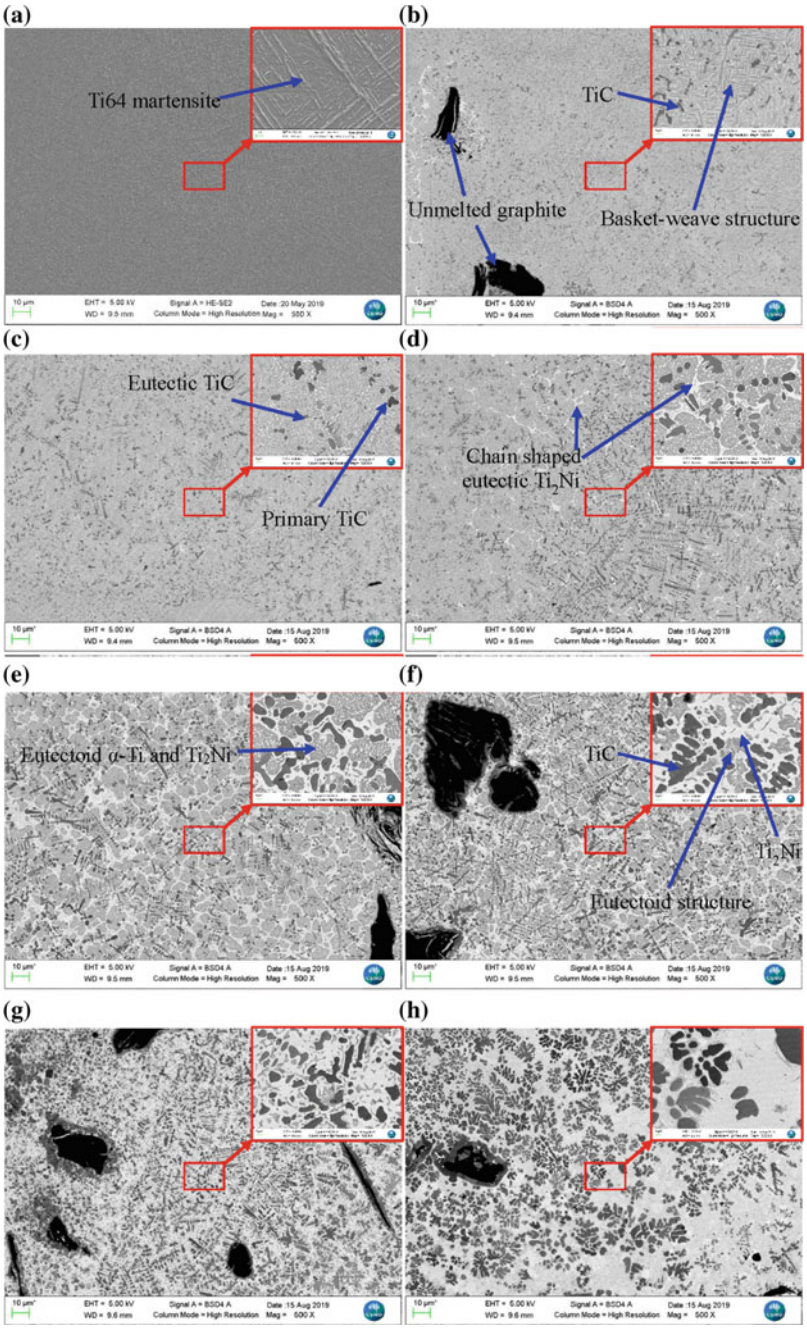

Fig. 3 Scanning microscopy images of microstructures at layers of different Ni coated graphite input, **a** 0 wt% Ni coated graphite, **b** 3 wt% Ni coated graphite, **c** 6 wt% Ni coated graphite, **d** 12 wt% Ni coated graphite, **e** 18 wt% Ni coated graphite, **f** 24 wt% Ni coated graphite, **g** 32 wt% Ni coated graphite, **f** 36 wt% Ni coated graphite

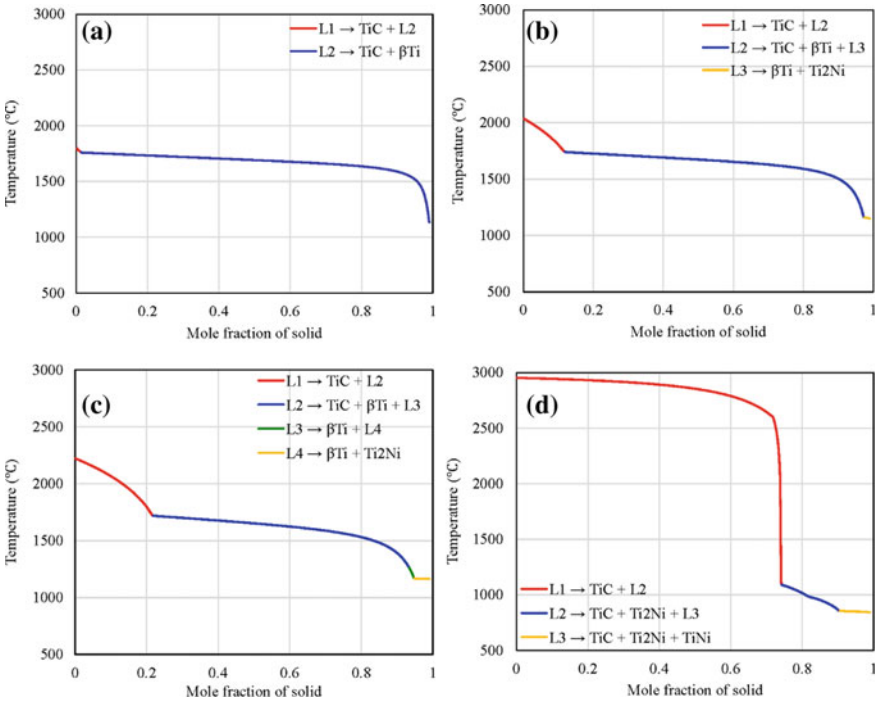

Fig. 4 Schiel solidification simulations of melt pools with different Ni coated graphite input, **a** 3 wt% Ni coated graphite, **b** 6% Ni coated graphite input, **c** 10% Ni coated graphite input, **d** 38% Ni coated graphite input

(6) producing β-Ti and Ti_2Ni_{ec}. At last, eutectoid reaction (7) takes place and turns β-Ti into α-Ti and Ti_2Ni_{ed} (subscript ed for eutectoid). Based on the solidification sequence, two different types of TiC phases and two different types of Ti_2Ni can be found in the microstructures. Primary TiC_p dendrites are generally larger in size and exist in the middle of a Ti grain since they act as nucleus in solidification process. Eutectic TiC_{ec} are in small flake shape and do not have obvious distributing preference. Eutectic Ti_2Ni_{ec} are in bigger sized granular or striped shape locating at grain boundaries, and thin laminar eutectoid Ti_2Ni_{ed} can be found distributing within α-Ti grains.

$$L_1 \rightarrow TiC_p + L_2 \tag{4}$$

$$L_2 \rightarrow TiC_{ec} + \beta{-}Ti + L_3 \tag{5}$$

$$L_3 \rightarrow \beta{-}Ti + Ti_2Ni_{ec} \tag{6}$$

$$\beta{-}Ti \rightarrow \alpha{-}Ti + Ti_2Ni_{ed} \tag{7}$$

When the Ni coated graphite input keeps increasing, Ti_2Ni phase takes more volumes and can be observed as thin but continuous chain shape structures at grain boundaries. Inside grains, stripe shape α-Ti and granular Ti_2Ni_{ed} distribute evenly with each other. The dendrites of TiC are coarser in size and more densely distributed (Fig. 3d). A solidification simulation of a melt pool having 10 wt% of Ni coated graphite is conducted (Fig. 4c), and solidification sequence can be expressed as formulas (8)–(11). Comparing above solidification process, a solidification stage from liquid to β-Ti (formula 10) is added between the two different eutectic reactions. In microstructures, this solidification from liquid to β-Ti will lead to a layer of TiC free eutectoid structure at outer parts of grains. With Ni coated graphite, input keeps increasing, and this solidification sequence is kept the same. But with more and more Ni and C in the melt pools, TiC dendrites and Ti_2Ni chains become coarser and take more volumes in the composite (Fig. 3e, f). The α-Ti phase is divided into smaller grains until disappears completely (Fig. 3g).

$$L_1 \rightarrow TiC_p + L_2 \tag{8}$$

$$L_2 \rightarrow TiC_{ec} + \beta{-}Ti + L_3 \tag{9}$$

$$L_3 \rightarrow \beta{-}Ti + L_4 \tag{10}$$

$$L_4 \rightarrow \beta{-}Ti + Ti_2Ni_{ec} \tag{11}$$

$$\beta{-}Ti \rightarrow \alpha{-}Ti + Ti_2Ni_{ed} \tag{12}$$

When the Ni coated graphite inputs reach a high level (≥36%), coralloid TiC precipitates can be observed distributing densely in Ti_2Ni background, and TiNi phase starts to emerge as very light spots in microstructure (Fig. 3h). The solidification simulation (Fig. 4d) and solidification formulas (13)–(15) show that β-Ti disappeared in solidification process, and as a result, no eutectoid Ti_2Ni and α-Ti can be found in the microstructures.

$$L_1 \rightarrow TiC_p + L_2 \tag{13}$$

$$L_2 \rightarrow TiC_{ec} + Ti_2Ni_{eu} + L_3 \tag{14}$$

$$L_3 \rightarrow TiC + Ti_2Ni + TiNi \tag{15}$$

Microstructures show a gradual but with a dramatic variation with increasing Ni coated graphite proportion from bottom to top of the sample. The morphologies and distribution densities of TiC dendrites are both changed. The morphologies of TiC change from small granular particles to dendrites and finally become coralloid

structures. The area percentage of TiC in microstructures increases from 7.61% (Fig. 3b) to 33.6% (Fig. 3h). The average size of TiC reinforcements increases from 0.53 to 6.4 μm^2. The area percentage of Ti_2Ni in microstructures increases from 3.8 to 47.9%.

Conclusions

In situ TiC reinforced Ti–Ni metal matrix composites were successfully additively manufactured with Ti64 and Ni coated graphite powders using the Laser Engineered Net Shaping (LENS™) process. This MMC has a chemical gradient because of the variation of raw material inputs. A gradually changing microstructure can be observed by optical and scanning electron microscopy. The characterization of microstructure evolution reveals the following features:

(1) The morphologies and fractions of in situ synthesized TiC reinforcements vary with the chemical gradient. TiC particles go through a changing of shapes from granular shape to dendrites and coralloid shape with their average particles size increasing from 0.5 to 6.4 μm^2. The area fraction of TiC increases from 7.6 to 33.6% with the Ni coated graphite input increasing from 6 to 40%.
(2) The phase composition and microstructure of Ti–Ni metal matrix are changed by the input of Ni coated graphite. The net shape eutectic Ti_2Ni structures grow coarser, and the eutectoid α-Ti grains wither away gradually with increasing Ni coated graphite inputs.
(3) Unmelted Ti64 and graphite particles can be observed between deposition layers, and their distribution is affected by the thermal status of melt pools.

The gradual variation of microstructures indicates that the properties of 3D printed Ti64 such as hardness, strength, and ductility may be greatly changed by the input of Ni coated graphite, which worthy further study.

Acknowledgements The authors thank Mr. Geoff Delooze and Dr. Robert Wilson from Lab 22 of CSIRO for their support in this work.

References

1. Rajabi A, Ghazali MJ, Daud AR (2015) Chemical composition, microstructure and sintering temperature modifications on mechanical properties of TiC-based cermet—a review. Mater Des 67:95–106
2. Huang CY, Chen YL (2017) Effect of varied alumina/zirconia content on ballistic performance of a functionally graded material. Int J Refract Metal Hard Mater 67:129–140
3. Ivasishin OM, Markovsky PE, Matviychuk YV, Semiatin SL, Ward CH, Fox S (2008) A comparative study of the mechanical properties of high-strength β-titanium alloys. J Alloy Compd 457(1–2):296–309

4. Nunes AR, Borborema S, Araújo LS, Dille J, Malet L, de Almeida LH (2018) Production, microstructure and mechanical properties of cold-rolled Ti-Nb-Mo-Zr alloys for orthopedic applications. J Alloy Compd 743:141–145
5. Hu Y, Zhao B, Ning F, Wang H, Cong W (2017) In-situ ultrafine three-dimensional quasi-continuous network microstructural TiB reinforced titanium matrix composites fabrication using laser engineered net shaping. Mater Lett 195:116–119
6. Vasanthakumar K, Karthiselva NS, Chawake NM, Bakshi SR (2017) Formation of TiC_x during reactive spark plasma sintering of mechanically milled Ti/carbon nanotube mixtures. J Alloy Compd 709:829–841
7. Liu W, DuPont JN (2003) Fabrication of functionally graded TiC/Ti composites by laser engineered net shaping. Scripta Mater 48(9):1337–1342
8. Balla VK, Bhat A, Bose S, Bandyopadhyay A (2012) Laser processed TiN reinforced Ti6Al4V composite coatings. J Mech Behav Biomed Mater 6:9–20
9. Das M, Balla VK, Basu D, Bose S, Bandyopadhyay A (2010) Laser processing of SiC-particle-reinforced coating on titanium. Scripta Mater 63(4):438–441
10. Bahraminasab M, Ghaffari S, Eslami-Shahed H (2017) Al_2O_3-Ti functionally graded material prepared by spark plasma sintering for orthopaedic applications. J Mech Behav Biomed Mater 72:82–89
11. Khor KA, Gu YW (2000) Effects of residual stress on the performance of plasma sprayed functionally graded ZrO2/NiCoCrAlY coatings. Mater Sci Eng A 277(1–2):64–76
12. Erdemir F, Canakci A, Varol T (2015) Microstructural characterization and mechanical properties of functionally graded Al2024/SiC composites prepared by powder metallurgy techniques. Trans Nonferrous Met Soc China 25(11):3569–3577
13. Bertolino N, Monagheddu M, Tacca A, Giuliani P, Zanotti C, Maglia F, Tamburini UA (2003) Self-propagating high-temperature synthesis of functionally graded materials as thermal protection systems for high-temperature applications. J Mater Res 18(2):448–455
14. Baran A, Polanski M (2018) Microstructure and properties of LENS (laser engineered net shaping) manufactured Ni-Ti shape memory alloy. J Alloy Compd 750:863–870
15. Gao F, Wang HM (2008) Dry sliding wear property of a laser melting/deposited Ti2Ni/TiNi intermetallic alloy. Intermetallics 16(2):202–208
16. Liu S, Liu Z, Wang Y, Yue P (2014) Ti-based composite coatings with gradient TiC x reinforcements on TC4 titanium alloy prepared by laser cladding. Sci China Technol Sci 57(7):1454–1461
17. Wang J, Li L, Tan C, Liu H, Lin P (2018) Microstructure and tensile properties of TiCp/Ti6Al4V titanium matrix composites manufactured by laser melting deposition. J Mater Process Technol 252:524–536
18. Ya B, Zhou B, Yang H, Huang B, Jia F, Zhang X (2015) Microstructure and mechanical properties of in situ casting TiC/Ti6Al4V composites through adding multi-walled carbon nanotubes. J Alloy Compd 637:456–460
19. Qiu C, Adkins NJ, Attallah MM (2013) Microstructure and tensile properties of selectively laser-melted and of HIPed laser-melted Ti–6Al–4V. Mater Sci Eng A 578:230–239
20. Wang T, Zhu YY, Zhang SQ, Tang HB, Wang HM (2015) Grain morphology evolution behavior of titanium alloy components during laser melting deposition additive manufacturing. J Alloy Compd 632:505–513
21. Huang LJ, Geng L, Xu HY, Peng HX (2011) In situ TiC particles reinforced Ti6Al4V matrix composite with a network reinforcement architecture. Mater Sci Eng A 528(6):2859–2862
22. Saheb N, Iqbal Z, Khalil A, Hakeem AS, Al Aqeeli N, Laoui T, Al-Qutub A, Kirchner R (2012) Spark plasma sintering of metals and metal matrix nanocomposites: a review. J Nanomater 2012:18
23. Massalski, TB, Murray, JL, Bennett, LH, Baker, H(1986). Binary alloy phase diagrams. American Society for Metals, Metals Park, OH

A Bibliometric Analysis of the Strategy and Performance Measurement of the Polymer Matrix Nanomaterials Development Scenario Globally, and the Participation of Brazil

Robson S. Costa and Esperidiana A. B. Moura

Abstract Extensive studies have been conducted worldwide on the strategy for the development of nanomaterials. One of the known strategies for this has aroused interest in the market is the incorporation of the nanoparticles, extracted from the residues in the matrices of the polymers for the production of environmentally correct nanocomposites. This work presents a survey of the scientific knowledge of nanomaterials of the polymer matrix and a panoramic view of the evolution of these nanomaterials are subject, in order to meet the criteria of sustainable development due to the environmental concerns. This study also intends to use bibliometric tools to database acquisition and analysis of bibliographic reviews for an evaluation of the scenarios in the world on the development of polymeric nanomaterials based on three different classes of polymeric nanocomposites: polymer/clay; polymer/graphene, and polymer/nanocellulose nanocomposites.

Keywords Polymeric matrix · Nanomaterials · Bibliometry · Status · Bibliographic

Introduction

Nanotechnology is one of the six technologies that provide substantial prospects for innovative products and applications' development worldwide, in sectors such as primary agricultural production, animal feed, food processing, novel foods, food additives and packaging, pharmaceutical products, industrial segments, and new material developments. Thus, the size reduction of the material to the nanoscale can change the physicochemical properties compared to conventional material even at larger scales, due to the high surface to volume ratio of nanomaterials.

Nanocomposite, the area of nanotechnology that uses the nanoscale technology to improve the properties of materials, is defined as a multiphase system in which

R. S. Costa (✉) · E. A. B. Moura
Nuclear and Energy Research Institute, Center for Chemical and Environmental Technology, 2242 Prof. Lineu Prestes Av., São Paulo, SP, 05508-000 Brazil São Paulo, Brazil
e-mail: rscosta@usp.br; rscosta.mktes@gmail.com

J. Li et al. (eds.), *Characterization of Minerals, Metals, and Materials 2020*,
The Minerals, Metals & Materials Series,
https://doi.org/10.1007/978-3-030-36628-5_31

one of the components has at least one of the dimensions in the nanometer size scale, ranging from about 1 to 100 nm. Polymer nanocomposites are defined as multiphase systems in which the nanofillers with at least one of dimensions is in nanoscale size are dispersed in the polymer matrix.

In recent decades, the polymer nanocomposite materials have been extensively studied since nanofillers reinforcement, even small loadings, provide substantial improvements in polymer properties. Nevertheless, as is known, their performance depends on several parameters and factors, such as the state of dispersion, compatibility, and nanofillers distribution into the polymer matrix. Despite the extensive research that has been carried out in worldwide in the field of polymer nanocomposites, their full potential in terms of flame retardance, mechanical, thermal, barrier, and other properties, yet remains a major challenge to achieve, in order to allow its application in various industrial sectors [1].

Regarding nanoscale components, several nanofillers such as carbon nanotubes, graphene, nanocellulose, nanosilica, and clay are being tested for their reinforcement capacity in the polymer matrix. Among these nanofillers, a particular interest in polymer/clay nanocomposites has extended since the last century. Recently, nanocellulose and graphene as fillers in the polymeric compound have gained the focus of research and industrial applications [2, 3].

Bibliometric

It is a field of science that studies and analyzes bibliographic references and thus creates data to assist in the development of testing and decision-making strategies. Bibliometrics has been a great method for conducting purpose studies and it provides insight into how research is being used or it studies the design of a specific topic and what has been completed for new projects and segmentation strategy.

For a good data analysis project, good planning is needed, especially with regard to bibliometric, because its databases are references, article selection, and keyword analysis for training and database building.

This work aims the use of bibliometric tools to database acquisition and analysis of bibliographic reviews for an evaluation of the scenarios in the world on the development of polymeric nanomaterials based on three different classes of polymeric nanocomposites: polymer/clay; polymer/graphene, and polymer/nanocellulose nanocomposites.

Methodology

To better guide the work, three nanofillers were selected from the various sub-areas of study nanotechnology materials including; polymer/clay, polymer/graphene, and polymer/nanocellulose nanocomposites. With the nanofillers selected, the bibliographic references of this work were selected and, later, the use of the bibliometric

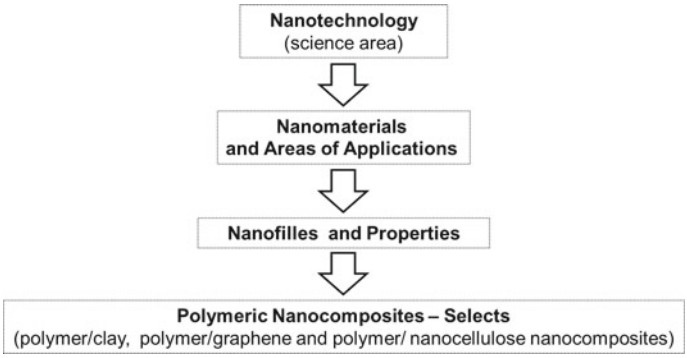

Fig. 1 Data collection information process

tool to understand the development scenario of the analyzed nanocomposites and meet the main objective of this study. Analyzing articles published primarily for this purpose from 2016 to 2019, bibliometric to development tools; these three nanofillers were selected, which helped in the analysis of segmentation data for current studies and research work. Together, they collected features and relevant information to selected objects of study in various fields of science. Figure 1, present in the process carried out for the start of database creation, this research was developed with the use of mind mapping tool, through which it was possible to align the concepts and the main ideas of this study. Subsequently, the defined study areas, and with the help of keywords (polymer/clay nanocomposites, polymer/graphene and polymer/nanocellulose), searched for references in the field of nanomaterials, nanofilters and finally, nanocomposite polymer to be studied, analyzed, and structured for the conclusion of this study.

It may be understood with these analyzes, and we will understand the main features that led to the development of nanocomposite materials based on a polymeric matrix and why some industries and some polymeric nanocomposites are not getting the desired benefits to conduct research related to them.

In Fig. 2, the process was performed to create the database from the beginning to the identification of the polymer matrix niches. The database was composed by keywords used for research development; in addition, some bibliometric methods were used. Bibliometrics use bibliometric indicators, examining the data, the bibliographic references, by him, provide the necessary information to describe the current situation, through articles published in a certain period that was analyzed and described today.

For careful and accurate analysis during this study, data were analyzed, information and data obtained from the references obtained through the analysis process for the preparation of this article. Initially, 317 articles were selected for analysis and then reduced 275 items, cleaning the obtained data. Keywords used: polymer/clay nanocomposites, graphene and/nanocellulose polymer/polymers nanocomposites; and selected the items in order of relevance in the first 10 pages of Google Scholar

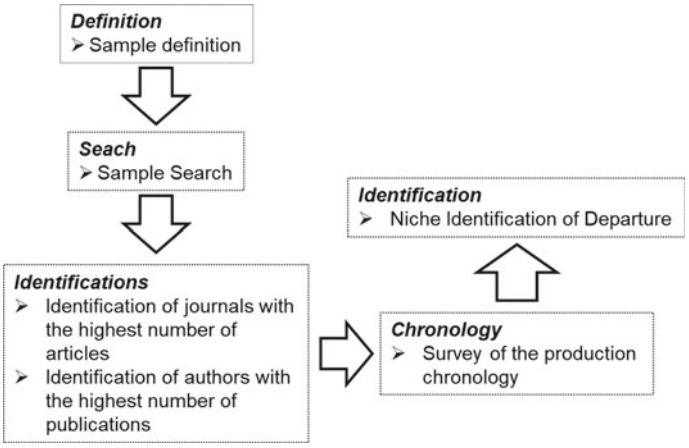

Fig. 2 Bibliometric organization flow

tool, and then organized the data according to the presentation, Fig. 2—bibliometric flow of the organization, so we can have a brief description of the proposed scenario in this study.

Scenario

Considering all the scenarios, the three segments previously selected by bibliometric tools and nanocomposite polymer matrix area were analyzed there between: clay, graphene, and nanocellulose.

Clay

Since the end of last century, the discovery of various clays and its increasing use in various applications resulted in continuous developments in polymer science and nanotechnology [4].

The material "clay" is actually composed of layered silicate/clay minerals (aluminum sheet silicates) containing metal oxides such as alkaline earth metal, alkali metal, magnesium, etc., and especially the organic matter present in small amounts [5] The field flourished after workers at Toyota Central Research Laboratories reported a nylon 6/clay nanocomposite that was used on a timing belt cover on the Toyota Camry.

This revelation led to an expansion of activity with a wide range of polymer types. Nylon 6/clay nanocomposites exhibited substantial improvements in the physical

properties of the composite over pure nylon 6 polymer [1, 6]. Clays are used in packaging development, different properties can be improved through the use of nanocomposites, as gas barriers, antimicrobial and other properties [7]. In addition, surface coatings can be used to modulate the surface affinity of the package for different liquids and pastes, for example, for a container-based water repellent paper [8] or easy-to-empty characteristics.

Polymer/Clay Nanocomposite Applications

In general, the real improvements in thermal properties, mechanical barrier, and the polymer nanocomposite/clay applications are indeed dependent on the level at which the clay particle is dispersed in the polymer matrix. The extent to which the clay nanoparticle is distributed in the polymer matrix depends on two factors, namely: (i) physical interaction capacity, or chemical between the material of the clay and the polymer matrix, and (ii) the technique used for preparing polymer/clay nanocomposite.

Classification of Clay Materials

Therefore, a brief discussion on clay classification is provided in this section. Two major classifications of clay materials include (i) natural clay and (ii) synthetic clay. The composition of all clay materials comprises of alternatively arranged "SiO_2" and "AlO_6" entities. According to their arrangement, natural clay materials are subdivided into (i) 2: 1 and (ii) 1: 1 clay types [5]. The broad classification of clay materials is shown in Fig. 3 for a better understanding of the readers.

The discussion of polymeric nanocomposite applications presupposes industrial growth. Many of the laboratory studies cited in this review use solution-based preparation methods for polymer/clay nanocomposites and others. Its fusion processing is the most practical and useful method for commercial production for those.

Polymer/clay nanocomposites, such as PE and nylon nanocomposites, are used as barrier materials in packaging and storage applications. Recently, biodegradable and bio-based polymer/clay nanocomposites, for example, PLA, PCL and PBS, have been used as packaging, especially for food and also for short shelf-life products such as containers, drinking glasses, and blister packs. Some other potential applications for polymer/clay nanocomposites that have good water barrier properties are protective coatings, adhesives, molding compounds, and dielectric materials for electronic applications, which also require high thermal stability and good mechanical properties of the polymer. PBI/clay nanocomposites have been used for membranes, for example, reverse osmosis membranes in seawater and brine desalination, and have also been developed for organic liquid barrier applications. Water-based polyurethane/clay nanocomposites are considered promising materials to be used as water-resistant coatings for wood finishing, fiberglass glue, automotive finishes and adhesives to reduce solvent emissions and retain good barrier properties [9].

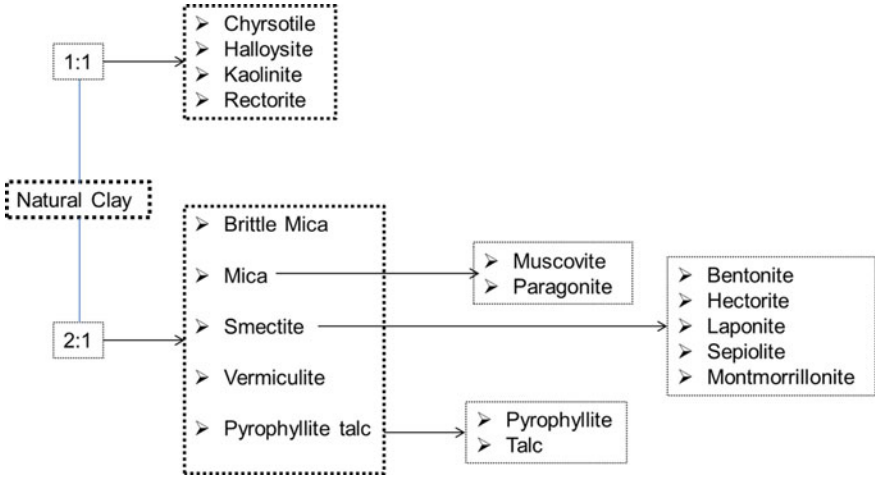

Fig. 3 Classification of clay materials

Approximately 80% of polymer/clay nanocomposites are intended for the automotive, aviation, and packaging industries. Auto parts such as handles, rearview mirror, timing belt, gas tank components, engine cover, bumpers, etc. They also used nanocomposites, mainly nylon (polyamide), produced by Bayer, Honeywell Polymer, RTP Company, Toyota Motors, UBE and Unitika [10]. Table 1 shows a summary of product application and areas in which polymer/clay nanocomposites are used.

And the setting corresponding to the areas in which the polymer/clay nanocomposite was used in the early twenty-first century is shown in Fig. 4.

Graphene

Graphene was successfully exfoliated a little over a decade ago. The discovery of autonomous graphene by Andre Geim and Konstantin Novoselov at the University of Manchester in 2004 led to the awarding of the 2010 Nobel Prize in Physics for groundbreaking experiments on two-dimensional material graphene. Since then, there has been tremendous interest from academia, industry, and government institutions in exploring graphene properties, production methods, and possible applications [11, 12].

Graphene is nothing more than a single layer of sp-bonded carbon arranged in a honeycomb structure. Unique electrical, thermal property, mechanical and chemical stability, and ease of chemical functionalization make graphene an attractive material [11, 13].

Graphene can be rolled up in a carbon nanotube (CNT) and can form 3D graphite stacking 2D graphene layers [14–16]. Graphene Oxide (GO) can be synthesized

Table 1 Application areas and products that use polymer/clay nanocomposites

Automotive	Packaging	Energy	Biomedical	Construction	Home furnishings
Footboards	Beer and soft drink bottles	Fuel cells	Artificial tissues	Tubes	Furniture
Friezes	Meat and cheese packaging	Lithium batteries	Dental and bone prosthesis	Cords	Home appliances
Station wagon	Internal films of juice boxes	Solar panels	Medicines		
Floors		Nuclear reactors			
Dashboards		Capacitors			
Timing belts					
Handle					
Gas tank					
Components					
Engine covers					
Bumpers					

Source Author

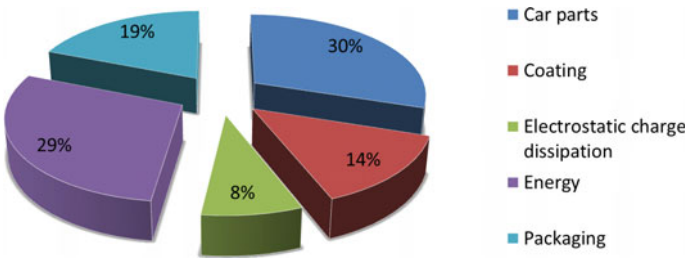

Fig. 4 Applications of polymer/clay nanocomposites

from graphite through Hummer's method. Resulting GO flakes contain various functional groups such as carboxyl, hydroxyl, epoxy, etc. Graphene exhibits high Young's modulus (~1 TPa), large surface area (2.630 $m^2\ g^{-1}$), and thermal conductivity (~5000 $W\ m^{-1}\ K^{-1}$). One of the most promising applications of graphene is incorporation as filler in polymer nanocomposites. There has been extensive research on GO-based polymer composites for energy application and will be detailed further. Another attractive property of graphene is that it can be chemically functionalized [9, 13]. However, this application of graphene is hampered by the poor solubility of pristine graphene in most common solvents. Also, the large surface area of graphene

results in significant aggregation in a polymer matrix due to large van der Waals interactions. A challenge is to achieve a good dispersion of the atomically thin sheets of graphene within the polymer matrix [9].

Polymer/Graphene Nanocomposite Applications

Polymer/graphene-based nanocomposites have been shown some remarkable moisture barrier properties and clearly have great potential for use as permeation protection materials. Potential applications are food and pharmaceutical packaging as well as corrosion protection coatings. Devices such as liquid crystal monitors and light-emitting organic diodes (OLEDs) are very sensitive to moisture and oxygen. Therefore, with these excellent barrier properties, graphene/polymer-based nanocomposites have obvious potential as ultra-barriers to organic electronics. Graphene is electrically conductive, while GO is not, therefore, the choice of graphene-based filler will depend on whether electrical conductivity is a requirement of polymer nanocomposite.

Transparency is another requirement for many of these applications. However, this can be difficult because some polymer/graphene-based films are opaque. However, where there is a very good dispersion of graphene or graphene oxide platelets, highly transparent, high barrier films can be produced that have the potential for use in electronic devices such as flexible electronic papers, OLEDs, flexible liquid crystal displays, cells. organic solar, and organic thin-film transistors [9].

Graphene nanocomposites have a large number of applications including engineering, electronics, medicine, energy, industrial, home design and more (Fig. 5). Metals such as Cu, Au, Fe, Ce, etc., have been incorporated into graphene as a composite for various applications such as sensing and imaging. With the success of graphene-metal nanoparticles (NPs), their most recently discovered counterpart, graphene–metal nanoclusters (NCs) have gained prominence in the field of materials science [16].

Nanocellulose

Cellulose as raw material has been in relevance for more than 15 decades, considering its annual biomass production of approximately 1.5×10^{12} tons. In addition, this biopolymer is viewed as an almost inexhaustible source with raw material produced mainly from wood pulp and to smaller extent cotton, ramie, flax, wheat straw, tunicate, fungi, bacteria, and algae (green, gray, red, yellow-green) with each having its unique characteristics (Fig. 6).

Nanocellulose is a form of nanostructured cellulose, which is typically used in the form of cellulose nanocrystals (CNCs), cellulose nanofibrils (CNFs), or bacterial nanocellulose (BNC) [17]. CNCs, also known as cellulose nanowhiskers, are

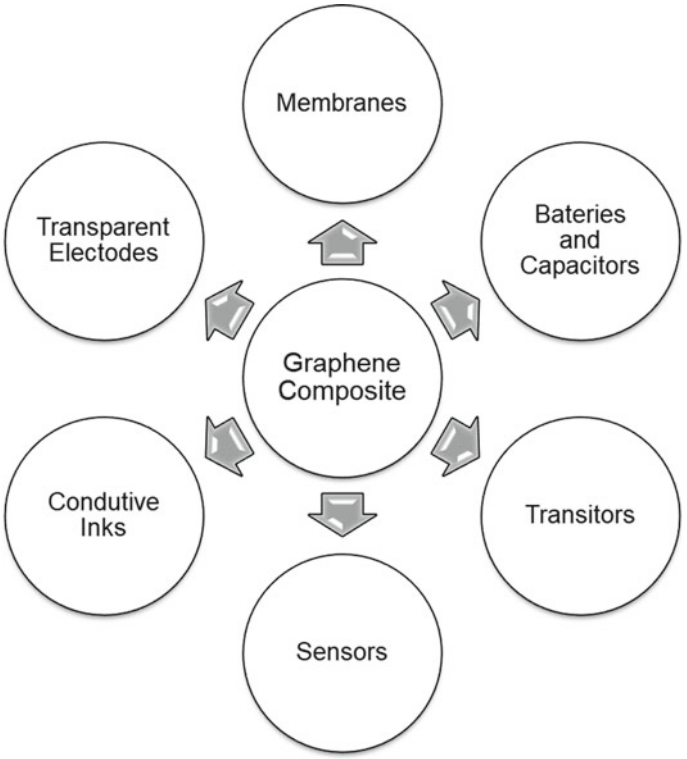

Fig. 5 Potential applications of graphene in different sectors ranging from conductive inks to chemical sensors, light-emitting devices, energy, touch panels, and high-frequency electronics

needle-like cellulose crystals with typical widths of 10–20 nm and lengths of 100–250 nm; they are produced from several biological sources, such as wood, cotton, wheat straw, rice husk, bamboo, potato tuber, sugar beet, ramie, bacteria, and algae, typically through strong acidhydrolysis. Acid treatments cause the removal of disordered regions from the source materials, forming highly ordered crystalline cellulose structures. CNFs contain amorphous cellulose in their structure and, therefore, are not as crystalline as CNCs. BNC, also known as microbial cellulose, is another form of nanostructured cellulose, which is produced by bacterial actions; It has a typical cross-section diameter of 20–100 nm and a degree of polymerization (DP) of 4000–10 000 [18].

The use of nanocellulose as reinforcement in nanocomposites has become a popular research topic. In addition to the numerous advantages of nanocellulose, such as low cost, low density, renewability, low energy consumption, high specific properties, biodegradability, and relatively good surface reactivity, it shows better properties as a reinforcing phase in nanocomposites as compared to micro or macro cellulose composites [19].

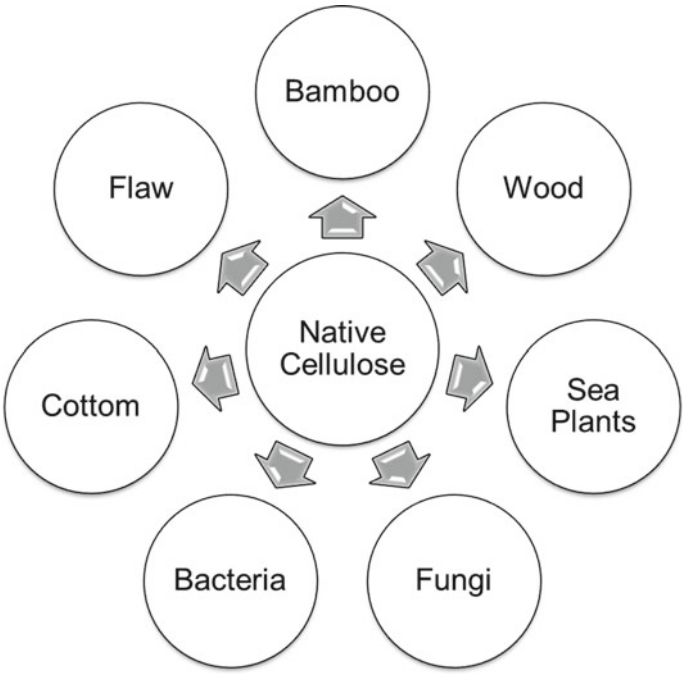

Fig. 6 Different sources of cellulose

Polymer/Nanocellulose Nanocomposite Applications

The nanocellulose–polymer composite designing and processing flexibility permit extensive, design flexibility; and process ability of nanocelulose–polymer composites permit extensive utilization in the automotive, packaging, electronics, and biotechnology industries, among others (Fig. 7) [19].

Besides cellulose, other polysaccharide nanoparticles can be obtained from starch or chitin which are also abundant renewable resources, usable in polymer [20].

Conclusions and Perspectives

Clay Panoramic

The perception of polymer nanocomposites is considered as an innovative approach for design of new materials with specialized properties. The different modification techniques used for the preparation of functionalized clay materials showed impact on the dispersion of clay fillers in the polymer matrices [21]. The desired properties for the polymer/clay nanocomposites are mainly dependent on the type of modifying

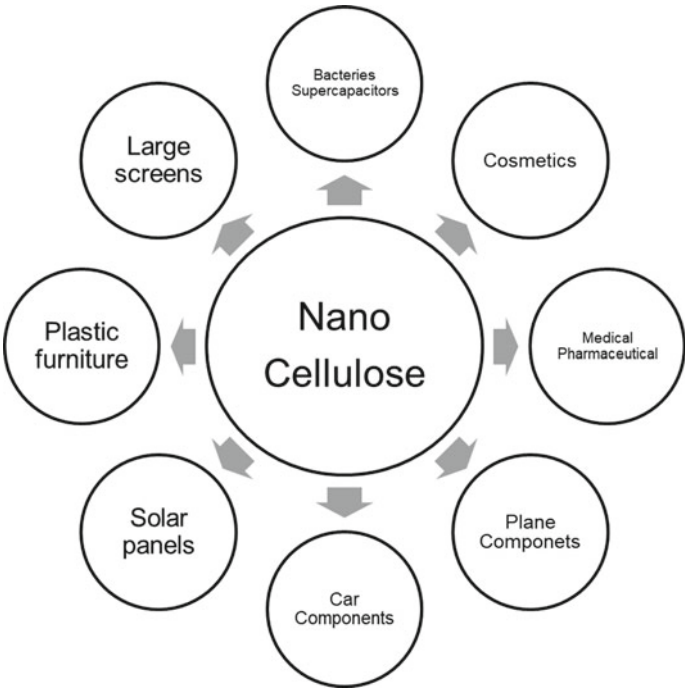

Fig. 7 Potential nanocellulose applications

agents used for functionalization of clay materials [22]. Solution casting technique appears to provide good dispersion of clay layers in polymer matrix in comparison with melt blending. This is due to low viscosity and high agitation power associated with solution blending. However, melt blending is considered as industrially viable as well as ecofriendly technique and exhibits high economic potential. The stabilizers and compatibilizers added during the processing are also found to exhibit impression on the properties of polymer/clay nanocomposites [23].

Graphene Panoramic

However, it is evident that graphene is an interesting material that exhibits excellent unique properties that make it a compelling candidate for various applications. But despite all these excellent properties, there are still a lot of challenges to be overcomed before the true potential of graphene becomes realizable. In this study, three aspects of graphene were been identified: properties, fabrication methods, and application in polymer composites. From the properties aspect of graphene, it is clear that it has a high potential for various applications including nanofiller for functional composites, energy storage devices, flexible electronics, sensors, etc., due to its superlative

properties. The top-down approaches for graphene exfoliation have been reviewed such as Hummer's method, and via GO routes. These methods utilize graphite as a starting material that is low cost and readily available. However, it is clear from the discussion that the most challenging problem that hinders the wider scale application of graphene is still the lack of an economically viable large-scale production method for high-quality graphene fabrication that is environmental-friendly [11]. The application of graphene in polymer nanocomposite was analyzed. It is evident that GO is the most widely used graphene-based nanofiller in polymer composites, largely because of the chemical interaction between the filler and the polymer matrix that enhances homogeneous dispersion of graphene in the matrix, thus improving the overall composite performance [11].

Nanocellulose Panoramic

As cellulose is almost inexhaustible as a resource, the development of cellulosic nanomaterials and their application to reinforce a synthetic polymer matrix are not only commercially beneficial but also environmentally beneficial [24]. According to bibliometric data, the topic of cellulose nanocomposites has been growing exponentially, and this growth is reflected in the increasing number of publications. However, many of these publications address the isolation of nanocelluloses from different sources of raw materials and the structure and properties of nanomaterials rather than nanocomposites and their processing. As such, interest in foaming and spinning of cellulose nanocomposite fibers has also increased in recent years [25]. The countries with the most publications on the subject are China, followed by the USA, Sweden, France, Canada, and Japan, showing, for example, that China is currently very active in this field and the USA assumes this role [25]. Although many publications report the use of nanocellulose reinforced polymer composites, some review articles have discussed this topic. Certain advanced and recent findings have not been satisfactorily addressed in the publications. Although few studies have evaluated the quality and/or shelf-life improvement of foods packaged with nanocellulose-based composites, they have been successfully applied to fruits, meats, and vegetables. And these studies have contributed significantly to understand the many properties, applications, and functionalization of nanocellulose [26]. One method of addressing these limitations is the synthesis of nanocellulose-based composites, where cellulose can be used as both reinforcement and matrix. Several studies have reported the synthesis of these compounds and shown promising results in advanced applications [26].

Acknowledgements The authors wish to thank IIAEA-CRP # 17760 RO, FAPESP, and CNPq to provide support for this work.

References

1. Müller K, Bugnicourt E, Latorre M, Jorda M, Sanz YE, Lagaron JM, Miesbauer O, Bianchin A, Hankin S, Bolz U, Pérez Jesdinszki M, Lindner M, Scheuerer Z, Castelló S, Schimd M (2017) Review on the processing and properties of polymer nanocomposites and nanocoatings and their applications in the packaging. Automot Solar Energy Fields Nanomater 7:47. https://doi.org/10.3390/nano7040074
2. Schmid M, Benz A, Stinga C, Samain D, Zeyer KP (2012) Fundamental investigations regarding barrier properties of grafted PVOH layers. Int J Polym Sci https://www.hindawi.com/journals/ijps/2012/637837/. Accessed 25 Jul 2019
3. Schmid M, Sängerlaub S, Miesbauer O, Jost V, Werthan J, Stinga C, Samain D, Stramm C, Noller K, Müller K (2014) Water repellence and oxygen and water vapor barrier of PVOH-coated substrates before and after surface esterification. Polymers 6:2764–2783. https://doi.org/10.3390/polym6112764
4. Powell CE, Beall GW (2006) Physical properties of polymer/clay nanocomposites. Curr Opin Solid State Mater Sci 10:73–80. https://doi.org/10.1016/j.cossms.2006.09.001
5. An overview of polymer/clay nanocomposites (PDF). https://www.researchgate.net/publication/312222191_An_Overview_of_PolymerClay_Nanocomposites?enrichId=rgreq-d6f92d84783f0cbe6764affc4a6f51d7-XXX&enrichSource=Y292ZXJQYWdlOzMxMjIyMjE5MTtBUzo0NjU1NDQwODk0NzcxMjFAMTQ4ODAwNTc2ODY2Ng%3D%3D&el=1_x_2&_esc=publicationCoverPdf. Accessed 31 Aug 2019
6. Bee S-L, Abdullah MAA, Bee S-T, Rahmat AR (2018) Polymer nanocomposites based on silylated-montmorillonite: a review. Prog Polym Sci 85:57–82. https://doi.org/10.1016/j.progpolymsci.2018.07.003
7. Arora A, Padua GW (2010) Review: nanocomposites in food packaging. J Food Sci 75:R43–R49. https://doi.org/10.1111/j.1750-3841.2009.01456.x
8. Mihindukulasuriya SDF, Lim L-T (2014) Nanotechnology development in food packaging: a review. Trends Food Sci Technol 40:149–167. https://doi.org/10.1016/j.tifs.2014.09.009
9. Tan B, Thomas NL (2016) A review of the water barrier properties of polymer/clay and polymer/graphene nanocomposites. J Membr Sci 514:595–612. https://doi.org/10.1016/j.memsci.2016.05.026
10. Anadão P (2012) Polymer/clay nanocomposites: concepts, researches, applications and trends for the future. Nanocomposites New Trends Dev https://doi.org/10.5772/50407
11. Phiri J, Gane P, Maloney TC (2017) General overview of graphene: production, properties and application in polymer composites. Mater Sci Eng B 215:9–28. https://doi.org/10.1016/j.mseb.2016.10.004
12. Novoselov KS, Geim AK, Morozov SV et al (2004) Electric field effect in atomically thin carbon films. Science 306:666–669. https://doi.org/10.1126/science.1102896
13. Gahlot S, Kulshrestha V (2019) Graphene based polymer electrolyte membranes for electrochemical energy applications. Int J Hydrog Energy. https://doi.org/10.1016/j.ijhydene.2019.06.047
14. Idowu A, Boesl B, Agarwal A (2018) 3D graphene foam-reinforced polymer composites—a review. Carbon 135:52–71. https://doi.org/10.1016/j.carbon.2018.04.024
15. Zhang Z, Qu J, Feng Y, Feng W (2018) Assembly of graphene-aligned polymer composites for thermal conductive applications. Compos Commun 9:33–41. https://doi.org/10.1016/j.coco.2018.04.009
16. Lawal AT (2019) Graphene-based nano composites and their applications. A review. Biosens Bioelectron 141:111384. https://doi.org/10.1016/j.bios.2019.111384
17. Ngwabebhoh (2019) Nature-derived fibrous nanomaterial toward biomedicine and environmental remediation: today's state and future prospects. J Appl Polym Sci. Wiley Online Library. https://onlinelibrary.wiley.com/doi/full/10.1002/app.47878. Accessed 2 Sep 2019
18. Patel DK, Dutta SD, Lim K-T (2019) Nanocellulose-based polymer hybrids and their emerging applications in biomedical engineering and water purification. RSC Adv 9:19143–19162. https://doi.org/10.1039/C9RA03261D

19. Kargarzadeh H, Mariano M, Huang J, Lin N, Ahmad I, Dufresce A, Thomas S (2017) Recent developments on nanocellulose reinforced polymer nanocomposites: a review. Polymer 132:368–393. https://doi.org/10.1016/j.polymer.2017.09.043
20. Feldman D. Cellulose nanocomposites. J Macromol Sci Part A 52(4). https://www.tandfonline.com/doi/abs/10.1080/10601325.2015.1007279. Accessed 3 Sep 2019
21. Liu P (2007) Polymer modified clay minerals: a review. Appl Clay Sci 38:64–76. https://doi.org/10.1016/j.clay.2007.01.004
22. Ummartyotin S, Bunnak N, Manuspiya H (2016) A comprehensive review on modified clay based composite for energy based materials. Renew Sustain Energy Rev 61:466–472. https://doi.org/10.1016/j.rser.2016.04.022
23. Loganathan S (2017) An overview of polymer/clay nanocomposites
24. Dhara K, Mahapatra DR (2019) Recent advances in electrochemical nonenzymatic hydrogen peroxide sensors based on nanomaterials: a review. J Mater Sci 54:12319–12357. https://doi.org/10.1007/s10853-019-03750-y
25. Oksman K, Aitomäki Y, Mathew AP, Siqueira G, Zhou Q, Butylina S, Tanpichai S, Zhou X, Hooshman S (2016) Review of the recent developments in cellulose nanocomposite processing. Compos Part Appl Sci Manuf 83:2–18. https://doi.org/10.1016/j.compositesa.2015.10.041
26. Shak KPY, Pang YL, Mah SK (2018) Nanocellulose: recent advances and its prospects in environmental remediation. Beilstein J Nanotechnol 9:2479–2498. https://doi.org/10.3762/bjnano.9.232

Evaluation of Biodiesel Obtained from Waste Cooking Oil Purified with a Modified Clay

C. G. Bastos Andrade, M. Shimba, G. Freitas, L. M. Kobayashi, S. M. Toffoli and F. R. Valenzuela Diaz

Abstract In order to meet the current environmental demand in the reduction of greenhouse gas emissions (GHG), and the preservation of water with the reduction of the incorrect disposal of residues, particularly soybean oil after consumption, the objective of this paper is to evaluate the biodiesel obtained from waste cooking oil (WCO) purified using a Brazilian clay after a modified acid treatment, less aggressive to the environment. The clay, before and after the treatment, was characterized by XRD, FTIR, and SEM/EDS. The biodiesel had its appearance, color, kinematic viscosity, density, water content, acidity level, saponification index, and combustion behavior measured. The results indicated that the biodiesel meets some of the main requirements of the Brazilian standard for biodiesels, with the exception of higher water content. Therefore, the effectiveness of the purification process of the WCO using the modified Brazilian clay was demonstrated.

Keywords Biodiesel · Modified clay · Nanotechnology · Recycling · Waste cooking oil

Introduction

An enormous increase in green energy research was observed at different countries in the last few years with the development of new technologies that minimize the environmental impact, and it is a necessary measure to combat the growing of GHG emissions. The United Nations determines several parameters and policies aiming to reduce the damages caused mostly by the use of fossil fuels [1–8]. The International Renewable Energy Agency (IRENA) presents some actions aiming to reduce the CO_2 emissions linked to energy, to prevent the temperature elevation to be higher than 2 °C, in accordance to the global agreement decided by COP 21. The reports

C. G. Bastos Andrade (✉) · M. Shimba · G. Freitas · L. M. Kobayashi · S. M. Toffoli · F. R. Valenzuela Diaz
Department of Metallurgical and Materials Engineering, Polytechnic School, University of Sao Paulo, Sao Paulo, SP, Brazil
e-mail: gianesic@usp.br

J. Li et al. (eds.), *Characterization of Minerals, Metals, and Materials 2020*,
The Minerals, Metals & Materials Series,
https://doi.org/10.1007/978-3-030-36628-5_32

also estimate that the energy produced from biomass could generate up to 180 EJ (180×10^{18} J) in a global scale, by 2050, with an increase of 2/3 in the share of renewable energy, highlighting the need for greater energy efficiency [9–13]. A study by the United States Department of Agriculture (USDA), soybean production in 2016/16 was 114.60 million tons and there was a growth in 2017/18 reaching a production of 119.50 million tons. According to ANP/ABIOVE estimate, in Brazil, 70% of biodiesel production uses pure soybean oil [14–16]. The waste cooking oil (WCO) recycling into the production of biodiesel permits a dramatic reduction of the biodiesel production total cost compared to the traditional process that uses refined vegetable oils, which represent approximately 80% of the total cost of the biodiesel production. Another issue is the land use, when biodiesel production competes with food production. This could be solved with the use of WCO as the main raw material [17–21].

The conventional industrial process of clay modification to oil purification is usually performed with high concentration of inorganic acids, which promotes an increase of the specific surface area (SSA), and pores, resulting in good properties. On the other hand, it may cause an almost complete destruction of the crystalline structure of the clay mineral. Modified clays—or activated clays—are widely used as fuller earths in bleaching process by the industry. In Brazil, the regulatory government agency—National Oil, Natural gas, and Biofuel Agency, ANP, in its directive No. 45:2014—sets the quality parameters for biofuels. The Brazilian bentonite used is a smectitic clay, with Ca^{2+} as the preponderant exchange cation, and with a significant iron content. This paper discusses the evaluation of a biodiesel obtained from WCO purified with a modified bentonite, using a process less aggressive to the environment than the traditional one.

Experimental

Materials

The clay sample was a natural bentonite from Brazilian Northern region, modified by acid attack using Drs. Bastos Andrade's and Valenzuela-Diaz's MAT methodology [22–27]. The waste cooking oil (WCO) purified was soybean oil. The catalytics used were KOH and NaOH, and for the transesterification process, methanol P.A. was employed.

Methods

Initially, the modified clay sample was sieved in #200 mesh, and then dried at 60 °C for 24 h. The WCO sample was filtered at 40 °C, and then purified using the same

amount of natural (or raw material) clay, and modified clay by MAT process. The purification process of the WCO was performed by a simplified bleaching test using the same procedure already reported in previous works [21, 22]. Different proportions of clay(g)/WCO (mL) were used, 1:20, 2:20, and 4:20, using MAT process modified bentonite (samples I, II, and III, respectively), or natural clay (samples IV, V, and VI). After being cooled to 40 °C, the samples were filtered, and centrifuged at 3000 rpm for 40 min.

The clay characterization consisted in analyzing images from SEM (EDAX Inspect 50), and from coupled energy dispersive spectroscopy spectra (EDS). The mineral content was obtained using a Rigaku diffractometer model MiniFlex600, with Cu-Kα radiation, scanned at 2°/min from 3 to 65° 2θ, at 30 kV and 10 mA. The clay mineral structure was studied by ATR-FTIR spectroscopy, using a Nicolet iS5 instrument with a spectrum range of 400–4000 cm^{-1}, and 16 sweeps with a 2 cm^{-1} resolution.

The biodiesel was obtained by a simple process using the best purified WCO among the six samples. The transesterification process used a molar ratio 1:9 WCO/methanol, 10 g of the WCO, and a ratio of 1 mol of triglycerides to 3 mols of KOH as catalyst. The alcohol and the catalyst were mixed by magnetic stirring. The WCO, heated to 90 °C to remove water and cooled to 40 °C, was added to the solution, and the stirring was continued for 30 min. After that, the solution was left to rest for 24 h, to separate the glycerin (denser). The biodiesel was then washed with distilled water to remove the excess of alcohol, catalyst, and soap formed during the transesterification process. After that, the mixture was left still, to allow the water to separate. This process was repeated until the water coloration became transparent. After this, biodiesel was heated to 90 °C, for 24 h, to remove any residual water. The same procedure was repeated for 100 g of WCO, in order to have enough material to perform the tests.

The biodiesel characterization consisted in the determination of the following parameters:

i. Appearance: the degree of turbidity by free water contamination, and/or particulate material was determined based on NBR 16048. The same procedure was used to verify the WCO purification.
ii. Kinematic viscosity: initially, the dynamic viscosity was obtained by Stokes Law, and then converted to kinematic viscosity (based on NBR 10441 standard). High values of viscosities could cause ignition delays, and thus may compromise the engine of vehicles.
iii. Density: the densities of purified WCO, and biodiesel, were measured at 25 °C based on NBR 14065 standard.
iv. Water content: the presence of water contributes to making biodiesel corrosive. The determination was based on ASTM 6304 and ASTM D4951.
v. Acidity index: performed based on NBR 14448 standard by the potentiometric titration method, preferably using KOH as titrant, and phenolphthalein as indicator.

vi. Saponification index: indicates the ability of biodiesel to form soap, which is totally undesirable as it could damage the engine of the vehicle. It is defined by the amount of KOH (in milligrams) required to saponify 1 g of oil.
vii. Combustion: the combustion test was a qualitative test aimed at proving that the product formed by transesterification is indeed a fuel. It was performed by burning a small amount of cotton saturated with virgin soybean oil, and another with the produced biodiesel. The flames were compared in their intensity and size.

Results and Discussion

Figure 1 presents the XRD results of the bentonite as-received and the modified clay using MAT process. It is possible to observe that there were no major changes between the curves, except for the reduction in the basal plane spacing, from 1.513 to 1.423 nm, indicated by shift in the corresponding peak, and the extinction of the peak associated to the interplanar distance of 0.157 nm.

Therefore, the obtained peaks are characteristic of smectitic clays [23, 24], and indicated that the MAT process used for the modification of the clay caused only a slight damage to the crystalline structure of the original clay.

Figures 2 and 3 show the results obtained by infrared spectroscopy analysis for natural and modified bentonite samples. It is possible to observe that the both curves are very similar, confirming that, in fact, there was no significant destruction of the

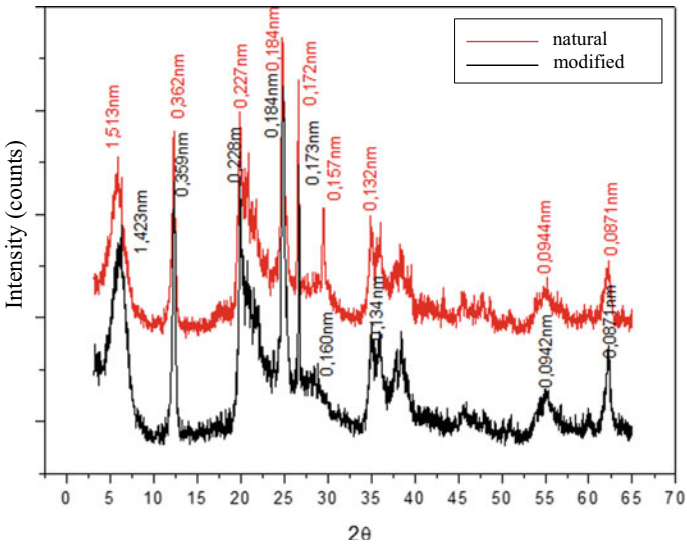

Fig. 1 XRD results to bentonite natural (raw material), and modified

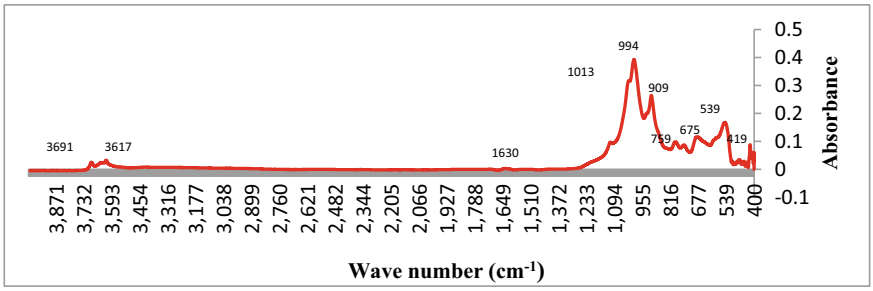

Fig. 2 Infrared spectroscopy of the natural clay sample

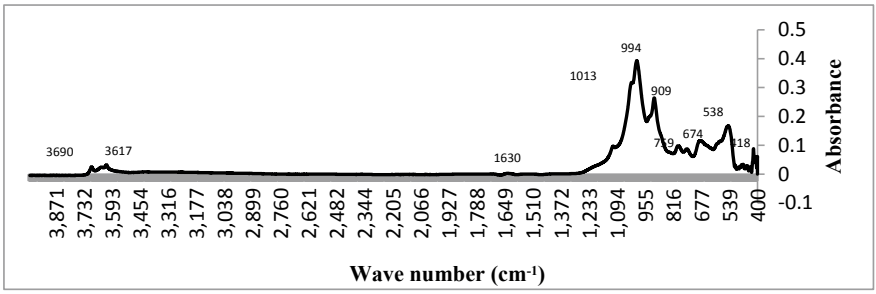

Fig. 3 Infrared spectroscopy of the modified bentonite sample

clay mineral structure caused by the MAT process modification. According to Farmer and Palmieri, Zhang et al. and Cortes et al. [25–27], the absorption bands in the range of 3616–3690 and around 1630 cm^{-1} can be associated with the stretching vibrations of the O–H group, and are typical of smectites with high content of Al. In the range of 994–1013 cm^{-1}, it is possible to observe peaks referring to the Si–O bond, typical of clay minerals.

The semi-quantitative chemical analysis by EDS of the bentonite, as-received and modified by MAT process, is presented in Table 1. It can be observed that a dramatic reduction in the iron, calcium, potassium, and titanium contents was caused by the acid activation process. On the other hand, both contents of silicon and aluminum remained similar.

The SEM images of the samples are shown in Figs. 4, 5, 6, and 7. The pictures show the typical agglomerates of small size clay particles, also showing their typical lamellar structure. For these magnifications, no apparent damage of the crystal structures was caused by the MAT process.

Table 1 EDS results for natural and modified bentonite

Element	Weight %		Atomic %	
	Natural	MAT	Natural	MAT
Si	28.0	28.5	24.3	21.0
Al	17.3	17.8	15.7	13.7
K	1.0	0.3	0.7	0.1
Ca	1.9	0.0	1.1	0.0
Ti	2.3	0.4	1.2	0.2
Mg	0.1	1.0	0.1	0.9
Fe	16.9	3.1	7.4	1.1
O	32.5	48.9	49.5	63.0
Total	100	100	100	100

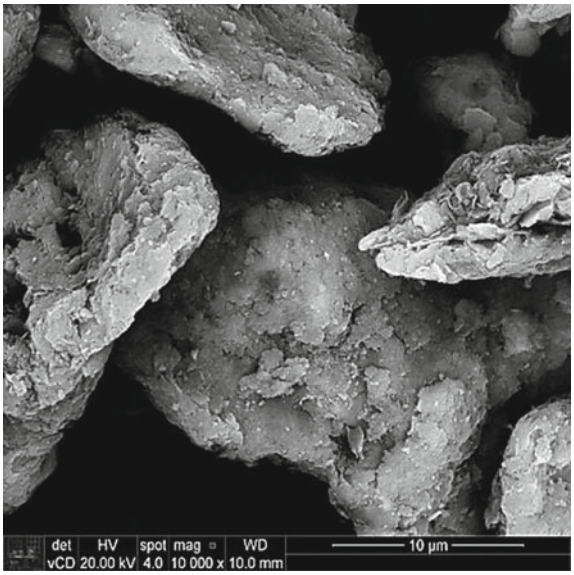

Fig. 4 SEM image of the as-received bentonite

Biodiesel Results

Dark color or cloudy appearance is an indication of a possible water content, and it is not desirable. Otherwise, a clear and crystalline color is the desirable condition, and it is established by the ANP 45/14 standard. The biodiesel obtained in this work was clear, without turbidity, free of impurities, and suspended particles. The biodiesel production started with 100 g of WCO purified, and yielded 91.5 g of biodiesel in the end (reaction efficiency of 91.5%).

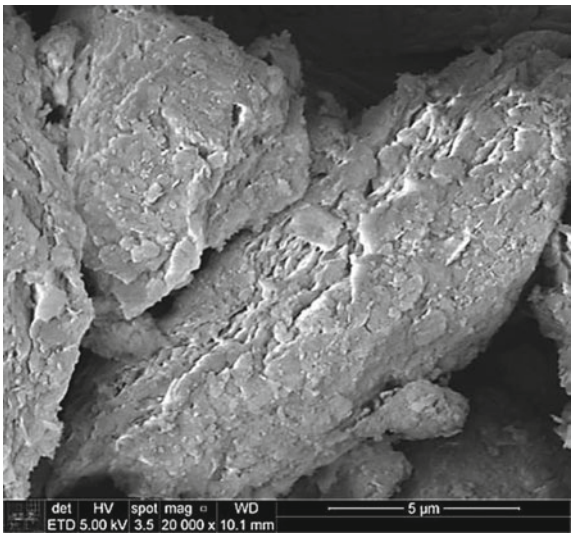

Fig. 5 SEM image of MAT sample

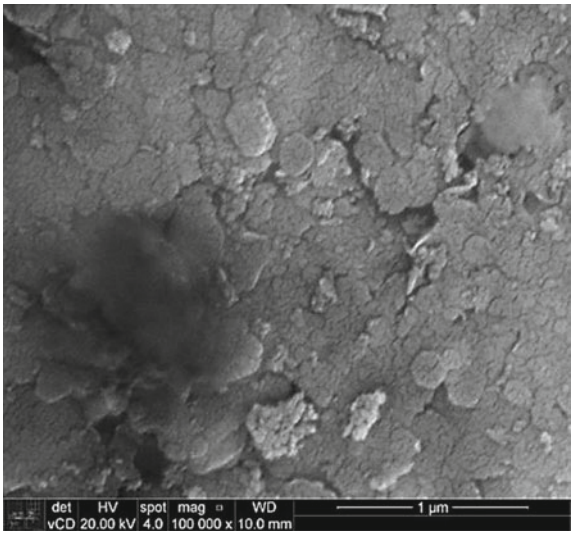

Fig. 6 SEM image of the as-received bentonite

The ANP regulates density values between 850 and 900 kg/m^3. The biodiesel density is not considered of extreme relevance to ASTM (USA) qualification of biodiesel. However, changes in density greater than 3 kg/m^3 require that all laboratory tests be redone to ensure biodiesel quality. The biodiesel density obtained

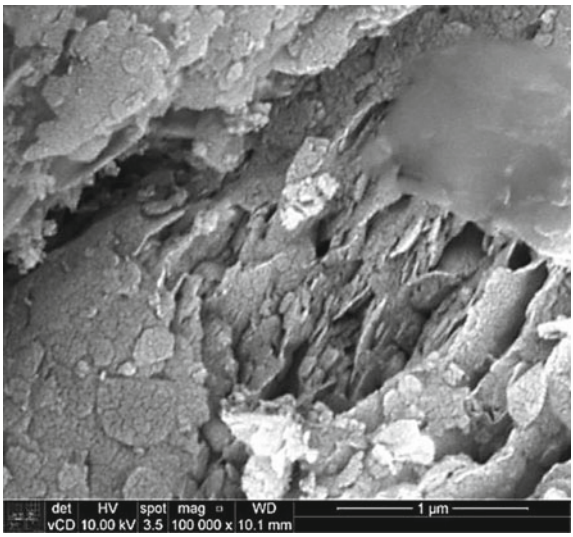

Fig. 7 SEM image of MAT sample

was 862 kg/m^3, thus in accordance to the standard. The Brazilian National Health Surveillance Agency (ANVISA) through RDC no. 270/2005—technical regulation for vegetable oils, vegetable fats, and vegetable creams, defines that the density value for a quality vegetable oil must be between 919 and 925 kg/m^3. The purified WCO density was 924 kg/m^3, being near the maximum limit of the standard, but still in accordance.

The dynamic viscosity calculation used Stokes law with Ladenburg's velocity correction factor considering the influence of the tube walls on the ball movement. The kinematic viscosities values of the purified WCO and biodiesel, at 25 °C, were 60.0 and 7.3 mm^2/s, respectively. At 40 °C, it was observed a reduction of 20% for purified WCO (48.5 mm^2/s), and 25% for biodiesel (5.5 mm^2/s). The kinematic viscosity obtained to the biodiesel is in accordance with the ANP standard, which establishes limits between 3 and 6 mm^2/s. The viscosity of the purified WCO at room temperature was approximately 63.5 mm^2/s, and it is also in accordance with values found in the literature [28]. As expected, and in accordance to the literature, the viscosity of the biodiesel is lower compared to the oil. This fact can be explained by the substitution of glycerin (formed in the transesterification process) by methanol, thus reducing the biodiesel viscosity [29].

In order to analyze if the purification process contributes to the reduction of the water content, a test was performed on the WCO and the purified WCO. The maximum water content allowed by ANP 45/14 standard is 200 mg/kg (H_2O/biodiesel). The tests were performed in triplicate to each sample. Table 2 presents the results.

Among the three samples of purified WCO, sample III, that used the ratio of 4:20 g/mL, presented the lowest water content compared to WCO. Thus, sample III parameters are indicated for the production of biodiesel, remembering that high water

Table 2 Results of water content in the WCO, sample III (purified WCO), and biodiesel samples

	WCO	Sample III	Biodiesel
Water content (mg H_2O/kg sample)	267.1	140.0	314.8

contents favor saponification during the transesterification reaction and increase the acidity index, which is not desirable. The water content result for the biodiesel produced was 314 mg/kg, above the 200 mg/kg allowed by the ANP standard. The value obtained could indicate inefficiency in the washing/drying process performed after the transesterification reaction indicating the need for further investigation.

The acidity is directly linked with the water content and mainly by the free fatty acid content. Therefore, high acidity indices indicate presence of water and fatty acids, which is not desired. The value obtained for biodiesel was 0.42 mg $_{KOH}$/g, thus below the maximum acid content of 0.5 mg $_{KOH}$/g, set by ANP 45/14.

The test for the saponification index (SI) calculation was performed in duplicate using the purified WCO and the biodiesel produced. This test contributes to the calculation of the amount of reagents to be used in the transesterification reaction to obtain biodiesel. The saponification index obtained for the purified WCO was 200 (mg $_{KOH}$/g$_{purified\ wco}$), and to the biodiesel was 160 (mg $_{KOH}$/g $_{biodiesel}$). Despite the ANP standard does not establish a limit for the biodiesel saponification index, it is desirable to obtain low values. High levels of saponification index indicate the presence of free fatty acids that could impair the quality of biodiesel. The SI result for the purified WCO was very close to the results found in the literature [30], indicating that the purified WCO is suitable for the biodiesel production. It was observed that the SI obtained for the biodiesel produced is lower than the one found for the purified WCO which could indicate a decrease in free fatty acids. Besides, Bellé [31] produced a biodiesel from post-consumption sunflower oil, with a SI of 161.5 mg $_{KOH}$/g $_{biodiesel}$, value quite similar to the results reported in this paper.

Figures 8 and 9 present the combustion test performed using a purified virgin soybean oil, and the obtained biodiesel. The virgin oil presented low flammability, exhibiting a flame with a yellowish tone of low incandescence and intensity, with reduced duration time, and a few seconds to start. The biodiesel sample presented a reaction time almost instantaneous, forming a long, and intense flame, with an intense yellowish color, and the reaction remained for a longer period than the one for virgin oil, typical characteristics of a biofuel.

Table 3 summarizes the various results obtained in the tests performed with the biodiesel obtained in this paper, comparing them with the parameters of ANP n. 45/14. It is observed that the biofuel results are within the limits established by the standard, except for the water content.

Fig. 8 Flame obtained by the combustion of virgin soybean oil

Fig. 9 Flame obtained by the combustion of the biodiesel

Table 3 Comparison of the results obtained from the tests performed with biodiesel obtained, and the parameters of ANP n. 45/14

	Aspect	Density at 25 °C (kg/m^3)	Viscosity at 40 °C (mm^2/s)	Water content (mg/kg)	Acidity index (mg_{KOH}/g)	Saponification index (mg $_{KOH}/g$)
ANP nº 45/14	Clear and free of impurities	850–900	3–6	200	0.50	–
Biodiesel	Clear and free of impurities	862	5.5	314	0.42	160.1

Conclusions

This paper evaluated the biodiesel obtained from purified waste cooking oil (WCO) using a Brazilian clay after an activation acid treatment, less aggressive to the environment than the current industrial treatments. The results of the characterization tests confirmed that the clay mineral is indeed a smectite, and the MAT process promoted slight modifications in its crystalline structure. The MAT process promoted a reduction in the contents of some metallic elements, without compromising the main characteristics of the crystalline structure, and improved the clay properties relevant to the purification process of the WCO. Among the several parameters established by the Brazilian standard for biodiesels, the produced biodiesel was tested for five of the most important ones. The results indicated that the product meets the requirements of four of them, with the exception of exhibiting a higher water content, parameter which can be, however, easily corrected by a more rigorous procedure in the washing/drying stages of the process.

Acknowledgements This work was supported by the São Paulo State Research Foundation—FAPESP.

References

1. Atabani AE et al (2012) A comprehensive review on biodiesel as an alternative energy resource and its characteristics. Renew Sustain Energy Rev 16:2070–2093
2. EC—European Commission (2009) Renewable Energy Directive 2009/28/EC. Report of the European Parliament and of the Council of 23 April 2009 on the promotion of the use of energy from renewable sources and amending and subsequently repealing Directives 2001/77/EC and 2003/30/EC. OJL 140:16–62
3. EPA—Environmental Protection Agency (2016) Renewable fuel standard program: Standards for 2017 and biomass based diesel Vol. for 2018, Final Rule. USA, Federal Register 81(238)
4. Haijjari M et al (2017) A review on the prospects of sustainable biodiesel production: a global scenario with an emphasis on waste oil biodiesel utilization. Renew Sustain Energy Rev 72:445–464

5. Pachauri RK, Meyer LA (eds.) (2014) IPCC climate change 2014: synthesis report. Contribution of working groups I, II and III to the fifth assessment report of the intergovernmental panel on climate change. Geneva, Switzerland
6. Pahl G (2005) Biodiesel: growing a new energy economy. Chelsea Green Publishing Company, Vermont
7. Tabatabaei M et al (2015) Renewable energy and alternative fuel technologies. Biomed Res Int 2015:245935
8. WRI (2004) The greenhouse gas protocol: a corporate accounting and reporting standard, Revised edn. World Resources Institute and World Business Council for Sustainable Development, USA
9. Souza GM, Victoria RL, Joly CA, Verdade LM. (eds) (2015) Bioenergy & sustainability: bridging the gaps. Paris, Scope, 779p (Scope 72)
10. Brasil, Ministério do Meio Ambiente—MMA (2015) Mudança do Clima—Convenção Quadro das Nações Unidas sobre Clima—Acordo de Paris
11. IRENA (2016) REmap: roadmap for a renewable energy future. 2016 edn. International Renewable Energy Agency (IRENA), Abu Dhabi
12. IRENA (2018) Global energy transformation: a roadmap to 2050, International Renewable Energy Agency, Abu Dhabi
13. Woods J et al (2015) Land and bioenergy. In: Souza GM, Victoria RL, Joly CA, Verdade LM (eds) Bioenergy & austainability: bridging the gaps. Scope, Paris, pp 256–299
14. Agência Nacional de Petróleo—ANP (2018) Associação Brasileira das Indústrias de Óleos Vegetais-ABIOVE. Cadeia Produtiva de Oleaginosas e Biodiesel—Estatística
15. Instituto Brasileiro de Geografia e Estatística—IBGE (2017)Agência Notícias, Editoria: Estatísticas Econômicas. Neto, J. Soja, milho e arroz representam mais de 90% da safra 2017
16. USDA—United States Department of Agriculture (2018) Foreign agricultural service circular series WAP8-18. World Agricultural Production
17. Ali C (2017) Biodiesel production from waste cooking oil using onsite produced purified lipase from *Pseudomonas aeruginosa* FW_SH-1: central composite design approach. Renew Energy 109:93–100
18. Anikulmar R, Virendra K (2018) Calcium diglyceroxide catalyzed biodiesel production from waste cooking oil in the presence of microwave: optimization and kinetic studies. Renewable Energy 121:757–767
19. Chiatti G, Chiavola O, Palmieri F (2016) Impact of waste cooking oil in biodiesel blends on particle size distributions from a city-car engine. J Energy Inst 91:262–269
20. Chuah L et al (2017) Kinetic studies on waste cooking oil into biodiesel via hydrodynamic cavitation. J Clean Prod 146:47–56
21. Gudeetal VG (2013) Biodiesel production from low cost and renewable feedstock. Central Euro J Eng 3(4):595–605
22. Bastos Andrade, CG et al (2016) Evaluation of white bentonite modified by acid attack. In: Characterization of minerals, metals, and materials. Wiley, pp 107–117
23. Bastos Andrade CG et al (2015) Evaluation of acid treatment on brown bentonite. In: Characterization of minerals, metals, and materials. Wiley, pp 735–742
24. Bastos Andrade CG et al (2015) Brazilian bentonite submitted to mild acid treatment under moderated conditions. In: Characterization of minerals, metals, and materials. Wiley, pp 361–368
25. Bastos Andrade CG et al (2014) Brazilian bentonite submitted to mild acid treatment. In: Characterization of minerals, metals, and materials. Wiley, pp 523–531
26. Bastos Andrade CG, Toffoli SM, Valenzuela Diaz FR (2018). Evaluation of Brazilian bentonite modified by acid attack in biofuel production. In: The minerals, metals & materials series. Springer International Publishing, pp 41–50
27. Bastos Andrade CG, Toffoli SM, Valenzuela Diaz FR (2018). Adsorption and surface area of modified bentonite used as bleaching clay. In: The minerals, metals & materials series. Springer International Publishing, pp 333–341
28. Souza-Santos P (1992) Ciência e Tecnologia de Argilas v.1, 2ª.ed. Edgar Blücher, Sao Paulo

29. Gomes CF (1998) Argilas: o que são e para que servem. 1ª edição, Fundação Calouste Gulbenkian, Lisboa, 457p
30. Farmer VC, Palmieri F (1975) The characterization of soil minerals by infrared spectroscopy. In: Giesekihg JE (ed) Soil components. Springer-Verlag, New York, pp 573–670
31. Zhang ZZ, Sparks DL, Scrivner NC (1993) Sorption and desorption of quaternary amine cations on clays. Environ Sci Technol 27(8):1625–1631
32. Cortes G et al (2018) Bentonitas do Brasil, características e uso. Congresso Nacional de Engenharia de Petróleo, Gás Natural e Biocombustíveis
33. Sivasamy A et al (2009) Catalytic applications in the production of biodiesel from vegetable oils. Chemsuschem 2(4):278–300
34. Quessada T (2017) Obtenção de biocombustíveis a partir de óleo vegetal utilizando diversos catalisadores. Universidade Estadual de Londrina
35. Espindola L et al (2011) Análise comparativa do rendimento e das características físico-químicas do biodiesel produzido a partir do óleo residual de frituras e de pinhão manso. Universidade Estadual do Mato Grosso do Sul
36. Bellé L (2016) Obtenção de biodiesel a partir de óleo de amendoim refinado, por transesterificação metílica em meio básico. Universidade Teconólgica Federal do Paraná, Pato Branco, Brasil

Part X
Characterization of Polymers and Composites II

Mechanical Behavior of Thermoplastic Filaments Fabricated with the Fused Modeling Deposition Technique

Elkin I. Gutiérrez and Henry A. Colorado

Abstract This article intends to evaluate the influence of the printing temperature on the maximum tensile strength for plastic specimens fabricated via 3D printing. The materials evaluated were Acrylonitrile Butadiene Styrene (ABS), Polylactic Acid (PLA), and Polyethylene Terephthalate Glycol Modified (PETG). The manufactured samples were evaluated in accordance with ASTM D638. The results obtained allow to establish how the temperature of the nozzle affects the ultimate tensile strength of plastics and some guidelines are given in relation to the appropriate temperature according to the material used.

Keywords Expanded polystyrene · Recycling · Strontium aluminate · Thermoplastic filaments · 3D printing · Fused deposition modeling · Asphalt coating

Introduction

3D printing, or additive manufacturing, is a group of manufacturing technologies that starting from a digital model, allowing you to automatically manipulate different materials, and adding them layer by layer very precisely to build an object in three dimensions [1]. By using 3D printing, it is possible to produce objects in almost every way. Today, different technologies and 3D printing materials are used. Recently, 3D printing tools are available for industrial manufacturing and for home use as well [2].

E. I. Gutiérrez
Faculty of Mechanic Electronic and Biomedical Engineering, Universidad Antonio Nariño, Cl. 52 #40-88, Medellín, Colombia

H. A. Colorado (✉)
CC Composites Laboratory, Universidad de Antioquia UdeA, Calle 70 N°. 52-21, Medellín, Colombia
e-mail: henry.colorado@udea.edu.co

Universidad de Antioquia, Facultad de Ingeniería, Bloque 20, Calle 67 no. 53-108, Medellín, Colombia

J. Li et al. (eds.), *Characterization of Minerals, Metals, and Materials 2020*,
The Minerals, Metals & Materials Series,
https://doi.org/10.1007/978-3-030-36628-5_33

3D printing allows you to create complex shapes and parts, many of which cannot be created using conventional manufacturing technologies. When using 3D printing, complex one-piece models can be produced without the need to make smaller parts and then assemble them together. In 3D printing, if there is a need to change the design of a particular product, the digital design would be changed without further expensive manufacturing processes or additional tools [3].

One of the advantages of 3D printing compared with traditional manufacturing is that the 3D printing process generally does not require any special tools to produce models or their parts. Therefore, it does not require additional costs or excessive waiting periods when a simple or medium complexity object is made. This is because the objects or their parts can be produced when they are needed, so the inventory storage costs and working time can be reduced. As an additional advantage, we can highlight that most processes use materials that can be recycled or reused for more than one figure, creating very little waste resulting from additive manufacturing processes [4].

However, 3D printing has some limitations: In general, it has higher cost for large production quantities, lower availability of materials, limitations in colors and finishes, lower mechanical strength, and the life and precision of the final pieces is lower. Likewise, most 3D printers are limited by scale and size. However, despite such limitations, 3D printing technologies are developing very fast and the costs of 3D printing tend to be reduced, so the use of this methodology is spreading vertiginously [5].

There is a wide variety of methods available for 3D printing. Their main differences are in the way in which the different layers are used to create pieces. Some methods such as fusion deposition modeling (FDM) or selective laser sintering (SLS) use melting or softening of the material to produce the layers, while others deposit liquid materials that are treated with different technologies. The International Organization for Standardization (ISO)/American Society for Testing and Materials (ASTM) 52900:2015 standard has classified additive manufacturing processes into seven categories [6]:

(1) binder jetting (BJ);
(2) directed energy deposition (DED);
(3) material extrusion (ME);
(4) material jetting (MJ); (5) powder bed fusion (PBF);
(5) sheet lamination (SL); and
(6) vat photopolymerization (VP).

Each method has its own advantages and disadvantages, so some companies offer alternatives between powders and polymers as raw materials, depending on the needs of the client. Generally, the main considerations to take into account when choosing a printer are the speed, the cost of the printed prototype, the cost of the machine, the choice and the cost of the work materials, and the capacity they offer to choose the color [7].

Finally, like for any new technology, it is easy to highlight the benefits of 3D printing. It opens a world of new possibilities for all industries and proposes the

reduction of transport costs, environmental impact, waste, etc. But 3D printers are still wasteful, potentially dangerous machines, and their social, political, economic, and environmental impacts have not yet been widely studied [8].

Materials and Methods

For this study, test specimens have been developed under ASTM D638 [9], in accordance with the type IV specimen. The geometry of the specimens was generated according to the dimensions shown in Table 1, according to Fig. 1.

The materials used for the printing of the specimens were Acrylonitrile Butadiene Styrene (ABS), Polylactic Acid or Polylactide (PLA), and Polyethylene Terephthalate Glycol Modified (PETG).

The specimens were made in a Creality 3D CR-10 printer, using 1.75 mm diameter filaments. The filament used was of the 3DBOTS® brand [10] without any modification. The specimens were printed so that the printed filaments were parallel to the section of calibrated length, as shown in Fig. 2. The head speed was adjusted to 60 mm/min for all samples and 0.15 mm layer thickness, for a total 2 mm sample thickness.

Table 1 Dimension of the specimens evaluated

Symbol	Parameter	Dimension (mm)
G	Gage length	50
W_c	With of narrow section	6
L	Length of narrow section	33
WO	Width overall	19
LO	Length overall	115
G	Gage length	25
R	Radius of fillet	14
RO	Outer radius	25
T	Thickness	2

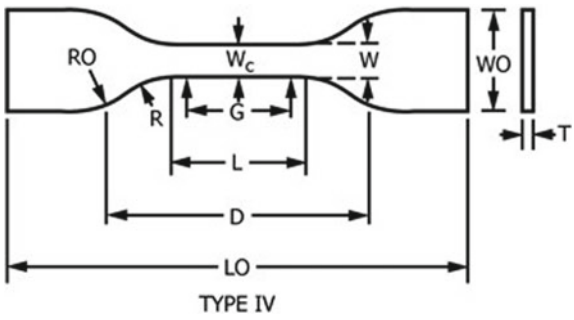

Fig. 1 Geometry of the specimens evaluated [9]

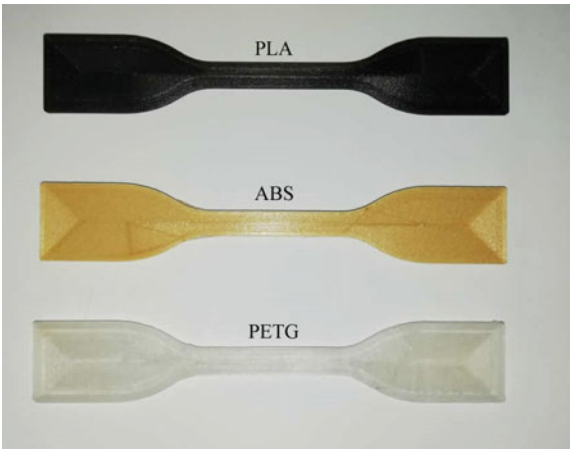

Fig. 2 Printed samples in PLA, ABS, and PETG

Table 2 Test temperatures

Material	Lower temperature (°C)	Upper temperature (°C)
ABS	220	240
PLA	190	220
PETG	220	240

Five specimens were tested for each of the materials evaluated. Tensile tests were performed using a universal testing machine with a 2500 kg load cell, at a loading speed of 5 mm/min.

In all cases, a bed temperature of 60 °C was used. The nozzle temperatures employed were based on those suggested by the filament manufacturer. In this study, variations in the printing temperature of 20 °C were evaluated. The temperatures of the printing nozzle at which the specimens were manufactured are shown in Table 2.

Results

The results obtained from stress tests are presented in Fig. 3. Figure 3a, b shows the stress–strain curves for the ABS samples at temperatures of 220 °C and 240 °C, respectively. Similarly, Fig. 3c, d, e, f shows the results obtained in the stress tests of the samples of PLA at 190 °C, PLA at 210 °C, PETG at 220 °C, and PETG at 240 °C, respectively.

In Table 3, the ultimate tensile strength and the standard deviations for the three materials evaluated are summarized. In the ABS samples at 220 °C, the highest standard deviation of all the samples tested was obtained, while the lowest standard deviation was obtained in the PLA specimens at 190 °C. However, the deviations obtained in general were less than 10%, except in the case of ABS at 220 °C, in which a standard deviation of around 11% was obtained.

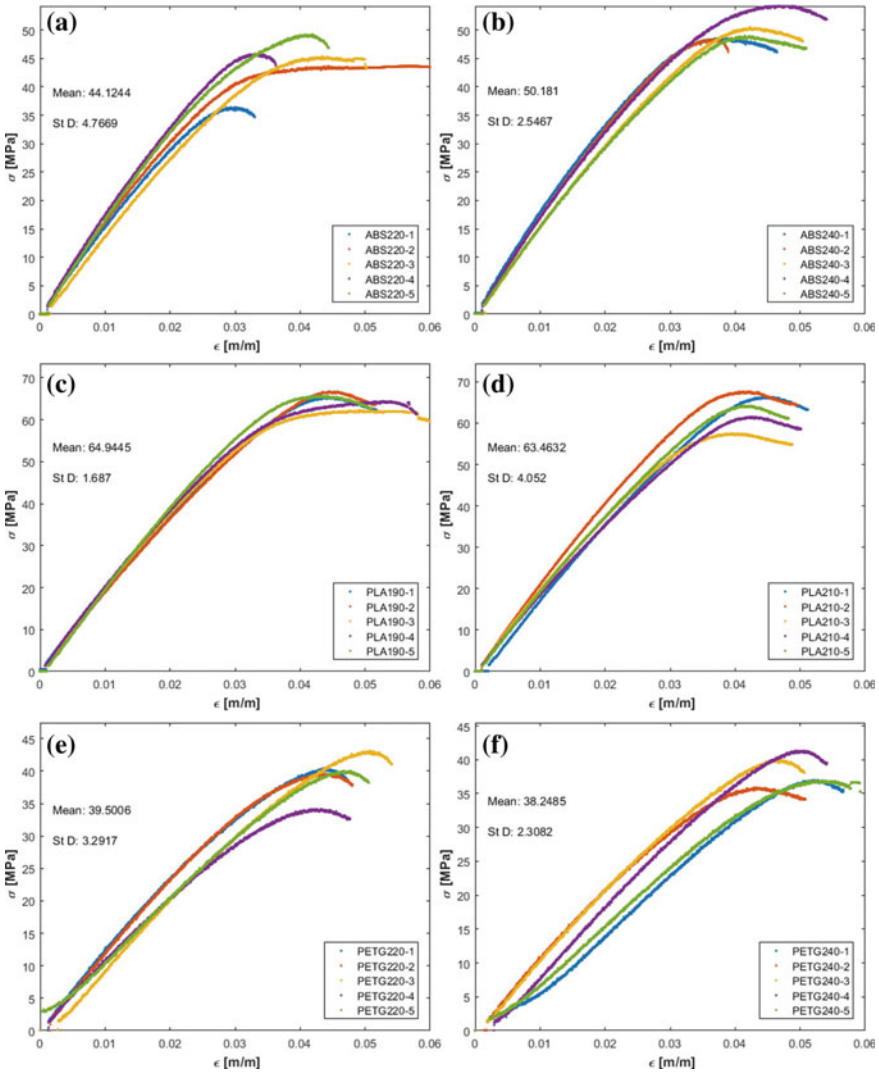

Fig. 3 Stress–strain graphs of the samples evaluated

From the results presented in Table 3, some relevant aspects can be seen in relation to the influence of the temperature of the printing nozzle. Initially, it can be seen how ABS is the only one of the three materials evaluated that presented an increase in its ultimate tensile strength. Likewise, the ABS was the material that presented the greatest variation in relation to its ultimate strength, greater than 13%. The variations of PLA and PETG show variations of less than 5%. These results are presented graphically in Fig. 4. A typical box diagram with its subparts is shown in Fig. 4a, and the results obtained in the present study are presented in Fig. 4b.

Table 3 Experimental results of the tension tests

Material	Temperature (°C)	Ultimate Strength (Mpa)	Standard deviation (MPa)	Percentage of variation (%)
ABS	220	44.1	4.8	13.7
ABS	240 °C	50.2	2.5	
PLA	190 °C	64.9	1.7	−2.3
PLA	210 °C	63.5	4.1	
PETG	220 °C	39.5	3.3	−3.2
PETG	240 °C	38.2	2.3	

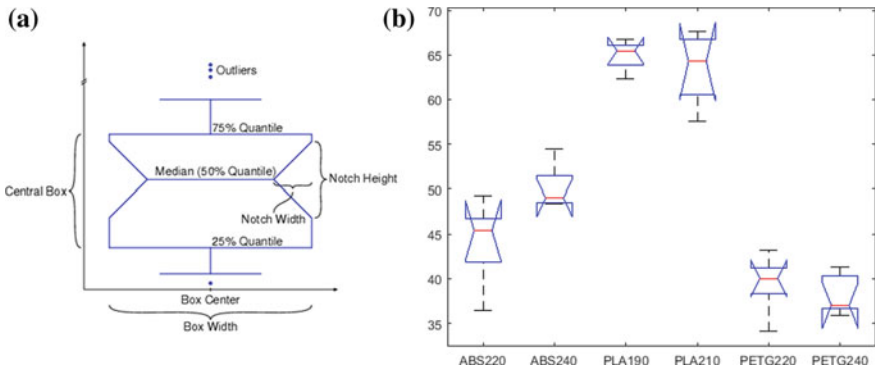

Fig. 4 Ultimate tensile strength results, **a** typical box diagram with its subparts [11]; **b** obtained results

Summary

In this investigation, the influence of the temperature of the extruder nozzle in the ultimate tensile strength of a set of test specimens has been investigated. Three inexpensive materials commonly used in 3D printing have been evaluated and compared. From the results, it was noticed that the material that is mostly affected with the increase in temperature in the printing nozzle was ABS. The other two materials, PLA and PETG, in addition to presenting a little significant variation (less than 5%), showed a decrease in their ultimate tensile strength.

Acknowledgements The authors thank the UAN University for the financing of the 2018221 project. This article is the result of the work carried out during the development of the project "Development, characterization, and manufacture of luminous asphalt and the thermo-mechanical device for its application" by grant PI/UAN-2019-656REM.

References

1. ASTM International (2010) ASTM F2792–10. Standard terminology for additive manufacturing technologies
2. Low ZX, Chua YT, Ray BM, Mattia D, Metcalfe IS, Patterson DA (2017) Perspective on 3D printing of separation membranes and comparison to related unconventional fabrication techniques. J Membr Sci 523:596–613.
3. Pirjan A, Petrosanu M (2013) The impact of 3D printing technology on the society and economy. J Inf Syst Oper Manag 1–11
4. Keleş Ö, Blevins CW, Bowman KJ (2017) Effect of build orientation on the mechanical reliability of 3D printed ABS. Rapid Prototyp J 23(2):320–328
5. Shahrubudin N, Lee TC, Ramlan R (2019) An overview on 3D printing technology: technological, materials, and applications. Procedia Manuf 35:1286–1296
6. Tofail SAM, Koumoulos EP, Bandyopadhyay A, Bose S, O'Donoghue L, Charitidis C (2018) Additive manufacturing: scientific and technological challenges, market uptake and opportunities. Mater Today 21(1):22–37.
7. Attaran M (2017) The rise of 3-D printing: the advantages of additive manufacturing over traditional manufacturing. Bus Horiz 60(5):677–688
8. Ford S, Elanie Despeisse M (2016) Additive manufacturing and sustainability: an exploratory study of the advantages and challenges
9. ASTM International (2014) ASTM D638-14 Standard test method for tensile properties of plastics
10. COBOL INGENIERÍA SAS, "Productos—3DBOTS," 2019 [Online]. Available: https://3dbots.co/productos/. Accessed 16 Sep 2019
11. MathWorks, "Statistical box plots—MuPAD—MathWorks América Latina" [Online]. Available: https://la.mathworks.com/help/symbolic/mupad_ref/plot-boxplot.html. Accessed 16 Sep 2019

Characterization of a Brazilian Kaolin and Its Sorption Ability to Mineral Oils

Gilmar Pinheiro, Thamires Carvalho, Bianca Michel, Jessica Arjona, Margarita Bobadilha, Maria Silva-Valenzuela, Tatiana Costa and Francisco Valenzuela-Diaz

Abstract Kaolins are clays with a wide range of uses, being one of them as a component in several types of cosmetics and pharmaceuticals products as excipient agents for chemical actives, considering its potential to meet international requirements described in pharmacopeias, so the use of kaolin in the cosmetic industry has been expanded based on the final properties achieved with its formulated products, like hydration capabilities, higher nutrition degree of the skin, and smoothness. There are not many published researches available concerning the sorption capacity of cosmetics oils in kaolin, like chestnut oil, pine oil, soybean oil, among others, mainly related to creams and emulsified products. This paper is focused on a commercial kaolin from the state of São Paulo, Brazil, aiming its use in the cosmetic industry as unguents and skin creams. Characterization was made using XRD, FTIR, SEM, particle size distribution, and cosmetic oil sorption capacity of the kaolin. Results obtained in some of the tested oil systems were superior to 150% oil absorption on a weight basis.

Keywords Kaolin · Cosmetics · Oil sorption · Characterization

Introduction

Kaolin is an important mineral widely used in different industries all over the world, consisting mainly of a kaolinite clay mineral which has a structure 1:1 type, being one layer a tetrahedron containing silicon in the center bounded to another layer structured like an octahedron with aluminum in the center. Several countries around the world have important reserves of kaolin being Brazil one of the biggest suppliers of high-quality kaolin, in terms of physical, chemical, and optical properties, compared to the majority types available worldwide [1].

G. Pinheiro (✉) · T. Carvalho · B. Michel · J. Arjona · M. Bobadilha · M. Silva-Valenzuela · T. Costa · F. Valenzuela-Diaz
USP-University of São Paulo, Polytechnic School of Engineering, São Paulo, Brazil
e-mail: go.pinheiro@uol.com.br

J. Li et al. (eds.), *Characterization of Minerals, Metals, and Materials 2020*,
The Minerals, Metals & Materials Series,
https://doi.org/10.1007/978-3-030-36628-5_34

Different industry segments are important users of kaolin, i.e., ceramic industry, cement, concrete, glass, adhesives, pulp and paper, among others. Special interest has been driven to the pharmaceutical and cosmetics industry whose demands for high quality and safety of products manufactured for personal care use have identified kaolin reservoirs from specific areas of Brazil which almost naturally match these requirements. This is the case of the present evaluated kaolin from an area located in Southeast of Brazil, which properties, after beneficiation, could be of high interest of the cosmetic industry chiefly in topics concerning different levels of oil sorption, the focus of this characterization. In general terms, the results here obtained can also be of important value for the coatings industry, especially considering the needs for adequate and sustainable, both technically and economically, extenders for titanium dioxide [2].

The main objective of this study is to contribute to leverage available information on the properties and technologies where and how Brazilian kaolins can be used as raw material in cosmetic industrial segments, since as of nowadays not many papers have been published covering these subjects [2].

Oils, both of mineral and vegetal origin, are among the main raw materials used by the cosmetic industry and are responsible, in general terms, for most of the key properties of several final products supplied by this industry, so the great importance of kaolin properties is to guarantee the achievability and stability of these cosmetic products over its forecasted life [3].

Brazil is one of the top world producers of kaolin accounting for important figures in the country foreign trade market, being ranked in the fifth position in worldwide production [3].

In the North of Brazil, deposits of secondary types are prevalent given its weather conditions favorable to sedimentary deposits. Areas of the Southeast and South of Brazil are recognized as important deposits of primary kaolin types, being the one focused here extracted from a deposit in Southeast Brazil, in an area of the interior of the state of São Paulo, positioned within economic logistic distance to important industrial consumers [4].

The structure of these materials determines their chemical and physical properties—high specific area, sorptive and ionic exchange capacities, rheological properties, chemically inertness, and low or null toxicity for the patient for which they are used in pharmaceutical formulations. Some authors report a decrease in the bioavailability of drugs due to the co-administration of clays in the formulation. However, the joint administration of drugs and kaolins in oral drugs or skin care products has widely accepted advantages from the biopharmaceutical, pharmacological, and chemical points of view [5–7].

Materials and Methods

A commercial beneficiated kaolin from the state of Sao Paulo. Firstly, material was screened to achieve uniformity in a 200 mesh sieve plate, and the material generated

was used for all the characterization tests. Oils used in the characterization are of common use in the cosmetic market, e.g., pine oil, soy bean oil, chestnut oil, Pará chestnut oil, passion fruit oil, sweet almond oil, fresh castor oil and a mean of comparison glycerin was evaluated [8, 9].

Dry and water based moisture evaluation test used thermal methods and final weight outcomes are compared and percentage of humidity is calculated [10].

Foster Swelling test was used to verify the capacity of clay swelling in the presence of different solvents is performed in a graduated cylinder of 100 ml volume, 50 ml of solvent, and 1 g of kaolin [10].

Oil incorporation is the method of manually shaping a sphere to the point of homogeneity and smoothness. The oil saturation point is determined by the plasticity point, adding more solvent to the sphere and disassembling with a spatula until a film formation is observed on the sample surface. The test was based on solvent adsorption test adopted ASTM F726-99 standards in a stainless steel basket [3, 6, 11].

X-Ray diffraction used Phillips X'Pert MPD equipment operating Cu Ka radiation, 40 kV and 40 mA [12]. FTIR analysis uses a Bomem model MB-100 spectrometer, KBr disc at the range 400–4000 nm [12]. Thermal analysis (TG and DSC) is to determine transformations of the kaolin during burning process. Thermogravimetric analysis (TG) performed in an ISI model ATAi 1500, temperature range from ambient up to 1000 °C, heating rate of 10 °C per minute [13]. Particle size analysis used a Malvern MSS Mastersizer particle analyzer.

Results

The determination of kaolin moisture resulted in a dry basis humidity of 3.7% value considered beneficial for the industrial processing of kaolin, because it does not require long drying periods before getting into manufacturing processes [9, 14]. Chemical analysis focused evaluation of material toxicity, with focus on Ni, Zn, Pb, and Cu. Results obtained assured trace values of these elements way below any legislation requirement. [6, 10, 15]. X-Ray diffraction represented in Fig. 1 is obtained by the powder method. The evaluated kaolin is formed by kaolinite (K) and quartz accessory mineral (Q). The typical peak for kaolinite clay mineral is at interplanar distance of 7.15 Å. The typical peak for the quartz accessory mineral is at the interplanar distance of 4.05 Å, and secondary peaks of the clay with interplanar distances are of 3.56 Å, 2.27 Å, and 1.81 Å, respectively [16].

Microscopy of sample sieved in a 200 mesh sieves showing kaolin and impurities, such as iron, quarts, agglomerates, is represented in Fig. 2.

Energy dispersing microscopy demonstrates a typical composition of this type of kaolin, i.e., Al, Si. High concentrations of Si and oxygen are associated with kaolinite structure [17].

Infrared Spectroscopy has bands between 3700 and 3623 cm^{-1} which correspond to the stretching vibrations of the hydroxyl group (OH), the bands at 1099 cm^{-1}, 692 cm^{-1}, and 470.56 cm^{-1} correspond to Si–O bond, in the range of 915 cm^{-1} is

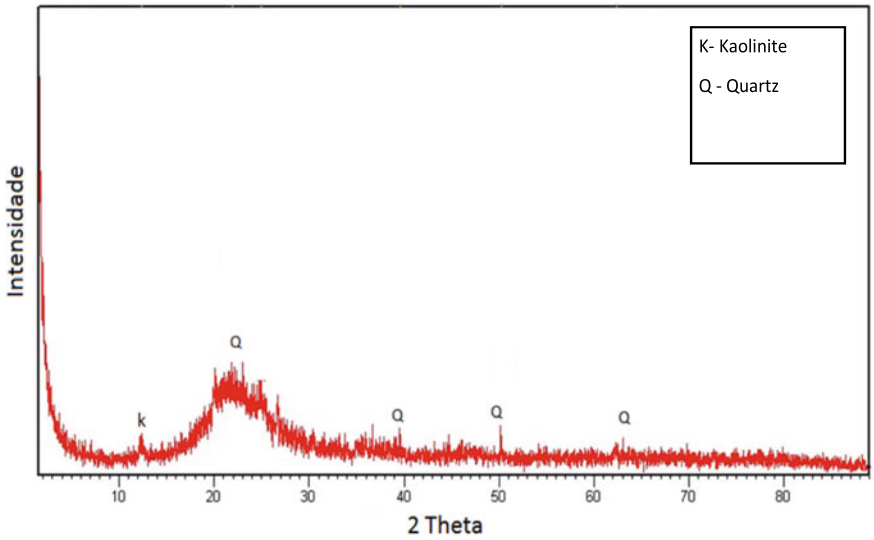

Fig. 1 X-Ray diffraction of evaluated kaolin

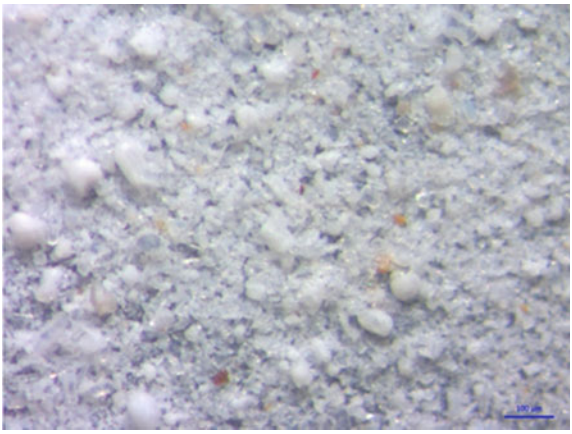

Fig. 2 Amplification of 25X of a 200 mesh sieved sample

the Al–OH strain band, the Si–O–Al bond band is 5424 cm^{-1} and 1639 cm^{-1} refers to the OH bond band of water [14, 17].

Regarding different levels of oil adsorption, numbers are expressed in terms of grams of oil per 1 g of kaolin, in Fig. 3. Sorption degree in weigh basis ranges from 56% for fresh castor oil up to 325% for soy bean oil, and oils, of key importance in the cosmetic industry, like passion fruit, sweet almond, pará chestnut, pine, and chestnut, all had sorption values higher than 240%. Glycerin, also an important raw material of this industry, was used as a mean of comparison, resulting in a sorption value of 781%.

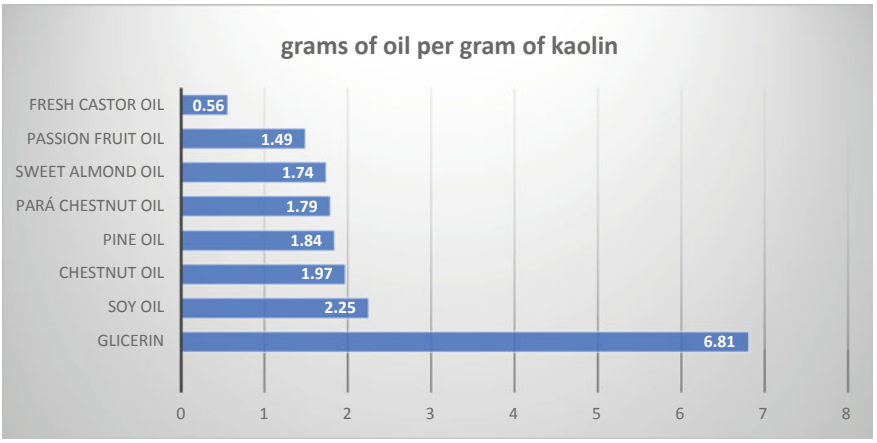

Fig. 3 Capacity of kaolin adsorption, in grams/gram of kaolin

Particle Size distribution of the evaluated kaolin sample resulted in 45% particles over 20 μm, 43% between 2 and 20 μm and 12% lower than 2 μm.

Thermogravimetric analysis is shown in Fig. 4. It demonstrates a mass loss of 4.11% in the temperature range from 28 to 340 °C and another loss of 1.21% in the temperature range of 354 to 559 °C. Dihydroxylation of peak is happening between 354.3 and 559.6 °C [17].

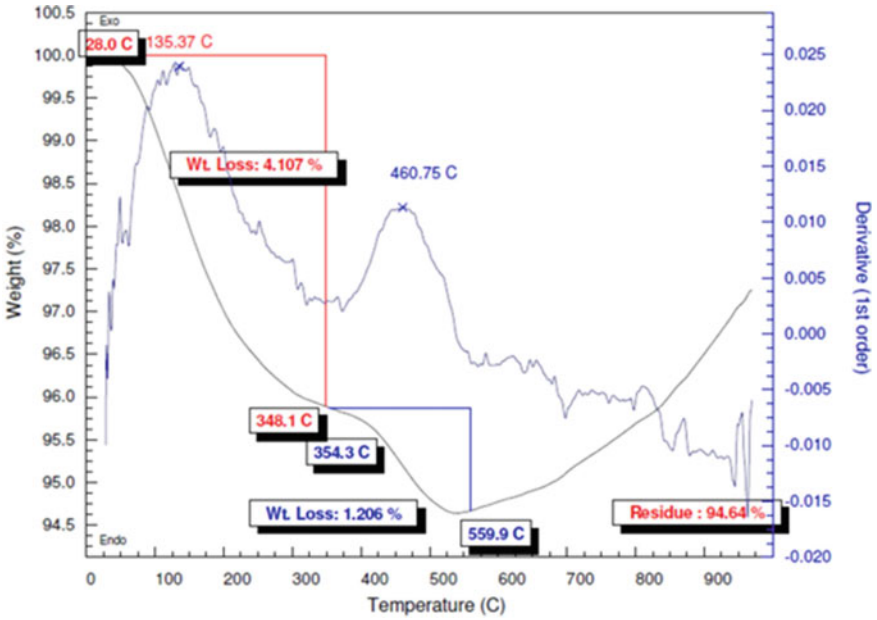

Fig. 4 Thermogravimetric analysis

Conclusions

The studies performed in the kaolin sample showed results consistent to a typical behavior of kaolinitic clays both in mineralogical and physicochemical characterizations, being considered a safe product in terms of health risk [18].

The kaolin material originated from the State of Sao Paulo was successfully evaluated and presented potential for the use at the cosmetic industry and could be adopted as an alternative raw material with great potential to reduce costs and improve products performance [5, 9, 18].

Considering the highly encouraging results here obtained, it is advisable to move further into more specific studies to support the ever-growing technological demands of the cosmetic market. Studies targeting the development of nanocomposites and rheology behavior are suggestions for future researches with this kaolin [9, 18].

Acknowledgements Authors are grateful to FAPESP—Fundação de Amparo à Pesquisa do Estado de São Paulo, for the financial support to this project, number 2019/01231-2.

References

1. Matos CM (2014) Estudo Comparativo das Propriedades de dois caulins brasileiros. Msc. Dissertation, USP—University of São Paulo
2. Freire et al (2013) Caracterização mineralógica e tecnológica do caulim. XVI Jornada de Iniciação Científica—CETEM, pp 174–180
3. Dixon JB (1989) Kaolin and serpentine group minerals. 2nd edn. Madison, New York
4. Coelho et al (2007) Argilas especiais: argilas quimicamente modificadas. Química Nova, v.30, pp 1282–1294
5. Brindley GW, Brown G (1980) Crystal structures of clay mineral and their identification. Mineralogical Society
6. Bertolino LC (2009) Caracterização mineralógica e tecnológica do caulim. Anuário do Instituto de Geociências 32:26–36
7. Cesar Viseras (2018) Characterization of kaolin as health care ingredients. Mineralogical Society Clay Minerals
8. Corrêa WL (2006) Contribuição à gênese e caracterização tecnológica das argilas. Ph.D. thesis. USP, São Paulo
9. Galesia DF (2005) Caracterização das principais argilas utilizadas na cerâmica industrial, v.10, pp 7–12
10. Gregg et al (1982) Adsorption surface area and porosity. Ed. J.W. New York
11. Huang et al (2001) Preparation and properties of montmorillonite hybrid materials prepared by a one-step approach. J Polym Sci 36:871–877
12. Jarek et al (2011) Characterization of natural and modified clay to the development of polymeric nanocomposites. In: Macromolecular symposium proceedings, pp 124–131
13. Kaiser K (2003) Mineral surfaces and soil organic matter. Eur J Soil Sci 54:219–236
14. Lopes et al (2011) Síntese e caracterização de argilas organofilicas. Quim Nova 7:1151–1156
15. Matos et al (2013) Caracterização de uma argila utilizada em produtos cerâmicos. Anais do 57°Congresso Brasileiro de Cerâmica, pp 194–202
16. Moore DM (2002) X-ray diffraction, identification and analysis of clay minerals. 2nd edn. Oxford University Press

17. Peralta-Sanchez MG (2011) Viabilidade do uso de argilas cauliniticas para a indústria cerâmica. Rev Cerâm 57:254–262
18. Toledo et al (2003) Caracterização dos argilominerais do grupo caulinita. Rev Cerâm Ind 8:19–25

Fabrication of Ultra-High Molecular Weight Polyethylene Membrane and Evaluation of Physical Characteristics for Wastewater Treatment

Shan Shan Xie, Zhang Fu Yuan and Yuan Tao Shi

Abstract A porous tubular-type ultra-high molecular weight polyethylene (UHMWPE) membrane with good filtration effect for turbid circulating water was designed and prepared. The physical-chemistry properties such as surface microstructure and tensile strength of tubular-type UHMWPE membrane were investigated. UHMWPE membrane consists of agglomerated particles with diameters of 127–229 μm. The UHMWPE membrane has a porous structure with pore diameter of 40–152 μm, which can enhance the permeability of UHMWPE membrane. The accumulation and distribution of oxide scale particles in UHMWPE membrane after having been used for 5 years were also analyzed. Oxide scale particles are mainly accumulated on the surface layer of UHMWPE membrane. And the fouling layer is about 2.052 mm. The accumulation of oxide scale particles decreases with the increase of distance from the inner surface of the UHMWPE membrane. The accumulation is about 0.96% at $L = 0.342$ mm, and the accumulation is about 0.36% at $L = 2.052$ mm in the UHMWPE membrane. UHMWPE membrane exhibits excellent antifouling property for long-term use.

Keywords Turbid circulating water · UHMWPE membrane · Filtration · Oxide scale

Introduction

In view of the increasing wastewater discharge and the ever-increasing demand for water in steel industries, recycling of wastewater has become the main measure to reduce the consumption of freshwater. Traditional filters are often applied to purify turbid circulating water during continuous casting. However, the filter element of traditional filters is prone to agglomerate and produce a blind spot, and block the nozzle of continuous casting machine, thereby affecting the production and quality

S. S. Xie · Z. F. Yuan (✉) · Y. T. Shi
Collaborative Innovation Center of Steel Technology, University of Science and Technology Beijing, Beijing, China
e-mail: zfyuan2016@ustb.edu.cn

J. Li et al. (eds.), *Characterization of Minerals, Metals, and Materials 2020*,
The Minerals, Metals & Materials Series,
https://doi.org/10.1007/978-3-030-36628-5_35

of casting [1–3]. Therefore, it is significant to develop a tubular-type composite membrane as the filter element, which has a significant effect on the purification and filtration of the turbid circulating water in steel and chemical industry.

The current organic polymeric membranes have the problems with repeated detection, repair, and replacement because of its low chemical stability and mechanical strength [4, 5]. In order to overcome the disadvantages of organic polymeric membranes, numerous research and development of organic membranes have been performed recently. Ultra-high molecular weight polyethylene membrane (UHMWPE) is extensively used in many fields, such as metallurgy, machinery, chemical industry, and various industrial wastewater filtration, due to its excellent mechanical properties, chemical stability, impact resistance, wear resistance, and self-lubrication [6–8]. Many studies have demonstrated that UHMWPE membrane can be used as microfiltration media [9, 10]. However, membrane fouling is an inevitable issue in microfiltration, which decreases the permeate flux over time and increases energy consumption [11–13].

Generally, major turbid circulating water foulants are oxide scale, metal dust, and lubricating grease. Luo [14] found that the preferential order of foulants was adsorbed organic compounds > particulate matter (iron and aluminum colloids) > metallic oxides. Hwang [15] indicated that the membrane showed irreversible particle adsorption during the early stages of seawater filtration. Therefore, it is meaningful to analysis the particles distribution in the internal structure of UHMWPE membrane after filtration, which is advantageous to decrease pore blocking and improve cross-flow microfiltration performance. In this paper, a porous tubular-type UHMWPE membrane was fabricated by sintered process, and its physical characteristics and antifouling performance for microfiltration were evaluated after use. The surface morphology, microstructures, and tensile performance of the UHMWPE membrane were characterized. The accumulation and distribution of particles in UHMWPE membrane after having been used for 5 years were also analyzed.

Experimental

Preparation of UHMWPE Membranes

Ultra-high molecular weight polyethylene was used as the main material. Aluminum stearate, hydroxypropyl methyl cellulose, and rare earth oxide were used as organic additives. The mixture was blended homogeneously and then placed in a tubular stainless steel mold with diameter of 150 mm. After being vibrations in a vibrators for 5–10 min, the stainless steel mold was dried in oven at 220 °C for about 2–3 h. Finally, the tubular-type UHMWPE membrane was obtained after cooling to room temperature.

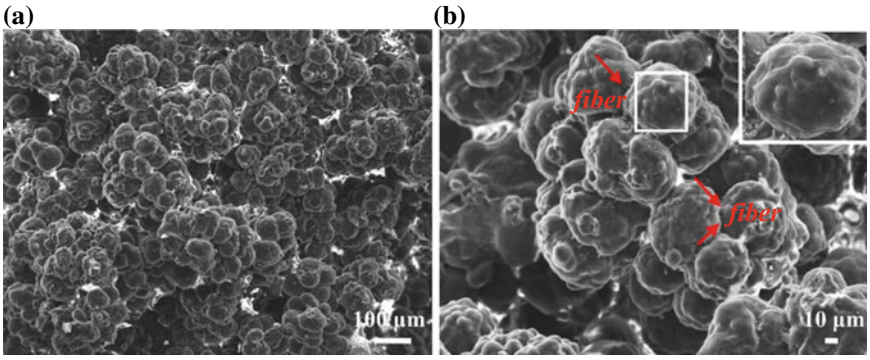

Fig. 1 Cross-sectional morphologies of tubular-type UHMWPE membrane. **b** is the magnification of **a**; The insert in **b** is the magnification of corresponding aggregated particles

Characterization of UHMWPE Membrane

Surface morphology of the tubular-type UHMWPE membrane was examined by using field emission scanning electron microscopy (FESEM) (JSM-7001F). The average aggregate particle size and average pore diameter were counted by nano-measurer according to SEM images of Fig. 1 in an area of about 1.06 mm^2. The functional groups of UHMWPE membrane were examined by using a Bruker Fourier transform infrared (FTIR) spectrometer (Nicolet iS50). Tensile tests of the UHMWPE membrane were conducted by using testing machine (2011SINO/BI002648) at ambient temperature. To evaluate the antifouling of the UHMWPE membrane, the accumulation of oxide scale in the UHMWPE membrane was investigated by optical microscope (OLYMPUS BX51M) according to the backscattered electron images of SEM in Fig. 4 in an area of about 0.042 mm^2.

Results and Discussion

Figure 1 shows the morphology of cross section of tubular-type UHMWPE membrane. It is found that the UHMWPE membrane exhibits a typical aggregated nodular structure, which is similar to those of most of traditional UHMWPE membrane formed by sintered process [16]. It consists of agglomerated particles 127–229 μm in diameter. These particles are agglomerated of numerous cauliflower-like secondary particles as demonstrated by the insert of Fig. 1b. The UHMWPE membrane has a porous structure with pore diameter of 40–152 μm, which can enhance the permeability of UHMWPE membrane. From the magnifications in Fig. 1b, it exhibits numerous fibrous structures between secondary particles, which is ascribed to the secondary particles are more likely to be oriented when they combine to form longer molecular chains.

The surface chemical structure of the UHMWPE membrane was characterized by FTIR spectroscopy. Figure 2 shows the FTIR results of the UHMWPE membrane in the 4000 to 500 cm^{-1} wave number. The absorption peaks at 2918 and 2850 cm^{-1} appear in samples owing to the C–H bond stretching. The peak at 1473 cm^{-1} is assigned to the asymmetry changing angle vibration of C–H bond. The peak at 718 cm^{-1} is due to the in-plane rocking vibration band of C–H bond. In addition, the absorption peaks of 3434 cm^{-1} may be attributed to the influence of moisture during the test.

Typical tensile stress–strain curve of UHMWPE is shown in Fig. 3. It can be seen that the specimen exhibits tensile strain-hardening behavior. It is well known that numerous of entanglements of UHMWPE prevent the lamellar transforming

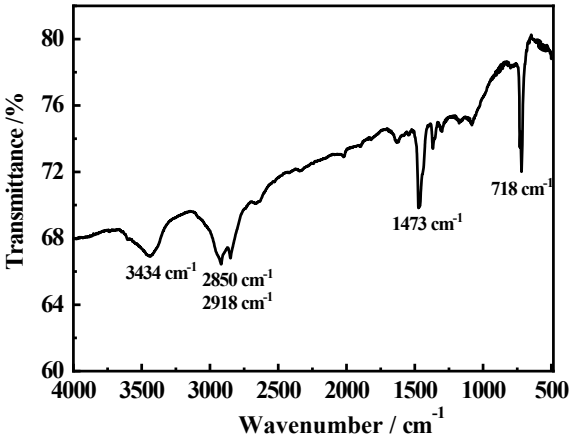

Fig. 2 FTIR spectra of tubular-type UHMWPE membrane

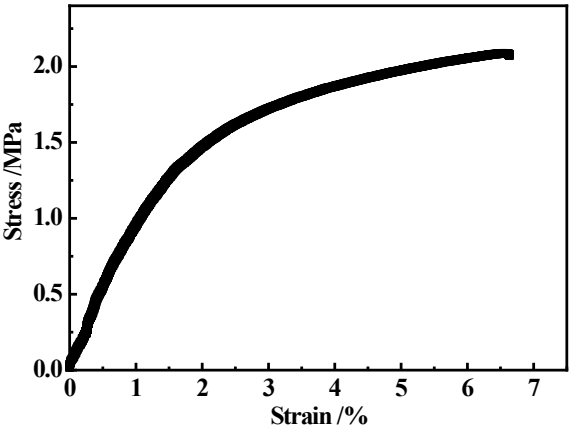

Fig. 3 Stress–strain curves of tubular-type UHMWPE membrane

fibrillar morphology at large deformation, thus resulting in the early onset of strain-hardening [17]. The tensile strength of the UHMWPE approaches 2.09 MPa. The corresponding elongation at break is 6.6%. It may be contributed to a highly oriented structure of UHMWPE leads to low elongation at break. The tensile elastic modulus of UHMWPE is obtained from the slope of tensile stress–strain curve and the value is 82.24 MPa.

To analyze the fouling mechanism, the distribution and accumulation of oxide scale in UHMWPE membrane after having been used for 5 years are shown in Fig. 4. The accumulation of oxide scale particles decreases with the distance from the inner surface of UHMWPE membrane. The accumulation of oxide scale particles decreases significantly by about 62.7% when the distance increases from 0.342 to 2.052 mm. The accumulation is only 0.36% at $L = 2.052$ mm in the UHMWPE membrane. While the oxide scale particles are hardly accumulated with the increase of distance. These results indicate that fouling layer is about 2.052 mm. The smaller oxide scale particles are apt to deposit on the internal structure of the UHMWPE membrane, thus resulting in pore blocking and irreversible fouling. While the larger particles are intercepted and deposited to form cake, preventing the smaller particles from further depositing on the membrane pores [18]. After backwashing, the attached cake is removed and the oxide scale particles would lead to a higher degree in pore fouling [19]. Such process repeats until the whole membrane surface is covered and equilibrium has been reached. Therefore, the oxide scale particles are mainly accumulated on the surface layer. Furthermore, the accumulation is only 0.96% at $L = 0.342$ mm in the UHMWPE membrane. As a result, UHMWPE membrane exhibits excellent antifouling property for long-term use.

The cross-sectional backscattered electron images of UHMWPE membrane after having been used for 5 years are shown in Fig. 5. It can be observed in Fig. 5 that two positions exhibit numerous oxide scale particles and suspended solids in the agglomerated particles surface and pores of the UHMWPE membrane. At the same

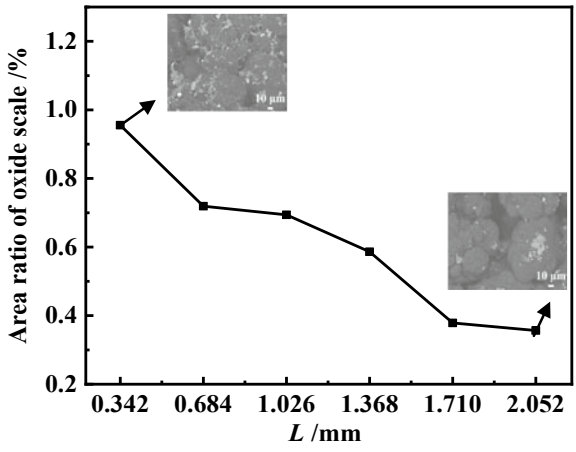

Fig. 4 Accumulation and distribution of oxide scale in the tubular-type UHMWPE membrane after having been used for 5 years

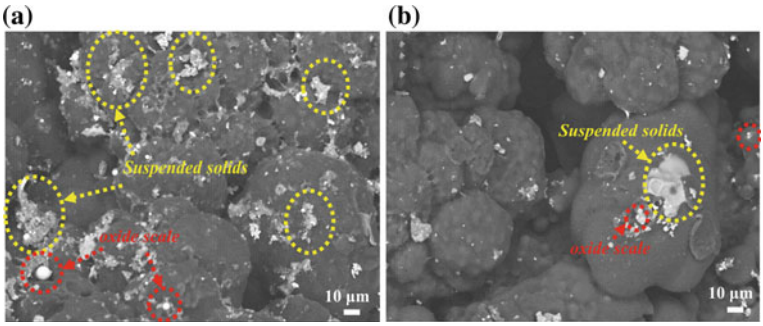

Fig. 5 Cross-sectional morphologies of the tubular-type UHMWPE membrane: **a** $L = 0.342$ mm and **b** $L = 2.052$ mm

time, comparing Fig. 5a, b, it is clear that the accumulation of oxide scale particles and suspended solids at $L = 0.342$ mm is much higher than that at $L = 2.052$ mm. This further indicates that the fouling of UHMWPE membrane at $L = 0.342$ mm is much more serious. And the oxide scale particles are mainly accumulated on the surface layer.

Conclusion

The tubular UHMWPE membrane with porous structure was used for filtration in turbid circulating water of continuous casting. UHMWPE membrane is composed of agglomerated particles and numbers different macro-pores. The average aggregated particle size is in the range of 127–229 μm. Excellent separation performance is presented. After filtration of the turbid circulating water, oxide scale particles are mainly accumulated on the surface layer of UHMWPE membrane. And the fouling layer is about 2.052 mm. The accumulation is about 0.96% at $L = 0.342$ mm, and the accumulation is about 0.36% at $L = 2.052$ mm in the UHMWPE membrane. UHMWPE membrane exhibits excellent antifouling property for long-term use.

Acknowledgements This research work was supported by the National Natural Science Foundation of China (Grant Nos. 51974022, U1738101) and Fundamental Research Funds for the Central Universities (Grant No. FRF-MP-18-007).

References

1. Jin JT, Wu GX, He K (2014) Effect of ions on carbon steel corrosion in cooling systems with reclaimed waste water as the alternative makeup water. Desal Water Treat 52:7565–7574
2. Xu JC, Chen G, Huang XF (2009) Iron and manganese removal by using manganese ore constructed wetlands in the reclamation of steel wastewater. J Hazard Mater 169:309–317

3. Yuan ZF, Xie SS, Yu XT (2018) Physical-chemical property and filtration mechanism of the porous polyvinyl chloride composite membrane as filter for waste water treatment. Desal Water Treat 105:35–40
4. Yun CY, Kim WY, Son DJ (2015) Fabrication of tubular-type MF ceramic membrane with enhanced permeability by addition of PMMA in the support and evaluation of physical characteristics for wastewater treatment. Ceram Int 41(9):10788–10794
5. Lee SJ, Dilaver M, Park PK (2013) Comparative analysis of fouling characteristics of ceramic and polymeric microfiltration membranes using filtration models. J Membr Sci 432:97–105
6. Liu H, Pei Y, Xie D (2010) Surface modification of ultra-high molecular weight polyethylene (UHMWPE) by argon plasma. Appl Surf Sci 256(12):3941–3945
7. Stojilovic N, Dordevic SV, Stojadinovic S (2017) Effects of clinical X-ray irradiation on UHMWPE films. Nucl Instrum Meth B 410:139–143
8. García A, Domínguez-Díaz M, Paniagua R (2019) Microhardness modification of ultrahigh-molecular-weight polyethylene by oxygen plasma: effect of the polymer crosslinking. Nucl Instrum Meth B 445:8–12
9. Liu S, Zhou C, Yu W (2011) Phase separation and structure control in ultra-high molecular weight polyethylene microporous membrane. J Membr Sci 379(1–2):268–278
10. Shen L, Peng M, Qiao F (2008) Preparation of microporous ultra high molecular weight polyethylene (UHMWPE) by thermally induced phase separation of a UHMWPE/liquid paraffin mixture. Chinese J Polym Sci 26(06):653–657
11. Wang C, Chen WN, Hu QY (2015) Dynamic fouling behavior and cake layer structure changes in nonwoven membrane bioreactor for bath wastewater treatment. Chem Eng J 264:462–469
12. Altunkaynak A, Chellam S (2010) Prediction of specific permeate flux during crossflow microfiltration of polydispersed colloidal suspensions by fuzzy logic models. Desalination 253(1–3):188–194
13. Park J, Lee S, You J (2018) Evaluation of fouling in nanofiltration for desalination using a resistance-in-series model and optical coherence tomography. Sci Total Environ 642:349–355
14. Luo M, Wang Z (2001) Complex fouling and cleaning-in-place of a reverse osmosis desalination system. Desalination 141:15–22
15. Hwang KJ, Wang SY, Iritani E (2016) Fine particle removal from seawater by using cross-flow and rotating-disk dynamic filtration. J Taiwan Inst Chem E 62:45–53
16. Gul RM, McGarry FJ (2004) Processing of ultra-high molecular weight polyethylene by hot isostatic pressing, and the effect of processing parameters on its microstructure. Polym Eng Sci 44(10):1848–1857
17. Yu KQ, Yu JT, Dai JG (2018) Development of ultra-high performance engineered cementitious composites using polyethylene (PE) fibers. Constr Build Mater 158:217–227
18. Lee JY, Choi BK, Ahn KH (2012) Characteristics of flux and gel layer on microfilter and non-woven fabric filter surface based on anoxicaerobic MBRs. Bioproc Biosyst Eng 35:1389–1398
19. Metzger U, Le-Clech P, Stuetz RM (2007) Characterisation of polymeric fouling in membrane bioreactors and the effect of different filtration modes. J Membr Sci 301(1–2):180–189

Part XI
Poster Session

A Comparison Between Graphene Oxide and Reduced Graphene Oxide as Reinforcement Agents in Polypropylene Nanocomposite Using Irradiated Polypropylene as Compatibilizer

Carlos Soares, Julyana Santana, Olgun Güven and Esperidiana A. B. Moura

Abstract Graphene is the material with the best mechanical resistance ever encountered. Various types of studies have been carried out on possible applications. The use as a reinforcement in nanocomposites has shown to be a promising field, but some studies indicate that the graphene oxide (GO) and reduced graphene oxide (RGO) have better results as reinforcement, due to the functional groups, which allow a better adhesion with the matrix. This study analyzes the production of polypropylene (PP) nanocomposite comparing the use of graphene oxide (GO) and reduced graphene oxide (RGO) as fillers and irradiated polypropylene as a coupling agent. A twin-screw extruder and injection molding machine were used to produce the nanocomposite PP reinforced with 0.2 wt% of GO and RGO by melt blending. The GO and RGO were characterized by XRD analysis. The nanocomposite samples were characterized by XRD, SEM, TG, DSC and mechanical test.

Keywords Graphene oxide · Polypropylene · Nanocomposite · Gamma radiation · Tensile tests

C. Soares (✉) · J. Santana · E. A. B. Moura
Nuclear and Energy Research Institute (IPEN), Center of Chemical and Environmental Technology, Av. Prof. Lineu Prestes 2242, Sao Paulo, SP 05508-000, Brazil
e-mail: carlos.soares@ifro.edu.br

C. Soares
Institute Federal of Education Science and Technology of Rondônia, BR 174, KM3 s/no, Vilhena, RO 76980-000, Brazil

O. Güven
Department of Chemistry, Polymer Chemistry Division, Hacettepe University, Beytepe, Ankara, Turkey

J. Li et al. (eds.), *Characterization of Minerals, Metals, and Materials 2020*,
The Minerals, Metals & Materials Series,
https://doi.org/10.1007/978-3-030-36628-5_36

Introduction

Graphene is the material with the best mechanical resistance ever encountered, composed by carbon only, it is the finest material in the world, reaching a plane with just one atom thickness in a sp^2-hybridized lattice [1, 2]. Novoselov and Geim were honored with Nobel Prize for Physics in 2010 for its synthesis [3]. Nowadays, graphene has attracted tremendous attention because of its remarkable properties in different areas such mechanical, electronic and thermal [4, 5], due to its atomic scale, it can be combined with others materials, bringing news kinds of nanocomposite with new kinds of properties, becoming a promising material for many applications [2, 6]. The discovery of how to combine polymer with nanoscale particles, by Toyota research group, create a lot of opportunities to applications with graphene [7, 8]. Polymers material are used in many applications, mainly in areas where weight is an important issue, such as automobile and aerospace when mixed with graphene it can keep its properties by conventional processing and fabricated in complex shaped [9]. The nanocomposite's properties are directly influenced by dispersion and interfacial interactions with the nanofillers [2, 10], but pristine graphene addition does not form homogeneous composites due to the van der Waals interaction, becoming incompatible with an organic polymer. Furthermore, the most promising area for this material is in polymer nanocomposites, where the exceptionally high elastic modulus and tensile strength of graphene or graphene derivatives (graphene oxide (GO)), a heavily oxygenated graphene, produced by oxidation of natural graphite, bearing functional groups like hydroxyl, epoxide and carboxyl groups, being more compatible and hydrophilic. GO and reduced graphene oxide (RGO) have presented noticeable improvement in the mechanical properties as reinforcement in nanocomposites [11], also both have high yield production and low cost in comparison to graphene [9].

Polymer matrix as polypropylene (PP) plays an important role due to its low cost, providing a good condition of commercialization and mechanical properties have become largely used in industrial application. However, as a hydrophobic polymer, it has poor adhesion hydrophilic reactive groups. According to Karsli et al., this problem can be solved by Gamma radiation, improving its properties and gaining compatibilization between PP and fillers such as carbon fiber [12]. Effects of the influence of radiation in polymers have become extensively studied in the last few decades, [13] the irradiation of polymers with high-energy radiation, like gamma and electron-beam, result in scission of the main chain, generally termed as "degradation" or cross-linking with the concomitant formation of covalent bonds among polymer chains and compatibility, between PP and filler, can be explained by induced oxidation and limited chain of PP [12]. Furthermore, radiation can be used to reduce GO, which is easily controlled, highly less destructive and eco-friendly, in comparison with a conventional chemical reduction [14], and it can further inhibit the graphene agglomeration, thereby contributing to a "well-dispersible graphene" [15].

To process the nanocomposite, there is some option as solution mixing, melt blending and in situ polymerization [9]. Solution mixing brings better results in dispersion, but the use of solvent made this option not environment-friendly. This

study took the option for melt extrusion, using a twin-screw extruder, where the filler can be mixed directly into the polymer matrix and feed into an extruder, an economical method and easy to apply to industrial production.

Materials and Method

Materials

For the preparation of polypropylene/GO nanocomposites (PPCNs) were used the following materials: polypropylene homopolymer H 301 with a melt flow index of 10 g/10 min (ASTM D 1238) and a density of 0.905 g/cm^3 (ASTM D 792) from Braskem S/A, graphite powder purchased from Labsynth Ltda.

Graphene Oxide

Graphene oxide was synthesized from natural graphite powder by a modified Hummers method [15]. The as-prepared graphene oxide was exfoliated in DMF/distillate water solution under ultra-sonication. The resulting GO was washed several times with HCl and distillate water until pH ~ 6 and freeze-dried to obtain the powder.

Reduced Graphene Oxide

A solution of distilled water (50 ml) , alcohol (50 ml) and GO were sealed and irradiated with gamma radiation (^{60}Co) at radiation dose of 80 kGy, using a multipurpose gamma irradiator located at Radiation Technology Center CTR-IPEN/CNEN-SP, at radiation dose rate of 6 kGy/h and room temperature. After irradiation, the aqueous solution containing RGO was frozen for 24 h and freeze-dried for 24 h to obtain the RGO powder.

Nanocomposite Preparation

The polypropylene/GO and /RGO nanocomposites (PPNCs) were prepared according to the composition presented in Table 1 using a co-rotating twin-screw extruder (Maplan). The temperature profile was 160/175/185/190/195 °C. The screw speed was set from 20 to 30 rpm. The extrudates materials were cooled down in water at room temperature for a better dimensional stability, pelletized and dried at 60 ± 2 °C for 24 h, subsequently fed into injected molding where the temperature profile used was 180/185/190/195 °C, and the mold temperature was set to 50 °C and specimens test samples were obtained.

Table 1 PPCNs nanocomposites composition

Materials	PP (wt%)	PPI (wt%)	GO (wt%)	RGO (wt%)
Neat PP	100	–	–	–
PP/GO	99.8	–	0.2	–
PP/RGO	99.8	–	–	0.2
PP/PPI/GO	94.8	5.0	0.2	–
PP/PPI/RGO	94.8	5.0	–	0.2

Characterization Methods

Thermogravimetric Analyses (TG)

The TG analysis was carried out using samples weighing 5.0 ± 0.5 mg. The temperature range was set from 25 to 600 °C with a heating rate of 10 °C/min, under nitrogen atmosphere (50 ml/min).

X-Ray Diffraction (XRD)

The XRD patterns of the GO, RGO and of the neat PP and its nanocomposites were obtained using Siemens-D5000 diffractometer operated at 40 kV and 40 mA, with copper Kα radiation ($\lambda = 1.54$ Å) and 2θ varying between 2 and 50°. The interlayer spacing (d) of the clays was calculated through Bragg's Eq. (1):

$$n * \lambda = 2d \sin\theta \tag{1}$$

where:

$n =$ whole number
$\lambda = 1.54$ Å is the incident radiation's wavelength
$d =$ interlayer spacing
$2\theta =$ diffraction angle

Mechanical Tests

The tensile tests for all samples were performed according to ASTM D 638 using a universal testing machine INSTRON, model 5564 at room temperature and loading rates of 50 mm/min.

Field Emission Scanning Electron Microscopy (FE-SEM)

FE-SEM of cryofractured samples under liquid nitrogen was carried out using a JEOL-JSM-6701 F, microscope with an accelerating voltage of 1–30 kV, using EDS Thermo-Scientific mod. Noran System Six software, in carbon sputtered samples.

Results and Discussion

Thermogravimetric Analysis Results

TGA curves of PP, PP/GO, PP/RGO, PPI/GO, PPI/RGO, GO and RGO under N_2 atmosphere are plotted in Fig. 1. The weight loss stage between 140 and 200 °C corresponds to the presence of moisture, and at 350 °C can be attributed to the weight loss of labile oxygen functional groups [2].

Table 2 has more information to analyses, the composites present a slight decrease in degradation temperature when compared to neat PP.

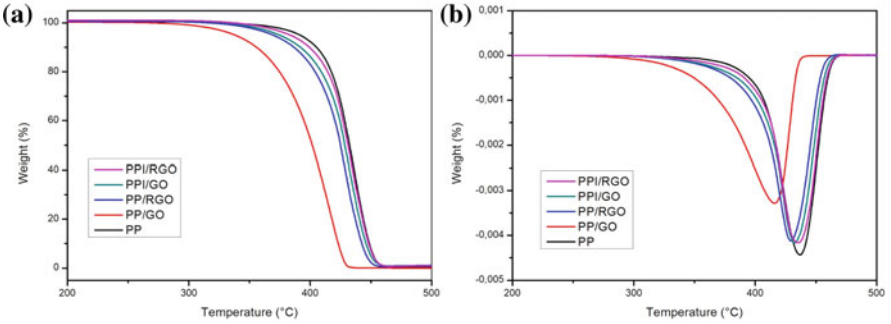

Fig. 1 Thermogravimetric (TG) (**a**) and derived thermogravimetric (DTG) (**b**) thermograms for the neat PP and its nanocomposites

Table 2 Decomposition temperatures and weight loss of PP and PPCNs

Materials	T_{onset} (°C)	$T_{máx}$ (°C)	Weight loss (%)
Neat PP	310	464	99.5
PP/GO	265	436	99.8
PP/RGO	297	459	99.3
PP/PPI/GO	295	462	98.6
PP/PPI/RGO	295	464	98.7

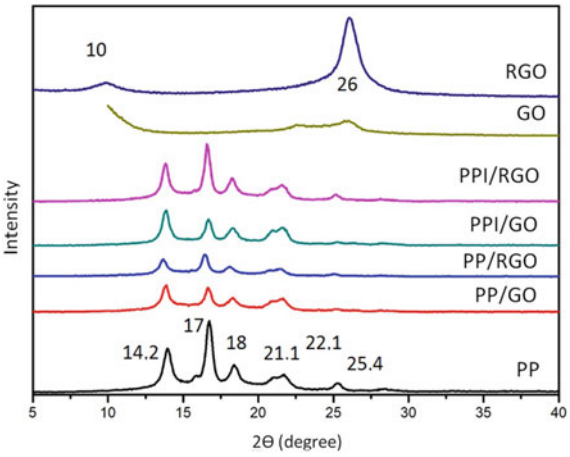

Fig. 2 XRD patterns to PP, GO, RGO and composites

X-Ray Diffraction (XRD) Analysis

The bulk crystal line structure of the powder was also characterized using XRD, which is presented in Fig. 2. The peaks in the diffractograms 2θ 14.2°, 17° and 18.8° correspond to (110), (040) and (130) planes of alpha crystal of PP [1], those bands presented strong intensities. The other three bands, at 21.13° reflection assigned to the (111) crystallographic plane, at 21.9° reflection assigned to the (041) and at 25.42° reflection assigned to the (060) crystallographic plane with lower intensities [16]. A diffraction peak corresponding to GO appears at 2θ 10.5° that appears too in RGO diffractogram with a weak peak. While GO exhibited a broad and weak peak at 2θ 26.0°, this peak is strong in RGO, like pristine graphite, which can indicate that nanosheets restack in RGO, because of the strong Van der Waals' forces in the interlayer [11]. The peaks exhibited by RO and RGO in X-ray diffractograms' not appear in the composites, that shows only the reflections of the crystallographic and amorphous planes of the PP matrix, indicated the total overlapped and good dispersion [16].

Mechanical Properties

Table 3 presents the results of tensile tests for neat PP and PP/PPI/GO/RGO composites. The results presented show the average values calculated from the data obtained in tests for ten test specimens. All the composites presented an increase in tensile stress at yield and tensile strength at break higher than 10% when compared to neat PP, except for the PP/PPI/RGO sample that presented a slight decrease in tensile strength at break. Regarding the Young's modulus, it can be observed a gain for all samples due to GO or RGO addition. The elongation reduced for all composites, a

Table 3 Mechanical properties of PP and PPCNs

Materials	Tensile stress at yield (MPa)	Tensile strength at break (MPa)	Elongation at break (%)	Young's modulus (MPa)
Neat PP	33.5 ± 0.9	20.9 ± 1.8	392.7 ± 35	364
PP/GO	38.6 ± 1.5	36.1 ± 2.1	17.8 ± 0.6	393
PP/RGO	39.1 ± 0.7	35.8 ± 1.7	21.7 ± 1.7	453
PP/PPI/GO	38.2 ± 2.4	35.3 ± 2.3	16.7 ± 1.1	430
PP/PPI/RGO	37.7 ± 1.0	15.1 ± 1.3	217.1 ± 19	335

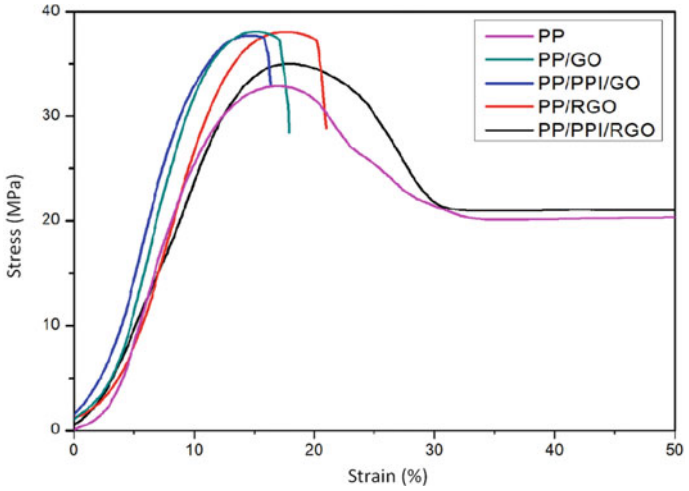

Fig. 3 Diagram stress × strain for neat PP and its composites

slightly decrease in PPI/RGO and a major decrease to all the others, its indicated good interfacial bonding between filler and the host polymer, that restrain the polymeric chain movement [17]. The increase in tensile stress and Young's modulus also means a good adhesion with matrix [18].

Figure 3 shows the diagram stress (MPa) × strain (%) for neat PP and its composites. The results show a significant reduction on elongation at break of PP/GO, PP/RGO and PP/PPI/GO when compared to neat PP, meaning good distribution of GO an RGO layer and good Interfacial bonding filler/matrix [19].

Field Emission Scanning Electron Microscopy (FE-SEM)

FE-SEM micrographs of cryofractured surfaces of the neat PP and its composites were studied to understand the failure mechanisms and also evaluate the presence of

GO/RGO aggregated and its dispersion in the PP matrix. FE-SEM image of neat PP and its composites in different magnifications are showed in Fig. 4.

In Fig. 4, the images show not a relevant difference between nanocomposites (Fig. 4c–f), all nanocomposites present an irregular fracture surface. When compared to neat PP (Fig. 4a) composites exhibits little more fragile fracture. Comparing Fig. 4b (10.000x) from Fig. 4c (500x), no expressive changes can be seen, indicating a homogeneous dispersion of GO/RGO nanosheets in the PP matrix.

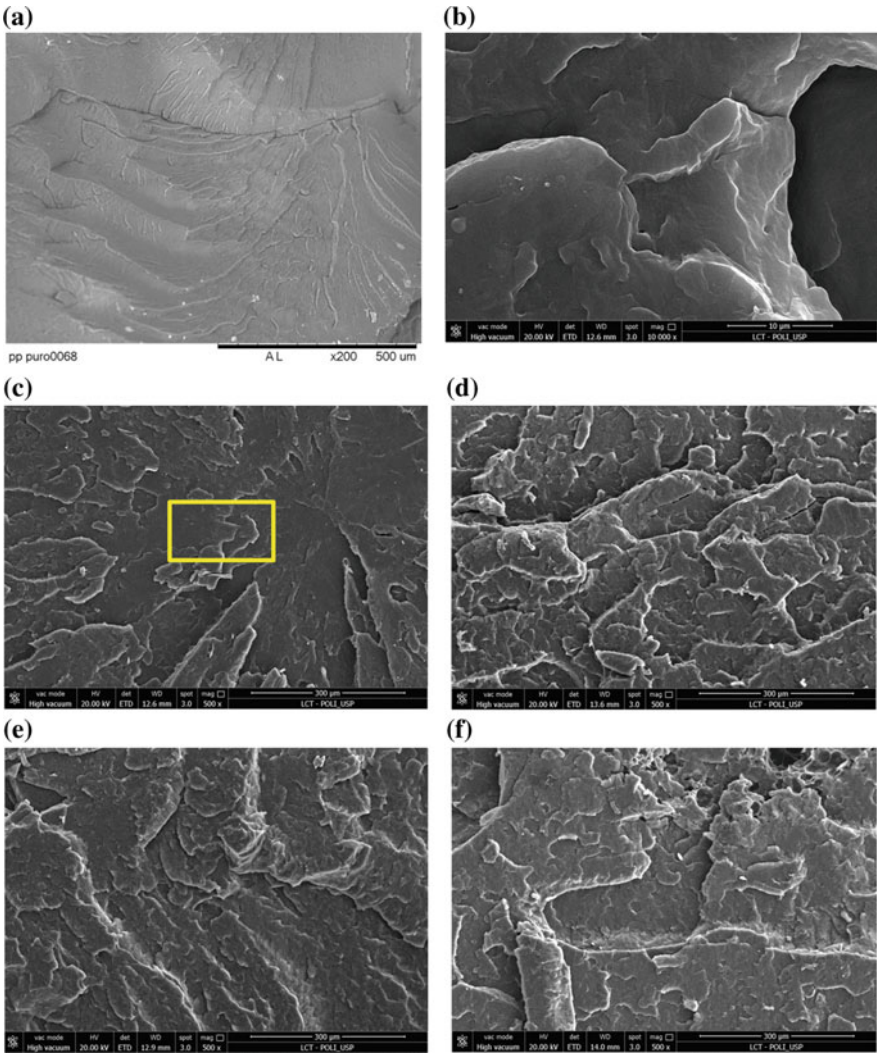

Fig. 4 FE-SEM image of **a** Neat PP and FE-SEM images of **b**-**c** PP/GO, **d** PP/RGO, **e** PPI/GO and **f** PPI/RGO

Conclusions

This study analyzed the synthesis of graphene oxide (GO), reduced graphene oxide (RGO) and their application as fillers in polypropylene (PP) matrix to produce nanocomposite, as well as using irradiated polypropylene as a coupling agent.

In conclusion, the thermogravimetric analysis results did not show much difference in the obtained nanocomposite samples. FE-SEM and XRD analysis results showed that synthesis of GO/RGO from graphite succeeded, and its combination with PP showed a good dispersion, resulting in a homogeneous nanocomposite. In addition, the mechanical tests showed good results, except for PP/PPI/RGO with decreased mechanic strength, indicating bad adhesion.

The other PPNCs showed improvement between 10 and 16% in tensile strength and 8–25% in Young's modulus.

Despite the GO/RGO synthesis showed good results, the PP/PPI/RGO indicated possible restack of RGO, due to the van der Waals force. The synthesis process followed the same steps, but yielded different results indicating the need for further investigation.

Acknowledgements The authors wish to thank IIAEA-CRP # 17760 RO, FAPESP, and CNPq for their financial support for this work.

References

1. Bafana AP, Yan X, Wei X, Patel M, Guo Z, Wei S, Wujcik EK (2017) Polypropylene nanocomposites reinforced with low weight percent graphene nanoplatelets. Composites B 109:101–107
2. Yua B, Bao C, Song L, Hong N, Liew KM, Hu Y (2014) Preparation of functionalized graphene oxide/polypropylene nanocomposites wit significantly improved thermal stability and studies on the crystallization behavior and mechanical properties. Chem Eng J 237:411–420
3. Ajayan PM, Schadler LS, Giannaris C, Rubio A (2000) Single-walled carbon nanotube-polymer composites: strength and weakness. Adv Mater 12:750–753
4. Dreyer RD, Park S, Bielawski CW, Ruoff RS (2010) The chemistry of graphene oxide. Chem Soc Rev 39:228–240
5. Wang G, Yang J, Park J, Gou X, Wang B, Liu H et al (2008) Facile synthesis and characterization of graphene nanosheets. J Phys Chem C 112:8192–8195
6. Geim AK, Novoselov KS (2007) The rise of graphene. Nat Mater 6:183–191
7. Vickery L, Patil AJ, Mann S (2009) Fabrication of graphene-polymer nanocomposites with higher-order three-dimensional architectures. Adv Mater 21:2180–2184
8. McAllister MJ, Li JL, Adamson DH, Schniepp HC, Abdala AA, Liu J, Herrera-Alonso M, Milius DL, Car R, Prud'homme RK, Aksay IA (2007) Chem Mater 19:4396–4404
9. Du J, Cheng HM (2012) The fabrication, properties, and uses of graphene/polymer composites. Macromol Chem Phys 213:1060–1077
10. Vaisanen T, Haapala A, Lappalainen R, Tomppo L (2016) Utilization of agricultural and forest industry waste residues in natural fiber-polymer composites: a review. Waste Manag 54:62–73
11. Lin Y, Liu Y, Zhang D, Guozhang Wu (2017) Radiation resistance of polypropylene composites by incorporating reduced graphene oxide and antioxidant: a comparison study. Compos Sci Technol 146:83–90

12. Karsli NG, Aytac A, Akbulut M, Deniz V, Guven O (2013) Effects of irradiated polypropylene compatibilizer on the properties of short carbon fiber reinforced polypropylene composites. Radiat Phys Chem 84:74–78
13. Haydaruzzaman Khan RA, Khan MA, Khan AH, Hossain MA (2009) Effect of gamma radiation on the performance of jute fabrics-reinforced polypropylene composites. Radiat Phys Chem 78:986–993
14. Li T, Park HG, Choi SH (2007) γ-Irradiation-induced preparation on Ag and Au nanoparticles and their characterizations. Mater Chem Phys 105:325–330
15. Sun M, Wang G, Li X, Li C (2014) Irradiation preparation of reduced graphene oxide/carbon nanotube composites for high-performance supercapacitors. J Power Sour 245:444–463
16. Parparita E, Darie RN, Popescu CM, Udin MA, Vasile C (2013) Structure—morphology—mechanical properties relationship of some polypropylene/lignocellulosic composites. Mater Des 56:736–772
17. Zhang Y, Zhang Q, Chen D, Lu P (2010) Enhanced mechanical properties of graphene-based polyvinyl alcohol composites. Macromolecules 43(5):2357–2363
18. Kim SW, Choi HM (2015) Enhancement of thermal, mechanical and barrier properties of ethylene-vinyl alcohol copolymer by incorporation of graphene nanosheets. High Perform Polym 27(6):694–704
19. Xue Y, Veazie DR, Glinsey C, Horstemeyer MF, Rowell RM (2007) Compos Part B Eng 38:152–158

A New Method to Obtain Cellulose Nanofiber from Wood

Miguel Sanchez, José Armando Spinoza and Leila Figueiredo Miranda

Abstract Cellulose nanofiber (CNF) can be obtained from natural or waste wood by acid hydrolysis. In this unprecedented research, we describe a process for producing CNF with nitric acid. Crystallinity index of approximately 84% was obtained. Eucalyptus certified by Forest Stewardship Council (FSC) was chosen as source aiming to ensure equal reproducibility of future experiments. A wood sample was treated by acid hydrolysis during almost 300 min. The resulting mass was filtered in a vacuum system and dried during one hour at temperature about 100 °C in an oven. The wood sample was also analyzed by X-Ray diffraction (XRD) to be sure of its crystallinity and submitted to a thermal analysis. Cellulose nanofiber has a greater axial elastic modulus (Young's modulus) than Kevlar, and its mechanical properties are within the range of other reinforcements materials. Cellulose nanofiber can be a good material to reinforce some polymeric filament like polylactic acid (PLA) or acrylonitrile butadiene styrene (ABS).

Keywords Wood · Hydrolysis · Cellulose nanofiber

Introduction

Cellulose is a very well-known material and the most abundant naturally polymer found in this planet [1]. It represents about $1.5–10^{12}$ tons (metric ton) of the total annual biomass production and is considered an inexhaustible and renewable material [2]. Cellulose nanofiber (CNF) promises to be a good material for the biopolymer composites industry [3]. Cellulose nanofiber has an axial elastic modulus (Young's modulus) greater than Kevlar (greater than 100 GPa) [4, 5], and its mechanical properties are within the range of other reinforcement materials. The natural source of cellulose fibers is trees because they furnish wood in abundance and are the renewable source of raw material. Said fibers have amorphous parts and crystalline parts. Figure 1 shows the structure of cellulose [1].

M. Sanchez · J. A. Spinoza · L. F. Miranda (✉)
Mackenzie Presbyterian University, Rua Da Consolação 930, São Paulo, SP 01302-907, Brazil
e-mail: leila.miranda@mackenzie.br

J. Li et al. (eds.), *Characterization of Minerals, Metals, and Materials 2020*,
The Minerals, Metals & Materials Series,
https://doi.org/10.1007/978-3-030-36628-5_37

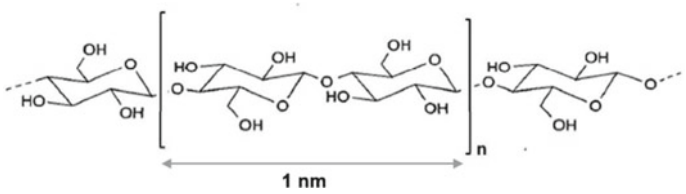

Fig. 1 Structure of cellulose

Cellulose is a linear chain and has a flat ribbon-like conformation [4]. There are four polymorphs of Cellulose (I, II, III, IV). Each of them has been extensively studied; however, Cellulose (I) is the crystalline cellulose naturally produced by a variety of organisms like trees and plants, and it is sometimes referred to as "natural" cellulose [4].

The selective elimination of the amorphous part is usually made by acid hydrolysis using strong acids like hydrochloric or sulfuric acid [6]. This article presents the preparation of cellulose nanofibers from wood pulp by acid hydrolysis with nitric acid. Crystallinity indexes were obtained near 84.4% which represent a better result than those obtained by other researchers, around 67.3% [7] and 70.0% [8]. The X-ray diffractograms showed peaks at 2θ near 18.9º, 23.1, and 35º indicating the presence of cellulose nanofibers and the index of crystallinity [9]. The method described herein is on a laboratory scale. Further studies can optimize industrial processors for the application of cellulose nanofibers on a large scale [10].

Experimental Procedure

A sample of wood from eucalyptus certified by FSC [11] was dried in an oven at 110 °C for near 24 h. Approximatively, 5 g of wood was shaken in HNO_3 (2.5 mol L^{-1}) at near 75 °C for 300 min. Subsequently, the cellulose nanofiber (CNC) suspension was filtered through a membrane with a 3.0μm pore size. The residue was then washed four times with ethanol and deionized water to remove impurities and then dried at 110 °C for 2 h and air cooled after the drying process.

X-Ray Diffraction (XRD)

The crystallinity index (CrI) of the obtained cellulose nanofiber was determined according to Teixeira et al. [9], by X-ray diffraction analysis (XRD) using a Rikacu Inc. MiniFlex II diffractometer equipped with Kα Cu radiation. ($\lambda = 0.15540$ nm) in a 2θ range from 5 to 90° to 30 kV and 15 mA.

Scanning Electron Microscopy (SEM)

The morphology of the cellulose nanofibers was observed using an electron microscope JEOL model JSM 6510. A sample was fixed on an aluminum stub using double-sided tape and then coated with gold to improve conductivity.

Thermal Analysis

A sample of cellulose nanofiber was placed in an open alumina capsule and analyzed in a NETZSCH thermogravimeter. Analysis was performed under a nitrogen gas (neutral atmosphere) at a constant flow rate of 50 mL min^{-1}. Thermogravimetric curves were obtained for sample from 50 to 600 °C, with a heating rate of 10 °C min^{-1}.

Results and Discussion

Yield Process

From 5 g of wood from eucalyptus certified, 2.1 g of cellulose nanofiber (CNF) was obtained.

This proposed process for obtaining CNF using nitric acid as hydrolysis agent produced cellulose nanofibers in 42% yield. Figure 2 shows the CNF obtained dried.

Fig. 2 CNF obtained dried

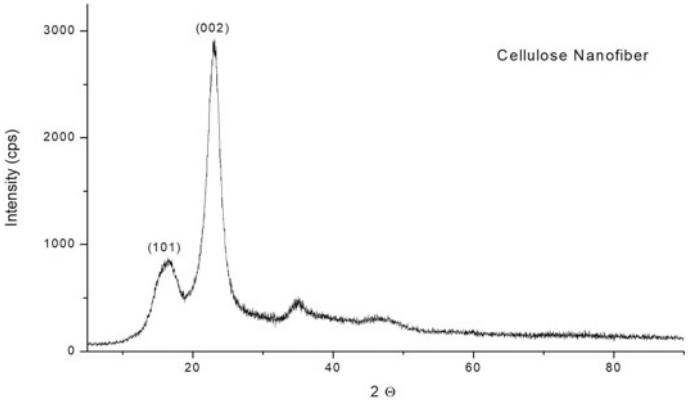

Fig. 3 XRD for obtained cellulose nanofiber

X-Ray Diffraction (XRD)

The crystallinity index (CrI = 84.4%) was determined using the relationship proposed by Segal et al. [9], Park et al. [12], and Mukwaya et al. [13], between the maximum intensity in arbitrary units of the 002 lattice diffraction ($2\theta = 22$–$24°$) and the minimum intensity of diffraction, in the same units, between lattices (101) and (002) peak ($2\theta = 16$–$19°$) representing amorphous material in cellulose nanofiber.

Figure 3 presents X-ray diffraction for obtained cellulose nanofiber.

As shown by Pääkkö et al. [14], hydrolysis mechanisms using strong acids remove amorphous regions, which increase the frequency of crystalline regions. Thus, the crystallinity index will always be higher for CNC than for CNF, although that determined for the CNF obtained in this study (84.4%) was higher than those obtained by traditional methods (78–81%).

It is assumed that materials with higher crystallinity indices are more resistant to thermal degradation, which would contribute to diversify the application of the obtained cellulose nanofibers, since the amorphous regions of cellulose are more susceptible to heat action and have lower thermal stability, when compared to the crystalline regions [15–17].

Scanning Electron Microscopy (SEM)

Figure 4 shows micrographs of surface of treated fibers showing its flat ribbon-like conformation.

As can be observed, a nanofibrillated cellulose (CNF) was formed, with an average width of 10–14 μm, a length of 60–100 μm, and a nanometric thickness (Fig. 4c). Nanofibrillated cellulose (Fig. 4b) is presented as a nanonetwork. This CNF network

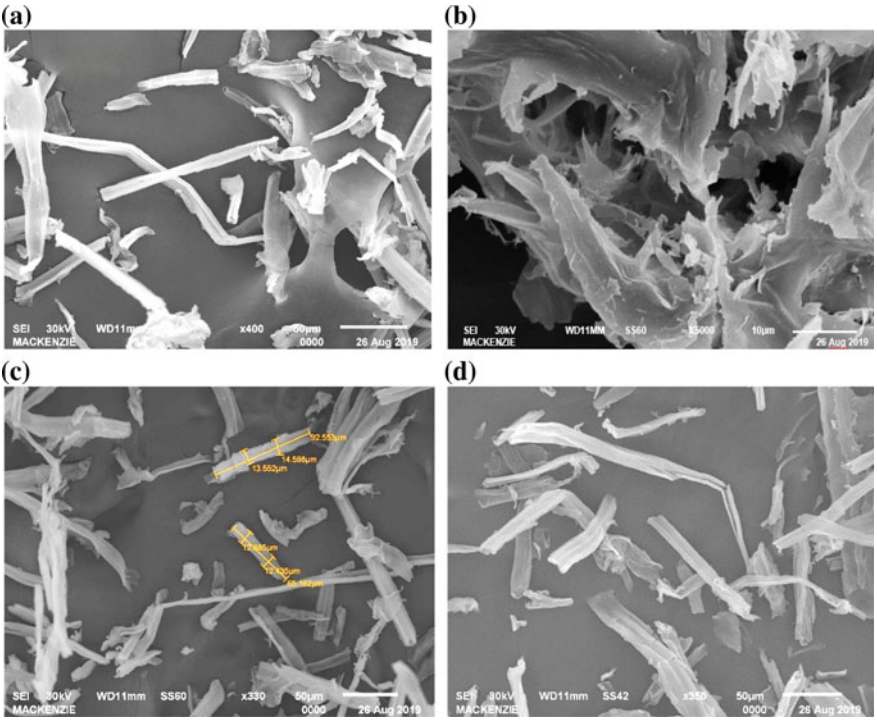

Fig. 4 SEM images of obtained CNF

is formed due to the entanglement of these nanofibrils since their active binding sites are exposed [18].

Thermal Analysis

Figure 5 shows the results to thermogravimetric analysis (TG/DTG). It is important to note that cellulose nanofibers degrade completely only near 340 °C. This temperature is close to those found for CNC in the literature [19, 20].

It can be observed that the initial degradation temperature of the CNF obtained (280 °C) is close to that of CNC (280–290 °C) and much higher than that of traditional CNF (240–250 °C) [19].

Thermal stability is essential for nanocelluloses to be used as an effective reinforcing material, as the processing temperature of thermoplastic polymers is above 180 °C, and their thermomechanical behavior should be evaluated [20].

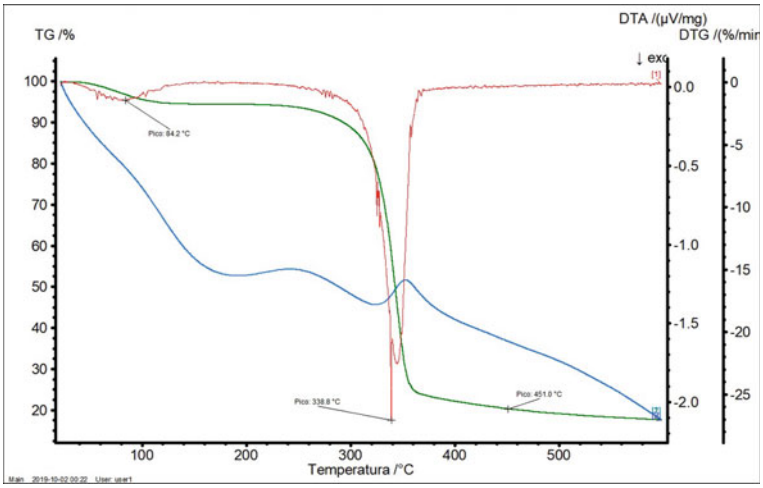

Fig. 5 Thermal analysis (TG, DTG and DTA) of obtained cellulose nanofiber

Conclusions

This research, with a yield close to 42%, shows a method with nitric acid to produce cellulose nanofibers (CNF) with good crystallinity (84.4%) and thermal stability above 280 °C.

This process can add real value to waste wood in the world. Construction and furniture industries discard large quantities of wood, which are often used to be burned in boilers. Future studies could improve this process and reinforce the application of cellulose nanofibers as a reinforcing material in polymers and concrete.

References

1. Silva DDJ, D'Almeida MLO (2009) Nanocristais de celulose. O Papel 70(7):34–52
2. Tang J, Sisler J, Grishkewich N, Tam KC (2017) Functionalization of cellulose nanocrystals for advanced applications. J Colloid Interf Sci 494:397–409
3. Taipina MO (2012) Nanocristais de celulose: obtenção, caracterização e modificação de superfície. Dissertação de Mestrado. Universidade Estadual de Campinas. Instituto de Química, Campinas, São Paulo
4. Moon RJ, Martini A, Nairn J, Simonsens J, Youngblood J (2011) Cellulose nanomaterials review; structura, properties and nanocomposites. Chem Soc Rev 40:3941–3994
5. Iwamoto S, Kai W, Isogai A, Iwata T (2009) Elastic modulus of single cellulose microfibrils from tunicate measured by atomic force microscopy. Biomacromolecules 10(9):2571–2576
6. Dufresne A (2015) Nanoparticles from renewable resources: extraction and applications. São Carlos

7. Teodoro KBR, Teixeira EDM, Corrêa AC (2011) Whiskers de fibra de sisal obtidos sob diferentes condições de hidrólise ácida: Efeito do tempo e da temperatura de extração. Polímeros 21(4):280–285
8. Teixeira EDM, Oliveira CRD, Mattoso LH (2010) Nanofibras de algodão obtidas sob diferentes condições de hidrólise ácida. Polímeros 20(4):264–268
9. Segal L, Creely JJ, Martin JAE, Conrad CM (1959) An empirical method for estimating the degree of crystallinity of native cellulose using the X-ray diffractometer. Text Res J 29(10):786–794
10. Borisyak S, Garbarczyk J (2003) Applying the WAXS method to estimate the supermolecular structura of cellulose fibres after mercerisation. Fibres Text West Eur, 104–106
11. FSC (2014) Global FSC certificates: type and distribution. Bonn, Alemanha
12. Park S, Baker JO, Himmel ME, Parilla PA, Johson DK (2010) Cellulose crystallinity index: measurement techniques and their impact on interpreting cellulase performance. Biotechnol Biofuels, 3–10
13. Mukwaya V, Yu W, Asad RA, Yagou HB (2015) An environmentally friendly method for the isolation of cellulose nano fibrils from banana rachis fibers. Text Res J
14. Pääkkö M, Ankerfors M, Kosonen H, Nykänen A, Ahola S, Osterberg M, Ruokolainen J, Laine J, Larsson PT, Ikkala O, Lindström T (2007) Enzymatic hydrolysis combined with mechanical shearing and high-pressure homogenization for nanoscale cellulose fibrils and strong gels. Biomacromolecules 8(6):1934–1941
15. Basch A, Lewin M (1973) The influence of fine structure on the pyrolysis of cellulose I: vacuum pyrolysis. J Polym Sci Polym Chem 11:3071–3093
16. Broido A, Javier-Son AC, Barrall ED (1973) Molecular weight decrease in the early pyrolysis of crystalline and amorphous cellulose. J Appl Polym Sci 17:3627–3635
17. Kim UJ, Eom SH, Wada M (2010) Thermal decomposition of native cellulose: influence on crystallite size. Polym Degrad Stab 95:778–781
18. Keplinger T, Wang X, Burgert I (2019) Nanofibrillated cellulose composites and wood derived scaffolds for functional materials. J Mater Chem A 7:2981–2992
19. Flauzino Neto WP, Silvério HA, Dantas NO, Pasquini D (2013) Extraction and characterization of cellulose nanocrystals from agroindustrial residue—soy hulls. Ind Crops Prod 42:480–488
20. Roman M, Winter WT (2004) Effect of sulfate groups from sulfuric acid hydrolysis on the thermal degradation behavior of bacterial cellulose. Biomacromolecules 5:1671–1677

Analysis of β' (Cu_4Ti) Precipitation During Isothermal Aging of a Cu–4 wt%Ti Alloy

Victor M. Lopez-Hirata, Felipe Hernandez-Santiago, Maribel L. Saucedo-Muñoz, Erika O. Avila-Davila and Jose D. Villegas-Cardenas

Abstract This work analyzed experimentally and numerically the growth kinetics of β' precipitation of a Cu–4 wt%Ti alloy after aging at 400, 500, and 600 °C for times from 0.0166 to 200 h. Results indicated that the precipitation process is almost controlled by nucleation and growth during aging at 400 °C, originating a slow growth kinetics of precipitation. In contrast, the coarsening of precipitates dominates the precipitation process during aging at 500 and 600 °C. The interfacial energy of interface between the α matrix phase and β' precipitates was determined to be about 0.1135, 0.0980, and 0.0725 Jm^{-2} for aging at 400, 500, and 600 °C, respectively. These values suggest a coherent interface, which is in agreement with the flat faces of β' cuboid precipitates. Calculated Time–Temperature–Precipitation diagram for the β' precipitation indicated good agreement with experimental results. Precipitation hardening was higher for the slower growth kinetics of precipitation.

Keywords Cu–Ti alloy · β' precipitation · Kinetics · Numerical analysis · Thermo-Calc

Introduction

Cu–Ti alloys are prone to have precipitation hardening after isothermal aging for alloy compositions of about 1–5 wt%Ti [1–3]. Age-hardenable Cu–Ti alloys have high tensile strength and good formability, and they are used as connector materials in electronic and electrical components [4]; nevertheless, its conductivity is less than the half of that corresponding to Cu–Be alloys. Therefore, the application of Cu–Ti alloys has been focused on mechanical properties. In order to obtain good mechanical properties, Cu–Ti alloys are solution treated above 800 °C and then quenched, and the aging process is carried out at temperatures of 400–500 °C. As a result of aging, the

V. M. Lopez-Hirata (✉) · F. Hernandez-Santiago · M. L. Saucedo-Muñoz · E. O. Avila-Davila · J. D. Villegas-Cardenas
Instituto Politécnico Nacional (ESIQIE-ESFM), UPALM Edif. 7, Mexico City, D.F 07300, Mexico
e-mail: vlopezhi@prodigy.net.mx

J. Li et al. (eds.), *Characterization of Minerals, Metals, and Materials 2020*,
The Minerals, Metals & Materials Series,
https://doi.org/10.1007/978-3-030-36628-5_38

fcc Cu-rich supersaturated solid solution decomposes spinodally to form a disordered fcc Ti-rich phase and then becomes order to form the metastable tetragonal β' Cu_4Ti phase which is responsible for the good mechanical properties of these alloys [1, 5, 6]. After prolonged aging, the cellular precipitation of the stable orthorhombic β Cu_4Ti phase takes place by nucleation and growth on grain boundaries which is the main cause for the decrease in the mechanical strength in the later stage of aging [1]. The mechanical strength of Cu–Ti alloys has been improved either by the addition of a third alloying element such as chromium, zirconium, carbon, nitrogen, or hydrogen [7–10] or by using cold work previously to the aging treatment [11]. In the former case, the precipitation sequence was similar to that observed in the binary alloy; however, the presence of a different precipitates such as titanium chromide, nitride, carbide, or hydride was also reported to occur during aging [9]. In the latter case, the cold work, used after solution treatment and quenching, has been reported [11] to promote the precipitation of titanium on dislocations and to inhibit the precipitation of the β' Cu_4Ti and β Cu_4Ti phases during aging.

Recently, TC-PRISMA software has been used to analyze the precipitation process of different aged alloys [12]. This software is based on the solution of the Langer–Schwartz (LS) and modified LS (MLS) theories and the Kampmann and Wagner numerical model (N model) [13], and it has been used to analyze the precipitation kinetics of different phases during aging in steels and nonferrous alloys [14].

This software permits, for example, to determine the size, distribution size, density number, and composition of precipitated phases, as well as the Time–Temperature–Precipitation (TTP) diagram in multiparticles, multiphases, and multicomponents alloy systems. Besides, the nucleation site can be selected among grain boundaries, bulk, and dislocations. Thus, the use of Thermo-Calc PRISMA would be a good alternative to complement the precipitation analysis of β' phase in the aged Cu–Ti alloys.

Thus, the purpose of this work is to study experimentally and numerically the growth kinetics of β' phase precipitation in an isothermally aged Cu–4 wt%Ti alloy in order to obtain the Time–Temperature–Precipitation (TTP) diagrams, as well as the determination of the interfacial energy between the α matrix and β' precipitates.

Experimental Procedure

A Cu–4wt%Ti alloy was melted with an electric furnace using 99.99% purity titanium and 99.999% purity copper in an alumina crucible under an argon gas atmosphere. The alloy ingot was homogenized at 950 °C for one week and subsequently cold rolled to obtain plate specimens of about 30 × 10 × 5 mm. These specimens were encapsulated in air-evacuated and Ar gas filled quartz tube and then solution treated at 900 °C for 1 h in an electrical resistance furnace, and subsequently quenched in ice-water in order to obtain solution treated specimens. These specimens were aged at temperatures of 400, 500, and 600 °C for times up to 200 h. The Transmission Electron Microscope (TEM) disc specimens of approximately 3 mm were thinned

using the twin-jet electropolishing technique in a solution of 75 vol.% methanol and 25 vol.% nitric acid at −60 °C. TEM specimens were mounted on a Be-specimen holder and observed with a TEM JEM-2000FX-II at 200 kV, equipped with a Noran EDXS.

Numerical Procedure

Thermo-Calc software was used to analyze the stability of phases and the coarsening constant and interfacial energy γ between matrix and precipitates. Likewise, the analysis of precipitation was pursued in the aged Cu−4 wt%Ti alloy employing the Thermo-Calc (TC) PRISMA software. The kinetic and thermodynamic data was determined from the Thermo-Calc databases for CUDEMO and MCUDEMO [12]. A homogeneous nucleation was assumed for the precipitation simulation in the austenite matrix, named bulk nucleation in TC-PRISMA. The precipitate shape was considered to be cuboid considering a cube elastic-strain energy for the α phase matrix and precipitate with the following elastic constants: $C_{11} = 168.4$ GPa, $C_{12} = 121.4$ GPa, and $C_{44} = 75.4$ GPa.

Results and Discussion

Temporal Evolution of Precipitation

The temporal evolution of precipitation of β' phase in the Cu-rich α phase matrix is illustrated in the Bright-Field (BF) Transmission Electron Micrographs corresponding to the Cu–4 wt%Ti alloy aged at 400 °C for different times, as shown in Fig. 1, respectively. The β' precipitates have a cuboid morphology, and they are aligned on the <100> direction of the α phase matrix for all aging temperatures because of its low value of elastic-strain energy [13, 15]. As aging progresses, the morphology changes to plates, also aligned with respect to the matrix phase. The electron diffraction pattern, shown in Fig. 1c, indicates clearly the presence of super-reflection spots between those corresponding to the matrix phase, which confirms that the β' phase has a Cu_4Ti crystalline structure. Table 1 shows the average equivalent radius determined for the β' precipitates after aging at 400, 500, and 600 °C for different times. An increase in precipitate radius can be noted with aging time and temperature. The discontinuous or cellular precipitation of the β' phase can be noted clearly for the alloy specimen aged at 600 °C, Fig. 1d. This type of precipitation was also observed to be present after aging at 400, 500, and 600 °C for 100, 0.5, and 0.166 h, respectively.

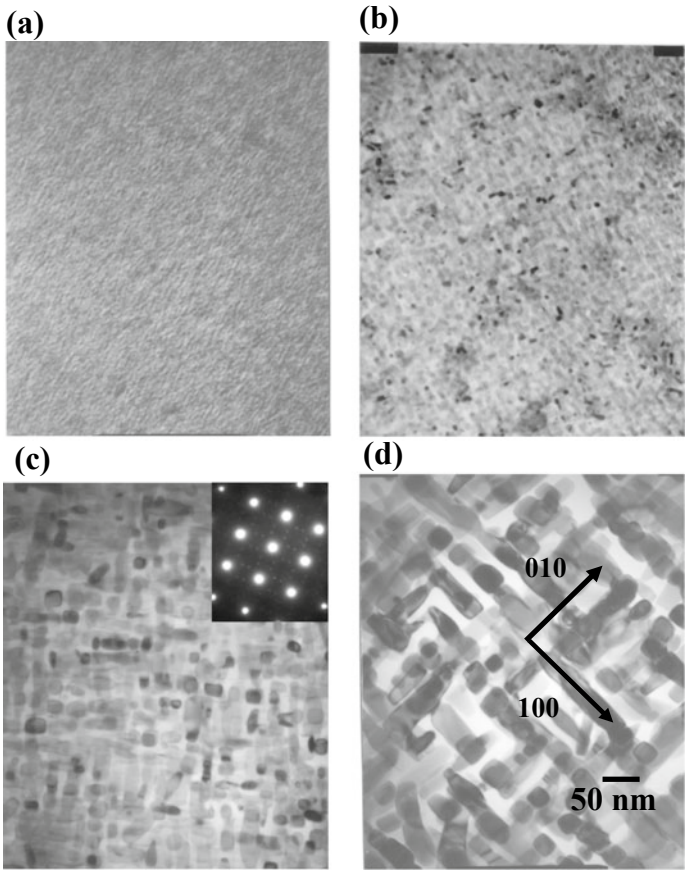

Fig. 1 BF-TEM micrographs of Cu–4 wt%Ti alloy aged at 400 °C for **a** 5 h and **b** 25 h include its corresponding electron diffraction pattern, **c** 100 h and **d** 200 h

Table 1 Variation of precipitate equivalent radius with time for aging at 400, 500, and 600 °C

Time (h)	Radius (nm)		
	400 °C	500 °C	600 °C
0.166	–	13.3	14.1
0.5	–	21.4	18.8
1	9.2	22.06	26.6
5	16.3	26.8	–
25	18.6	–	–
75	19.2	–	–
100	19.8	–	–
150	20.5	–	–
200	22.2	–	–

Thermo-Calc Analysis of Precipitation

The Thermo-Calc calculated amount of all phases versus temperature is shown in Fig. 2. This plot indicates clearly that the α and β' phases are present at temperatures between 500 and 840 °C. This figure also suggests that the precipitation reaction:

$$\alpha_{sss} \rightarrow \alpha + \beta' \tag{1}$$

It may occur after aging at those temperatures. The volume fraction of β' precipitates increases with the decrease in temperature.

Table 2 shows the Thermo-Calc calculated values of interfacial energy for the interface of α matrix and β' precipitate. This value decreases with the increase in temperatures, as expected in the case of free energy due to the increase in entropy [12]. The magnitude order, 0.03 Jm^{-2}, suggests a coherent interface [15]. This table also indicates the values of coarsening constant k for 400, 500, and 600 °C. Unsurprisingly, this parameter increases with temperature because of the increase in atomic diffusion [12].

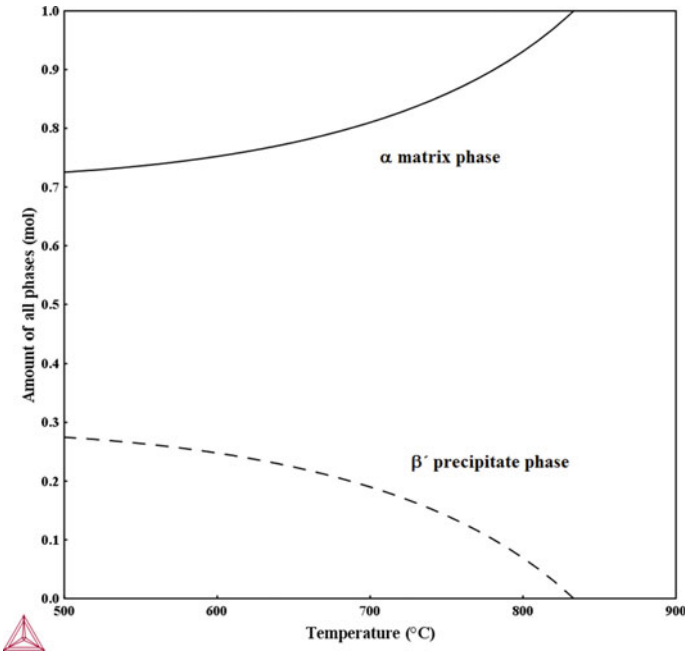

Fig. 2 Thermo-Calc calculated plot of amount of all phases versus temperature

Table 2 Thermo-Calc calculated interfacial energy between precipitate and matrix and coarsening constant, and experimental interfacial energy for aging temperatures

T (°C)	Thermo-Calc		Experimental
	γ (J m^{-2})	k (m^3 s^{-1})	γ (J m^{-2})
400	0.0339	1.1041×10^{-31}	0.1135
500	0.0325	2.2334×10^{-29}	0.0980
600	0.0309	1.2776×10^{-27}	0.0725

Thermo-Calc PRISMA Analysis of Precipitation

The experimental and calculated variation of equivalent radius for β' precipitates with time are shown in Fig. 3a–c for the Cu–4 wt%Ti alloy aged at 400, 500, and 600 °C.

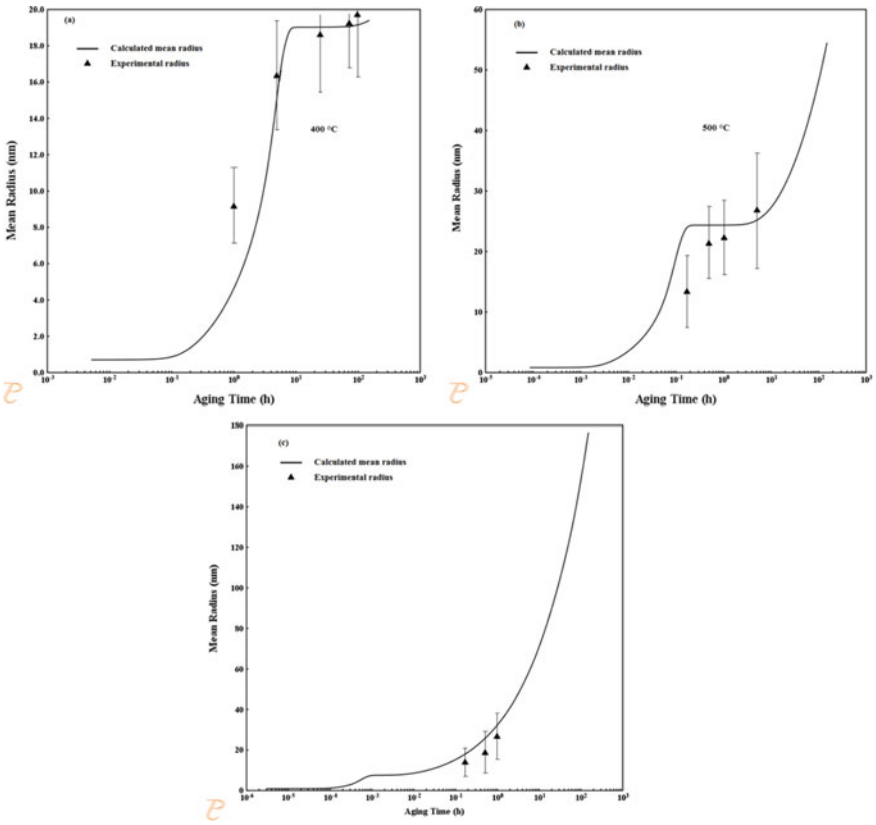

Fig. 3 TC-PRISMA calculated plot of mean radius of β' precipitate versus time for Cu–4 wt%Ti alloy aged at **a** 400 °C, **b** 500 °C, and **c** 600 °C

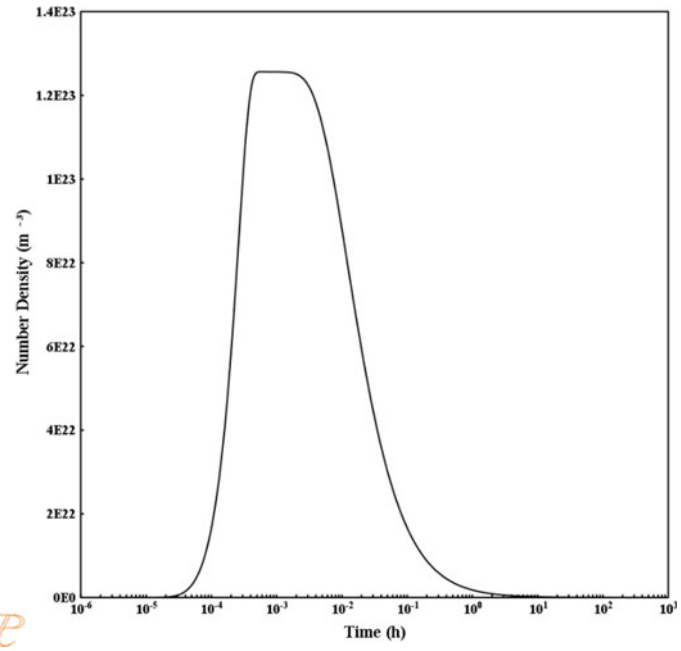

Fig. 4 TC-PRISMA calculated plot of number density of β' precipitate versus time for Cu–4 wt%Ti alloy aged at 600 °C

The continuous line and triangle points correspond to the calculated and experimental values, respectively. This plot shows clearly three characteristic stages: a continuous and slow increase in precipitate radius for short aging times, Fig. 3a, because of the rise of nucleation rate with time. The number density of precipitates also increases with aging time, as shown in Fig. 4. Then, the radius increases more rapidly after 1 h of aging time, following a parabolic law of $t^{1/2}$ which can be attributable to the growth stage. The nucleation rate subsequently becomes zero because either the solute supersaturation turns into zero or all nucleation sites are used [12]. As a result of this, the number density and the precipitate radius remain constant, as shown in Figs. 3a and 4, respectively. As aging progresses, the number density starts decreasing with time, following a t^{-1} power law, and the growth kinetics of precipitate radius with time follows a slope of 1/3, $t^{1/3}$. That is, the growth kinetics corresponds to the coarsening stage of precipitates, and it follows the Lifshitz–Slyozov–Wagner theory for diffusion-controlled theory [12]. According to the previously mentioned explanation, most of the experimental points for the growth kinetics of precipitates at 400 °C are located in the nucleation and growth stage, while the experimental points at 500 and 600 °C correspond to the coarsening stage. It is important to mention that the interfacial free energy γ was changed in order to find the best fit of experimental values with the calculated curves. They are shown in Table 2 and decrease as aging temperature increases. These values are higher than the Thermo-Calc determined

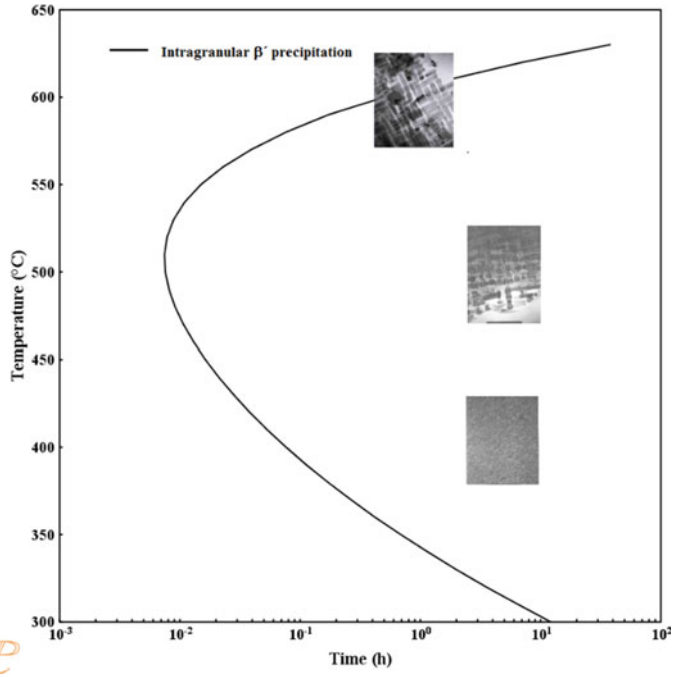

Fig. 5 TC-PRISMA calculated TTP diagram

ones. Nevertheless, these values show a good agreement with the values of 0.1–0.2 J m^{-2} reported for coherent β' precipitates in the literature [12, 15]. These low values suggest that the interface between matrix and precipitates should be coherent [15], which is in agreement with the cuboid morphology of β' precipitates, as shown in Fig. 1.

The TC-PRISMA calculated Time–Temperature–Precipitation (TTP) diagram of the Cu–4 wt%Ti alloy is shown in Fig. 5. This was calculated using an average value of 0.0946 J m^{-2} determined from the experimental ones shown in Table 2. This figure shows that the fastest precipitation kinetics corresponds to an aging at about 500 °C for 0.01 h. This figure also includes the TEM micrographs for the alloy specimens aged at 400 °C for 5 h, and 500 and 600 °C for 0.166 and 1 h. These TEM images suggests that the start of β' precipitation is very similar for aging at 500 and 600 °C which is in good agreement with the growth kinetics of precipitation shown in the calculated TTP diagram. Nevertheless, the growth kinetics of precipitation at 400 °C is much faster than that detected experimentally, Fig. 1. This can be attributable to the constant value of interfacial energy, 0.0946 J m^{-2}, used for the present calculation. That is, the energy value should be higher at 400 °C, which might cause a higher activation energy for nucleation, and consequently, the nucleation rate would be expected to be slower [12] than that of the TTP diagram.

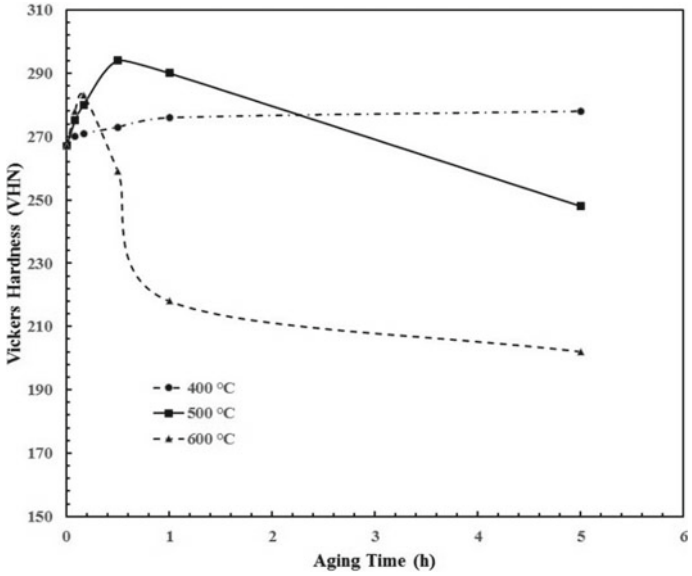

Fig. 6 Aging curves of Cu–4 wt%Ti alloy aged at 400, 500, and 600 °C

Aging Curves

Figure 6 shows the aging curves, plot of hardness as a function of aging time, for the Cu–4 wt%Ti alloy aged at 400, 500, and 600 °C. The aging curves corresponding to 500 and 600 °C show an increase in hardness; then, the hardness peak is reached, and finally, this decreases as a result of the discontinuous precipitation and coarsening process of precipitates. In contrast, aging at 400 °C presents a slow increase in hardness and the hardness peak, 370 VHN, is obtained after aging for 200 h, not shown in Fig. 6. The highest and lowest hardness peaks correspond to the alloy specimens aged at 400 and 600 °C. The hardness peaks of aging at 500 and 600 °C were reached more rapidly than that at 400 °C which agrees very well with the faster growth kinetics of precipitation, as shown in the calculated TTP diagram.

Conclusions

The numerical and experimental analysis of β' precipitation during aging at 400, 500, and 600 °C permitted to state the following conclusions:

1. The numerical analysis of precipitation indicated that the nucleation and growth stage is dominant during aging at 400 °C, while the precipitation during aging at 500 and 600 °C is mainly controlled by the coarsening stage.

2. The interfacial energy between matrix and precipitates was determined to be about 0.1135, 0.0980, and 0.0725 J m^{-2} for aging at 400, 500, and 600 °C, respectively, which is in agreement with the coherent interface of cuboid β' precipitates.
3. Calculated TTP diagram showed a good concordance with the experimental results. The slowest growth kinetics at 400 °C promoted the highest precipitation hardening, while the fastest kinetics causes the lowest hardness.

Acknowledgements The authors wish to thank the financial support from SIP-COFAA-IPN and CONACYT.

References

1. Soffa WA, Laughlin DE (2004) High-strength age hardening copper–titanium alloys: redivivus. Prog Mater Sci 49:347–366
2. Nagarjuna S, Balasubramanian K, Sarma DS (1995) Effect of cold work on precipitation hardening of Cu–4.5 mass %Ti alloy. Metall Trans JIM 36:1058–1066
3. Saji S, Hornbogen E (1978) Combined recrystallization and precipitation reactions in Cu–4%Ti alloys. Zeitschrift Metallkunde 69:741–746
4. Hernandez-Santiago F, Cayetano-Castro N, Lopez-Hirata VM, Dorantes-Rosales HJ (2004) Cruz-rivera JJ Precipitation kinetics in a Cu–4 mass %Ti alloy. Mater Trans JIM 45:2312–2315
5. Nagarjuna S, Srinivas M, Balasubramanian K, Sarma DS (1999) On the variation of mechanical properties with solute content in Cu–Ti alloys. Mater Sci Eng A 259:34–42
6. Ikeda J, Semboshi S, Iwase A, Gao W, Sugawara A (2015) Precipitation behavior and properties of Cu–Ti alloys with added nitrogen. Mater Trans JIM 56:297–302
7. Semboshi S, Nishida T, Numakura H (2009) Microstructure and mechanical properties of Cu–3 at.%Ti alloy aged in a hydrogen atmosphere. Mater Sci Eng A 517:105–113
8. Wang F, Li Y, Wakoh K, Koizumi Y, Chiba A (2014) Cu–Ti–C alloy with high strength and high electrical conductivity prepared by two-step ball-milling processes. Mater Des 61:70–74
9. Markandeya R, Nagarjuna S, Sarma DS (2004) Precipitation hardening of Cu–Ti–Cr alloys. Mater Sci Eng A 371:291–305
10. Donoso E (2010) Influence of cobalt and chromium additions on the precipitation processes in a Cu–4Ti alloys. Rev Metal 46:542–547
11. Nagarjuna S, Srinivas M (2008) Grain refinement during high temperature tensile testing of prior cold worked and peak aged Cu–Ti alloys: evidence of superplasticity. Mater Sci Eng A 498:468–474
12. Thermo-Calc software (2018) Cudemo-Mocudemo, Version 2018b
13. Kostorz G (2001) Phase transformations in materials. Wiley-VCH, Germany
14. Saucedo-Muñoz ML, Ortiz-Mariscal A, Lopez-Hirata VM, Villegas-Cardenas JD, Soriano-Vargas O, Avila-Davila E (2017) Precipitation analysis of as-cast HK40 steel after isothermal aging. Int J Min Metall Mater 24:1125–1133
15. Hernandez-Santiago F, Lopez-Hirata VM, Saucedo-Muñoz ML, Dorantes-Rosales HJ (2007) Gibbs-Thomson relationship for the precipitation in Cu–Ti alloys. Mater Charact 58:303–306

Analysis of Nanoscale Iron Oxide Morphology

Tianhao Sun, Suju Hao, Wufeng Jiang and Yuzhu Zhang

Abstract Two different forms of nano-scale Fe_2O_3 were prepared by the hydrothermal method using $Fe(NO_3)_3{\cdot}9H_2O$ as the starting material, ethylenediamine and ethylene glycol methyl ether as surfactants. The structure, surface morphology, and composition of nano-scale Fe_2O_3 samples were analyzed by XRD and SEM/EDS. The results show that the sample has two forms, one *nano*-Fe_2O_3 form is rod-shaped, and the rod-like structure is hexagonal columnar, the particles are closely arranged in disorder; the other *nano*-Fe_2O_3 is spherical, and there are clusters between particles. The formation mechanism of the nano-oxidized iron was analyzed.

Keywords Fe_2O_3 · Hydrothermal method · Nanometer material

Introduction

Nano-iron oxide has good light resistance, magnetic resistance and good absorption and shielding effect on ultraviolet light. It can be widely used in flash paints, inks, plastics, leather, automotive topcoats, electronics, high magnetic recording materials, magnetic fluids, catalysts. And biomedical processes. At present, the commonly used methods for preparing nano-iron oxide can be generally divided into a dry method and a wet method. Wet methods include forced hydrolysis, gel-sol method [1], chemical vapor deposition [2], hydrothermal method [3], precipitation method [4], microemulsion method [5], colloidal chemical method [6] Etc. Dry method includes vapor deposition [7], flame thermal decomposition [8], microwave method [9], laser thermal decomposition method, and the like. The wet method has the characteristics of easy availability of raw materials and can be directly used (only need

T. Sun · S. Hao (✉) · W. Jiang · Y. Zhang
Key Laboratory of Modern Metallurgical Technology, Ministry of Education, School of Metallurgy and Energy, North China University of Science and Technology, Tangshan 063009, China
e-mail: sujuh@sina.com

T. Sun
e-mail: 15633710607@163.com

J. Li et al. (eds.), *Characterization of Minerals, Metals, and Materials 2020*,
The Minerals, Metals & Materials Series,
https://doi.org/10.1007/978-3-030-36628-5_39

to be properly purified), easy to operate, and controllable particles, so it is generally valued, especially in industrial production; dry method has short process flow, operating environment Well, the product quality is high, the particles are ultra-fine, uniform, and well dispersed, but the technical difficulty is high, and the structure and material requirements of the equipment are high. This paper uses the hydrothermal method for research.

Experimental

Preparation of Nanometer Iron Oxide

Configure 90 ml water and ethanol mixture system (volume ratio is 1:1), weigh 4 g $Fe(NO_3)_3 \cdot 9H_2O$, dissolve it in water and ethanol mixture, stir for 5 min, when the stirring is about to be completed 10 ml of ethylenediamine was added dropwise to the reaction solution, and a brownish yellow precipitate was rapidly formed in the system. The mixed solution after the completion of the reaction was transferred to a 120 ml polytetrafluoroethylene-lined autoclave, and solvothermally reacted in a constant temperature oven at 180 °C for 4 h. After naturally cooling to room temperature, the sample was washed three times with deionized water and absolute ethanol, suction filtered, and the resulting sample was placed in an oven at 60 °C for 6 h.

In the same way, 90 ml of deionized water was added, 10 ml of ethylene glycol methyl ether and 2.5 g of $Fe(NO_3)_3 \cdot 9H_2O$ were added, stirred for 30 min, and then 2.5 g of urea was added and stirred for 30 min. After the completion of the stirring, the solution was transferred to an autoclave and solvothermally reacted in a constant temperature oven at 180 °C for 12 h. After naturally cooling to room temperature, the sample was washed three times with deionized water and absolute ethanol, suction filtered, and the resulting sample was placed in an oven at 60 °C for 6 h.

Sample Characterization

The image of the sample was determined by the X-ray diffractometer (Model: D/MAX2500PC03030502) of the Japanese Society of Science and Technology. The instrument uses a graphite crystal as a monochromator and a CuKa ray with a scanning range of 10–90°. The morphology of the sample was studied by a focused ion beam field emission scanning electron microscope (Model: Scios03040702) manufactured by FEI Czech Ltd.

Experimental Results and Analysis

SEM Characterization

Figure 1 is the SEM image of a sample prepared when the surfactant is ethylenediamine. It can be seen from Fig. 1 that the sample prepared by the reaction is a single-crystal rod-like structure, the size distribution of the nanorods is relatively uniform, and the rod ends are curved and curved. Further observations revealed that the prepared samples were approximately 500–600 nm and 50–60 nm in length and width, respectively. The arrow in Fig. 1b points to the bottom surface of the nano-iron oxide particles. It can be clearly seen from the figure that the shape of the bottom surface is hexagonal, and it can be inferred that the rod-like structure is hexagonal prism. The reason for the hexagonal prism shape may be that ethylenediamine provides an adsorption ligand for iron ions, and iron ion adsorption mainly occurs on the hexagonal side of the crystal. Liu et al. found the same phenomenon on ZnO nanorods [10]. This proves that the addition of ethylenediamine to the ethanol and water system can be directly reacted to obtain rod-shaped nano-iron oxide, instead of being obtained by calcining the precursor α-FeOOH.

Figure 2 is the SEM image of a sample prepared when the surfactant is ethylene glycol methyl ether. It can be clearly seen from the figure that the nano-iron oxide particles have a spherical shape, the particle size is relatively uniform, the arrangement is relatively tight, and there is slight adhesion between the particles, and the particle diameter is about 50–60 Nano.

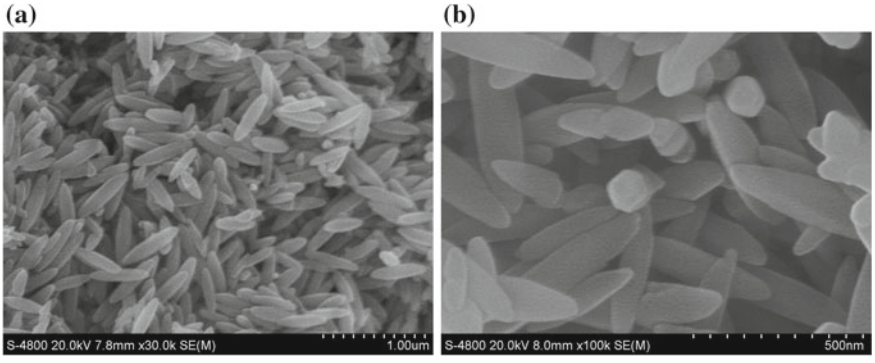

Fig. 1 SEM image of nanometer iron oxide

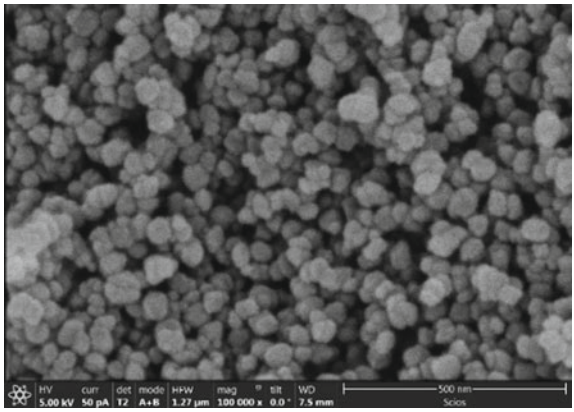

Fig. 2 SEM image of the sample under the influence of ethylene glycol methyl ether

XRD Analysis

Figure 3 is the X-ray diffraction spectrum of a nano-iron oxide sample. It can be concluded from the figure that the experimental iron oxide sample is trigonal α-Fe_2O_3, which clearly shows (012), (104), (110), (113), (024), (116). And (214) (300) and other main surface diffraction peaks of Fe_2O_3, the X-ray diffraction spectrum of the sample is consistent with the standard spectrum, indicating that the crystallization performance of the sample is very good, and there are no other redundant peaks (such as FeOOH) in the diffraction peak. It is proved that the sample prepared by the experiment has high purity.

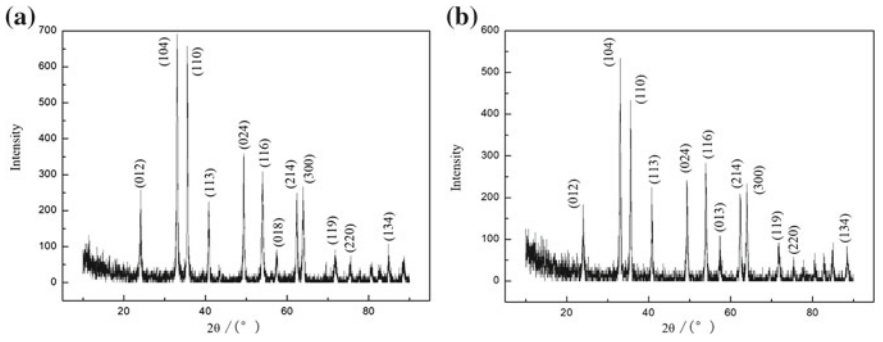

Fig. 3 X-ray diffraction spectrum of iron oxide sample

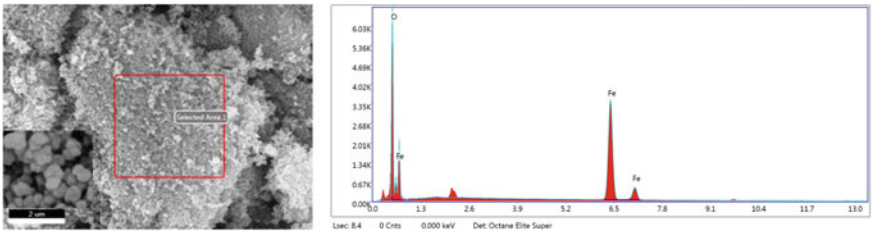

Fig. 4 Sample EDS under the influence of ethylene glycol methyl ether

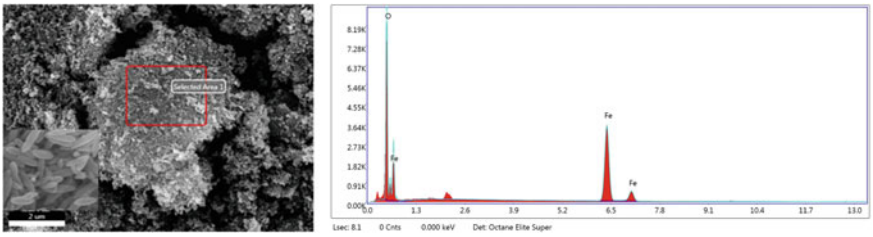

Fig. 5 Sample EDS under the influence of ethylenediamine

EDS Analysis

Figures 4 and 5 are the EDS samples under the influence of EDS and ethylenediamine under the influence of ethylene glycol methyl ether. It can be clearly seen from the figure that there are obvious Fe and O peaks, and there are no other peaks. The conclusion of the sample XRD analysis.

Formation Mechanism

The hydrothermal method is to crystallize the hydroxide in a solution environment under a certain pressure to obtain a fully grown nanocrystal. In the process, since the liquid resistance is small, the crystal grains are formed under a non-compressed state, and the growth unit can be freely Move, connect to form a crystal nucleus and grow up. The reaction of hydrothermal preparation of nanometer iron oxide is as follows

$$\mathrm{Fe^{3+} + OH^- \rightarrow Fe(OH)_3 \downarrow}$$
$$\mathrm{Fe(OH)_3 \rightarrow FeOOH + H_2O}$$
$$\mathrm{FeOOH \rightarrow Fe_2O_3 + H_2O}$$

Conclusion

In this paper, two kinds of nano-sized iron oxides were prepared by the hydrothermal method using $Fe(NO_3)_3 \cdot 9H_2O$ as the starting materials, which are spherical nano-iron oxides of spherical nano-iron oxide. The rod-shaped nano iron oxide can be synthesized in one step by adding ethylenediamine in a mixed solvent of ethanol and water.

Funding National Natural Science Foundation of China (No. 51274084), Hebei Natural Science Foundation (E2018209323, E2017209231), and Project of North China University of Science and Technology GP201507.

References

1. Zhang L, Li H, Zhang H et al (2019) Research progress in application and preparation of nano-Fe_3O_4. Powder Metall Technol 37(3):233–238
2. Wang X, Yu Y, Hu X et al (2000) Preparation of oxide films by liquid phase deposition. Func Mater 31(4):341–343
3. Li F, Liu L, An Y et al (2016) Hydrothermal liquefaction of three kinds of starches into reducing sugars. J Clean Prod 112:1049
4. Yu G, Zhang T, Zhang J et al (2007) Preparation and morphology of nano-sized ferric oxide (Fe_3O_4). Adv Chem 19(6):884
5. Li C, Qi H, Zhang Y (2009) Progress in chemical preparation and application of magnetic nano-sized Fe_3O_4 particles. Shanghai Met 31(4):54
6. Zhang R (2012) Progress in preparation of semiconductor nanocrystals by colloidal chemistry. Success (Education) 12(1):118–119
7. Zhuang X, Li R, Xing Y et al (2019) Preparation of lithium titanate electrode materials by solid phase method. Mater Report 33(16):2654–2659
8. Song X (2012) Continuous preparation of lithium iron phosphate nanocathode material by supercritical method and its carbon coating. Shanghai Jiaotong University (2012)
9. Meng T, Li C, Xhao H et al (2019) Nitrogen doped carbon quantum dots prepared by microwave one step method and their application in Fe^{3+} detection. Analyt Laboratory 38(7):777–781
10. Liu B, Zeng HC (2003) Hydrothermal synthesis of ZnO nanorods in the diameter regime of 50 nm. J Am Chem Soc 125:4430–4431

Analysis of the Effect of Marine Salinity in Durability of Red Ceramics Calcinated in Different Temperature

M. T. Marvila, A. R. G. Azevedo, M. S. S. Souza, E. B. Zanelato, J. Alexandre, G. C. Xavier, S. N. Monteiro, C. M. F. Vieira and G. C. G. Delaqua

Abstract In the Brazilian coast, the ceramic materials are affected by saline exposures, which cause losses of properties. This work evaluated the alteration that the materials undergo when exposed to the marine environment. Prismatic specimens were molded by the extrusion process and then calcined at different temperatures. After burning, the chemical attack was carried out by immersion cycles using synthetic sea water and the effects on the mechanical resistance and the water absorption were verified. In the absorption of water, the marine salinity interfered in a superficial way. In the mechanical resistance, salinity interfered in a significant way, but not enough to cause problems as far as the normative limits. Finally, it was verified that the crystalline phases identified at all the burning temperatures studied were the same for the intact samples and for the immersion cycles, except for halite (NaCl), from synthetic sea water.

Keywords Marine salinity · Durability · Red ceramics

M. T. Marvila (✉) · A. R. G. Azevedo · M. S. S. Souza · E. B. Zanelato · J. Alexandre · G. C. Xavier
LECIV—Civil Engineering Laboratory, UENF—State University of the Northern Rio de Janeiro, Av. Alberto Lamego, 2000, Campos dos Goytacazes, Rio de Janeiro 28013-602, Brazil
e-mail: markssuel@hotmail.com

A. R. G. Azevedo · C. M. F. Vieira · G. C. G. Delaqua
LAMAV-Advanced Materials Laboratory, UENF—State University of the Northern Rio de Janeiro, Av. Alberto Lamego, 2000, Campos dos Goytacazes, Rio de Janeiro 28013-602, Brazil

A. R. G. Azevedo
Engineering School, Department of Agricultural Engineering and Environment, UFF—Federal Fluminense University, R. Passo da Pátria, 156-209 São Domingos, Niterói, Rio de Janeiro 24210-240, Brazil

S. N. Monteiro
Department of Materials Science, IME—Military Institute of Engineering, Square General Tibúrcio, 80, Rio de Janeiro 22290-270, Brazil

J. Li et al. (eds.), *Characterization of Minerals, Metals, and Materials 2020*,
The Minerals, Metals & Materials Series,
https://doi.org/10.1007/978-3-030-36628-5_40

Introduction

Most of the Brazilian population is located in the coastal region, which determines the strong presence of buildings in these areas [1, 2]. Due to this, there is a constant iteration between the marine environment and the main Brazilian urban buildings. The durability of ceramic materials is directly affected by saline haze, a natural phenomenon that occurs in coastal regions and which winds down from coastal areas to remote areas, with sea salt being the main reason for the degradation of building materials used in these environments [3].

Among the various salts that contribute to the salinity of seawater, the two that cause major durability problems in building materials are chlorides and sulfates [4, 5]. Studies show that the average distribution of chlorides in seawater is around 55%, while sulfate salts are around 7.5% [6]. Knowledge of this salt distribution is important to produce the saline solution that will be used to attack the samples produced in this research, since it aims to replicate the salt attack in ceramic materials.

Sulfates can cause adverse reactions in building materials by producing an expansive gel known as Candlot salt, which is more common in cementitious components, and can cause cracking that causes the material structure to break. Chlorides may react with iron, aluminum, and calcium-based compounds, which may form chloroaluminates, causing increased porosity and consequently decreasing concrete strength [7, 8].

The salinity of seawater can enter the ceramic materials in various ways, through rain, through the action of saline fog coming from the sea and also when the material is in direct contact with the soil [6]. Salt transport mechanisms are absorption, migration, diffusion, and permeation. Absorption is a fluid transport mechanism that occurs through the capillary pores due to the surface tension of the liquid [9]. In this mechanism, the chlorides in the liquid medium penetrates the material. Crauss [9] explains that the entrance of chlorides in the material depends on the characteristics of the liquid, such as density, viscosity, and surface tension. In materials already saturated absorption does not occur; For this to occur, the pores must be totally or partially dry. This type of mechanism occurs when the material is susceptible to wetting and drying cycles.

Regarding migration, this mechanism occurs due to the movement of substances with electric charges present inside the solution, caused by the application of a difference of electric potential [10]. The mechanism of chloride ion migration is an electrolytic process governed by the conductivity of the pore solution, and depends on the concentration of the various ions present in the solution. The most active ions in the conductive process are Na^+, K^+, Ca^{2+} , and OH^-. The conductivity of Na^+ and K^+ ions is lower than the conductivity of chloride ions. The participation of Ca^{2+} ion is quite reduced, since its concentration in the pore solution is very small. Regarding the OH^-ion, its conductivity is high when compared to other ions [9].

Diffusion is a transport mechanism that can be defined as the mass movement that happens from a high concentration area to a low concentration area, due to a

concentration gradient or due to the chemical potential difference resulting from the displacement of the salt into the materials [10].

Chloride penetration by diffusion occurs in the material-filled pore network. Penetration does not require water movement, but an ion concentration gradient between the interior and the surface of the material. The chloride transport through the permeation mechanism occurs when the solution reaches the entire porous structure of materials, but only in materials already saturated. In this mechanism, the solution is transported due to the pressure difference. Cruz [10] states that permeation is considered only in structures that are subjected to high hydrostatic pressure.

In this context, the objective of this work is to evaluate the durability of calcined red ceramic materials at different temperatures subjected to the attack of saline seawater, and their influence on the mechanical strength and water absorption of these materials.

Materials and Methods

For the analysis, a ceramic mass from Campos dos Goytacazes, RJ was used. This materials has been studied in previous work [11–15] in ceramic and cementitious materials and presents good technological parameters when used in red ceramics. The characterization of the ceramic mass is presented through Fig. 1, which shows the particle size distribution, and Fig. 2, which presents the mineralogical analysis. Figure 3 shows the thermal analysis and Table 1 shows the chemical composition of the studied mass. The specimens were produced by the extrusion process and burned in an oven model Ricardo A900 at temperatures of 600, 800, 950 and 1050 °C.

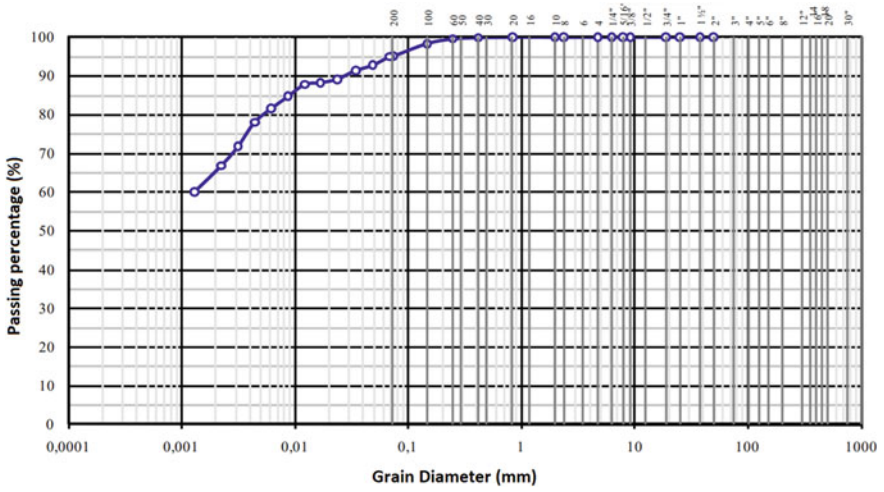

Fig. 1 Particle size distribution of the studied mass

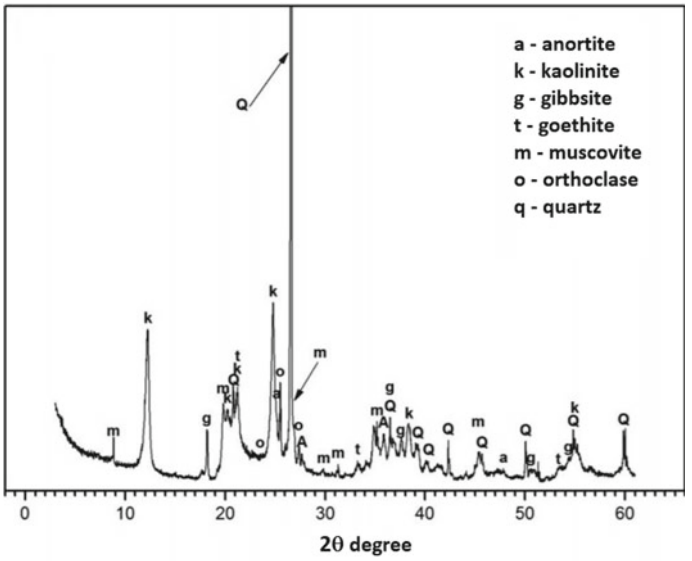

Fig. 2 Mineralogical analysis of the studied mass

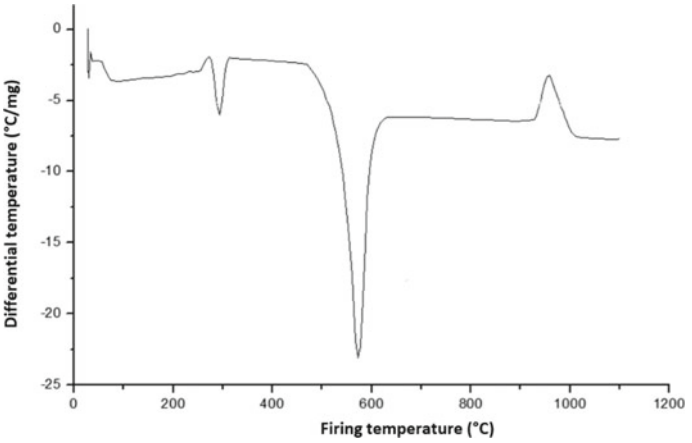

Fig. 3 Thermal analysis of the studied mass

The specimens produced were tested for the technological parameters of water absorption according to NBR 15270-2: 2018 [16], and for the three-point flexural strength using an EMIC DL-30 universal speed tester. Load rating of 1 mm/min, with a capacity of 30 kN, following the recommendations of the same standard.

The specimens were changed in the laboratory following a wetting and drying procedure for a total of 150 24-h cycles, where in 12 h, the samples were immersed in saline prepared for the test and in the other 12 h, the specimens were exposed

Table 1 Chemical analysis of the studied mass

Oxide	Mass (%)
SiO_2	43.83
Al_2O_3	36.85
Fe_2O_3	11.46
K_2O	2.73
TiO_2	1.95
CaO	0.82

to the sun, simulating environmental conditions. The saline solution was produced using distilled water and using chlorides and sulfates in 55 and 7.5% concentration, respectively. These values were chosen to simulate the concentrations of the two most aggressive salts to the building materials. The trial lasted five months, corresponding to 3600 h. The volume of solution used was at least four times the volume of the samples used. The pH of the used solution was controlled by maintaining a value of approximately 7, measured using a WTW - Profiline OXI 3205 portable concentration meter. After the specimens were changed, water absorption and flexural strength tests were performed.Three points in order to compare with the values obtained by the unchanged samples.

Finally, a mineralogical analysis of the samples burned at 1050 °C, both altered and intact, was performed to verify the formation of new compounds in the material.

Results

Figure 4 presents the results obtained for water absorption in specimens burned at different temperatures for unchanged and degraded samples. The same pattern of results was observed for both intact and degraded samples: water absorption increased as the firing temperature increased, except for the 1050 °C where there was a large fall of this property. This pattern can be attributed to the reaction that occurs in kaolinitic clays around 1000 °C (as can be seen in Fig. 3), where kaolinitic undergoes a phase transformation and becomes mainly mullite [17, 18] (as can be seen from Figs. 6 and 7). This mineral, besides being highly resistant, has a structure that substantially reduces the porosity of the material, reducing water absorption.

Regarding water absorption levels, intact masses show values above 20% absorption in almost all temperatures, except 1050 °C. On the other hand, degraded samples showed a reduction in water absorption when compared to intact specimens at temperatures of 600, 800, and 950 °C. This indicates that salts from the saline used in the degradation tests penetrated the material surface by the penetration mechanisms described in the introduction and caused capillary pore shielding, reducing water absorption in the degraded masses. Therefore, in this view, saline degradation positively affects the material.

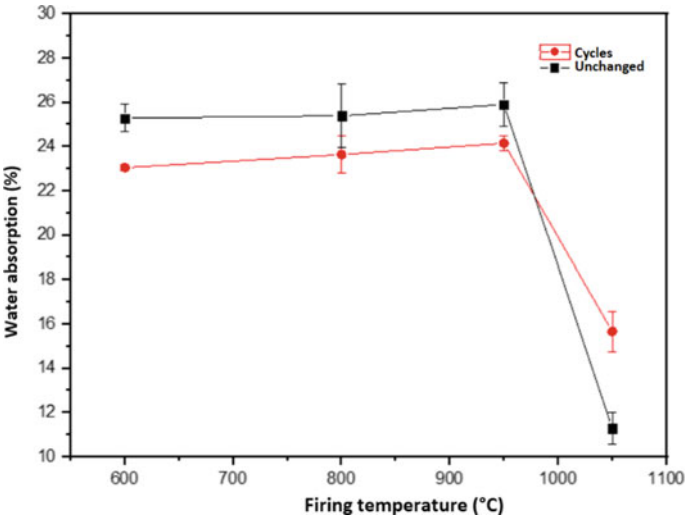

Fig. 4 Water absorption for the studied specimens

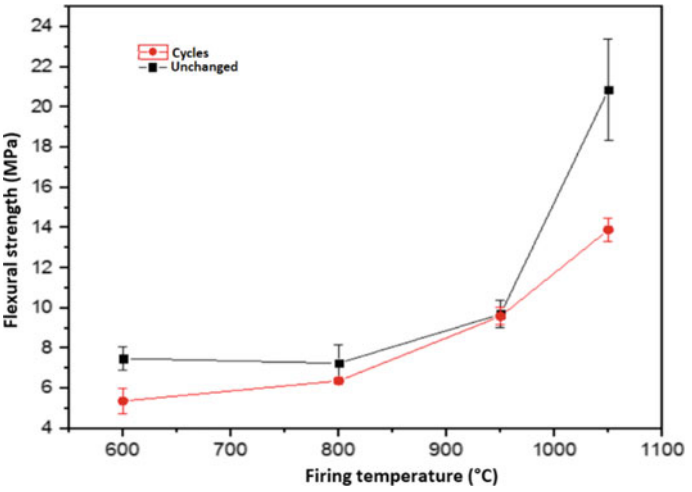

Fig. 5 Flexural strength for the studied specimens

This pattern does not occur with samples burned at 1050 °C, due to the transformation of kaolinite into mullite that occurs around 1000 °C. At this temperature, the degraded samples showed higher water absorption than intact samples, since the formation of the mullite made it impossible to penetrate the solution salts into the internal structure of the samples.

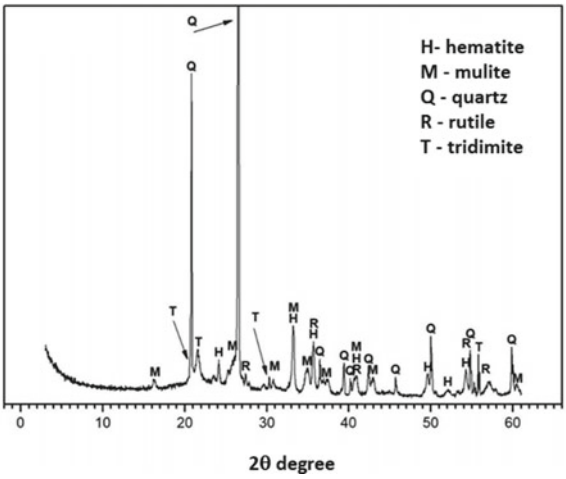

Fig. 6 Mineralogical analysis of uncharged samples

Figure 5 presents the results obtained for flexural strength in specimens burned at different temperatures for unchanged and degraded samples. Except for the temperature of 950 °C in which there was equivalence, all degraded samples presented resistance decrease when degraded in saline solution. In addition, it was found that the effect of the temperature increase was beneficial as expected. However, it is noteworthy that there was a significant jump in the resistances obtained at the temperature of 1050 °C, which again shows the fact that kaolinite turned into mullite around the temperature of 1000 °C. Regarding the minimum values, Santos [19, 20] recommends that the minimum resistance should be approximately 6.5 MPa. From this point of view, the only viable temperatures are at 950 and 1050 °C for both intact and degraded samples.

Figures 6 and 7 show the results obtained for mineralogical analysis of samples burned at 1050 °C without degradation tests and submitted to saline attack, respectively. The material under analysis was taken from the inside of the samples to verify the penetration of salts within the material. It was found that in the samples subjected to degradation (Fig. 7), there were peaks of halite, the typical chloride mineral, showing the penetration of this material in the samples. In addition, both figures showed the presence of mullite peaks, which proves the transformation of kaolinite (present in the peaks of Fig. 2 that presents the mineralogical analysis of the clayey mass studied), and validates the discussions made in the previous paragraphs.

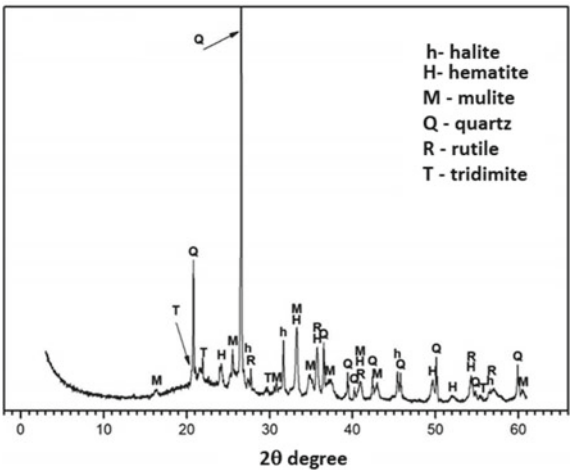

Fig. 7 Mineralogical analysis of degradation samples

Conclusion

Samples burned at temperatures of 600, 800, and 950 °C showed reduced sea water absorption when submitted to durability tests, indicating that the penetration of salts occurred inside the material structure, creating a barrier for water penetration. At 1050 °C, however, there was a sharp reduction in water absorption values due to the transformation of kaolinite into mullite. The mullite prevented the penetration of salts inside the samples and, therefore, the degraded specimens showed increased absorption values. The ceramic products that complied with the Brazilian normative values were the samples burned at 1050 °C (intact and degraded), since they presented water absorption below 20%. Other burning temperatures are not feasible.

Mechanical resistance gain was verified as the temperature increase occurred. It was possible to identify a jump in the resistance value obtained at a temperature of 1050 °C due to the formation of the mullite phase. Regarding the viability, it was found that the masses burned at 950 and 1050 °C presented resistance higher than 6.50 MPa, both intact and degraded, and as a result are feasible to be used.

The ceramic mass showed kaolinite peaks, not detected in the analysis of samples burned at 1050 °C, indicating the transformation of this clay mineral into mullite, as it is also possible to be identified in the thermal analysis. The mullite acted as a barrier to chloride entrance, although halite peaks were detected in the analysis of the degraded material, demonstrating that even in smaller quantities, the salts penetrated the material internal structure.

The samples burned at 1050 °C are possible to be used in harsh marine environments, and that the lower temperature masses are not viable because they presented problems regarding water absorption, mechanical resistance, and temperature no formation of mullite, which acts as a barrier to the entrance of chlorides in the material.

References

1. Soares LP, Carneiro PBM, Fujii MT (2018) New records of red seaweeds to the coast of Ceará State, northeastern Brazil. Hoehnea 45(2):323–347
2. Marques C, Frey H (2015) Housing changes in Brazilian metropolitan areas, urbe. Rev Bras Gestão Urbana (Braz J Urban Manag) 7(2):250–267
3. Trevisol CA, Silva PRP, Paula MMS, Pelisser F (2017) Evaluation of corrosion inhibitors for reinforced concrete structures. Revista Matéria 22:4
4. Medeiros MHF, Souza DJ, Filho JH, Adorno CS, Valdecir A (2016) Quarcioni, Eduardo Pereira. Red-clay waste and limestone filler added in Portland cement composite: effects on sulfate attack and alkali-silica reaction. Rev Matér 21(2):282–300
5. Li K, Zhang D, Li Q, Fan Z (2019) Durability for concrete structures in marine environments of HZM project: design, assessment and beyond. Cem Concr Res 115:545–558
6. Fonseca BMS (2012) Influence of saline fog on the degradation of ceramic materials applied in buildings. Masters dissertation UnB
7. Sulikowski J, Kozubal J (2016) The durability of a concrete sewer pipeline under deterioration by sulphate and chloride corrosion. Proced Eng 153:698–705
8. Mazzarelli CCM, Santos MR, Amorim RV, Augusto A (2015) Effect of salinity on the metabolism and osmoregulation of selected ontogenetic stages of an amazon population of Macrobrachium amazonicum shrimp (Decapoda, Palaemonidae). Braz J Biol 75(2):372–379
9. Crauss C (2010) Chloride penetration of concrete with different types of cement subjected to surface treatment. Masters dissertation UFSM
10. Cruz CJAC (2010) Behavior and durability of ceramic tiles in marine environment. Masters dissertation UA
11. Azevedo ARG, Marvila MT, Fernandes WJ, Alexandre J, Xavier GC, Zanelato EB, Cerqueira NA, Pedroti LG, Mendes BC (2019) Assessing the potential of sludge generated by the pulp and paper industry in assembling locking blocks. J Build Eng 23:334–340
12. França BR, Azevedo ARG, Monteiro SN, Filho FCG, Marvila MT, Alexandre J, Zanelato EB (2018) Durability of soil-cement blocks with the incorporation of limestone residues from the processing of marble. Mater Res 21(Suppl. 1):e20171118
13. Azevedo ARG, França BR, Alexandre J, Marvila MT, Zanelato EB, Xavier GC (2018) Influence of sintering temperature of a ceramic substrate in mortar adhesion for civil construction. J Build Eng 19:342–348
14. Marvila MT, Azevedo ARG, Alexandre J, Zanelato EB, Azeredo NG, Simonassi NT, Monteiro SN (2019) Correlation between the properties of structural clay blocks obtained by destructive tests and ultrasonic pulse tests. J Build Eng 26:100869
15. Marvila MT, Alexandre J, Azevedo ARG, Zanelato EB, Xavier GC, Monteiro SN (2019) Study on the replacement of the hydrated lime by kaolinitic clay in mortars. Adv Appl Ceram 118(7):373–380
16. Brazilian Association of Technical Standards—ABNT (Associação Brasileira de Normas Técnicas) (2009) NBR 15310—Ceramic components—tiles—terminology, requirements and test methods. ABNT, Rio de Janeiro
17. Moreno EAX, Scian NA (2015) High purity mullite by slip casting method from calcined alumina and kaolinitic clay. Proced Mater Sci 8:245–250
18. Sánchez-Soto PJ, Eliche-Quesada D, Martínez-Martínez S, Garzón-Garzón E, Pérez-Villarejo L, Rincón JM (2018) The effect of vitreous phase on mullite and mullite-based ceramic composites from kaolin wastes as by-products of mining, sericite clays and kaolinite. Mater Lett 223:154–158
19. Santos OS (1989) Clay science and technology, 2nd edn, vol 1. Edgard Blucher, S. Paulo, SP
20. Vieira CMF, Morais ASC, Monteiro SN, Delaqua GCG (2016) Industrial test of heavy clay ceramic incorporated with fluorescent lamp waste. Cerâmica 62:364

Application of Nanoparticles of ZnO and ZnO-Doped-Ag in Polymeric Blend of HMSPP/SEBS for Biocide Activity

Luiz Gustavo Hiroki Komatsu, Washington Luiz Oliani, Camila Basseti Oliveira, Vijaya Kumar Rangari and Duclerc Fernandes Parra

Abstract In this study, the nanoparticles of Zinc oxide (ZnO) and Zinc oxide doped with Silver (ZnO/Ag) were synthesized in laboratory. The incorporation of these nanoparticles in the blend of high melt strength polypropylene (HMSPP) and styrene–ethylene/butadiene–styrene (SEBS) was carried by melt processing. The obtained materials were evaluated by X-ray diffraction (XRD), Raman Spectroscopy, Differential Scanning Calorimetry (DSC), biocidal tests against the bacteria *Escherichia coli* and *Staphylococcus aureus*. The nanoparticles showed size between 150 and 200 nm and spherical form. HMSPP/SEBS/AgNPs/ZnO films incorporated with the nanoparticles have demonstrated biocidal effect against the bacteria *E. coli* and *S. aureus* when irradiated at 12.5 kGy.

Introduction

Metals and metal oxides have been well-known antimicrobial agents for a very long time [1]. Among the many types of antimicrobial metal and metal oxide nanoparticles, including silver, gold, TiO_2 nanoparticles [2], ZnO nanoparticles are a well-known and very prominent antimicrobial metal oxide because of their interesting properties [3].

Antimicrobial pack is a type of active packaging which interacts with the product environment to reduce, inhibit, or retard the growth of microorganisms that may be on food surfaces [4].

The bactericidal properties of ZnO nanoparticles are due to electrostatic interaction between the nanoparticles and the cell surface, and increasing association with the nanoparticles results in enhance of cell damage. The toxic effect of ZnO

L. G. H. Komatsu (✉) · W. L. Oliani · C. B. Oliveira · D. F. Parra
Nuclear and Research Institute, IPEN, CNEN/SP, Av. Prof. Lineu Prestes, 2242, Cidade Universitária, São Paulo-SP, CEP 05508-000, Brazil
e-mail: luizkomatsu@gmail.com

V. K. Rangari
Department of Materials Science and Engineering, Tuskegee University, Tuskegee AL36088, USA

J. Li et al. (eds.), *Characterization of Minerals, Metals, and Materials 2020*,
The Minerals, Metals & Materials Series,
https://doi.org/10.1007/978-3-030-36628-5_41

nanoparticles towards the pathogenic species depends on prolonged contact between the bacterium cell membrane and the nanoparticles. The bacterium and fungal lipid bilayer get ruptured due to the cytotoxic behavior of ZnO nanoparticles resulting in the drainage of the cytoplasmic contents [5].

In general, there are different approaches to incorporate the antimicrobial agents into a food packaging. Nevertheless, the procedure can possibly raise a crucial problem because the fabricated composites would perform lower or none antimicrobial activity. One of the possible reasons for these unfavorable characteristic is that a majority of the incorporated antimicrobial agents are totally trapped inside the composite matrixes, so they cannot be released or leached out to provide antibacterial properties [6, 7].

Following that comments on the incorporation process of the antimicrobial agents, the aim of this work is on the processability and the microbial efficiency, following the JIZ 2801 standard, of the blend of high melt strength polypropylene (HMSPP) and styrene–ethylene/butadiene–styrene (SEBS) incorporation of antimicrobial agent: zinc oxide (ZnO) and zinc oxide doped with nano silver (ZnO/Ag).

Experimental Procedure

Synthesis of ZnO and ZnO-Doped-Ag-Powder

The solution of 0.5 M $Zn(NO_3)_2 \cdot H_2O$ was added to the solution of 1 M of NaOH drop by drop under constant stirring using the Mili-Q water as solvent. After, the solution of NaOH was heated to the temperature of 75 °C. The suspension was dried and washed, according to the literature [8].

For dopping the ZnO with silver (Ag), the solution of silver nitrate $AgNO_3$ was heated at boiling point, and the sodium citrate was added as reductant agent. After resting 15 min, the PVP (poly-vynilpirrolidone) was incorporated to the solution as core-shell agent followed by addition of 1 g of synthesized ZnO, according to adaptation of the literature [9].

Melt Processing of the Samples

For the blend of HMSPP/SEBS, a sample of isotactic polypropylene (H603—Braskem) was placed in plastic container and irradiated (^{60}Co) in acetylene atmosphere in order to obtain the HMSPP [10]. A sample of SEBS (KRATON—G1633) was mixed with paraffinic oil form Nynas (Nyflex 3030), antioxidant IRGANOX 1010 from BASF and PP-*graft*-MA from Additivant. HMSPP/SEBS blend in proportion of (75/25), respectively, was processed in a Single Screw Extruder—Thermo-Haake Polymer Lab., at temperature range of 160–210 °C. The extruded materials in

pellets were mixed in concentrations of 0.3 wt%; 1 wt% of ZnO and 0.3 wt%; 1 wt% of ZnO/Ag.

Differential Scanning Calorimetry

Thermal properties of specimens were analyzed using a differential scanning calorimeter (DSC) 822, Mettler Toledo. The enthalpy behavior of the films was obtained under: (1) heating from 25 to 280 °C at a heating rate of 10 °C min^{-1} under nitrogen atmosphere, (2) holding for 5 min at 280 °C, (3) then cooling to 25 °C, and reheating to 280 at 10 °C min^{-1}, according to ASTM D 3418-08. The crystallinity was calculated according to the equation:

$$X_C = P \times \frac{\Delta H_f \times 100}{\Delta H_0}$$

where ΔH_f is melting enthalpy of the sample, ΔH_0 is melting enthalpy of the 100% crystalline PP which is assumed to be 209 kJ kg^{-1}.

X-Ray Diffraction

X-ray diffraction measurements were carried out in the reflection mode on a Rigaku diffractometer Mini Flex II operated at 30 kV voltage and a current of 15 mA with CuKα radiation.

Biocide Tests

This test was carried to evaluate the results of diffusion of the nanoparticles before and after the melt processing, and the films for biocide tests were evaluated before and after sterilization under gamma irradiation at dose of 12.5 kGy.

The bacteria utilized for this test was the *Escherichia coli* (Gram—negative) ATCC 8739 e *Staphylococcus aureus* (Gram—positive) (ATCC 6538p).

With an sterile swab, the inoculums of the bacteria were seeding in all directions in sterile Petri dish with Müeller-Hinton agar, and after drying, the samples were placed in contact to the agar and incubated for 24 h. All the tests were performed according to JIZ 2801 standard.

Results and Discussion

DLS analysis show a media of particles size as 150 nm for ZnO and 200 nm for ZnO-doped-Ag. Figure 1 shows the XRD diffractogram of the ZnO power and the blend of HMSPP/SEBS doped with the particles.

The characteristics peak of scattering angle (2θ) identified was 4.15°, which refers to the lattice parameter of ZnO presence [8]. The other peaks indicate silver (Ag^0) presence in the polymer, from the doping of ZnO. The presence of ZnO on the polymer was indentified also by Raman Spectroscopy Fig. 2.

The more intense peak of 460 cm^{-1} corresponds to ZnO [11]. In fact, the presence and addition of the particles with nano sized dimensions can cause some alterations in the polymer matrix as shown in Table 1.

The result observed on Table 1 is expected to the elastomeric phase of SEBS and hinders the crystallization process of HMSPP, especially because the block of ethylene-butadiene increases the amorphous area [7]. However, the composites have shown alterations in addition of particles, increasing the crystallinity, in comparison the neat blend and the composites with the nanosized particles. The particles nanometric sized can act as nucleating agent, increasing the crystallinity instead. This effect was also observed, due to the higher concentration of HMSPP in respect of SEBS concentration.

The knowledge of the interaction of the particle and the polymer matrix is one of the key points to understanding the biocidal effects against the bacteria. Table 2 shows the results of microbial activity of the films after irradiation.

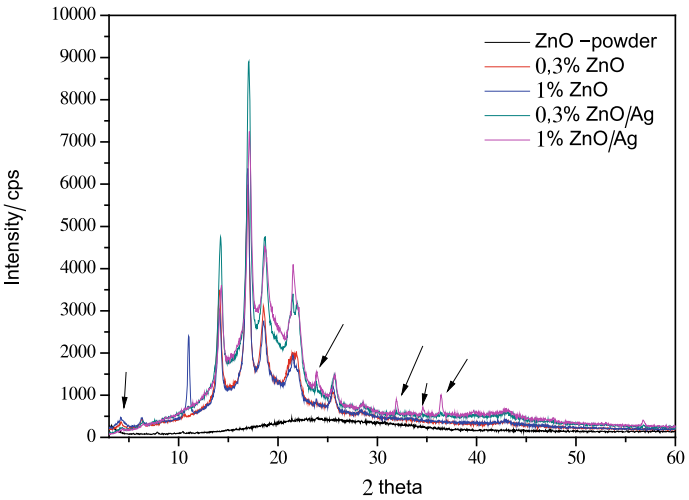

Fig. 1 XRD diffractogram of the ZnO powder and the films of HMSPP/SEBS doped with ZnO and ZnO-doped-Ag

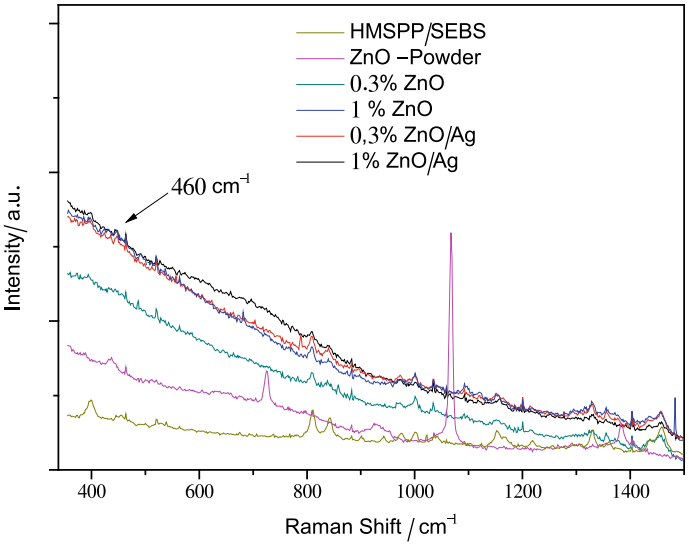

Fig. 2 Raman Spectroscopy of the composites and the synthesized powder

Table 1 DSC of the composites; Tm_2 = melting temperature and X_c = crystallinity

Samples	Tm_2 (°C)	X_c (%)
Zero	161.46	23.89
1% ZnO	159.63	31.10
0.3% ZnO	159.98	32.10
1% ZnO/Ag	159.95	30.89
0.3% ZnO/Ag	158.96	31.03

Table 2 Biocidal activity of irradiated films

Samples	Bacteria counting in zero time—*S. aureus* ATCC6538P	Bacteria counting after 24 h—*S. Aureus* ATCC6538P	Bacteria counting in zero time—*E. coli* ATCC 8739	Bacteria counting after 24 h—*E. coli* ATCC 8739
HMSPP/SEBS	2.1×10^5	2.1×10^5	2.3×10^5	2.6×10^5
Ag/ZnO 0.3%	2.1×10^5	1.3×10^2	2.3×10^5	5.6×10^2
Ag/ZnO 1%	2.1×10^5	9.8×10	2.3×10^5	4.3×10^2
ZnO 0.3%	2.1×10^5	9.1×10	2.3×10^5	2.7×10^2
ZnO 1%	2.1×10^5	8.6×10	2.3×10^5	2.5×10^2

The films before the irradiation process were tested; however, they did not show any biocidal effect. After irradiation, the result observed on Table 2 is possible to affirm that ZnO has more intense biocide activity than the doped particle. This reason can be correlated to the protective membrane of the bacteria cells. The most important cellular function of external membrane is work as protective barrier to prevent or retard the entry of biocide agents that can kill or cause injury on the bacteria [12]. For this reason when the particle has a nanosized dimension is possible to rupture the bacterial membrane and then to kill the bacteria.

Conclusion

The HMSPP/SEBS blend was successfully processed as well as the laboratory synthesis of ZnO and ZnO@Ag on the nanometer scale. The HMSPP/SEBS films with ZnO and ZnO@Ag nanocomposites showed significant results against *E. coli* and *S. aureus* bacteria when irradiated at 12.5 kGy.

Acknowledgements The authors thank the CAPES/PROEX for the grants. Multipurpose gamma irradiation facility at the CTR-IPEN and ControlBio for the Microbiology Analysis.

References

1. Stoimenov PK, Klinger RL, Marchin GL, Klabunde KJ (2002) Metal oxide nanoparticles as bactericidal agents. Langmuir 18(17):6679–6686
2. Rai VR, Bai AJ (2011) Nanoparticles and their potential application as antimicrobials. In Mendez-Vilas A (ed) Science against microbial pathogens: communicating current research and technological advances, pp 197–209
3. Klingshirn CF, Meyer BK, Waag A, Hoffmann A, Geurts J (2010) Zinc oxide: from fundamental properties towards novel applications. Springer-Verlag, Berlin, Heidelberg
4. Espitia PJP, Soares NFF, Coimbra JSR, Andrade NJ, Cruz RS, Medeiros EAA (2012) Zinc oxide nanoparticles: synthesis, antimicrobial activity and food packaging applications. Food Bioprocess Technol 5:1447–1464
5. Sharma D, Rajput J, Kaith BS, Kaur M, Sharma S (2010) Synthesis of ZnO nanoparticles and study of their antibacterial and antifungal properties. Thin Solid Films 519:1224–1229
6. Paisoonsin S, Pornsunthorntawee O, Rujiravanit R (2013) Preparation and characterization of ZnO-deposited DBD plasma-treated PP packaging film with antibacterial activities. Appl Surf Sci 273:824–835
7. Vuluga Z, Panaitescu DM, Radovici C, Nicolae C, DoinaIorga M (2012) Effect of SEBS on morphology, thermal, and mechanical properties of PP/organoclay nanocomposites. Polym Bull 69:1073–1091
8. Gusatti M, Rosario JA, Barroso GS, Campos CEM, Riella HG, Kunhen NC (2009) Synthesis of ZnO nanostructures in low reaction temperature. Chem Eng Trans 17:1017–1021
9. Oliveira GM, Costa LMM, Carvalho AJF, Basmaji P, Pessan LA (2011) Novel LDPE/EVA nanocomposites with silver/titaniumdioxide particles for biomedical applications. J Mater Sci Eng 1:516–522

10. Komatsu LGH, Oliani WL, Lugao AB, Parra DF (2014) Environmental ageing of irradiated polypropylene/montmorillonite nanocomposites obtained in molten state. Rad Phys Chem 97:233–238
11. Jadhav J, Biswas S (2018) Hybrid ZnO: agcoreshell nanoparticles for wastewater treatment: growth mechanism and plasmonically enhanced photocatalytic activity. Appl Surf Sci 456:49–58
12. Li X, Xing Y, Jiang Y, Ding Y, Li W (2009) Antimicrobial of ZnO powder-coated PVC film to inactive food pathogens. Inter J Food Sci Tech 44:2161–2168

Characterization and Metallurgical Performance of Titangarnet

Gang Li, Xuewei Lv, Xuangeng Zhou and Guibao Qiu

Abstract Titangarnet ($Ca_3Fe_2Si_1{\cdot}58Ti_1{\cdot}42O_{12}$), a significant mineral phase in sinter with vanadium–titanium magnetite (VTM), was rarely investigated on its strength and metallurgical properties. In this study, high purity (95%) of titangarnet was firstly prepared by chemical synthesis. The results of compressive strength tests showed that the compressive strength of titangarnet (14.21 Mpa) is much lower than that of calcium ferrite (37.46 Mpa). The melting performance of titangarnet was measured by hemisphere method, and results indicated that the softening, melting, and flowing temperatures of titangarnet are 1453, 1483, and 1509 K, respectively. The reduction tests carried out by thermal analysis showed that the maximum reduction degree of titangarnet and calcium ferrite reached 0.65 and 0.94, respectively.

Keywords Titangarnet · Preparation · Melting performance · Reduction behavior

Introduction

Titangarnet, an important titanium-containing phase in iron ore sinter with vanadium–titanium magnetite (VTM), was rarely investigated previously especially in the aspects of strength, melting, and reduction performance. VTM is a typical polymetallic iron ore with high comprehensive utilization value and is becoming an important alternative source of iron ore due to the shortage of high grade ores. However, for the high content of titanium in VTM, the sinter parameters and sinter quality still exist many issues that need to be solved. HE [1] carried out the sinter pot tests where titanium concentrate was adopted to the sinter blend to explore the effects of TiO_2 on the sintering properties of high titanium VTM, results showed that the strength and the yield of sinter decreased, meanwhile the RDI and the droplet property

X. Lv (✉) · X. Zhou · G. Qiu
College of Materials Science and Engineering, Chongqing University, Chongqing 400044, China
e-mail: lvxuewei@163.com

G. Li · X. Lv · X. Zhou · G. Qiu
Chongqing Key Laboratory of Vanadium-Titanium Metallurgy and New Materials, Chongqing University, Chongqing 40044, China

J. Li et al. (eds.), *Characterization of Minerals, Metals, and Materials 2020*,
The Minerals, Metals & Materials Series,
https://doi.org/10.1007/978-3-030-36628-5_42

of sinter deteriorated when TiO_2 content increased from 6 to 10%. Microstructure showed that Ti mainly distributed in perovskite, titangarnet, and titanaugite. Zhou [2] studied the effect of basicity on high-chromium vanadium–titanium magnetite sintering via sintering pot tests, and results showed that perovskite, the main titanium-containing phase, concentrated in certain microstructural areas, which weakened the sinter strength due to its high fragility. In addition, the distribution of perovskite aggravated the degradation of V–Ti sinter through weakened bonding effect and resulted in increased cracking. To improve the sintering of VTM, understanding of the basic and metallurgical properties of titangarnet that distributes in V–Ti sinter is necessary and significant.

Previous studies on titangarnet mainly involved its behavior in mineralogy and geology including crystal structure test and geological formation. However, its high-temperature performance was scarcely concerned. Some authors [3] considered that titangarnet does not undergo the phase change and volume expansion in the process of cooling, and thus, sinter is not easy to disintegrate and suitable for storage. Nevertheless, support information can not be found, and the details are missing.

In this study, titangarnet was prepared in laboratory, and its purity was checked by X-ray diffraction and scanning electron microscope. Furthermore, the compressive strength, melting performance, and reduction behavior of titangarnet were also tested for the first time.

Sample Preparation and Characterization

Preparation

The raw materials for titangarnet preparation were Fe_2O_3, TiO_2, SiO_2, and $CaCO_3$, and their mass percentages are shown in Table 1. The raw materials were first uniformly mixed and then roasted at 1523 K for 10 h in a resistance furnace. After roasting, the samples were cooled down and finally ground to particles for subsequent investigations. The entire process was in the air condition.

X-ray diffraction (XRD) analysis using RIGAKU D/max2500/PC was conducted to examine the phase composition of roasted samples, which were scanned at an angular range of 10–90° with a rate of 4°/min. The XRD patterns of roasted samples and standard titangarnet were shown in Fig. 1. The results indicate that there was almost no impure peak, and the purity of sample was high enough.

Table 1 Mass percentage of raw materials for titangarnet preparation (wt%)

Fe_2O_3	TiO_2	SiO_2	CaO
29.83	21.18	17.67	31.32

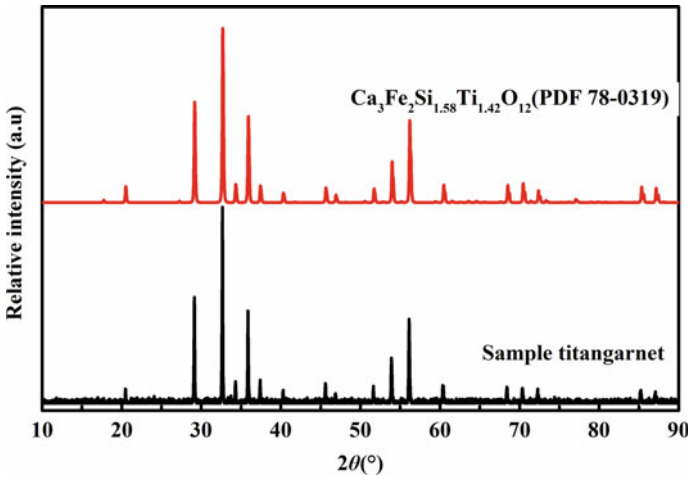

Fig. 1 XRD patterns of roasted samples and standard titangarnet

Morphology Observation

The micrographs obtained by scanning electron microscope (SEM, model TESCAN VEGA 3 LMH) are expressed in Fig. 2. Mass percent of atoms at three spots *A*, *B*, *C* were analyzed by energy disperse spectroscopy (EDS). It can be reasonably speculated that the compounds existed at plots *A*, *B*, *C* were all titangarnet, which further proved the high purity of titangarnet samples.

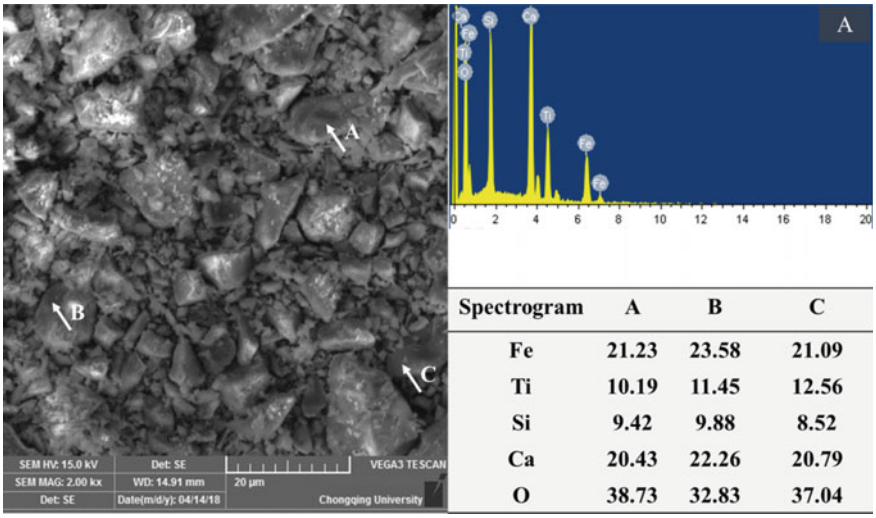

Spectrogram	A	B	C
Fe	21.23	23.58	21.09
Ti	10.19	11.45	12.56
Si	9.42	9.88	8.52
Ca	20.43	22.26	20.79
O	38.73	32.83	37.04

Fig. 2 SEM image and spot scanning of titangarnet

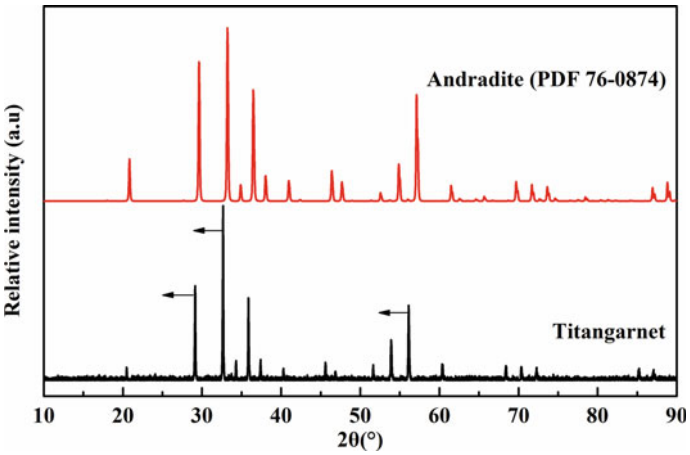

Fig. 3 XRD patterns of andradite and titangarnet

Crystal Structure

Titangarnet is a variant of andradite ($Ca_3Fe_2Si_3O_{12}$) under titanium-rich conditions. Titangarnet has similar structure with andradite, but the cation distribution of Ti and Fe among the crystallographic sites is comparatively complex. Ti is typically interpreted as tetravalent and accommodated predominantly in the octahedral sites [4–7], whereas the presence of Ti^{3+} in the six-fold octahedron was also reported by some investigations [8–10]. Extensive reports found that Fe^{3+} is one of the major substituents for Si [10–12]. Another possible occupancies for tetrahedral sites are Ti^{4+} [10, 11, 13], and the preference for tetrahedral sites is $Si^{4+} \gg Fe^{3+} > Ti^{4+}$.

XRD patterns of standard andradite and sample titangarnet are shown in Fig. 3. Diffraction peaks of titangarnet appear similar to that of andradite, but there are a few transpositions to the left side of 2θ axis, which is caused by the substitution of titanium in andradite.

Metallurgical Properties

Compressive Strength

Sample calcium ferrite was adopted in the compressive strength test (SANS CMT-5150) for a comparison with titangarnet. The samples were heated to 1573 K, kept warm for 1 h, and then cooled down in the air. Subsequently, the cooled samples were cut and sanded into a cube shape (10 mm). The compressive strength of titangarnet

Table 2 Compressive strength (Mpa) of titangarnet and calcium ferrite

Samples	Compressive strength	Avg.
Titangarnet	16.27	14.21
	11.35	
	15.01	
Calcium ferrite	42.14	37.46
	33.47	
	36.77	

and calcium ferrite was determined by the average value of three repeated experiments, which were shown in Table 2. The compressive strength of calcium ferrite varied from 33.47 to 41.14 Mpa. However, the compressive strength of titangarnet was much lower than that of calcium ferrite. From this point of view, the content of titangarnet phase should be controlled in a limited value when sintering with VTM.

Melting Performance

The melting performance of titangarnet was measured by hemisphere method. Temperatures at tested sample with 3/4, 1/2, and 1/4 of initial height in the melting stages are defined as its softening, melting, and flowing temperature. Titangarnet sample, after melting, cooled, and solidified, was ground to a cuboid of 10 * 5 * 5 mm for the melting performance test. The measurement results of titangarnet are shown in Fig. 4. Results indicate that the softening, melting, and flowing temperatures of titangarnet are 1453, 1483, and 1509 K, respectively. From the melting performance test of titangarnet, its melting temperature is relative low, and the generation of liquid phase

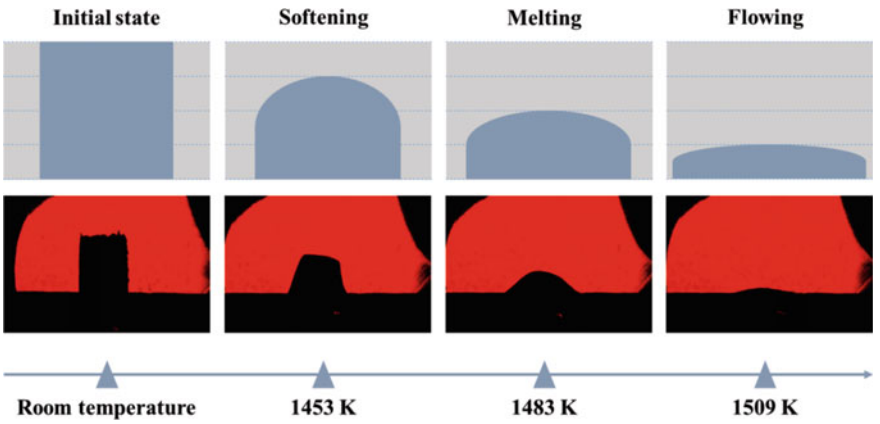

Fig. 4 Melting performance measured by hemisphere method for titangarnet

can be promoted by the melting of titangarnet in the sintering process. In addition, titangarnet as a titanium-containing phase should reduce the content of perovskite to some extent. Thus, an appropriate proportion of titangarnet generated at the sinter may can not only improve the sinter quality but also reduce the fuel consumption in the sintering process.

Reduction Performance

Although the reduction behavior of VTM sinter has been extensively reported [14–16], unfortunately, the reduction of titangranet was rarely investigated. The reduction behavior of titangarnet was examined by thermal analysis using a Setaram analyzer (Model Setsys Evo TG-DTA 1750), and schematic of the equipment is shown in the previous study [17]. Samples (30 mg) in an alumina crucible (Φ6 × 8 mm) were heated from room temperature to 1173 K under N_2 atmosphere and then reduced at 1173 K under 30% CO and 70% N_2 gas mixtures at a flow rate of 20 ml/min. Gas flow rate was set at 20 ml/min in accordance with it previously determined to exclude the influence from external diffusion [18]. Weight loss data was obtained from isothermal reduction stage, and the reduction degree is defined as the ratio of weight loss at a certain time to theoretically maximum weight loss.

$$\alpha = \frac{\Delta m_t}{\Delta m_m}, \tag{1}$$

where α is the reduction degree; Δm_t and Δm_m refer to the weight loss at a certain time t and the theoretically maximum weight loss, respectively. Figure 5 shows the reduction degree of titangarnet and calcium ferrite at 1123 K and indicated that the maximum reduction degree of titangarnet and calcium ferrite reached 0.65 and 0.94, respectively. The complete reduction of titangarnet takes more than 15 h, whereas that of calcium ferrite takes less than 2 h under CO atmosphere. Based on previous study on powdery reduction, the reduction kinetics of iron oxide can be described by an exponential function [17, 18]. The following equation fitted by Origin® 9.0 describes the relationship of reduction degree and time,

$$\alpha = -0.74 \exp\left(-\frac{t}{403.91}\right) + 0.74 \tag{2}$$

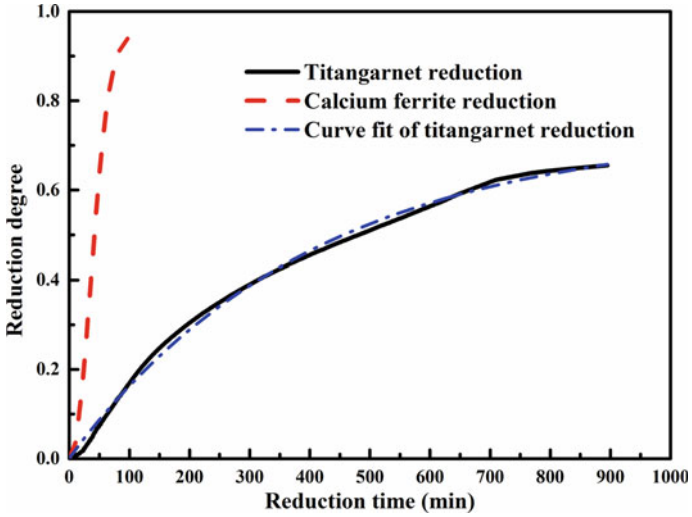

Fig. 5 Isothermal reduction of titangarnet and calcium ferrite at 1123 K

Conclusions

In this study, titangarnet was prepared with high purity by chemical synthesis. The compressive strength, melting performance, and reduction behavior of titangarnet were tested. The conclusions are summarized as follows:

(1) Titangarnet with high purity can be synthesized by solid phase sintering in the laboratory.
(2) Crystal structure of titangarnet is a variant of andradite by Ti substitution, XRD results showed that diffraction peaks of titangarnet appear similar to that of andradite, but there are a few transpositions to the left side of 2θ axis.
(3) The compressive strength of titangarnet varies from 11.35 to 16.27 Mpa, which is much lower than that of calcium ferrite.
(4) Hemisphere method was carried out to test the melting performance of titangarnet, and results show that the softening, melting, and flowing temperatures of titangarnet are 1453, 1483, and 1509 K, respectively.
(5) The reduction behavior of titangarnet was investigated via TG measurement under 1173 K with 30% CO and 70% N2 gas mixtures, and it was found that the maximum reduction degree of titangarnet and calcium ferrite reached 0.65 and 0.94, respectively.

Acknowledgements This study was performed with the financial support of National Key Research and Development Program of the Ministry of Science and Technology (2018YFC1900500) and National Natural Science Foundation of China (Grant No. 51674055).

References

1. Mu-Guang HE, Plant I (2016) Effect of w(TiO_2) on sintering properties of high titanium vanadium-titanium magnetite. Iron Steel
2. Zhou M, Yang S, Jiang T (2015) Influence of basicity on high-chromium vanadium-titanium magnetite sinter properties, productivity, and mineralogy. JOM 67(5):1203–1213
3. Liu X-R, Qiu G-Z, Cai R-Z (2001) Effects of Al_2O_3/SiO_2 ratio on mineralizing laws for low-temperature sintering. Iron Steel 36(3):5–8
4. Armbruster T, Birrer J, Libowitzky E (1998) Crystal chemistry of Ti-bearing andradites. Eur J Mineral 5:907–9277
5. Chakhmouradian A, McCammon C (2005) Schorlomite: a discussion of the crystal chemistry, formula, and inter-species boundaries. Phys Chem Miner 32(4):277–289
6. Orlando A, BoRRiNi C, di Mineralogia P (2001) Solubility of Ti in andradite in upper mantle conditions: preliminary results. Period Mineral 70(1):99–110
7. Locock A A, Luth RW, Cavel RG (1995) Spectroscopy of the cation distribution in the schorlomite species of garnet. Am Miner 80(1–2):27–38
8. Waychunas GA (1987) Synchrotron radiation XANES spectroscopy of Ti in minerals; effects of Ti bonding distances, Ti valence, and site geometry on absorption edge structure. Am Miner 72(1–2):89–101
9. Kühberger A, Fehr T, Huckenholz H (1989) Crystal chemistry of a natural schorlomite and Ti-andradites synthesized at different oxygen fugacities. Phys Chem Miner 16(8):734–740
10. Schwartz KB (1977) Mössbauer spectroscopy and crystal chemistry of natural Fe-Ti garnets. Massachusetts Institute of Technology
11. Gongbao W, Baolei M (1986) The crystal chemistry and Mössbauer study of schorlomite. Phys Chem Miner 13(3):198–205
12. Amthauer G, Annersten H, Hafner S (1977) The Mössbauer spectrum of 57 Fe in titanium-bearing andradites. Phys Chem Miner 1(4):399–413
13. Huggins F, Virgo D, Huckenholz H (1977) Titanium-containing silicate garnet; I, the distribution of Al, Fe (super 3+), and Ti (super 4+) between octahedral and tetrahedral sites. Am Miner 62(5–6):475–490
14. Liu J, Cheng G, Liu Z (2015) Reduction process of pellet containing high chromic vanadium–titanium magnetite in cohesive zone. Steel Res Int 86(7):808–816
15. Cheng G-J, Xue A-X, Gao Z-X (2016) Effect of Cr_2O_3 on the reduction and smelting mechanism of high-chromium vanadium-titanium magnetite pellets. ISIJ Int 56(11):1938–1947
16. Zhou M, Yang S-T, Jiang T (2015) Influence of MgO in form of magnesite on properties and mineralogy of high chromium, vanadium, titanium magnetite sinters. Ironmaking Steelmaking 42(3):217–225
17. Ding C, Lv X, Xuan S (2017) Powder reduction kinetics of dicalcium ferrite, calcium ferrite, and hematite: measurement and modeling. Adv Powder Technol 28(10):2503–2513
18. Ding C, Lv X, Li G (2018) Isothermal reduction of powdery $2CaO{\cdot}Fe_2O_3$ and $CaO{\cdot}Fe_2O_3$ under H_2 atmosphere. Int J Hydrogen Energy 43(1):24–36

Characterization by FTIR of Oxidized Pyrargyrite with Sodium Sulfide

Yessica Paulina Gómez Espinoza, M. Reyes Pérez, Elia Guadalupe Palacios Beas, J. C. Juárez Tapia, M. Pérez-Labra, Iván A. Reyes Domínguez, Mizraim Uriel Flores Guerrero and Víctor Esteban Reyes Cruz

Abstract Pyrargyrite is a silver-rich sulfosal of formula Ag_3SbS_3, considered a refractory species to leaching with cyanide solutions. In this research work, the characterization by infrared spectroscopy by Fourier transform and X-ray diffraction (XRD) of the oxidation of pyrargyrite with sodium sulfide is presented. The XRD results of the oxidation with sodium sulfide show that the pyrargyrite PDF 00-019-1135 is transformed into silver sulfide acanthite identified with PDF 96-901-1415, and the rosinckyite phase was also detected PDF 96-901-2782 as well as Ag_2O_3 PDF 96-150-9693. The characterization by FTIR shows the absorption bands in 534, 760, 1019, and 1384 cm^{-1} characteristics of the presence of Sb–O bonds of Sb_2O_3, and these oxides decisively influence the leaching of silver, due to the formation of a passivation layer on the mineral affecting the success of the leaching.

Keywords Pyrargyrite · Acanthite · Oxidation · FTIR

Y. P. G. Espinoza (✉) · M. R. Pérez (✉) · J. C. Juárez Tapia · M. Pérez-Labra · V. E. R. Cruz
Autonomous University of the State of Hidalgo, Academic Area of Earth Sciences and Materials, Road Pachuca-Tulancingo Kilometer 4.5, Mineral de La Reforma 42180, Hidalgo, Mexico
e-mail: yessicagmz13@gmail.com

M. R. Pérez
e-mail: mreyes@uaeh.edu.mx

E. G. P. Beas
National Polytechnic Institute Unit ESIQUIE. C.P. 07738, México City, D.F., Mexico

I. A. Reyes Domínguez
Autonomous University of San Luis Potosí, Metallurgy Institute Av. Sierra Leona 550 Lomas Second section, 78210 San Luis Potosí, S.L.P., Mexico

M. U. F. Guerrero
Technological University of Tulancingo, Industrial Electromechanics Area. Road to Ahuehuetitla #301 Col. Presas, 43642 Tulancingo, Hidalgo, Mexico

J. Li et al. (eds.), *Characterization of Minerals, Metals, and Materials 2020*,
The Minerals, Metals & Materials Series,
https://doi.org/10.1007/978-3-030-36628-5_43

Introduction

Silver is associated with polymetallic and sulfosalt sulfide minerals, among which the most abundant sulfur phase is silver sulfide acanthite (Ag_2S) other minerals that contain silver are pyrargyrite, Ag_3SbS_3, proustite Ag_3AsS_3, aguilarita Ag_4SeS, tenantite $Cu_6(Cu_4(Fe, Zn)_2)As_4S_{13,}$ and tetrahedrite $(Cu, Fe, Ag, Zn)_{12}Sb_{14}S_{13}$ with silver inclusions [1]. The most common mineral that contains silver is the acanthite and responds relatively quickly to leaching with cyanide [2].

In the literature, a common theme is reported with silver sulfosalts and is refractoriness; this is due to the retarding effect caused by the Ag–Sb and Ag_2S bonds [3]. Refractory mineral is understood as the one that presents little leaching of silver from the mineral. This problem, due to the refractoriness of minerals such as pyrargyrite, has been tried to overcome through treatments such as roasting [4].

As well as the hydrometallurgical route, through pressure oxidation and leaching with bacteria. However, the first route involves the generation of reaction gases such as SO_2 or volatile antimony oxides, while the aqueous route contains difficulties, such as high operating costs and long reaction periods [4].

Pyrargyrite is a mineral with a high silver content of around 59%, and due to its refractoriness characteristic, alternative treatment routes have been considered with variants of the previously described [5], as is a prior treatment with an agent oxidant such as ozone before cyanide leaching. The results found indicate that both silver and antimony dissolve in a considerable percentage of 80%, under conditions of 0.18 M sulfuric acid and 0.079 g of ozone (O_3) per liter [4].

The strong acidic conditions of this process could generate repercussions of both economic and environmental nature. In another work, a pre-treatment of intensive grinding was studied, seeking the mechanical activation of the refractory mineral components. This produces significant changes in the surface of the mineral that has a decisive influence on refractoriness; however, prolonged grinding times are inconvenient for this process [6].

The integration of the previous process consists of a chemical mechanically leaching, which involves grinding and leaching operations in a single stage, which would improve the development of active grinding [6]. In another process, the leaching of silver and antimony from minerals such as tetrahedrite Cu_3SbS_3 containing silver has been studied, using sodium sulfide Na_2S and sodium hydroxide NaOH, describing the chemistry of mineral leaching with Na_2S Eq. 1 [7].

$$Cu_3SbS_3 + Na_2S = 3Cu_2S + 2NaSbS_2 \quad (1)$$

Therefore, in this research work, the oxidation of antimony of a pyrargyrite mineral is studied, through the use of different concentrations of sodium sulfide, characterizing the products formed after oxidation, by X-ray diffraction techniques (XRD) and Fourier transform infrared spectroscopy (FTIR).

Experimental Methodology

For this investigation, a pure pyrargyrite mineral was used, and it was previously characterized by scanning electron microscopy (SEM) in conjunction with energy dispersion microanalysis (EDS), Fourier transform infrared spectroscopy (FTIR), and X-ray diffraction (XRD). The pyrargyrite ore was sprayed in an agate mortar to avoid contamination of the ore, it was screened wet using a series of Tyler sieves, and the mesh size in particular used for this work was the 400 mesh (37 μm).

For all experiments, 1 g of pyrargyrite ore, a glass reactor, and 1 L of deionized water were used testing different concentrations of sodium sulfide, 0.416×10^{-2}, 0.833×10^{-2}, 1.25×10^{-2}, 1.67×10^{-2}, 2.08×10^{-2}, 2.5×10^{-2}, and 2.91×10^{-2} M, and the mineral pulp was continuously agitated using a four blade stir propeller inert to the leaching solution.

The reaction time was 12 h, the solid was allowed to settle, was decanted, and washed copiously with abundant deionized water, and then the mineral was allowed to dry at room temperature and was characterized by the instrumental techniques described above. The expected chemical reaction is as shown in Eq. 2.

$$2Ag_3SbS_3 + Na_2S + H_2O + 1/2O_2 = 3Ag_2S + Sb_2S_4^{2-} + 2NaOH \quad (2)$$

Results

The pyrargyrite mineral used in this investigation was analyzed via SEM in conjunction with EDS and elementary mapping; the results found show that it is a high purity silver sulfosal of the pyrargyrite type with contents of 60.22% Ag, 19.08% Sb, 16.86% of S, and 3.84% of Cu. The morphology of the particles is elongated, with smooth edges and with a conchoidal fracture.

Figure 2 shows the X-ray diffraction spectrum (XRD) of the pyrargyrite mineral with a particle size of 37 μm without treatment, indexed with the diffraction pattern PDF 00-019-1135 with the Match Software, which corresponds to of a high purity pyrargyrite. Meanwhile, the spectrum corresponding to the solid resulting after oxidation of antimony with sodium sulfide using a concentration of 2.5×10^{-2} M and reaction time of 12 h, as presented in Eq. 2, $Na_2S * 9H_2O$ does not only leach to the antimony forming a stable aqueous antimony sulfide at an alkaline pH of 13, but also, transforming the structure of the pyrargyrite mineral from hexagonal to monoclinic corresponding to the silver sulfide PDF 96-900-0254 (Fig. 1).

Similar spectra are obtained when the concentration of sodium sulfide is 2.91×10^{-2} M and 12 h of reaction, lower concentrations of sodium sulfide lead to increase reaction time and partially oxidize the pyrargyrite mineral. However, the valuable information obtained in the diffraction technique does not provide conclusions about

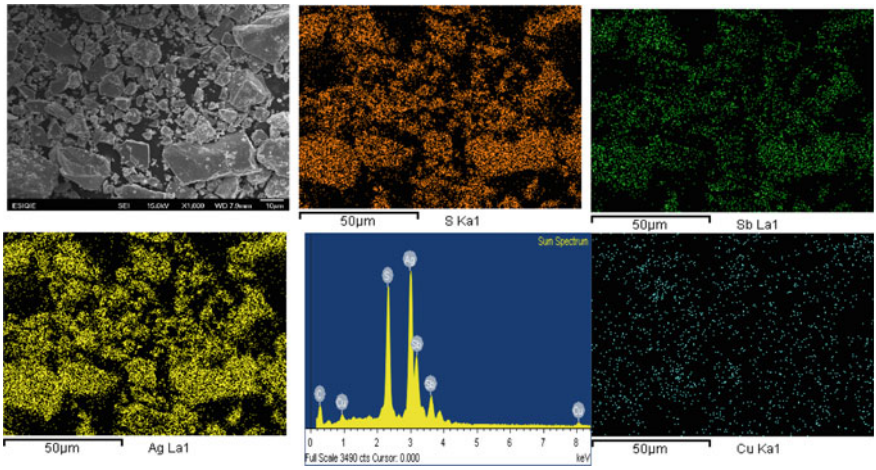

Fig. 1 Micrograph of SEM, EDS, and mapping of the majority elements of the mineral

the state of the antimony in the mineral; for this reason, the solids obtained were characterized by FTIR.

Figure 3 shows the Fourier transform infrared spectra (FTIR) of the pyrargyrite particles; untreated, oxidized, and that of a pure chemical reagent of Sb_2O_3. When the pyrargyrite is sprayed in the mortar, the fresh surfaces of the mineral are exposed to the oxidizing atmosphere, forming species such as sulfate ion bound in a monodentate manner with the mineral metal, and this is due to the cleavage of the main ion absorption band SO_4^{-2} in three characteristic bands in 1056, 1114, and 1160 cm^{-1}.

In addition, the only pulverized pyrargyrite shows the formation of weak absorption bands at 534, 689, 1020, and 1384 cm^{-1}, corresponding to the Sb–O bond of the antimony trioxide Sb_2O_3 the nature of these links as a first approximation are related to the formation of a passivation layer, where the antimony oxide III creates a barrier that can prevent access to the leaching reagent affecting the success of cyanidation.

With the oxidation of the antimony using sodium sulfide, it is expected that in its entirety, it will be transformed into $Sb_2S_4^{-2}$ antimony sulfide; however, from the infrared spectrum of the oxidized pyrargyrite, it is observed that it is not entirely, demonstrated by the intense bands of absorption of the Sb–O bonds of the Sb_2O_3 at about 1384, 1020, 760, 689, and 534 cm^{-1}.

In addition to the absorption bands of antimony trioxide, intense absorption bands of the sulfate ion bound in a monodentate manner with three absorption bands in 1160, 1115, and 1033 cm^{-1} are observed. The band at around 419 cm^{-1} indicates the presence of the S–S bonds present in silver sulfide (Figs. 2 and 3).

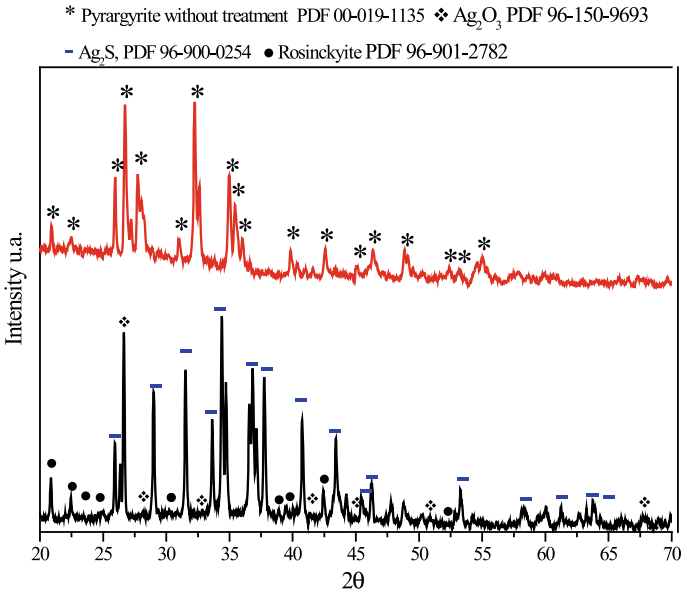

Fig. 2 XRD spectra of non-oxidized and oxidized pyrargyrite with $Na_2S * 9H_2O$, 2.5×10^{-2} M

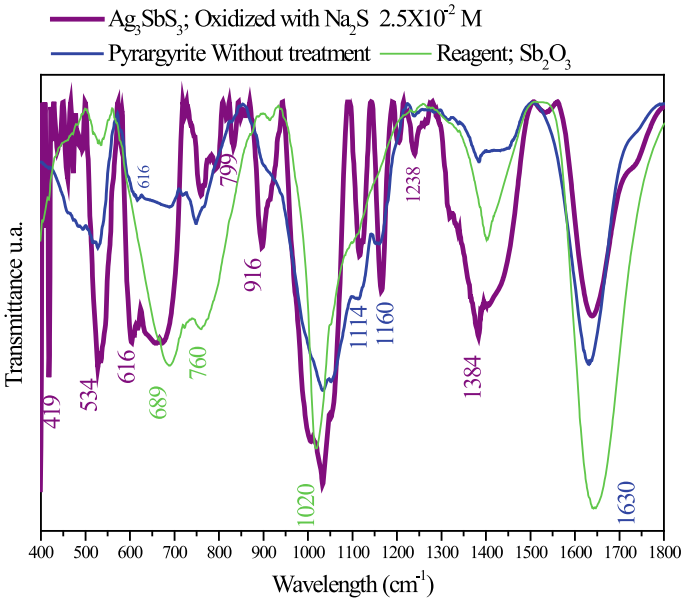

Fig. 3 FTIR infrared spectra of pyrargyrite not oxidized and oxidized with sodium sulfide

Conclusions

The mineral used in this investigation corresponds to a high purity pyrargyrite with contents of 60.22% Ag, 16.86% S, 19.08% Sb, and 3.84% Cu. Sodium sulfide acts as a strong oxidizing agent of antimony, passing into aqueous $Sb_2S_4^{-2}$, and the resulting solid corresponds to a silver sulfide identified with the diffraction pattern PDF 00-019-1135. However, infrared spectroscopy shows that the antimony is not completely eliminated by remaining superficially the Sb–O bonds of the antimony trioxide, the presence of this species results in the formation of a passivation layer where as a first approximation it is expected to delay the cyanidation of silver.

Acknowledgements The authors would like to thank the Autonomous University of the State of Hidalgo, the Program for Professional Development PRODEP, and the National Polytechnic Institute unit ESIQUIE for their financial support.

References

1. Khalid M, Larachi F, Adnot A (2017) The role of silver minerals on the cyanidation of gold particles embedded within multi-sulphidic mineral matrices. Can J Chem Eng 95:1875–1884
2. Zhou J (2010) Paper presented at the 42nd annual meeting of Canadian mineral processors, Ottawa, Ontario, Canada, Jan 2010
3. Celep O, Bas AD, Yazici EY, Alp I, Deveci H (2015) Improvement of silver extraction by ultrafine grinding prior to cyanide leaching of the plant tailings of a refractory silver ore. Miner Process Extr Metall Rev 36:227–236
4. Rodríguez Rodríguez C, Nava Alonso F, Uribe Salas A, Viñals J (2016) Pyrargyrite (Ag_3SbS_3): silver and antimony dissolution by ozone oxidation in acid media. Hydrometallurgy 164:15–23
5. Fraser KS, Walton RH, Wells JA (1991) Processing of refractory gold ores. Miner Eng 4:1029–1041
6. Balaz P (2000) Extractive metallurgy of activated minerals. Elsevier, Amsterdam
7. Balaz P, Ficeriova J, Villachica Leon C (2203) Silver leaching from a mechano chemically pretreated complex sulfide concentrate. Hydrometallurgy 70:113–119

Characterization by FTIR of Sphalerite Obtained in the Flotation Without Collector in the Presence of Ferric Iron

J. A. Granados Oliver, M. Reyes Pérez, A. M. Teja Ruiz, E. G. Palacios Beas, M. Pérez Labra, F. R. Barrientos Hernández, J. C. Juárez Tapia and J. A. Cobos Murcia

Abstract Sphalerite is generally recovered by flotation; however, it has been established that the success of this stage is affected by surface contamination with ferric iron precipitates during grinding. In this work, the flotation of sphalerite was carried out in the presence of iron precipitates 5, 25, 50, and 75 mgL^{-1} of Fe^{+3} as ferric sulfate. The results show that the cumulative flotation of sphalerite, without collector at pH 6.4, with 60 mgL^{-1} of frother, improves, with the increase in ferric ion, and thus, with 75 mgL^{-1} and 2 min of flotation, 94% cumulative recoveries are achieved. Infrared analysis shows absorption bands of the Zn–O vibration at 1737, 1378, 1244, and 1021 cm^{-1}, in addition, the presence of the main band of the tetragonal sulfate ion at 1115 cm^{-1}, and an absorption band corresponding to Fe–O vibration of goethite at 619 cm^{-1}.

Keywords Sphalerite · Flotation · Activation · FTIR

Introduction

Flotation is a physicochemical separation process, which takes advantage of the superficial differences between valuable minerals and the gangue that comes along with mineral [1]. The complex mineralogy of mineral deposits is accompanied by the presence of a mixture of several species such as copper sulfide, lead sulfide, zinc sulfide, among others, which must be separated by sequential flotation.

J. A. Granados Oliver (✉) · M. Reyes Pérez (✉) · A. M. Teja Ruiz · M. Pérez Labra · F. R. Barrientos Hernández · J. C. Juárez Tapia · J. A. Cobos Murcia
Autonomous University of the State of Hidalgo, Academic Area of Earth Sciences and Materials, Road Pachuca-Tulancingo Kilometer 4.5, 42180 Mineral de la Reforma, Hidalgo, Mexico
e-mail: mreyes@uaeh.edu.mx

M. Reyes Pérez
e-mail: jago_madara@hotmail.com

E. G. Palacios Beas
National Polytechnic Institute Unit ESIQUIE. C.P., 07738 Mexico City, D.F., Mexico

J. Li et al. (eds.), *Characterization of Minerals, Metals, and Materials 2020*,
The Minerals, Metals & Materials Series,
https://doi.org/10.1007/978-3-030-36628-5_44

In the sequential flotation of the concentrator plants, zinc sulfide is the last species to be floated, to keep it depressed, and depressing reagents such as sodium cyanide, zinc sulfate, sodium sulphite, among others [2] are generally used. For flotation of sphalerite, xanthate is used as the collector reagent and copper sulfate as a surface activator at alkaline pH [3], and however, flotation can be carried out similarly at slightly acidic pH [4]. In other research, it has been established that lead ions can activate the surface of sphalerite and benefit flotation [5, 6].

Similarly, the surface activation mechanism of sphalerite has been evaluated due to the presence of lead ion, this with the help of the technique X-ray electronic photospectroscopy (XPS) and Fourier transform infrared spectroscopy (FTIR). Establishing that the intentional addition of lead ions in the flotation pulps improves the recovery by flotation of sphalerite. In this way, sphalerite can be significantly activated by lead ions from the oxidation of sulfides or mineral species of lead oxide [5].

In addition, surface activation of sphalerite mineral particles can be carried out by the effect of the metal atoms present in the mineral reticulate parameter [7, 8]. Thus, it has also been established in the literature that sphalerite can float well without the presence of an activating reagent, and this, at a pH less than 6 where the elements contained in the surface of the mineral, can be solubilized to form zinc xanthate (ZnX_2). Other research has suggested activation with ferric hydroxide species in acidic medium [9], proposing activation mechanisms under these conditions [10].

As previously mentioned, Fe^{+3} ions derived from the surface oxidation of the marmatite-sphalerite mineral oxidize xanthate to form di-xanthate and achieve the flotation of the mineral successfully [10]. The investigations establish the role of activation in the flotation of sphalerite; however, the works are scarce in the study of infrared spectroscopy of flotation products derived from the activation of the mineral with Fe^{+3} precipitates.

In this research work, the influence of the ferric ion Fe^{+3}, from the salt of ferric sulfate in the activation and flotation without sphalerite collector was studied using as a frother pine oil, considering a broad range of concentrations and their effect on flotation efficiency and on the surface state of the mineral, characterized by Fourier transform infrared spectroscopy (FTIR).

Experimental Methodology

To carry out this experimental work, a zinc sulfide mineral, practically pure ZnS sphalerite, was used, which was previously characterized by instrumental techniques of XRD, SEM-EDS. Sphalerite ore was pulverized in an agate mortar, screened dry using a series of Tyler sieves 170, 200, 270, 325, and 400 mesh and the fine. Sphalerite flotation tests were carried in a Denver-type flotation cell using 1 L of deionized water and mineral particles retained in the 200 mesh for each test.

To determine the effect of Fe^{+3} iron precipitates on sphalerite flotation, analytical grade reagent such as ferric sulfate $Fe_2(SO_4)_3$ * H_2O was used in concentrations of 5, 25, 50, and 75 mgL^{-1}, to reduce the surface tension of the pulp, frother was used, pine oil in concentration of 60 mgL^{-1} provided by the company Alkemin S.A. de S.R.L. Using flotation times of 30 s, 1–10 min obtaining the recovery curves versus the flotation time.

During the conditioning of the pulp and at the end of the flotation, the hydrogen ion potential (pH), the oxide-reduction potential (ORP), and the electrical conductivity (k) are monitored. Concentrates obtained at different flotation times 30 s and 1 min were characterized by FTIR to determine the surface state of mineral particles during flotation without sphalerite collector.

Results

Figure 1 shows the micrographs of SEM of the sphalerite particles in general and in detail, and particles of irregular morphology, elongated edges, and appearance in layers with smooth edges are observed. From the EDS energy dispersion microanalysis, the mineral has the following semi-quantitative chemical composition 54.46% Zn, 26.26% S, 14.59% Fe, and 4.69% O_2. Figure 2 shows the X-ray diffraction analysis of the mineral used in this investigation. It is observed that it is a single crystalline phase of zinc sulfide identified with the diffraction pattern PDF 00-005-0566.

The results of the flotation tests without collector of the sphalerite mineral at pH 6.36, using 60 mgL^{-1} of frother pine oil, and concentrations of 5, 25, 50, and 75 mgL^{-1} of ferric ion Fe^{+3}, are shown in Fig. 3, generally the cumulative recovery of the mineral increases with the flotation time obtaining about 99% cumulative separation of sphalerite in a time of 10 min, and with a ferric ion concentration of 75 mgL^{-1}.

The Fe^{+3} ion in the pulp at pH 6.3 precipitates as FeO * OH ferric hydroxide (goethite) as established by thermodynamics, and Fig. 4 shows the Eh-pH diagram of the Fe–H_2O system at 25 °C 1.3×10^{-3} m, obtained from the Hsc software Chemistry V5.11 where iron under the conditions of flotation precipitates as ferric hydroxide, goethite.

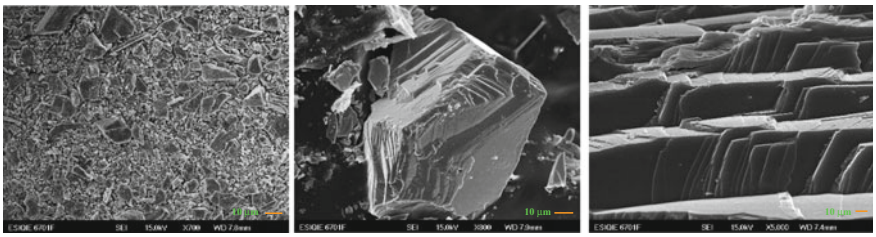

Fig. 1 SEM micrographs, general, and detailed image of the sphalerite particles

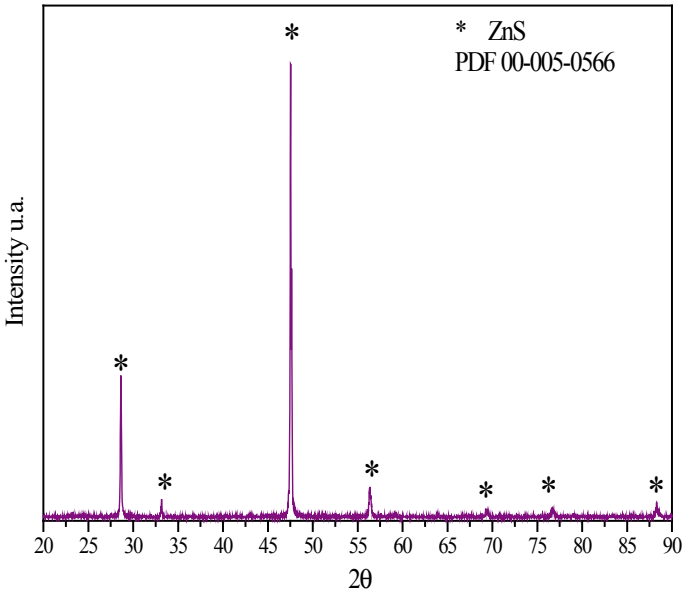

Fig. 2 X-ray diffraction spectra of sphalerite ore

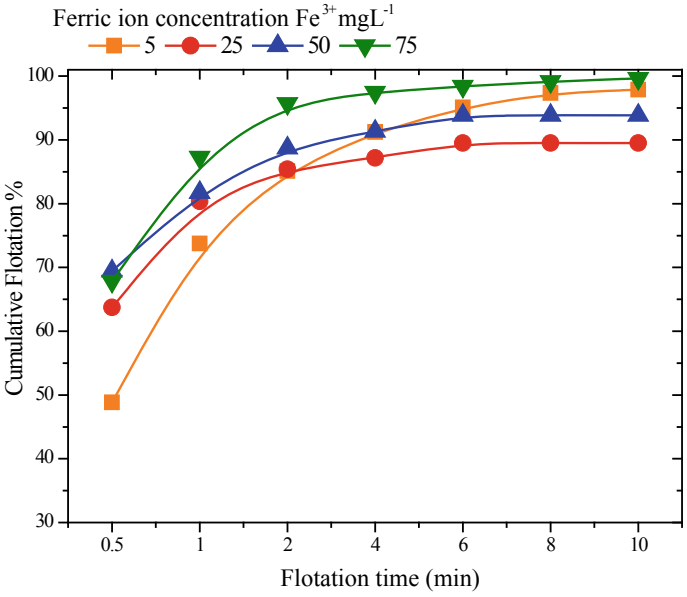

Fig. 3 Percentage of cumulative recovery of ZnS versus flotation time for ferric ion concentrations of 5–75 mgL^{-1}

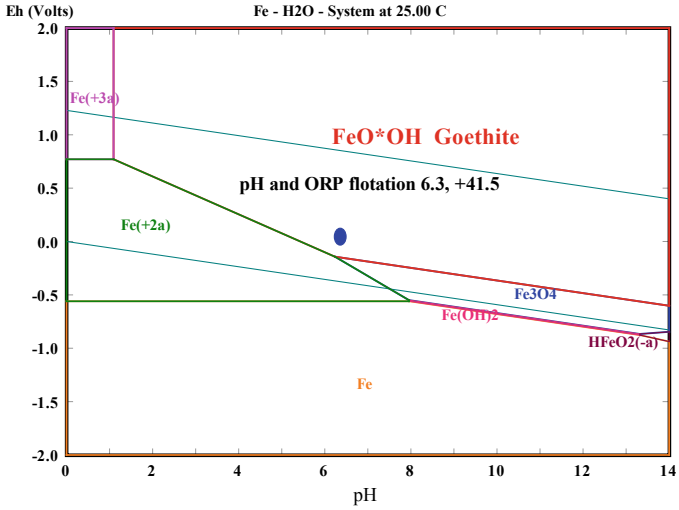

Fig. 4 Diagram of Eh-pH for the Fe–H_2O system for 1.3×10^{-3} m of Fe^{+3}

Infrared spectroscopy analysis of the sphalerite solids floated in the first 30 s and 1 min, for tests with 75 mgL^{-1} of ferric ion Fe^{+3}, is shown in Fig. 5. This figure also contains the infrared spectra of sphalerite fresh. The absorption band at around

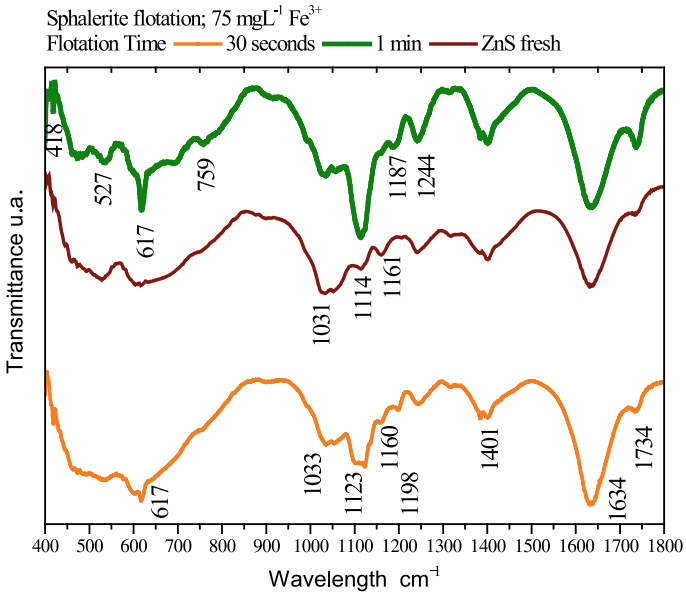

Fig. 5 Infrared spectra of sphalerite, obtained during the flotation with 75 mgL^{-1} of Fe^{3+}, 30 s and 1 min

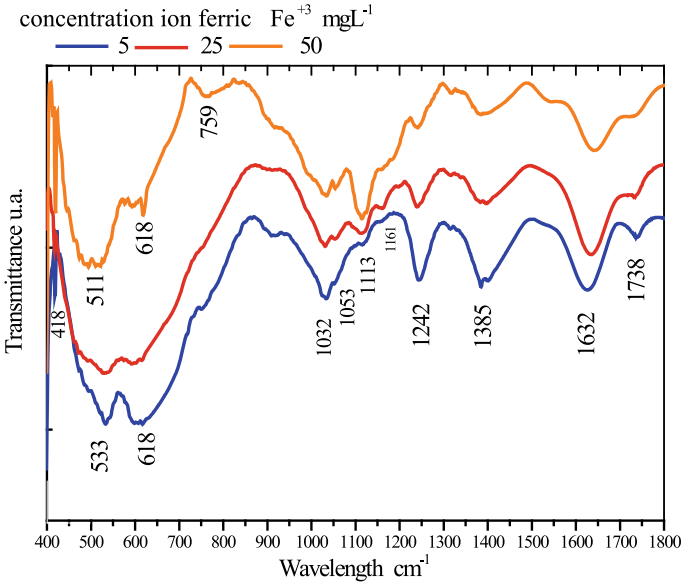

Fig. 6 Infrared spectra of sphalerite, obtained in the flotation with 5, 25, and 50 mgL^{-1} of Fe^{3+}, during 30 s

617 cm^{-1} corresponds to the vibrations Fe–O of the chemical species precipitated goethite iron [10], and it should be mentioned that this band was not detected in the FTIR spectra of the floated sphalerite using as a ferric ion surface activator in concentrations of 5, 25, and 50 mgL^{-1} Fig. 6.

On the other hand, the vibrations bands in 1031, 1244, 1378, and 1737 cm^{-1}, especially for the sphalerite floating in the first 30 s correspond to the Zn–O. Therefore, the presence of the Zn–O and Fe–O vibration bands on the surface of the sphalerite is essential for the success of flotation without a collector. At 1120 cm^{-1}, there is an absorption band corresponding to the free tetragonal sulfate ion, that is, no bonds are formed with the metal on the surface of the mineral.

Conclusions

The mineral used in this investigation is one of the high purity with significant iron contents which are housed in the network parameter. Sphalerite flotation can be carried out successfully without the use of a collector and with 60 mgL^{-1} of frother agent using ferric ion as surface activating reagents from its sulfate salts. The strong binding bands of Zn–O and Fe–O detected in the infrared spectra when flotation is performed with 75 ppm of either Fe^{+3} significantly improve the cumulative recovery of sphalerite. Infrared analysis shows absorption bands of the Zn–O vibration at

1737, 1378, 1244, and 1021 cm^{-1}, in addition, the presence of the main band of the tetragonal sulfate ion at 1115 cm^{-1}, and an absorption band corresponding to Fe–O vibration of goethite at 619 cm^{-1}.

References

1. Wills BA, Finch JA (eds) (2016) Mineral processing technology, 8th edn. Butterworth-Heinemann, Boston, pp 1–29
2. Song S, Lopez Valdivieso A, Reyes Bahena JL, Lara Valenzuela C (2001) Floc flotation of galena and sphalerite fines. Miner Eng 14(1):87–98
3. Shen WZ, Fornasiero D, Ralston J (1998) Effect of collectors, conditioning pH and gases in the separation of sphalerite from pyrite. Miner Eng 11:145–158
4. Harmer SL, Mierczynska Vasilev A, Beattie DA, Shapter JG (2008) The effect of bulk iron concentration and heterogeneities on the copper activation of sphalerite. Miner Eng 21:1005–1012
5. Basilio CI, Kartio IJ, Yoon RH (1996) Lead activation of sphalerite during galena flotation. Miner Eng 9(8):869–879
6. Houot R, Ravenau P (1992) Activation of sphalerite flotation in the presence of lead ions. Int J Miner Process 35:253. https://doi.org/10.1016/0301-7516(92)90037-W
7. Finkelstein NP, Allison SA (1976) Fuerstenau MC (ed) Flotation, A.M. Gaudin memorial volume. SME/AIME, New York, p 414
8. Marouf B, Bessiere J, Houot R, Blazy P (1986) Trans Inst Min Metall 95:C1
9. Leroux M, Rao SR, Finch JA (1987) CIM Bull 80(902):41
10. Nakamoto K (1978) Infrared and Raman spectra of inorganic and coordination compounds, 3rd edn. Wiley, New York

Characterization of Bentonite Beneficiation Residue for Use in Structural Ceramics

Larissa Maia dos Santos, Vinícius Macedo Brito Medeiros, Maria das Graças da Silva Valenzuela, Francisco Rolando Valenzuela Diaz and Orley Magalhães de Oliveira

Abstract In this work, the use of residues from the bentonite mining of the State of Bahia, Brazil, in the manufacture of structural ceramic bodies for application in bricks, blocks, and tiles is studied. The methodology used in this study consisted of the preparation of common clay specimens with the substitution of clay for the bentonite beneficiation residue in 0, 5, and 10% in weight. After the conformation were done ceramic tests based on ABNT standards for tests such as bending stress, retraction, and water absorption. The clay and the residue were characterized by techniques such as DRX. The beneficiation residue showed potential use in the manufacture of structural ceramic products.

Keywords Structural ceramics · Ceramic materials · Beneficiation of bentonite residue

L. M. dos Santos (✉) · V. M. B. Medeiros · O. M. de Oliveira
Instituto Federal de Educação, Ciência e Tecnologia, Campus Vitória da Conquista, Vitória da Conquista, Brazil
e-mail: larissamaia1011@gmail.com

V. M. B. Medeiros
e-mail: vinhtp97@gmail.com

O. M. de Oliveira
e-mail: orleyestudo10@yahoo.com.br

M. das Graças da Silva Valenzuela · F. R. V. Diaz
Escola Politécnica da Universidade de São Paulo, São Paulo, Brazil
e-mail: gracavalenzuela@gmail.com

F. R. V. Diaz
e-mail: frrvdiaz@usp.br

J. Li et al. (eds.), *Characterization of Minerals, Metals, and Materials 2020*,
The Minerals, Metals & Materials Series,
https://doi.org/10.1007/978-3-030-36628-5_45

Introduction

Pottery is one of the oldest artificial materials. According to the National Association of Ceramics Manufacturers, it is estimated that the production of this material already took place about 10,000 years ago. In Brazil, the ceramics industry contributes about 1% of the country's GDP.

Ceramic materials consist essentially of clays [1]. Common clays that vary widely in chemical, mineralogical, and physical composition, so the mechanical properties of ceramic-based products depend on the clay composition and processing conditions [2].

Bentonite is a mineral clay with a high montmorillonite content, which is a type of clay that has expansion properties and high plasticity in the presence of samples [3]. In the process of beneficiation of bentonite, there is a waste production that has a fine grain size and a high silica content, the residues that end up becoming an environmental passive.

Brazil has one of the ten largest bentonite reserves in the world. In Vitória da Conquista, in the Pradoso district, there is a quarry for exploration and processing of this material; this region is located in a transition area between the Caatinga and the Atlantic forest; in this context, these residues are configured as environmental liabilities [4].

Based on the variation of the properties of ceramics from the clay composition, it is possible to help the development of the ceramic material and thus obtain a better quality product with specific characteristics through changes or additions in its formulation [5]. Thus, it is possible to work the characteristics of ceramic materials with the use of mining industry residues, in this specific case, the residues from the processing of bentonite, in order to contribute with new technologies to the construction market, thus reducing it of environmental impacts.

Materials and Methods

Bentonite Residue Characterization

The characterization of the bentonite residue using the clay as a substitute for making ceramic specimens was the initial step of the research. XDR was used to determine the atomic and molecular structure of a ceramic crystal. The results showed that the bentonite residue has main smectic clay minerals, kaolinite, and quartz. In Fig. 1, we can observe the first peak as being of a smectic argilomineral as a function of the base material that generates the residue, bentonite, being a smectic argilomineral. The second peak shows kaolinite as a constituent material, kaolinite is a clay constituent of clays, bentonite is a clay, and kaolinite was expected to be found as part of the main constituents of the residue. The third peak shows quartz as a constituent material,

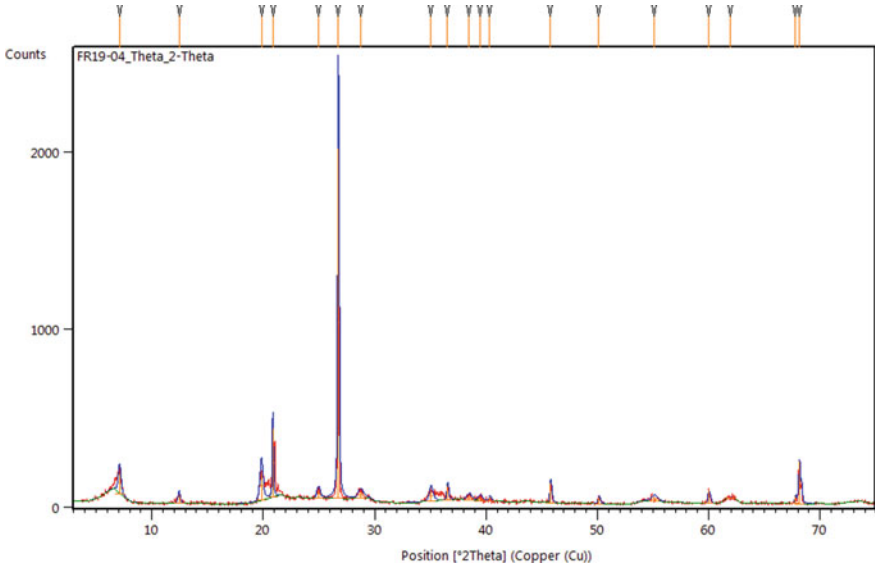

Fig. 1 XDR result. *Source* (Own Authorship)

quartz is one of the crystalline forms of silica; thus, together with the clay, it helps the vitrification process of the silica, besides controlling the shrinkage phenomenon.

Material Preparation

Initially, a clay sample was collected in a ceramics industry in the city of Vitória da Conquista, the Simonassi Ceramics of Bahia. The sample was oven-dried at 110 ± 5 °C. It was then torn apart in a ball mill approximately 2.0 cm in diameter for about twenty minutes.

A sample of the residue from the bentonite beneficiation process was also collected from the Companhia Brasileira de Bentonita (CBB), located in the city of Vitória da Conquista. The sample was oven-dried at 110 ± 5 °C.

Both clay and bentonite residues were sieved through the ABNT 80-mesh sieve (0.18 mm) to reduce particle size and also to prevent organic matter residues from remaining in the sample.

Specimen Preparation

After sieving, 10 aliquots of 15 grams each of clay each were weighed and 10% moisture added. Deionized water was used for this experiment. The clay was homogenized

with moisture manually using containers and spatulas so that the entire aliquot was uniformly moist. After homogenization, the aliquots were placed in a closed metal container in a moisture-holding vat for 24 h.

The specimens were then molded into a rectangular mold with dimensions of $2.03 \times 6.00 \times 0.85$ cm. The mold was greased with a very thin layer of oil to prevent material from adhering to the mold surface. Then, the sample was evenly distributed within the mold and then subjected to uniaxial dry pressing above 4Tf for shaping of the specimens.

After molding the specimens were weighed, measured, and identified for comparison purposes, the process was completed and subjected to natural drying for 24 h. Then, the specimens were placed for drying in the oven at 105 ± 5 °C for 24 h. The final process took place in the muffle furnace where the specimens are burned with a heating speed of 5 °C per minute at temperature levels of 270, 540, and 950 °C.

After the firing process is completed, the ready-made specimens are reweighed, measured, and accommodated in an impact-free location for characterization testing. The same procedure is repeated for aliquots with replacement of clay by bentonite mining residue in percentages of 5 and 10%.

Specification of Specimens

The characterization of the specimens was made by linear shrinkage tests, three-point bending test, and water absorption test.

Linear Shrinkage Test

This test consists of obtaining the difference in the width, length, and height dimensions of the clay specimens after molding and immediately after firing.

Three-Point Bending Test

After the firing process, the specimens were submitted to the three-point bending test in a hand press with the application of a force until the state of rupture of the material. With this data, it is possible to calculate the flexural strength through Eq. (1).

$$\sigma_{RF} = \frac{3 * F * L}{2 * b * d^2} \tag{1}$$

where F = applied force (N), L = distance between supports (m), b = specimen width (m), and d = specimen thickness (m).

Water Absorption Test

The ceramic specimens were immersed in a container with water for a period of 24 h, after which the specimens were removed from the water and superficially dried to lose excess water. The wet specimens were weighed, thus obtaining the wet mass (Mu) and then placed in the oven at 110 ± 5 °C for 24 h for their complete drying. Again the specimens were weighed thus obtaining the dry mass (Ms). The percentage absorption rate of water is given following equation piece.

$$\text{Absorption} = \frac{\text{Mu} - \text{Ms}}{\text{Ms}} * 100 \quad (2)$$

Results and Discussion

Shrinkage on Drying and Burning of Specimens After Sintering

Tables 1, 2, and 3 show the shrinkage results after the firing process at 950 °C.

It is noticed that in the specimens without the replacement of clay by the residue from the bentonite processing, the average weight variation after drying is 20.5%. For specimens with 5% and 10% substitutions, the percentage weight variation was

Table 1 Retraction after sintering of clay specimens with 0% incorporation of bentonite residue

Sample	Before the burn		After burning		Percentage change	
	Weight (g)	Length (m)	Weight (g)	Length (m)	Weight (g)	Length (m)
1	16.284	6.04	12.886	2.01	20.87	2.98
2	16.382	6.03	12.891	1.98	21.31	2.82
3	16.337	6.03	12.901	1.98	21.03	2.99
4	16.059	6.03	12.843	1.99	20.03	2.82
5	16.339	6.03	12.964	2.01	20.66	2.82
6	16.446	6.03	12.978	2.00	21.09	2.82
7	16.229	6.03	12.869	2.00	20.70	2.99
8	16.015	6.04	12.933	2.01	19.24	2.98
9	16.064	6.03	12.931	1.99	19.50	2.99
10	16.182	6.03	12.897	1.99	20.30	2.82
Average	*16.23*	*6.03*	*12.91*	*2.00*	*20.47*	*2.90*

(*Source* Own Authorship)

Table 2 Retraction after sintering of clay specimens with 5% incorporation of bentonite residue

Sample	Before the burn		After burning		Percentage change	
	Weight (g)	Length (m)	Weight (g)	Length (m)	Weight (g)	Length (m)
1	16.28	6.03	12.93	5.83	20.61	3.32
2	16.11	6.03	12.87	5.83	20.09	3.32
3	16.17	6.03	12.85	5.83	20.50	3.32
4	16.24	6.03	12.90	5.84	20.57	3.15
5	16.20	6.05	12.82	5.82	20.87	3.80
6	16.29	6.03	12.93	5.84	20.61	3.15
7	16.10	6.03	12.86	5.83	20.08	3.32
8	16.09	6.03	12.88	5.83	19.96	3.32
9	16.17	6.03	12.92	5.82	20.07	3.48
10	16.06	6.03	12.79	5.83	20.32	3.32
Average	*16.17*	*6.03*	*12.88*	*5.83*	*20.37*	*3.35*

(*Source* Own Authorship)

Table 3 Retraction after sintering of clay specimens with 10% incorporation of bentonite residue

Sample	Before the burn		After burning		Percentage change	
	Weight (g)	Length (m)	Weight (g)	Length (m)	Weight (g)	Length (m)
1	15.926	6.03	12.664	5.83	20.48	3.32
2	16.155	6.03	12.726	5.83	21.23	3.32
3	15.931	6.03	12.676	5.83	20.43	3.32
4	16.123	6.04	12.726	5.84	21.07	3.31
5	15.992	6.04	12.699	5.84	20.24	3.31
6	15.939	6.03	12.658	5.84	20.58	3.15
7	16.111	6.03	12.775	5.83	20.83	3.32
8	16.071	6.03	12.767	5.83	20.56	3.32
9	16.131	6.03	12.724	5.83	21.12	3.32
10	16.052	6.03	12.645	5.84	21.22	3.15
Average	*16.04*	*6.03*	*12.71*	*5.84*	*20.78*	*3.28*

(*Source* Own Authorship)

20.4% and 20.8%, respectively. The weight variation between the different percentages of waste substitution is very small, which shows that the increase of the residue does not interfere with this property.

As for the variation of dimensions, the specimens with 0% of residue replacement presented, in their length, an average retraction of 2.9%. For the percentages of 5 and 10%, the average retraction was 333%. The shrinkage increase, although very small, can be explained by the behavior of the bentonite base element, the montmorillonite,

which tends to absorb moisture causing its swelling; consequently, after burning, there is greater shrinkage of the material. The shrinkage, being in small proportions, does not tend to damage the final ceramic product. In large proportions, shrinkage generates tensions that can lead to the appearance of defects that compromise the quality of the final product.

Three-Point Bending

Observing the results of this test, shown in Table 4, it is clear that the average flexural strength of the specimens with 0% replacement is 6.16 MPa. In samples with 5% and 10% of clay substitution by the bentonite mining residue, the average flexural strength observed is, respectively, 4.74 MPa and 5.25 MPa.

It is observed that there is a decrease in flexural strength for the 5% percentage of clay substitution by bentonite beneficiation residue; however, the resistance has an increase for specimens with 10% replacement compared to those of 5%, indicating that possibly a replacement increase above the 10% range would improve material strength.

When comparing the results related to shrinkage and flexural strength, it is clear that specimens with 5% replacement present negative results to these properties when compared to specimens with 0% addition. However, when comparing the material

Table 4 Tensile strength of specimens after firing

Sample	0% replacement		5% replacement		10% replacement	
	Burst stress (N)	Flexural strength (MPa)	Burst stress (N)	Flexural strength (MPa)	Burst stress (N)	Flexural strength (MPa)
1	64	6.43	50	4.73	53	5.06
2	61	6.03	50	4.51	68	6.34
3	Invalid data	–	Invalid data	–	47	4.51
4	59	5.98	47	4.45	53	4.88
5	54	5.59	46	4.26	50	4.74
6	75	7.57	57	5.24	54	5.17
7	65	6.55	48	4.43	62	5.92
8	51	4.97	46	4.22	51	4.68
9	66	6.68	53	4.86	65	5.97
10	59	5.64	64	5.94	Invalid data	–
Average	*61.56*	*6.16*	*51.22*	*4.74*	*55.89*	*5.25*

(*Source* Own Authorship)

Table 5 Water absorption rate results

Sample	0% replacement		5% replacement		10% replacement	
	Mu (g)	Ms (g)	Mu (g)	Ms (g)	Mu (g)	Ms (g)
1	7.14	6.02	7.30	6.09	7.39	6.20
2	7.44	6.27	6.54	5.44	6.95	5.81
3	8.11	6.89	8.20	6.86	7.82	6.55
4	7.98	6.65	8.85	7.40	8.18	6.91
Average absorption rate	*1874%*		*198%*		*1915%*	

(*Source* Own Authorship)

with 5 and 10% replacement, the 10% specimens have positive shrinkage and flexural strength characteristics.

Due to the characteristics of bentonite, the residual material used tends to absorb more moisture, thus presenting greater shrinkage when this moisture is removed. On the other hand, the probable high silica content causes this material, when subjected to high temperatures, greater vitrification, and therefore greater resistance, thus causing a balance between strength and shrinkage in certain percentages, that is, in an optimum percentage.

Water Absorption

Water absorption is a property of the ceramic body; it is a direct function of the porosity and permeability of the ceramic part. Water absorption has a direct influence on the material performance in terms of breaking load, wear resistance, among other factors. Table 5 shows the data obtained from the water absorption test.

The results show that the average absorption shrinkage rate for the 0% replacement specimens is 18.74%, while in the 5% and 10% replacement specimens, the water absorption rate is, respectively, 19.8% and 19.15%. Note that when the bentonite residue is replaced the water absorption rate increases, that is, there is a higher porosity in the ceramic material; however, with the increase of the percentage of clay substitution by the residue, the water absorption rate begins to reduce, thus indicating the possibility of an optimum percentage maintaining or improving the rate of water absorption, thus making the bentonite residue clay composition an applicable material.

Conclusions

The specimens with 5 and 10% substitution presented negative shrinkage characteristics, resistance, and water absorption when compared to the specimens with 0% substitution, because the quantity of silica present in the sample was not able to cause sufficient vitrification to compensate for shrinkage and excessive porosity and consequently loss of strength. However, when comparing specimens with clay substitution (5 and 10%), the best indices of resistance, shrinkage, and water absorption were presented in specimens with higher percentage.

By replacing more clay with the waste material, the amount of silica in the total mass is increased, favoring vitrification and, consequently, resistance, balancing the shrinkage effects, and improving water absorption rates. Due to the positive resistance, shrinkage, and water absorption characteristics of the 10% replacement specimens compared to the 5% replacement specimens, it can be assumed that there is an optimal replacement percentage, so it is possible make use of the clay composition with an optimal percentage of bentonite residue for the production of structural ceramic materials.

New research is being done with increasing the percentage of clay substitution to find the optimum percentage content and thus finding a ceramic product with attractive properties for the construction industry in tandem with the reduction in environmental liabilities caused by the mining industry.

References

1. Hagemann SE (2011) Materiais de construção básicos. [*S. l.*]: Instituto Federal Sul-rio-grandense. Available in http://tics.ifsul.edu.br/matriz/conteudo/disciplinas/_pdf/apostila_mcb.pdf. Access in 20 Mar 2019
2. Pinheiro BCA, Holanda JNF (2010) Efeito da temperatura de queima em algumas propriedades mecânicas de cerâmica vermelha. Cerâmica, UENF - Campos dos Goytacazes. Available in http://www.scielo.br/pdf/ce/v56n339/a0556339.pdf. Access in 3 maio 2019
3. Silva ARV, Ferreira HC (2008) Argilas bentoníticas: conceitos, estruturas, propriedades, usos industriais, reservas, produção e produtores/fornecedores nacionais e internacionais. Revista Eletrônica de Materiais e Processos, [*S. l.*], 22 ago. Available in http://www2.ufcg.edu.br/revista-remap/index.php/REMAP/article/viewFile/77/91. Access in 8 maio 2019
4. Jesus RM (2012) Análise socioambiental do processo produtivo do minério bentonita no distrito de pradoso: Vitória da Conquista-BA. Universidade Federal da Bahia. Available in https://repositorio.ufba.br/ri/bitstream/ri/19785/1/Roberta%20Batista%20de%20Jesus.ppd. Access in 28 abril 2019
5. Andrade FLF (2009) Estudo da formulação de massa cerâmicas provenientes da região do Seridó-RN para fabricação de telhas. Tese (Mestrado em engenharia mecânica) - Universidade Federal do Rio Grande do Norte, [*S. l.*], 2009. Available in https://repositorio.ufrn.br/jspui/handle/123456789/15569. Access in 03 maio 2019

Characterization of Clay Mix with Incorporation of Granite Waste for the Production of Ceramic Tiles

A. R. G. Azevedo, D. Cecchin, N. F. Luiz, V. F. Cruz, M. T. Marvila, E. B. Zanelato, S. N. Monteiro, G. Morais and J. Alexandre

Abstract The municipality of Cachoeiro do Itaperimirim, located in Espírito Santo, has a well-established ornamental stone industry, being one of the main cutting and extraction poles of this material. However, industry stimulation caused the waste produced to be disposed of in inappropriate places, threatening the environment and human life. In the present work, a study was carried out aiming at the reuse of wastes as raw material for red ceramics, from chemical, physical, and mineralogical analyses, besides the characterization of the samples regarding the granulometry, plasticity, and basic properties, in order to better investigation of these materials. The preliminary study showed that, in general, the essentially kaolinite ceramic mass tends to enrich with the addition of ornamental rock wastes due to the presence of flux oxides.

Keywords Ceramic · Granite waste · Tiles · Clay

A. R. G. Azevedo (✉) · D. Cecchin · N. F. Luiz
TER—Department of Agricultural Engineering and Environment, UFF—Federal Fluminense University, Rua Passo da Pátria, 341, Niterói, Rio de Janeiro 24210-240, Brazil
e-mail: afonso.garcez91@gmail.com

A. R. G. Azevedo · E. B. Zanelato
IFF—Federal Institute Fluminense, DIRINF—Directorate of Infrastructure Rectory, Rua Cel. Valter Kramer, 357—Parque Vera Cruz, Campos dos Goytacazes, Rio de Janeiro 28080-565, Brazil

V. F. Cruz
Department of Animal Science, University of Évora, Largo dos Colegiais 2, 7000 Évora, Portugal

M. T. Marvila · E. B. Zanelato · G. Morais · J. Alexandre
LECIV—Civil Engineering Laboratory, UENF—State University of the Northern Rio de Janeiro, Av. Alberto Lamego 2000, Campos dos Goytacazes, Rio de Janeiro 28013-602, Brazil

S. N. Monteiro
Department of Materials Science, IME—Military Institute of Engineering, Square General Tibúrcio 80, Rio de Janeiro 22290-270, Brazil

J. Li et al. (eds.), *Characterization of Minerals, Metals, and Materials 2020*,
The Minerals, Metals & Materials Series,
https://doi.org/10.1007/978-3-030-36628-5_46

Introduction

In general, all industrial activities have impacts on the environment, caused by the excessive use of non-renewable raw materials and the increased production of waste that is incorrectly disposed of in the environment. The biggest challenge of the twenty-first century is finding solutions to these problems in the industrial sector.

One of the main sectors that generate waste is ornamental rock, because its disposal is often problematic in settling tanks or landfills, often without component removal treatment processes [1].

In Brazil, the export of ornamental rock from January to May 2019, a total of 407.5 million dollars to the production process generates 80% of waste from extraction to polishing [2].

The main pole of ornamental rocks in the country is located in the municipality of Cachoeiro de Itapemirim, in the state of Espirito Santo, where much of its production is destined for exports. Its production accounted for 76.2% of the total volume of Brazilian chemical substances in 2017, and also for less than 65% by volume of total quantities of ornamental rocks in the Brazil [2].

In the use of ornamental rocks in the construction sector, it is necessary to dismantle its blocks to result in mud wastes. According to NBR 10004 [3], these mud-forming wastes are classified in class II A and are called non-inert wastes. This mud is usually deposited in yards, which can contaminate rivers, lakes, and streams [4].

Given this scenario, it is necessary to reuse waste more efficiently to reduce its impact on the environment and minimize its disposal. Since the rock waste has a composition favorable for incorporation with a ceramic mass, this fact makes the waste favorable for this case, as it consists mainly of silicon oxide (SiO_2), aluminum oxide (Al_2O_3), calcium oxide (CaO), iron oxide (Fe_2O_3), and alkaline oxides (K_2N e Na_2O) [5].

Several studies show that the addition of ornamental rocks in the ceramic masses [4–7] has great potential for this incorporation, varying according to the compositions analyzed, but surpassing the technological properties indicated by the Brazilian technical norms of the tiles, depending on the burning temperature.

Thus, this work is focused on the physical, mineralogical, and chemical characterization of clays used industrially for the production of ceramic tiles, aiming to evaluate their suitability to this ceramic process.

Materials and Methods

The clay used in this study is provided by Campos dos Goytacazes-RJ, using a local ceramic. 40 kg of clay was collected inside ceramics, in its natural state. In addition to clay, an ornamental rock waste was collected in the municipality of Cachoeiro de Itapemirim-ES-Brazil, and 20 kg of mud-shaped wastes were collected, which result in a significant decrease in mass after drying.

Table 1 Composition of ceramic masses (% by weight)

Sample	Ceramic mass	Waste
Clay mixed with 0% waste (AM0)	100	0
Clay mixed with 5% waste (AM5)	95	5
Clay mixed with 10% waste (AM10)	90	10
Clay mixed with 15% waste (AM15)	85	15

Particle size, Atterberg limits, and humidity of the material were characterized. These tests were performed for clay as well as for waste, except the Atterberg limits that were not possible with rock waste.

Particle size analysis of the raw materials was performed by sieving and sedimentation according to NBR 7181 (2016) [8]. Initially, the materials were sieved with up to 10-mesh sieves (coarse sieving) and also up to 200-mesh sieves (fine sieving). For the sedimentation test, as the raw materials used in the 200-mesh sieve, this amount was sufficiently reduced for the addition of sodium hexametaphosphate solution with sodium carbonate to disaggregate particles.

The determination of the moisture content was made by the gravimetric method; the wet sample was weighed and then submitted to oven drying at ±110 °C. The determination of the real grain density was performed according to NBR 6457 (ABNT, 1986) [9] and NBR 6508 (ABNT, 1984) [10], where a pycnometer was used.

The material used at the Atterberg boundaries was torn apart and passed through the 0.42-mm aperture sieve. The plasticity limit test was performed according to NBR 7180 (ABNT, 2016) [11], while the liquidity limit was performed according to NBR 6459 (1984) [12].

The chemistry of the clays and the waste was characterized using X-ray fluorescence spectroscopy and the SHIMADZU EDX-700 equipment, performed at the Civil Engineering Laboratory—LECIV of UENF.

The test result is aimed to establish a reduced model, which consists in the optimization of the most appropriate mixture of raw materials: clays and rock wastes. Compositions with different waste percentages were prepared for each mixed clay, as masses had 0, 5, 10, and 15% waste for each clay weight percentage, as shown in Table 1, these compositions were characterized and burned at three temperatures, 850, 950, and 1050 °C, and subsequently subjected to technological tests. The tests performed in the characterization were linear variation, apparent porosity, water absorption, apparent specific mass, and flexural strength at three points.

Results

The analysis of the particle size of the clays and the waste (Table 2) showed large quantities of particles smaller than 2 μm in diameter, being the mixed clay presented 58.3% of particles with this diameter, and when summed the amount of silt and clay,

Table 2 Soil grain size

Percentage particle size								
Sample	Boulder			Sand			Silt	Clay
	Thick	Medium	Fine	Thick	Medium	Fine		
Clay	–	–	–	0.6	6.0	15.8	19.2	58.3
Waste	–	–	–	–	–	5.2	60.7	34.1

we have a total of 77.5%. The waste has 34.1% of clay and 60.7% of silt. The result of particle size analysis means that the raw materials are formed by the fraction of clay and silt which are the major part, followed by the fine sand fractions, and in all materials, the percentage of boulders present was 0%.

Already in Fig. 1 can be observed the particle size distribution in terms of curve, after the screening test, thus determining a general characteristic of the clay studied for this composition, according to the Brazilian normative standard.

The plasticity limit determines the minimum amount of water for the plastic state to be achieved, and the liquidity limit determines the minimum amount of water for the material to reach a mud consistency. Clay presented a liquidity limit of 44.0% and a plasticity limit of 25.3%; this is due to the granulometric behavior of the clay, since the smaller the surface area of the material, the higher the water absorption. And the plasticity index of 18.7%, being suitable for ceramic masses, is between 18.0 and 23.0% [13], and when above 15.0% are considered highly plastic [14]; in another study [15], the liquidity limit varies between 30 and 60.0%, the plasticity limit between 15.0 and 30.0%, and the plasticity index between 10.0 and 30.0%.

The real specific mass of the grains is presented in Table 3, and it is possible to observe that the higher the percentage, heavier waste will be the piece produced.

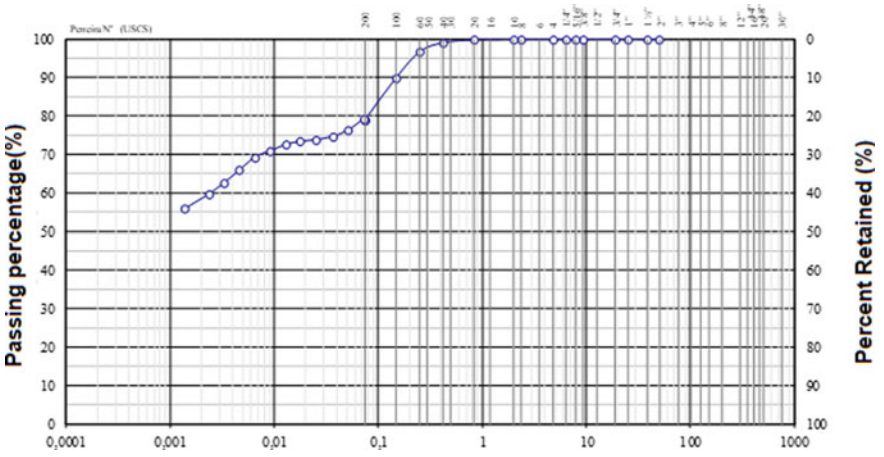

Fig. 1 Clay particle size curve

Table 3 Specific mass of ceramic masses

Ceramic mass	Specific mass (g/cm^3)		
	850 °C	950 °C	1050 °C
AM0	1.45	1.46	1.49
AM5	1.50	1.52	1.56
AM10	1.52	1.57	1.59
AM15	1.60	1.65	1.68

Table 4 Chemical characterization of raw materials (% by weight)

Raw materials	SiO_2	Al_2O_3	Fe_2O_3	K_2O	TiO_2	SO_3	CaO
Clay mix	56.46	34.01	3.31	2.26	1.42	1.78	0.66
Waste	86.22	7.15	0.26	2.15	0.10	1.59	2.34

Table 4 shows the chemical compositions of clays and rock wastes, and it can be seen that all raw materials consist essentially of silicon oxide (SiO_2) and aluminum oxide (Al_2O_3), corresponding to 90.47% in the clay and 93.37% in the waste, and this means that this clay comes from metamorphic rocks. The least prevalent in both raw materials are iron oxide, potassium oxide, titanium dioxide, and sulfur oxide.

The incorporation of rock wastes in clay tends to enrich the mass with flux oxides (sodium oxide), because in high temperatures, they contribute to a greater synthesis and densification of the pieces [16].

Figure 2 shows the crystalline phases of quartz, kaolinite, mica/illite in the mixed clay sample, confirming the results of the chemical analysis. Through this analysis,

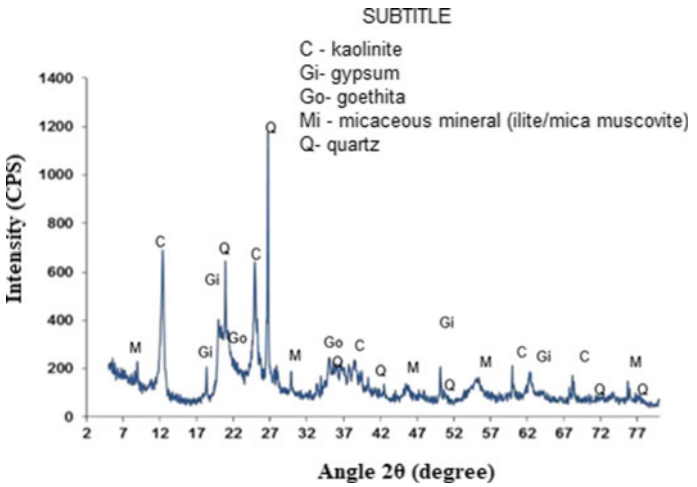

Fig. 2 X-ray diffractometry of ceramic masses

it is possible to verify the presence of silicon oxide in large quantity, which indicates reduction in shrinkage and deformation and support to the ceramic body, and from it can be classified the mixed clay with a tendency to be strong [17].

This clay has a higher amount of aluminum oxide, which indicates greater plasticity and mechanical strength [18, 19]. The relationship between these oxides indicates that the predominant clay is kaolinite, which has difficult dispersion in water and moderate plasticity, being commonly verified by researchers from the region. The illicit peaks of Fig. 2 act as flux oxides [5].

Conclusion

The clay particle size distribution seem to be typical for material used in the production of red ceramics, with a high percentage of clay fraction and the waste with a high percentage of silt fraction, which makes them suitable for incorporation and use in the manufacture of red ceramic pieces. Chemical and mineralogical analysis shows that the clay is typically kaolinitic ($SiO_2 + Al_2O_3 = 90.47\%$) Campos dos Goytacazes region with presence of flux oxides ($CaO = 0.66\%$) and that the rock waste has values above 90%.

The characterization allows us to predict, based on the knowledge of the behavior of ceramics, through the firing cycles, the suitability of the raw materials for tile production. This is because ornamental rock waste has promising properties in the manufacture of these products.

Therefore, it can be concluded that the samples have potential for use as raw material in the red ceramic industry due to their mineralogical composition, convenient particle size distribution, and highly plastic performance, favoring material conformation, burning, and final material performance.

Acknowledgements The authors thank the Brazilian agencies: CNPq, CAPES, and FAPERJ for the support provided to this investigation.

References

1. Sato VY, Galina APL, Teixeira JESL (2018) Contribution to the rheological study of cementitious pastes with addition of wastes from the processing of ornamental rocks. Rev IBRACON Estruturas e Mater 11(6):1284–1307. https://doi.org/10.1590/s1983-41952018000600007
2. Brazilian Association of Ornamental Rocks (2019) In: Exportações e Importações Brasileiras de Rochas. http://www.abirochas.com
3. Brazilian Association of Technical Norms (2004) NBR 10004—solid waste—classification
4. Moreira JMS, Manhaes JPVT, Holanda JNF (2005) Reaproveitamento de resíduo de rocha ornamental proveniente do Noroeste Fluminense em cerâmica vermelha. Cerâmica 51(319):180–186. https://doi.org/10.1590/S0366-91320050003000002

5. Taguchi SP, Santos JC, Gomes TM, Cunha NA (2014) Avaliação das propriedades tecnológicas de cerâmica vermelha incorporada com resíduo de rocha ornamental proveniente do tear de fio diamantado. Cerâmica 60(354):291–296. https://doi.org/10.1590/S0366-69132014000200020
6. Rodrigues DV, Xavier GC, Saboya F, Maia PCA, Alexandre J (2012) Durabilidade de peças cerâmicas vermelhas com adição de rejeito de rocha ornamental isenta de granalha. Cerâmica 58(347):286–293. https://doi.org/10.1590/S0366-69132012000300003
7. Souza AJ, Pinheiro BCA, Holanda JNF (2011) Efeito da adição de resíduo de rocha ornamental nas propriedades tecnológicas e microestrutura de piso cerâmico vitrificado. Cerâmica 57(342):212–218. https://doi.org/10.1590/S0366-69132011000200013
8. Brazilian Association of Technical Norms (2016) NBR 7181: particle size analysis—soil
9. Brazilian Association of Technical Norms (1986) NBR 6457: soil samples—preparation for compaction assays and characterization assays
10. Brazilian Association of Technical Norms (1984) NBR 6508: grains of soil passing through the 4.8 mm sieve—determination of specific mass
11. Brazilian Association of Technical Norms (2016) NBR 7180: determination of plasticity limit—test method
12. Brazilian Association of Technical Norms (2016) NBR 6459: determination of liquidity limit—test method
13. Dondi M (2003) Technological characterization of clay materials: experimental methods and data interpretation. Int Ceram J 55–59
14. Maestrelli SC, Roveri CD, Nunes AGP, Faustino LM, Aielo GF, Pinto LPA, Manochio C, Cal TML, Ribeiro FF, Mariano NA (2013) Estudo de caracterização de argilas não plásticas da região de Poços de Caldas, MG. Cerâmica 59(350):242–248. https://doi.org/10.1590/S0366-69132013000200008
15. Santos PS (1992) Ciência e Tecnologia das Argilas. Publishing Company Edgard Blucher Ltda, São Paulo
16. Azevedo ARG, Alexandre J, Zanelato EB, Marvila MT (2017) Influence of incorporation of glass waste on the rheological properties of adhesive mortar. Constr Build Mater 148:359–368
17. Xavier GC, Azevedo ARG, Alexandre J, Monteiro SN, Pedroti LG (2019) Determination of useful life of red ceramic parts incorporated with ornamental stone waste. J Mater Civ Eng 31:328–335. https://doi.org/10.1061/(ASCE)MT.1943-5533.0002590
18. Marvila MT, Alexandre J, Azevedo ARG, Zanelato EB, Xavier GC, Monterio SN (2019) Study on the replacement of the hydrated lime by kaolinitic clay in mortars. Adv Appl Ceram 10:20–30. https://doi.org/10.1080/17436753.2019.1595266
19. Azevedo ARG, Alexandre J, Picanço RO, Souza RC, Zanelato EB, Monteiro SN (2015) Evaluation of the industrial raw material used for ceramic production in Sa-o Jose- de Uba-, State of Rio de Janeiro, Brazil. Mater Sci Forum (Online) 820:3–7

Characterization of Hydrogels for Release of Cosmetic Assets Containing Nanoemulsions of Mandellic Acid in Different Concentrations of Pseudoboehmite

Leila Figueiredo de Miranda, Isabella Tereza Ferro Barbosa, Terezinha Jocelen Masson, Antonio Hortêncio Munhoz Junior, Leonardo Gondim de Andrade e Silva and Aleksandra Aparecida Arceno Gonçalves

Abstract Hydrogel is a gel formed by a three-dimensional network of hydrophilic polymers that are used as advanced asset release systems with good biocompatibility. The use of ionizing radiation to obtain hydrogels promotes cross-linking with the concomitant sterilization of the hydrogels. Aiming at the release of the mandelic acid (an active cosmetic), hydrogels were prepared using different concentration of poly(N-vinyl-2-pyrrolidone) (PVP), poly(ethylene glycol) (PEG) and agar containing nanoparticles of the pseudoboehmite, mandelic acid and Palmarosa and Rosa Mosqueta oils nanoemulsions, submitted to irradiation dose of 25 kGy. Hydrogels containing 7.5 wt% PVP showed better absorption, slip, odor results, and those with 10 wt% PVP were found to be inadequate. Nanoemulsions were characterized by acidity, density and optical microscopy; hydrogels samples were put under isothermal dehydration with air entrainment and dehydration was examined as a function of time. The results showed that the composition of hydrogels is stable, and the increase of the concentration of pseudoboehmite in hydrogels sample containing Palmarosa oil suffers less dehydration and those containing the two oils showed an increase in dehydration. The hydrogels obtained with 7.5 wt% of PVP and 3 wt% of pseudoboehmite, Rosa Mosqueta vegetable oil and mandelic acid are most suitable to be used in cosmetic products.

Keywords Release of cosmetic assets · Pseudoboehmite · Hydrogel · Poly(N-vinyl-2-pyrrolidone) (PVP) · Mandelic acid

L. F. de Miranda (✉) · I. T. F. Barbosa · T. J. Masson · A. H. Munhoz Junior
Mackenzie Presbyterian University, 930 Consolação St, Sao Paulo, SP 01302-907, Brazil
e-mail: leila.miranda@mackenzie.br

I. T. F. Barbosa · A. A. A. Gonçalves
Senac University Center, 823 Eng. Eusébio Stevaux Ave, Sao Paulo, SP 04696-000, Brazil

L. G. de Andrade e Silva
Nuclear and Energy Research Institute (IPEN/CNEN—SP), 2242 Prof. Lineu Prestes Ave, Sao Paulo, SP 05508-000, Brazil

J. Li et al. (eds.), *Characterization of Minerals, Metals, and Materials 2020*,
The Minerals, Metals & Materials Series,
https://doi.org/10.1007/978-3-030-36628-5_47

Introduction

Anti-aging cosmetics contain active ingredients to suit the physiological and anatomical conditions of the skin in their individual variations. Care with its functional and anatomical integrity allows effective intervention with the objective of aesthetic improvement of the skin [1].

For the decades, the skin has been used as a route of administration of dermatologically active substances, that is, with pharmacological action in the skin tissues. In these therapies, it is considered that drug molecules diffuse into the tissue at the site of application to produce their therapeutic effects [2].

Hydrogels represent advanced asset release systems, capable of offering advantages over conventional pharmaceutical forms by having good biocompatibility, adequate mechanical properties and promoting controlled release of assets [3].

Hydrogel based on PVP, obtained by ionizing radiation, is widely used as a biomaterial because it has no toxicity and the presence of agar in small concentrations favors the gelation of the solution, providing physical form before cross-linking [4]. Ionizing radiation is widely used in the industry for sterilization at a minimum dose of 25 kGy [5].

In order to improve the performance of cosmetic and dermatological products emerge nanoemulsion technology. This consists of placing assets in carrier systems used for controlled release.

Various materials, such as polymeric, ceramic, lipid, protein among others [6], can form these carriers.

Pseudoboehmite type fine ceramics, fall into the non-toxic category [7, 8], obtained by the sol gel process, have advantages such as low cost, easy handling and enable the obtaining of nanoscale materials adding different properties compared to conventional materials [9].

In view of these considerations, this paper aims to contribute to the cosmetic area by presenting hydrogels containing concentrations of 5, 7.5 and 10% by mass of PVP, submitted to 25 kGy dose by ionizing radiation, maintaining the concentration of 3 wt% PEG and 1 wt% agar containing anti-aging cosmetic active and mandelic acid. This acid promotes the renewal of the epidermis, causing slight peeling, slight burning and flushing, acting on the removal of superficial spots, helping the skin deriving from skin aging [10].

Experimental

Materials

The used reagents were the following: aluminum nitrate $Al(NO_3)_3$, supplied by Dinâmica LTDA; ammonium hydroxide (NH_4OH), supplied by Audaz Reagente

Tecnológico; polyvinyl alcohol, supplied by Bandeirante Química; poly(N-vinyl-2-pyrrolidone) (PVP), supplied by GAF Co.; poly(ethylene glycol), supplied by Oxiteno Brasil; agar, supplied by Oxide; and mandelic acid, Palmarosa and Rosa Mosqueta oils and Tween 20, supplied by Labsynth.

Methods

Obtainment and Characterization of Base-Hydrogels

Different hydrogel types containing different concentrations of PVP (HB1—10 wt%, HB2—7.5 wt%, HB3—5 wt%) and at 25 kGy radiation doses were prepared, maintaining the concentrations of PEG (3 wt%) and agar (1 wt%) based on literature studies [11]. These hydrogels were produced for the purpose of defining the most suitable composition for the final product. To obtain the hydrogels, the reagents were previously dissolved in water and hot mixed. The concentration of the components in the final solution was adjusted by adding sufficient water to achieve 100 mass% (Fig. 1).

After sample preparation, they were irradiated at room temperature in an electrostatic electron accelerator of the "Radiation Dynamics" model "Dynamitron" with a maximum energy of 1.5 MeV, maximum current of 15 mA and dose of 11.3 kGy/s to promote cross-chain cross-linking. The samples were irradiated at 25 kGy dose.

After obtaining the physical gel, pH and density were determined at room temperature. Dehydration was determined as a function of time every 30 days, and the samples were kept in their original packaging at room temperature.

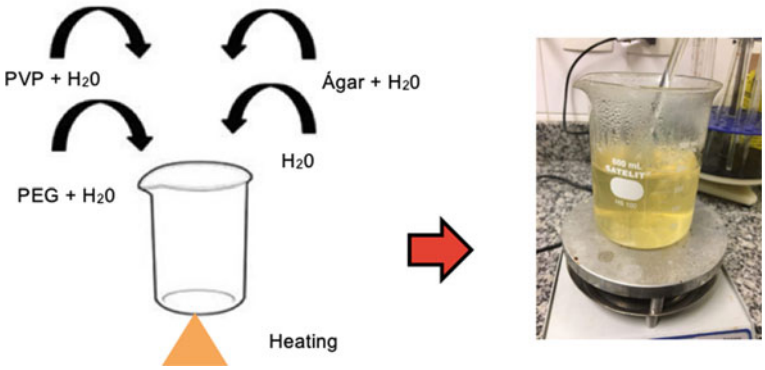

Fig. 1 Preparation of hydrogels

Table 1 Composition of mandelic acid nanoemulsions

Samples	Composition (wt%)				
	Pseudoboehmite (PSB)	Palmarosa (PR)	Rosa Mosqueta (RM)	Mandelic Acid (MA)	Tween 20
A	1.0	7.0	–	2.1	8.8
B	1.0	–	7.0	2.1	8.8
C	3.0	7.0	–	2.1	8.8
D	3.0	–	7.0	2.1	8.8
E	5.0	7.0	–	2.1	8.8
F	5.0	–	7.0	2.1	8.8

The characterization of hydrogels was also obtained through a sensory analysis with a group of 100 people linked to the area of aesthetics and cosmetics, by a probabilistic method not for convenience, and used the Likert scale to evaluate absorption, the slip, the aspect, the odor and feeling of comfort after application.

Obtainment Nanoemulsions

Nanoemulsions were prepared from pseudoboemite (1, 3 and 5 wt%), mandelic acid (2.1 wt%), surfactant, Tween 20 (8.8 wt%) and Palmarosa essential oil (7 wt%) and/or Rosa Mosqueta vegetable oil (7 wt%) presented in Table 1.

Initially, the pseudoboehmite was solubilized in water, and later, the active principle (mandelic acid) was added, and the system was kept under stirring for 30 min and heated to 40 °C (aqueous phase). Tween 20 surfactant (polysorbate) was solubilized in the oil phase (Palmarosa essential oil or Rosa Mosqueta vegetable oil), and the system was stirred for 30 min and heated to 40 °C. The obtained aqueous phase was poured (still heated) onto the oil phase under constant and continuous stirring of 600 rpm on the Solab Model SL-9 magnetic heating stirrer and was kept until cooled to room temperature at 25 ± 3 °C. The prepared emulsion was placed in Eppendorf model 5804R centrifuge at speeds of 1000 rpm, 2500 rpm and 3500 rpm for 15 min. The nanoemulsions obtained were characterized by density and pH before and after thermal stress. The homogeneity and morphology of the dispersion were observed in a Philips series 062698 optical microscope. All slides were analyzed in the 40x objective and recorded through the Opton model 0345 microscopic camera.

Obtainment Hydrogels Containing Different Nanoemulsions

Through the results of the sensorial analysis, the most suitable composition of PVP (7.5% by mass), PEG (3% by mass) and agar (1% by mass) were observed. Thus,

Table 2 Hydrogels with varying addition of different nanoemulsions

Dose	Hydrogels	Nanoemulsions samples (3 mL)	Nanoemulsions samples (3 mL)
25 kGy	HI	–	–
	HII	A	–
	HIII	–	B
	HIV	A	B
	HV	C	–
	HVI	–	D
	HVII	C	D
	HVIII	E	–
	HIX	–	F
	HX	E	F

new hydrogels were prepared keeping the best concentrations and adding different nanoemulsions according to Table 2.

The obtained hydrogels were characterized by isothermal dehydration with air drag, through the forced air circulation and temperature controlled stove, under strictly isothermal conditions at 37 °C, with 50 mL/min synthetic airflow. Dehydration as a function of time was maintained on the same criteria as before.

Results and Discussion

Preparation and Characterization of Base-Hydrogel

The base-hydrogels had a similar viscous appearance, and the HB3 sample (5% PVP-25 kGy) had a consistency not suitable for the final cosmetic product as can be seen in Fig. 2.

The research of sensory analysis on absorption, the slip, the aspect, odor and comfortable feeling after application is presented in Table 3, indicating the sum

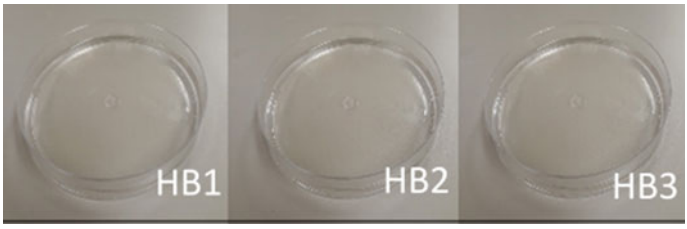

Fig. 2 Base-hydrogels obtained: HB1 (10%PVP-); HB2 (7.5%PVP); HB3 (5%PVP)

Table 3 Satisfaction degree obtained for the evaluated dimensions

Hydrogels	Satisfaction degree of hydrogels (%)					
	Absorption	Slip	Aspect	Odor	Comfortable feeling	Total
HB1	36	71	24	33	52	216
HB2	56	78	48	38	55	275
HB3	45	67	52	38	64	266

Table 4 Variation of dehydration percentage over time after irradiation

	Time (days)							
Dehydration (%)	Hydrogels	30	60	90	120	150	180	210
	HB1	8.77	15.78	23.36	34.01	39.70	45.09	52.69
	HB2	11.26	19.96	31.77	54.26	54.84	58.10	62.91
	HB3	12.29	26.59	40.76	58.53	66.24	74.35	79.51

score of partially satisfied and fully satisfied by the Linkert scale to determine the highest degree of satisfaction of the surveyed population. In this type of treatment, the degree of patient/user satisfaction is important for the continuity of treatment [13].

The pH behavior of the base-hydrogels presented a range from 2.9 to 3.4 decreasing with the decrease of PVP. This determination and control from the cosmetic and/or dermatological point of view are extremely useful, since the skin has a slightly acidic pH, which contributes to the bactericidal and fungicidal protection on its surface [14].

The density of the base-hydrogels remained stable, very close, even with PVP concentration variations (5, 7.5 and 10%) and the values obtained were slightly below 1.00 g cm^{-3}.

Dehydration as a function of time was followed for all formulations according to Table 4 and Figs. 3 and 4 showing the variation of the percentage of dehydration as a function of time after irradiation.

The hydrogels obtained were observed to have a viscous appearance;

All samples were observed of same aspect and samples HB3 (5% PVP-25 kGy) had a consistency not suitable for the final cosmetic product. The hydrogel HB2 formulation showed a prevalently elastic rheological behavior, as recommended in the literature [13].

Nanoemulsions Characterization

The macroscopic analysis of the emulsions was milky, white in color. After the centrifugation test, phase separation was evidenced at a speed of 1000 rpm. This

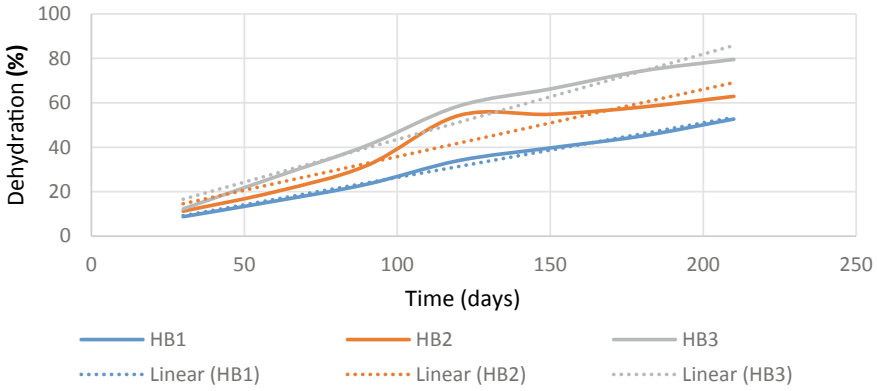

Fig. 3 Variation of dehydration percentage as a function of composition

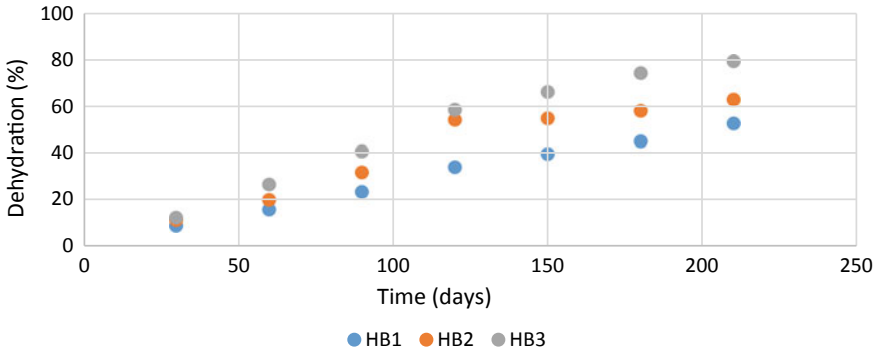

Fig. 4 Variation of dehydration percentage as a function of time after irradiation

proves their stability and from the speed of 2500 rpm, all formulations were slightly modified and at the speed of 3500 rpm, all formulations were phase separated (Fig. 5).

The pH measured before and after the samples was subjected to stress showing no significant changes. The pH of nanoemulsions formulated with Rosa Mosqueta

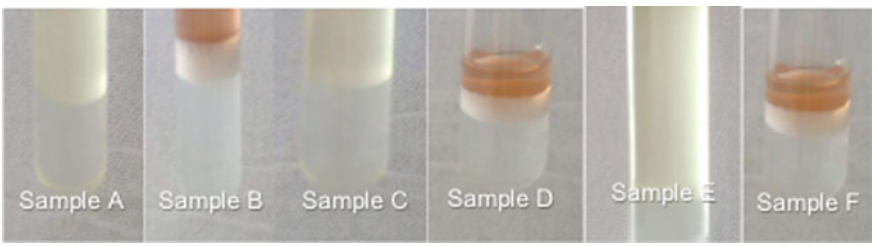

Fig. 5 Appearance of samples after centrifugation

vegetable oil and Palmarosa essential oil decreased progressively to less than 3.0, due to chemical degradation of the components such as release of carboxylic acids in the oil phase and surfactants.

After seven days, the pH of the nanoemulsions obtained increases with the concentration of pseudoboemite. It is observed that the increases in pH are higher for formulations containing Rosa Mosqueta vegetable oil, with these increases being 3.84% (1% pseudoboehmite), 7.69% (3% pseudoboehmite) and 48.27% (5% pseudoboehmite). For nanoemulsions containing Palmarosa essential oil, the increases were 21.73% (1% pseudoboehmite), 20.83% (3% pseudoboehmite) and 74.07% (5% pseudoboehmite) The pH behavior is shown in Fig. 6.

The results are in accordance with the literature [12], which state that emulsions and nanoemulsions prepared with vegetable oils may exhibit a decrease in pH due to hydrolysis of fatty acid esters in free fatty acids, which is the major product of degradation.

The skin has a slightly acidic pH (4.6–5.8), which contributes to bactericidal and fungicidal protection on its surface, and all formulated samples have an acidic pH, and formulations C, D, E and F have skin-like pH.

The density of nanoemulsions as a function of time, measured at 25 °C, shows values close to water 1.00 g/cm^3 (major component), and the results obtained are compatible [10]. All nanoemulsions obtained had a density lower than 1.0 g/cm^3 and the hydrolysis products presented a reduction, ranging from 0.82 to 0.90 g cm^{-1}.

In optical microscopy (Fig. 7) (400x magnification), samples A (1% pseudoboehmite/Palmarosa), D (3% pseudoboehmita/Palmarosa) and E (5% pseudoboehmita/Palmarosa) were the ones with the highest uniformity, and sample D was which presented beyond uniformity a good dispersion of the particles. Sample F (5% pseudoboehmite/Rosa Mosqueta) presented the worst particle dispersion, as well as low uniformity.

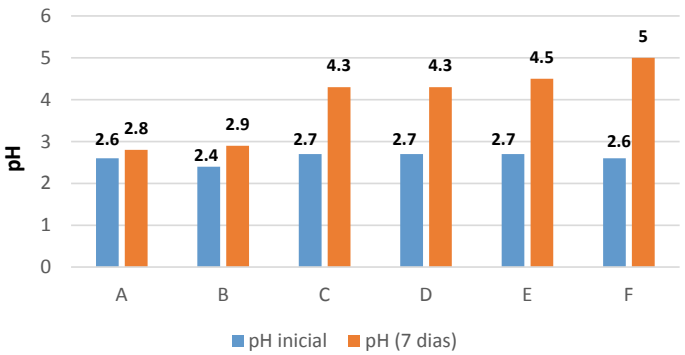

Fig. 6 pH behavior over time

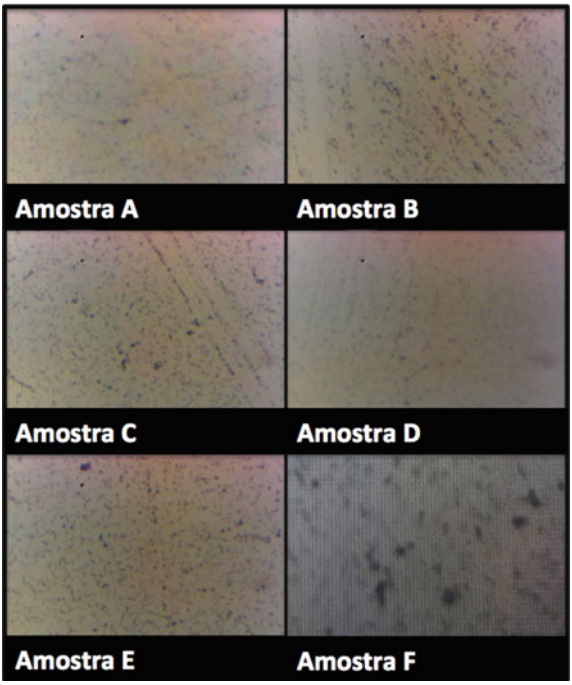

Fig. 7 Microphotographs: samples A (1% pseudoboehmite/Palmarosa); B (1% pseudoboehmite/Rosa Mosqueta); C (3% pseudoboehmite/Palmarosa); D (3% pseudoboehmita/Rosa Mosqueta); E (5% pseudoboehmita/Palmarosa); F (5% pseudoboehmita/Rosa Mosqueta)

Characterization of Hydrogels Containing Different Concentrations of Pseudoboehmite in Nanoemulsion

Isothermal dehydration (37 °C) with air drag was followed as a function of time for hydrogels based on 7.5% PVP, 3.0% PEG and 1.0% agar plus the different nanoemulsions obtained according to Table 2. Dehydration was measured every 20 min and the results are presented in Table 5.

By results, it was observed that in isothermal dehydration (37 °C), in air-entrained greenhouse, the hydrogels presented very close dehydration percentages ranging between 7 and 9%.

The greatest dehydration occurred in the HIX type and most presented 7% dehydration as shown in Fig. 8.

The objective of this investigation was to verify if changes in the composition of hydrogels interfere with dehydration behavior when in contact with human skin, allowing varying the absorption time of the active. However, as noted, dehydration in the range of interest for use as a topical product is independent of composition.

Dehydration as a function of time was measured every 30 days and the results obtained are presented in Table 6 and Figs. 9 and 10.

Through the experiments, it was observed that: the HVI hydrogels presented the lowest dehydration: hydrogels containing Palmarosa oil also lose less water when the percentage of pseudoboehmite increases (hydrogels II, V and VIII); hydrogels

Table 5 Variation in the percentage of isothermal dehydration of the obtained hydrogels

	Hydrogels	Time (min)					
Dehydration (%)		0	20	40	60	80	100
	HI	1	0.97	0.95	0.94	0.93	0.93
	HII	1	0.97	0.94	0.92	0.92	0.92
	HIII	1	0.96	0.95	0.93	0.93	0.93
	HIV	1	0.96	0.94	0.93	0.93	0.93
	HV	1	0.96	0.95	0.94	0.93	0.93
	HVI	1	0.97	0.95	0.94	0.93	0.93
	HVII	1	0.96	0.95	0.94	0.93	0.93
	HVIII	1	0.96	0.95	0.94	0.93	0.93
	HIX	1	0.97	0.96	0.95	0.91	0. 91
	HX	1	0.96	0.93	0.92	0.92	0.92

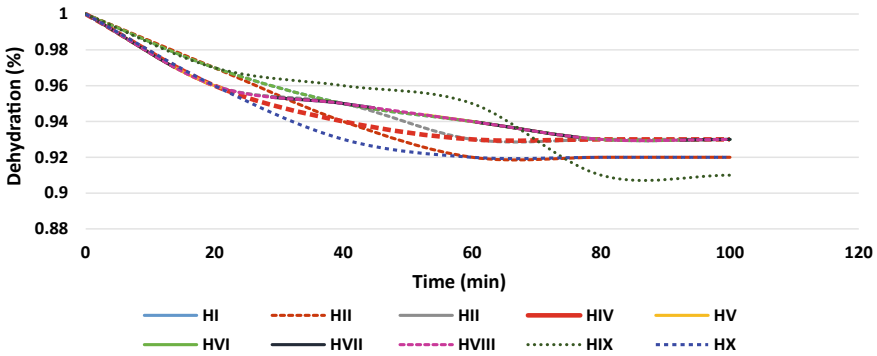

Fig. 8 Variation in the percentage of isothermal dehydration of the obtained hydrogels

IV, VII and X containing Palmarosa oil and Rosa Mosqueta oil increase dehydration with increasing pseudoboemite concentration; the greatest dehydration was from the composition with 1% pseudoboehmite and Rosa Mosqueta oil (hydrogel III) and compared to hydrogel I without Palmarosa or Rosa Mosqueta oils, hydrogel V suffered less dehydration.

Conclusions

From the obtained results, it can be concluded that: the hydrogel base compositions with concentration of PVP (7% by mass), PEG (3% by mass) and agar (1% by mass) are the most appropriate and the one with the worst performance is base-hydrogel with concentration of PVP (10 wt%), PEG (3 wt%) and agar (1 wt%); the

Table 6 Variation in the percentage of dehydration of hydrogels with mandelic acid nanoemulsions containing different concentrations of pseudoboehmite as a function of time

	Hydrogels	Time (min)				
Dehydration (%)		30	60	90	120	150
	HI	2.63	4.28	5.94	7.91	6.73
	HII	3.27	4.69	6.02	8.57	7.29
	HIII	3.11	5.03	6.71	9.51	8.00
	HIV	2.59	3.65	4.55	5.94	4.52
	HV	2.27	3.21	4.01	5.27	4.28
	HVI	1.44	3.06	4.14	5.23	4.64
	HVII	1.63	2.80	4.30	5.74	5.15
	HVIII	1.89	2.77	3.99	5.34	4.73
	HIX	2.09	3.72	5.40	6.42	5.32
	HX	1.60	2.66	4.05	6.00	6.08

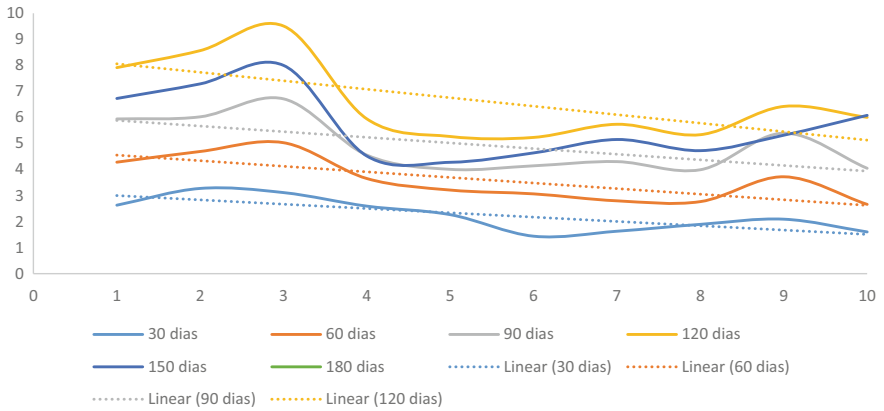

Fig. 9 Variation of dehydration of hydrogels with mandelic acid nanoemulsions containing different concentrations of pseudoboemite as a function of composition

nanoemulsions obtained presented acidic pH (compatible with that of the skin) with density close to that of water and the nanoemulsions containing 3% pseudoboehmite and Rosa Mosqueta vegetable oil presented the best homogeneity and uniformity; and the hydrogel with different concentrations that presented the best performance was the one containing 7.5 m% PVP and 5 m% pseudoboehmite in the nanoemulsion which presented the lowest degree of isothermal dehydration (37 °C).

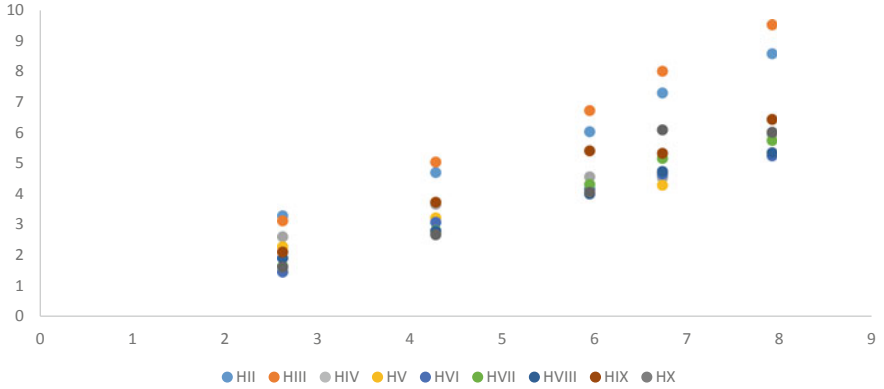

Fig. 10 Variation of dehydration percentage as a function of time after irradiation with hydrogels with mandelic acid nanoemulsions containing different concentrations of pseudoboehmite

References

1. Ferreira IF, Spanol CM, Colombo F, Correa MA, Salgado HRN (2016) Validação de método analítico para a quantificação de ácido ursólico em emulsão cosmética utilizando espectrometria no UV. Rev Ciências Farmacêuticas Básica Aplicada 37(Supl. 1) 08/2016
2. Chien YW (1987) Advances in transdermal systemic medication. In: Chien YW (ed) Transdermal controlled systemic medications. Marcel Dekker, New York, NY, pp 1–22
3. Santos MMS (2015) Estudo de nanocompósitos poliméricos siloxanopoliéter como dispositivos de liberação modificada de princípios ativos. Dissertação de Mestrado em Ciências e Tecnologia em Saúde, Universidade de Brasília, Brasília
4. Rogero SO, Lorenzetti SG, Chin G, Lugão AB (2002) Hidrogel de poli(1-vinil-2-pirrolidona) (PVP) como matriz polimérica para o sistema de liberação de fármaco. Rev Bras Pesquisa Desenvolvimento 44:1447–1449
5. Porto KMBG (2013) Efeitos da radiação gama (Cobalto-60) nas propriedades físicas e químicas de embalagens compostas por papel grau cirúrgico e filme plástico laminado. destinadas à esterilização de produtos para a saúde. Dissertação (Mestrado em Ciências na área de Tecnologia Nuclear) – Instituto de Pesquisas Energéticas e Nucleares – IPEN – São Paulo. São Paulo
6. Souza VM, Antunes Júnior D (2013) Ativos Dermatológicos: Dermocosméticos e Nutracêuticos. Pharmabooks Editora, São Paulo
7. Munhoz Junior AH, Novicks RW, Faldini SB, Ribeiro RR, Maeda CY, Miranda LF (2010) Development of pseudoboehmites for nanosystems to release acyclovir. Adv Sci Technol 76:184–189
8. Souza AMT (2013 Avaliação de toxicidade da pseudoboemita para liberação controlada de fármacos. Dissertação (Mestrado em Engenharia de Materiais), Universidade Presbiteriana Mackenzie – SP, São Paulo
9. Paganini PP (2012) Síntese e caracterização de nanoparticulas de óxido misto de estanho/tintânio dopadas com lantanídeos para marcação biológica. Tese de Doutorado em Ciências na Área de Tecnologia Nuclear. São Paulo
10. Pimentel AS (2008) Peeling. máscaras e acne: seus tipos e passo a passo do tratamento estético. Livraria Médica Paulista, São Paulo

11. Miranda LF, Cunha KLG, Barbosa ITF, Masson TJ, Munhoz Júnior AH (2018) Obtaining hydrogels based on PVP/PVAL/chitosan containing pseudoboehmite nanoparticles for application in drugs. In: Haider S, Haider A (eds) Hydrogels, vol 1, 1st edn. IN TECH, Croatia, pp 1–20
12. Silva Junior E, Zanon Junior GB, Zanella I, Raffin R, Cielo V, Rossato J, Bulhões LOS (2013) Formação de nanoemulsões do tipo óleo em água contendo óleo de semente de romã, vol 14(1). Ciências Naturais e Tecnológicas, Santa Maria, pp 115–122
13. Arosa S, Gupta S, Narang RK, Budhiraja RD (2011) Amoxilin Ioaded chitosan-alginate polyelectrolyte complex nanoparticles as mucopenetrating delivery system for H. Pylori Sci Pharmaceutica 79(3):673–694
14. Leonardi GR (2004) Cosmetologia aplicada. Medfarma, São Paulo

Chemical and Mineralogical Characterization of a Cuprite–Miargyrite Ore and Proposal of Elimination of Semimetals by Alkaline Bath

Aislinn Teja Ruiz, Kinardo Flores Castro, Migue Pérez Labra, Martin Reyes Perez, Elia G. Palacios Beas, Víctor Esteban Reyes Cruz and Julio Cesar Juárez Tapia

Abstract Complex sulfides such as pyrargyrite and miargyrite contain important concentrations of silver. However, the presence of semimetals in its structure hinders recovery by traditional methods. The present study shows the characterization of a cuprite mineral with miargyrite inclusions, with the purpose of proposing the oxidation and elimination of the antimony contained in the sulfosalt by means of an alkaline bath. The chemical characterization of the mineral sample reported the presence of Cu (58.6% Wt), Ag (4.4% Wt), Sb (3.8% Wt), As (1.1% Wt), and Zn (0.2% Wt). The composition of the majority species was identified by the X-ray Diffraction (XRD) technique, whereby it was confirmed that ore matrix corresponds to Cu_2O [96-900-5770] and $AgSbS_2$ [96-900-2734]. Both species were identified

A. T. Ruiz · K. F. Castro · M. P. Labra · M. R. Perez · V. E. R. Cruz · J. C. J. Tapia (✉)
Autonomous University of the State of Hidalgo, Academic Area of Earth Sciences and Materials, Pachuca-Tulancingo Highway, Kilometer 4.5, 42180 Mineral de la Reforma Hidalgo, Mexico
e-mail: jcjuarez@uaeh.edu.mx

A. T. Ruiz
e-mail: aislinn_teja@uaeh.edu.mx

K. F. Castro
e-mail: kinardo_flores@hotmail.com

M. P. Labra
e-mail: MIGUELABRA@hotmail.com

M. R. Perez
e-mail: mreyes@uaeh.edu.mx

V. E. R. Cruz
e-mail: reyescruz16@yahoo.com

E. G. Palacios Beas
National Polytechnic Institute, Higher School of Chemical Engineering and Extractive Industries, Adolfo López Mateos, Av. IPN s/n, Lindavista Colony, 07738 Mexico City, Mexico
e-mail: epalacios@ipn.mx

J. Li et al. (eds.), *Characterization of Minerals, Metals, and Materials 2020*,
The Minerals, Metals & Materials Series,
https://doi.org/10.1007/978-3-030-36628-5_48

using the Polarizing Light Microscopy (PLM) technique, and the elemental relation presented in the mapping was obtained by Scanning Electron Microscopy-Dispersive Energy Analysis (SEM-EDS). Both the metallic content and the trace species were corroborated by the X-ray fluorescence (XRF) technique.

Keywords Characterization · Cuprite · Miargyrite · Semimetals · Alkaline bath

Introduction

Copper ores are species commonly related to the formation of silver sulfosalts, which have an extremely complex structure that makes it difficult to extract the metallic content. Some of the most abundant gray coppers are polybasite and tetrahedrite, species related to the formation of pyrite, chalcopyrite, marcasite, and Argentinian galena [1]. However, the presence of simpler minerals such as covelite, digenite, and cuprite functions as nuclei of mineralogical growth where the formation of secondary minerals of greater structural complexity is generated, as is the case of sulfosalts [2]. The type of deposits where this type of sulfosalts is found consists mainly of quartz veins where the presence of simple iron and zinc sulfides scattered [3, 4]. The existence of mineral species related to noble metals is commonly located at greater depths of the deposit, and the process of mineral extraction decreases its profitability by not achieving the efficient dissolution of silver concentrations, promoting the permanence of complex species in metallic concentrates or leaching wastes solids [5]. In search of alternatives that allow the extraction of metallic values of these species, previous studies have determined that, when previously treating a complex mineral rich in tetrahedrite, the extraction of semimetals such as antimony and arsenic depends mainly on the concentration of sulfur and concentration of hydroxide, as well as the influence of variables such as temperature and reaction time on the efficiency of the dissolution process [6]. It is well known that gold is often encapsulated by secondary sulfides such as arsenopyrite, so a previous oxidation treatment is required for gold recovery, where the regulation of a highly alkaline medium ensures the conversion into arsenic solution and the release of the precious metal [7]. Authors such as B. Xu et al. and S. L. Mesa-Espitia et al. have also proposed alkaline pretreatments that allow these sulfosalts to be oxidized by varying factors such as the concentration of NaOH, temperature, and pressure, with the aim of obtaining simple minerals from complex minerals that can be leached by alternative leaching processes [8, 9]. This study aims to identify the mineralogical species that contains silver and check the dissolution of semimetals such as As and Sb through the bath of highly alkaline solutions.

Experimentation

The mineral sample was obtained from a sampling conducted in the mining district of Fresnillo, Zacatecas. This sample consisted of a single gray-reddish-colored crystal with a thin mountain range of green hue, which was identified as malachite and removed from the sample to avoid contamination of the dusts subjected to the different characterization techniques.

Said powders were reduced to 74 microns and subjected to an acid solution, whereby a diluted solution was obtained that allowed the chemical analysis of the sample through the technique of Induction-Coupled Plasma Emission Spectroscopy (ICP) using a spectrometer, model PerkinElmer 8300. Subsequently, the powders of cuprite sample were analyzed using X-ray Fluorescence (XRF) techniques, for which the sample powders were analyzed using a X-ray Fluorescence spectrometer, model Bruker S2 PUMA with Palladium tube and X-ray Diffraction (XRD) technique using a diffractometer, model INEL EQUINOX 2000 X-ray with a Cu–Ka1 radiation of 1,540,598, operating at 30 mA and 20 kV, 220 V and a resolution of 0.095 FWHM; this with the purpose of corroborating the elementary content and identifying the majority species of the sample, respectively. The mineralogical identification and morphological description of the sample were performed using the Scanning Electron Microscopy—Energy Dispersion Analysis (SEM-EDS) techniques, using a JEOL Scanning Electron Microscope, model JSM 6701F at 25 kV, and Optical Polarization Microscopy (PLM) using a microscope, model BH41 with different magnifications.

The alkaline bath to which the powders of the mineral sample were subjected were performed under the following experimental conditions: $V = 0.25$ L, mineral $= 8$ gL^{-1}, tr $= 720$ min, $d_0 = 74$ μm, [NaOH] $= 3$ mol L^{-1}, $T = 338$ K, and RPM $= 1000$ min^{-1}, and a glass reactor with a capacity of 0.3 L was used on a Thermo Scientific Super-Nuova brand heating grill equipped with magnetic stirring. The aliquots obtained from the reaction monitoring were analyzed using the ICP technique, making readings for As, Sb, and Ag.

Results and Discussion

The results obtained from the chemical–mineralogical characterization and the elimination of antimony and arsenic made to the cuprite sample obtained from the mining district of Fresnillo, Zacatecas, are presented below.

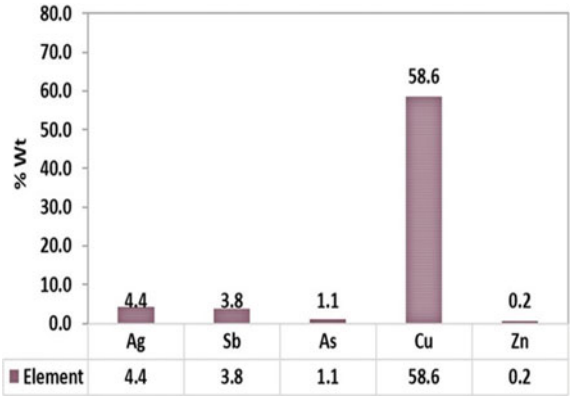

Fig. 1 Chemical analysis of the mineral sample of cuprite obtained by ICP

Induction-Coupled Plasma Emission Spectroscopy (ICP)

The chemical analysis performed on the powder sample using the ICP technique reported a weight percentage equivalent to 58.6% of Cu, this being the most abundant element in the mineral, as shown in Fig. 1.

The rest of the minoritary elements correspond to 4.4% of Ag and 3.8% of Sb, elements related to the formation of complex sulfides, and associated with base metal sulfides. The presence of arsenic is also usually related to some sulfosalts, although in a minimal quantity, since arsenic species such as proustite (Ag_3AsS_3) can be found as inclusions of pyrargyrite (Ag_3SbS_3) and miargyrite ($AgSbS_2$) [10–12].

X-Ray Fluorescence (XRF)

The elementary analysis obtained by the XRF technique allowed to identify, in addition to the abundant content of Cu, the presence of trace elements such as Al, Si, Ca, and K, as observed in Table 1. The oxygen reading recorded a percentage in weight of 21.80%; this element is mainly related to the cuprite species, which is the matrix of the mineral sample. The content of Ag and Sb shows equivalent concentrations with a slight increase in the content of Ag that is attributed to the presence of silver sulfosalts related to a minor arsenic content.

X-Ray Diffraction (XRD)

The XRD technique identified that the majority species corresponds to a copper oxide identified as cuprite ([96-900-5770]). The mineralogical species where the majority silver content was identified corresponds to miargirite ([96-900-2734]), a

Table 1 Elemental content of the mineral sample of cuprite obtained by XRF

Element	Al	Si	S	K	Ca	Cu	Zn	As	Ag	Sb	Au	O
Cuprite-A	0.40	0.40	11.09	0.06	0.05	57.14	0.10	1.06	4.38	3.94	0.01	23.01
Cuprite-B	0.42	0.42	11.09	0.06	0.05	57.99	0.08	1.06	3.99	3.23	0.01	20.07
Cuprite-C	0.38	0.46	11.08	0.05	0.05	57.86	0.08	1.06	4.25	4.09	0.01	22.31
Average	0.40	0.43	11.09	0.06	0.05	57.66	0.09	1.06	4.21	3.75	0.01	21.80

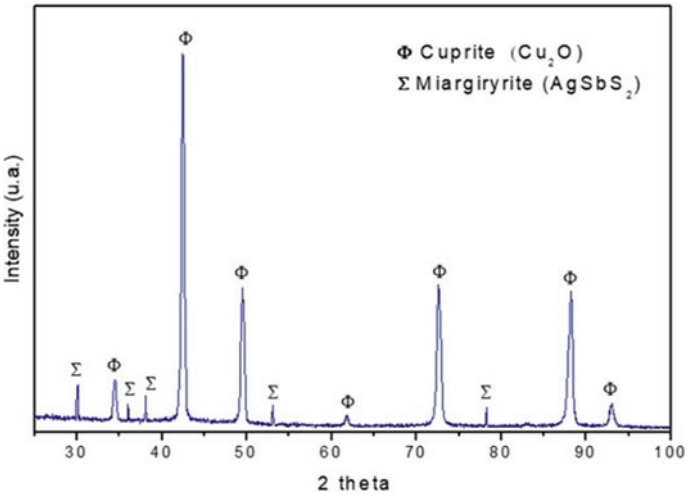

Fig. 2 Diffractogram of the mineral sample of cuprite

double silver sulfide with antimony, which differs from the pyrargyrite by its lower silver content (Fig. 2) [13, 14]. The contents of Sb and Ag reported by ICP and XRF correspond stoichiometrically to the miargyrite specie identified through this technique.

Polarization Optical Microscopy (PLM)

Figure 3 shows a micrograph obtained at 20× with polarized nicoles, where a matrix of lumpy texture and dark hue corresponding to the cuprite species is observed. In the micrograph, inclusions corresponding to quartz and fringes of clear hue corresponding to the silver sulfosalt (miargyrite) are also observed.

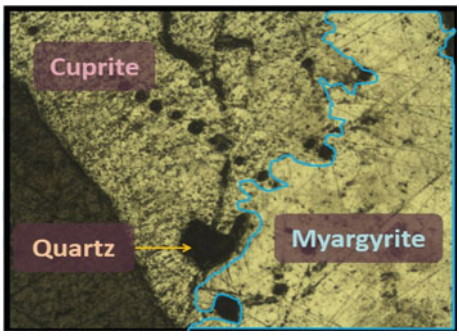

Fig. 3 Micrograph of the mineral sample of cuprite obtained by PLM

Scanning Electron Microscopy—Energy Dispersion Analysis (SEM-EDS)

The morphology of the mineral sample has a surface with slight relief and homogeneous texture (Fig. 4a). The semi-quantitative analysis performed on the sample reports mainly a metallic content corresponding to Cu, As, Sb, and Ag, as shown in Fig. 4b.

In order to know the association of these elements in the sample, the mapping technique was used by which the matrix of the mineral was corroborated (Fig. 5), determining a specific relationship of the elements Cu and O, in addition to their abundance in the same zone of the particle. The relationship between Ag and Sb is disseminated, in addition to the minor presence of As [15, 16].

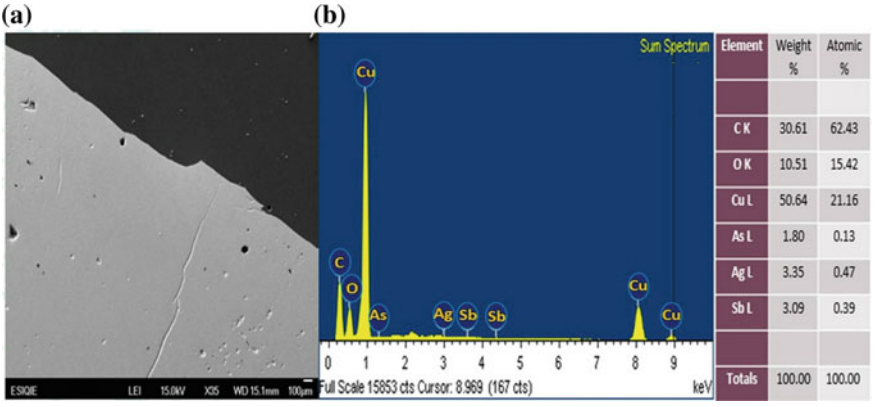

Element	Weight %	Atomic %
C K	30.61	62.43
O K	10.51	15.42
Cu L	50.64	21.16
As L	1.80	0.13
Ag L	3.35	0.47
Sb L	3.09	0.39
Totals	100.00	100.00

Fig. 4 **a** Micrograph obtained with backscattered electrons from the mineral sample of cuprite. **b** Spectrum of dispersive energies obtained from the cuprite sample

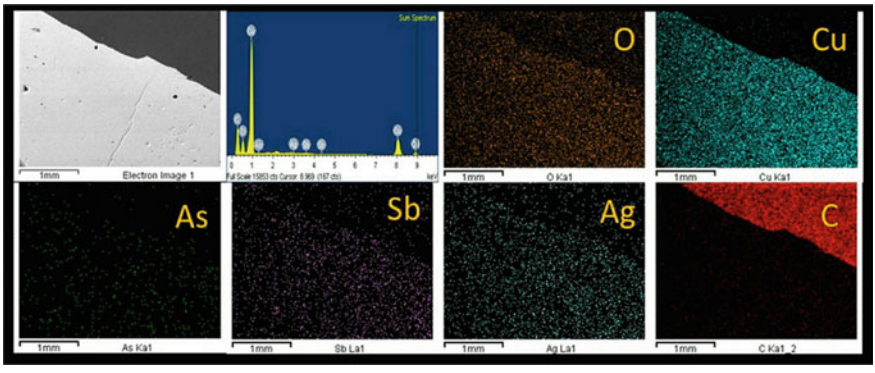

Fig. 5 Mapping obtained from the mineral sample of cuprite

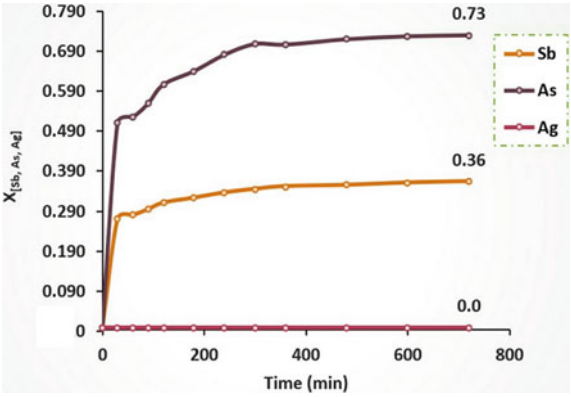

Fig. 6 Conversion in solution of semimetals contained in silver sulfosalts

Dissolution of As, Sb, and Ag by Alkaline Baths

Through dissolution tests carried out in NaOH solutions, a greater dissolution of the As semimetal was observed, reaching a solution conversion of 73%. In the case of Sb, the semimetal that makes up the majoritary silver sulfosalt in mineral sample only achieved the dissolution of 36% under the conditions established for experimental tests. As shown in Fig. 6, the use of NaOH solution represents a feasible dissolution medium for semimetal leaching; however, no silver conversion in solution is shown, so it is assumed that said metal remains in the mineral sample as a species in solid state.

Conclusions

Through the technique of ICP, XRF, and the analysis of dispersive energies by SEM-EDS, it was possible to know and confirm the concentration of Sb, Ag, and S corresponding to the complex sulfide, which is present in the cuprite sample from Zacatecas, Mexico. The elementary relationship and the stoichiometry of said sulfosalt, identified as miargyrite, were confirmed by the mapping technique by SEM-EDS and the diffractogram obtained by XRD, respectively. The matrix of the mineral sample was identified as cuprite, a copper oxide, whose elemental content was reported in the chemical analysis and XRF technique, in addition to the presence of trace elements that reveal the presence of silicates. The micrograph obtained by PLM shows the association of the cuprite species as a matrix of the mineral and the double sulfide of silver and antimony, the latter being differentiated, by the contrast of a smooth texture and clear tones. Through most of the techniques used, the presence of As is observed in low concentrations; however, the SEM-EDS mapping technique confirms the presence of the semimetal associated mainly to areas where the contents of

Sb and Ag predominate. The NaOH solution has a greater efficiency for the dissolution of As than for the dissolution of Sb, making it a feasible alternative for complex arsenic species related to noble metals such as silver. Although the dissolution of Sb is less, the kinetic study of the reaction could establish optimal operating conditions.

References

1. Klein C, Jr Hurlburt CS (1996) Manual de Mineralogía, vol 1. Editorial Reverté. 2da. Ed. Madrid. ISBN: 978–84-291-4606-6
2. Kettanah YA (2019) Copper mineralization and alterations in Gercus Basalt within the Gercus formation, northern Iraq. Ore Geol Rev 111:102–124. 0.1016/j.oregeorev.2018.04.023
3. Deer WA, Howie RA, Zussman J (1998) An introduction to the rock-forming minerals, 2nd edn. Longman, Hong Kong
4. Martínez-Frías J, Marín-Ramos JD (1995) Sulfuros y Sulfonales de Metales Nobles, 1st edn. Textos Universitarios, Madrid. ISBN 9788400074968
5. Teja-Ruiz AM, Juárez JC, Reyes IA, Hernández-Cruz LE, Reyes M, Patiño F, Flores MU (2017) Kinetic study of Ag leaching from arsenic sulfosalts in the $S_2O_3^{2-}$-O_2-NaOH system. Metals 7(411):1–12. https://doi.org/10.3390/met7100411
6. Awe S, Sandström A (2010) Selective leaching of arsenic and antimony from a tetrahedrite rich complex sulphide concentrate using alkaline sulphide solution. Miner Eng 23:1227–1236
7. Celep O, Paktunç D, Thibault Y (2014) Influence of potassiumhydroxide pretreatment on the extraction of gold and silver from a refractory ore. Hydrometallurgy 146:64–71
8. Mesa-Espitia SL, Lapidus GT (2015) Pretreatment of a refractory arsenopyritic gold ore using hydroxyl ion. Hydrometallurgy 153:106–113
9. Xu B, Yang Y, Li Q, Jiang T, Liu S, Li G (2016) The development of an environmentally friendly leaching process of a high C, As and Sb bearing sulfide gold concentrate. Miner Eng 89:138–147
10. Harlov DE, Sack RO (1995) Thermochemistry of Ag_2S-Cu_2S sulfide solutions: constraints derived from coexisting Sb_2S_3- and As_2S_3-bearing sulfosalts. Geochim Cosmochim Acta 59, 21: 4351–4365. 0016-7037 (95)00308-8
11. Harlov DE, Sack RO (1994) Thermochemistry of polybasitepearceite solutions. Geochim Cosmochim Acta 58:4363–4375
12. Harlov DE, Sack RO (1995) Ag-Cu exchange equilibria between pyargyrite, high-skinnerite, and polybasite. Geochim Cosmochim Acta 59:867–874
13. Schmidt JA, Sagua AE (1990) Phase equilibrium of ($Ag_{1.55}Cu_{0.45}S + Ag_{1.2}Cu_{0.8}S + CuS$) and thermodynamic quantities for the ternary phase $Ag_{1.2}Cu_{0.8}S$. J Chem Therm 22:1207–1212
14. Schmidt JA, Sagua AE, Bazan JC (1990) Phase equilibrium of ($CuS + Ag_2S + Ag_{1.55}Cu_{0.45}S$) and thermodynamic quantities for the ternary phase jalpaite from e.m.f. measurements in solidstate galvanic cells. J Chem Therm 22:181–187
15. Kharbish S (2011) Raman spectroscopic investigations of some Tl-sulfosalt minerals containing pyramidal (As, Sb)S_3 groups. Am Miner 96:609–616. https://doi.org/10.2138/am.2011.3653
16. Gągor A, Pawlowski A (2009) Pietraszko, Silver transfer in proustite Ag_3AsS_3 at high temperatures: conductivity and single-crystal X-ray studies. J Solid State Chem 182:451–456. https://doi.org/10.1016/j.jssc.2008.11.005

Chemical Characterization and Mineralogical Analysis of Mining-Metallurgical Tailing from the State of Morelos

Jesús Iván Martínez Soto, Aislinn Michelle Teja Ruiz, Martin Reyes Perez, Migue Pérez Labra, Víctor Esteban Reyes Cruz, José A. Cobos Murcía, Gustavo Urbano Reyes and Julio Cesar Juárez Tapia

Abstract The benefit of noble metals, such as silver contained in mining-metallurgical waste, is considered a challenge for the metallurgist because they are low-grade minerals, fine granulometry, and complex minerals by their refractoriness. To address this problem, a tailings characterization of the state of Morelos was carried out, using techniques such as atomic absorption spectrophotometry and Induction Coupled Plasma Emission Spectrometry that gave similar silver concentrations of 104.8 and 106 g ton^{-1}, respectively. In addition, a XRD study was carried out, which identified the presence of Xancotonite, in addition to Cu and Fe sulfides, and both species are contained in a silicon matrix. To abound in the mineralogical study, samples were observed in optical microscopy revealing mainly pyrite associated with quartz, sphalerite, arsenopyrite, and some particles with the appearance of a sulfosal, which were confirmed through SEM since elements such as S, Ag, As, and Sb were revealed through microanalysis to different particles.

J. I. M. Soto · A. M. T. Ruiz · M. R. Perez · M. P. Labra · V. E. R. Cruz · J. A. Cobos Murcía · G. U. Reyes · J. C. J. Tapia (✉)
Autonomous University of the State of Hidalgo, Academic Area of Earth Sciences and Materials, Road Pachuca-Tulancingo Kilometer 4.5 Mineral de la Reforma, Hidalgo 42180, Mexico
e-mail: jcjuarez@uaeh.edu.mx

J. I. M. Soto
e-mail: ivan_kai@outlook.es

A. M. T. Ruiz
e-mail: aislinn_teja@uaeh.edu.mx

M. R. Perez
e-mail: mreyes@uaeh.edu.mx

M. P. Labra
e-mail: MIGUELABRA@hotmail.com

V. E. R. Cruz
e-mail: reyescruz16@yahoo.com

G. U. Reyes
e-mail: Gustavo_urbano@uaeh.edu.mx

J. Li et al. (eds.), *Characterization of Minerals, Metals, and Materials 2020*,
The Minerals, Metals & Materials Series,
https://doi.org/10.1007/978-3-030-36628-5_49

Keywords Mining waste · Chemical characterization · Mineralogical characterization

Introduction

Usually, the studies carried out to assess a mineral deposit imply knowing only the concentration of metallic values, without giving greater importance to the mineralogical characterization, which is very relevant, because it allows the identification of mineral species and the associations between them. Additionally, the elementary analysis performed by techniques such as atomic absorption spectroscopy (AAS) and Induction Coupled Plasma Emission Spectrometry (ICP), it is necessary to use other conventional techniques such as polarization optical microscopy (LPM) and Scanning Electron Microscopy with dispersive energy analyzer (SEM-EDS), in order to corroborate the information obtained by the rest of the techniques, since these are last allow the observation of the metallic values that are usually occluded within other mineral species such as pyrite, galena, or quartz, thus confirming the mineralogical associations [1]. Due to the above, it is very important to carry out a thorough study on the chemical and mineralogical characterization of raw materials (minerals, concentrates, metallurgical residues, etc.) that contain metallic values of interest for their extraction [2, 3].

At present, there is a deficit to meet the demand for noble metals of simple minerals, due to the massive exploitation of Au–Ag–Cu–Zn deposits, which has led to the search for alternatives to recover these metals [4]. Although there are options, such as recycling, re-extraction of mining waste [5, 6] through leaching with pretreatments, which represents an important source of recovery, based on the fact that there is a large amount of residues with important values of gold and silver, metals that remain in the residues because the minerals benefited through conventional metallurgical processes did not achieve a complete dissolution of these values [7, 8]. Additionally by having a metallurgical mining residue for the development of this research, it is inevitable to address the issue of contamination and the benefits obtained by reprocessing and removing these wastes due to their negative impact on the environment [6, 9].

Nowadays, it is possible to achieve a profitable recovery of these precious metals, using alternative metallurgical processes, capable of extracting a significant percentage of the metallic content; however, the reprocessing of these residues still represents a challenge for metallurgy because the noble metals are related to other elements or encapsulated in more complex mineral species [10]. With respect to this, the dissolution of silver contained in mining waste with concentrations of 71 gr Ag ton^{-1} has been reported in previous works, reaching maximum solutions of 97% by means of the copelation technique [11].

On the other hand, Alp et al., analyzed the influence of pretreatment with potassium hydroxide with a concentration of 5 mol L^{-1} at a temperature of 80 °C in the extraction of gold and silver from a refractory mineral leading to recoveries of 49.3%

and 18.7% to 87.6 and 94.5%, respectively, by removing antimony from the mineral which is the reason for the refractory nature of it [8].

Unlike previous work, Li et al., in 2016, carried out the extraction of silver to a refractory mineral with a low Au–Ag law through a cyanidation process and a pretreatment of reductive leaching in the presence of copper, in alkaline solution of ammonium and ammonium sulfate, with concentrations of 2 mol L^{-1} and 1 mol L^{-1}, respectively, 4 g of copper wire and using a stirring speed of 300 min^{-1} over a period of 4 h, obtaining a recovery of 78.96% [12].

Subsequently, Celep et al., in the year 2019, by means of an analysis of mineral release and a diagnostic leaching, subjected an extremely complex arsenical silver ore to an ultra-fine grinding of up to 8 μm leading to cyanide leaching 71–84% recovery [13].

The purpose of this study is to obtain detailed information on gold and silver concentrations through quantitative techniques, as well as mineral associations for the evaluation of metallurgical mining waste (mine wastes), from the state of Morelos, for possible generation of a proposal viable of silver recovery.

Experimental Methodology

The sampling of the mine wastes was carried out in the state of Morelos, Mexico, these mining wastes were homogenized, and using the method of quarter, a representative sample was obtained to perform the chemical-mineralogical characterization and the granulometric analysis.

The chemical analysis was performed using the atomic absorption spectrophotometry (AAS) technique, using a Perkin Elmer Analyst 200 model, and using an air-acetylene flame. To complement the chemical characterization, the sample was analyzed by the X-ray Fluorescence (XRF) technique, and the equipment used was a Bruker X-ray fluorescence spectrometer model S2 PUMA with palladium tube.

Through the X-ray Diffraction (XRD) technique, the majority mineral species were identified, using an X-ray diffractometer, INEL EQUINOX 2000, with a Co-Ka1 radiation (1.789010 Å), operated under the following analysis conditions: 30 mA and 20 kV, voltage of 220 V, and resolution of 0.095 FWHM.

In order to identify the mineralogical constituents of mining waste, their particle sizes and textures, a cold stuffed sample was prepared in epoxy resin, which was roughened in abrasive paper and polished with 6 and 1 μm diamond paste, until obtaining a flat and polished surface with mirror finish, to later be observed with an Olympus polarization optical microscope model BH41 at different magnifications.

To deepen in the identification of the presence of silver and elements associated with the precious metal, several specific analyzes were carried out on various particles of the order of 10 μm using the Scanning Electron Microscopy technique with dispersive energy analyzer (SEM-EDS), using a JEOL brand equipment model JSM 6701F at 25 kV and different magnifications.

On the other hand, to determine the distribution by size of the particles present in the mine wastes, a granulometric analysis was carried out by dry route. 100 g of sample were weighed on an analytical balance, which was deposited in the Tyler series sieves, ordered in descending order of the following mesh numbering, 65, 100, 150, 200, 325, and 400. The fractions obtained were heavy, subsequently dissolved with 0.01 L of perchloric acid for 15 min at a temperature of 200 °C, and finally allowed to cool for 20 min, and the final solution was filtered, brought out at 0.1 L, and analyzed by the Plasma Emission Spectrometry technique Induction coupled (ICP) using a Perkin Elmer model 8300 spectrometer; to determine the silver content for each particle size, the sample was bounded. The above with the purpose of determining the distribution of the precious metal for its subsequent metallurgical process.

Results

The chemical and mineralogical characterization carried out on the sample of mine wastes from the state of Morelos, Mexico, and the results obtained from the granulometric analysis are presented below.

Granulometric Chemical Analysis

The results of the granulometric chemical analysis of the mineral revealed that the highest silver content (54.61%) is present in the −400# mesh, equivalent to particle diameters smaller than 37 μm (Table 1). This particle size is peculiarly fine for the metallurgical extraction of the metallic content, either by hydrometallurgical or pyrometallurgical route, so when discarding this particle diameter, it is attributed that the ideal particle size for conducting experimental tests is 44 μm (−200 + 325#) where a distribution of silver of 19.35% is observed [14].

Chemical Characterization

Atomic Absorption Spectroscopy (AAS)

The chemical analysis performed on the sample of tailings revealed a majority Fe content corresponding to 2.73% followed by the minor concentration of base metals such as Cu and Zn. The presence of noble metals was also identified, where the concentration of Ag corresponding to 104.8 g ton^{-1} stands out, as can be seen in Table 2.

Table 1 Granulometric chemical analysis, mining waste from Morelos

Sample mining waste Morelos							
Product		%	%	Test		Distribution	
				Ag	Au	Ag	Au
Mesh	Microns	Weight	Accumulative (–)	(g ton^{-1})	(g ton^{-1})	%	%
+65#	220	0	100	0	0	0	0
−65 + 100#	149	14.46	85.54	32.50	0.05	4.24	5.882
−100 + 150#	105	10.41	75.13	77.80	0.07	7.30	6.723
−150 + 200#	74	10.26	64.87	117.80	0.07	10.89	6.723
−200 + 325#	44	15.07	49.80	142.50	0.16	19.35	21.008
−325 + 400#	37	3.25	46.55	123.20	0.18	3.61	5.042
−400#		46.55		130.20	0.14	54.61	54.622
F_{80} = 124.38		100.00	CAB. CALC.	110.967	0.119	100.00	100.00
			CAB. ENS.	112.00	0.120		

Table 2 Chemical composition, mining waste from Morelos

Element	Percentage
Fe	2.7395
Cu	0.0238
Zn	0.3565
Ag	0.0104

Induction Coupled Plasma Emission Spectrophotometry (ICP)

In order to corroborate the concentration of noble metals in the tailings, the ICP technique was applied, which confirmed that silver and gold values are similar to those obtained by the AAS technique, which is shown in Table 3.

Table 3 Concentration of base metals contained in the sample of mining waste

Element	Concentration
Silver	106 g ton^{-1}
Gold	0.14 g ton^{-1}

Table 4 Elementary content of the mining waste sample

Element	Al	Si	Mn	S	Fe	K	Ca	Ti
% Wt	0.47	6.25	0.1	0.06	3.97	2.51	2.25	0.15
Element	Rb	Au	Fe	Ag	Sb	Cu	Zn	As
% Wt	0.01	**0.0013**	3.97	**0.0104**	**0.0049**	0.02	0.32	**0.0141**

3X-Ray Fluorescence (XRF)

To complement the chemical characterization, the XRF technique was used, which corroborates the concentrations of Ag, Au, Zn, Cu, and Fe, obtained by AAS and ICP. In addition to the presence and concentration of elements related to Ag (0.0104% Wt) such as As (0.0142% Wt) and Sb (0.005% Wt), suggesting the presence of silver sulfosalts in the tailings, as can be seen in Table 4. It is worth mentioning that these results are only from the analysis of minor elements and traces, which is why 100% of the elements are not presented.

Mineralogical Characterization

X-Ray Diffraction (XRD)

This technique identified the presence of a metallic species corresponding to an Argentine antimony sulfide identified as pyrargirite (Ag_3SbS_3) [96-900-9267], which is contained in a silicon matrix (SiO_2) [96-901-3322], as seen in Fig. 1, where quartz

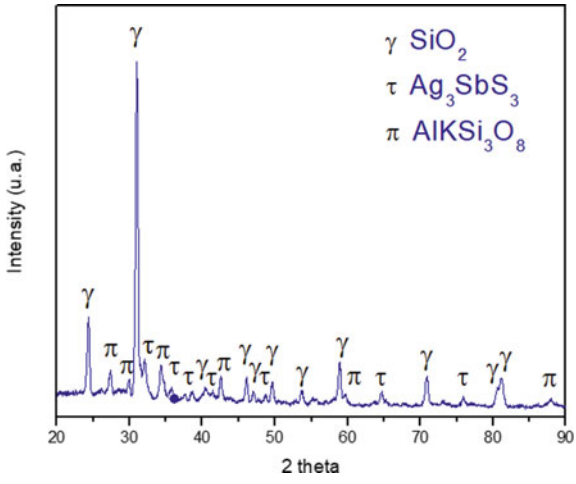

Fig. 1 X-ray diffractogram, sample of mining waste from Morelos

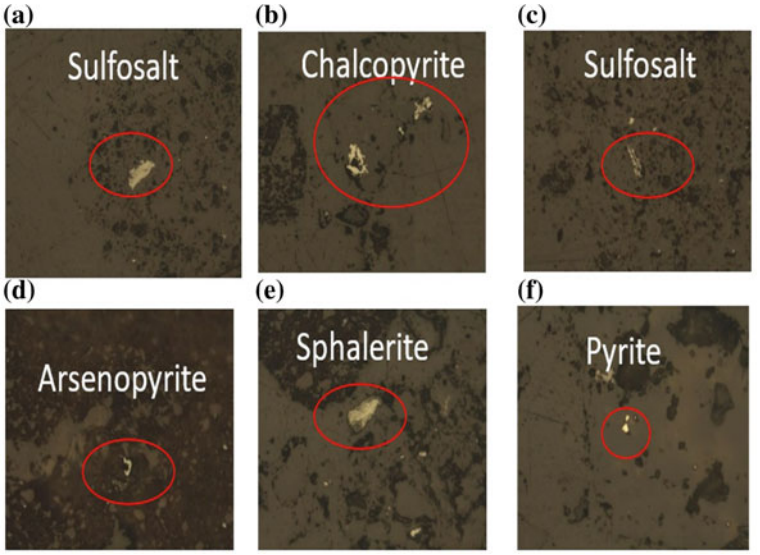

Fig. 2 Micrographs obtained at 20 X, sample of mining waste from Morelos. **a** Sulfosal, **b** Chalcopyrite, **c** Sulfosal, **d** Arsenopyrite, **e** Sphalerite, and **f** Pyrite

is presented as majority species of the mine wastes sample and shows the presence of a other gangue species such as potassium silicoaluminates ($AlKO_8Si_3$) [96-900-6349] [15].

Polarization Optical Microscopy (LPM)

Through LPM, it was possible to identify abundant fragments of quartz, silicates, and little metallic mineralization. Said mineralization consists mainly of pyrite (FeS2) associated with quartz (SiO_2), sphalerite (ZnS), and arsenopyrite (FeAsS). Due mainly to the fine size of the sample, the morphology, the texture and the coloration, it was possible to identify some sulfosal particles as seen in Fig. 2a, c.

Scanning Electron Microscopy (MEB-EDS)

Using the gray-scale contrast, the micrographs presented in Figs. 3 and 4 were obtained, in which an irregular and varied morphology can be observed in the sample of tailings, composed mainly of C, O, Al, Si, S, Ag, and Sb, and according to the results obtained from the X-ray microanalysis presented in Figs. 3b and 4b, it is

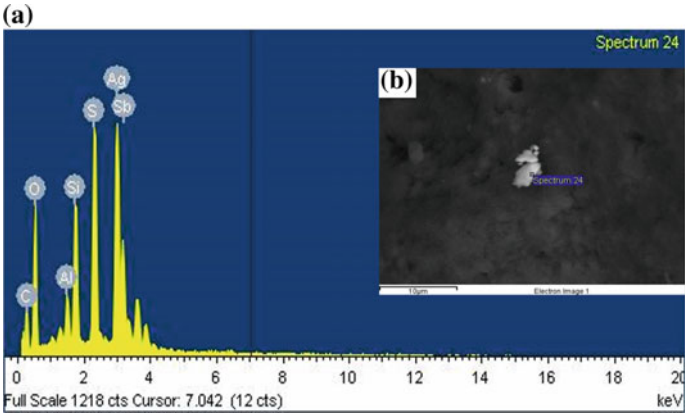

Fig. 3 **a** and **b** Micrograph with backscattered electrons and X-ray microanalysis, respectively, of the Morelos mining waste sample

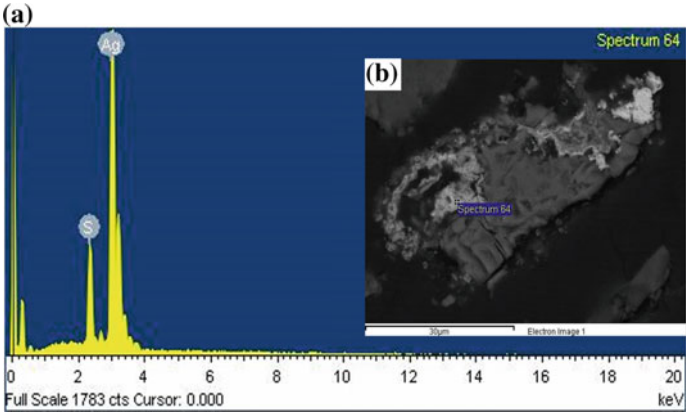

Fig. 4 **a** and **b** Micrograph with backscattered electrons and X-ray microanalysis, respectively, of the Morelos mining waste sample

important to note that these results are consistent with those obtained in the chemical analysis performed by ICP, where the presence is reported Sb and Ag [16].

Through the use of backscattered electrons, metal particles of different densities were identified, corresponding to the mineral species that contain silver. According to the literature and the results obtained, it can be determined that mineral species that contain silver correspond to simple sulfides such as argentite or acantite, as well as more complex species known and identified as sulfosalt of arsenic and antimony argentiferous, as confirmed by microanalysis of X-ray. Another aspect that should also be highlighted is that the silver particles are occluded in different galena and silicon matrices, which make the leaching process difficult because the leaching agent interacts partially with the particles of silver.

Conclusion

Granulometric analysis revealed a higher concentration of Ag contained at −400 mesh (<37 μm) with a weight percentage of 46.55%; however, the use of 44 μm particles (weight percentage equivalent to 15.07%) reduces the risk of agglomerates in hydrometallurgical treatments. The content of 104.8 g Ag ton^{-1}, the significant content of Fe (2.73% Wt), and the abundant presence of trace elements were corroborated by AAS and ICP, to later complement the chemical analysis of the sample of tailings by XRF, confirming the association of Ag, As, Sb, Au, Zn, Cu, and Fe.

Through LPM, it was possible to identify the presence of a sulfosal where an irregular and varied morphology was observed, which was an analysis consistent with the results obtained in SEM-EDS that allowed to observe the presence of Sb and Ag.

The chemical, mineralogical, and granulometric characterization of the mine wastes from the state of Morelos showed silver contents mainly associated with a sulfosal called pyrargirite (Ag_3SbS_3) and simple sulfides such as argentite and acantite (Ag_2S) occluded in a silicon matrix. The presence of potassium silicoaluminates ($AlKO_8Si_3$) was also observed, by XRD.

References

1. Melgarejo J, Proenza J, Galí, S, Llovet X (2010) Técnicas de caracterización mineral y su aplicación en exploración y explotación minera. Boletín de la Sociedad Geológica Mexicana 62(1):1–23
2. Rollinson G, Moon C (2014) Quantitative mineralogical and chemical assessment of the Nkout iron ore deposit, Southern Cameroon. Ore Geol Rev 62:25–39. https://doi.org/10.1016/j.oregeorev.2014.02.015
3. Baum W (2014) Ore characterization, process mineralogy and lab automation a roadmap for future mining. Miner Eng 60:69–73. http://dx.doi.org/10.1016/j.mineng.2013.11.008
4. Lopez C (2014) México: Política en Materia Minera. (Diálogo Unión Europea-América Latina Sobre Materias Primas). Available online: europa.eu/geninfo/query/index.do?queryText=plata&query_source=GROWTH& summary=summary&more_options_source=restricted&more_options_date=*&more_options_date_from=&more_options_date_to=&more_options_language=es&more_options_f_formats=*&swlang=en
5. Jamieson H, Walker S, Parsons M (2015) Mineralogical characterization of mine waste. Appl Geochem 57:85–105. http://dx.doi.org/10.1016/j.apgeochem.2014.12.014, 0883-2927
6. Murciego A, Alvarez E, Aldana S, Sanz A, Medina J, Rull F, Villar P (2019) Characterization of secondary products in arsenopyrite-bearing mine wastes: influence of cementation on arsenic attenuation. J Hazard Mater 373:425–436. https://doi.org/10.1016/j.jhazmat.2019.03.086
7. Parga J, Carrillo F (1996) Avances en los métodos de recuperación de oro y plata de minerales refractarios. Rev Metal Madrid 32(4):254–261
8. Alp I, Celep O, Paktunç D, Thibault Y (2014) Influence of potassium hydroxide pretreatment on the extraction of gold and silver from a refractory ore. Hydrometallurgy 146:64–71. https://doi.org/10.1016/j.hydromet.2014.03.007
9. Jamieson H, Walker S, Parsons M (2015) Mineralogical characterization of mine waste. Appl Geochem 57:85–105. https://doi.org/10.1016/j.apgeochem.2014.12.014 0883-2927

10. Teja A, Juarez J, Reyes M, Hernandez L, Flores M, Reyes I, Perez M, Moreno R (2017) Characterization and leaching proposal of Ag(I) from a Zn concentrate in an $S2O_3^{2-}$–O_2 medium. In: Characterization of minerals, metals, and materials. Springer, Cham, Switzerland, vol 146, pp 567–575
11. Juarez J, Patiño F, Roca A, Teja A, Reyes I, Reyes M, Perez M, Flores M (2018) Determination rates of Ag contained in metallurgical and mining residues in the $S_2O_3^{2-}$–O_2–Cu^{2+} system: kinetic analysis. Minerals 8:309. https://doi.org/10.3390/min8070309
12. Li W, Liu Z, Huang Q, Tang Y, Qiu X (2016) Extraction of low-grade silver from a refractory Au–Ag ore in cyanidation by pretreatment with reductive alkaline leaching. Hydrometallurgy 164:257–264. https://doi.org/10.1016/j.hydromet.2016.06.021
13. Celep O, Yazici E, Altinkaya P, Deveci H (2019) Characterization of a refractory arsenical silver ore by mineral liberation analysis (MLA) and diagnostic leaching. Hydrometallugy 189:105106. https://doi.org/10.1016/j.hydromet.2019.105106
14. Osseo-Asare K (1989) Solution chemistry and separation processes in precious and rare metal systems. In: Torma AE, Gundilo IH (eds) Precious and rare metals technologies. Elsevier, Amsterdam
15. Rocha-Castro E (2000) Principios Básicos de Espectroscopia; Editorial Uach, México, 123–203
16. Martínez-Frías J, Martín-Ramos J (1995) Sulfuros y Sulfosales de metales nobles, 1st edn. Textos Universitarios, Madrid, España, pp 44–48

Development and Characterization of a Luminescent Coating for Asphalt Pavements

Elkin I. Gutiérrez and Henry A. Colorado

Abstract In the present study, the performance of a photoluminescent asphalt coating made from recycled expanded polystyrene (EPS) and strontium aluminate particles deposited on asphalt pavements was characterized and evaluated, in order to give an alternative use to the problem which represents the large volumes of ESP in landfills worldwide. This study used two solvent mixtures for the degradation of recycled EPS: ethyl acetate and acetone. The characterization was conducted using scanning electron microscopy and tensile and shear tests. The purpose of this work was to develop a coating with particles that absorb light from the sun and became activated during the night. It is expected that this coating can be used in the demarcation of roads in order to improve road safety, reduce energy consumption at night, and give aesthetics to the roads, producing artificial lighting that does not generate electricity consumption.

Keywords Expanded polystyrene · Recycling · Strontium aluminate · Asphalt coating

Introduction

Expanded polystyrene (EPS) is one of the most widely produced basic polymer products in the world due to its versatile application in different fields [1]. The EPS has a coefficient of thermal conductivity of 0.03 W/mK, which has led to its extensive use for thermal insulation purposes [2]. Another important application is the packaging of food, electronic products, and other fragile materials due to its low density. The EPS, which is often used as packaging, contains 98% air and 2% polystyrene (PS).

E. I. Gutiérrez
Faculty of Mechanics, Electronic and Biomedical Engineering, Universidad Antonio Nariño, Cl. 52 #40-88, Medellín, Colombia

H. A. Colorado (✉)
CCComposites Laboratory, Universidad de Antioquia UdeA, Calle 70 N°. 52-21, Medellín, Colombia
e-mail: henry.colorado@udea.edu.co

J. Li et al. (eds.), *Characterization of Minerals, Metals, and Materials 2020*,
The Minerals, Metals & Materials Series,
https://doi.org/10.1007/978-3-030-36628-5_50

This material occupies large landfill space and is not biodegradable, being also an important component of urban waste and marine debris. Because it has a very low density (<50 kg/m^3), it spreads easily due to wind, which increases the environmental pollution [3]. EPS waste recycling has recently received great attention worldwide due to changes in regulatory standards and its associated environmental issues.

The two main approaches used to manage polystyrene waste are (i) energy recycling, where waste is incinerated [4] and (ii) mechanical recycling, where waste is recycled into secondary raw materials without changing the basic structure [5]. The incineration of PS can produce dangerous chemicals. In mechanical recycling, the process of recovering these wastes is usually more expensive than producing virgin plastic. These recycling processes are also not economical due to the cost of transportation involved due to the voluminous nature of the material. Therefore, the recycling of EPS in products with good economic value and appreciable end use is highly necessary. Taking these facts into account, other processing routes are explored to reduce the cost and environmental impact of the recycling process. One of the methods by which this can be achieved is by dissolving EPS in suitable solvents and having processes that transport the moving process equipment to reduce the transport of EPS. Through this method, it can be obtained a volume reduction of more than 100 times and a recovery of PS in forms such as foams, nano/microparticles, laminates, and other materials [6–8].

On another hand, there are several materials that have been used as luminous materials for various applications. Particularly, strontium aluminate particles have been used on asphalt surfaces, applied in coatings, and this is because these particles have luminescence by UV radiation, and with the addition of doping elements can also have mechano-luminescence, caused by mechanical deformations [9–11].

Materials with photoluminescent properties are widely used in light paints, textiles, and safety notices. Strontium aluminate is commonly used doped with Europium (Eu^{2+}) and Disprocio (Dy^{3+}), and its phosphorescent properties can be enhanced by co-doping with ions such as rare earths or other metal ions [11, 12]. The properties that highlight these materials are high radiation intensity, color purity, high luminescence, chemical, and non-radioactive stability [13]. However, these particles are sensitive to environmental conditions and may lose photoluminescent properties due to oxidation, which is why they are often dispersed or coated in a polymer matrix, which can greatly increase the stability of the compounds. Bem et al. [13] made compounds of strontium aluminate doped with Europium and Dysprosium, in a low density polyethylene matrix. The results showed that the particles slightly decreased the crystallinity of the polymer but considerably improved its stability, which is attributed to the immobilization of the polymer chains. The objective of this study is to give an alternative use to EPS waste (Fig. 1a).

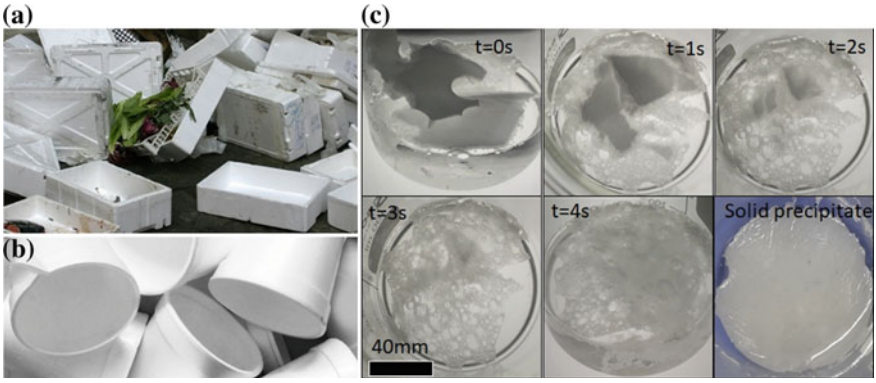

Fig. 1 EPS waste and its degradation process in the solvent

Materials and Methods

The EPS used for this study was taken from clean EPS food containers (Fig. 1b), which were manually crushed and subsequently degraded in the solvent until a homogeneous precipitate was obtained. Then, the excess of solvent was removed (Fig. 1c).

The degradation of EPS was carried out by mixing mixtures of two solvents commonly used in the degradation of polystyrene: acetone and ethyl acetate.

According to preliminary tests, it was observed that the solution in pure acetone produces a thicker and more opaque precipitate than that obtained using pure ethyl acetate; however, the adhesive characteristics of pure ethyl acetate did not show a good performance. Therefore, mixtures of ethyl acetate (EA) and acetone (Ace) were made in different proportions, in order to establish that the proportion of solvents has better characteristics in terms of adhesiveness and translucency of the EPS precipitate. For this, a design of experiments was carried out to establish a solvent with good characteristics to be used as the basis for an asphalt coating. The proportions and solvents used in this experimental design are presented in Table 1.

From the solvents obtained, tensile and shear tests were performed in order to establish the adhesive characteristics of the resulting EPS precipitate. For standard stress tests, the standard AASHTO TP-XX-11 (Standard Method of Test for Determining Asphalt Binder Bond Strength by Means of the Bitumen Bond Strength (BBS) Test) was used, while for the performance of shear stress tests, the ASTM D1002

Table 1 Design of experiments to establish the volume proportions of the solvent for the degradation of EPS

Designation	Ethyl acetate (%)	Acetone (%)
EA80	80	20
EA50	50	50
EA20	20	80

Table 2 Design of experiments for the determination of the persistence time and the degree of luminosity of the projected coating

Designation	Solvent composition	Weight of SA (%)
AE50SA5	EA 50% Ace 50%	5
AE80SA5	EA 80% Ace 20%	5
AE100SA5	EA 100% Ace 0%	5
AE50SA10	EA 50% Ace 50%	10
AE80SA10	EA 80% Ace 20%	10
AE100SA10	EA 100% Ace 0%	10
AE50SA20	EA 50% Ace 50%	20
AE80SA20	EA 80% Ace 20%	20
AE100SA20	EA 100% Ace 0%	20

(Standard Test Method for Apparent Shear Strength of Single-Lap-Joint Adhesively Bonded Metal Specimens by Tension Loading (Metal-to-Metal)) was used. The tests have two replicas for each condition, in order to quantify the average values and the standard deviations of the measurements made.

Additionally, a characterization of the strontium aluminate used in the development of the proposed asphaltic coating was carried out, and subsequently, based on the adhesion results previously obtained, a design of experiments was considered in which the weight percentage aluminate was taken into consideration in relation to the content by weight of EPS precipitates (obtained with the solvent mixtures). This procedure was followed in order to establish the appropriate ratio of EPS/strontium aluminate precipitate that allows obtaining an adequate light intensity and the persistence time of luminescence in the coating. The design of experiments projected to determine the luminosity and the persistence time of this is presented in Table 2.

The shear and tensile tests were conducted in a Shimadzu AG250KN universal testing machine at 1 mm/min crosshead speed. Scanning electron microscopy (SEM) images were obtained in a JEOL JSM 6700R operated in high vacuum mode, in samples coated with a thin film of gold.

Results and Discussion

The residues obtained with the different solvent mixtures generate a significant amount of bubbles during the solidification process. In Fig. 2, the appearance of the bubbles generated by using the solvent mixtures referred to in Table 1 is presented.

The tensile tests were performed based on the AASHTO TP-XX-11 standard. This test method quantifies the tensile force necessary to remove a piece (pullout stub) adhered to a solid substrate with asphalt binder. The samples were prepared under ambient conditions of temperature (23 °C) and relative humidity (69%). The assembly used to perform the stress tests as well as the post-removal state of the pullout stub is shown in Fig. 3a. In these tests, it is evidenced that all the failures

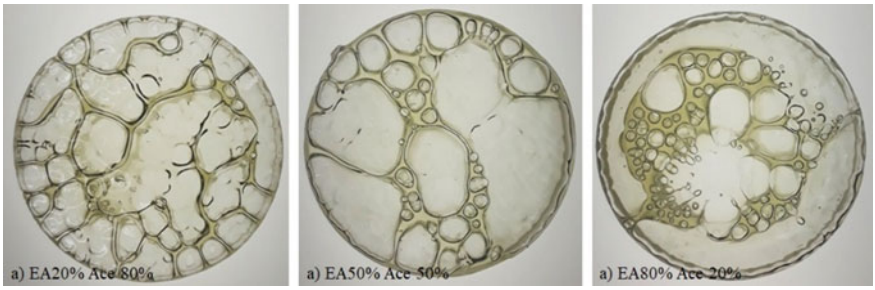

Fig. 2 Bubble formation during the solidification process

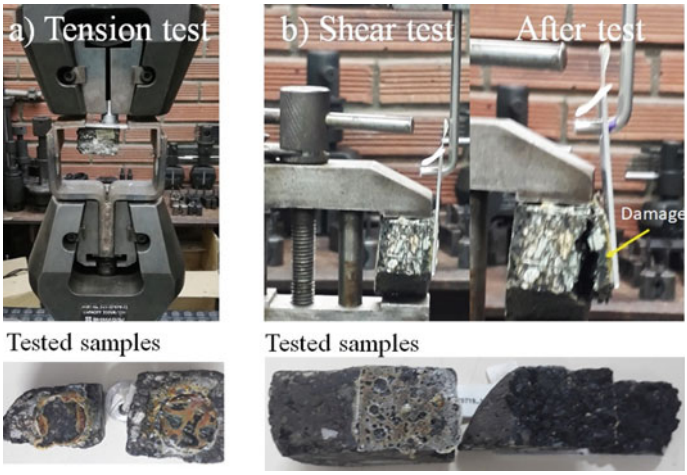

Fig. 3 Assembly used in tension and shear tests

were caused by adhesive failure. Similarly, in Fig. 3b, the assembly used and the state of two samples are shown after the shear stress test. In this figure, it can be seen how the EPS precipitate used as an asphalt adhesive produces a tear of the asphalt substrate, which infers that some of the EPS precipitates exhibit a fracture of the substrate, so that the asphalt coating would be oversized for application.

The results obtained in the stress and shear stress tests are shown in Fig. 4, and the means and their standard deviations are shown in Table 3.

The previous results show that solvent mixtures with a higher proportion of acetone provide EPS precipitates with good adhesion. However, for the shear stress tests adhesion, a fracture of the asphalt substrate appeared, which is not desirable for this application.

Figure 5 shows strontium aluminate microparticles obtained with the scanning electron microscopy. The images revealed the particles size ranged from about 2–30 μm, with an amorphous morphology.

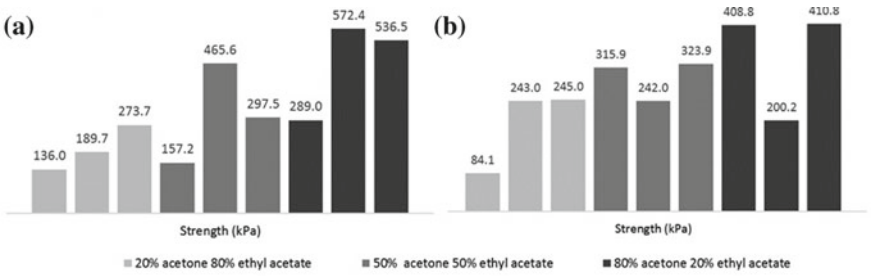

Fig. 4 Maximum load results. **a** in tension tests, **b** in shear stress tests

Table 3 Results obtained in tension and shear stress tests

Solvent composition	Tension test		Shear test	
	Mean	Std. dev.	Mean	Std. dev.
EA80	199.8	69.4	190.7	92.3
EA50	306.8	154.4	294.0	45.1
EA20	466.0	154.3	339.9	121.0

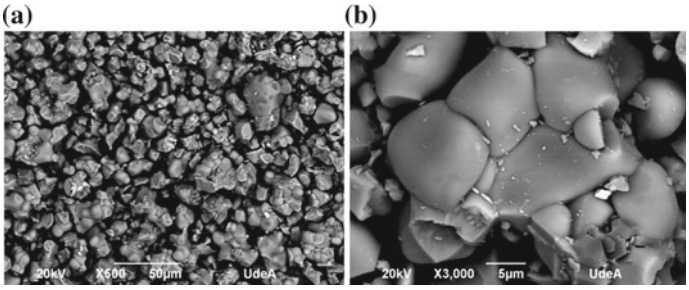

Fig. 5 Scanning electron microscopy images for the strontium aluminate particles

Finally, the coating samples were prepared using the design of experiments proposed in Table 2. The samples prepared are shown in Fig. 6.

The overall results suggest that several transparent or semitransparent polymer derived waste materials and resins can be used in combination with fluorescent particles aiming its use in infrastructure applications. Among those, Poly-DCPD [14] vinyl ester [15], epoxy resin [16] PET [17], and PP [18] particle matrix composites can be used. It also can be combined with other photoluminescence materials [19]. Therefore, there is a great possibility of using a large amount of recycled expanded polystyrene (EPS) in replacing electric road lighting or in not heavy traffic roads that require less illumination. Therefore, there are two contributions for a better environment: a new use for a solid waste and the reduction in the electrical energy

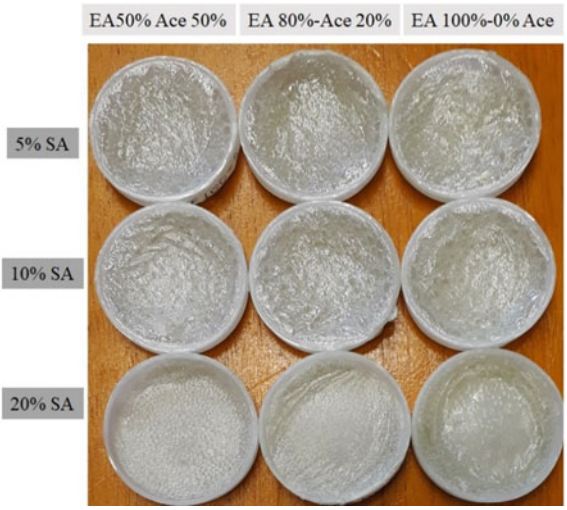

Fig. 6 Samples made using different proportions by weight of strontium aluminate

consumption by putting fluorescence materials that operate only with the sunlight and with the cars lights.

Summary

The present investigation has shown novel result regarding the use of a problematic and harmful solid waste available worldwide: expanded polystyrene (EPS) waste. This recycled EPS was used in combination with strontium aluminate as luminescence particles. These particles gave the composite properties of a multifunctional material, not only giving a solution for the waste, but also contributing for the lighting of remote area rods that require illumination and also in potentially reducing the need of electrical power, which certainly is a need nowadays with the issues associated with the increasing pollution. The mechanical properties of the film were acceptable, and all the manufactured system requires further investigation and optimization.

Acknowledgements The authors thank UAN University for the financing of the 2018221 project. This article is the result of the work carried out during the development of the project "Development, characterization, and manufacture of luminous asphalt and the thermo-mechanical device for its application" by grant PI/UAN-2019-657REM.

References

1. Chauhan RS, Gopinath S, Razdan P, Delattre C, Nirmala GS, Natarajan R (2008) Thermal decomposition of expanded polystyrene in a pebble bed reactor to get higher liquid fraction yield at low temperatures. Waste Manag 28(11):2140–2145. https://doi.org/10.1016/J.WASMAN.2007.10.001C
2. Aciu C, Manea DL, Molnar LM, Jumate E (2015) Recycling of polystyrene waste in the composition of ecological mortars. Proc Technol 19:498–505. https://doi.org/10.1016/J.PROTCY.2015.02.071
3. Kan A, Demirboğa R (2009) A new technique of processing for waste-expanded polystyrene foams as aggregates. J Mater Process Technol 209(6):2994–3000. https://doi.org/10.1016/J.JMATPROTEC.2008.07.017
4. You J-H, Chiang P-C, Chang K-T, Chang S-C (1994) Polycyclic aromatic hydrocarbons (PAHs) and mutagenicity of soot particulates in air emissions from two-stage incineration of polystyrene. J Hazard Mater 36(1):1–17. https://doi.org/10.1016/0304-3894(93)E0045-4
5. Gutiérrez C, García MT, Gracia I, Lucas A, Rodríguez JF (2012) Recycling of extruded polystyrene wastes by dissolution and supercritical CO_2 technology. J Mater Cycles Waste Manage 14(4):308–316. https://doi.org/10.1007/s10163-012-0074-9
6. Rajeev A, Erapalapati V, Madhavan N, Basavaraj MG (2016) Conversion of expanded polystyrene waste to nanoparticles via nanoprecipitation. J Appl Polym Sci 133(4). https://doi.org/10.1002/app.42904
7. Gutiérrez C, Rodríguez JF, Gracia I, de Lucas A, García MT (2014) Preparation and characterization of polystyrene foams from limonene solutions. J Supercrit Fluids 88:92–104. https://doi.org/10.1016/J.SUPFLU.2014.02.002
8. Wang Z, Bai R (2005) Preparing microgranules from waste polystyrene through a novel temperature- and nonsolvent-induced phase separation method for potential adsorbent. Ind Eng Chem Res 44(4):825–831. https://doi.org/10.1021/ie049258e
9. Akiyama M, Xu C-N, Liu Y, Nonaka K, Watanabe T (2002) Influence of Eu, Dy co-doped strontium aluminate composition on mechanoluminescence intensity. J Lumin 97(1):13–18. https://doi.org/10.1016/S0022-2313(01)00419-7
10. Chandra BP, Sonwane VD, Haldar BK, Pandey S (2011) Mechanoluminescence glow curves of rare-earth doped strontium aluminate phosphors. Opt Mater 33(3):444–451. https://doi.org/10.1016/J.OPTMAT.2010.10.014
11. Mishra SB, Mishra AK, Revaprasadu N, Hillie KT, Steyn WJ vdM, Coetsee E, Swart HC (2009) Strontium aluminate/polymer composites: morphology, luminescent properties, and durability. J Appl Polym Sci 112(6):3347–3354. https://doi.org/10.1002/app.29933
12. García CR, Diaz-Torres LA, Salas P, Guzman M, Angeles-Chavez C (2015) Photoluminescent and photocatalytic properties of bismuth doped strontium aluminates blended with titanium dioxide. Mater Sci Semicond Process 37:105–111. https://doi.org/10.1016/J.MSSP.2015.02.032
13. Bem DB, Luyt AS, Dejene FB, Botha JR, Swart HC (2009) Structural, luminescent and thermal properties of blue $SrAl_2O_4:Eu^{2+}$, Dy^{3+} phosphor filled low-density polyethylene composites. Phys B 404(22):4504–4508. https://doi.org/10.1016/j.physb.2009.09.050
14. Colorado HA, Yuan W, Guo Z, Juanri J, Yang J-M (2014) Poly-dicyclopentadiene-wollastonite composites toward structural applications. J Compos Mater 48(16):2023–2031. https://doi.org/10.1177/0021998313494098
15. Zhang X, Bitaraf V, Wei S, Guo Z, Zhang X, Wei S, Colorado HA (2014) Vinyl ester resin: rheological behaviors, curing kinetics, thermomechanical, and tensile properties. AIChE J 60(1):266–274. https://doi.org/10.1002/aic.14277
16. Wang Z, Colorad HA, Guo Z-H, Kim H, Park C-L, Hahn HT, Lee SG, Lee KH, Shang Y-Q (2012) Effective functionalization of carbon nanotubes for bisphenol F epoxy matrix composites. Mater Res 15(4):510–516. https://doi.org/10.1590/S1516-14392012005000092

17. Mariscal LB, Carmona-Téllez S, Alarcón-Flores G, Meza-Rocha AN, Murrieta HS, Falcony C (2015) Synthesis of Al_2O_3: Eu^{3+} powder and PET films with this powder incorporated: a luminescence study. ECS J Solid State Sci Technol 4(7):R97–R104. https://doi.org/10.1149/2.0111507jss
18. Ambid M, Mary D, Teyssedre G, Laurent C, Montanari GC (2005) Investigation of electrical and luminescent properties of polypropylene-based nanocomposite materials. In: Proceedings of 2005 international symposium on electrical insulating materials, (ISEIM 2005), vol 1, 227–230. https://doi.org/10.1109/ISEIM.2005.193384
19. Dhage SR, Colorado HA, Hahn HT (2013) Photoluminescence properties of thermally stable highly crystalline CdS nanoparticles. Mater Res 16(2):504–507. https://doi.org/10.1590/S1516-14392013005000020

Effect of Alloying Elements on Age Hardening and Coarsening of β′ Precipitates in Isothermally Aged Fe–Ni–Al Based Alloys

Victor M. Lopez-Hirata, Hector J. Dorantes-Rosales, Nicolas Cayetano-Castro, Maribel L. Saucedo-Muñoz and Jose D. Villegas-Cardenas

Abstract Precipitation and coarsening processes of Fe-10 at.% Ni-15 at.% Al, Fe-10 at.% Ni-15 at.% Al-1 at.% Cr, and Fe-10 at.% Ni-15 at.% Al-1 at.% Cu alloys were carried out during isothermal aging at temperatures of 750, 850, and 950 °C using experimental and numerical analysis methods. Thermo-Calc numerical results indicated that the Cu addition promoted higher volume fraction of β′ precipitates, which caused better response to the age hardening than the other two alloys. The coarsening resistance was also detected to be higher for the Cu-containing alloy in comparison with the other alloys because of its lower solubility and volume diffusion in the ferrite matrix. The Cu and Cr alloying elements were observed to be located in the precipitate and matrix, respectively, according to their expected thermodynamic behavior.

Keywords Fe–Ni–Al alloys · β′ precipitation hardening · Cu and Cr additions · Aging · Thermo-Calc

Introduction

Fe–Ni–Al based alloys are important for the development of different engineering alloys such as PH stainless steels and Fe–Cr–Ni–Al alloys. [1]. They have been selected to fabricate industrial components which require a good combination of mechanical strength and oxidation resistance at temperatures of about 800 °C [1, 2]. Their enhanced mechanical strength is promoted by a hardening precipitation treatment which is related to the formation of an ordered NiAl-type phase with a B2 (CsCl) crystalline structure, designated as the β′ phase [3, 4]. Another advantage of Fe–Ni–Al alloys is their density of approximately 5.7 g/cm^3 in comparison with that

V. M. Lopez-Hirata (✉) · H. J. Dorantes-Rosales · N. Cayetano-Castro · M. L. Saucedo-Muñoz · J. D. Villegas-Cardenas
Instituto Politécnico Nacional (ESIQIE-ESFM), UPALM Edif. 7, 07300 Mexico, D.F., Mexico
e-mail: vlopezhi@prodigy.net.mx

J. Li et al. (eds.), *Characterization of Minerals, Metals, and Materials 2020*,
The Minerals, Metals & Materials Series,
https://doi.org/10.1007/978-3-030-36628-5_51

of Ni based super alloys, about 8 g/cm^3. As mentioned previously, the mechanical strength of this type of alloy is usually obtained by forming coherent precipitates in a soft matrix. Likewise, the mechanical properties of precipitation hardened alloys are closely related to the morphology, spatial distribution, volumetric fraction, and average radius of the precipitated particles in the matrix phase. These microstructural characteristics can be controlled by means of aging heat treatments; nevertheless, they are also changed during the operation of industrial components at high temperatures for prolonged times [3].

The precipitate coarsening of alloys is a metallurgical phenomenon, which occurs at high temperatures, and it involves the dissolution of small precipitates and subsequently atomic diffusion to the larger precipitates during aging process. This phenomenon, also known as Ostwald ripening, has a considerable effect on the alloys' mechanical properties [4]. The Lifshitz–Slyozov–Wagner (LSW) theory for diffusion-controlled coarsening predicts growth kinetics dependence with time, t, of $t^{1/3}$ considering spherical precipitates without elastic interaction with the matrix phase, equilibrium matrix composition near zero, and precipitate volume fraction close to zero [5, 6].

Additionally, several studies for precipitation process have been carried out in Fe–Ni–Al based alloys. Results have shown that the coarsening growth kinetics of the NiAl-type β′ phase precipitation in a Fe-rich matrix phase follows the LSW theory for diffusion-controlled coarsening [5, 6]. Furthermore, the addition of alloying elements such as Cr and Cu has been shown [7] to have influence on the coarsening kinetics of these alloys.

The application of Thermo-Calc software has been recently [7, 8] applied successfully to analyze the precipitation process of different alloy systems. Therefore, the purpose of the present work is to analyze the precipitation and coarsening processes of β′ precipitates in a ferritic matrix for the Fe-10 at.% Ni-15 at.% Al, Fe-10 at.% Ni-15 at.% Al-1 at.% Cr, and Fe-10 at.% Ni-15 at.% Al-1 at.% Cu alloys aged artificially at high temperatures to understand its effect on aging hardness using numerical and experimental methods.

Experimental Procedure

Three alloy compositions, Fe-10 at.% Ni-15 at.% Al, Fe-10 at.% Ni-15 at.% Al-1 at.% Cr, and Fe-10 at.% Ni-15 at.% Al-1 at.% Cu, were melted with an electric arc furnace under an argon atmosphere using high-purity Fe (99.9%), Ni (99.99%), Al (99.7%), Cu (99.99%), and Cr (99.9%). The chemical composition of alloys was verified pursuing the chemical analysis by the atomic absorption method. The actual composition was very close to the nominal one, ±0.5%. The alloy ingots were heated at 1100 °C for one week to destroy the as-cast microstructure and to homogenize the chemical composition. Specimens of 30 mm × 30 mm × 10 mm were cut and encapsulated in a quartz tube under argon atmosphere to conduct the solution treatment at 1100 °C for 1 h, and then aged at 750, 850, and 950 °C for times from 5 to 1500 h. The

solution treated and aged specimens were prepared metallographically and etched with an etchant composed of 2 vol% nitric acid in methanol and then observed with a scanning electron microscope (SEM) equipped with an energy dispersive spectrometer (EDS) at 25 kV. The equivalent radius of precipitates was measured by means of the precipitate area on SEM images with an image analyzing system. In order to get representative data, 200 measurements were pursued in different zones of the specimens. These measurements mainly corresponded to precipitates with a cuboid morphology. Scanning transmission electron microscopy (STEM) analysis of some aged specimens was carried out with a high-angular annular dark field (HAADF) detector to obtain a Z-contrast, and it was combined with STEM-EDS analysis to know the distribution of chemical elements in matrix and precipitates of some aged specimens. The Vickers hardness, HV 0.1 kg/12 s, was measured in all the aged specimens.

Numerical Procedure

The analysis of phase stability was conducted using Thermo-Calc (TC) Software along with the thermodynamic database for Ni based alloys [8]. To simulate with Thermo-Calc, the chemical composition and temperature are usually specified. This software also enables us to determine the coarsening rate constant based on the LSW theory and the interfacial free energy between matrix and precipitate based on the nearest-neighbor broken-bond model [9].

Results and Discussion

Thermodynamic Stability of Phases and Interfaces

Figure 1a–c shows the equilibrium pseudo-ternary Fe–Ni–Al phase diagrams at 850 °C for the Fe-10 at.% Ni-15 at.% Al, Fe-10 at.% Ni-15 at.% Al-1 at.% Cu, and Fe-10 at.% Ni-15 at.% Al-1 at.% Cr alloys, respectively. These diagrams show the presence of the following phases: bcc α ferrite, fcc γ austenite, β' phase, and γ' phase. The γ austenite phase becomes more stable as the Ni content increases, while the ferrite and β' phases are more stable with the increase in Al content. The γ' phase is present as both the Al and Ni contents increase. The alloy compositions of the present work are located in the phase field of the α ferrite and β' phases, indicated by a black circle in Fig. 1a–c. The addition of 1 at.% Cr slightly decreases the field of $\alpha + \beta'$ phases, while the contrary effect is observed for the 1 at.% Cu addition. This behavior was also observed at higher temperatures.

The amount of all phase in equilibrium versus temperature is shown in Fig. 2a–c for the Fe-10 at.% Ni-15 at.% Al, Fe-10 at.% Ni-15 at.% Al-1 at.% Cu, and Fe-10

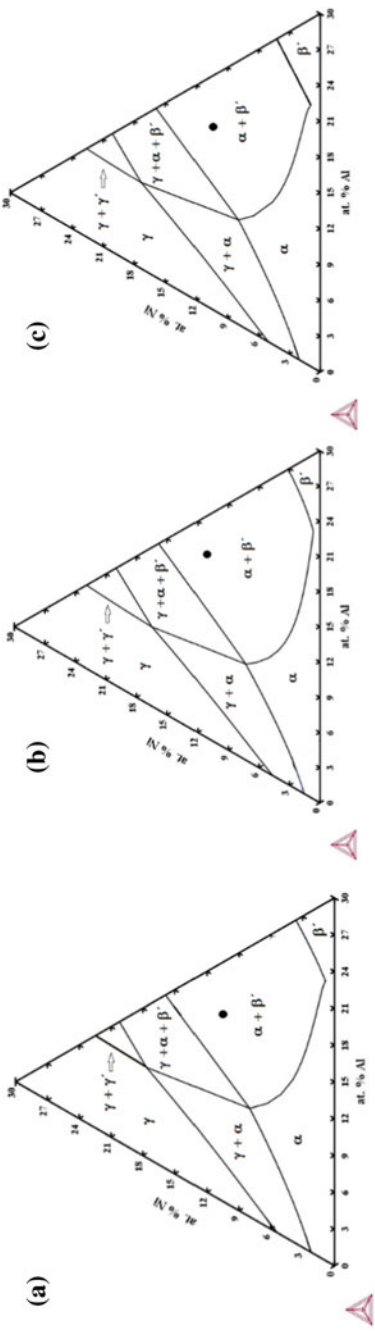

Fig. 1 Thermo-Calc calculated equilibrium pseudo-ternary phase diagrams at 850 °C for **a** Fe-10 at.% Ni-15 at.% Al, **b** Fe-10 at.% Ni-15 at.% Al-1 at.% Cu, and **c** Fe-10 at.% Ni-15 at.% Al-1 at.% Cr alloys

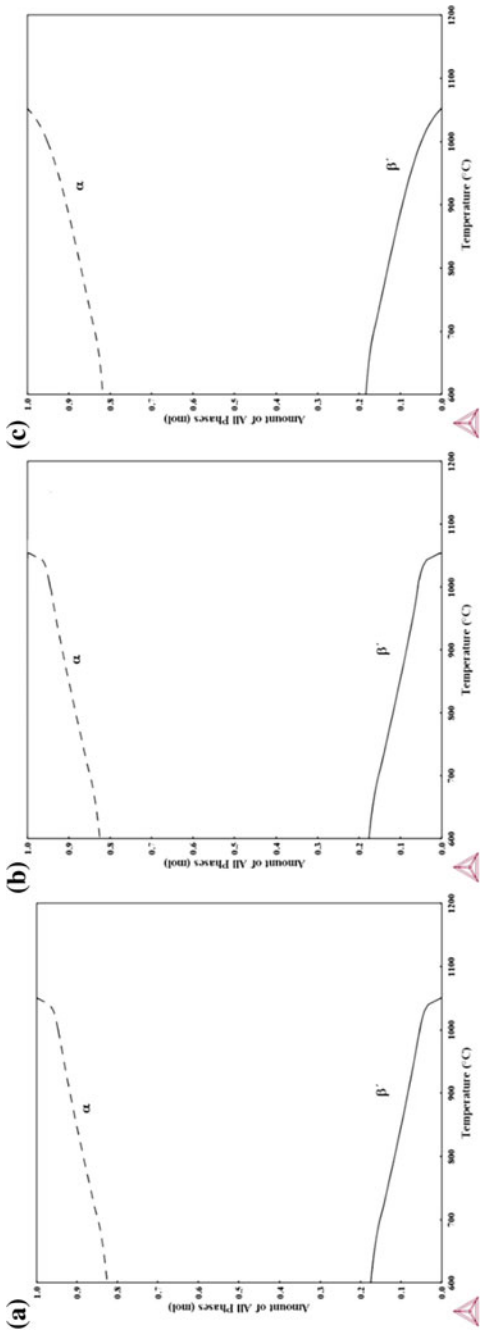

Fig. 2 Thermo-Calc calculated plot of the amount of all equilibrium phases versus temperature for **a** Fe-10 at.% Ni-15 at.% Al, **b** Fe-10 at.% Ni-15 at.% Al-1 at.% Cu, and **c** Fe-10 at.% Al-1 at.% Cr alloys

Table 1 Equilibrium chemical composition of the α and β′ phases at 750 °C

Alloy	α phase				
	at.% Fe	at.% Ni	at.% Al	at.% Cr	at.% Cu
Fe-10 at.% Ni-15 at.% Al	83.48	4.96	11.54	–	–
Fe-10 at.% Ni-15 at.% Al-1at.% Cr	82.47	4.91	11.48	1.12	–
Fe-10 at.% Ni-15 at.% Al-1 at.% Cu	83.74	4.68	11.21	–	0.43
Alloy	β′ phase				
Fe-10 at.% Ni-15 at.% Al	37.48	42.76	19.76	–	–
Fe-10 at.% Ni-15 at.% Al-1 at.% Cr	19.38	42.83	37.67	0.11	–
Fe-10 at.% Ni-15 at.% Al-1 at.% Cu	17.14	41.05	37.08	–	6.44

at.% Ni-15 at.% Al-1 at.% Cr alloys, respectively. These figures indicate that the ferrite phase is stable at temperatures higher than approximately 1050 °C for the three alloys. As temperature decreases, the following phase reaction takes place:

$$\alpha \rightarrow \alpha + \beta' \tag{1}$$

That is, the β′ phase precipitates in the α ferrite phase. Table 1 indicates, for instance, the equilibrium composition of the α and β′ phases at 750 °C. It can be confirmed that Cu is dissolved in the β′ phase, while Cr is contained in the α ferrite matrix phase. This fact was also observed to occur at temperatures of 850 and 950 °C. Furthermore, the Fe content of the β′ precipitates decreases notably with the addition of Cr or Cu and with the decrease in temperature. Another interesting point is that the largest volume fraction of the β′ precipitate is formed for the Cu-containing alloy, while the smallest amount is obtained for the ternary alloy. This suggests that the Cu addition favors the precipitation of the β′ phase, which can be attributable to the lower solubility of precipitates, since it promotes a higher solute supersaturation enhancing the driving force of precipitation in spite of the high interfacial free energy [6], as will be shown later.

Microstructure Characterization of β′ Precipitates

SEM micrographs of the precipitation evolution are shown in Fig. 3a–f for the Fe-10 at.% Ni-15 at.% Al, Fe-10 at.% Ni-15 at.% Al-1 at.% Cu, and Fe-10 at.% Ni-15 at.% Al-1 at.% Cr alloys, respectively, aged at 750 °C for 200 and 500 h. The morphology of the β′ precipitates is spheroidal for the three alloys aged at all aging temperatures for very short times, shorter than 25 h, because the interfacial free energy γ is higher than the elastic-strain energy. As the aging progresses, the precipitate morphology changes to rounded cuboids due to the increase in elastic-strain energy [6]. The straight sides of cuboid precipitates suggest the presence of a coherent interface between precipitates

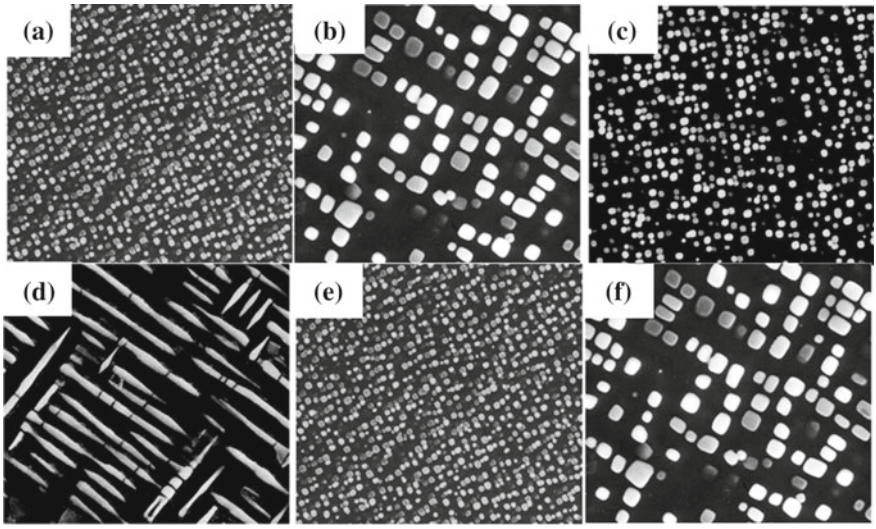

Fig. 3 SEM micrographs of the precipitation evolution for **a**, **b** the Fe-10 at.% Ni-15 at.% Al alloy, **b**, **c** Fe-10 at.% Ni-15 at.% Al-1 at.% Cu alloy, and **e**, **f** Fe-10 at.% Ni-15 at.% Al-1 at.% Cu alloy aged at 750 °C for 200 and 500 h, respectively

and matrix, and thus, the elastic-strain energy seems to become dominant [10]. The precipitates turn out to be aligned with the ferrite matrix over the course of time, Fig. 3b. This alignment has been reported [8] to occur in the <100> crystallographic direction of the ferrite matrix since it corresponds to the softest direction for the bcc crystalline structure. Further aging promotes the coarsening process of precipitates for the aged alloys. The precipitate size increases with the aging temperature. Aging for longer times shows a tendency to form square or rectangular arrays of cuboid precipitates for the three alloys; however, this fact seems to be greater in the ternary alloy aged at 750 and 850 °C than that at 950 °C, Fig. 3a, b. In the case of aging at 950 °C, arrays of elongated precipitates are aligned with respect to the ferrite matrix. Some coalescence of precipitates is also observed in these arrays, and the straight sides of some precipitates become curved. This suggests the loss of coherency between the precipitates and matrix. This characteristic is more notorious in the case of the aged ternary alloy. This behavior seems to be related to the higher elastic-strain effect in this alloy [8]. No splitting of precipitates was observed to occur in all the aged alloys. The lowest experimental volume fraction at all aging temperatures corresponds to the ternary alloy, and the highest one is for the Cu-containing alloy, which is in agreement with the Thermo-Calc calculated values. It is interesting to notice that the end of plates is like a rounded-tip for the aged Fe-10 at.% Ni-15 at.% Al-1 at.% Cu alloy, Fig. 3d, while it is more or less flat for the other aged alloys, Fig. 3e, f. This suggests that the coherency between matrix and precipitates is lost in the former alloy, and thus, the plate grows more easily in that direction [6], causing a larger length of plates in this case. This fact can be attributed to a higher

interfacial free energy, as will be shown later, which may be caused by a larger lattice-misfit because of the Cu addition [10]. The preferential alignment of precipitates on elastically softest directions occurred faster in the Cu-containing alloy.

Figure 4a illustrates the HAADF-STEM image of the Fe-10 at.% Ni-15 at.% Al-1 at.% Cr alloy aged at 950 °C for 50 h. Some β′ precipitates and the ferrite matrix can be observed in this micrograph. The STEM intensity profiles corresponding to Fe, Ni, Al, and Cr elements, following the straight line indicated in Fig. 4a, are shown in Fig. 5b. The presence of chromium is slightly higher in the ferrite matrix than that observed in the β′ precipitates. The iron content of precipitates is higher than that of

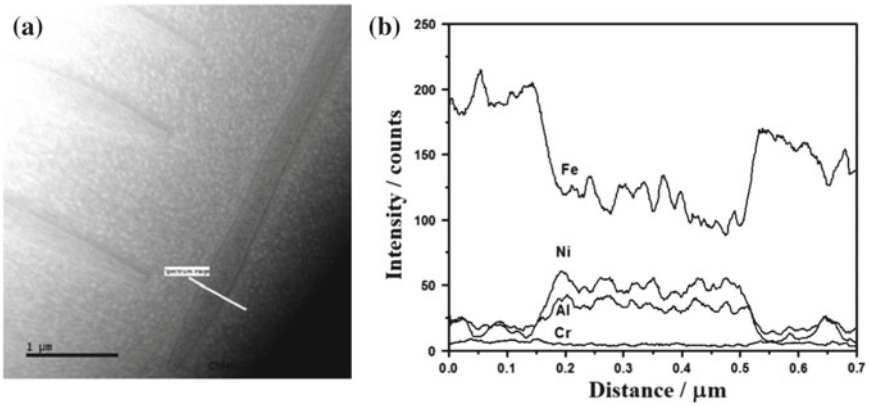

Fig. 4 **a** HAADF-STEM image of β′ precipitates in a Fe matrix and **b** Intensity profile of Fe, Ni, Al, and Cr

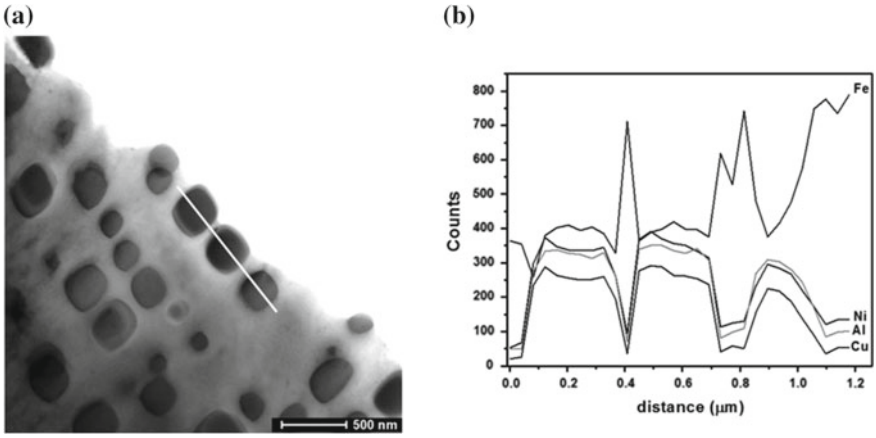

Fig. 5 **a** HAADF-STEM image of β′ precipitates in a Fe matrix and **b** Intensity profile of Fe, Ni, Al, and Cu

nickel and aluminum. This result is consistent with the equilibrium composition of the α ferrite matrix phase calculated by Thermo-Calc, as shown in Table 1.

In contrast, Fig. 5a shows a HAADF-STEM image of the Fe-10 at.% Ni-15 at.% Al-1 at.% Cu alloys aged at 750 °C for 100 h. The corresponding HAADF-STEM-EDS line scan profile is also shown for this specimen in Fig. 5b. It is evident the Fe-rich content of the ferritic matrix. In contrast, the β′ precipitates are composed of Fe, Ni, Al, and Cu. Furthermore, most of the Cu content is located within the β′ precipitates, which is in agreement with Thermo-Calc results in Table 1.

Coarsening Process

To show the coarsening kinetics in Fe–Ni–Al alloys, the average equivalent circle radius, r, of β′ precipitates, expressed as $r^3 - r_o^3$, is plotted as a function of aging time in Fig. 6a–c for the aged Fe-10 at.% Ni-15 at.% Al, Fe-10 at.% Ni-15 at.% Al-1 at.% Cu, and Fe-10 at.% Ni-15 at.% Al-1 at.% Cr alloys, respectively. These figures show straight line curves for the different cases, which suggest that the LSW theory for diffusion-controlled coarsening is followed in this study. The LSW theory and modified LSW theories [5, 6] express mathematically the variation of particle radius with time as follows [6]:

$$\bar{r}_t^3 - \bar{r}_0^3 = k\,t \tag{2}$$

where r_o and r are the average radius of precipitates at the onset of coarsening and time t, respectively, and k a rate constant, which is expressed by the following equation [6]:

$$k = \frac{8}{9}\frac{D\gamma C_\alpha V_\mathrm{m}}{RT} \tag{3}$$

where D is the diffusion coefficient, γ the interfacial free energy between precipitate and matrix, C_α the equilibrium solubility of precipitate, V_m the molar volume of precipitate, R the gas constant, and T the temperature. The constant k can be determined from the slope of straight lines in Fig. 6. The r_o value was determined from the linear regression analysis for each case. Table 3 shows the experimental values of rate constant k for each case, and they indicate that the coarsening process takes place more rapidly for the Fe-10 at.% Ni-15 at.% Al alloy aged at the three temperatures than that of the other two alloys. In general, the slowest growth kinetics can be observed for the aged Fe-10 at.% Ni-15 at.% Al-1 at.% Cu alloy. This behavior suggests that there is a considerable effect of chromium and copper on the Ostwald ripening process in Fe–Ni–Al alloys.

Table 2 shows the Thermo-Calc calculated values of interfacial free energy γ and coarsening rate constant k for these alloys. It can be noted that the interfacial free energy decreases with the increase in aging temperature for the three alloys.

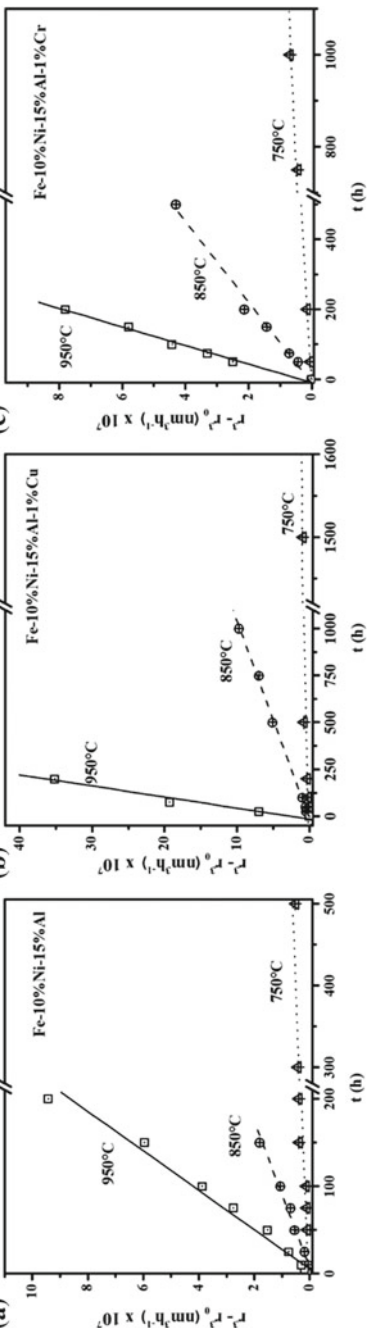

Fig. 6 Plot of r^3 versus t for the **a** Fe-10 at.% Ni-15 at.% Al, **b** Fe-10 at.% Ni-15 at.% Al-1 at.% Cu, and **c** Fe-10 at.% Ni-15 at.% Al-1 at.% Cr alloys aged at 750, 850, and 950 °C

Table 2 Thermo-Calc calculated coarsening rate constant k and interfacial free energy γ of β' precipitate in Fe–Ni–Al based alloys

Alloy	Coarsening rate k ($m^3\ s^{-1}$)			Interfacial energy γ ($J\ m^{-2}$)		
	750 °C	850 °C	950 °C	750 °C	850 °C	950 °C
Fe-10 at.% Ni-15 at.% Al	0.406×10^{-26}	10.040×10^{-26}	117.600×10^{-26}	0.1248	0.0755	0.0322
Fe-10 at.% Ni-15 at.% Al-1 at.% Cu	0.3582×10^{-26}	9.581×10^{-26}	110.800×10^{-26}	0.1358	0.0796	0.0387
Fe-10 at.% Ni-15 at.% Al-1 at.% Cr	0.409×10^{-26}	10.077×10^{-26}	117.200×10^{-26}	0.1243	0.0768	0.0341

Besides, the Cu-containing alloy presents the highest values of γ, while the lowest values correspond to the ternary alloy. In contrast, the lowest and highest values of coarsening rate constant k are observed to occur for the Cu-containing and ternary alloys, respectively. This tendency is in good agreement with the experimental values shown in Table 3; however, the experimental k values are lower than those determined numerically by Thermo-Calc, which can be attributable to the software-estimated parameters of Eq. (3) for these alloys.

The lower k values for the Cu and Cr-containing alloys, in comparison with the ternary alloy, can be explained as follows: according to Eq. (3), the constant k depends on the diffusion coefficient D, the interfacial energy γ, and the equilibrium solubility of precipitates C_α. In the case of Cu-containing alloy, the interfacial energy γ increases with the Cu addition, as shown in Table 3. Thus, the coarsening resistance can be enhanced only by the decrease in either D or C_α. In this case, the decrease in k values can be attributable to the decrease in the solubility of the β' precipitate, Table 1, and the decrease in volume diffusion promoted by the Cu addition, while the coarsening resistance of the Cr-containing alloy seems to be only related to the decrease in the volume diffusion process [6]. The highest values of k for studied alloys are observed to occur at 950 °C, which can be originated by the increase in volume diffusion and solubility of precipitates.

Table 3 Experimental values of coarsening rate constant k of β' precipitate in Fe–Ni–Al based alloys

Alloy	Coarsening rate k ($m^3\ s^{-1}$)		
	750 °C	850 °C	950 °C
Fe-10 at.% Ni-15 at.% Al	0.297×10^{-26}	3.333×10^{-26}	11.944×10^{-26}
Fe-10 at.% Ni-15 at.% Al-1 at.% Cu	0.153×10^{-26}	1.330×10^{-26}	10.550×10^{-26}
Fe-10 at.% Ni-15 at.% Al-1 at.% Cr	0.177×10^{-26}	1.805×10^{-26}	11.220×10^{-26}

Age Hardening Curves

The plots of Vickers hardness versus aging time are shown in Fig. 7a–c for the Fe-10 at.% Ni-15 at.% Al, Fe-10 at.% Ni-15 at.% Al-1 at.% Cu, and Fe-10 at.% Ni-15 at.% Al-1 at.% Cr alloys, respectively, aged at 750, 850, and 950 °C. The highest hardness of the solution treated alloy corresponded to the Cu-containing alloy, which may be attributed to the formation of Cu cluster in the ferrite matrix [7], since there is practically no solid solution in the ferrite. In the case of the Cr-containing alloy, a solid solution hardening can be noted because of the wide solubility of Cr in ferrite [11]. On the other hand, the lowest hardness value was observed to occur for the ternary alloy. An increase in hardness can be noted in all the aged alloys as a result of the process of β′precipitation. The highest and lowest increases in hardness took place at the lowest aging temperature of 750 °C and the highest one of 950 °C, respectively. This can be related to the precipitate size, which is the smallest for an aging temperature of 750 °C. Regarding the alloy composition, the highest and lowest hardness peak were detected for the Cu-containing and ternary alloys, respectively. In the former case, the age hardening can be attributable to the Cu content of the β′ precipitates, as shown in Table 1. That is, the Cu addition increases the volume fraction of the β′ precipitates, as shown in Fig. 2. Additionally, this decreases the iron content of the β′ precipitates and its chemical composition is closer to the composition of NiAl intermetallic. The ternary alloy presented the lowest volume fraction of precipitates, and thus, the lowest hardness. The fastest overaging stage occurred at temperatures of 850 and 950 °C. This is associated with the most rapid coarsening of precipitates because of the fastest atomic diffusion process at these temperatures [7].

Conclusions

A numerical and experimental study of the precipitation and coarsening processes was carried out during the isothermal aging at temperatures of 750, 850, and 950 °C for Fe-10 at.% Ni-15 at.% Al, Fe-10 at.% Ni-15 at.% Al-1 at.% Cr, and Fe-10 at.% Ni-15 at.% Al-1 at.% Cu alloys. The key findings are summarized as follows:

1. Thermo-Calc calculated results indicated that both the Cu and Cr addition promoted higher volume precipitation of β′ precipitates than that of the ternary alloy, and the Fe content in precipitates is also reduced. The Cu and Cr alloying elements are located mainly in the β′ precipitate and ferrite matrix, respectively.
2. The aging hardening of Cu-containing alloy was higher than that of the other alloys because of the higher volume fraction of β′ precipitates and its chemical composition close to the NiAl intermetallic compound.
3. The coarsening resistance of Cu-containing alloy was higher than that of the two other alloys, which can be attributable to the decrease of volume diffusion and solubility in the ferrite matrix.

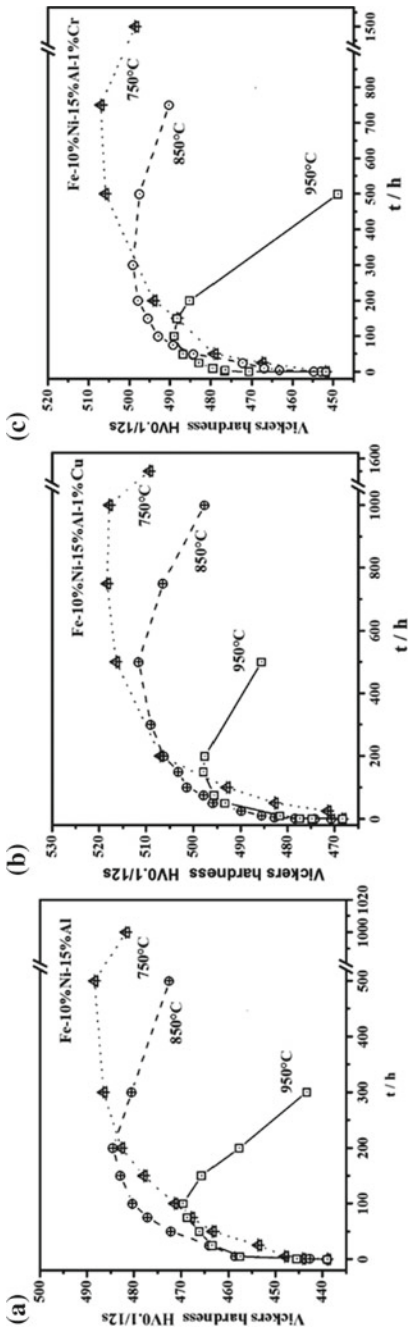

Fig. 7 Aging curves for the **a** Fe-10 at.% Ni-15 at.% Al, **b** Fe-10 at.% Ni-15 at.% Al-1 at.% Cu, and **c** Fe-10 at.% Ni-15 at.% Al-1 at.% Cr alloys aged at 750, 850, and 950 °C

Acknowledgements The authors wish to thank the financial support from SIP-COFAA-IPN and CONACYT.

References

1. Guo Z, Sha W, Vaumosse D (2003) Microstructural evolution in a PH13-8 stainless steel after ageing. Acta Mater 51:101–106
2. Stallybrass Sauthoff G (2004) Ferritic Fe–Al–Ni–Cr alloys with coherent precipitates for high-temperature applications. Mater Sci Eng, A 387:985–990
3. Stallybrass C, Schneider A, Sauthoff G (2005) The strengthening effect of (Ni,Fe)Al precipitates on the mechanical properties at high temperatures of ferritic Fe–Al–Ni–Cr alloys. Intermetallics 13:1263–1268
4. Muñoz-Morris MA, Morris DG (2007) Microstructure and mechanical behavior of a Fe–Ni–Al alloy. Mater Sci Eng A 444:236–241
5. Baldan A (2002) Progress in Ostwald ripening theories and their applications to nickel-base superalloys. J Mater Sci 37:2171–2202
6. Kostorz G (2001) Phase transformations in materials. Wiley-VCH, Germany
7. Saucedo-Muñoz ML, Ortiz-Mariscal A, Lopez-Hirata VM, Villegas-Cardenas JD, Soriano-Vargas O, Avila-Davila EO (2017) Precipitation in HK49 steel. Int J Min Met Mater 24:1125–1129
8. Thermo-Calc Software. TFe7.Version 2019a
9. Janssens KGF, Raabe D, Kozeschnik E, Miodownik MA, Nestler B (2007) Computational materials engineering. Academic Press, London
10. Cayetano-Castro N, Saucedo-Muñoz ML, Dorantes-Rosales HJ, Gonzalez-Velazquez LL, Villegas-Cardenas JD, Lopez-Hirata VM (2014) Ostwald ripening process of coherent β' precipitates during aging in $Fe_{0.75}Ni_{0.10}Al_{0.15}$ and $Fe_{0.74}Ni_{0.10}Al_{0.15}Cr_{0.01}$ alloys. Adv Mater Sci Eng 5:1–7
11. ASM (1992) ASM handbook, vol 3: Alloy phase diagrams. ASM International, USA

Effect of Different Ti-Sn Intermetallic Compounds Addition on Synthesis of Ti_2SnC by Self-Propagating High-Temperature Combustion Technique

Hongyan Sun, Xin Kong and Guiyang Liu

Abstract The higher purity of Ti_2SnC ternary compounds has been successfully synthesized by self-propagating high-temperature synthesis (SHS) technique with elemental Ti, Sn, C, and some different Ti-Sn intermetallic compounds powders as raw materials. The molar ratio of Ti/Sn/C was set 2:1:1. The results show that the additions of Ti_5Sn_3 and Ti_2Sn play a different role in the synthesis of Ti_2SnC and the optimum addition content are both 20%. Meanwhile, the reaction mechanism for the formation of Ti_2SnC in the system is confirmed that the Ti_5Sn_3 intermetallic compound reacts with TiC to form Ti_2SnC, rather than Ti_2Sn. And Ti_2SnC will partly decompose into Ti_5Sn_3 and TiC at higher temperatures.

Keywords Combustion synthesis · Ti_5Sn_3 · Ti_2Sn · Reaction mechanism · Ti_2SnC

Introduction

Titanium tin carbide (Ti_2SnC) is one of the most interesting materials in the family of the layered ternary compounds which has attracted much worldwide attention because it exhibits a number of excellent properties. It has high electrical and thermal conductivity, low hardness, good self-lubricity, easy machinability, resistance to corrosion, damage tolerant capability, etc. [1–4]. It is a promising candidate replacement material of graphite for diverse applications. There are several processing routes have been adopted to prepare Ti_2SnC including hot isostatic pressing (HIP) [5, 6], hot pressing (HP) [7, 8], pressureless sintering [9], and self-propagating high-temperature synthesis (SHS) [10–12]. However, the high purity of Ti_2SnC powder is difficult to obtain because TiC, Ti-Sn compounds or Sn as unwanted impurities always accompanying Ti_2SnC. The presence of TiC will deteriorate the high electrical conductivity and other properties of Ti_2SnC [9].

H. Sun · X. Kong · G. Liu (✉)
Department of Chemistry, College of Science, Honghe University, Mengzi 661199, Yunnan, China
e-mail: liuguiyang@tsinghua.org.cn

Local Characteristic Resource Utilization and New Materials Key Laboratory of Universities in Yunnan, Honghe University, Mengzi 661199, Yunnan, China

J. Li et al. (eds.), *Characterization of Minerals, Metals, and Materials 2020*,
The Minerals, Metals & Materials Series,
https://doi.org/10.1007/978-3-030-36628-5_52

Self-propagating high-temperature synthesis (SHS), developed by Merzhanov and Borovinskaya [13] in the late 1960s, is a new kind of method to produce ceramic [14], ceramic matrix composites [15], and so on. It has many attractive advantages, such as high purity of products, low processing cost, and energy and time efficiency, and non-polluting traits. Yeh and Kuo [10] have successfully synthesized Ti_2SnC powders with Ti/Sn/C and Ti/Sn/TiC powder mixtures with this method.

The main purpose of the paper is to prepare Ti_2SnC powders adopting a novel mixture system of Ti/Sn/C/Ti-Sn intermetallic compounds by using the SHS technique. The effect of different kinds of Ti-Sn intermetallic compounds on the high purity of Ti_2SnC is discussed in detail. And the reaction mechanism for the synthesis of Ti_2SnC phase is also researched.

Experimental Procedures

Commercial Ti (average particle size: 500 mesh, 99.7 purity), Sn (average particle size: 200 mesh, 99.6 purity), carbon black (average particle size: 330 mesh, 99.5 purity), and self-made intermetallic compounds of Ti_5Sn_3 and Ti_2Sn (average particle size: 200 mesh) powders were used in the present study. The powders of Ti, Sn, C with stoichiometric ratio of Ti_2SnC (Ti:Sn:C = 2:1:1). Different Ti_2SnC samples were prepared by SHS method under the assistance of different Ti-Sn intermetallic compounds as previously described [16, 17]. The phase composition of products was identified by the X-ray diffraction analysis (XRD). Scanning electron microscopy (SEM) was used to observe the microstructure morphology. The relative quantity of Ti_2SnC was represented by F value (the ratio of diffraction intensities of non-overlapping Ti_2SnC (002, $2\theta = 12.97°$) and TiC (111, $2\theta = 35.9°$).

Results and Discussion

Effect of Different Ti-Sn Intermetallic Compounds Addition on Phase Compositions of Combustion Product Ti_2SnC

Figure 1 shows XRD patterns of the SHS synthesized products by green compact with different Ti_5Sn_3 addition amounts (0, 15, 20, 30, 40%). From Fig. 1, it can be observed that the predominating phase is always Ti_2SnC. Some Sn, TiC, and Ti_5Sn_3 phases are also detected but the peaks are very weak. Furthermore, the relative content of Ti_2SnC phase increases firstly and then decreases with the increasing of Ti_5Sn_3 addition content. The dominant phase of Ti_2SnC is the most when the addition amount of Ti_5Sn_3 is 20%. At the same time, the impurity phases of Sn, TiC, and Ti_5Sn_3 are trivial. The above results reveal that the addition of Ti_5Sn_3 is not the more the better. The optimum addition amount of Ti_5Sn_3 is 20%.

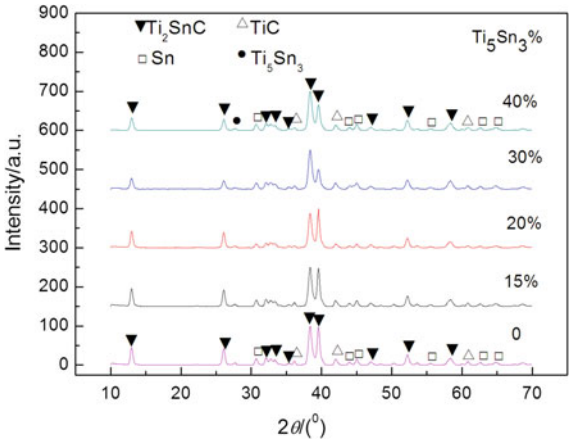

Fig. 1 XRD patterns of combustion products with different Ti_5Sn_3 addition in Ti-Sn-C system

The relationship between F values (the relative quantity of Ti_2SnC) and different Ti_5Sn_3 addition amount is provided in Fig. 2. It can be found in Fig. 2 that the relative quantity of Ti_2SnC increases with the increasing of Ti_5Sn_3 addition contents from 0 to 20%. While when the content of Ti_5Sn_3 increases furthermore, the F value begins to decrease sharply indicating that the addition of more Ti_5Sn_3 is not beneficial for the synthesis of Ti_2SnC which is in good agreement with the XRD results.

Typical XRD patterns of the combustion products obtained from reactant compacts with the different addition amount of $TiSn_2$ is presented in Fig. 3. The XRD profiles of all samples indicate that the Ti_2SnC is the dominant phase. Some TiC, Ti_5Sn_3, and Sn as secondary phases always accompany with Ti_2SnC. What's interesting is that the reactant $TiSn_2$ is not detected in the final products. The results indicate that $TiSn_2$ is as a reactant rather than an intermediate in the formation of Ti_2SnC. From the above results, the reaction mechanism of Ti_2SnC formation can be deduced that Ti reacts with $TiSn_2$ to form Ti_5Sn_3 firstly, then TiC (coming from

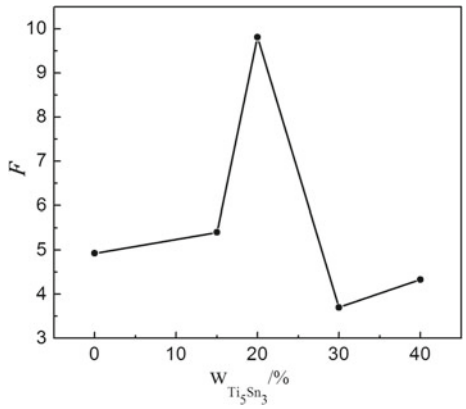

Fig. 2 F values(the relative quantity of Ti_2SnC) of the products after addition different Ti_5Sn_3 contents in the Ti-Sn-C system

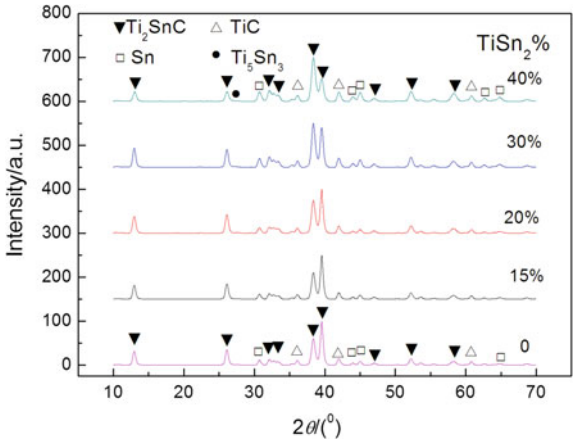

Fig. 3 XRD patterns of combustion products with different $TiSn_2$ addition in Ti-Sn-C system

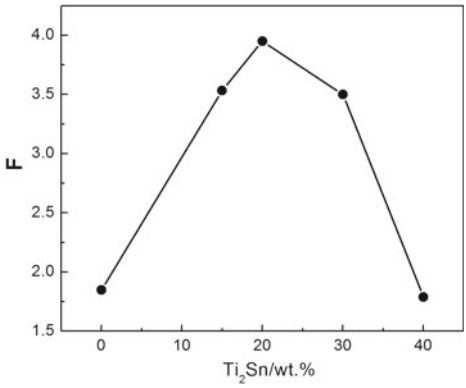

Fig. 4 *F* values (the relative quantity of Ti_2SnC) of the products after addition different Ti_2Sn contents in the Ti-Sn-C system

reaction of Ti and C) reacts with Ti_5Sn_3 compounds to form Ti_2SnC, which has been also confirmed in ref. [7].

Figure 4 plots the relationship between *F* values (the relative quantity of Ti_2SnC) as a function of $TiSn_2$ addition amounts. From Fig. 4, it is clearly shown that the relative quantity of Ti_2SnC increases before 20% ($TiSn_2$ addition amount) and then decreases with further increasing of $TiSn_2$ addition amount.

The Effect of Different Ti-Sn Intermetallic Compounds Addition on Combustion Temperature of Product Ti_2SnC

Figure 5 provides the relationship between the maximum reaction temperature and Ti_5Sn_3 addition content. The plot shows that the maximum reaction temperature is substantially affected by Ti_5Sn_3 addition content and decreases approximately

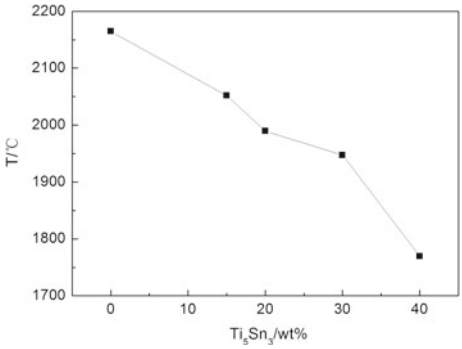

Fig. 5 Effect of Ti_5Sn_3 content on combustion temperature of Ti-Sn-C system

linearly with increasing Ti_5Sn_3 content, which is consistent with the phenomena observed in experiments.

The reaction temperature-Ti_2Sn content profile of the combustion reaction is given in Fig. 6. From Fig. 6, it can be seen that the maximum combustion temperature decreases with the increasing of Ti_2Sn content. From Figs. 5 and 6, it is both found that the maximum reaction temperature decreases with the increase of Ti-Sn intermetallic compounds addition content. So it can be deduced that both Ti_5Sn_3 and Ti_2Sn have a similar dilution effect [18] as the TiC on solid-state combustion of the Ti-Sn-C powder compacts. However, the decrease of reaction temperature is highly beneficial to stabilize Ti_2SnC (shown in Figs. 2 and 4) because Ti_2SnC will decompose at temperatures higher than 1250 °C [9].

Meanwhile, from the XRD results provided by Figs. 1 and 3, it is found that TiC, Ti-Sn compounds (Ti_5Sn_3), and Sn as unwanted phases always accompany with Ti_2SnC whether addition some Ti_5Sn_3 or Ti_2Sn. The reason of the existence of Ti_5Sn_3 is due to lack of insufficient reaction time attributing for rapid propagation of the reaction front in the SHS process. And the main reason for the existence of Sn and TiC is that Ti_2SnC begins to decompose at temperatures higher than 1250 °C [9] through the following reaction $Ti_2SnC = TiC + Sn$. To decrease the above impurities, the TiC-added samples will undergo further research.

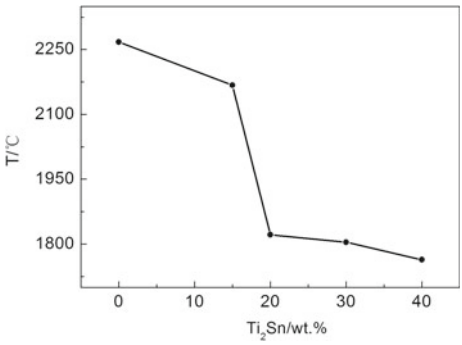

Fig. 6 Effect of Ti_2Sn content on combustion temperature of Ti-Sn-C system

The Effect of Different Ti-Sn Intermetallic Compounds Addition on Microstructure of Product Ti_2SnC

Figure 7 shows the SEM photographs of Ti_2SnC with different addition content of Ti_5Sn_3. The Ti_2SnC grains are plate-like, with coarse surface. Some small, coarse, and round-shaped granules of TiC and Ti_5Sn_3 are identified by EDS (Fig. 7a). When the addition of Ti_5Sn_3 is 20%, well-developed plate-like shape, and smooth surface Ti_2SnC structures evidently increase and the rounded-TiC and Ti_5Sn_3 decrease (Fig. 7b). The plate-like grains are less than 5 μm in size and less than 2 μm in thickness. When the content of Ti_5Sn_3 is 30%, the morphology of Ti_2SnC grains become coarse once more and the size becomes smaller and thicker (Fig. 7c). Figure 7d indicates that Ti_2SnC grains are in the shapes of long rods with thickness of about 0.25 μm and length in the range of 5–10 μm. In addition, the amount of Ti_5Sn_3 and TiC granules is noticeably increased. The crystal structure morphology of Ti_2SnC is determined by the grain growth rate in different planes reported by Boulliard and Sotto [19]. Based on the study of Li et al. [20], the growth environment with sufficient liquid phases is one of the reasons that benefits Ti_2SnC to develop a rod-like microstructure. Therefore, it is believed that the increase of Ti-Sn compounds amount results in the formation of more molten compound in the synthesis, which favors the growth of Ti_2SnC in the form of rods instead of platelets.

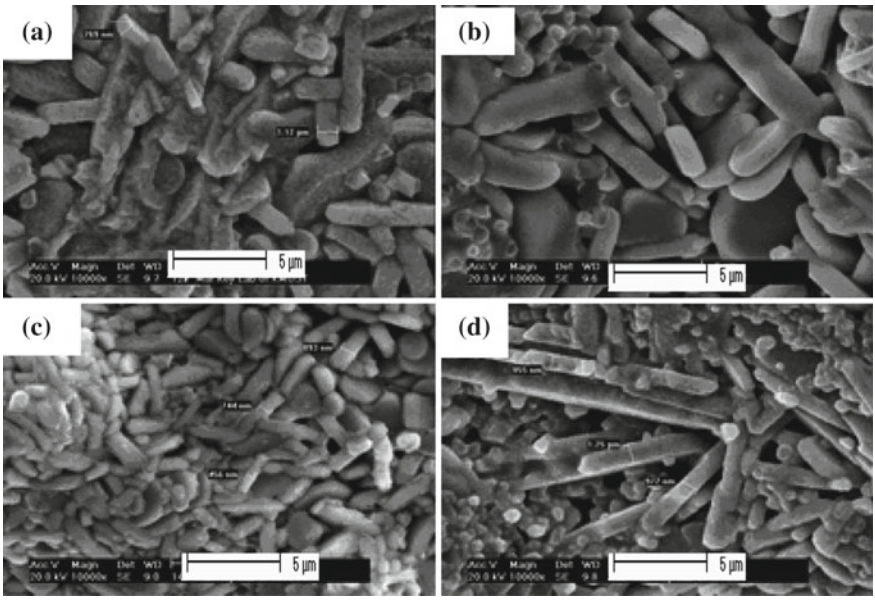

Fig. 7 SEM results for the fracture surfaces of the samples prepared with different Ti_5Sn_3 contents: **a** 15%, **b** 20%, **c** 30%, **d** 40%

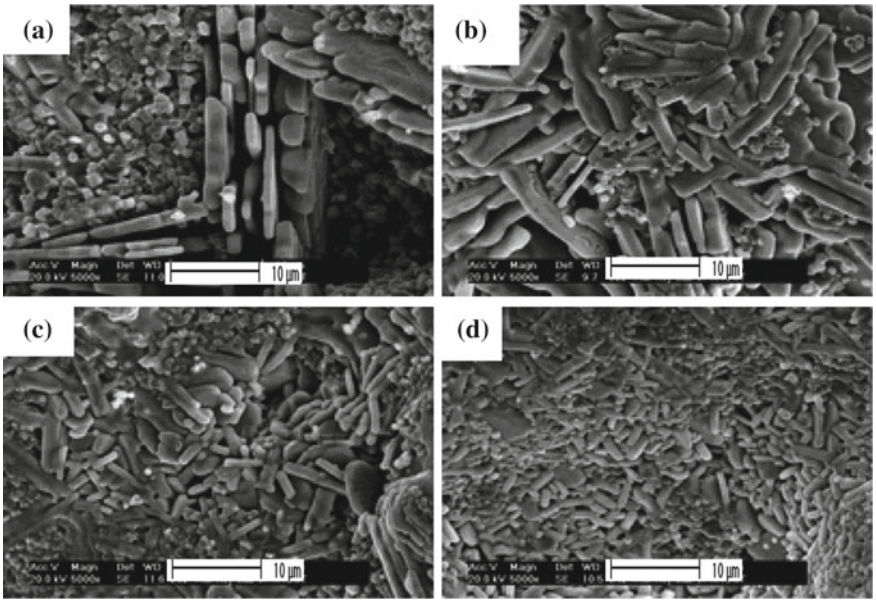

Fig. 8 SEM micrographs of the fracture surfaces of the samples prepared with different Ti_2Sn contents: **a** 15%, **b** 20%, **c** 30%, **d** 40%

The morphologies of Ti_2SnC with different Ti_2Sn contents are given in Fig. 8. The observation from Fig. 8 is similar to that shown in Fig. 7. With the increasing of Ti_2Sn contents from 15 to 20%, the plate-like structure of Ti_2SnC has a better development and the round-shaped granules of TiC and Ti_5Sn_3 obviously decrease (Fig. 8a–b). However, with the content of Ti_2Sn increases further, it is found that some rod-like Ti_2SnC grains appeared and the amount of TiC and Ti_5Sn_3 also evidently increased (Fig. 8c–d). The reason has been explained above in detail.

Conclusions

Higher purity of Ti_2SnC has been successfully synthesized by SHS process with a novel powder mixture of Ti/Sn/C/Ti-Sn compounds. And the relative quantity of Ti_2SnC in final product will increase with the increasing of Ti_5Sn_3 and Ti_2Sn firstly (0–20%), and then decrease with further increasing (30–40%). It is confirmed that Ti_2SnC is formed from a reaction between TiC and Ti_5Sn_3 instead of with Ti_2Sn in the system of Ti/Sn/C/Ti-Sn compounds.

Acknowledgements The authors thank the financial support from the National Natural Science Foundation of China (No. 51362012, No. 51662007 and U1602273), the Yunnan Local Colleges (part) Applied Basic Projects Joint Special Foundation (2017FH001-120) and the Yunnan Applied Basic Research Project (No. 2017FD157).

References

1. Lu C, Wang Y, Wang XF, Zhang JF (2018) Synthesis of Ti_2SnC under optimized experimental parameters of pressureless spark plasma sintering assisted by Al addition. Adv Mater Sci Eng 4:1–9
2. Li YX, Bai PK, Liu B (2011) Effect of C/Ti ratio on self-propagating high-temperature synthesis reaction of Sn-Ti-C system for fabricating Ti_2SnC ternary compounds. J Alloys Compd 509(35):L328–L330
3. El-Raghy T, Yaroschuk G, Barsoum MW (2000) Synthesis and characterization of Hf_2PbC, Zr_2PbC and M_2SnC (M = Ti, Hf, Nb or Zr). J Eur Ceram Soc 20(14–15):2619–2625
4. Jeschko W, Nowotny H, Benesovsky F (1963) Kohlenstoffhaltige ternäre verbindungen (H-Phase). Monatsh Chem 94:672–676
5. Li SB, Bei GP, Zhai HX, Zhou Y, Li CW (2007) Synthesis of Ti_2SnC at low-temperature using mechanically activated sintering process. Mater Sci Eng A 457(1–2):282–286
6. Bei GP, Li SB, Zhai HX, Zhou Y (2007) Reaction mechanism for synthesis of Ti_2SnC. Mater Res Bull 42(12):1995–1998
7. Barsoum MW, Yaroschuk G, Tyagi S (1997) Layered machinable ceramics for high temperature applications. Scripta Mater 36(5):535–541
8. Wu JY, Zhou YC, Wang JY (2006) Tribological behavior of Ti_2SnC particulate reinforced copper matrix composites. Mater Sci Eng A 422(1–2):266–271
9. Li SB, Bei GP, Zhai HX, Zhou Y (2006) Synthesis of Ti_2SnC from Ti/Sn/TiC powder mixtures by pressureless sintering technique. Mater Lett 60(29–30):3530–3532
10. Yeh CL, Kuo CW (2010) Effects of TiC addition on formation of Ti_2SnC by self-propagating combustion of Ti-Sn-C-TiC powder compact. J Alloys Compd 502(2):461–465
11. Li YX, Bai PK, Liu B (2011) Effect of C/Ti ratio on self-propagating high-temperature synthesis reaction of Sn–Ti–C system for fabricating Ti_2SnC ternary compounds. J Alloys Compd 509:L328–L330
12. Li YX, Bai PK (2011) The microstructural evolution of Ti_2SnC from Sn–Ti–C system by self-propagating high-temperature synthesis (SHS). Int J Refract Met Hard Mater 29(6):751–754
13. Merzhanov AG, Borovinskaya IP (1972) Self-propagating high-temperature synthesis of inorganic compounds. Dokl Akad Nauk 204(2):366–369
14. Li HP (2003) The numerical simulation of the heterogeneous composition effect on the combustion synthesis of TiB_2 compound. Acta Mater 51(11):3213–3224
15. Hoke DA, Meyers MA (1996) Combustion synthesis/dynamic compaction of TiB_2-SiC composite. J Eur Ceram Soc 79:177–182
16. Sun HY, Kong X, Yi ZZ, Wang BS, Liu GY (2014) The difference of synthesis mechanism between Ti3SiC2 and Ti3AlC2 prepared from Ti/M/C(M = Al or Si) elemental powders by SHS technique. Ceram Inter 40(8):12977–12981
17. Sun HY, Kong X, Sen W, Yi ZZ, Wang BS, Liu GY (2014) Effects of different Sn contents on formation of Ti_2SnC by self-propagating high-temperature synthesis method in Ti–Sn–C and Ti–Sn–C–TiC systems. Mater Sci Poland 32(4):696–701
18. Yeh CL, Shen YG (2008) Effects of TiC addition on formation of Ti_3SiC_2 by self-propagating high-temperature synthesis. J Alloys Compd 458:286–291
19. Boulliard JC, Sotto MP (1991) On the relations between surface structure and morphology of crystals. J Cryst Growth 110(4):878–888
20. Li SB, Bei GP, Xiang WH, Zhai HX (2009) Controlling the oriented growth of Ti_2SnC grains with carbon fiber as a reactive template in the Ti–Sn–C system. Mater Res Bull 44(5):966–969

Dynamic Mechanical Behaviour of Lean Duplex Stainless Steel 2101

E. C. Yeo, J. P. Escobedo-Diaz and A. A. H. Ameri

Abstract The effect of the history of plastic deformation on the mechanical response of hot rolled Lean Duplex Stainless Steel 2101 (LDSS2101) was investigated at high strain rates. Samples of LDSS2101 were quasi-statically compressed up to 25% strain to introduce an intermediate state of plastic deformation before high strain rate compression. Microstructural analyses were conducted using optical microscopy to correlate the mechanical responses with microstructural evolution. Results show that the dynamic yield stress of LDSS2101 increases with pre-deformation. However, significant work-softening was also observed at high strain rates. Microstructural analyses of LDSS2101 revealed the phase transformations which likely affect the mechanical response. Our findings support the use of LDSS2101 in applications that involve a combination of serial quasi-static and dynamic loadings.

Keywords Compression · Duplex steel · LDSS2101 · Microstructure · Mechanical properties

Introduction

Lean Duplex Stainless Steel (LDSS2101) is a relatively new duplex stainless steel alloy which offers improved mechanical properties compared to single-phase steel alloys and to conventional duplex stainless steel, e.g. DSS2205. Moreover, LDSS2101 is comparatively cheaper to manufacture and has a more stable cost than DSS2205. LDSS2101 was designed by partially substituting the more expensive elements (nickel, molybdenum, chromium) with cheaper elements such as nitrogen and manganese. The mechanical properties of the LDSS2101 are a result of its unique crystallography. LDSS2101 is made up of the ferritic (α) and austenitic (γ) phases of steel in a close to equal proportion of each phase. The presence of the austenitic phase gives the LDSS2101 its high corrosion resistance. Therefore, the

E. C. Yeo · J. P. Escobedo-Diaz (✉) · A. A. H. Ameri
University of New South Wales at the Australian Defence Force Academy, Canberra 2600, ACT, Australia
e-mail: j.escobedo-diaz@unsw.edu.au

J. Li et al. (eds.), *Characterization of Minerals, Metals, and Materials 2020*,
The Minerals, Metals & Materials Series,
https://doi.org/10.1007/978-3-030-36628-5_53

combination of high strength, excellent corrosion resistance, and reasonable pricing has promoted the study of and potential use of LDSS2101 in the oil, gas and chemical industry, and even in nuclear engineering applications. However, the mechanical response of LDSS2101 to high strain rate processes—and resulting microstructural changes—have not yet been comprehensively studied to instil levels of confidence for its widespread application. Furthermore, the nature of duplex steels increases the complexity of study due to the different ways in which the individual phases of steel respond to high strain rates. Nevertheless, a systematic exploration of the mechanical responses of LDSS2101 hopes to address the uncertainties described.

The aim of this research is to determine the effect of the history of plastic deformation on the mechanical response of LDSS2101 at high strain rates. The research focused upon the following areas:

- The mechanical response of LDSS2101 when it is quasi-statically deformed to known levels of strain
- The mechanical response of LDSS2101 when it is deformed at high strain rate to known levels of strain
- The mechanical response of LDSS2101 when it is first quasi-statically deformed then further deformed at high strain rate to known levels of strain
- Microstructural changes with this history of plastic deformation and subsequent high strain rate deformation
- Determine the dominant influencing factor of the mechanical response at high strain rates.

Material and Experimental Methods

20 mm thick hot rolled plates of LDSS2101 were used. A 140 mm thick cast slab was hot rolled at temperatures between 1100 and 1300 °C to the final thickness (20 mm). Then, the plate was heat treated at 1050 °C followed by water quenching. The chemical composition of the used material is shown in Table 1. The as-received samples of LDSS2101 had about 44% and 56% volume fractions of the ferritic phase and austenitic phase, respectively, as revealed by EBSD scans [1].

Cylindrical samples were machined for compression tests. A three-dimensional axis system as in Fig. 1 was used to define the three main directions for testing and optical analysis. The directions considered were defined as the rolling direction (RD) to which the sample was hot rolled, the transverse direction (TD) perpendicular to the rolling direction, and the normal direction perpendicular to the plane which the RD and TD lies. The samples were compressed parallel to the RD for all tests conducted in this study. The as-received dimensions of the samples were 4.5 mm thick in the RD and 7.5 mm in diameter in the ND-TD plane. The dimensions of the sample were chosen to minimise the friction and inertia effects associated with SHPB testing [1].

The compression of LDSS2101 samples at quasi-static strain rate (10^{-3} s^{-1}) to 25% strain was conducted using a Shimadzu® Universal Testing Machine calibrated

Table 1 Chemical composition of the studied material measured by inductively coupled plasma atomic emission spectroscopy, spark emission spectroscopy, and Leco methods

Elements	C	Mn	Si	S	P	Ni	Cr	Mo	Cu	N	Fe
Bulk composition	0.03	4.08	0.59	0.01	0.03	1.55	21.5	0.34	0.24	0.23	Bal.

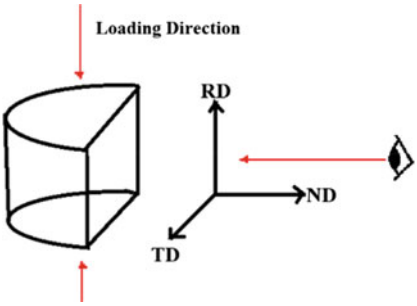

Fig. 1 Diagram of a sample cut in half, showing the three defined directions, loading, and observation directions

at 100 kN of force. The high strain rate (4000 s^{-1}) compression tests of the pre-deformed samples were conducted using a Split-Hopkinson pressure bar (SHPB) with pulse shapers. The pulse shaper was used in order to achieve constant strain rates during the individual tests [2, 3]. They are thin discs of LDSS2101 material attached to the incident bar at the interface of the incident and striker bars as shown in Fig. 2.

The Vickers hardness was conducted using the Shimadzu® Micro Hardness Tester HMV-G21. Measurements were done with a test load of HV0.01 (98.07 mN) at locations of austenite, ferrite, and martensite phases. For each sample, the hardness of the three different phases was recorded for comparison. As in Fig. 3, the austenitic phase was identified by the visible twin boundaries [4] within the grains, ferritic phase were identified by uniform darker regions, and dark regions within the austenite grains were identified as the martensitic phase. At least HV measurements were conducted for each phase, for each sample.

Optical microscopy was conducted using the Zeiss Axio optical microscope. Images were taken at 5X, 10X, 20X, and 50X magnifications to acquire different levels of data for analysis. The higher magnification images were taken at multiple positions within the same samples to confirm the existence of martensite phases

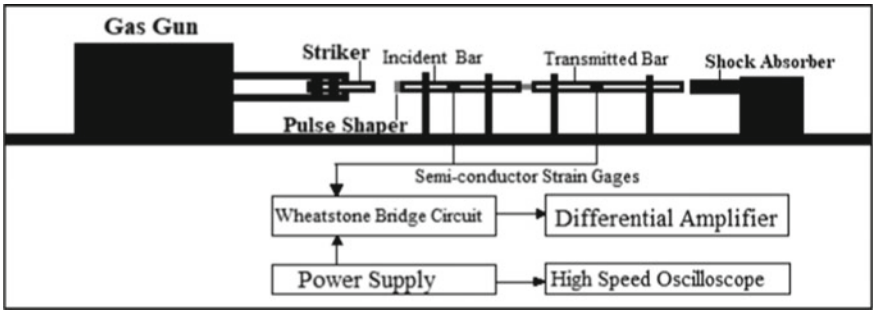

Fig. 2 Schematic diagram of a Split-Hopkinson pressure bar set-up

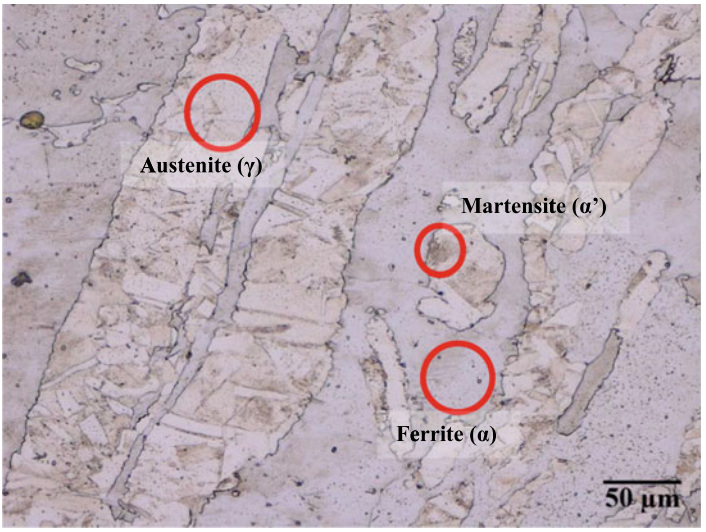

Fig. 3 Optical microscopy image of LDSS2101 at 25% strain, with the three different phases identified

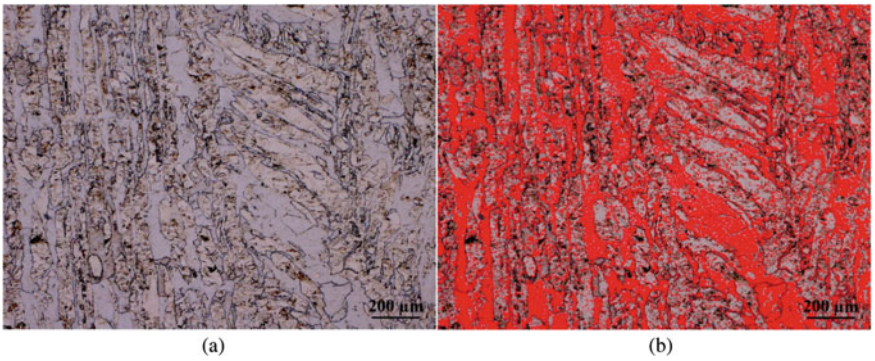

Fig. 4 Optical micrographs of **a** LDSS2101 sample; **b** processed image showing red ferritic grains

within the deformed samples and verify that martensitic transformation has occurred. Images were processed using the software Image J to measure the volume fraction of the different phases based on colour differences. An example is shown in Fig. 4.

Results and Discussion

The mechanical responses in the SHPB tests were measured by using the concept of one-dimensional elastic wave propagation in bars as explained by Ameri et al. [2].

The true stress-strain curves of the LDSS2101 samples are shown in Fig. 6. Figure 6 shows an obvious difference in mechanical responses of the LDSS2101 samples when subjected to compressive deformation of different rates.

The increase in yield stress of the LDSS2101 samples increased by about 550 MPa as the strain rate increased from 10^{-3} to 4000 s^{-1}. This increase in yield stress of LDSS2101 due to the increase in the strain rate is likely caused by the existence of the ferritic phase (BCC) in LDSS2101 [5].

The same increase in yield stress was observed when the pre-deformed LDSS2101 samples (25% strain) were deformed at high strain rates. Figure 5 shows the same increase in yield stress of about 550 MPa, from 1050 to 1600 MPa when changing the strain rate from 10^{-3} to 4000 s^{-1}. The higher true stress value at 1050 MPa at 25% strain aligns with present understanding of the response of LDSS2101, in which the increase in strain of the material leads to increase in dislocation densities, resulting in higher stress responses. Furthermore, this suggests that even though the quasi-static deformation of LDSS2101 had introduced greater dislocation densities within the LDSS2101 samples, this had minimal effect on the way the ferritic phase reacts to increasing strain rates. This has allowed the yield stress to increase similarly even after 25% strain. Therefore, the relative yield point of the LDSS2101 material remains the same even after history of plastic deformation.

Moreover, it is noted in [1] that martensitic transformation of the austenitic phase would have occurred after quasi-static deformation to 25% strain, and this is confirmed in Fig. 3. Hence, it is likely that the austenitic phase (FCC) and body-centred tetragonal (BCT) martensitic phase have minimal effect on the yield stress of LDSS2101.

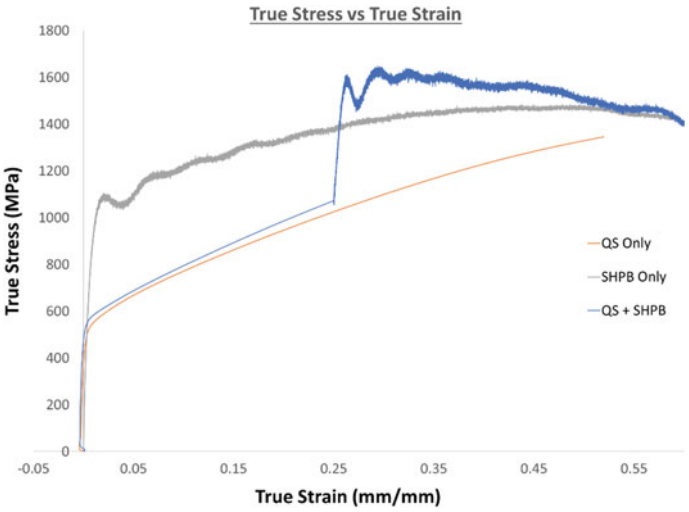

Fig. 5 True stress-strain curves from the compressive deformations of LDSS2101 samples at different strain rates

The true stress-strain curves in Fig. 5 indicate the higher flow stresses following the increase in strain rate of the LDSS2101 sample. When comparing the single-process deformation at 10^{-3} s^{-1} strain rate and 4000 s^{-1}, the increase in flow stresses of LDSS2101 is likely due to the increased generation of dislocations within the material when deformed at higher strain rates [1, 5]. As a result, when comparing the single-process deformation of LDSS2101 at 4000 s^{-1} to the deformation of the pre-deformed LDSS2101 also at 4000 s^{-1}, it is interesting to note the overall higher flow stresses. This is shown in Fig. 6 where the blue curve is higher than the grey curve up till about 50% strain. Therefore, the introduction of the 25% strain in LDSS2101 prior to high strain rate deformation has induced a high flow stress response of the material.

Images of LDSS2101 samples deformed at high strain rate to 25% strain (Fig. 6a) were compared to the LDSS2101 samples which were deformed quasi-statically to 25% strain (Fig. 6b). The analysis revealed that the quasi-statically deformed sample at 25% strain had a higher percentage of martensite (5.70%) compared to the sample deformed to 25% at high strain rate (2.7%). This agrees with findings from Ameri et al. [1] that the rate of martensitic transformation is lower when strain rate is

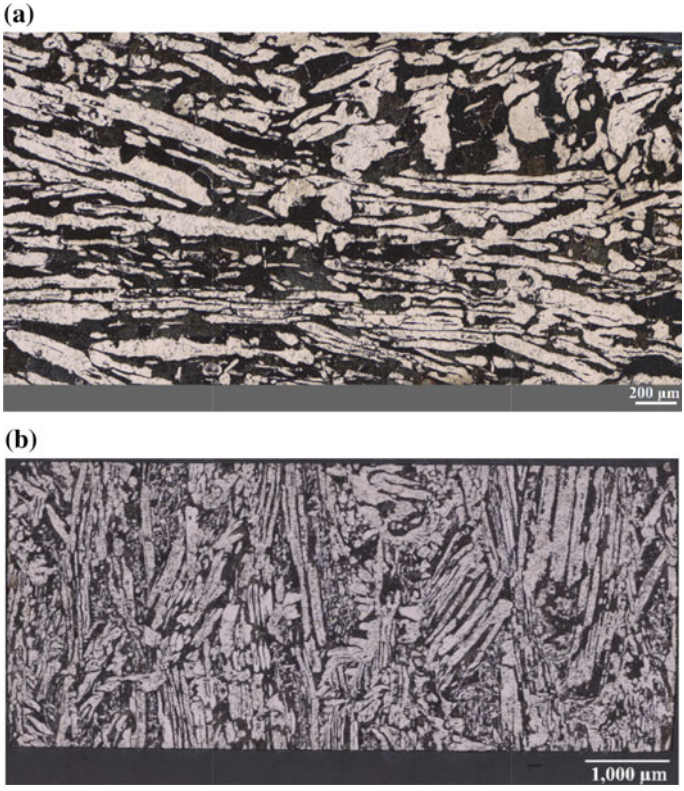

Fig. 6 **a** LDSS2101 deformed at 10^{-3} s^{-1} to 25%; **b** LDSS2101 deformed at 4000 s^{-1} to 25%

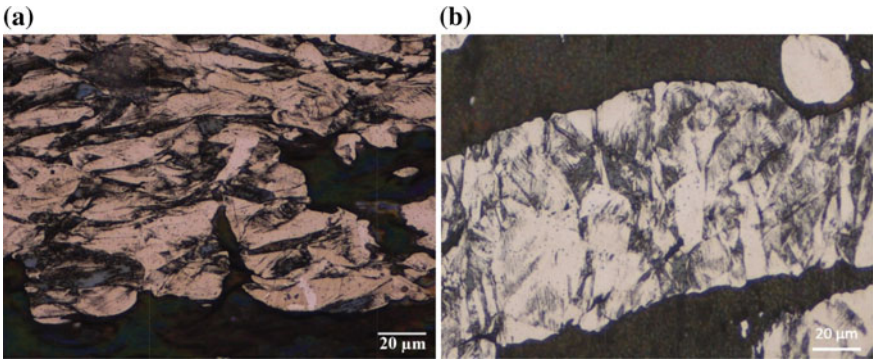

Fig. 7 **a** LDSS2101 deformed at 4000 s^{-1} to 50%; **b** LDSS2101 deformed at 10^{-3} s^{-1} to 50%

increased. Hence, the higher flow stresses of the pre-deformed sample are likely due to the higher volume fraction of the martensite phase, which the existence within the austenite increases the material flow stress due to reduction of free dislocation paths [5, 6].

The microstructure of the LDSS2101 samples at 50% strain was also compared between the quasi-static deformation and the high strain rate deformation processes. Examples of the images used for comparison are shown in Fig. 8. Analysis of the respective images revealed that the pre-deformed LDSS2101 sample had about 11.1% volume fraction of martensite after high strain rate deformation. In addition, the quasi-statically deformed sample of LDSS2101 had about 15.9% volume fraction of martensite. Even then, the pre-deformed sample recorded higher levels of flow stresses than the solely quasi-statically deformed LDSS2101 sample. Thus, the flow stresses of LDSS2101 are likely to be dependent on the amount of martensite and dislocation density (Fig. 7).

The work-hardening rate of the LDSS2101 samples was plotted against true strain in Fig. 8. The high strain rate deformation processes have as expected shown a lower rate of work-hardening than the quasi-static compression process. This is partly due to the decreased martensitic transformation with increased strain rates and the resulting increase in free dislocation paths as described above. Hence, there are two known mechanisms at play when LDSS2101 is deformed at high strain rates: (1) the material is softened due to quasi-adiabatic heating [5], and (2) the martensitic transformation of austenite causes hardening.

In this case, the history of quasi-static deformation causes work-softening of LDSS2101, as indicated by the negative in Fig. 6 and the negative values in Fig. 8, after about 37% strain. Similar work-softening of LDSS2101 was observed by Krüger et al. in [5] and was determined to be caused by quasi-adiabatic heating inherent in deformation at high strain rates. While that seemed reasonable given the high amount of energy generated when compressing the LDSS2101 sample from 0 to 50% strain at high strain rates, the pre-deformed LDSS2101 sample could cool to room temperature

Fig. 8 Work-hardening rate of the LDSS2101 sample at different rates of deformation

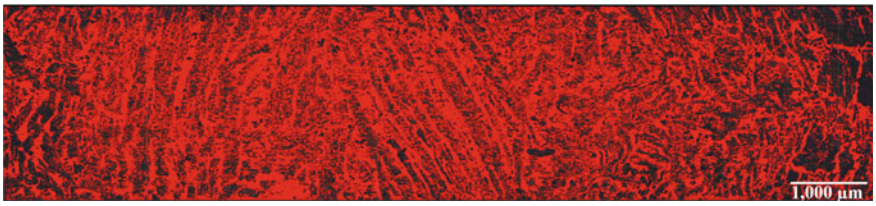

Fig. 9 Processed image (black–austenite) of LDSS2101 sample deformed at 4000 s^{-1} from the 0 to 50% strain

before it was subjected to high strain rate deformation. The toughness of the pre-deformed LDSS2101 sample from 25 to 37% was calculated to be about 156.17 MJ, whereas the toughness of the SHPB-only sample from 0 to 50% (where it experiences work-softening) was calculated to be 665.03 MJ. Therefore, the significant work-softening of the pre-deformed LDSS2101 sample is believed to be caused by the combination of both the quasi-adiabatic heating and the lower rate of martensitic transformation.

Microstructural analyses by comparing the microstructural evolution resulting from the deformation of LDSS2101 samples from the as-received state and the pre-deformed state have revealed the volume fractions of martensite in both samples. Firstly, the pre-deformed LDSS2101 had about 11.1% martensite, whereas the LDSS2101 that only underwent SHPB compression (Fig. 9) had about 12.7% marten-

Table 2 Vickers hardness data from the pre-deformed LDSS2101 sample

	Vickers hardness (HV)		
	Austenite (γ)	Ferrite (α)	Martensite (α')
25% strain	425	300	470
50% strain	500	315	550
Difference	73	16	78

site. Hence, the work-softening of the pre-deformed LDSS2101 sample when subjected to high strain rate could be due to the reduced rate of martensitic transformation as well as the softening effects due to quasi-adiabatic heating.

However, the lower volume fraction of martensite in the pre-deformed sample is contrary to the theory that martensitic transformation reduces with high strain rate [5]. Otherwise, the pre-deformed sample, with history of quasi-static compression would be expected to have higher volume fractions of martensite. Hence, it is believed that the material with history of plastic deformation behaves differently than the LDS2101 would when deformed from the as-received state. The fact that the pre-deformed sample (25% strain) was left to cool to room temperature first then deformed again at high strain rate may be a factor at play since the material will respond differently when it is at a different temperature at 25% strain.

The Vickers hardness test results were compared for the pre-deformed sample, between the sample at 25% strain and the sample at 50% strain. Results are presented in Table 2. This revealed the extent of hardening of the different phases of steel within the LDSS2101 samples.

The hardness measurements revealed that the austenitic phase and martensitic phase of LDSS2101 experience the significant portion of the work-hardening, whereas the ferritic phase experiences a comparatively low extent of work-hardening. Moreover, the martensitic phase undergoes more work-hardening than the austenitic phase. This further suggests that as the rate of martensitic transformation decreases (volume fraction of austenite is relatively higher), the work-hardening rate of LDSS2101 will also decrease. Hence, the effects of work-softening of the LDSS2101 could have been amplified further due lower rate of austenite compared to martensite.

Conclusions

The effect of the history of plastic deformation in LDSS2101 on those mechanical responses has been systematically tested and results analysed based on the present field of knowledge of LDSS2101 and general duplex stainless steels. Our main findings are as follows:

1. The increase in yield stress of LDSS2101 due to an increase in strain rate is not affected by the history of plastic deformation on the material. This increase in

yield stress is due to the ferritic phase of steel in LDSS2101, but the austenitic and martensitic phase has minimal effect on the yield stress of LDSS2101.

2. The history of plastic deformation in LDSS2101 induces relatively higher flow stresses when the pre-deformed sample is subjected to high strain rate deformation. The higher flow stress compared to a non-pre-deformed sample undergoing high strain rate deformation is likely due to the increased volume fraction of martensite in the pre-deformed sample. The higher flow stresses compared to a non-pre-deformed sample undergoing quasi-static deformation is likely due to the dominance of the increased rate of dislocation formation over the lower rate of martensitic transformation in high strain rate compressed LDSS2101.
3. Pre-deformed samples of LDSS2101 undergo work-softening when subjected to high strain rate compression. This is likely due to the combined effects of quasi-adiabatic heating and lower rate of martensitic transformation. However, the exact mechanism that caused the final volume fraction of martensite to be higher in the non-pre-deformed sample is yet to be understood.

Acknowledgements Authors would like to acknowledge the support by the Air Force Office of Scientific Research under grant number FA2386-17-1-4095.

References

1. Ameri A, Escobedo-Diaz J, Quadir MZ, Ashraf M, Hutchison W (2018) Strain rate effect on the mechanical response of duplex stainless steel. In: AIP conference proceedings, vol 1979(1). AIP Publishing, p 070001
2. Ameri A, Brown A, Ashraf M, Hazell P, Quadir MZ, Escobedo-Diaz J (2019) An effective pulse-shaping technique for testing stainless steel alloys in a split-Hopkinson pressure bar. J Dyn Behav Mater, 1–12
3. Sunny G, Yuan F, Prakash V, Lewandowski J (2009) Design of inserts for split-Hopkinson pressure bar testing of low strain-to-failure materials. Exp Mech 49(4):479
4. Galindo-Nava EI, Rivera-Díaz-del-Castillo P (2017) Understanding martensite and twin formation in austenitic steels: a model describing TRIP and TWIP effects. Acta Mater 128:120–134
5. Krüger L, Schwarz F, Martin U, Roven HJ (2014) Strain rate and temperature effects on the flow behavior and microstructure of X2CrNiMoN22-5-3 duplex stainless steel. Mater Sci Eng A 592:6–11
6. Herrera C, Ponge D, Raabe D (2011) Design of a novel Mn-based 1 GPa duplex stainless TRIP steel with 60% ductility by a reduction of austenite stability. Acta Mater 59(11):4653–4664

Capillary Absorption Evaluation of Different Mortars Applied in Civil Construction

A. R. G. Azevedo, M. T. Marvila, J. P. Reis, E. B. Zanelato, A. L. F. Manhães, S. N. Monteiro, L. G. Pedroti, B. C. Mendes, N. A. Cerqueira and V. Souza

Abstract The absorption by capillarity is one of the main characteristics of the mortars, connected directly to the internal flow of water through their pores and consequently their durability over time. The objective of this work is to evaluate the influence of the conditions of the materials, as the granulometry of the sand, in the internal capillary flow of cement- and lime-based mortar, according to the Brazilian standard. Thus, prismatic specimens ($4 \times 4 \times 16$ cm) with sands of different particle sizes ($D_{max} = 1.2$ and 2.4 mm) were made, evaluating the capillary absorption and the capillary coefficient of the mortars with 1:1:6 (cement: lime: sand), following the Brazilian regulations. The results showed that the larger the average grain size, the greater the number of voids indicating an increase in the capillary flow, damaging applications of these mortars in construction.

Keywords Mortar · Pores · Durability

A. R. G. Azevedo (✉)
TER—Department of Agricultural Engineering and Environment, UFF—Federal Fluminense University, Rua Passo da Pátria, 341, Niterói, Rio de Janeiro 24210240, Brazil
e-mail: afonso.garcez91@gmail.com

M. T. Marvila · E. B. Zanelato · A. L. F. Manhães
LECIV—Civil Engineering Laboratory, UENF—State University of the Northern Rio de Janeiro, Av. Alberto Lamego, 2000, Campos dos Goytacazes, Rio de Janeiro 28013-602, Brazil

J. P. Reis · A. L. F. Manhães
UCAM—Cândido Mendes University, Av. Anita Peçanha, 100, Campos dos Goytacazes, Rio de Janeiro 28030-335, Brazil

S. N. Monteiro
Department of Materials Science, IME—Military Institute of Engineering, Square General Tibúrcio, 80, Rio de Janeiro 22290-270, Brazil

L. G. Pedroti · B. C. Mendes
UFV—Federal University of Viçosa, DEC, Av. Peter Henry Rolfs, S/N - Campus Universty, Viçosa, Minas Gerais 36570-000, Brazil

N. A. Cerqueira · V. Souza
UNIREDENTOR—Redentor University Center, BR-356, 25 - Pres. Costa E Silva, Itaperuna, Rio de Janeiro 28300-000, Brazil

J. Li et al. (eds.), *Characterization of Minerals, Metals, and Materials 2020*,
The Minerals, Metals & Materials Series,
https://doi.org/10.1007/978-3-030-36628-5_54

Introduction

The mortars are widely used in Brazilian civil construction as wall and ceiling covering and for settlement laying masonry. The composition of this material is formed by Portland cement (binder), lime, and sand (aggregate) [1]. In civil construction, water is used as a raw material in many stages including the preparation of mortars, concretes, in the concrete curing process and even in soil compaction, and moreover, water is essential for the occurrence of cement hydration reactions, which is a hydraulic binder [2].

The amount of water absorbed by mortars, in the hardened state, is directly related to capillarity. This property is defined as the upward movement in a fluid, which is usually water, through a capillary formed by pores for mortars between 0.01 and 10 μm in diameter [3]. This mechanism occurs when there is a physicochemical affinity between the molecules of the liquid and the molecules present in the pores, due to the intermolecular interactions of the water and mortar molecules [4]. These forces cause the fluid to displace when the tube molecule that is just above the surface of the liquid attracts the rising liquid in alignment with the molecule that attracted it, the upward movement occurs when this cycle repeats itself. The phenomenon of capillarity, as mentioned above, occurs in mortars due to a capillary formed by pores. Mortar porosity can be characterized as open porosity, in which voids are interconnected by capillaries of varying diameters, or closed porosity, in which voids are not interconnected [5]. Figure 1 is a scheme of water flow in the capillary pores.

Importantly, the voids in the mortar are not truly empty, and are filled with water or air. In 28 days of mortar hydration, the voids are occupied by air, the size of these pores and the type of porosity (open or closed) influence the coefficient of capillarity and water absorption [6]. The capillarity for mortars commonly used in construction is poorly studied; however, it is very important to predict and understand the characteristics, such as durability of mortars. Studies prioritize the analysis of the mechanical resistance of materials, but the durability of mortars is not investigated with due attention and importance. [7]

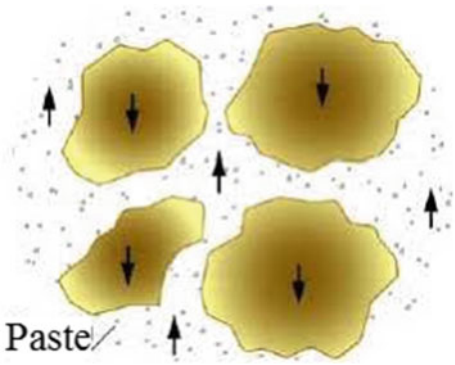

Fig. 1 Capillary water flow model in mortars [6]

Another important factor of mortars that should be researched is the appearance, as this material is widely used as masonry laying and finishing of ceiling and wall coverings. For a better analysis of mortar durability, it is necessary to analyze how this material behaves with respect to parameters such as the transport of fluids into the mortar, either by analyzing traditional durability or static durability in the material in question [4]. One of the mechanisms that must be studied in mortars is the absorption by capillarity, because it is through it that impurities penetrate the pores. This phenomenon is related to the size of existing pores, so it is necessary to do this test so that we can estimate and quantify the greater or less susceptibility of new materials to degradation [6].

Materials and Methods

Materials used in this study was provided by Portland Cement CPII-E-32, hydrated lime CH-III and natural sand with a maximum diameter of 1.2 and 2.4 mm. Lime, being thinner than cement, fills the voids of mortars, in addition to hydrating the cement due to its role as a water retainer [1].

The mortars were used with a ratio of their elements in mass of 1:2:9, 1:1:6 (cement: lime: sand), and 1:3 (cement: sand), which have great application in the construction sector. Two distinct groups of mortar were used: three traces with natural sand with a maximum diameter of 1.2 mm and three traces with a maximum diameter of 2.4 mm.

To determine the proportions of water in the desired mortars, the consistency test was performed, regulated by NBR 13276 [8]. It is recommended by the standard that there is a range of 260 ± 5 mm in mortar diameter on the chopping table. The test consisted of molding the mortar into a 6.5 cm high conical trunk shape, 12.5 cm base diameter, and 8 cm top diameter on the chopping table. The form is removed after filling and the table is driven to cause 30 consecutive drops at a height of 15 mm, so that the mortar receives the impact caused by the table falls. Three different diameters must be measured, and the result of averaging these values is the consistency index. The amount of water present in the mortar that obtained the index of 260 ± 5 mm was the defined proportion for each mortar trait studied in the present research [2].

Initially, the sand to be used was passed through the sieves with $D_{max} = 1.2$ mm and $D_{max} = 2.4$ mm. The sand was oven dried at a temperature of 110 °C for 24 h, as determined by previous analyzes. Subsequently, the material was removed from the greenhouse to cool to room temperature. The mortar mixing procedure followed the recommendations of NBR 13276 [8]. With dry sand, all materials are homogenized separately, and placed in a mixer, including water defined on the basis of the consistency test. The mortar is mixed at low speed for 90 s. At the end of the set time, the material is left to stand for 15 min, and then manually homogenized the mortar for a maximum of 30 s [8].

After preparing the mortar, with the mold fixed on the table, introduce the first layer in all molds, applying 30 consecutive drops to the table, at a height of 15 mm, at the end of the falls, and introduces the final layer, applying again 30 consecutive drops at the same height on the densification table. At the end, the excess mortar is removed with steel knives and unifies the surface. For each mortar, three specimens were molded in a 40 × 40 × 160 mm prismatic mold [4].

The specimens were kept in the mode for 48 h. The samples are kept in the laboratory at a temperature and relative humidity of 23 ± 2 °C and 60 ± 5%, respectively. Upon completion of 28 days of curing, water absorption and capillary coefficient determination tests are performed. Before starting the test for determination of water absorption by capillarity, it is necessary to even the surface of the specimens with coarse sandpaper, as recommended by NBR 15259 [9].

The test recommended by the standard is basically to determine the initial mass of the dry specimens, to put their square face in contact with water at a constant level 5 mm above the face and to determine the mass, in grams, of the specimens by test at 10 and 90 min. The weight increase of the specimens over a period of time is due to the absorption of water by capillarity. To obtain the capillary coefficient, the masses obtained are subtracted in 90 and 10 min of the test [9].

After the determined time of each test, excess surface water should be removed from the specimens to be tested, avoiding that the results do not reflect the actual amount of water trapped in the internal capillary pores of the cementitious matrix.

Results

At the beginning, the capillary rise of water, via capillary absorption, can be observed in visual analysis, where it is observed the advance of water penetration in the specimens. In Figs. 2 and 3, it is possible to observe the capillary rise in the different mortars immediately after the specimens are placed in contact with water and 60 min after the beginning of the test, respectively.

It can be seen from Figs. 2 and 3 that with increased exposure time of the specimens in the absorption front test condition, that is, the height of the water slide increases noticeably. To determine the capillarity absorption of mortars, the tests are provided for in NBR 15259 (ABNT 2005) was performed [9]. The results presented by the average values found in the assay according to Tables 1, 2, and 3.

After analyzing the data presented in Tables 1 and 2 that indicate the absorption by capillaries in the prismatic specimens, it is possible to see that the mortars that have larger average grain size, have better efficiency in water absorption.

However, it is possible to observe that the traces with the highest amount of lime in its composition presented higher water absorption by capillarity. The 1:3 trait mortar (cement: sand) that has no lime in its composition and showed greater efficiency by inhibiting capillary absorption. The results presented in Table 3 show that the capillarity coefficient increased when the mortar had a larger amount of lime in its

Fig. 2 Capillary rise after the specimens come into contact with water. *Source* Own author

Fig. 3 Capillary rise of specimens 60 min after contact with water. *Source* Own author

Table 1 Water absorption by capillarity of sand mortars with $D_{max} = 2.4$ mm

Mix design (cement: lime: sand)	Absorption (g/cm^2)	
	$t = 10$ min	$t = 90$ min
1:3:0	0.34	0.83
1:1:6	0.44	1.09
1:2:9	0.54	1.30

Table 2 Water absorption by capillarity of sand mortars with $D_{max} = 1.2$ mm

Mix design (cement: lime: sand)	Absorption (g/cm^2)	
	$t = 10$ min	$t = 90$ min
1:3:0	0.26	0.62
1:1:6	0.43	1.02
1:2:9	0.60	1.49

Table 3 Capillarity coefficient of mortars with different sand diameters

	Mix design (cement: lime: sand)	Sand diameter	
		2.4 mm	1.2 mm
Capillarity coefficient ($g/dm^2 min^{1/2}$)	1:3:0	7.79	5.63
	1:1:6	10.41	9.44
	1:2:9	12.19	14.18

composition. It is also observed that the larger the average grain size, the higher the capillarity coefficient.

Some studies in the literature have already indicated the importance of the capillarity coefficient and the influence of the average aggregate grain size as an influence on the internal compactness of the cementitious matrix and consequently on the water absorption, which is related to the capillarity [3]. Components, such as lime, have a direct influence on the potential for capillary ascension and internal porous flow [5, 10, 11].

Conclusion

- The 1:1:6 (cement: lime: sand) and 1:2:9 (cement: lime: sand) mortars had better capillary water absorption compared to the 1:3 (cement: sand). This may be because the first two samples have lime in their composition and this component has a huge ability to retain water around its particles.
- The specimens formed by 1:1:6 and 1:2:9 mortars with a maximum sand diameter of 2.4 mm showed that the larger the average grain size, the higher the water absorption efficiency by capillarity, as well as the higher capillarity coefficient, as it had a higher void index.
- Capillary water absorption is an important property for civil construction applications, and the characteristics of compositional materials such as aggregate (sand) have a significant influence.

Acknowledgements The authors thank the Brazilian agency: CNPq, CAPES, and FAPERJ for their support to this research.

References

1. Azevedo ARG, Alexandre J, Xavier GC, Pedroti LG (2018) Recycling paper industry effluent sludge for use in mortars: a sustainability perspective. J Clean Prod 193:335–346
2. Azevedo ARG, Alexandre J, Zanelato EB, Marvila MT (2017) Influence of incorporation of glass waste on the rheological properties of adhesive mortar. Constr Build Mater 148:359–368

3. Le MT, Tribout C, Escadeillas G (2019) Durability of mortars with leftover recycled sand. Constr Build Mater 215:391–400
4. Corinaldesi V, Moriconi G, Naik TR (2010) Characterization of marble powder for its use in mortar and concrete. Constr Build Mater 24:113–117
5. Azevedo ARG, França BR, Alexandre J, Marvila MT, Zanelato EB, Xavier GC (2018) Influence of sintering temperature of a ceramic substrate in mortar adhesion for civil construction. J Build Eng 19:342–348. https://doi.org/10.1016/j.jobe.2018.05.026
6. Vladimir GH, Graça V, Paulo BL (2011) Influence of aggregates grading and water/cement ratio in workability and hardened properties of mortars. Constr Build Mater 156(3):2980–2987
7. Bravo M, Brito J, Pontes J, Evangelista L (2015) Mechanical performance of concrete made with aggregates from construction and demolition waste recycling plants. J Clean Prod 99:59–74
8. Brazilian Association of Technical Norms. NBR 13276 (2016) Mortars applied on walls and ceilings—preparation of mortar for unit masonry and rendering with standard consistence index (in Portuguese)
9. Brazilian Association of Technical Norms. NBR 15259 (2005) Mortars applied on walls and ceilings—determination of water absorption coefficient due to capillary action (in Portuguese)
10. Mendes BC, Pedroti LG, Fontes MPF, Ribeiro JCL, Vieira CMF, Pacheco AA, Azevedo ARG (2019) Technical and environmental assessment of the incorporation of iron ore tailings in construction clay bricks. Constr Build Mater 227:116–669
11. Marvila MT, Alexandre J, Azevedo ARG, Zanelato EB, Xavier GC, Monteiro SN (2019) Study on the replacement of the hydrated lime by kaolinitic clay in mortars. Adv Appl Ceram 10:20–30

Fundamental Study on Wettability of Pure Metal by Liquid Sodium

Jun-ichi Saito, Hideo Shibutani and Yohei Kobayashi

Abstract Liquid sodium is used as a coolant of a fast reactor owing to its high thermal conductivity and high melting temperature. Wettability is an important property for designing the apparatus of the fast reactor. It is well known that the wettability of liquid sodium changes owing to factors such as surface roughness and type of metal. This study proposes an atomic interaction between metal and liquid sodium related to wettability. The purpose of this study is to understand the wettability of pure metal by liquid sodium by using both experimental and theoretical approaches. High-purity metal plates of titanium, vanadium, iron, nickel copper, and molybdenum were used in the experiment. Wettability was evaluated using the contact angle obtained using the tangent method, and simple surface models were constructed for theoretical calculation. The contact angle was evaluated using two kinds of atomic bonds, and the result showed a relation between the contact angle and the atomic bond.

Keywords Liquid sodium · Wettability · Contact angle · Atomic bonding · Electronic structure

Purpose

Liquid sodium is used as a coolant of a fast reactor because of its high thermal conductivity and high melting temperature. Liquid sodium is always in contact with a lot of equipment and pipes in a plant, and there is a difference in the performance of the contact state required by equipment. For example, it is required that the heat exchanger tubes in the heat exchanger and sodium oxide trap mesh in the cold trap

J. Saito (✉)
Japan Atomic Energy Agency, 1 Shiraki Tsuruga, Fukui 919-1279, Japan
e-mail: saito.junichi78@jaea.go.jp

H. Shibutani
Kurume Institute of Technology, 2228-66 Kamitsu-Cho Kurume, Fukuoka 830-0052, Japan

Y. Kobayashi
Maizuru College, National Institute of Technology, 234 Shiroya Maizuru, Kyoto 625-8511, Japan

J. Li et al. (eds.), *Characterization of Minerals, Metals, and Materials 2020*,
The Minerals, Metals & Materials Series,
https://doi.org/10.1007/978-3-030-36628-5_55

have good wettability. On the other hand, it is required that sodium pipes and a part of valves have low wettability. If the wettability of the surface can be controlled, equipment performance improves. The wettability of structure materials by liquid sodium is an important property in designing the apparatus of the fast reactor. It is well known that wettability is affected by factors such as surface roughness and type of metal [1–3]. The purpose of this study is to understand the wettability of pure metal by liquid sodium by using both experimental and theoretical approaches.

Experimental Evaluation of Wettability

Experimental Procedure

High-purity metal plates of titanium, vanadium, iron, nickel copper, and molybdenum were used in an experiment to evaluate wettability. Stainless steel (SUS304), which is the typical structural material for the fast reactor, was utilized as the reference material. High-purity sodium was also used in the experiment to avoid an adverse impact of impurity elements to surface tension. The experiment was carried out in a grove box filled with high-purity argon gas because the chemical reactivity of liquid sodium with oxygen and moisture is very high. The oxygen and moisture concentrations in argon gas were less than 3 and 0.54 ppm, respectively. Wettability was evaluated using the contact angle obtained using the tangent method. The temperature of the metal plate and liquid sodium during the experiment was 140 °C. Experiments were repeated more than three times, and the contact angle was evaluated using the average of these experimental values.

The surface roughness values of all of the plates used in the experiment were evaluated using Mitutoyo SJ-410. A typical result of nickel plate surface roughness measurement is shown in Fig. 1. The arithmetic mean roughness (Ra) was

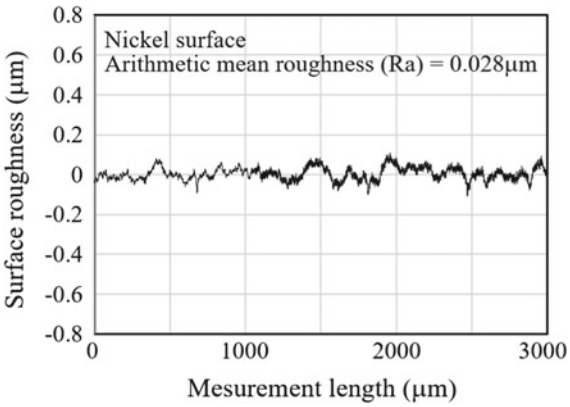

Fig. 1 Surface roughness of the nickel plate used in the experiment

0.028E−6 m. All of the plates used in the experiments had similar surface roughness values to that of nickel. Hence, it could be suggested that surface roughness has a negligible effect on wettability in this study.

Experimental Result

The experimental result of a sodium droplet on a titanium plate is shown in Fig. 2. It was confirmed that there was no oxidation of the droplet because of its mirror surface. Contact angles were measured using both A and B sides of this picture. The average value of A and B was defined as the experimental value.

The experimental results of contact angles for each metal plate with liquid sodium are shown in Fig. 3. There is a small variation of experimental values for each metal,

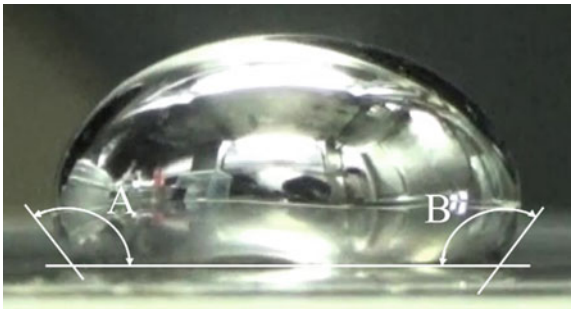

Fig. 2 Sodium droplet on the titanium plate

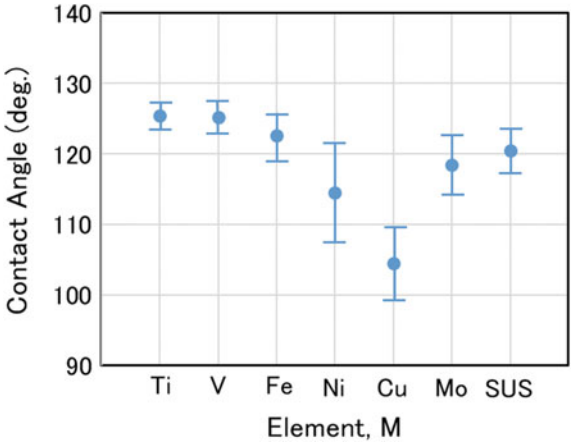

Fig. 3 Change of contact angle by plate metal

but its change depends on the melting temperature of each metal. It is interesting that the trend of change depends on the periodic table. The change of the contact angle decreases as the atomic number increases. This possibly means that the contact angle relates to the atomic interaction between metal of the plate and sodium.

Calculation of the Electronic Structure of the Interface

Molecular Orbital Calculation

An electronic structure of the interface between metal and sodium was calculated to understand atomic interactions. The discrete variational (DV)–$X\alpha$ molecular orbital method [4–7] was used in the calculation of the electronic structures of the interface.

Calculation Model of the Interface

Simple surface models of the interface were constructed for the calculation. A schematic representation of the wetting state of the metal plate with liquid sodium is shown in Fig. 4 using a simple atomic model. There are three kinds of atomic bonds in this interface. One is the M–M bond between metal and metal in the metal plate, which corresponds to the surface tension of metal. Another bond is the M–Na bond between metal and liquid sodium, which corresponds to the interface tension

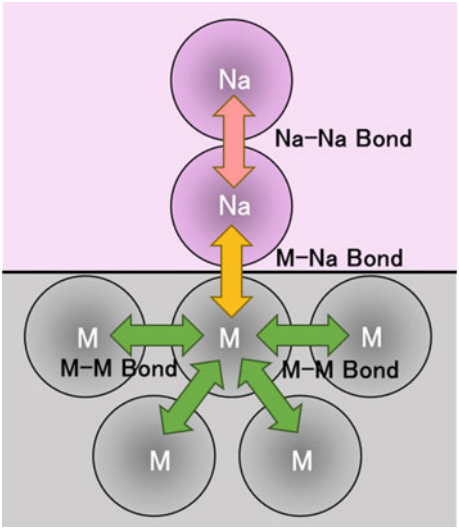

Fig. 4 Schematic of the atomic level of the wetting surface

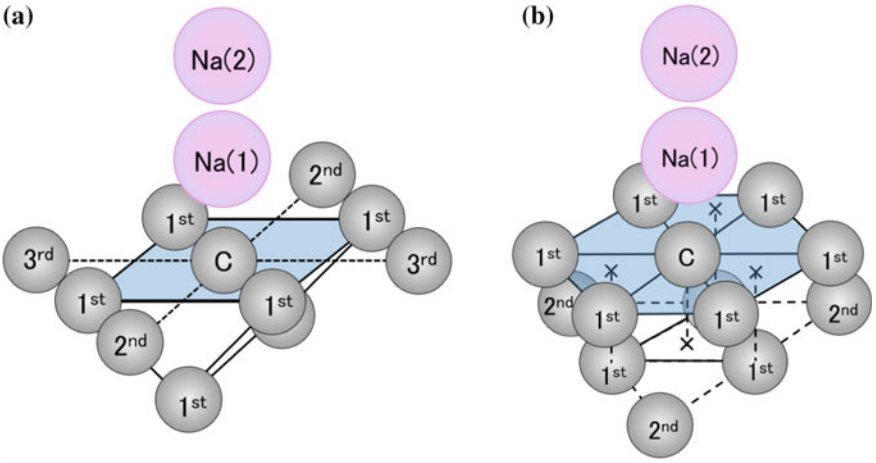

Fig. 5 Cluster models used for electronic structure calculation: **a** body-centered cubic type and **b** face-centered cubic or close-packed hexagonal crystal type

between solid and liquid. There is also the Na–Na bond between liquid sodium and liquid sodium, which corresponds to the surface tension of liquid metal. If the surface condition is the same as the surface roughness and oxidation layer, it is expected that wettability depends on atomic interaction. On the basis of this atomic model of the interface, a cluster model for calculation was constructed.

The cluster models used in the calculation are shown in Fig. 5a, b. Two types of the interface model were constructed because there are three types of crystal structure (body-centered cubic, face-centered cubic, and close-packed hexagonal crystal) of the metal plate. The same cluster model is used for the face-centered cubic or close-packed hexagonal crystal because the difference is only in layer stacking. Figure 5a shows the cluster model for a body-centered cubic metal. Figure 5b shows the cluster model for metal possessing a face-centered cubic or close-packed hexagonal crystal. Sodium atom is located on the centered plate metal atom. This location is called on-top site and represents the general contact site between two kinds of metal.

Calculation Results

Electron Density of States

The electron density of states of the iron and sodium interface is shown in Fig. 6. From these figures, most of the electronic density of states near the Fermi energy level is composed of the Fe–3d band, Na–3s band, and Na–3p band. In particular, the Fe–3d band is located near the Fermi energy level (Ef). The main features shown

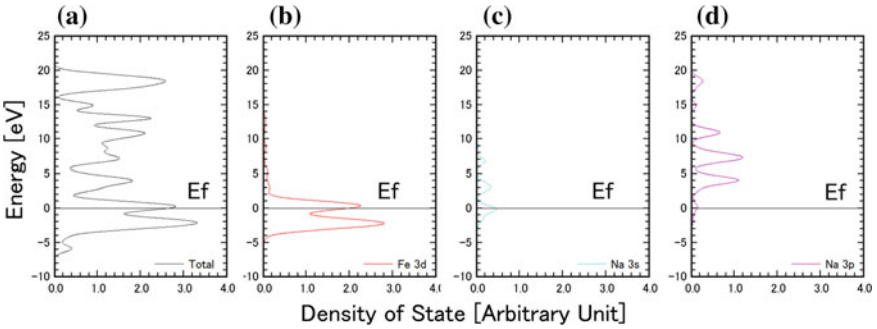

Fig. 6 Electron density of states of the interface between the iron plate and sodium

in Fig. 6b for the Fe–3d band quite resemble the results obtained from the band calculation [8–10] despite the use of the small cluster model shown in Fig. 5a.

Charge Transfer

The calculation results for ionicity are shown in Table 1. Ionicity expresses the charge transfer between atoms. A negative value means receiving electrons, and a positive value means releasing electrons. The centered metal atom and the first neighbor atoms have negative iconicity, whereas the second neighbor atoms and sodium atoms almost have positive ionicity. It is clear from this result that the charge transfer took place from the surrounding second neighbor metal atom and sodium atom to the center and the first neighbor atoms. The amount of charge transfer relates to the difference in the electronegativity of metal and sodium.

Table 1 Ionicity of each atom in the cluster model

Plate metal	Atom				
	Center	1st neighbor	2nd neighbor	Na (1)	Na (2)
Ti	−0.1774	−0.0633	0.1488	−0.1310	0.0717
V	−0.2276	0.0087	0.1919	−0.0649	0.0501
Cr	−0.1449	−0.0412	0.2008	−0.0642	0.1055
Fe	−0.1395	−0.0337	0.1018	0.0224	0.1613
Ni	−0.1689	−0.0838	0.0541	0.1267	0.1775
Cu	−0.1418	−0.0472	0.0169	0.1590	0.1693
Mo	−0.2606	−0.0144	0.0432	0.0497	0.2110

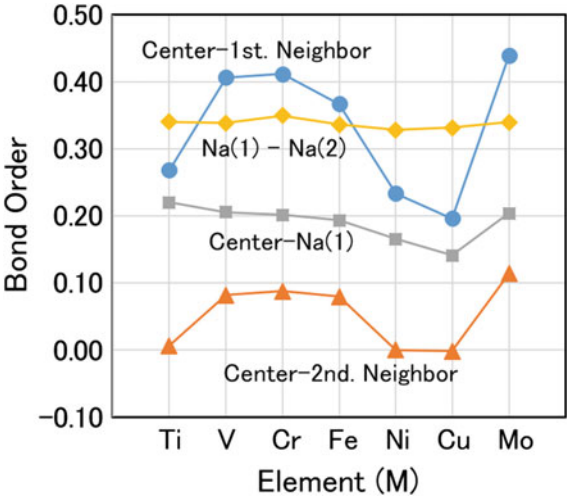

Fig. 7 Change of bond order with plate metal

Atomic Bonding

The atomic bonding of the interface is shown in Fig. 7. The vertical axis, which is the bond order, denotes the strength of atomic bonding. When the bond order is large, the atomic bonding force between atoms is strong. This figure shows that the bond order between the center atom of the plate metal and the first neighbor atom is larger than the other bond orders, and it changes with the atomic number. The bond order between the center atom and the second neighbor atom is very small. These results mean that the atomic bonding of the surface metal largely depends on the kind of metal. It is interesting that the bond order between the center atom and the sodium atom on the center atom changes with the atomic number of metals. It means that the atomic bond strength of the interface is influenced by the kind of metal and that wettability is influenced by the atomic bonding of the interface. The bond order between sodium atoms is almost constant, and this result means that the atomic bonding between sodium atoms is not influenced by the kind of metal. This calculation result shows that the atomic bond of the interface plays an important role in understanding interface behavior (Fig. 7).

Relationship Between Wettability and Atomic Interaction of the Interface

This study considers the relation between the contact angle and atomic interaction. The contact angle shown in Fig. 8 is expressed by Young's equation [Eq. (1)] [11].

$$\gamma_{SV} = \gamma_{SL} + \gamma_{LV} \cos\theta. \tag{1}$$

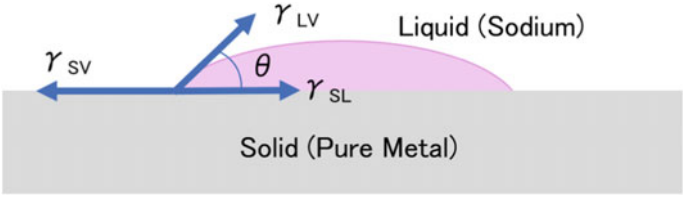

Fig. 8 Schematic of the contact angle and surface force

In this equation, the surface tension of plate metal γ_{SV} corresponds to the atomic bonding between metal atoms of the present calculation. The surface tension of liquid sodium γ_{LV} corresponds to the atomic bonding between sodium atoms, and the interface tension between plate metal and liquid sodium γ_{SL} corresponds to the atomic bonding between the plate metal atom and sodium atom.

The contact angle was evaluated using the calculated atomic bonding. The atomic bonding between sodium atoms remains almost the same with the kind of plate metal in Fig. 6. Therefore, it hardly affects wettability. On the other hand, the atomic bonding of the interface between the plate metal atom and sodium atom and the atomic bonding of the surface between plate metal atoms are very important in theoretically understanding wettability because they change with the kind of plate metal. The contact angle was evaluated using the atomic bonding between plate metal atoms and the atomic bonding between the plate metal atom and sodium atom. The evaluated results are shown in Fig. 9.

In this figure, the vertical axis denotes the contact angle, and the horizontal axis denotes the bond order ratio. It is clear that the contact angle decreased with the increase of the atomic bonding ratio. When the atomic bonding between plate metal and sodium is stronger than that between metals, the contact angle becomes smaller.

Fig. 9 Relationship between contact angle and bond order ratio

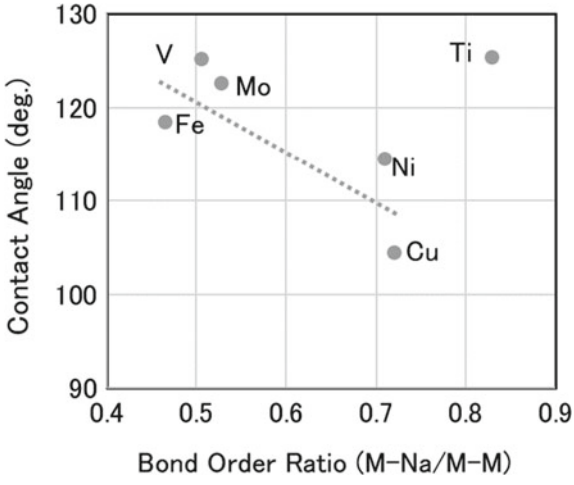

In other words, compared to the surface tension of the plate metal, when the interface tension between the plate metal and sodium becomes stronger, wettability becomes good. From these results, it is expected that the atomic bonding of the interface affects wettability. However, the contact angle of the titanium plate is not consistent with this concept. It is considered that the following reasons cause this inconsistency. In general, the surface of metal has a very thin oxidation film. Sodium has high reducing character, so when liquid sodium comes into contact with metal, the oxidation film on the metal disappears. By the reduction of the oxide film, liquid sodium comes into direct contact with metal. However, titanium oxide is thermodynamically more stable than sodium oxide. Titanium oxide remains on the metal, and the titanium plate does not come into direct contact with liquid sodium. The experimental results of the titanium plate are not a true value and include the value of the oxide film. For this reason, it is expected that the experimental result for titanium is not consistent with the calculated atomic bonding.

Conclusion

The experiments of wettability and the calculation of the electronic structure were carried out in order to understand the wettability of pure metal by liquid sodium. The contact angles for wettability were evaluated using atomic bonding. As a result, it became clear that there was a relation between the contact angle and atomic bonding.

Acknowledgements We greatly appreciate the contribution of Hana Ishiguro, a student at the National Institute of Technology, Maizuru College, who helped to measure the surface roughness of specimens.

References

1. Toyoda H, Ide T, Yagi H, Mori Y, Hirose K (1998) J Jpn Soc Precision Eng 64(5) (1998)
2. Imabayashi S (2008) Rev Polarography 54(2)
3. Fukuyama K (2009) J Surf Finish Soc Jpn 60(1)
4. Adachi H (1978) J Phys Soc Jpn 45:875
5. Adachi H (1978) J Phys Soc Jpn 45:1333
6. Adachi H (1979) J Phys Soc Jpn 47:1528
7. Adachi H (1980) J Phys Soc Jpn 49:1994
8. Cornwell JF, Hum DM, Wong KG (1968) Phys Lett 26A:8
9. Spicer WE (1966) J Appl Phys 36:947
10. Petersson L-G, Melander R, Spears DP, Hagstrom SBM (1976) Phys Rev B 14:4177
11. Young T (1805) Philos Trans R Soc 95:65

How to Measure High-Temperature Heat Capacity Reliably by Drop Calorimetry

Guishang Pei, Junyi Xiang, Lilian Yang, Dapeng Zhong, Gang Li, Feifei Pan and Xuewei Lv

Abstract High-temperature heat capacity measurements can be a very powerful means to investigate and understand the properties of materials, and high-temperature heat capacity values are also the key thermodynamic data can be used for calculating phase diagram, chemical reaction, and multi-phase equilibrium. As one of the most promising method, drop calorimetry has attached much attention during the past years due to its special 3D thermal sensor, which provides more accurate measurement of high-temperature heat capacity. All the subsequent insightful analyses and further discussion should be based on correct experimental data. A few critical concerns about high-temperature heat capacity measurements by drop calorimetry were summarized in this study. Various possibilities in the measurements will be given to show how much the experimental data deviated from their exact values, and those concerns should be taken seriously during actual measurements in order to obtain reliable high-temperature heat capacity values. The sample properties such as water absorption capability, particle size, weight test, surface roughness are critical for Drop calorimetry. The stable room temperature is essential for measuring heat content of the sample. Various integration methods should be carefully considered and selected when face the different heat flow types before and after the Drop test.

Keywords Drop method · Sample property · Operation procedure · Data treatment

X. Lv (✉)
The State Key Laboratory of Mechanical Transmissions, Chongqing University, No. 174 Shazheng Street, Shapingba District, Chongqing 400044, China
e-mail: lvxuewei@163.com

G. Pei · J. Xiang (✉) · L. Yang · D. Zhong · G. Li · F. Pan · X. Lv
School of Materials Science and Engineering, Chongqing University, No. 174 Shazheng Street, Shapingba District, Chongqing 400044, China
e-mail: xiangjunyi126@126.com

Chongqing Key Laboratory of Vanadium-Titanium Metallurgy and New Materials, Chongqing University, Chongqing 400044, China

J. Li et al. (eds.), *Characterization of Minerals, Metals, and Materials 2020*,
The Minerals, Metals & Materials Series,
https://doi.org/10.1007/978-3-030-36628-5_56

Introduction

Chemical thermodynamics is widely used in comprehensive evaluation of preparation related with material synthesis, which is regarded as a powerful tool to deep understand the interrelationship among chemical composition, structure, and properties [1–8]. The calculation of thermodynamic equilibria and chemical reaction require basic knowledge of inputting essential thermodynamic data for each substance involved, namely the values of formation enthalpies and formation entropies at 298.15 K, as well as the expression of high-temperature heat capacity. Above all, heat capacity at constant pressure is one of the essential thermophysical characteristics determining the thermal behavior of a thermoelectric materials, which can convert energy directly between heat and electricity [9]. With the development of experimental phase equilibria and computational thermodynamics, CALPHAD [10] (computer coupling of phase diagram and thermochemistry) is extensively applied in the past years, and the high-temperature heat capacity is the critical thermodynamic propertied to establish the model of the stoichiometric compounds for reassessing the phase diagrams by CALPHAD method. Theoretical calculation and experimental test are two kinds of the frequently used ways to obtain the reliable heat capacity values both at low-temperature and high-temperature. While, the big challenge for high-temperature heat capacity measurements still remains when theoretical calculation is applied in this filed based on ab-initio principle and molecular dynamics simulation for mixed oxides. Therefore, the experimental test based on calorimetric technology is still the most common and reliable method from the literature.

Although heat capacity is a relatively easily accessible property from the experimental point of view and can be measured for mixed solids over a broad temperature range from near 0 K up to their melting temperature. Generally, the calorimetric technology can be clarified as two kinds, namely low-temperature calorimetric technology and high temperature calorimetric technology. The PPMS (physical property measurement system) has been taken for low-temperature *Cp* measurements, and the calibration in PPMS instrument must be often operated to avoid getting incorrect heat capacity values [11]. As for calorimetric experiment at high temperature (when temperature beyond 273.15 K), although a standard measurement process is set by American Society for Testing Material (ASTM) standard [12, 13], the heat capacity measured by DSC (differential scanning calorimetry) still has bad repeatability from time to time and from person to person even when using the same sample and instrument [9]. As for another calorimetric method, drop calorimetry with the specific 3D thermos-pile shows good data repeatability and reliability, thus receiving great interest in recent calorimetric field [14–16]. The aspects of sample preparation, operational procedure, and data treatment have a big impact on the final test results, which should be paid close attention during test procedure.

In this paper, the principle and instrument of drop calorimetry were first introduced, and subsequently, a few key concerns during high-temperature heat capacity measurements by drop calorimetry were analyzed and discussed with detail. Various possibilities in the measurements will be given to show how much the heat

capacity values deviate from their exact values. These concerns should be taken seriously during measurements in order to obtain reliable high-temperature heat capacity values.

The Basic Principle of Drop Calorimetry

The main theory of drop calorimetry is the measurement of the enthalpy changes of the specific sample that is being dropped from T_1 to the detector which is kept at higher temperature (T_2), and the schematic diagram of drop calorimetry can be shown in Fig. 1. When a sample at the room temperature drops into the furnace, the additional heat must be delivered to the system to maintain the preset temperature. This heat is proportional to the heat content of the sample. Through conducting the experiment for several temperatures, enthalpy changes as a function of temperature are been determined, and subsequently, the high-temperature heat capacity is obtained from its derivative as shown in Eq. (1):

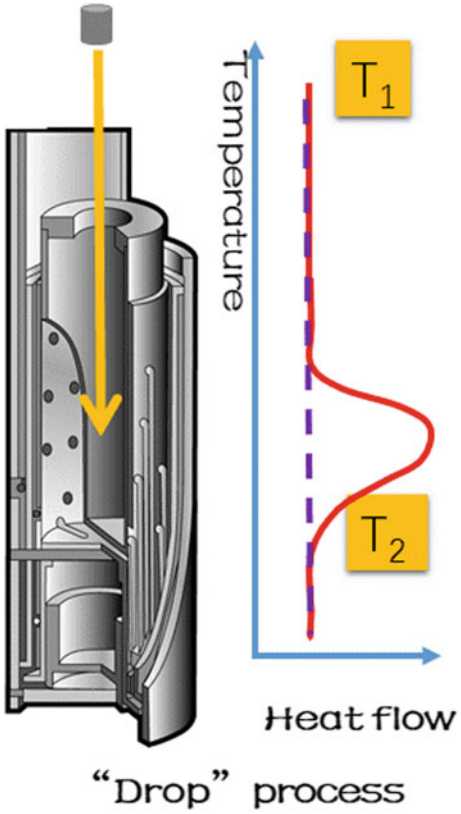

Fig. 1 Schematic diagram of drop calorimetry

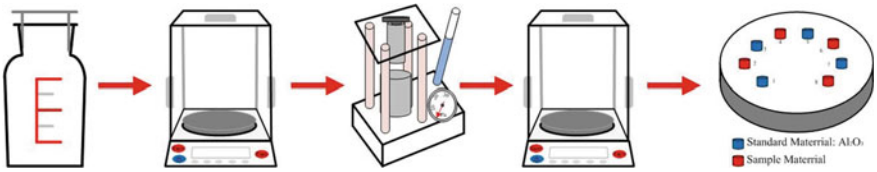

Fig. 2 General step of preparing the drop sample

$$Cp = \left(\frac{\mathrm{d}H}{\mathrm{d}T}\right)_P \tag{1}$$

where T and H were the absolute temperature (K) and enthalpy (J), respectively. The subscript p denoted that the heat capacity values based on Eq. (1) were measured under atmospheric conditions.

The equipment of the enthalpy changes was performed with a Multi-detector High Temperature Calorimeter (MHTC 96 line, Setaram. France) with installed drop sensor. Since the drop calorimetry is the comparison method, it is necessary that during each experiment a standard material with known heat capacity is measured during each Drop test. However, since small heat quantities are measured due to the small temperature increase of the dropped sample, on an absolute scale, the enthalpy error for this temperature range is acceptable, and these results can be considered in the heat capacity evaluation.

The general step for preparing the sample is shown in Fig. 2. Before the drop calorimetry instruments, it is required to compact pieces of the powder material. Generally, cylindrical pellets with 4 mm diameter and 2 mm height should be prepared using a hydraulic press. The mass of samples ranges from 80 to 100 mg due to keep the weight of a standard sapphire (α–Al_2O_3) consistent.

In addition, the most considered aspects during the Drop process such as sample properties, operational procedure, and data treatment should be typically taken into account due to obtain more available calorimetric data.

Sample Properties

Sample is the center and the main factor during the whole Drop test, which not only affect the sample preparation but also subsequent calorimetric test. Different samples may have diversity of particle size, surface roughness, and moisture and which cased various results according to sample property.

Weight test should be as directly and clearly as possible, and the high precision weighting instrument will be suggested when measuring the sample mass.

Particle size of the powder sample mainly has an influence on the pellet process. With regard to the drop calorimetry instruments, it is required to have compacted pieces of the material. Usually, cylindrical pellets are suggested. The large particle

size may make the bad condition for balling process, and the surface roughness of the as-prepared pellets was on good enough to perform the Drop test.

Surface roughness also affects the process when the sample drops from the room temperature to the detector which is kept at high temperature, and when the sample has a rough surface, it may be crushed during the Drop process.

Moisture is also the typical factor, which always is faced when carried out the Drop test. Taking $NaCO_3$ as an example, water absorption capability on the sample surface should not be neglected. Hence, the sealed storage of the roasted sample should be taken when bringing it into the Drop instrument inner, and the inner atmosphere must be turned to pure Ar gas due to prevent further pollute of the sample.

Operational Procedure

Operation is another critical aspect, which affects the veracity of the experimental accuracy. For best of our knowledge, those concerns should be taken seriously and avoided as much as possible during the actual operation. As for operational procedure, the follow point should be paid more attention.

Room temperature has a little influence on the heat flow curve when temperature beyond than 573 K. Although the drop calorimetry was always performed, the stability of room temperature is necessary for measuring the heat flow of the sample when temperature is lower than 573 K because any changes on the room temperature may cause an obvious fluctuation of heat flow curve. Figure 3a presents a specific heat flow curve changes when the room temperature is not stable in contrast to Fig. 3b. What the worst, if this heat flow changes take place just as the sample is dropping from the top to the constant temperature zone. As a result, the experimental data of this Drop test should be repeated. Therefore, the stability of the heat flow before and after Drop test is necessary and essential to avoid the undesired trouble.

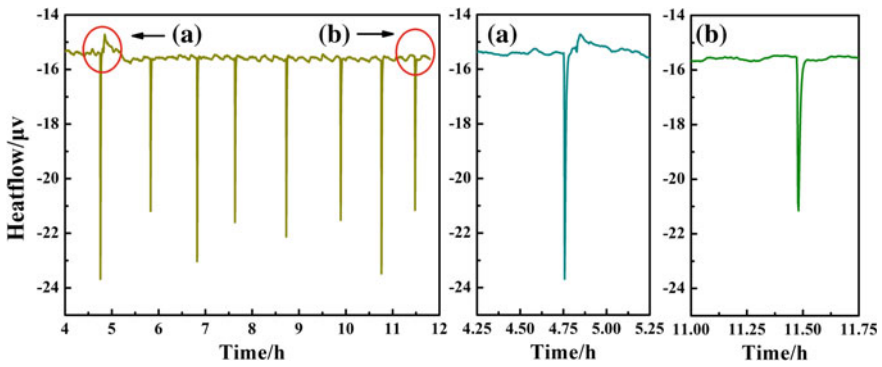

Fig. 3 Typical heat flow changes caused by room temperature unstable

Discussion

The typical heat flow curve of one sequence can be shown in Fig. 4, which concludes four Drops of sapphires (α–Al_2O_3) (No: I, III, V, and VII) and four Drops of sample (No: II, IV, VI, and VIII), and each endothermic peak should be individually integrated to compute the heat content Q_{sample} and $Q_{\text{reference}}$ terms from equations as shown in Eq. (2), subsequently to calculate the heat capacity values. By the heat flow curve, enthalpy changes as a function of temperature are obtained according to Eq. (2):

$$\Delta_{T_a}^{T_m} H_m = \frac{Q_{\text{sample}}}{Q_{\text{reference}}} \times \frac{m_{\text{reference}}}{m_{\text{sample}}} \times \frac{M_{\text{sample}}}{M_{\text{reference}}} \times \int_{T_a}^{T_m} Cp(T)\mathrm{d}T_{\text{reference}} \qquad (2)$$

where T_a and T_m are the room and detector temperatures, m and M are the mass and the molar mass of the reference material and studied sample, respectively. $Cp(T)$ is the temperature function of the sapphire reference molar heat capacity in the literature, and Q_{sample} and $Q_{\text{reference}}$ are heat content by integrated individually each peak of the heat flow signal using Origin Software.

However, the different results could be obtained when using the various integration methods. In this part, the various integration methods according to different experimental curve will be discussed with detail.

It is also evident that a slight variation of the temperature appears during the experiment which is due to the shock upon the drop of the low-temperature material into the hot sensor. However, this phenomenon has no negative effect on the final enthalpy increment determination as the temperature always re-equilibrates at the programmed value.

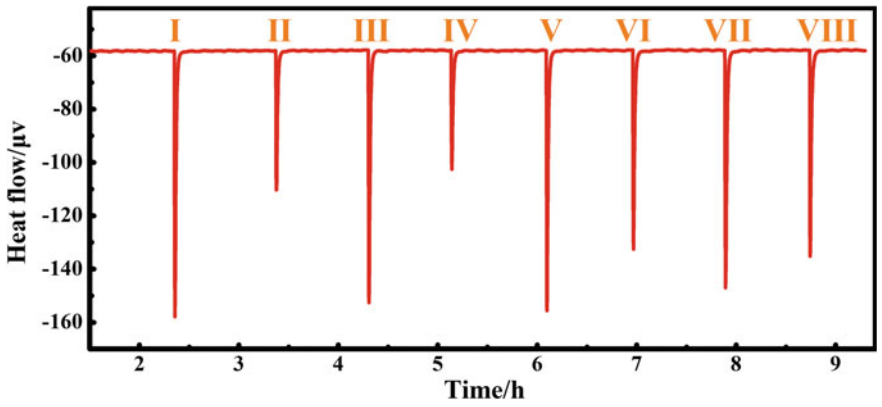

Fig. 4 Typical heat flow curve of one sequence

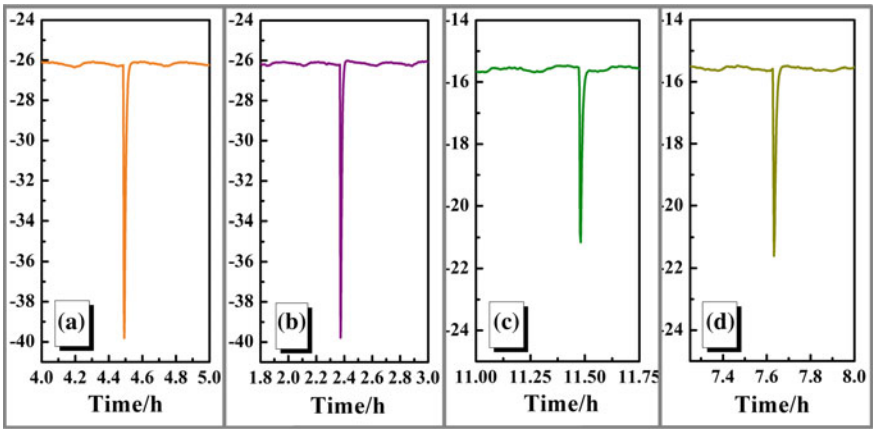

Fig. 5 The enlarged insight near endothermic peak

The enlarged insight near endothermic peak is presented as shown in Fig. 5, which includes four kinds of endothermic peak typical A, B, C, and D. The S-S methods should be considered in priority when integrated the endothermic peak from the literature, and this integration method is very suitable for the endothermic peak of Drop test.

Another common method such as interpolation method and extrapolation method also should be taken into consideration when dealing with the real situation.

Conclusions

Several concerns that may be caused incorrect data during the Drop test were presented in this study. The basic principle of drop calorimetry was first introduced with detail. The sample properties such as water absorption capability, particle size, weight test, surface roughness are critical for Drop calorimetry. The stable room temperature is essential for measuring heat content of the sample. Various integration methods should be carefully considered and selected when face the different heat flow types before and after the Drop test. It is suggested that the drop calorimetry is the most promising method and will be widely applied in the further.

Acknowledgements This work was supported by the National Key R&D Program of China (2018YFC1900500) and Graduate Scientific Research and Innovation Foundation of Chongqing, China (Grant No. CYS19001).

References

1. Kubaschewski O (1972) High Temp High Press 4:1
2. Pankratz LB (1982) Thermodynamic properties of elements and oxides. US Bureau of Mines, Washington
3. Knacke O, Kubaschewski O, Hesselmann K (1991) Thermochemical properties of inorganic substance, 2nd ed, Springer
4. Saxena SK, Chatterjee N, Fei Y, Shen Y (1993) Thermodynamic data on oxides and silicates. Springer, Berlin
5. Kopp H (1863) Investigations of the specific heat of solid and liquid bodies. Proc Royal Soc London 13:229–239
6. Moiseev GK, Sesták J (1995) Prog Cryst Growth Charact 30:23
7. Spencer PJ (1998) Thermochim Acta 314:1
8. Leitner J, Chuchvalec P, Sedmidubsky D, Strejc A, Abrman P (2003) Estimation of heat capacities of solid mixed oxide. Thermochim Acta 395:27–46
9. Wei TR, Guan M, Yu J, Zhu T, Chen L, Shi X (2018) How to measure thermoelectric properties reliably. Joule 2:2183–2188
10. Saunders N, Miodownik AP (2005) CALPHAD (Calculation of phase diagrams): a comprehensive guide. Elsevier
11. Calvin JJ, Asplund M, Zhang Y, Huang BY, Woodfield BF (2017) Heat capacity and thermodynamic functions of γ–Al_2O_3. J Chem Thermodyn 112:77–85
12. Board CA, Burean C, Loan FH, Board R (1999) American Society for Testing and Materials (ASTM) Trf5.jus.br:55
13. Ditmars DA, Ishihara S, Chang SS, Bernstein G, West ED (1982) Enthalpy and heat-capacity standard reference material: synthetic sapphire (Alpha-Al_2O_3) from 10 to 2250 K. J Nation Bure Stand 87:159
14. Pei GS et al (2019) A literature review of heat capacity measurements method. In: Paper presented at the 148st TMS annual meeting, San Antonio, Texas, 10–14 March 2019
15. Pei GS, Xiang JY, Lv XW, Li G, Wu SS, Zhong DP, Lv W (2019) High-temperature heat capacity and phase transformation kinetics of $NaVO_3$. J Alloy Compd 794:465–472
16. Leitner J, Vonka P, Sedmidubsky D, Svoboda P (2010) Application of Neumann-Kopp for the estimation of heat capacity of mixed oxides. Thermochim Acta 497:7–13

Improvement Properties of Polypropylene by Graphene Oxide Incorporation

Tatiane Yumi Tatei, Eric Hossein Fontes, Renan Paes Moreira, Francisco Valenzuela Días, Rene R. Oliveira, Vijaya Rangari and Esperidiana A. B. Moura

Abstract Due to the remarkable properties of graphene oxide (GO) and its possibility of functionalization, GO has been used in many applications such as nanocomposites. GO nanosheets have been shown to improve the properties of the polypropylene (PP) matrix, for instance, its strength, gas barrier, thermal, and electrical conductivity. As PP has relatively low cost and varied applications, this work aims to study the changes in its thermal, morphological, and mechanical properties, due to the incorporation of GO in the PP matrix. GO was synthesized from graphite by a modified Hummers method. The nanocomposites PP/GO with 0.1, 0.2, and 0.3 wt% of GO in the PP matrix were obtained using a twin-screw extruder and an injection molding machine via a melt blending process. The nanocomposites PP/GO were characterized by FE-SEM and Izod impact test. In addition, the GO nanosheets were also characterized by Raman spectroscopy, ATR-FTIR, FE-SEM, and XRD, therewith correlation between properties was discussed.

Keywords Polypropylene · Graphene oxide · Nanocomposite

T. Y. Tatei (✉) · E. H. Fontes · R. P. Moreira · E. A. B. Moura
Center for Chemical and Environmental Technology, Nuclear and Energy Research Institute, 2242 Prof. Lineu Prestes Av, São Paulo, SP 05508-000, Brazil
e-mail: tatiane.tatei@usp.br

F. V. Días
Metallurgical and Materials Engineering Department, Polytechnic School, University of São Paulo, Prof. Mello de Moraes, 2463, São Paulo, PA 05508-030, Brazil

R. R. Oliveira
Nuclear and Energy Research Institute, Center for Materials Science and Technology, 2242 Prof. Lineu Prestes Av., São Paulo, SP 05508-000, Brazil

V. Rangari
Department of Materials Science and Engineering, Tuskegee University, Tuskegee, AL 36088, USA

J. Li et al. (eds.), *Characterization of Minerals, Metals, and Materials 2020*,
The Minerals, Metals & Materials Series,
https://doi.org/10.1007/978-3-030-36628-5_57

Introduction

Carbon nanostructures have been extensively studied due to their excellent properties and numerous applications such as nanocomposites [1]. Graphene nanosheets can be obtained by mechanical exfoliation (scotch-tape method) of bulk graphite [2] and by epitaxial chemical vapor deposition [3]. Although preferred for synthesis, these methods require devices that make large-scale manufacturing difficult. In contrast, chemical methods are easy to perform for large-scale synthesis of graphene materials [4]. In 1859, Brodie first showed the synthesis of graphene oxide (GO) by adding a portion of potassium chlorate to a graphite paste in fuming nitric acid [5]. In 1898, Staudeninaier improved this procedure by using a mixture of concentrated sulfuric acid and fuming nitric acid, followed by the gradual addition of chlorate to the reaction mixture. This change provided a simple protocol for producing highly oxidized GO [6].

In 1958, Hummers reported an alternative method for the synthesis of graphene oxide using $KMnO_4$ and $NaNO_3$ in concentrated H_2SO_4 [7]. The Hummers method has received much relevance in the last decades due to its high efficiency and satisfactory reaction safety; however, it still has some disadvantages. For example, the oxidation procedure releases toxic gases such as NO_2 and N_2O_4, while residual Na^+ and NO_3^- ions are difficult to remove from wastewater formed by the synthesizing and purifying processes of GO. For this reason, in this work, the graphite oxidation was performed by a modified Hummers method, as it has several advantages and is safer compared to the usual techniques. Among the adjustments made, $KClO_3$ was replaced with $KMnO_4$ to improve reaction safety and eliminate the release of ClO_2 (explosive) [8]. The adjustment used in the present work was successful in increasing the reaction product and further reducing the release of toxic gas while using a different ratio of $KMnO_4$ and H_2SO_4 as required by the Hummers method.

Graphite has a similar layered structure as GO, but the plane of carbon atoms in GO contains oxygen, which expands the distance between the layers and makes the atomic thick layers hydrophilic. Therefore, these oxidization layers can be exfoliated under moderate ultrasonication. When these sheets contain only one or a few layers of carbon atoms they are called graphene oxides (GO) [9, 10]. Graphene oxides are extremely relevant for applications in various areas, such as composite materials, polymer-composite, solar energy, and among others. Polymeric nanocomposites are two-phase materials in which one of the phases is formed by nanoparticles dispersed in a polymeric matrix represented by the continuous phase, providing new and improved properties compared to conventional polymer composites [11]. The implementation of graphene oxide as nanocomposite has been widely reported due to improvements in the properties of several matrices as a result of the addition of functional groups [10].

Polypropylene (PP) is one of the most widely used industrial-scale polymer matrices in today's world thanks to its great versatility, due to its chemical structure, processability, and properties, as well as its recycling potential [12]. In order to study

ways to improve the PP matrices, such as their thermal, morphological, and mechanical properties, the present work considers the incorporation of GO as essential. Thus, producing PP/GO nanocomposites with 0.1, 0.2, and 0.3 wt% GO in the PP matrix.

Methodology

Synthesis of GO by the Modified Hummers Method

The graphene oxide (GO) was produced from exfoliated graphene using the Hummers method. However, this method has been slightly modified with respect to the process times and reagents proportions.

In a 600 mL beaker, 5 g of exfoliated graphite and 15 g of $KMnO_4$ were added. The beaker was subjected to an ice cube "water bath" and 100 mL of H_2SO_4 was added dropwise, whereupon gas was released under magnetic stirring for 30 min. Still in the ice bath, 400 mL of distilled water was added to the beaker, in which gases were also released. This solution was then placed in a water bath at 90 °C for 1 h.

Then a prepared solution of 70 mL H_2O and 30 mL H_2O_2 was added to the beaker, under magnetic stirring and heating at 50 °C for 4 h (due to technical limitations, it was 3 h in one day and 1 h in the next), which showed no reaction. The resulting solution was taken to the vacuum pump with the addition of a solution of 50 mL of HCl and 450 mL of distilled water for filtration in a Büchner hopper in a vacuum system. Then the material retained on the filter was dialysed in a 2 L beaker for 5 days, changing the water twice a day, until reaching a pH between 5 and 6.

Finally, the powder material was frozen and separated into small beakers for 1 day and lyophilized to obtain the GO, which was then subjected to 4-cycle ultrasound in a 200 mL beaker for 15 min each.

Preparation of Composites

Polymeric composites were prepared in different compositions by weight: 0.1, 0.2, and 0.3 wt% of GO. The GO nanosheets were incorporated into neat polypropylene (PP) using a twin-screw extruder model Haake Rheomix with 16 mm and $L/D = 25$ rate from Thermo Scientific. The temperature profile was 185/195/195/190/190/190 °C. The screw speed was set from 15 to 60 rpm. The extruded materials were cooled down in room temperature water for better dimensional stability, pelleted, dried at 60 °C ± 2 °C for 24 h, and fed with injected molds from 180 to 185 °C. Then, the mold temperature was set to 50 °C and test samples for tensile and impact test were obtained.

Characterization of Graphene Oxide Nanosheets and Polypropylene Based on Graphene Oxide Nanocomposites

The characterization of GO nanosheets were made by the analysis Raman Spectroscopy using model MacroRam Horiba Scientific, $\lambda = 785$ nm, power 7%, 40 for acquisition, and 5 spectra for accumulation. X-ray diffraction (XRD) was performed on a model Bruker D8 Advance 3 kW diffractometer equipped with Cu-K alpha radiation tube and scintillation detector. The samples were analyzed in the form of powder at room temperature, and the angular range was 3.0 ° up to 60.0 ° with an increment of 0.05. Attenuated total reflectance Fourier transform infrared and spectroscopy (ATR-FTIR), the spectra were acquired by Fourier transform infrared spectroscopy using a total attenuated reflectance sensor in powder samples of GO and the PP/GO nanocomposite. For PP/GO nanocomposites were performed tensile tests using an INSTRON Testing Machine model 5564, according to ASTM D 882-91 in order to evaluate the mechanical behavior of the materials studied. Each value obtained represented the average of five samples. Morphological characterization of PP/GO 0.3 wt% composite was carried out using field emission scanning electron microscopy (FE-SEM), cryofractured samples under liquid nitrogen were carried out using a model JEOL-JSM-7401 F, microscope with an accelerating voltage of 1–30 kV, using EDS Thermo-Scientific mod. Noran System Six software, in gold-coated powder samples using sputter coater.

Results and Discussion

GO Characterization Results

Field Emission Scanning Electron Microscopy (FE-SEM)

Figure 1 shows FE-SEM micrographs of surface of the PP/GO 0.3 wt% in 500 × magnification and 1.000 × magnification. The micrographs of the PP/GO 0.3 wt% cryofractured surface shown in the figures show a relatively uneven rough surface with aggregated domains.

Raman Spectroscopy Analysis Results

Figure 2 shows the Raman spectrum of GO after the background subtraction. The characteristics *D* (disorder band) and *G* (in phase vibrations band) of GO are present, so as the 2D band. The *D* band is located at 1345 cm^{-1} and the *G* band at 1600 cm^{-1}. These values agree with ones reported in literature [13, 14]. They are also associated with the representation E_{2g} first-order scattering of the D_{6h} symmetry group in graphene and the breathing mode in aromatic rings [13, 15].

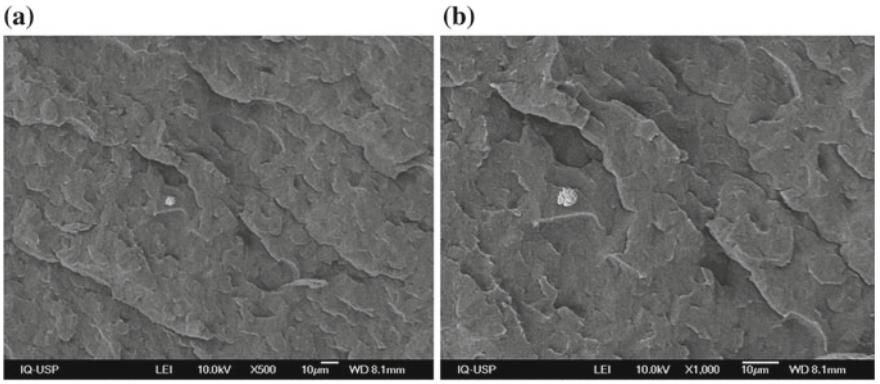

Fig. 1 FE-SEM images of PP/GO 0.3% **a** 500 × magnification and **b** 1.000 × magnification

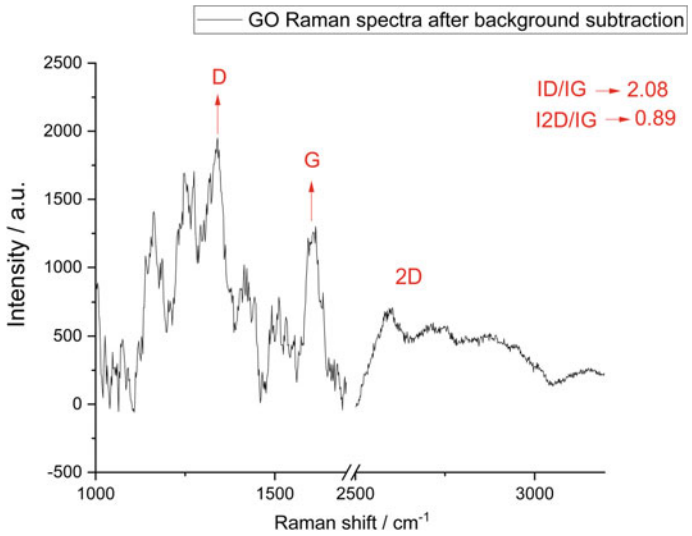

Fig. 2 Raman spectroscopy of graphene oxide in powder form

The ratio between the intensity of the overtone 2D and the intensity of the *G* band, together with the intensity ratio of *D* and *G* bands, can show to us the approximate number of layers in the GO structure [16]. According to our measures, the ratio between the *D* and *G* bands was about 2.08, and the ratio between the 2D and *G* bands was about 0.89. The value of 0.89 suggests that we have a few layers of graphene in our system. The high value of ID/IG, 2.08, can be attributed to the graphitic phase also present in our system [17].

To measure the crystallite size of the GO, we used the modified Tuinstra Koenig relation suitable for low crystallite sizes L_a [18, 19]:

$$\Gamma_G\left(\mathrm{cm}^{-1}\right) = 71 - 5.2\,L_a \tag{1}$$

We found the value of 8.5 nm. According to [7], it is quite impossible to compare the extracted value by fitting technique with other results in literature, since there are different methodologies employed in each work. But we can make a comparison of this value with the one extracted by Scherrer's equation within XRD analysis.

XRD Analysis Results

Figure 3 shows the crystalline structure of GO obtained by XRD. It is possible to observe the Bragg's angle approximately in $2\theta = 10°, 25°$, and $55°$. They are associated, respectively, with the (001) hexagonal crystalline structure of GO, (002) and (004) hexagonal crystalline structure of graphite [14, 20].

According to Bragg's law, the interplanar distance for the GO (001) crystalline plane is about 7.97 Å. This result is very similar to what is reported in [20], also, this value is an intermediate value between 6.1 Å (dry GO) and 12 Å (hydrated GO). The hydrophilic oxygen in the functional groups in GO formed at the basal plane of GO sheets absorbed water molecules, increasing the interplanar distance or the commonly said d-space relatively to the dry GO [20]. Applying the Scherrer's equation, we can determine the approximate crystallite size. The value found was 4.39 nm, which is almost the half of the one we have obtained through Raman spectroscopy: 8.5 nm. Both models to calculate the crystallite size have their limitations, but nevertheless, it is important to use both to obtain complementary information about the system. So, the results are divergent by the form factor used in the calculation of the average crystallite size used in the Scherrer equation.

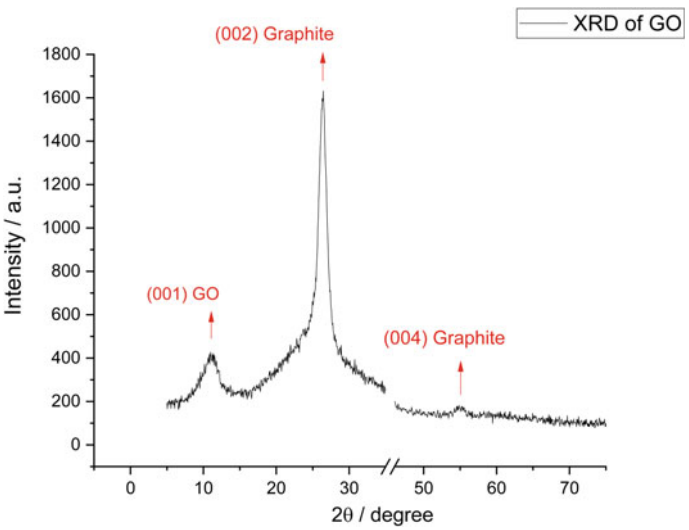

Fig. 3 Crystalline structure of GO in powder form obtained by XRD

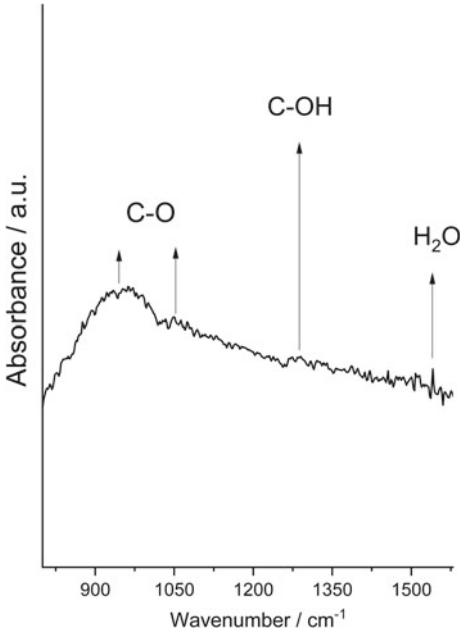

Fig. 4 Infrared spectroscopy with ATR accessory for the identification of GO nanosheets and its functional groups

ATR-FTIR Analysis Results

ATR-FTIR-spectra of GO nanosheets shown in Fig. 4.

According to [13, 21], the IR bands at 1049 and 965 cm^{-1} correspond to the CO stretching mode of vibration, while the 1280 cm^{-1} is associated with the C–OH vibration mode. These results are very important, since the formation of functional groups are characteristics of GO nanosheets. Also, it was possible to notice the presence of H_2O molecules at the nanopowder. The IR band associated with water is approximately 1540 cm^{-1}.

Mechanical Test Results

Table 1 shows the mechanical test results by Izod impact.

Table 1 Izod impact test results

Samples	E^{a}_{Izod} ($J.m^{-1}$)
Neat PP	1.15 ± 10
PP/GO 0.1 (0.1 wt%)	3.12 ± 7
PP/GO 0.2 (0.2 wt%)	1.47 ± 7
PP/GO 0.3 (0.1 wt%)	1.17.5

[a] E_{Izod} Energy required to fracture

The Izod impact test results are imported since represents the energy needed to break the nanocomposite structure. The main goal here is to compare the GO loadings and verify what composition has a better performance. The nanocomposite PP/GO 0.1 (with 0.1 wt% GO) has presented the highest energy required to fracture: 3.125 J m^{-1}. This could be explained by the high nanoparticle dispersion into PP matrix, as can be seen in SEM results.

Conclusion

In this work, graphene oxide (GO) was synthesized from graphite by a modified Hummers method and incorporated in the PP matrix by melting extrusion process and characterized. The nanocomposites PP/GO were characterized by FE-SEM and Izod impact test. In addition, the GO nanosheets were also characterized by Raman spectroscopy, ATR-FTIR, FE-SEM, and XRD. The results showed that the functional groups C–OH present in the nanocomposite was responsible for adsorb water molecules and according to SEM the PP/GO 0.1 (with 0.1 wt% GO) has the better dispersion and because of that has the better impact results. This can be observed in the FE-SEM images, in which the PP/GO 0.3 wt% showed a roughness surface with aggregated domains.

References

1. Geim AK, Novoselov KS (2007) The rise of graphene. Nat Mater 6:183–191. https://doi.org/10.1038/nmat1849
2. Novoselov KS, Geim AK, Morozov SV, Jiang D, Zhang Y, Dubonos SV, Grigorieva IV, Firsov AA (2004) Electric field effect in atomically thin carbon films. Science 306:666–669. https://doi.org/10.1126/science.1102896
3. Berger C, Song Z, Li X, Wu X, Brown N, Naud C, Mayou D, Li T, Hass J, Marchenkov AN, Conrad EH, First PN, De Heer WA (2006) Electronic confinement and coherence in patterned epitaxial graphene. Science 312:1191–1196. https://doi.org/10.1126/science.1125925
4. Higginbotham AL, Lomeda JR, Morgan AB, Tour JM (2009) Graphite oxide flame retardant polymer nanocomposites. Appl Mater Interfaces 1:2256–2261. https://doi.org/10.1021/am900419m
5. Brodie BC (1859) On the atomic weight of graphite. Philos Trans R Soc Lond 149:249–259. https://doi.org/10.1098/rstl.1859.0013
6. Staudenmaier L (1898) Verfahren zur Darstellung der Graphitsaure. Ber Dtsch Chem Ges 31:1481–1487. https://doi.org/10.1002/cber.18980310237
7. Hummers WS, Offeman RE (1958) Preparation of graphitic oxide. J Am Chem Soc 80:1339. https://doi.org/10.1021/ja01539a017
8. Ramakrishnan MC, Thangavelu RR (2013) Synthesis and characterization of reduced graphene oxide. Adv Mater Res 678:56–60. https://doi.org/10.4028/www.scientific.net/AMR.678.56
9. Stankovich S, Dikin D, Piner RD, Kohlhaas KA, Kleinhammes A, Jia Y, Wu Y, Nguyen SBT, Ruoff RS (2007) Synthesis of graphene-based nanosheets via chemical reduction of exfoliated graphite oxide. Carbon 45:1558–1565. https://doi.org/10.1016/j.carbon.2007.02.034

10. Wang G, Yang J, Park J, Gou X, Wang B, Liu H, Yao J (2008) Facile synthesis and characterization of graphene nanosheets. J Phys Chem C 112:8192–8195. https://doi.org/10.1021/jp710931h
11. Wang KH (2001) Synthesis and characterization of maleated polyethylene/clay nanocompósitos. Polymer 42:9819–9826
12. Washburger MR (2006) Compósito de polipropileno com nanocarga – Dissertação de mestrado pela Universidade Federal do Rio Grande do sul
13. Pérez LA, Bajales N, Lacconi GI (2019) Raman spectroscopy coupled with AFM scan head: a versatile combination for tailoring graphene oxide/reduced graphene oxide hybrid materials. Appl Surf Sci 495:143539
14. Muniyalakshmi M, Sethuraman K, Silambarasan D (2019) Mater Today Proc
15. Gelessus A, Thiel W, Weber W (1995) Multipoles and symmetry. J Chem Educ 72:505
16. Instanano, in
17. Malard LM, Pimenta MA, Dresselhaus G, Dresselhaus MS (2009) Raman spectroscopy in graphene. Phys Rep 473:51–87
18. Okuda H, Young RJ, Wolverson D, Tanaka F, Yamamoto G (2018) Okabe TCarbon 130:178–184
19. Mallet-Ladeira P, Puech P, Toulouse C, Cazayous M, Ratel-Ramond N, Weisbecker P, Vignoles GL, Monthioux M (2014) A Raman study to obtain crystallite size of carbon materials: a better alternative to the Tuinstra–Koenig law. Carbon 80:629–639
20. Al-Gaashani R, Najjar A, Zakaria Y, Mansour S, Atieh MA (2019) XPS and structural studies of high quality graphene oxide and reduced graphene oxide prepared by different chemical oxidation methods. Ceram Int 45:14439–14448
21. Han Lyn F, Chin Peng T, Ruzniza MZ, Nur Hanani ZA (2019) Effect of oxidation degrees of graphene oxide (GO) on the structure and physical properties of chitosan/GO composite films. Food Packag Shelf Life 21:100373

Influence of Sealing Mortar in the Strength of Compression of the Structural Masonry Ceramic

M. T. Marvila, A. R. G. Azevedo, J. Alexandre, R. P. Oliveira, M. P. Oliveira, E. B. Zanelato and S. N. Monteiro

Abstract Seeking to reduce costs, one of the constructive alternatives that have been employed in Brazil is structural masonry. In this study, the influence of the mortar on the strength of the masonry was analyzed by two block prisms. The thickness of the joint was varied in five levels and the unit used was the ceramic structural block 14 × 19 × 29 cm. After the 28 days of age of the prisms, their resistance to simple compression and the modules of longitudinal deformation were determined. According to the results of the average resistance of the samples, the resistance of the prism is inversely proportional to the thickness of the mortar. However, after analysis of variance tests, it was concluded that the resistance of the prism to the thicknesses of 10, 15, and 20 mm are significantly equal; the same was concluded for the grouping of the thicknesses of 15, 20, and 25 mm.

M. T. Marvila (✉) · A. R. G. Azevedo · J. Alexandre · R. P. Oliveira · E. B. Zanelato
UENF—State University of the Northern Rio de Janeiro, LECIV—Civil Engineering Laboratory, Av. Alberto Lamego, 2000, Campos dos Goytacazes, Rio de Janeiro 28013-602, Brazil
e-mail: markssuel@hotmail.com

M. T. Marvila · A. R. G. Azevedo · M. P. Oliveira
UENF—State University of the Northern Rio de Janeiro, LAMAV-Advanced Materials Laboratory, Av. Alberto Lamego, 2000, Campos dos Goytacazes, Rio de Janeiro 28013-602, Brazil

A. R. G. Azevedo
Engineering School, Department of Agricultural Engineering and Environment, UFF—Federal Fluminense University, R. Passo da Pátria, 156 - 209 - São Domingos, Niterói, Rio de Janeiro 24210-240, Brazil

A. R. G. Azevedo · R. P. Oliveira · E. B. Zanelato
IFF—Federal Fluminense Institute, Square Dr. Siqueira, 273, Parque Dom Bosco, Campos dos Goytacazes, Rio de Janeiro 28030-130, Brazil

M. P. Oliveira
UFES—Federal University of Espirito Santo, Alto Universitário, S/N Guararema, Alegre, ES 29500-000, Brazil

S. N. Monteiro
Department of Materials Science, IME—Military Institute of Engineering, Square General Tibúrcio, 80, Rio de Janeiro 22290-270, Brazil

J. Li et al. (eds.), *Characterization of Minerals, Metals, and Materials 2020*,
The Minerals, Metals & Materials Series,
https://doi.org/10.1007/978-3-030-36628-5_58

Keywords Mortar · Compression · Structural masonry ceramic

Introduction

The use of structural masonry in the construction sector has seen a large increase in recent years, due to government policies that encourage the construction of more housing units in order to meet the constant housing deficit in the country [1]. As a result, studies with the components of this building material have gained importance in the Brazilian scenario, with a major focus on the main property of these materials: the characteristic compressive strength [2, 3].

With these studies, it was found that the compressive strength of structural masonry depends on a number of factors, such as the shape and size of the structural walls, the anisotropy of the units that form the system, the horizontal and vertical arrangements of the joints, mechanical properties of the components, quality of the workforce that performed the services, conditions of cure, and others [4].

Among these factors, one of the main investigated by several researchers is the non-monolithic behavior of the system that is influenced by the fact that the structural masonry walls are composed of ceramic or concrete blocks, joined by a settlement mortar [5]. The strength of these two materials and how they behave together when receiving the applied masonry loads totally interferes with the compressive strength of the structural walls.

Hamdy et al. [6] studied the use of additives in mortar applied to masonry walls, in order to verify how the modification of the resistance patterns and workability of the material affected the overall strength of the building system. The authors concluded that the modifications of the mortar resistance and the water retention of the material are positive, but could not establish any correlation between the compressive strength of the masonry walls and the properties studied for the mortars.

Drougkas et al. [7] studied the influence of the mortar Poison coefficient on the overall behavior of masonry walls when subjected to compression. The authors proposed a micro-mechanical analysis model and performed experimental tests and numerical modeling. The results of the authors proved that the variation of the mortar parameters directly affects the compressive strength of the studied walls, indicating that further study of the behavior of mortars is necessary to correctly understand the structural masonry system.

In this context, the objective of this work was to evaluate the influence of the compressive strength of mortars, using two different types of material with 2.72 and 7.41 MPa, and the thickness of the joint used for laying the blocks, with values ranging between 5 and 25 mm, verifying how these factors affect the compressive strength of structural masonry.

Materials and Methods

In this study, 140 × 190 × 290 mm hollow ceramic blocks were used, as illustrated by Fig. 1. The blocks were granted by a construction company located in Campos dos Goytacazes-RJ, Brazil, which uses these units to perform its services. Thirteen blocks with this pattern were submitted to water absorption [8] and compressive strength [9] tests following the Brazilian methodologies.

For laying mortars, two mixed mortar compositions were used, the dosages of which were supplied by the same company that gave the structural blocks. It is noteworthy that both compositions are also commonly used by this company. CP II E 32 cement and hydrated lime CH I were used, as well as natural river sand. Mortar 1 has a ratio of 1:0.80:5.67:1.57 and mortar 2 has a ratio of 1:0.35:4.50:1.05 (cement: hydrated lime: sand: water), both mass compositions. Both compositions were tested for consistency index tests [10], mechanical tensile strength at flexion and compression [11], water retention [12], and all methodologies according to Brazilian standards.

Finally, the analysis of the prisms was performed using two blocks joined with mortars of different thicknesses. The Brazilian standard [13] recommends the use of 10 mm thick joints. In this work, was used 5, 10, 15, 20 and 25 mm joints with the mortar 1. For mortar 2 only prisms with a mortar joint 10 mm thick were used. Six specimens were used for each composition studied.

In the tests of resistance used a press Shimadzu Corporation model UH-F500KNI, with a maximum capacity of 500 kN, with displacement rate of 0.5 mm per minute.

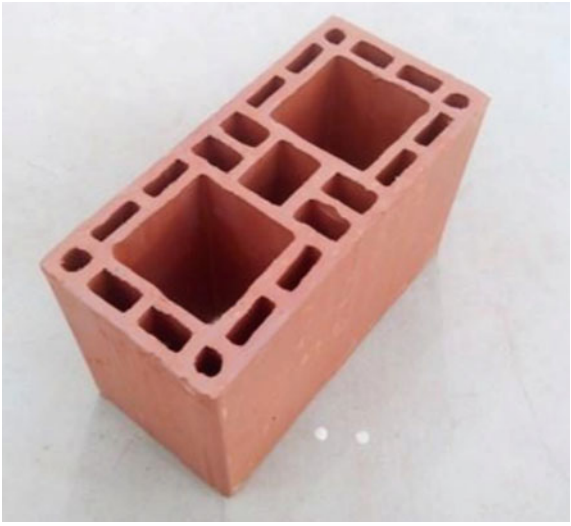

Fig. 1 Ceramic structural block

Results and Discussion

Table 1 presents the results obtained individually for blocks and mortars. The values obtained are consistent in comparison with the values obtained with the bibliography for both blocks [1–4] and mortar [14–17]. The focus of the work is not to discuss the parameters of blocks and mortars individually, but to discuss the influence of varying mortar thickness on block strength, as will be detailed below.

Table 2 presents the results obtained for the studied prisms. Figure 2 complements the table showing the relationship between the thickness of mortar joints 1 and the compressive strength of the blocks. From this figure, the inverse relationship between compressive strength and mortar thickness is obvious, where the greater the thickness of the joint, the lower the resistance of the studied prisms. It should be noted, however, that the thicknesses of 10, 15, 20, and 25 mm have statistical equivalence. This fact demonstrates the importance of rigorous control in the execution of mortar joints in masonry walls, since any deviation in the control of joint thickness can cause significant decreases in the strength of the evaluated material.

Regarding mortar 1 and 2, based on the 10 mm prisms, it is found that mortar 2 provides a very high resistance to the prepared prisms, which can be directly related to the resistance of the mortar itself (shown in Table 1). Thus, it is noteworthy that, although it is an obvious fact, the higher the resistance of the mortars used, the greater the compressive strength of the structural masonry made with this mortar.

Figure 3 presents the linear analysis between compressive strength and inverse mortar joint thickness. The graph clearly demonstrates the relationship between these two parameters and further highlights how increasing the thickness of joints of

Table 1 Parameters of blocks and mortars

Parameter	Block	Mortar 1	Mortar 2
Water absorption (%)	23.2	–	–
Compressive strength (MPa)	5.99	2.72	7.41
Flexural tensile strength (MPa)	–	1.25	3.11
Consistency index (mm)	–	275	259
Water retention (%)	–	90.4	86.8

Table 2 Parameters of prisms

Prism	Nomenclature	Compressive strength (MPa)
Mortar 1 with 5 mm	P05	2.79 ± 0.49
Mortar 1 with 10 mm	P10	1.64 ± 0.29
Mortar 1 with 15 mm	P15	1.40 ± 0.08
Mortar 1 with 20 mm	P20	1.37 ± 0.13
Mortar 1 with 25 mm	P25	1.29 ± 0.07
Mortar 2 with 10 mm	P2.10	3.44 ± 0.34

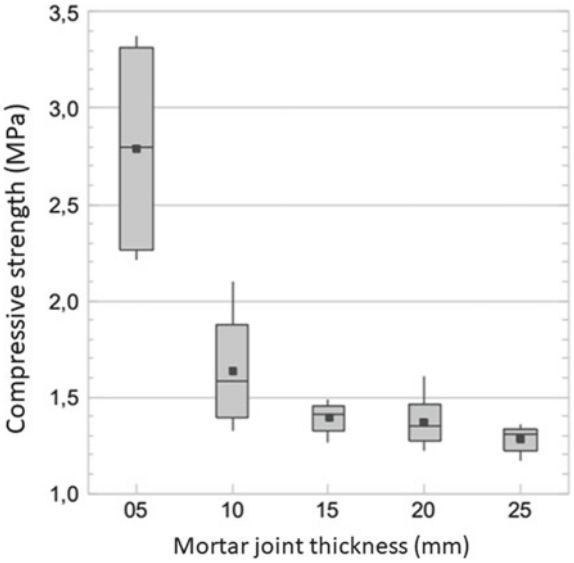

Fig. 2 Relationship between joint thickness and compressive strength of prisms

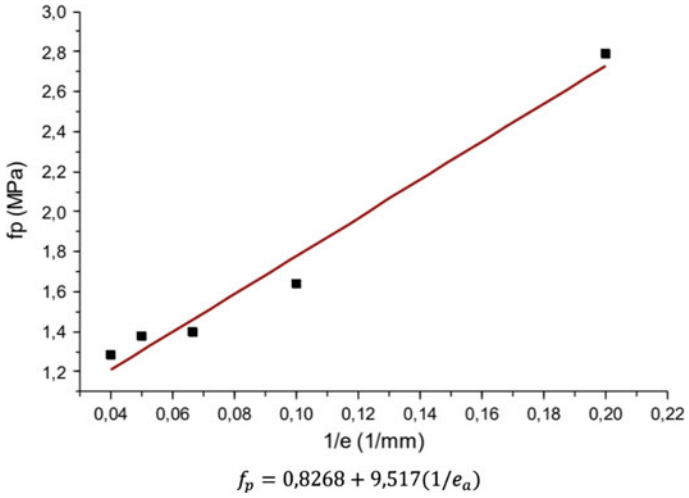

Fig. 3 Linear relationship between compressive strength and inverse joint thickness

structural masonry walls is detrimental to the strength of the material, proving the importance of rigorous control in the execution of this type of structure.

Still in Fig. 3, it is worth noting lastly that the R^2 of the equation shown in the figure is 0.9751, which proves a high regression in the proposed model. Finally, Fig. 4 shows the relationship between strength factor and mortar thickness. The resistance

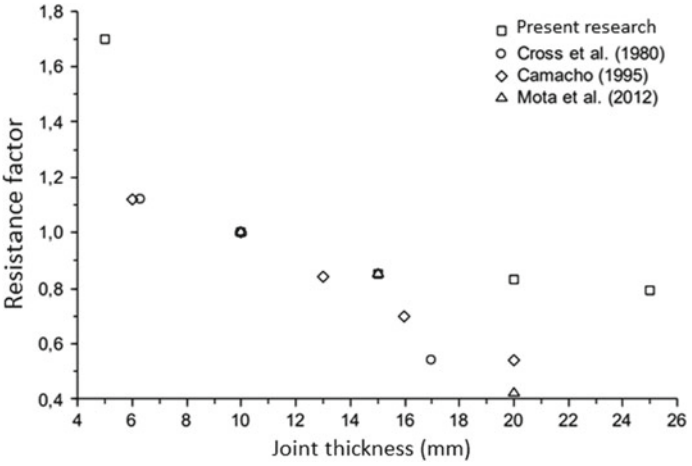

Fig. 4 Linear relationship between compressive strength and inverse joint thickness

factor is a parameter widely used in structural masonry research and is calculated by dividing the resistance of the structural unit (ceramic block) by the resistance obtained by the prism. In this same graph, the values obtained by other researchers who performed similar research are plotted: Camacho [18] shows that the distribution of points approximates a distribution of a decreasing linear function; that of the present study demonstrates that the results are close to a hyperbole whose horizontal and vertical asymptotes are values close to 0.8 MPa/MPa and 5 MPa, respectively; Cross et al. [19] and Mota et al. [20] present only three points in their study and little can be said about the behavior of the points as a function; however, a visual analysis shows that the distribution resembles a descending portion of a parable. Due to the confinement of the mortar by the blocks the expected results are: the stabilization of the resistance value with the thickness increase from a given joint thickness value; and the exponential increase in resistance as thickness is decreased. In the present research, it was possible to confirm the above, since we worked from a very small joint to a high thickness joint, with several repetitions for each joint thickness. Therefore, the influence of the joint thickness relationship on the compressive strength of structural masonry prisms is proved.

Conclusions

Based on the results, it is possible to conclude that:

– The increased thickness of the masonry wall joints reduces the compressive strength of the structural masonry prisms, highlighting the need to control the services performed with this material;

– There is a practically linear relationship between the inverse joint thickness and the compressive strength of the prisms or between the resistance factor of the prisms and the joint thickness itself, as observed with the results obtained in this research and in the research of other authors;
– Increasing the compressive strength of mortars is effective in increasing the compressive strength of structural masonry prisms. Both values have a directly proportional relationship.

References

1. Marvila MT, Azevedo ARG, Alexandre J, Zanelato EB, Azeredo NG, Simonassi NT, Monteiro SN (2019) Correlation between the properties of structural clay blocks obtained by destructive tests and Ultrasonic Pulse Tests. J Build Eng 26:100869
2. Foraboschi P (2019) Masonry does not limit itself to only one structural material: interlocked masonry versus cohesive masonry. J Build Eng 26:100831
3. Santos CFR, Alvarenga RCSS, Ribeiro JCL, Castro LO, Silva RM, Santos AAR, Nalon GH (2017) Numerical and experimental evaluation of masonry prisms by finite element method. IBRACON Struct Mater J 10(2):477–508
4. Martins ROG, Nalon GH, Alvarenga RCSS, Pedroti LC, Ribeiro JCL (2018) Influence of blocks and grout on compressive strength and stiffness of concrete masonry prisms. Constr Build Mater 182:233–241
5. Leite HAL, Júnior ALM, Torres DL (2016) Design of masonry walls in situations of fire: a contribution for a future Brazilian standard. Ambiente Construído, Porto Alegre 16(2):89–107
6. Hamdy GA, El-Hariri MOR, Farag MF (2019) Use of additives in mortar to enhance the compression and bond strength of masonry exposed to different environmental conditions. J Build Eng 25:100765
7. Drougkas A, Verstrynge E, Hayen R, Balen KV (2019) The confinement of mortar in masonry under compression: experimental data and micro-mechanical analysis. Int J Solids Struct 162:105–120
8. Brazilian Association of Technical Standards - ABNT (Associação Brasileira de Normas Técnicas) (2017) NBR 15270-2—ceramic components—clay blocks and bricks for masonry part 2: test methods. ABNT, Rio de Janeiro
9. Brazilian Association of Technical Standards - ABNT (Associação Brasileira de Normas Técnicas) (2005) NBR 15310—ceramic components part 3: Structural and non-structural ceramic blocks—test methods. ABNT, Rio de Janeiro
10. Brazilian Association of Technical Standards - ABNT (Associação Brasileira de Normas Técnicas) (2016) NBR 13279—mortars applied on walls and ceilings—determination of the consistence index. ABNT, Rio de Janeiro
11. Brazilian Association of Technical Standards - ABNT (Associação Brasileira de Normas Técnicas) (2005) NBR 13279—mortars applied on walls and ceilings—determination of the flexural and the compressive strength in the hardened stage. ABNT, Rio de Janeiro
12. Brazilian Association of Technical Standards - ABNT (Associação Brasileira de Normas Técnicas) (2005) NBR 13277—mortars applied on walls and ceilings—determination of the water retentivity. ABNT, Rio de Janeiro
13. Brazilian Association of Technical Standards - ABNT (Associação Brasileira de Normas Técnicas) (1985) NBR 8949—structural masonry walls—single compression test—test method. ABNT, Rio de Janeiro
14. Marvila MT, Alexandre J, Azevedo ARG, Zanelato EB (2019) Evaluation of the use of marble waste in hydrated lime cement mortar based. J Mater Cycles Waste Manage 21:1250–1261

15. Zanelato EB, Alexandre J, Azevedo ARG, Marvila MT (2019) Evaluation of roughcast on the adhesion mechanisms of mortars on ceramic substrates. Mater Struct 52:53
16. Azevedo ARG, Marvila MT, Barroso LS, Zanelato EB, Alexandre J, Xavier GC, Monteiro SN (2019) Effect of granite residue incorporation on the behavior of mortars. Materials 12:1449
17. Marvila MT, Alexandre J, Azevedo ARG, Zanelato EB, Xavier GC, Monteiro SN (2019) Study on the replacement of the hydrated lime by kaolinitic clay in mortars. Adv Appl Ceram 118(7):373–380
18. Camacho JS (1995) Contribution to the study of reduced physical models of ceramic structural masonry. Thesis (Doctorate in Civil Engineering) - São Paulo, Escola Politécnica da Universidade de São Paulo - EPUSP, 157p
19. Cross AN, Mohamd G, Bavastri EYN (2015) Development of a new geometric design for non-modular concrete blocks for structural masonry. Ambiente Construído, Porto Alegre 15(2):127–152
20. Mota JMF, Oliveira RA, Silva AJ, Barbosa FR, Carvalho JR (2012) Influence of laying mortar thickness on the axial compressive strength of ceramic block prisms. In: Proceedings of the 54th Brazilian concrete congress CBC2012, IBRACON, Maceió

Influence of the Reduced Graphene Oxide Incorporation on Properties of Acrylonitrile Butadiene Styrene (ABS)

Bianca S. Santos, Andre L. N. Inácio, Suellen S. Bartolomei, Taise B. S. Silva, Karina L. S. Carmo, Rene R. Oliveira and Esperidiana A. B. Moura

Abstract The purpose of this study was to evaluate the influence of incorporation of the reduced graphene oxide on properties of acrylonitrile butadiene styrene (ABS). The incorporation of 0.5 and 1.5 wt% of RGO into ABS matrix was carried out by melting extrusion process using a twin-screw extruder and injection molding machine. The properties of ABS/RGO nanocomposite samples were investigated by tensile and impact Izod tests, FE-SEM, and XRD analysis. The results showed that the incorporation of small amount of RGO into ABS matrix led to obtaining of polymeric nanocomposite with superior mechanical properties when compared with original properties of ABS matrix.

Keywords RGO · ABS · Mechanical tests · SEM · DRX

Introduction

Graphene is a 2D material and it derivatives such as graphene oxide (GO) and reduced graphene oxide (RGO) has received much attention in recent years as nanofillers to produce polymer nanocomposites due to of their outstanding properties, as ultra-high conductivity, good thermal stability, mechanical and optical properties, excellent structural flexibility, and extremely large ratios [1, 2]. Therefore, graphene is considered a promising material for application in polymer nanocomposites and many other fields, as sensors, transistors, and fields related to energy and also biological applications [3–5]. It is considered to be a potentially superior electronic circuit material compared to other carbon-based nanofillers. Therefore, graphene

B. S. Santos (✉) · A. L. N. Inácio · S. S. Bartolomei · T. B. S. Silva · K. L. S. Carmo · E. A. B. Moura
Center for Chemical and Environmental Technology, Nuclear and Energy Research Institute, 2242 Prof. Lineu Prestes Av., São Paulo 05508-000, Brazil
e-mail: bianca.bibiliki@gmail.com

R. R. Oliveira
Center for Materials Science and Technology, Nuclear and Energy Research Institute, 2242 Prof. Lineu Prestes Av., São Paulo 05508-000, Brazil

J. Li et al. (eds.), *Characterization of Minerals, Metals, and Materials 2020*,
The Minerals, Metals & Materials Series,
https://doi.org/10.1007/978-3-030-36628-5_59

is considered one of the most important conductive fillers for conductive polymer composites. Nanocomposite of graphene-based polymer can be prepared by incorporating graphene in polymer materials. However, there is a low solubility in polar and non-polar solvents and homogeneous dispersion in the polymer matrix exfoliation limited to preparation and applications of nanocomposites based on graphene. Graphene tends to form irreversible agglomerates into the polymer matrices resulting from Vander Waals attractive forces [6–8].

These nanocomposites agglomerations can prevent the charge transfer to the matrix and produce points of stress concentration. Therefore, it is essential to improve compatibility between the matrix polymer and graphene with the modification of the graphene surface. Due to their abundant oxygen, such groups as hydroxyl, epoxy, carbonyl, and carboxyl, graphene oxide (GO) can be easily swollen and dispersed even in water, which has been applied in many polar polymers, such as poly (methyl) and methacrylate, (PMMA). For higher electrical conductivity and thermal stability, GO can be reduced, improving the dispersion of graphene in the material and the interface between graphene and the polymeric matrix [8].

Acrylonitrile butadiene styrene (ABS) copolymer is one of the engineering thermoplastics most widely used in the world in many electronics components, as televisions and monitors and also in automotive field, because it has an excellent abrasion resistance, good chemical resistance, and excellent surface appearance. However, ABS has very low conductivity for application in electronic devices, and modifications should be made to improve the electrical conductive. In addition of conducting fillers as carbon black, carbon nanotubes, graphene, and graphene oxide can be used in order to form an electrical conducting composite. Carbon black, graphene, and its derivatives have been widely studied to increase the conducting performance of the ABS composites [9–12].

The purpose of this study was to evaluate the influence of reduced graphene oxide's incorporation on properties of acrylonitrile butadiene styrene (ABS).

Materials and Methods

Materials

For the preparation of nanocomposite by acrylonitrile butadiene styrene (ABS) with reduced graphene oxide, following materials were used: The acrylonitrilebutadiene styrene (ABS) was produced by BASF, the graphite flakes used in this experiment is from Química Ltda (Sao Paulo, Brazil), and the reagents for preparing nanocomposites are: Sulfuric acid (H_2SO_4, 98%); Potassium permanganate ($KMnO_4$, 99.9%); Hydrogen chloride (HCl, 37%); Hydrogen peroxide (H_2O_2, 30%); Dimethylformamide (DMF); Ethyl alcohol (Ethanol—C_2H_6O—99.5% Synth).

Preparation of GO

Graphene oxide (GO) was produced following a modified Hummers method [5]. First, graphite homogenized (5 g) and potassium permanganate (15 g) were added with concentrated sulfuric acid (100%—98 ml) on an ice bath. The mixture was mechanically mixed for 30 min then 400 ml of distillated water was added, after that a solution was placed at 90 °C and maintained at that temperature for 60 min. Second, a hydrogen peroxide solution (30 ml) and distilled water (70 ml) (30/70%) was added and placed in a mechanical blender for 4 h. The resulting solution was washed with hydrochloric acid and distilled water then it was washed with a mix of 200 ml of water and 200 ml of alcohol, repeatedly, until the pH around 6.0. Then the solid was dispersed in dimethylformamide (DMF) (30 ml) with distilled water (70 ml) and sonicated using a high-intensity ultrasonic device (20 kHz and 450 W/cm^2) for 2 h.

Reduction of GO

GO solution was washed several times with distilled water to remove DMF and subsequently GO was added to a mixture of distilled water and ethanol (50 ml/50 ml). The mixture has been brought to a high-intensity ultrasonic device for 15 min and irradiated with gamma radiation (60 °C) at a radiation dose of 100 kGy (RGO100) using a multipurpose gamma irradiator located on Radiation Technology Center CTR-IPEN/CNEN-SP, radiation dose of 6 kGy/h. After irradiation, the aqueous solution containing RGO was frozen for 24 h and freeze-dried for 24 h to obtain the powder. Schematic illustration of preparation procedure of the GO and RGO is shown in Fig. 1.

Composite Preparation

The composites material based on ABS and graphene according to Table 1, were prepared by melt extrusion using a twin-screw extruder Haake Rheomix with 16 mm and $L/D = 25$ rate from Thermo Scientific. The temperature profile was 210–215 °C. The extrudate materials were cooled down in water at room temperature for a better dimensional stability, pelletized were dried again and fed into injection moulding at 195–225 °C temperature profile and specimens test samples were obtained. The compositions of nanocomposite are presented in Table 1.

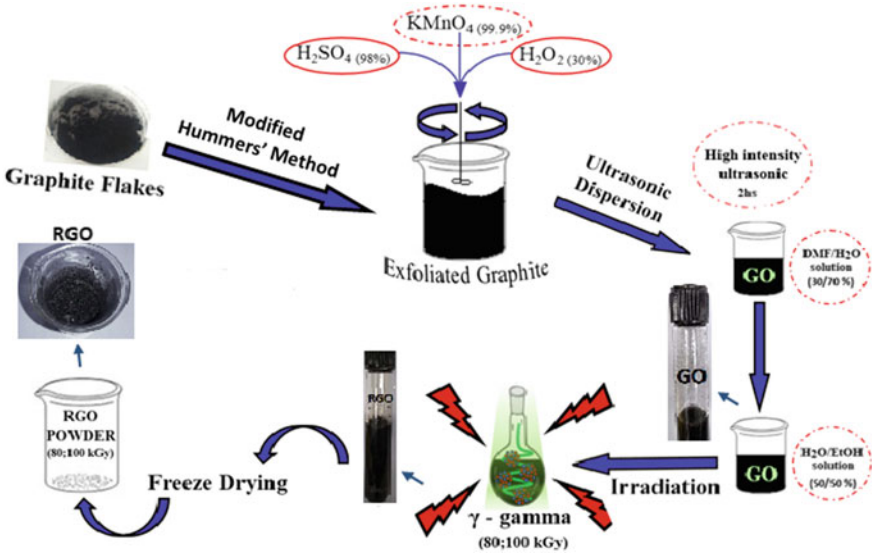

Fig. 1 Schematic illustration of preparation procedure of the GO and RGO

Table 1 Components percentage in the formulations

Materials	ABS (wt%)	RGO (wt%)
Neat ABS	100	–
ABS/RGO	99.5	0.5
ABS/RGO	98.5	1.5

Characterization

X-Ray Diffraction (XRD)

The XRD analysis of the ABS and its composites materials were carried out using a Philips XPERT-MPD diffractometer with CuKα radiation ($\lambda = 1.54$ nm) operated at 40 kV, 40 mA, with 2θ varying between 2° and 90°.

Raman Spectroscopy

The Raman spectra of RGO nanosheets were obtained using a Raman spectrometer HORIBA Jobin Yvon, France, with a confocal microscope equipped with a solid-state laser crystal ($\lambda = 532$ nm) as the excitation source. The spectra obtained were adjusted by the image acquisition software (LabSpec 5.1; Horiba Jobin Yvon) supplied with the instrument.

Field Emission Scanning Electron Microscopy (FE-SEM)

FE-SEM of RGO nanosheets and its nanocomposites materials with ABS were carried out using a JEOL-JSM-7401 F, microscope with an accelerating voltage of 1–30 kV, using EDS Thermo-Scientific mod. Noran System Six software, in cryofractured samples under liquid nitrogen and covered with gold.

Mechanical Tests

The tensile tests were carried out for all samples using an INSTRON Universal Testing Machine, model 5564, according to ASTM D 638, at room temperature and loading rates of 50 mm/min.

Results and Discussion

XRD Analysis Results

Figure 2 shows the XRD patterns of the RGO, neat ABS, and its nanocomposites.

As can be seen in Fig. 2 the RGO XRD patterns show a sharp reflection peak at $2\theta = 12.6°$ (d001) characteristic of GO nanosheets, and a large peak at $2\theta = 26.6°$ (d-spacing 3.35 Å) characteristic of graphite, which can suggest that graphite was partially converted into reduced graphene oxide. Regarding the XRD patterns of the ABS with 0.5 wt% of RGO addition, the characteristic peak of RGO was

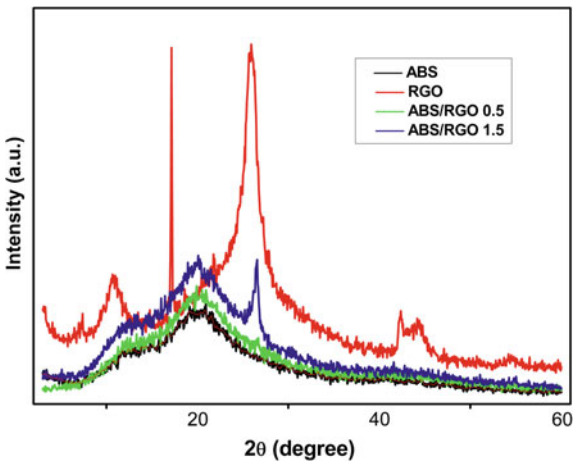

Fig. 2 XRD patterns of the RGO, neat ABS and its nanocomposites

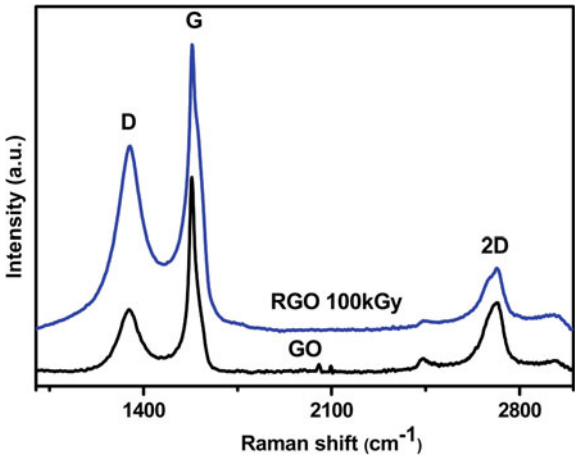

Fig. 3 Raman spectra of GO and RGO 100 kGy

not observed, suggesting that GO nanosheets have been intercalated between ABS molecular chains. On the other hand, for ABS with 1.5 wt% of RGO addition, it can be seen the characteristic graphite peak, but with reduced intensity, suggesting that part of RGO nanosheets remained non-dispersed into ABS matrix.

Raman Spectroscopy Analysis Results

Raman spectroscopy is an important technique to characterize the electronic and structural properties of RGO nanosheets including your disorders, defects, and doping levels. The Raman spectra of RGO are presented in Fig. 3.

The Raman spectra of RGO reveals a prominent peak in the *G* band, at 1581 cm^{-1}. The G band is broadened and reveals a peak at 1581 cm^{-1} due to the oxygenation of the graphite planes, suggesting the formation of new sp^3 carbon atoms. The *D* band at 1347 cm^{-1} is also broadened and with a low intensity which is due to the reduction in size of in-plane sp2 domains of graphite induced by the creation of defects, vacancies, and distortions of the sp2 domains after oxidation. The intensity ratios D/G band of Raman provides information about the structure of graphene. The intensity radio ID/IG represents defects (edges, vacancies, etc.).

FE-SEM Analysis Results

Figure 4 shows FE-SEM micrographs of cryofractured surfaces of the neat ABS (Fig. 4a), ABS with 0.5 wt% of RGO (Fig. 4b), and ABS with 1.5 wt% of RGO (Fig. 4c) with 30.000 X magnification.

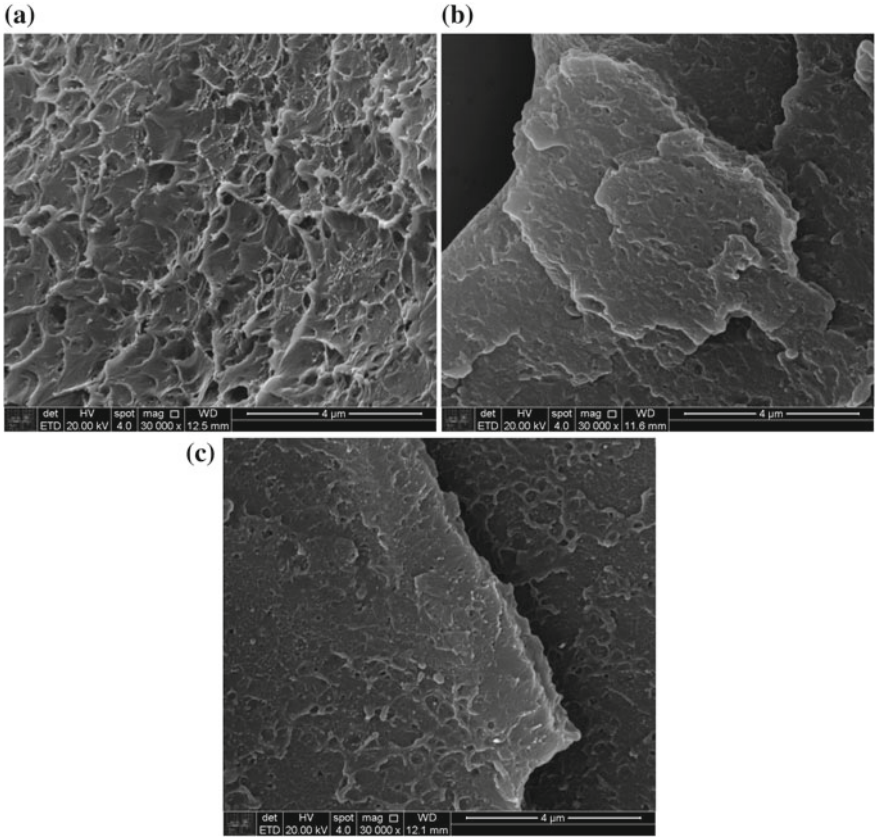

Fig. 4 FE-SEM micrographs surfaces of neat ABS (**a**) and ABS/0.5% RGO (**b**) and ABS/1.5%RGO (**c**) with 30.000 X of magnifications, respectively

As can be seen from Fig. 4a, pure ABS shows the presence of two phases. The first of them in light color and elliptical shape refers to butadiene, the second continuous phase and without visible separations refer to the other monomers: acrylonitrile and styrene. The image of cryofractured surfaces of ABS/RGO (0.5 wt%) presented a homogeneously dispersion of GO without any aggregation in the surface of ABS matrix (Fig. 4b). However, when 1.5 wt% of GO are addition in ABS matrix it can be seen some small GO aggregated on the surface of ABS, which are related with the non-homogeneous distribution of GO in the matrix. These results were late confirmed by X-ray diffraction (XRD) pattern of the ABS with 0.5 and 1.5 wt% of RGO.

Table 2 Izod impact test results of neat ABS and its nanocomposites

	neat ABS	ABS/RGO 0.5	ABS/RGO 1.5
Izod impact strength (J/M)	28.82	24.18	31.76

Mechanical Analysis Results

Table 2 presents the Izod impact test results of neat ABS and its nanocomposites. The results presented in the table below shows the average values calculated from the data obtained in tests for five test specimens. From the table, it is possible to observe that the addition of RGO nanosheets into neat ABS leads to a decreasing in impact strength. However, there was an increase in impact strength when 1.5% RGO was added in ABS.

Conclusions

This work investigated the effects of incorporating a small amount of graphene oxide into ABS. The results showed that the incorporation of RGO nanoparticles in the ABS matrix led to a higher impact resistance when compared to pure ABS, only 0.5% ABS is well dispersed and a loss for this composition occurred. The 1.5% ABS has some small RGO clusters and the DRX also showed a peak of the RGO, indicating that it is not well dispersed in the ABS matrix.

Acknowledgements The authors wish to thank IIAEA-CRP # 17760 RO, FAPESP, and CNPq to provide support for this work.

References

1. Bollella P, Fusco G, Tortolini C et al (2017) Beyond graphene: electrochemical sensors and biosensors for biomarkers detection. Biosens Bioelectron 89:152–166. https://doi.org/10.1016/j.bios.2016.03.068
2. He K, Zeng Z, Chen A et al (2018) Advancement of Ag–graphene based nanocomposites: an overview of synthesis and its applications. Small 14:1800871. https://doi.org/10.1002/smll.201800871
3. de Luna LAV, de Moraes ACM, Consonni SR et al (2016) Comparative in vitro toxicity of a graphene oxide-silver nanocomposite and the pristine counterparts toward macrophages. J Nanobiotechnol 14:12. https://doi.org/10.1186/s12951-016-0165-1
4. Kim H, Abdala A, Macosko C (2010) Graphene/polymer nanocomposites. Macromolecules. https://doi.org/10.1021/ma100572e
5. Preparation of graphitic oxide. https://pubs.acs.org/doi/pdf/10.1021/ja01539a017. Accessed 29 Aug 2019

6. Bindumadhavan K, Srivastava S, Srivastava I (2013) Green synthesis of graphene. J Nanosci Nanotechnol 13:4320–4324. https://doi.org/10.1166/jnn.2013.7461
7. Kruk T, Socha RP, Szyk-Warszyńska L, Warszyński P (2019) Flexible and ultrathin polyelectrolyte conductive coatings formed with reduced graphene oxide as a base for advanced new materials. Appl Surf Sci 484:501–510. https://doi.org/10.1016/j.apsusc.2019.04.051
8. Yang X, Wang X, Yang J et al (2013) Functionalization of graphene using trimethoxysilanes and its reinforcement on polypropylene nanocomposites. Chem Phys Lett 570:125–131. https://doi.org/10.1016/j.cplett.2013.03.069
9. Wang F, Zhang Y, Zhang BB et al (2015) Enhanced electrical conductivity and mechanical properties of ABS/EPDM composites filled with graphene. Compos Part B Eng 83:66–74. https://doi.org/10.1016/j.compositesb.2015.08.049
10. Gao A, Zhao F, Wang F et al (2019) Highly conductive and light-weight acrylonitrile-butadiene-styrene copolymer/reduced graphene nanocomposites with segregated conductive structure. Compos Part Appl Sci Manuf 122:1–7. https://doi.org/10.1016/j.compositesa.2019.04.019
11. An J, Kim C, Choi B, Lee J (2014) Characterization of acrylonitrile–butadiene–styrene (ABS) copolymer blends with foreign polymers using fracture mechanism maps. Polym Eng Sci 2791–2798
12. Ford P, Fisher J (2019) Designing consumer electronic products for the circular economy using recycled Acrylonitrile Butadiene Styrene (ABS): a case study. J Cleaner Prod 236

Inhibition of Flame Propagation in Nanocomposites with Expanded Polystyrene Recycled Clay, Gypsum, and Titanium Dioxide

S. S. Bartolomei, E. A. B. Moura and H. Wiebeck

Abstract The large amount of plastic waste found in the environment, landfills, and dumps boost research into the recycling of polymer materials, which could reduce the amount of polymer discarded. In Brazil, the sector that most consumes polymers is the civil construction that could consume recycled polymers without concerns with the properties due to applications of low mechanical exigency. However, for applications in this sector, it is necessary that the materials have some resistance to the propagation of flames. This work discusses the flame retardance in nanocomposites with recycled polystyrene matrix and particles of nanoargila, titanium dioxide, and gypsum. The results of the X-ray diffraction (XRD), differential scanning calorimeter (DSC), field emission scanning electron microscopy (FE-SEM), and flammability test. The results showed that glycerol, added during recycling, can plasticize recycled expanded polystyrene while maintaining the flame resistance properties of the material with flame retardant. It can also be concluded that some particles may delay the propagation of the flame in the composite.

Keywords Clay · Titanium dioxide · Gypsum · Expanded polystyrene · Flame retardance

S. S. Bartolomei (✉)
José Crespo Gonzales Faculty of Technology (Fatec Sorocaba), Av. Engenheiro Carlos Reinaldo Mendes 2015, Sorocaba, SP 18013-280, Brazil
e-mail: suellen.signer@gmail.com

E. A. B. Moura
Center of Chemical and Environmental Technology, Nuclear and Energy Research Institute (IPEN), Av. Prof. Lineu Prestes 2242, Sao Paulo, SP 05508-000, Brazil

H. Wiebeck
Polytechnic School of USP, Metallurgical and Materials Engineering Department, University of Sao Paulo (USP), Av. Prof. Mello Moraes 5643, Sao Paulo, SP 05508-010, Brazil

J. Li et al. (eds.), *Characterization of Minerals, Metals, and Materials 2020*,
The Minerals, Metals & Materials Series,
https://doi.org/10.1007/978-3-030-36628-5_60

Introduction

Polymeric materials are present in various industrial sectors and in different applications, but in Brazil, the main consumer of polymers is the construction sector. In order for a material to be used in construction, fire safety standards must be met. However, the most consumed material in this sector, polystyrene (PS), is highly flammable, releases large amounts of heat and toxic smoke when exposed to a flame, limiting its applications [1–4].

To reduce flame propagation in PS, halogenated compounds are used effectively, especially in synergy with antimony oxide, but these additives generate toxic fumes and intense smoke during combustion. These factors then influenced the emergence of halogen-free flame retardants that were effective for PS, with phosphorus-containing retardants and intumescent flame retardant systems emerging, but these systems reduce the thermal stability and mechanical properties of PS. This justifies the development of less environmentally aggressive retardants that meet the requirements [5–11].

Polymeric nanocomposites, formed by inorganic nanoparticles, have many advantages in flame retardation, such as low heat release rate, low smoke, and toxic gas production. Montmorillonite clay (MMT) is often used in PS nanocomposites due to reduction in the maximum heat release rate. But for the clay can be homogeneously distributed in the polymer matrix, it is necessary to organophilization, turning the hydrophilic MMT in organoclay MMT. For this, cation exchange is performed replacing the cations present with Na^+ ions, allowing the swelling of MMT to occur in water, which facilitates the bonding of surfactant, usually quaternary ammonium salt, on the surfaces of the MMT layers, increasing the spacing between the layers, or basal spacing, facilitating the exfoliation of clay in the polymer matrix. However, for the clay to achieve the results required by the standards, it is necessary to add a large amount of particles, which generate agglomerates in the material and losses in the mechanical properties. Therefore, the use of clays to provide flame spread resistance to the material must be accompanied by the use of other flame retardants. Thus, the clay will provide the reduction inflammability, and the secondary flame retardant will provide the ignition resistance [5–12].

Metal oxides have been employed in polymeric materials to improve the performance of flame retardants. Results show that the addition of TiO_2 extends ignition time by reducing combustion speed, inhibits dripping, and reduces smoke production, while also improving mechanical properties, thermal stability, and electrical properties of polymers [11, 13–15]. The authors Wu, Y. et al., added TiO_2 nanotubes modified with phenoldichlorophosphate (PDCP) in polystyrene matrix. The addition of 7 wt% of TiO_2 modified resulted in a reduction in the maximum heat release rate and an increase in thermal stability, probably due to the inhibition of some stages of PS thermal degradation [16]. In addition, TiO_2, in the presence of nitrogen (N) containing compounds, such as the quaternary ammonium salt used for organofilization of clays, can accelerate the release of NH_3 and H_2O during decomposition, further reducing the combustion speed [15].

This paper presents a study of the influence of white clay Cubati-PB, TiO_2, and gypsum addition on flame propagation and thermal stability of recycled polystyrene (REPS) using solvent from expanded polystyrene (EPS). Glycerol (2 wt%) was added as plasticizers during recycling of the EPS. The samples were characterized by DRX, TG analyses, FEG-SEM images, and flammability tests.

Experimental

Materials

Materials used in this study include recycled expanded polystyrene (REPS) with flame retardant, recycled post-consumption gypsum, organophilized white clay from Cubati-PB, titanium dioxide (Degussa AG, Dusseldorf, Germany), and glycerol (Synth) were used for composite preparation.

Clay Organofilization

White clay from Cubati-PB was modified with sodium carbonate (Na_2CO_3), then quaternary ammonium salt was added into the resulting product and mixed. The dispersed organophilized clay mixture was filtered and washed with deionized water, thus obtaining the organophilized white clay in a paste.

Composites Preparation

Firstly, the organophilized clay paste was dispersed in ethyl acetate. Then, 1000 ml of solvent for each 500 g of polymer was added to EPS. Then, 2% glycerol was added, and the mixture was stirred for 2 h at room temperature. Finally, the mixture was allowed to stand for solvent evaporation. Recycled gypsum was obtained from post-consumption gypsum by milled and heating in an oven at 100 °C for 2 h. Titanium dioxide (TiO_2) was oven dried at 60 °C for 24 h to remove moisture. Four composites were prepared, containing 5% plaster, 5% clay, 5% plaster and 5% clay, 2.5% clay and 2.5% TiO_2. The mixture of REPS with glycerol and REPS without glycerol was also used to compare the results. These materials were prepared by melt extrusion using a twin-screw extruder HAAKE Rheomex P332, with thread diameter of 16 mm and $L/D = 25$ rate from Thermo Scientific. The temperature profile used during processing was 115/120/130/135/135/135 °C, and the screws' rotation was 15 RPM. The extrudates coming out of the extruder were cooled in air

Table 1 Composition and nomenclature of samples

Name	White clay	Gypsum	TiO_2	Glycerol
REPS	–	–	–	–
REPS-G	–	–	–	2.0%
REPS-G-C	5.0%	–	–	2.0%
REPS-G-G	–	5.0%	–	2.0%
REPS-G-CG	5.0%	5.0%	–	2.0%
REPS-G-CT	2.5%	–	2.5%	2.0%

and pelletized by a pelletizer. At last, specimens were molded by pressing. Thus, the samples were obtained and named as shown in Table 1.

Characterization Methods

DSC analysis for each sample was performed using DSC Q20 from TA Instruments. Firstly, the thermal history of each sample was eliminated by heating the samples from 25 to 300 °C at a scanning rate of 10 °C/min. Subsequently, the samples were cooled down to room temperature at a rate of 10 °C/min. Finally, DSC curves were obtained by heating the samples from 25 to 300 °C at a rate of 10 °C/min.

X-ray diffraction (XRD) patterns for the samples were recorded on a Philips XPERT-MPD diffractometer with CuKα radiation ($\lambda = 1.54$ nm) operated at 40 kV and 40 mA, with 2θ varying between 10° and 60°.

The specimens were fractured at cryogenic temperature; the fracture region was covered with gold and observed in a scanning electron microscope (Phillips XL-30 FEG-SEM).

The flammability tests of composites were performed in accordance with ASTM D635.

Results and Discussion

DSC

Figure 1 shows DSC thermograms for all compositions. The glass transition temperature (Tg) shown in Table 2 indicates 1° reduction in Tg when glycerol was added in REPS. This reduction indicates that the polymer may be toughened by the lubricant. For PS, toughening would be beneficial as this polymer is fragile and has low impact resistance, but to confirm toughening, mechanical tests would need to be performed [17, 18]. However, when clay, plaster, and TiO_2 particles were added to

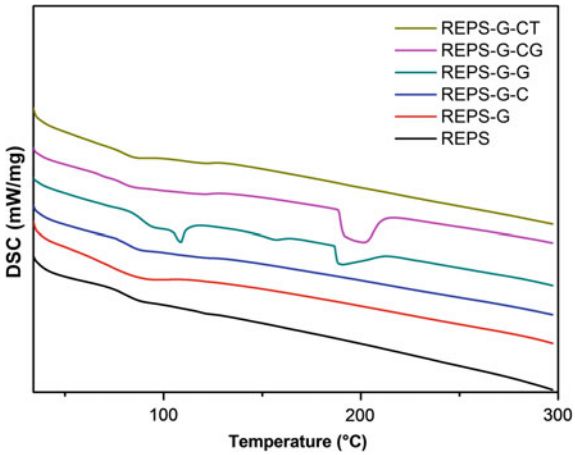

Fig. 1 DSC melting curves

Table 2 Glass transition temperature (Tg)

Sample	REPS	REPS-G	REPS-G-C	REPS-G-G	REPS-G-CG	REPS-G-CT
Tg (°C)	80.5	79.5	82.5	89.5	79	79

the polymer, Tg increased again. The largest increase, approximately 10%, was for samples containing 5% gypsum (REPS-G-G), expected result due to high particle fragility [19–21]. When clay, along with gypsum and TiO_2 (REPS-G-CG and REPS-G-CT), was added to the polymer, Tg returned to the levels of recycled material with glycerol, which may be an indication that clay particles improved tenacification of the material together with glycerol. However, the addition of only clay (REPS-G-C) also increased the Tg of the material, indicating that the clay improved the thermal stability of the polymer, which corroborates the literature data [14, 22, 23].

XRD

XRD spectrum presented in Fig. 2 shows characteristic peaks of the studied particles and the nanocomposities. For white clay, these peaks correspond to those found for montmorillonite clay (12, 20, 25, and 26.5°) [9, 24, 25]. The TiO_2 sample presented 2θ degree around of 25.3, 37.8, 48, 27.4, and 36° [24]. Recycled gypsum shows characteristic peaks of bassanite (β-$CaSO_4$0, $5H_2O$) and anhydrite ($CaSO_4$). The absence of hydrated calcium sulphate ($CaSO_4$ $2H_2O$) characteristic peak of high intensity, $2\theta = 12°$, indicates that the recycling process was effective in removing moisture present in the material [19, 20].

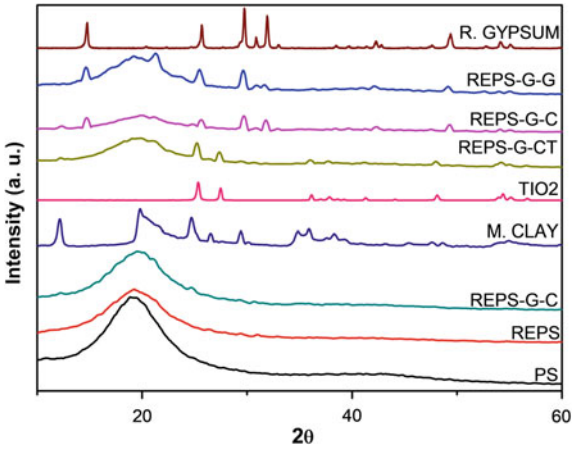

Fig. 2 XRD spectrum

By observing nanocomposites XRD patterns, it is possible to conclude that the peaks present are characteristic of the polymeric matrix and of the particles added with less intensity.

FEG-SEM

Figure 3 shows SEM micrographs of (a) REPS-G-G, (b) REPS-G-C, (c) REPS-G-CG, and (d) REPS-G-CT taken at with 2500 × magnifications. These images show an overview of the polymer composite and cryogenic fracture. The images show that samples containing gypsum have rounded pores from the pullout of these particles during the fracture, which represents a poor interfacial adhesion between the gypsum and the polymeric matrix.

Particulars of the particles and polymer matrix can be seen in Fig. 4, where the images (a) REPS-G-G, (b) REPS-G-C, and (c) REPS-G-CG have 25,000 × magnifications, and the image (d) REPS-G-CT has 50,000 × magnifications; this image required a larger magnification for the TiO_2 particles to be visualized. In image 4 (a), the circles highlight clays embedded in the polymer matrix. In image 4b, the circles show voids generated by the low adhesion of the plaster to the polymers, the same can be seen in image 4c, in the area highlighted by the squares, in addition to the clay particles within the circles. In image 4d, it is possible to visualize the interface of the clay with the polymer, the empty space between them shows that there was no good adhesion of the particle in the polymeric matrix, in this same image, but in the checkered area, a TiO_2 particle cluster is visualized. In the images of Fig. 4, it is also possible to visualize a spherical roughness along the entire polymeric matrix; these spheres may come from the blowing agent present in the recycled EPS, which upon reaching the expansion temperature generated these small droplets in the matrix.

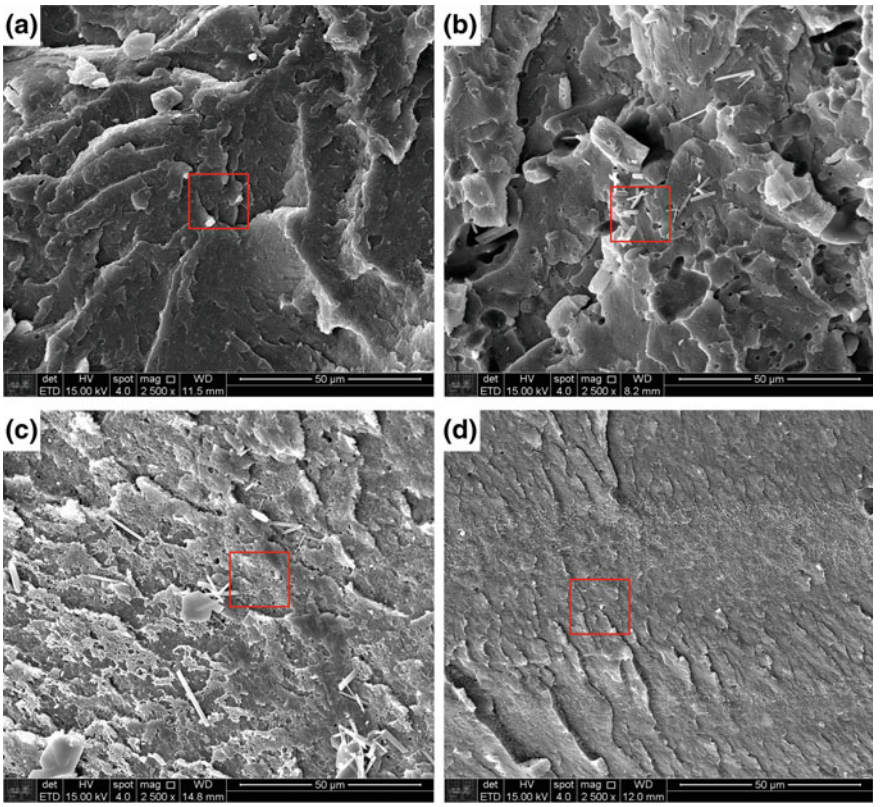

Fig. 3 SEM micrographs: **a** REPS-G-G, **b** REPS-G-C, **c** REPS-G-CG, and **d** REPS-G-CT

Flammability Test

The flammability test was performed by exposing the samples to a flame for 30 s. Then, the flame propagation time was timed until the flame was extinguished or until it reached 240 s. Table 3 shows the ignition time in seconds, the burnt length during the test in millimeters, and the flame propagation velocity in mm/min. REPS and REPS-G samples self-extinguished within 2 and 9 s, respectively, when the induced flame was extinguished. The flame specimen was 100 mm long, and for the REPS-G-G sample, this length was completely consumed after 240 s. In REPS-GC, REPS-G-CG, and REPS-G-CT samples, flame propagation was slower, the material was not fully consumed during the test time, and the lowest flame propagation velocity was presented in sample REPS-G-CG. Thus, it can be concluded that the presence of clay together with plaster in the polymeric matrix improved flame retardant effect.

According to Standard D635, a material can be classified as *HB* if the burn rate does not exceed 40 mm/min over a range of 75 mm for samples with thickness from 3.0 to 13 mm, or not burning greater than 75 mm/min over a 75 mm interval

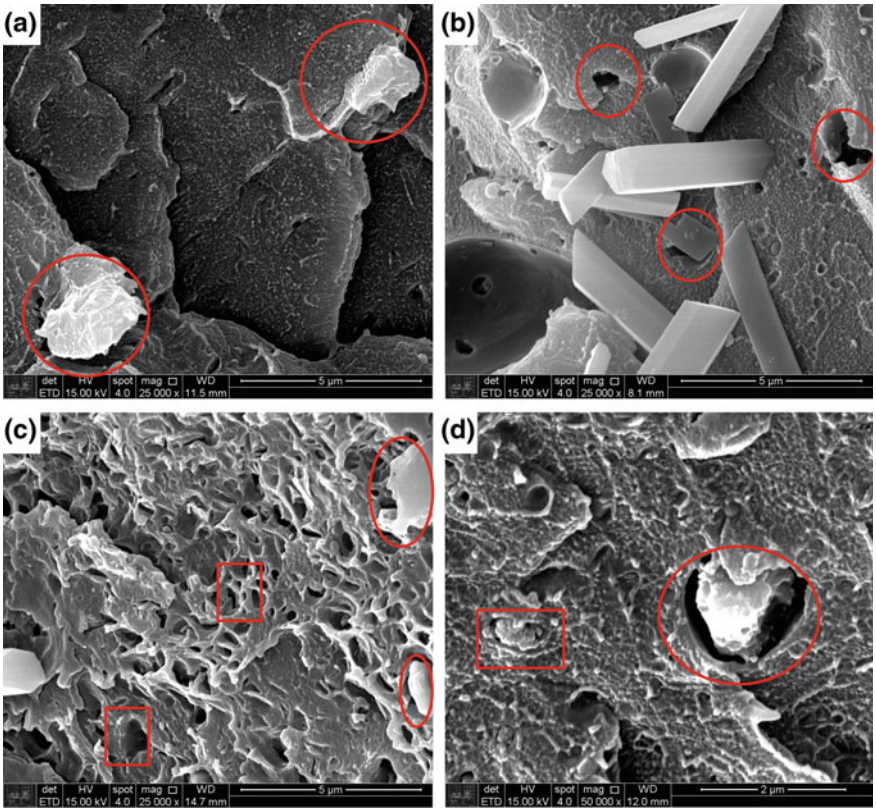

Fig. 4 FEG-SEM micrographs: **a** REPS-G-10 and **b** REPS-G-15

Table 3 Time of ignition, length burning, and burn rate

Sample	REPS	REPS-G	REPS-G-G	REPS-G-C	REPS-G-CG	REPS-G-CT
Essay time (s)	32	39	240	240	240	240
Length burning (mm)	19	23	100	66	24	68
Burn rate (mm/min)	Extinction of flame in 2 s	Extinction of flame in 9 s	25	16.5	6.2	17.2

for samples less than 3.0 mm thickness, or if the material stops burning before the 100 mm reference mark. In this study, samples with 3 mm thickness, 20 mm width, and 100 mm length were used. Therefore, it can be concluded that REPS and REPS-G samples can be classified as HB, whereas REPS-G-G samples cannot be classified as HB because the flames consumed all material, with 100 mm length. However,

the REPS-GC, REPS-G-CG, and REPS-G-CT samples had a burn rate of less than 40 mm/min, but the assay was not performed until the burnt length reached 100 mm, so it cannot classify these samples in accordance with D635. Even though, it was recorded that the REPS-G-CG sample presented the lowest burning rate among the samples that did not auto extinguish the flame.

Conclusions

This study showed that EPS with flame retardant can be recycled without losing the low flame propagation properties, while maintaining flame self-extinguishing, even in the presence of a plasticizer, such as glycerol. However, when clay, plaster, and TiO_2 particles were added to the polymer, the material no longer extinguished the flame. Among the composites studied, the smallest flame propagation velocity was found for the REPS-G-CG sample; yet during the 240 s of flame propagation test, it did not self-extinguish the flame.

References

1. Abiplast - Associação Brasileira da Indústria. Indústria Brasileira de Transformação e Reciclagem de Material. (2018) In: Perfil 2018. Brazilian plastic processed and recycling industry. http://www.abiplast.org.br/wp-content/uploads/2019/08/perfil-2018-web.pdf. Accessed 16 Aug 2019
2. ABNT - Associação Brasileira De Normas Técnicas (1986) NBR9442 - Materiais de construção - determinação do índice de propagação superficial de chama pelo método do painel radiante. Rio de Janeiro
3. Secretaria Do Estado Dos Negócios Da Segurança Pública (2011) Polícia Militar. Instrução Técnica n° 08 - Resistência ao fogo dos elementos de construção. Corpo de Bombeiros, pp 191–202
4. Secretaria Do Estado Dos Negócios Da Segurança Pública (2011) Polícia Militar. Instrução Técnica n° 10 - Controle de materiais de acabamento e de revestimento. Corpo de Bombeiros, pp 217–226
5. Kiliaris P, Papaspyrides CD (2010) Polymer/layered silicate (clay) nanocomposites: an overview of flame retardancy. Prog Polym Sci 35(7):902–958
6. Laoutid F et al (2009) New prospects in flame retardant polymer materials: from fundamentals to nanocomposites. Mater Sci Eng 63(3):100–125
7. Leszczyńska A et al (2006) Polymer/montmorillonite nanocomposites with improved thermal properties. Thermochim Acta 453(2):75–96
8. Morgan AB (2003) Flame retarded polymer layered silicate nanocomposites: a review of commercial and open literature systems. Polym Advan Technol 17(4):206–217
9. Morgan AB et al (2003) Flammability of polystyrene layered silicate (clay) nanocomposites: carbonaceous char formation. Fire Mater 26(6):247–253
10. Ning W, Jiugao Y, Xiaofei M (2008) Review new developments in flame retardancy of styrene thermoplastics and foams. Polym Int 57:431–448

11. Xing W et al (2016) Enhanced thermal stability and flame retardancy of polystyrene by incorporating titanium dioxide nanotubes via radical adsorption effect. Compos Sci Technol 133:15–22
12. Paiva LB, De Morales AR, Díaz FRV (2008) Argilas organofílicas: características, metodologias de preparação, compostos de intercalação e técnicas de caracterização. Cerâmica 54:213–226
13. Chen T et al (2019) Fire, thermal and mechanical properties of TPE composites with systems containing piperazine pyrophosphate (PAPP), melamine phosphate (MPP) and titanium dioxide (TiO_2). Plast Rubber Compos 48(4):149–159
14. Rahmani H et al (2011) Synergistic effects of titanium dioxide with layered double hydroxides in EVA/LDH composites. Polym Eng Sci 2166–2170. https://doi.org/10.1002/pen
15. Pang XY, Chang R, Weng MQ (2018) Halogen-free flame retarded rigid polyurethane foam: the influence of titanium dioxide modified expandable graphite and ammonium polyphosphate on flame retardancy and thermal stability. Polym Eng Sci 58(11):2008–2018
16. Wu Y, Song L, Hu Y (2012) Thermal properties and combustion behaviors of polystyrene/surface-modified TiO_2 nanotubes nanocomposites. Polym-Plast Technol 51(6):647–653
17. Sjoerdsma SD (1986) The effect of glycerol on the crazing behaviour of polystyrene in relation to the craze boundary temperature. Polymer 27(2):164–168
18. Ani KEA, Ramadhan AE (2015) Kinetic study of the effect of plasticization on photodegradation of polystyrene solid films. Mater Sci Appl 6:617–633
19. Bartolomei SS, Moura EAB, Wiebeck H (2018) Addition of glycerol and plaster particles for toughening recycled polystyrene. Paper presented at the 8th Isnapol, Águas de São Pedro, São Paulo, 27–30 May 2018
20. Machado MDS (2016) Nanocompósito de poliestireno reciclado, bentonita sódica e hemi-hidrato de sulfato de cálcio: Obtenção e Caracterização. Ph.D. thesis, University of São Paulo
21. Šeputytė-Jucikė J et al (2014) Impact of granules from crushed expanded polystyrene package on properties of thermo—insulating plaster. J Civ Eng Manag 20(4):581–589
22. Li T et al (2016) Polyaniline/montmorillonite nanocomposites as an effective flame retardant and smoke suppressant for polystyrene. Synth Met 221:28–38
23. Zhu J, Wilkie CA (2000) Thermal and fire studies on polystyrene-clay nanocomposites. Polym Int 49(10):1158–1163
24. Kango S et al (2013) Surface modification of inorganic nanoparticles for development of organic-inorganic nanocomposites—a review. Prog Pol Sci 38(8):1232–1261
25. Li H et al (2018) 3D flowerlike TiO_2/GO and TiO_2/MoS_2 heterostructures with enhanced photoelectrochemical water splitting. J Mater Sci 53:7609–7620
26. Bartolomei SS et al. (2018) Investigation of the effect of titanium dioxide and clay grafted with glycidyl methacrylate by gamma radiation on the properties of EVA flexible films. Radiat Phys Chem Apr 1–9

Investigating the Effect of Sintering Temperature on Structural and Tribological Properties of a Nanostructured Ti–20Nb–13Zr Alloy for Biomedical Applications

Mamoun Fellah, Naouel Hezil, Karima Abderrahim, Mohammed Abdul Samad, Alex Montagne, Alberto Mejias, Alain Iost, Stephania Kossman, Timofey Chekalkin, Aleksei Obrosov and Sabine Weiss

Abstract β-type Ti–20Nb–13Zr alloys with low Young's modulus were prepared at different sintering temperatures (950, 1050, 1150, and 1250 °C). The morphological and structural characteristics of as-prepared samples were investigated by several methods. Wear tests were conducted using a ball-on-plate type oscillating tribometer under different applied loads (2, 10, and 20 N). The morphological characterization indicated that the mean pore and crystallite size continuously decreased with increasing sintering temperature to reach lowest values of 40 nm and 38 nm at 1250 °C, respectively. The relative density of the 1250 °C sintered sample was as

M. Fellah (✉)
Mechanical Engineering Department, ABBES Laghrour University, P.O 1252, 40004 Khenchela, Algeria
e-mail: mamoun.fellah@yahoo.fr

Tribology and Materials Group, Laboratory of Foundry, BADJI Mokhtar University BO, 12 CP 23000 Annaba, Algeria

N. Hezil
Mater Sciences Department, ABBES Laghrour—University, P.O 1252, 40004 Khenchela, Algeria

K. Abderrahim
Surface Engineering Laboratory (L.I.S), Badji Mokhtar University, B.P. 12, 23000 Annaba, Algeria

M. Abdul Samad
Mechanical Engineering Department, KFUPM, Dhahran 31261, Kingdom of Saudi Arabia

A. Montagne · A. Mejias · A. Iost · S. Kossman
Laboratory of Mechanics Surfaces and Materials Processing, ARTS ET METIERS ParisTech, 8, Boulevard Louis XIV, 59046 Lille Cedex, France

T. Chekalkin
Research Institute of Medical Materials, Tomsk State University, 634050 Tomsk, Russia

A. Obrosov · S. Weiss
Department of Physical Metallurgy and Materials Technology, Brandenburg Technical University, 03046 Cottbus, Germany

J. Li et al. (eds.), *Characterization of Minerals, Metals, and Materials 2020*,
The Minerals, Metals & Materials Series,
https://doi.org/10.1007/978-3-030-36628-5_61

high as 98.7%. Moreover, the higher sintering temperature resulted in higher relative density and closed porosity of the sample. Both the friction coefficient and wear rate were lower in the sample sintered at 1250 °C as compared to other samples. This enhancement in tribological properties was attributed to a closed porosity.

Keywords Ti-20Nb-13Zr · Nanobiomaterials · Tribological behaviour · Nanotribology · Sintering · Biomedical applications

Introduction

A biomaterial alloy should show good corrosion resistance and high biocompatibility and have suitable mechanical characteristics such as strength and young's modulus [1]. The most commonly used biomaterials include, ceramic (Al_2O_3 and ZrO_2), stainless steels, Co alloys, and Ti alloys [1–4]. Ti alloys have been used as implant materials due to their high corrosion resistance and excellent biocompatibility. They are gradually replacing the Co–Cr alloys and stainless steels 316L in biomedical applications [5–8]. Development and characterization of Ti alloys with different alloying elements such as Ni, V, Al, and Cr, were in focus of many studies [9].

Up to now, the Ti–6Al–4V alloy is the most widely used titanium alloy. However, it has two major problems. The first is the toxic effect of V [7–9] which can cause mutagenic cytology and allergic reactions [1–5]. For this reason, titanium alloys without these toxic elements such as Ti–6Al–4Fe and Ti–6Al–7Nb have been developed [10]. On the other hand, Young's modulus is generally considered to be important for implant materials, because implant failure can occur due to the mismatch in Young's modulus between the implant materials and the human bone. It is well known that the most widely used Ti implant material, ($\alpha + \beta$) type Ti–6Al–4V, exhibits a Young's modulus of 110 GPa, which is significantly higher than that of the human bone (30 GPa) [1–10]. Thus, in the past few decades, a β-type Ti alloy with lower Young's modulus has attracted more attention such as Ti–Mo, Ti–Nb, Ti–Zr, and Ti–Ni. These β-type titanium alloys not only have lower young's modulus, but they also exhibit better wear and corrosion resistance [11–13]. Hence, in order to develop the Ti alloy biomaterials, selection of suitable chemical components is very important. For this purpose, Zr and Nb have been extensively used and investigated as the non-toxic elements for the development of these biomaterials [14, 15].

However, more recently, β-stabilizing elements such as Nb and Mo have gained a lot of attention to develop low young's modulus titanium alloys for biomedical applications, [16]. Additionally, a neutral alloying element such as Zr has also been used as an alloying element, [17]. It has been reported that Zr and Nb show good biocompatibility [16–18]. Studies on Ti–Nb alloys have shown that the β phase was almost retained at 30 wt% of Nb and higher [19, 20]. Also, Ta has also been used with Nb to stabilize the bcc β–phase, such as Ti–35Nb–5Ta–7Zr, with low young's modulus. Nevertheless, their tensile strength is also low. The commercialized Ti–13Nb–13Zr is the most successful alloy in the Ti–Nb–Zr system [21]. Recently, the

Ti–20Nb–13Zr alloys with a favorable near-structure were developed for clinical use [22]. However, their tribological properties have not been investigated which are very important for the developed biomaterial to be successfully used for biomedical applications.

Therefore, the tribological behaviour of Ti–20Nb–13Zr alloys produced from mechanically milled powders and sintered at different temperatures needs to be investigated [22]. The correlation between sintering temperature and tribological properties of Ti–20N–13Zr alloys is crucial for biomedical applications. However, in the case of Ti–20Nb–13Zr alloy, this correlation has not been investigated. Thus, for the first time, this work aims to report the effect of sintering temperature on the structural and tribological behaviours of Ti–20Nb–13Zr alloys.

Materials and Methods

Sample Preparation and Characterization

Elementary powders (Fig. 1) of Ti, Nb, and Zr supplied by SIGMA-Aldrich society, Germany, were used to produce Ti–Nb–Zr alloy. The chemical compositions and characteristics of elementary powders are listed in Table 1.

Mechanical alloying was performed under an argon atmosphere using the Fritsch Pulverisette P7 planetary ball mill equipped with hardened steel vial (100 mL) and balls (Ø = 8 mm) with a speed of rotation of 450 rpm. The ball-to-powder weight ratio was 20:1. The synthesis was performed by milling cycles of 35 min and followed with equal rest periods (pauses of 40 min) to avoid an excessive rise of temperature inside the vials. The powders were milled for 48 h, were uniaxially pressed at 2.5×10^8 Pa into cylindrical samples of 13 mm diameter and 15 mm in height, and were subsequently hot isostatically pressed (HIPed) at 1273 K and at an isostatic pressure of 400 MPa.

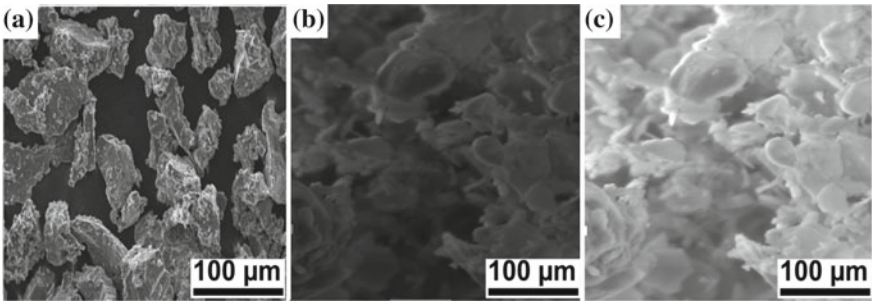

Fig. 1 SEM micrographs of as-received powders particles of **a** pure Ti, **b** pure Nb, and **c** pure Zr

Table 1 Characteristics of elementary powders used in the preparation of Ti–20Nb–13Zr samples

Characteristics	Ti	Nb	Zr
Purity	99.99%	99.98%	99.98%
Particle size (μm)	<50	<51	<45
O (wt%)	0.055	0.313	0.212
Fe (wt%)	0.0051	0.00032	0.0002
N (wt%)	0.0012	0.0013	0.0031
H (wt%)	0.008	0.0023	0.0009
C (wt%)	0.02	0.007	0.001
Melting point (°C)	1672	2477	1852
Particle morphology	Angular	Angular	Angular
Density	4.5	8.57	6.49

The compacted samples were then sintered in a vacuum furnace at 4×10^{-12} MPa at sintering temperatures ranging from 950 to 1250 °C at a heating rate of 5 K/s. Changes in the powder particles morphology (changes in crystallite size, lattice parameters, and microstrain) were evaluated by scanning electron microscopy (SEM) using a Zeiss DSM 960A microscope.

The tribological tests were conducted using a ball-on-plate type oscillating tribometer (tribotester) [23, 24], (Fig. 2), in accordance with the ASTM G 133–95, ISO 7148–1:2012, and ASTMG 99 standards under wet conditions using phosphate-buffered saline solution in accordance with ASTM F2129. The chemical composition of the used PBS is specified in the following Table 2.

Tests were carried out under different applied loads of 2 N, 10 N, and 20 N, respectively, at a sliding speed of 5 mm/s and a stroke length of 5 mm. An alumina ball (Al_2O_3), 5 mm in diameter, for which the young modulus $E = 320$ GPa, hardness $HV_{0.02} = 2500$, and density $= 3.96$ g/cm^3, was used as a counter face. Wear rate was calculated using the following equation:

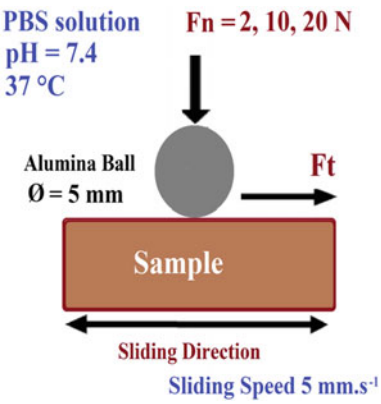

Fig. 2 Ball-on-disk type oscillating tribometer testing machine *(tribotester).* [23, 24]

Table 2 The most common composition of PBS solution at 37 °C, in accordance with ASTM F2129

Reagent	NaCl	KCl	Na_2HPO_4	KH_2PO_4
Concentration (g/L)	8.0	0.2	1.44	0.24
Concentration (mmol/L)	137	2.7	10	1.8
pH	7.4 ± 0.04			

$$W = \frac{V}{F.L} \tag{1}$$

where V: wear volume (μm^3), F: normal load (N), and L: sliding distance (μm). The wear volume was determined directly by laser profilometry. It was subsequently confirmed by the integration of the worn track profile obtained by laser and mechanical profilometry.

Results and Discussion

Lattice and Crystallite Size Parameter Measurement

Figure 3 shows the evolution of lattice parameters, average crystallite size, and internal microstrain of sintered Ti–20Nb–13Zr samples. The average crystallite size slowly decreased with increasing sintering temperature, which was also accompanied by an increase in the average microstrain rate {Ɛ} [25]. The crystallite size

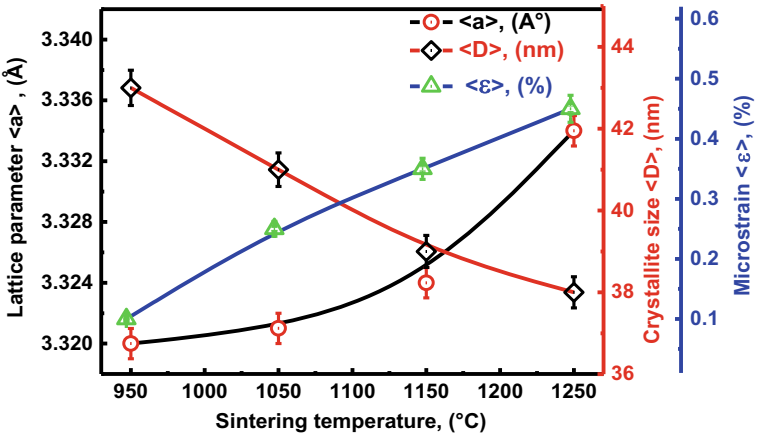

Fig. 3 Evolution of lattice parameters {a}, (Å), average crystallite size {D}, (nm), and internal microstrain {Ɛ}, (%) of sintered Ti–20Nb–13Zr samples

of studied sample at 950 °C was 43 nm which then reduced and reached a lowest value of 38 nm for samples sintered at 1250 °C. Similar dependency was reported in various works [10, 26, 27]. The mean internal strain values increased from 0.1 to 0.45% with an increase in the sintering temperature from 950 to 1250 °C. Furthermore, the lattice parameter {a} increases with increasing sintering temperature, from 3.320 to 3.334 Å, with a rising sintering temperature from 950 to 1250 °C, and only the β-phase was observed, which represents an extension of 1.1% in cell volume (Fig. 3). The variation of lattice parameter {a} of Ti–20Nb–13Zr alloy corresponds to the bcc-structure as previously reported elsewhere [28, 29].

Samples Porosity

Figure 4 displays the evolution of porosity, mean pore size, and the relative density of Ti–20Nb–13Zr versus sintering temperature. Porosity and mean porosity size decrease significant with an increase in sintering temperature. Also, as shown in Fig. 4, the porosity frequency decreased from 0.15 to 0.08% and the mean porosity size reduced from 50 to 40 nm, at sintering temperatures changing from 950 to 1250 °C, respectively.

The relative density of sintered Ti–20Nb–13Zr alloys increased with sintering temperature. Additionally, samples sintered at 1250 °C show higher density of 98.5% than the sintered samples at 950 °C, 1050 °C, and 1150 °C with values of 97%, 96%, and 89%, respectively.

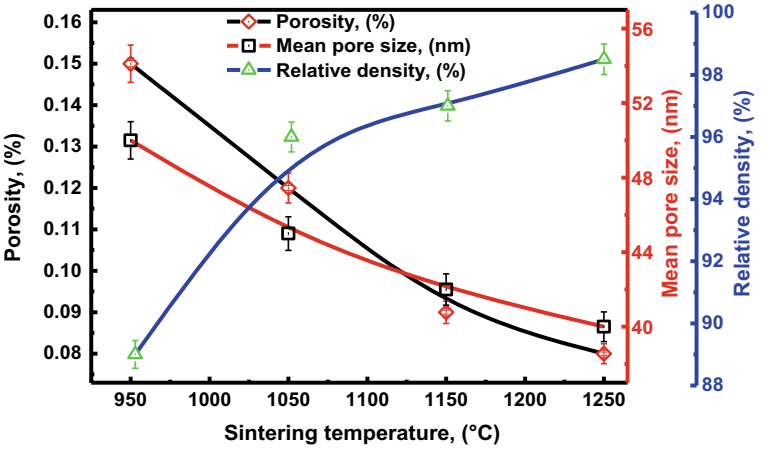

Fig. 4 Evolution of porosity (%), mean pore size (nm), and the relative density (%) of Ti–20Nb–13Zr as function of sintering temperature (°C)

Tribological Characterization

Frictional Behaviour

Figure 5 presents the evolution of an average friction coefficient, wear volume, and wear rate of sintered Ti–20Nb–13Zr alloys under different sintering temperatures and applied loads. The average mean values of the friction coefficient throughout the test were ranging from 0.49 to 0.58 at 950 °C to (0.18 to 0.25) at 1250 °C, respectively, (Fig. 5a).

According to this result, the friction resistance was improved with increasing sintering temperature which can be attributed to the closed porosity and grain size refinement. Additionally, as indicated in Fig. 5b, the wear volume of the sintered Ti–20Nb–13Zr samples decreases with increasing sintering temperature. The wear volume varied from 3.56 to 4.12 × 10^3 at 950 °C to (2.91 to 3.45 × 10^3) μm^3 at 1250 °C, respectively. Additionally, as shown in Fig. 5c, the wear rate decreases with increasing sintering temperature. The specific wear rate ranges from (16.4 to 19.01 × 10^{-3}), (8.82 to 13.95 × 10^{-3}), (7.65 to 12.43 × 10^{-3}) to (6.75 to 11.93 × 10^{-3}) $\mu m^3\ N^{-1}\mu m^{-1}$ for sintered samples at 950 °C, 1050 °C, 1150 °C, and

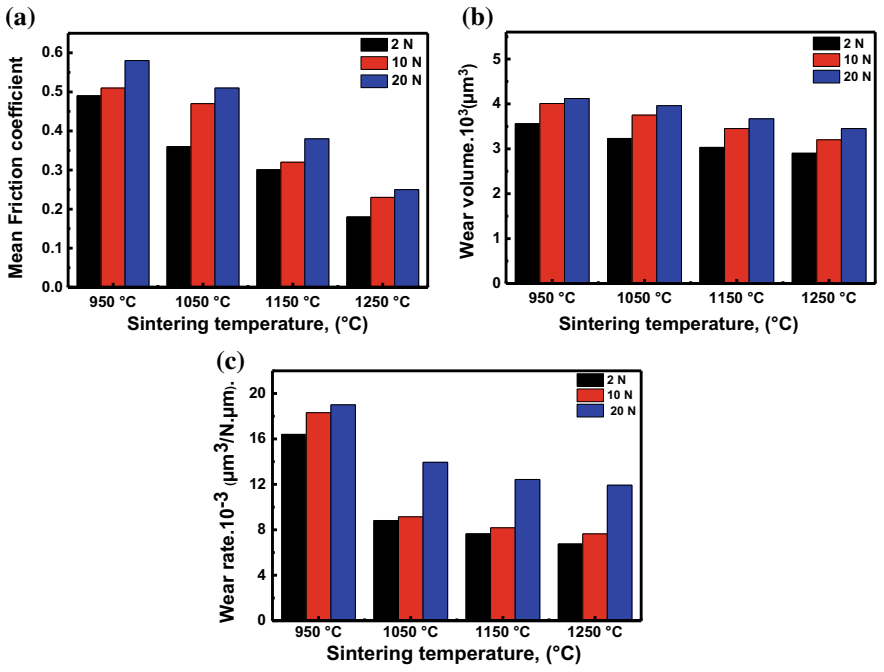

Fig. 5 Evolution of **a** mean friction coefficient, **b** wear volume (× 10^7 μm^3), and **c** wear rate (× 10^{-3} $\mu m^3\ N^{-1}\ \mu m^{-1}$) of sintered Ti–20Nb–13Zr alloys under different sintering temperatures and applied normal loads

1250 °C, respectively. The above results suggest that the tribological behavior of Ti–20Nb–13Zr alloys do not only depend on the sintering temperature, but also on experimental parameters such as the applied load, sliding speed, testing environment, and friction couple. As described in Fig. 5a–c, the specimens sintered at 1250 °C exhibit a high wear resistance and good tribological properties. This behaviour can be attributed to the enhanced mechanical properties due to closed fine porosity and grain size refinement.

Wear Scars Morphology

Figure 6a–d illustrates SEM micrographs of worn surface of sintered Ti–20Nb–13Zr alloys, after sliding. For specimens sintered at 950 and 1050 °C, abrasion was the main wear mechanism, while at medium and high sintering temperatures 1150 and 1250 °C, adhesion was found to be the main wear mechanism. For sample sintered at 950 °C and 1050 °C (Fig. 6a, b), the wear tracks consisted of deep grooves produced by plowing or micro-cutting action from hard asperities or due to the adherent transfer deposits on the counter face. All tested specimens presented a

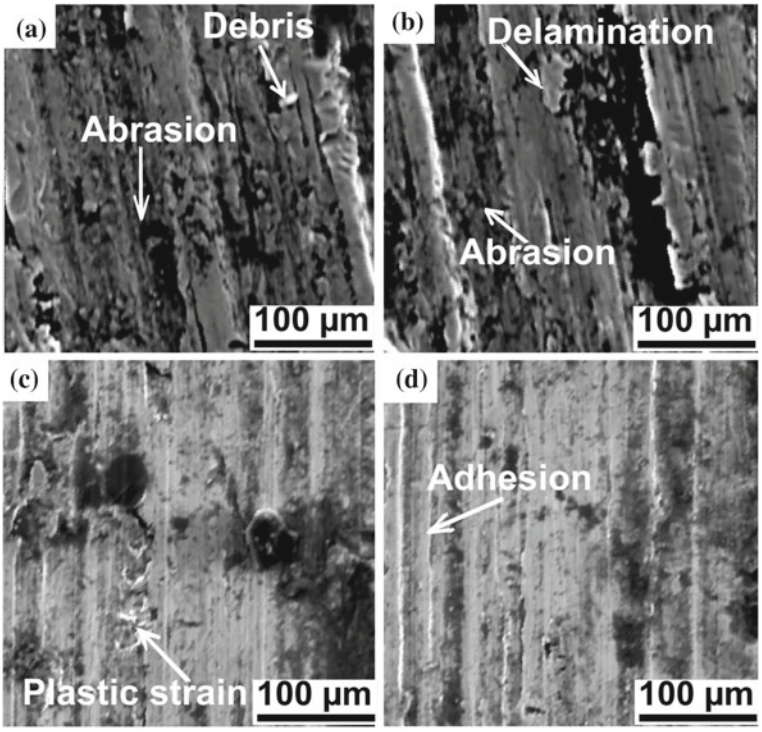

Fig. 6 SEM micrographs of Ti–20Nb–13Zr alloys vs sintering temperature at: **a** 950 °C, **b** 1050 °C, **c** 1150 °C, and **d** 1250 °C, tested at 10 N

similar wear mechanism. Irregular areas and a non-homogeneous wear, which was suggestively caused by the movement of abrasive debris particles from the inside to the sides of wear track, were detected in the case of the alumina ball counter face [25, 30, 31]. In particular, this phenomenon was predominantly observed for samples sintered at 1250 °C.

At 1150 °C sintering, it was difficult to identify the friction mechanism. The wear did not follow a conventional outline as in the case of 950 and 1050 °C. Samples sintered at 1150 °C (Fig. 6c) displayed parallel grooves running along the sliding direction which are covered by wear debris. The sintering at 1150 °C performed as a repellant to the failure mechanisms of traditional sliding wear, resulting in small areas of wear that are isolated and irregularly shaped [31–34]. Noise and vibration were not apparent.

Sample sintered at 1250 °C displayed the lowest wear, as shown in Fig. 5. The low coefficient of friction (0.23–0.35) (Fig. 5), high density, and porosity (Fig. 4) are the most important parameters that lead to high wear resistance. The wear scars morphology shows detachment of the particles. Nevertheless, there was no significant difference in wear morphology of samples sintered at 1150 and 1250 °C. In most cases, samples sintered at 1250 °C presented a good wear performance. In addition, the worn surfaces were protected by compressed wear debris forming a smooth transfer film showing very few marks on the samples as can be seen from Fig. 6c, d.

As expected, in the present study also, the Ti–20Nb–13Zr alloy with the smallest grain size showed the lowest wear rate, which was obtained for the samples sintered at 1250 °C leading to its closed porosity and higher density as compared to the un-sintered samples and sintered at lower temperatures (1050 °C).

Conclusions

Nanostructured Ti–20Nb–13Zr alloys were successfully synthesised by powder metallurgy methods, aiming to improve the tribological behavior. The effect of sintering temperature on lattice parameters, relative density, porosity, friction, and wear behavior was evaluated. The following conclusions can be drawn:

- Ti–20Nb–13Zr alloys sintered at 1250 °C indicated an improved relative porosity, density, and frictional behavior due to the grain size refinement and high relative density.
- With increasing sintering temperature and densification, the wear rate and friction coefficient decreased.
- At 1250 °C, the Ti–20Nb–13Zr alloys showed the lowest friction coefficient and wear rate as compared to alloys sintered at lower temperatures (950 and 1050 °C).
- Decreased average crystallite size, increased lattice parameter, internal microstrain, and sintering temperature played a significant role in controlling the wear rate.
- The higher wear resistance of alloys sintered at 1250 °C is attributed to the enhanced structural properties.

References

1. Assala O, Fellah M, Mechachti S, Touhami MZ, Khettache A, Bouzabataf B, Weiβ H, Jiang X (2018) Preparation and characterization of diamond-like carbon films prepared by MW/ECR-PACVD process deposited on 41Cr-Al-Mo7 nitrided steel. Trans IMF 96(3):1–10
2. Fellah M, Labaïz M, Assala O, Dekhil L, Iost A (2013) Tribological behavior of AISI 316L stainless steel for biomedical applications. Tribol-Mater, Surf Interf 7(3):135–149
3. Hezil N, Fellah M (2019) Synthesis, structural and mechanical properties of nanobioceramic (α–Al_2O_3). J Aust Ceram Soc 00:1–9. https://doi.org/10.1007/s41779-019-00333-7
4. Fellah M, Labaïz M, Assala O, Dekhil L, Iost A (2013) Friction and wear behavior of Ti-6Al-7Nb biomaterial alloy. J Biomater Nanobiotechnol 4(4):374–384
5. Fellah M, Abdul Samed M, Labaïz M, Assala O, Dekhil L, Iost A (2015) Sliding friction and wear performance of the nano-bioceramic α–Al_2O_3 prepared by high energy milling. Tribol Int 91:151–159
6. Dekhil L, Louidi S, Bououdina M, Fellah M (2019) Microstructural, magnetic, and nanoindentation studies of the ball-milled Ti80Ni20 alloy. J supercond Nov Magn. https://doi.org/10.1007/s10948-019-05145-1
7. Fellah M, Labaïz M, Assala O, Iost (2013) 5th world tribology congress. WTC 1:470
8. Fellah M, Assala O, Labaiz M (2014) Comparative study on tribiological behavior of Ti-6Al-7Nb and SS AISI 316L alloys, for total hip prosthesis. TMS 2014 Suppl Proc 32:237–246
9. Fellah M, Aissani L, Iost A, Zairi A, Montagne A, Mejias A (2018) Comportement à l'usure et au frottement de deux biomatériaux AISI 316L et Ti6Al7Nb pour prothèse totale de hanche. Matériaux Tech 106(402):1–10. https://doi.org/10.1051/mattech/2018051
10. Fellah M, Aissani L, Abdul Samad M, Iost A, Touhami MZ, Montagne A, Nouveau C (2017) Effect of replacing vanadium by nobium and iron on the tribological behavior of HIPed titanium alloys. Acta Metall Sin (Engl Lett) 30(11):1089–1099
11. Hou YP, Guo S, Qiao XL, Tian T, Meng QK, Cheng XN, Zhaob XQ (2016) Origin of ultralow Young's modulus in a metastable β-type Ti–33Nb–4Sn alloy. J Mech Behav Biomed 59:220–225
12. Geetha M, Singh AK, Asokamani R, Gogia AK (2008) Ti based biomaterials, the ultimate choice for orthopaedic implants—a review. Progr Mater Sci 54:397–425
13. Fellah M, Hezil N, Abdul Samad M, Montagne A, Kosman S, Megias A, Iost A, Obrosov A, Weiß S (2019) Biotribocorrosion behaviour of newly developed nanostructured near β-types titanium based alloys for biomedical applications. In: NanoMAT2019–2nd international conference on nanomaterials and their applications -170
14. Meng Q, Guo S, Liu Q, Hu L, Zhao X (2014) A β-type TiNbZr alloy with low modulus and high strength for biomedical applications. Proc Nat Sci-Mater 24(2):157–162
15. Cui Y, Li Y, Luo K, Xu H (2010) Microstructure and shape memory effect of Ti–20Zr–10Nb alloy. Mater Sci Eng A 527:652–656
16. Congqin N, Dongyan D, Kerong D, Wanyin Z, Lei C (2010) The effect of Zr content on the microstructure, mechanical properties and cell attachment of Ti–35Nb–x Zr alloys. Biomed Mater 5:045006, 8
17. Rao X, Chu CL, Zheng YY (2014) Phase composition, microstructure, and mechanical properties of porous Ti–Nb–Zr alloys prepared by a two-step foaming powder metallurgy method. J Mech Behav Biomed 34:27–36
18. Abdel-Hady M, Fuwa H, Hinoshita K, Kimura H, Shinzato Y, Morinaga M (2007) Phase stability change with Zr content in β-type Ti–Nb alloys. Scr Mater 57:1000–1003
19. Jae IK, Hee YK, Tomonari I, Hideki H, Shuichi M (2006) Effect of annealing temperature on microstructure and shape memory characteristics of Ti–22Nb–6Zr(at%) biomedical alloy. Mater Trans 47(3):505–512
20. Brailovski V, Prokoshkin S, Gauthier M, Inaekyan K, Dubinskiy S, Petrzhik M, Filonov M (2011) Bulk and porous metastable beta Ti–Nb–Zr(Ta) alloys for biomedical. Mater Sci Eng C 31(3):643–657

21. Cui CY, Ping DH (2009) Microstructural evolution and ductility improvement of a Ti–30Nb alloy with Pd addition. J Alloys Compd 471:248–252
22. Hussein MA, Abdul Samad M, Al-Aqeeli N (2015) Wear characteristics of metallic biomaterials: a review. Materials 8:2749–2768
23. Fellah M, Hezil N, Abdul Samad M, Touhami MZ, Montagne A, Iost A, Mejias A, Kossman S (2019) The effect of milling time on structural, friction and wear behavior of hot isostatically pressed Ti–Ni alloys for orthopedic applications. In: TMS 2019 148th annual meeting & exhibition supplemental proceedings. The minerals, metals & materials series. Springer, Cham, 2019. PA: TMS, pp 865–875. https://doi.org/10.1007/978-3-030-05861-6_85
24. Fellah M, Aissani L, Abdul Samad M, Purnama A, Djbaili H, Montagne A, Iost A, Nouveau C (2018) Effect of Zr content on friction and wear behavior of Cr-Zr-N coating system. Int J Appl Ceram Tec 15(3):701–715
25. Fellah M, Labaïz M, Assala O, Dekhil L, Iost A (2015) Tribological behavior of biomaterials for total hip prosthesis. Trends Biomater Artif Organs 29(01):22–30
26. Hagihara K, Nakano T, Maki H, Umakoshi Y, Niinomi M (2016) Isotropic plasticity of β-type Ti-29Nb-13Ta-4.6 Zr alloy single crystals for the development of single crystalline β-Ti implants. Sci Rep 6:29779
27. Fellah M, Labaïz M, Assala O, Dekhil L, Iost A (2014) Tribological behavior of Ti–6Al–4V and Ti–6Al–7Nb alloys for total hip prosthesis. Adv Tribol 7:13
28. Geetha M, Singh AK, Gogia AK, Asokamani R (2004) Effect of thermomechanical processing on evolution of various phases in Ti–Nb–Zr alloys. J Alloys Compd 384:131–144
29. Hari Kumar KC, Wollants P, Delaey L (1994) Thermodynamic assessment of the Ti–Zr system and calculation of the Nb–Ti–Zr phase diagram. J Alloys Compd 206:121–127
30. Fellah M, Labaiz M, Assala O (2013) Tribological behavior of friction couple: metal/ceramic (used for head of total hip replacement). Adv Bioceram Porous Ceram VI, 34(6):45–57
31. FellahM Labaiz M, Assala O, Dekhil L, Zerniz N, Iost A (2014) Tribological behavior of biomaterial for total hip prosthesis. Matériaux Tech 102(6–7):601–612
32. Fellah M, Hezil N, Touhami MZ, Obrosov A, Weiß S, Kashkarov EB, Lider AM, Montagne A, Iost A (2019) Enhanced structural and tribological performance of nanostructured Ti–15Nb alloy for biomedical applications. Results Phys 15: 102767
33. Fellah M, Hezil N, Hussein MA, Abdul Samad M, Touhami MZ, Montagne A, Iost A, Obrosov A, Weiss S (2019) Preliminary investigation on the bio-tribocorrosion behaviour of porous nanostructured β-type titanium based biomedical alloy. Mater Lett 257:126755
34. Fellah M, Hezil N, Abdul Samad M, Djellabi R, Montagne A, Mejias A, Kossman S, Iost A, Purnama A, Obrosov A, Weiss S (2019) Effect of molybdenum content on structural, mechanical, and tribological properties of hot isostatically pressed b-type titanium alloys for orthopedic applications. J Mater Eng Perform 28(10): 5988–5999

Investigation on Mechanical and Thermal Behaviours of PBAT/PLA Blend Reinforced with Reduced Graphene Oxide Nanosheets

Marcio R. X. Bartolomei, Karina H. S. Carmo, Bianca S. Santos, Suellen S. Bartolomei, Rene R. Oliveira and Esperidiana A. B. Moura

Abstract The aim of this study was to process and investigate the changes in the mechanical and morphological properties of the biodegradable nanocomposites based on polybutylene adipate-co-terephthalate (PBAT)/poly(lactic acid) (PLA) blend (PBAT/PLA blend) due to the incorporation of reduced graphene oxide (RGO) nanosheets. The biodegradable polymeric nanocomposites were prepared by melting extrusion process using a twin-screw extruder machine. The influence of the RGO nanosheets incorporation on mechanical and thermal properties of PBAT/PLA blend was investigated by tensile Thermogravimetric (TG), X-Ray diffraction (XRD), differential scanning calorimetry (DSC), and tensile test analysis. Results showed that incorporation of the small amount of RGO (0.1 wt.%) of RGO nanosheets in the blend matrix of PBAT/PLA resulted in an important gain of mechanical properties of the blend. This result indicates that a very small amount of RGO nanosheets addition in the PBAT/PLA can lead to obtaining materials with superior properties suitable for several industrial applications.

Keywords RGO · Biodegradable polymer · PBAT/PLA blend · Mechanical tests · SEM · XRD

Introduction

The increasing pollution of the environment, on land, oceans, and rivers by plastics, in its most different forms, types, and composition, discharged in nature as used plastic packaging, industrial waste, personal hygiene waste, and even soap used in washing machines has raised the concern of governments, the scientific community,

M. R. X. Bartolomei (✉) · K. H. S. Carmo · B. S. Santos · S. S. Bartolomei · R. R. Oliveira
Nuclear and Energy Research Institute (IPEN), Center of Chemical and Environmental Technology, Av. Prof. Lineu Prestes 2242, 05508-000 São Paulo, SP, Brazil
e-mail: marciorxb@gmail.com

E. A. B. Moura
Nuclear and Energy Research Institute, Center for Materials Science and Technology, 2242 Prof. Lineu Prestes Av., 05508-000 São Paulo, SP, Brazil

J. Li et al. (eds.), *Characterization of Minerals, Metals, and Materials 2020*,
The Minerals, Metals & Materials Series,
https://doi.org/10.1007/978-3-030-36628-5_62

and society at large for plastic waste. Plastic debris, especially during the degradation process, can release a large number of chemicals including such as nonylphenols, bisphenols, phthalates, and benzophenones and result in significant pathologies and morbidity of the animals. In this process of degradation, the plastic also breaks into smaller and smaller parts, turning into microplastics [1, 2].

Microplastics from all these wastes eventually enter the food chain of animals such as fish and seafood and return to humans by consuming these foods or even when drinking theoretically potable water, with effects on our health that are still being studied by science. Of course, this is a serious global health problem because plastics can travel across the planet through ocean currents [1–5].

Flexible or rigid plastic packaging is an important part of plastic waste in nature, especially single use plastic packaging. Researches are being carried out in universities and industries around the world with the intention of developing biodegradable plastics, but without losing the same characteristics of conventional plastic packaging. For plastic packaging used in food storage, the aim is that packaging must have not only biodegradable characteristics but also food safety characteristics that conserve the food like barrier properties for example [1–6].

For the aim of developing materials for the manufacture of green plastic packaging and also food safety parameters, this work is being developed. Biodegradable food packaging can bring a more sustainable and green future. The biodegradable nanocomposites based on polybutylene adipate-co-terephthalate (PBAT)/poly(lactic acid) (PLA) blend (PBAT/PLA blend) by itself does not guarantee the mechanical characteristics required for flexible plastic packaging, as water vapor or oxygen barrier characteristics and thermal degradation, not as efficiently as their equivalent petroleum-derived ones. The challenge is to simultaneously enhance these characteristics, but the compact lamellar microstructure and the hydrophobicity of the reduced graphene oxide (RGO) core barrier ensure the excellent barrier properties. With the addition of a very small amount of reduced graphene oxide (RGO) in a blend like PBAT/PLA, can bring significant changes in mechanical characteristics, a substantial 87.6% reduction in the water vapor permeability is thanks to the junction of the barrier and the protective encapsulation [7–12].

While properties such as oxygen barrier and thermal properties were well developed using the RGO, optical, electrical, and mechanical properties also improved considerably. Adding a small amount of the of RGO (0.1 wt%) of RGO nanosheets in the blend matrix of PBAT/PLA results in a large gain of mechanical properties of the blend, and as a result, it can be used in a large scale of industrialized products, including of course, flexible packaging such as single use packaging [7–12].

Graphite is an allotropic form of carbon, which is a solid crystalline material of lamellar structure composed of two-dimensional sheets chemically linked together by Van der Waal forces, and each sheet is called graphene. The term graphene can be used from one to ten overlapping sheets. In order to obtain graphene, it is first necessary to obtain graphene oxide, which must be reduced until one of the sheets can be isolated, with only the carbon on the surface. As described in various lit-

erature, graphene oxide can be obtained from the oxidation of graphite powder by the modified Hummers method. Graphene oxide reduction is a process that can be thermal, chemical, mechanical, and also by radiation, but it cannot be total, with the current technology, leaving at the most reduced graphene oxide [7–13].

In this work, nanocomposites of PBAT/PLA biodegradable blend, commercially called ECOVIO, were processed with 0.1 and 0.5% wt. RGO. They were characterized by XRD, TG, DSC, and tensile test.

Experimental

Materials

Biodegradable nanocomposites based on polybutylene adipate-co-terephthalate (PBAT)/poly(lactic acid) (PLA) blend (PBAT/PLA blend), commercial name Ecovio (Basf, Ludwigshafen on the Rhine, Germany), graphite flakes (Quimesp Química Ltda., Guarulhos, Brazil).

Preparation of Graphene Oxide (GO) and Reduced Graphene Oxide (RGO)

In the preparation of GO, the flake graphite was exfoliated by ultrasonication, with solution of 10% ethanol, 10% DMF, and 80% water, in each 100 ml was used 20 g of commercial graphite, the solution was prepared and taken for 2 h in the ultrasound machine. The result was the exfoliated graphite, that was washed with water to take off the DMF also using the centrifuge in this process. Then it was frozen and freeze-dried to produce the exfoliated graphite. GO was made with the modified Hummers method. Five grams of exfoliated graphite and 15 g of potassium permanganate have gone through a process of homogenized to dry into a beaker. This beaker was then taken to an ice bath and after that, 100 ml of concentrated sulfuric acid was added, and then it was mechanically stirred for 30 min. Then it was added 400 ml of distilled water slowly in an ice bath, to change the solution to effervescent. For 60 min, the mixture was put in a bath of water at 90 °C to rest.

After all, a solution of distilled water (70 ml) and hydrogen peroxide (30 ml) was taken to mechanical stirring for 4 h at 50 °C and then removed the excess acid in the centrifuge, and then it was washed with a solution of hydrochloric acid (450/50 mL) and water with the help of Büchner funnel with a vacuum pump. The result was a mass fixed in the filter and that was scattered in a solution of 50% ethanol (400 ml) and 50% water and dialyzed for five days. The pH must be between 5 and 6. The ultrasonic equipment was used with an intensity adjustment of 20 kHz and 450 W/cm^2

Table 1 Composition and nomenclature of samples

Name	ECOVIO (%)	RGO
ECOVIO	100	–
ECOVIO 0,1 RGO	99.9	0.1%
ECOVIO 0,5 RGO	99.5	0.5%

in this mixture with 200 ml for one hour to obtaining the solution of GO, that will be reduced by radiation.

The RGO will be obtained reducing the GO, using a gamma radiation (60Co) with 100 kGy radiation dose at the Radiation Technology Center CTR-IPEN/CNEN-SP. The radiation was performed with the solution in air presence, sealed in a pot in a room temperature was applied a dose rate of 6 kGy/h. Then it was filtered and dispersed in 150 ml of distilled water, frozen and freeze-dried for 48 h, thus obtaining the RGO as a fine and homogeneous powder.

Composites Preparation

The nanocomposites with ECOVIO matrix and percentage of RGO of 0.1 and 0.5% wt. were prepared by melt extrusion using a twin-screw extruder HAAKE Rheomex P332, 16 mm and L/D = 25 rate from Thermo Scientific. The temperature profile used during processing was 120/140/135/135/130/125 °C and the screws rotations were 15 RPM. The extrudates coming out of the extruder were cooled down by air and pelletized. The nanocomposite materials were fed into a flat die single extruder for films preparation. Table 1 shows the compositions analyzed and the nomenclature used in the work.

Characterization Methods

X-Ray Diffraction (XRD) Analysis

X ray diffraction (XRD) patterns for the samples were recorded on a Philips XPERT-MPD diffractometer with CuKα radiation ($\lambda = 1.54$ nm) operated at 40 kV and 40 mA, with 2θ varying between 3° and 60°.

Thermogravimetric Analysis

TG analysis was carried out using TGA Q500 from TA Instruments. The samples were heated from 30 to 600 °C under a nitrogen atmosphere (40 ml/min) at heating rate of 10 °C/min.

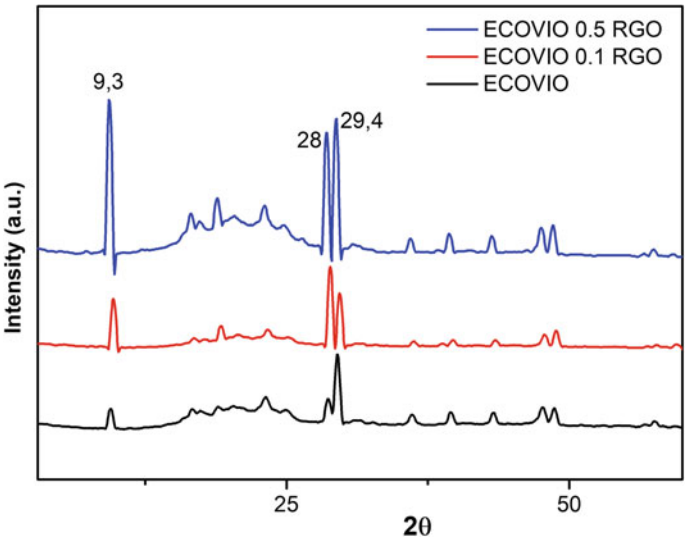

Fig. 1 XRD patterns for the RGO, ECOVIO, and its nanocomposites

Differential Scanning Calorimetry (DSC) Analysis

DSC analysis for each sample was performed using DSC Q20 from TA Instruments. Firstly, the thermal history of each sample was eliminated by heating the samples from 30 to 280 °C at a scanning rate of 10 °C/min. Subsequently, the samples were cooled down to room temperature at a rate of 10 °C/min. Finally, DSC curves were obtained by heating the samples from 30 to 280 °C at a rate of 10 °C/min.

Tensile Tests

Tensile specimens were obtained by thin film processing in single screw extruder; specimens were prepared according to ASTM D882-91. The tests were carried out using an INSTRON Universal Testing Machine, model 5564 at 25 °C and a loading rate of 50 mm/min, in six test specimens of each prepared nanocomposite and the average values were reported.

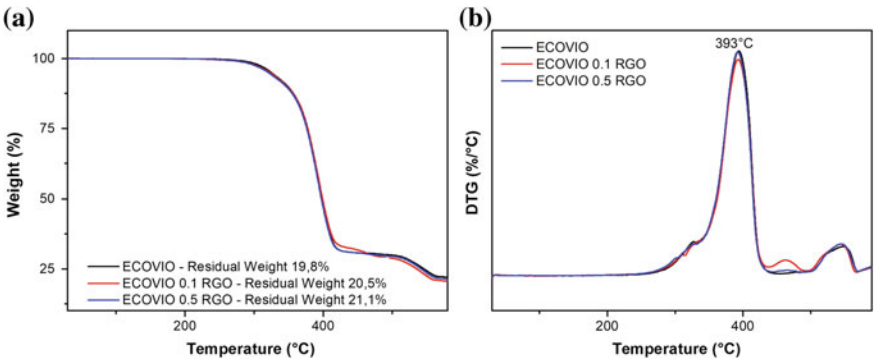

Fig. 2 TG thermograms (**a**) and DTG (**b**) of ECOVIO and its nanocomposites

Results and Discussion

X-Ray Diffraction (XRD) Analysis Results

Figure 1 shows the XRD curves. The peaks $2\theta = 9.3$, 16.5, 19, 23, 25, 28 and 29.4º are characteristic of the PBAT and PLA polymers present in the ECOVIO, material used for sample preparation. High intensity peaks of RGO particles can be observed at $2\theta = 10.9$º, the absence of this peak in nanocomposites indicates exfoliation of RGO particles in the polymer matrix.

Thermogravimetric (TG) Analysis Results

Figure 2 shows the thermograms obtained from TG analysis for the ECOVIO, ECOVIO 0.1 RGO and ECOVIO 0.5 RGO samples, with Fig. 2a TG curves and Fig. 2b DTG curves. According to Fig. 2a the residual mass increased according to the RGO content, the values found were 19.8, 20.5, and 21.1, respectively, for the samples ECOVIO, ECOVIO 0.1 RGO, and ECOVIO 0.5 RGO. Expected behaviour is due to high RGO degradation temperature. In Fig. 2b, it can be seen that the degradation temperature did not vary significantly between the samples, reaching a value of 393 °C [1].

Differential Scanning Calorimetry (DSC) Analysis Results

The heating curves of the ECOVIO, ECOVIO 0.1 RGO, and ECOVIO 0.5 RGO samples are shown in Fig. 3. Table 2 shows the glass transition temperatures of

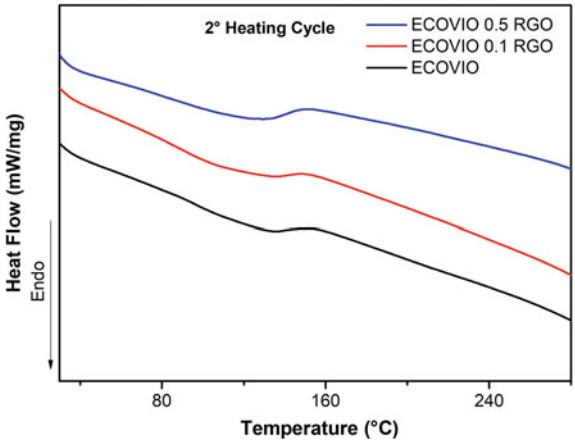

Fig. 3 DSC melting curves of the ECOVIO, ECOVIO 0.1 RGO and ECOVIO 0.5 RGO samples

Table 2 Glass transition temperature (*Tg*)

Sample	ECOVIO	ECOVIO 0, 1 RGO	ECOVIO 0, 5 RGO
Tg (°C)	152	147	140

these samples, taken from the DSC analysis curves. Looking at these data, it was found that *Tg* decreased with increasing amount of RGO. In scientific work using RGO nanocomposites, the glass transition temperatures increase, but in this work the opposite occurred, the nanocomposite temperatures decreased. According to the literature, the increase in *Tg* is an indication that RGO particles have strong interfacial adhesion with the polymeric matrix. In order to verify the adhesion of the RGO in the ECOVIO, tensile tests were performed in the samples ECOVIO and ECOVIO 0,1 RGO [1, 2].

Tensile Tests Results

The samples were submitted to the tensile test and the results are presented in Fig. 4 and Table 3. The two samples did not show significant differences for maximum tensile strength, but for the elongation, the ECOVIO 0.1 RGO sample showed a 30% gain over the ECOVIO. For the modulus of elasticity, there was a 30% reduction of ECOVIO 0.1 RGO compared to ECOVIO. The increase in the ductility of the RGO-containing nanocomposite corroborates the reduction of Tg presented earlier, being these phenomena characteristic of a toughening material, that is, the RGO particles added to ECOVIO acted as plasticizer increasing the mobility of the polymeric chain. The toughening mechanism in the presence of RGO occurs due to crack propagation during material rupture. Due to graphene's unique geometry, microcrack evolution can occur in a direction where there will be greater energy absorption, in addition

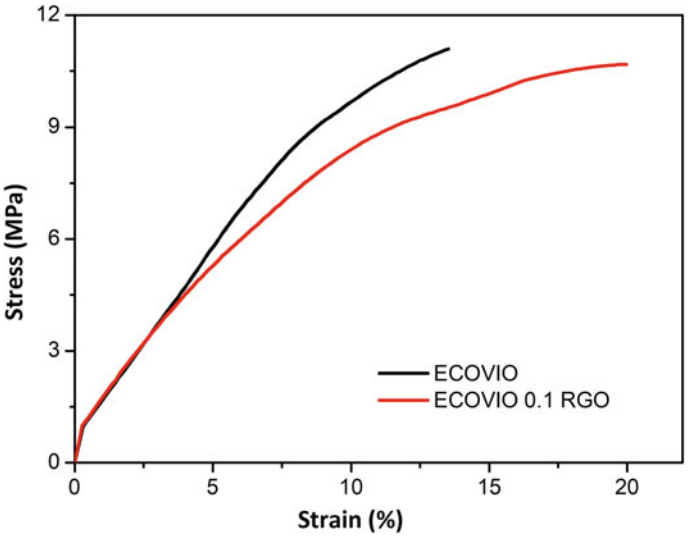

Fig. 4 Diagram stress (MPa) X strain (mm/mm) for ECOVIO and its nanocomposites

Table 3 Tensile test results

Sample	Tensile strength at break (MPa)	Elongation at break (%)	Young's modulus (MPa)
ECOVIO	12.1 ± 0.7	15.5 ± 2.5	171.6 ± 0.4
ECOVIO 0.1 RGO	11.1 ± 0.5	20.4 ± 0.2	142.8 ± 8.6

to interfacial slippage, tearing, and fracturing of graphene layers, further increasing energy absorption and material toughening [3, 4].

Conclusions

According to the results obtained, it can be concluded that the RGO particles were exfoliated in the ECOVIO polymer matrix by double screw extruder processing. Graphene acted as a toughening agent by increasing material ductility while reducing TG. The modulus of elasticity in a complementary manner also shows the toughness of the material as it significantly reduced when only 0.1% wt. of RGO was added to the polymer matrix [14–17].

Acknowledgements The authors wish to thank IIAEA-CRP# 17760 RO, FAPESP, and CNPq to provide support for this work.

References

1. Earth Day—Plastic Pollution Primer and Action Toolkit (2018). https://www.earthday.org/wp-content/uploads/Plastic-Pollution-Primer-and-Action-Toolkit.pdf. Accessed 15 Feb 2019
2. Nelms SE, Barnett J, Brownlow A, Davison NJ, Deaville R, Galloway TS, Lindeque PK, Santillo D, Godley BJ (2019) Microplastics in marine mammals stranded around the British coast: ubiquitous but transitory? Nature 1075(9):1–23
3. Ivankovic A, Zeljko K, Talic S, Bevanda AM, Lasic M (2017) Biodegradable packaging in the food industry. J Food Saf Food Qual 2(68):23–52
4. Kaur S, Puri D (2017) Active and intelligent packaging: a boon to food packaging. Int J Food Sci Nutr 4(2):15–18
5. Metak AM, Nabhani F, Connolly SN (2015) Migration of engineered nanoparticles from packaging into food products. Food Sci Technol 2(64):781–787
6. Dobrucka R, Cierpiszewski R (2014) Active and intelligent packaging food, research and development—a review. Pol J Food Nutr Sci 64(1):7–15
7. Rong MZ, Zhang MQ, Ruan WH (2006) Surface modification of nanoscale fillers for improving properties of polymer. Mater Sci Technol 22:787–796
8. Yoo BM, Shin HJ, Yoon HW, Park HB (2014) Graphene and graphene oxide and their uses in barrier polymers. J Appl Polym Sci 131:1–23
9. Zhang B, Li L, Wang Z, Xie S, Zhang Y, Shen Y, Yu M, Deng B, Huang Q, Fana C, Li J (2012) Radiation induced reduction: an effective and clean route to synthesize functionalized graphene. J Mater Chem A 22:7775–7781
10. Huang X, Qi X, Boeyab F, Zhang H (2011) Graphene-based composites. RSC. pp 1–21
11. Potts JR, Dreyer DR, Bielawski CW, Ruoff RS (2011) Graphene-based polymer nanocomposites. Int J Sci Technol Polym, 1–21
12. Singh RK, Kumar R, Singh DP (2016) Graphene oxide: Strategies for synthesis, reduction and frontier applications. RSC, 1–19
13. Kim H, Abdala AA, Macosco CW (2010) Graphene/polymer nanocomposities. Macromolecules 16(43):6515–6530
14. Ansón-Casaos A, Puértolas JA, Pascual FJ, Hernández-Ferrer J, Castell P (2014) The effect of gamma-irradiation on few-layered graphene materials. Appl Surf Sci 301:264–272
15. Kuilla T et al (2010) Recent advances in graphene based polymer composites. Prog Polym Sci Oxford 11(35):1350–1375
16. Pinto AM et al (2013) Effect of incorporation of graphene oxide and graphene nanoplatelets on mechanical and gas permeability properties of poly(lactic acid) films. Polym Int 1(62):33–40
17. Wang J et al (2019) Graphene and graphene derivatives toughening polymers: toward high toughness and strength. Chem Eng J 370:831–854

Iron Ore Fines Granulation in a New High Speed Mixing Granulator

Shanshan Wu, Zhongci Liu and Xuewei Lv

Abstract A new type of mixing granulation equipment is proposed, which can improve the mixing degree of raw materials, improve the granulation efficiency, and have the function of "self-purification". The results show that the particle size is uniform and chemical composition segregation of particles is decreased after granulation. The strength of the granules can be effectively improved to control the particle size distribution of the particles. With the rotational speed increasing, the particles of +10 mm increase and the fractions of −1 mm are few. As the rotational speed is 70 rev. min^{-1}, the median particle size *D* (50) of granules is the maximum value. The fractal dimension tends to decrease gradually with the increase of rotating speed. It indicates that the particle size distribution in the high speed stirring granulator is very concentrated. The particle size grading is very small and the fine powder particles mostly adhere to the mother particles.

Keywords High speed granulating · Particle size distribution · Fractal dimension · Granulation effect

Introduction

In iron-making, most of iron ore is mixed with the addition of cokes and limestone and granulated using water with a drum mixer for the following sintering process [1]. In order to make the mixture particles, form a larger particle in a collision with each other. The particle size distribution is an appropriate size range and strength of granules [2–4]. The granulation operation is important for the iron-making because it

S. Wu · Z. Liu · X. Lv (✉)
College of Materials Science and Engineering, Chongqing University, Chongqing 400044, China
e-mail: lvxuewei@163.com

J. Li et al. (eds.), *Characterization of Minerals, Metals, and Materials 2020*,
The Minerals, Metals & Materials Series,
https://doi.org/10.1007/978-3-030-36628-5_63

is the first stage in the blast furnace method. The granulation process can reasonably control the composition and particle size distribution of the particles to keep high permeability and reactivity of granules bed and to achieve high productivity in the sintering process [5, 6].

Granulation efficiency should be dependent on three factors: the characteristics of iron ores, the moisture content of mixtures, and the operational conditions of drum mixers. Operational conditions are mixture charge ratio, drum mixer length, and rotational size [7–9]. But there is no greater change in the mixer [10]. Powder mixing and granulation in a high speed mixer are fundamental operations in the agriculture, food, pharmaceutical, and chemical industries [11–13]. They have great advantages that the operations can be completed in a relatively short time and the equipment is very simple in construction [14–17]. A new method of using granulation in a high speed mixer has been proposed. In addition, the effects of particle size distribution of iron ores on granulation performance in high speed mixer are widely researched. This paper describes setting up a new high speed mixer of granules and find out the method to optimize the granulation through studying the particle size distribution.

Materials and Methods

Properties of Raw Materials

Seven raw materials were used, which came from sintering production site. The filling rate of the mixture was 12%. Their chemical and contents are shown in Table 1.

The sintered raw materials have differences in the composition of SiO_2, Al_2O_3, and MgO. These factors are advantageous for adjusting the chemical composition of the sintering mixture. The experiment controls the compounding of the mixture according to the particle size distribution.

Table 1 Chemical composition of sintering raw materials (%)

Items	TFe	CaO	SiO_2	Al_2O_3	MgO
Ore blender	60.11	0.58	4.48	1.46	0.17
Dolomite	0.36	31.44	2.07	0.34	19.74
Limestone	0.35	52.24	2.38	0.89	1.12
Quicklime	–	89.88	2.33	–	–
Serpentine	4.90	1.99	37.31	0.88	37.81
Return fines	57.43	10.01	5.04	1.73	1.31
Sintered powder	57.12	10.21	5.17	1.75	1.50

Granulation Experiment

The experiment was performed using a new designed granulating equipment. It is to explore the influence of the process parameters of the equipment on the granulation effect during the granulation process. The granulation mixer is shown in Fig. 1. Sinter mixture was granulated in a high speed mixer of 400 mm in diameter and 500 mm long. The granulator speed in this experiment was the only variable. The granulation process parameters in the experiment are shown in Table 2.

The rotational load of the granulator during the granulation experiment and the granulation state of the granules in the granulator were all considered. There are four items in the experiment. Sintering materials were weighed according to the corresponding filling rate and mixed with suitable moisture. Before the granulation, all the mixtures were mixed in high speed mixer which the mixture time is 1 min with rotational speed of 100 rev. min^{-1}. Then all the mixtures were granulated for 12 min with different rotational speed and the experimental process is shown in Fig. 2.

After granulation, samples were taken to measure granule size distribution and the particle size compositions. Granule size distribution and permeability presented the granulating effectiveness. Sampled granulated mixture was initially screened into six

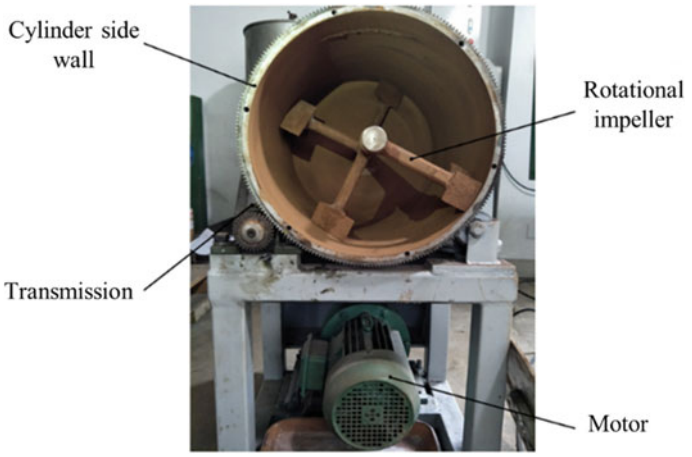

Fig. 1 High speed mixing granulating equipment

Table 2 Parameters of high speed mixer

Items	Water content/g	Times/min	Rotational speed/rpm
No. 1	345	12	40
No. 2	345	12	50
No. 3	345	12	60
No. 4	345	12	70

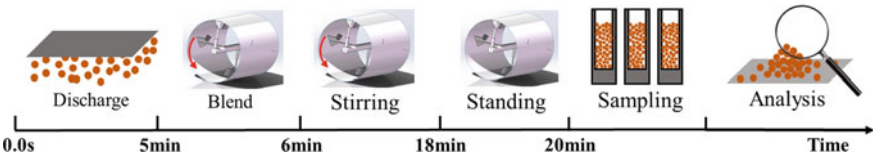

Fig. 2 The flow sheet of experiment

fractions, which were +10 mm, 8–10 mm, 5–8 mm, 3–5 mm, 2–3 mm, and 1–2 mm, respectively. Then each fraction was weighed to calculated size distributions and average diameter.

Results and Discussion

Factors Affecting Granulation Efficiency

Sampled mixture before granulated was screened into seven fractions, as shown in Table 3, the particles of 1–2 mm and 0.5–1 mm are the maximum. The content and the specific surface area of −0.5 mm were the adhesive fines.

As can be seen from Fig. 3, the particle size is uniform and the chemical composition segregation of the particles can be effectively reduced during the granulation process. The strength of the granules can be effectively improved to control the particle size distribution of the particles.

Figure 4 shows Particle size distribution of four granulation experiments. When the high speed granulator rotates at 40 revolutions, the particle size of the particles larger than 10 mm accounts for 40%, 10 ~ 8 mm is about 28%. There are fewer fine powders in the mixture. With the rotational speed increasing, the particles of + 10 mm increase, while the fractions of −1 mm are few.

The particle size distribution of the mixture after granulation at four different speeds is as shown in Fig. 5. As the rotation speed of granulation increases, the median particle size D (50) of the granules increases, the average particle size increases. As the rotational speed is 70 rev. min^{-1}, the granules have very low content of

Table 3 Particle size analysis of sinter mix before granulation

Granule size	+8 mm	5–8 mm	3–5 mm	2–3 mm	1–2 mm	0.5–1 mm	−0.5 mm
No. 1	9.31	9.68	18.26	11.89	25.72	20.41	4.73
No. 2	10.24	9.87	16.47	14.68	22.58	20.25	5.90
No. 3	9.02	9.03	13.90	12.27	20.20	27.16	8.42
No. 4	6.85	7.94	13.81	12.31	21.45	28.10	9.54

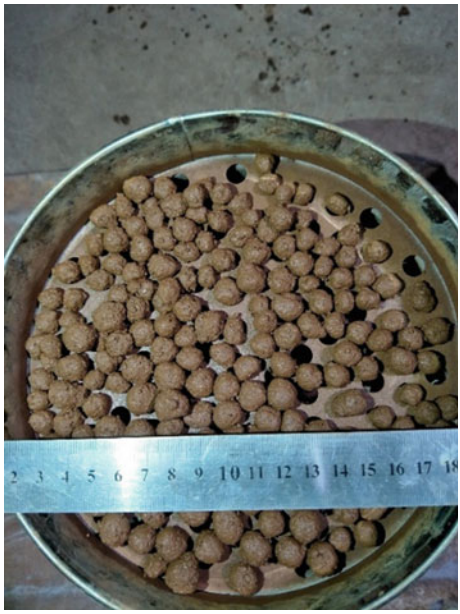

Fig. 3 Particle size screening morphology

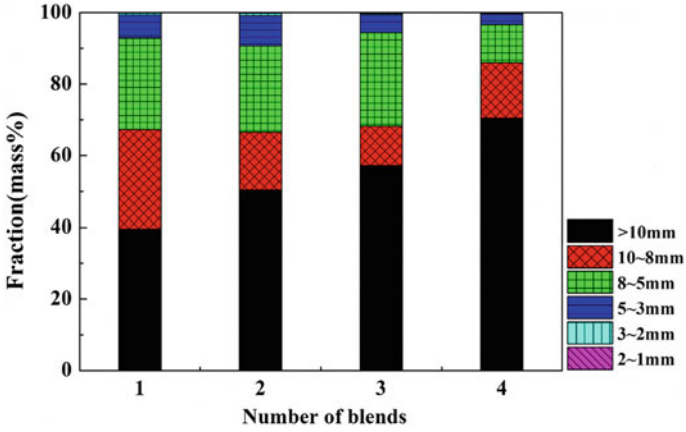

Fig. 4 Particle size distribution at different speeds

fine powders, uniformity of particle size distribution, and good concentration. The particle size distribution of the No. 3, particles satisfies the optimum permeability for the sinter bed.

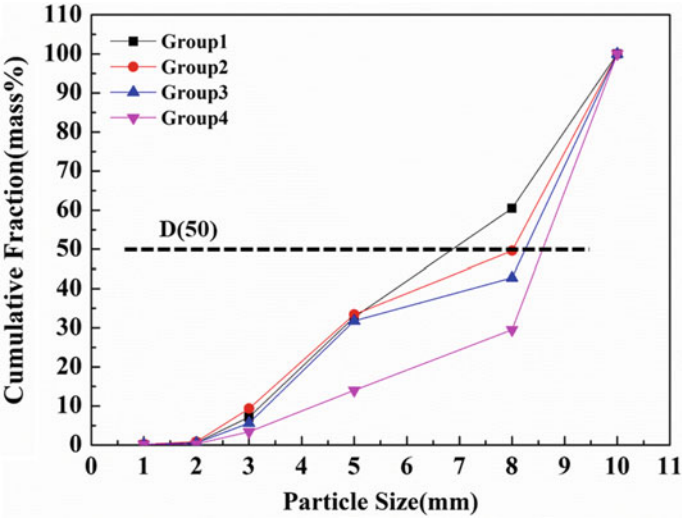

Fig. 5 The median particle size of the granules

Fractal Dimension Analysis

Fractal dimension is representation of the particle size composition. Mineral particles are generally considered to have fractal characteristics after the beneficiation process.

$$Y_n(r) \propto r^{-D} \tag{1}$$

where Y_n (r) is the ratio of particles smaller than r (mm) in size to the total number of particles. And D is the fractal dimension. The formula is given as follows:

$$\mathrm{d}Y_n(r) \propto \mathrm{d}r^{-1-D}\mathrm{d}r \tag{2}$$

From the above formula, the particle mass $\mathrm{d}W$ (kg) in the range of $r \sim r + \mathrm{d}r$ can be obtained:

$$\mathrm{d}W = \rho k_v r^3 N \mathrm{d}Y_n(r) \tag{3}$$

where kv is the particle volume shape factor and N is the total number of particles.

$$Y_W(r) = \left(\frac{Nk_v}{W}\right) r^3 \mathrm{d}Y_n(r) \tag{4}$$

$$\mathrm{d}Y_W(r) \propto r^{2-D}\mathrm{d}r \tag{5}$$

$$Y_W(r) \propto r^{3-D} \tag{6}$$

The formula (6) is the fractal relationship between the mass fraction of the particle size $-r$ and the corresponding particle size r.

The experiment divides the particles into several fixed particle sizes, obtains the mass percentage of the particles under each particle level, and then draws a dot map on the cumulative mass percentage and the grain level integral, and uses the linear regression to find the slope of the line, and then it gets the particles fractal dimension.

When there is only one particle size, the fractal dimension of the particle cluster is the smallest ($D = 0$). As the particle size of the particle cluster is classified, the mass fraction of the particles under each particle size is small and the difference is small. Then the fractal dimension will be larger.

Before granulation, the fractal dimension of particle size composition of the mixture is 2.996, which is close to 3. The particle size fraction of the particle cluster is large. As shown in Fig. 6, fractal dimension ($D = 3 - \mathrm{k}$) analysis is available in the four experimental results. It can be concluded that, with the increase of rotating speed, the fractal dimension tends to decrease gradually, indicating that the particle size distribution in the high speed stirring granulator is very concentrated, the particle size grading is very small, there is almost no small particle size, and the fine powder particles mostly adhere to the mother particles.

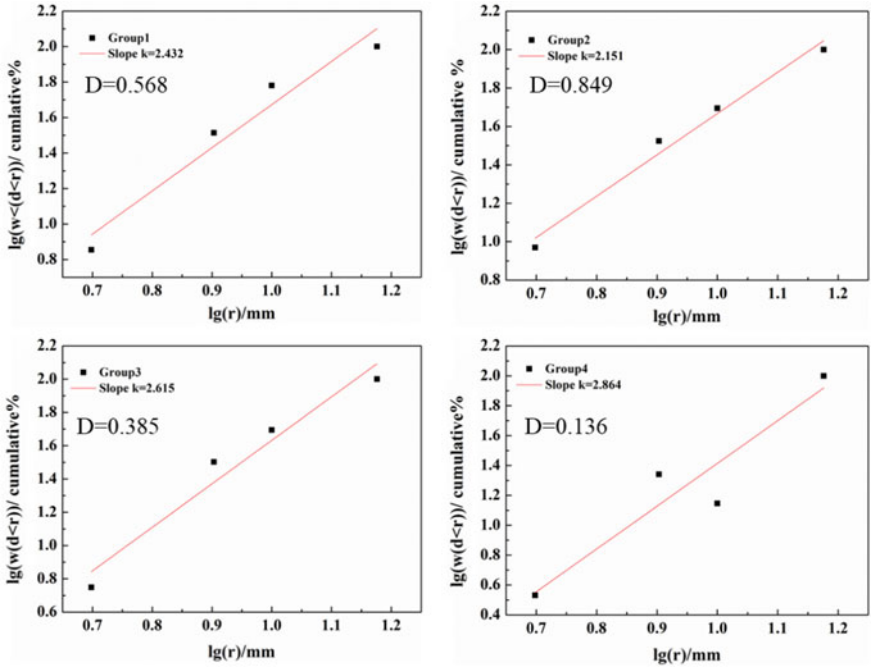

Fig. 6 The fractal dimension of granulators in each experiment

Conclusions

In this paper, the effect of the granulator speed on the particle size distribution of the mixture after granulation is studied under the same raw material conditions. The relationship between the rotational speed and the fractal dimension of the particles after granulation is established. The main conclusions can be summarized as follow:

(1) The particle size is uniform and chemical composition segregation of particles is decreased after granulation. The strength of the granules can be effectively improved to control the particle size distribution of the particles.
(2) With the rotational speed increasing, the particles of $+10$ mm increase and the fractions of -1 mm are few. As the rotational speed is 70 rev. min^{-1}, the median particle size D (50) of granules is the maximum value.
(3) The fractal dimension tends to decrease gradually with the increase of rotating speed. It indicates that the particle size distribution in the high speed stirring granulator is very concentrated. The particle size grading is very small and the fine powder particles mostly adhere to the mother particles.

References

1. Kano J, Kasai E, Saito F, Kawaguchi T (2005) Numerical simulation model for granulation kinetics of iron ores. ISIJ Int 45(4):500–505
2. Khosa J, Manuel J (2007) Predicting granulating behaviour of iron ores based on size distribution and composition. ISIJ Int 47(7):965–972
3. Rankin WJ, Roller PW (1985) The measurement of void fraction in beds of granulated iron ore sinter feed. Trans Iron Steel Inst Jpn 25(10):1016–1020
4. Cores A, Muñiz M, Ferreira S, Robla JI, Mochón J (2012) Relationship between sinter properties and iron ore granulation index. Ironmaking Steelmaking 39(2):85–94
5. Dawson PR (1993) Recent developments in iron ore sintering new development for sintering. Ironmaking Steelmaking 20(2):135–136
6. Oliveira D, Wu SL, Dai YM, Xu J, Chen H (2012) Sintering properties and optimal blending schemes of iron ores. J Iron Steel Res Int 19(6):1–5
7. Kapur PC, Kapur P, Fuerstenau DW (1993) An auto-layering model for the granulation of iron ore fines. Int J Miner Process 39(3–4):239–250
8. Gan M, Fan XH, Ji ZY, Chen XL, Yin L, Jiang T, Huang YS (2015) Optimising method for improving granulation effectiveness of iron ore sintering mixture. Ironmaking Steelmaking 42(5):351–357
9. Litster JD, Waters AG (1990) Kinetics of iron ore sinter feed granulation. Powder Technol 62(2):125–134
10. Yang LX (2005) Sintering fundamentals of magnetite alone and blended with hematite and hematite/goethite ores. ISIJ Int 45(4):469–476
11. Sato Y, Nakamura H, Watano S (2008) Numerical analysis of agitation torque and particle motion in a high shear mixer. Powder Technol 186(2):130–136
12. Ghanta SR, Srinivas R, Rhodes CT (1984) Use of mixer-torque measurements as an aid to optimizing wet granulation process. Drug Dev Ind Pharm 10(2):305–311
13. Litster JD, Hapgood KP, Michaels JN, Sims A, Roberts M, Kameneni SK (2002) Scale-up of mixer granulators for effective liquid distribution. Powder Technol 124(3):272–280

14. Kuo HP, Knight PC, Parker DJ, Tsuji Y, Adams MJ, Seville JPK (2002) The influence of DEM simulation parameters on the particle behaviour in a V-mixer. Chem Eng Sci 57(17):3621–3638
15. Kuo HP, Knight PC, Parker DJ, Adams MJ, Seville JPK (2004) Discrete element simulations of a high-shear mixer. Adv Powder Technol 15(3):297–309
16. Kopcha M, Roland E, Bubb G, Vadino WA (1992) Monitoring the granulation process in a high shear mixer/granulator: an evaluation of three approaches to instrumentation. Drug Dev Ind Pharm 18(18):1945–1968
17. Knight PC, Seville JPK, Wellm AB, Instone T (2001) Prediction of impeller torque in high shear powder mixers. Chem Eng Sci 56(15):4457–4471

Leaching of Pre-Oxidated Pyrargyrite with $Na_2S_2O_5$

Vicente Gonzáles Martínez, Isabel Hernández Martínez, M. Reyes Pérez, M. Pérez Labra, J. C. Juárez Tapia, Iván A. Reyes Domínguez, Mizraim Uriel Flores Guerrero and Gustavo Urbano Reyes

Abstract Recently, Mexico has established itself as the largest producer of silver in the world; however, the minerals extracted have a very complex mineralogy. Pyrargyrite presents problems of leaching with cyanide. For this reason, the effect of oxidation with metabisulfite prior to leaching with cyanide is studied. The characterization of the mineral confirmed the presence of a single phase of Ag_3SbS_3, identified in the pattern of DRX PDF 00-019-1135. The MEB–EDS analysis shows the elements of pyrargyrite, antimony 22.90, sulfur 17.4, and silver with 59.6%. From analysis by FTIR, the presence of antimony oxides was found and the formation of sulfates. The leaching of silver with cyanide [0.03]M pre-oxidized with metabisulfite [0.105]M and 96 h, reaches a percentage of silver extraction of 25% in 68 h. The increase in the concentration of oxidizing agent at [0.210]M and the leaching time contributes to achieve recoveries of 37%.

Keywords Leaching · Oxidation · Metabisulfite · Pyrargyrite · Cyanide

Introduction

Pyrargyrite (Ag_3SbS_3) is one of the most important silver ores, it crystallizes in the hexagonal system, and it contains 59.7% silver (Ag), 22.5% antimony (Sb), and 18.8% sulfur (S). It occurs abundantly in mineral deposits in mining areas such

V. G. Martínez · I. H. Martínez · M. R. Pérez (✉) · M. P. Labra · J. C. Juárez Tapia · G. U. Reyes
Autonomous University of the State of Hidalgo, Academic Area of Earth Sciences and Materials, Road Pachuca-Tulancingo Kilometer 4.5 Mineral de La Reforma, Pachuca 42180, Hidalgo, Mexico
e-mail: mreyes@uaeh.edu.mx

I. A. Reyes Domínguez
Autonomous University of San Luis Potosí, Metallurgy Institute, Av. Sierra Leona 550, Lomas Second Sect., Potosí 78210, San Luis Potosí, Mexico

M. U. F. Guerrero
Technological University of Tulancingo, Industrial Electromechanics Area, Road to Ahuehuetitla #301 Col. Presas, Tulancingo 43642, Hidalgo, Mexico

J. Li et al. (eds.), *Characterization of Minerals, Metals, and Materials 2020*,
The Minerals, Metals & Materials Series,
https://doi.org/10.1007/978-3-030-36628-5_64

as Zacatecas and Guanajuato, Mexico. It is refractory to cyanide, and therefore, the leaching of silver in the standard cyanidation process is slow [1]. Worldwide, cyanidation is considered as the main method used for the extraction of precious metals.

The depletion of easily leachable silver ores and the increase in silver prices have forced the mining industry to process complex minerals that can be refractory to cyanide. A mineral is considered refractory when less than 80% is extracted during cyanide leaching. Cyanide was introduced industrially more than a century ago, and since then, it has been used in various types of mining applications, such as leaching and flotation, which act as a sphalerite depressant [2, 3].

Because silver and gold refractory minerals do not respond to direct cyanidation, they require a pretreatment to release gold and silver before cyanidation to improve extraction. The methods that have been practiced industrially to increase precious metal recoveries are roasting [4] pressure oxidation [5] bio oxidation [6], ultra-fine grinding [7]. Another technique to increase the recovery of silver is the pre-reaction with lime and lead nitrate in order to passivate mineral impurities. This technique increases leaching [8].

It has been previously shown that leaching with alkali sulfides is effective pretreatment methods that increase leaching with cyanide by extracting more silver and gold from the antimony refractory minerals contained in species such as Zinkenite ($Pb_4Sb_{22}S_{42}$) and andurite (Sb_2PbAgS_6) [9], and this is because sodium hydroxide can dissolve antimony from minerals such as stibnite [10].

Therefore, the minerals that have refractoriness to be leached with cyanide are those that contain antimony in their structure, which need a pretreatment to improve the recovery of gold and silver. This research study evaluates the influence of a pretreatment process before leaching with cyanide, using sodium metabisulfite by evaluating the concentration of pretreatment reagent, time, and cyanide concentration.

Experimental Methodology

To study the leaching of silver, from the previously pre-oxidized or pre-treated ore, pure pieces of Ag_3SbS_3 pyrargyrite ore from the mining region of Guanajuato, Mexico, were used. Macroscopically, these are high purity specimens, and no other mineralogical phases that contaminate the mineral are observed as shown in Fig. 1.

The pyrargyrite ore was pulverized in an agate mortar, sieved wet using a series of Tyler sieves, 100 mesh, 200, 270, 325, 400 and the fine, with particle sizes of (180 μm, 75 μm, 53 μm, 43 μm, 37 μm, and <37 μm), respectively. The sieved product was allowed to dry at room temperature, characterized by DRX, MEB–EDS. For the performance of all experimental tests, it was decided to use the particle size of the mesh +325 (43 μm).

Fig. 1 Pyrargyrite mineral used in this work

To carry out the experimentation, 1 L of deionized water was used, placed in a glass reactor, and mechanically stirred with a four-blade propeller made of inert material (plastic), and subsequently, 0.5 g of pyrargyrite mesh +325 weighed on a precision scale (0.001 g). Both pH and ORP were monitored during all tests, and then, in separate tests, sodium metabisulfite ($Na_2S_2O_5$) was added in concentrations of 0.052, 0.105, 0.210M.

The investigated pre-oxidation with metabisulfite was 4, 7, 48, 72, 96, and 120 h, continuously monitoring the pH and ORP, and the reactor was covered to avoid evaporation volume losses as much as possible. At the end of each pretreatment time, the pH was adjusted to around 9 with sodium hydroxide, subsequently a concentration of potassium cyanide of 3.07×10^{-2}M was added for each of the tests, and different times of study were studied. cyanidation 68, 96, 100, 180, and 200 h.

The evaluated times of pre-oxidation with metabisulfite were 4, 7, 48, 72, 96, and 120 h, monitoring the pH and the ORP, continuously, and the reactor was covered to avoid as much as possible loss of volume by evaporation. At the end of each pretreatment time, the pH was adjusted to around 9 with sodium hydroxide, subsequently a concentration of potassium cyanide of 3.07×10^{-2} M was added for each of the tests, and different times were studied. cyanidation 68, 96, 100, 180, and 200 h.

During the entire leaching time with cyanide, samples of the solution were collected, filtered, and determined via ICP at its concentration of Ag, Sb, and it should be noted that the reaction system was monitored all the time of cyanidation, measuring the pH and the ORP. The equation used to determine the progress of the reaction is

$$\%\mathrm{Ag} = \frac{L * \text{Bring out} * \text{dilution}}{W_m * 10000} \tag{1}$$

where L is the reading obtained in the ICP in PPM (mgL^{-1}), the bring out is the total volume (ml) of water of the experiment, the dilution is the dilution factor which

is obtained by dividing the volume of the capacity (ml) between the volume of the aliquot (ml), W_m is the sample weight in grams, and 10,000 is the conversion factor of the units of this ratio. The residual solids from the leaching tests were recovered, washed with plenty of water, and characterized by Fourier FTIR transform infrared spectroscopy and MEB scanning electron microscopy in conjunction with EDS energy dispersion micro analysis.

Results

Figure 2 shows the X-ray diffraction spectra (DRX) of the mineral, which was indexed with the Match software database, and it was found that pyrargyrite is the only crystalline mineralogical phase present, identified with the diffraction pattern PDF 00-019-1135. The analysis by MEB and elementary mapping of the pyrargyrite is shown in Fig. 3. It is observed that it contains the characteristic elements of this mineral phase in some of the tests the presence of copper was detected, which due to its lower percentage is not possible detect by X-ray diffraction.

Table 1 shows the semi-quantitative microanalysis by dispersion of energies of the pyrargyrite ore, where the majority element is silver, which makes it an important ore of this valuable metal; however, the high content of antimony makes it impossible to leach silver by processes traditional, which necessarily involves a previous stage of oxidation to improve cyanidation of silver.

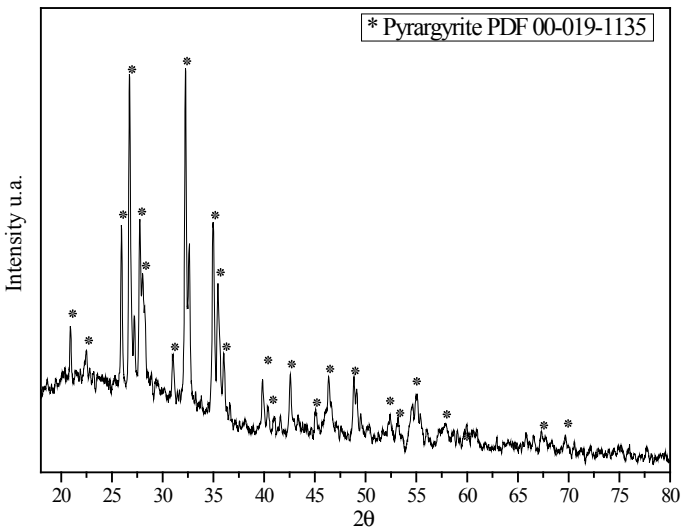

Fig. 2 X-ray diffraction spectra (DRX) of the pyrargyrite

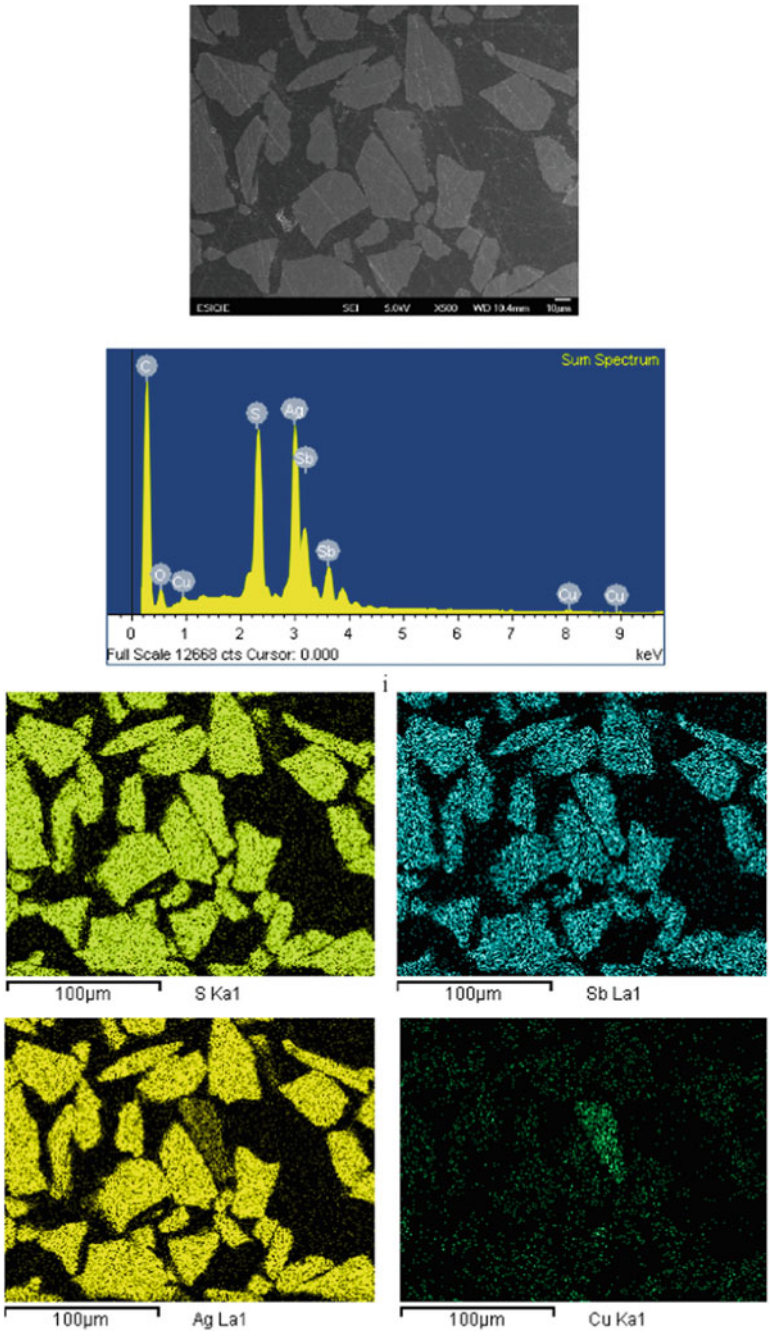

Fig. 3 Micrographs of SEM and elementary mapping of the pyrargyrite

Table 1 Semi-quantitative analysis of the pyrargyrite mineral by EDS

Element	Percentage % w/w
Sulfur	16.25
Oxygen	7.90
Copper	2.19
Silver	52.78
Antimony	20.89

The results of the pre-oxidation and leaching tests of silver with cyanide are shown in Fig. 4, and in general, it is observed that the percentage of extraction constantly increases with the reaction time. Better recoveries of silver with longer oxidation time 120 h and 0.052M of $Na_2S_2O_5$ (2.5% Ag extraction) would be expected; however, for the same concentration of metabisulfite and 68 h of leaching with a cyanide concentration of 0.037M, the silver recovery of the oxidized ore is significantly higher, obtaining around 25%.

The expected cyanidation reaction would be as indicated in Eq. 2. On the other hand, when a concentration of 0.210 M of $Na_2S_2O_5$ and 200 h of leaching is used, maximum silver extraction is achieved at around 37%.

$$2Ag^{\circ} + 4CN^{-} + 2H_2O + O_2 = 2\left[Ag(CN)_2\right]^{-} + H_2O_2 + 2OH^{-} \qquad (2)$$

From the monitoring of the pH and the ORP carried out during all the tests, it is necessary that, with the increase in leaching time, the pH of the pulp tends to

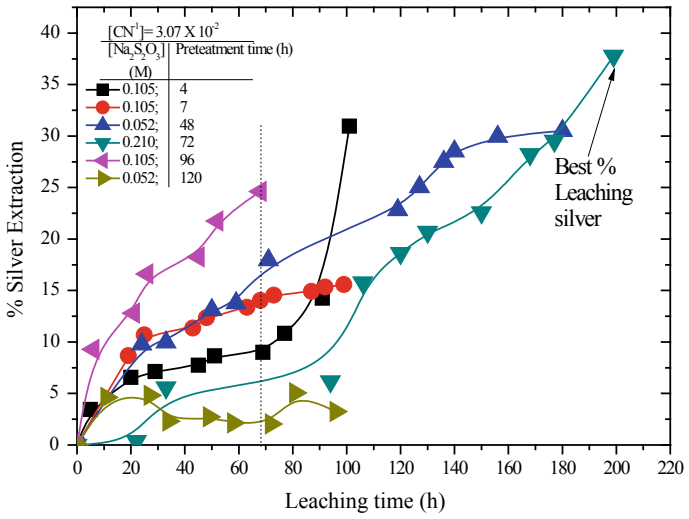

Fig. 4 % Silver extraction versus leaching time (h) for the different concentrations of metabisulfite and pre-oxidation times

decrease, this is due to the leaching of the rest of the components of the pyrargyrite, such as sulfur which forms $(SO_4)^{-2}$ sulfate ion in solution by lowering the pH, and in addition, from the analysis of antimony carried out via ICP, it was detected that solubilize is achieved up to about 20%.

With regard to ORP, this decreases its reducing character, that is, its negative value is lower with the increase in leaching time, due to the nature of the species formed during cyanidation. Figure 5 shows the micrograph of MEB–EDS and the elementary mapping of the residual powders, 180 h of leaching with pre-oxidized

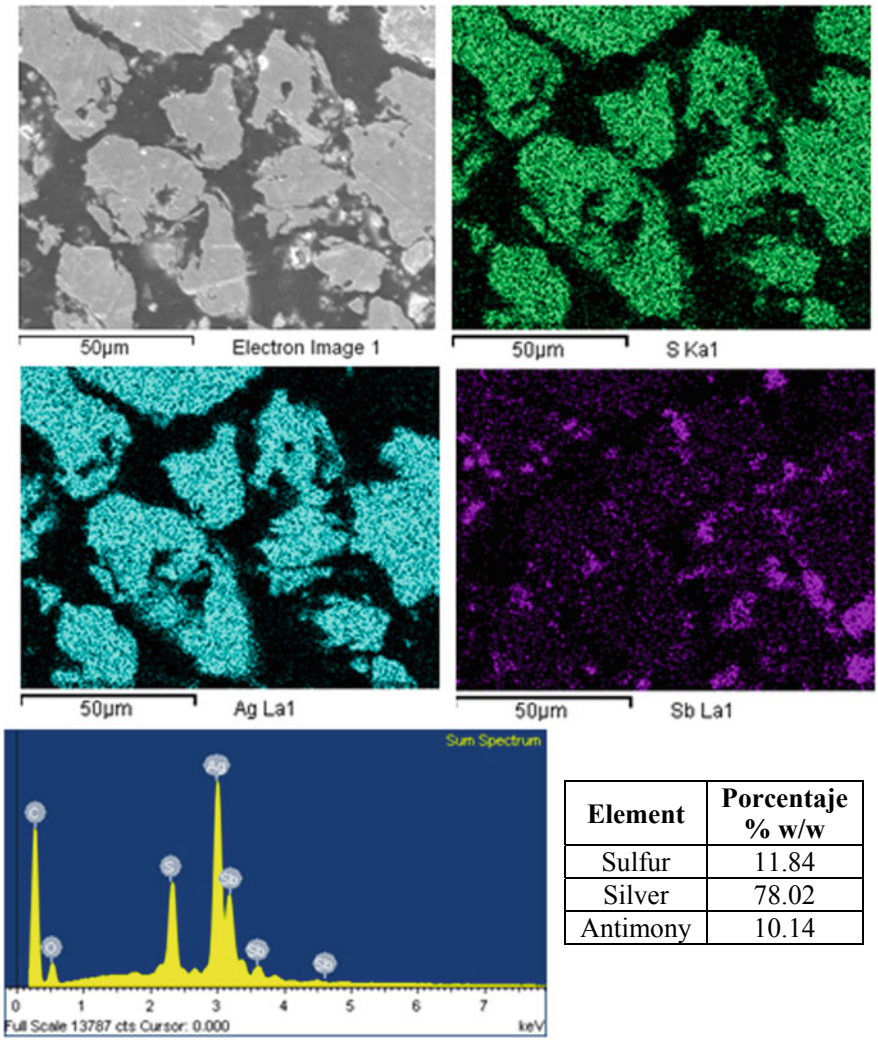

Element	Porcentaje % w/w
Sulfur	11.84
Silver	78.02
Antimony	10.14

Fig. 5 Micrograph of MEB–EDS and elementary mapping of the pyrargyrite mineral. Leach 180 h with 3.02×10^{-2}M cyanide, pre-oxidized with 0.052M $Na_2S_2O_5$

cyanide with 0.052M of sodium metabisulfite. As shown in Fig. 4, the extraction of silver is not total for this reason in the elementary mapping both sulfur, silver and antimony are detected, this presents a phenomenon of areas of greater concentration generally around the surfaces of pyrargyrite.

Figure 6 presents the analysis by Fourier transform infrared spectroscopy of the residual powders from the leaching of pyrargyrite for 180 h with 3.07×10^{-2}M of cyanide and pre-oxidized for 48 h with 0.210M of $Na_2S_2O_5$, as well as the spectra of oxidized pyrargyrite and antimony oxide Sb_2O_3. When the pyrargyrite remains without oxidizing, it is formed in the spectral region of the sulfate ion, the cleavage of the main band with three absorption bands where the sulfate is bound in a monodentate manner.

The absorption bands at 618, 875, 988, 1112, and 1455 cm^{-1} correspond to the Sb–O vibrations, which confirm the strong presence of these antimony oxides which affect success of leaching generating a layer of difficult access to carry out the extraction of silver.

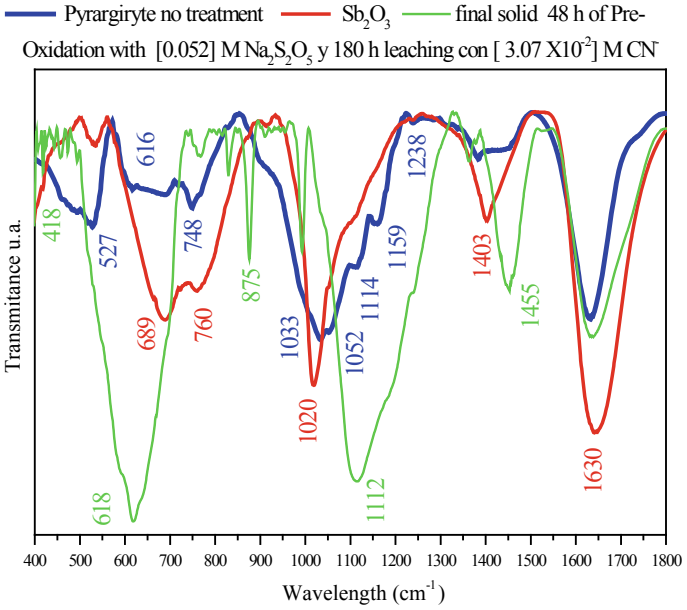

Fig. 6 Infrared spectra untreated pyrargyrite, final powders of the leaching process, and chemical reagent of antimony trioxide Sb_2O_3

Conclusions

Using the MEB–EDS and DRX techniques, it was found that the mineral studied corresponds to an Ag_3SbS_3 pyrargyrite and was the only crystalline phase detected by DRX indexed with the diffraction pattern PDF 00-019-1135. The best percentage of leaching of pyrargyrite is achieved when it is pre-oxidized for 68 h with 0.210M of metabisulfite and a cyanidation of 200 h with 3.07×10^{-2}M, and the increase in the concentration of metabisulfite and the pretreatment time does not contribute to achieve better recoveries. The low recoveries are attributed to the formation of species of antimony oxides detected by FTIR, around the surface forming a species refractory to the passage of cyanide, this Sb_2O_3 oxide passive the mineral surface and prevents the cyanidation from being carried out successfully.

Acknowledgements The authors would like to thank the Autonomous University of the State of Hidalgo, the Program for Professional Development PRODEP, and the National Polytechnic Institute unit ESIQUIE for their financial support.

References

1. Rodríguez-Rodríguez C, Nava-Alonso F, Uribe-Salas A (2014) Silver leaching from pyrargyrite oxidation by ozone in acid media. Hydrometallurgy 149:168–176
2. Logsdon MJ, Hagelstein K, Mudder Tl (1999) The management of cyanide in gold extraction. Int Counc Met Environ
3. Guo B, Peng Y, Espinosa-Gómez R (2014) Cyanide chemistry and its effect on mineral flotation. Miner Eng 66:25–32
4. La Brooy SR, Linge HG, Walker GS (1994) Review of gold extraction from ores. Miner Eng 7(10):1213–1241
5. Gunyanga FP, Mahlangu T, Roman RJ, Mungoshi J, Mbeve K (1999) An acidic pressure oxidation pre-treatment of refractory gold concentrates from the Kwekwe roasting plant—Zimbabwe. Miner Eng 12(8):863–875
6. Ciftci E (2000) Mineralogy, paragenetic sequence, geochemistry and genesis of the gold and silver bearing upper cretaceous mineral deposits, Northeastern Turkey, PhD Thesis, University of Missouri-Rolla, Faculty of the Graduate School, Geology and Geophysics, p 278
7. Corrans IJ, Angove JE (1991) Ultra fine milling for the recovery of refractory gold. Miner Eng 4(11):763–776
8. Rajala J, Deschênes G, Romanov A, Kolosay G (2011) Kupol mill leach operation in 2008–09. CIM J 2(2):79–84
9. Alp I, Celep O, Paktunç D, Thibault Y (2014) Influence of potassium hydroxide pretreatment on the extraction of gold and silver from a refractory ore. Hydrometallurgy 146:64–71
10. Raschman P, Sminčáková E (2011) Hydrometallurgy 113–114:60–66

Mechanical and Morphological Properties of Hybrid Composites Based on Recycled LDPE/EVA Blend Reinforced with Clay and Babassu Fiber Residues

Caroline S. Tamura, Mariana Arantes, Karina H. S. Carmo, Bianca S. Santos, Rene R. Oliveira and Esperidiana A. B. Moura

Abstract Over the years the consumption of plastic products made of conventional polymers has produced a large amount of waste which has led to disposal problems worldwide. Among the alternatives to minimize these problems are reuse and recycling practices. Then, the recycling of plastic and the use of recycled materials to produce new materials reinforced with nanoparticles from natural resources can be an alternative to reduce inappropriate waste disposal. The objective of this study is to investigate the effects of the addition of clay and non-treated babassu fiber residues on the mechanical and morphological properties of composite based on recycled LDPE/EVA blend. Composite materials containing 1–3 wt% of babassu residues and 1 wt% of clay were prepared using a twin-screw extruder machine and flat die single extrusion process, in order to prepare hybrid composites sheets. The sheets prepared by recycled LDPE/EVA blend and its composites were characterized by tensile tests, XRD, and FE-SEM analysis and the correlation between properties was discussed.

Keywords Blend · Recycled polymer · Flexible film · Babassu residues · Hybrid composite

Introduction

The petroleum-based polymers have been largely used due to its excellent characteristics and processing possibilities [1–3]. Large amount of waste has been generated increasing environmental concerns due to improper disposal of the residues. These

C. S. Tamura (✉) · M. Arantes · K. H. S. Carmo · B. S. Santos · E. A. B. Moura
Nuclear and Energy Research Institute (IPEN), Center of Chemical and Environmental Technology, Av. Prof. Lineu Prestes 2242, Sao Paulo, SP 05508-000, Brazil
e-mail: carolinetamura@gmail.com

R. R. Oliveira
Nuclear and Energy Research Institute, Center for Materials Science and Technology, Av. Prof. Lineu Prestes 2242, Sao Paulo, SP 05508-000, Brazil

J. Li et al. (eds.), *Characterization of Minerals, Metals, and Materials 2020*,
The Minerals, Metals & Materials Series,
https://doi.org/10.1007/978-3-030-36628-5_65

residues take many years to decompose by the fact that they have high degradation resistance and can generate many negative effects on the environment. This includes contamination of soil, groundwater sources, beyond the big volume occupied by them in the municipal solid waste landfills, and garbage dumps. One of the alternatives is to reuse and recycle the materials to minimize these problems and give a new application for these materials [4–7].

Recycling polymer materials followed by their reinforce with vegetal fiber residues can be a potential alternative to substitute conventional polymeric composites, based on neat polymer matrix and synthetic fibers, in certain applications. Despite the fact that mechanical properties of vegetal fibers are not high like that of many synthetic fibers, its origin from renewable sources, low density, and cost compared to synthetic ones, today it can be observed a great growth of their use in areas where high mechanical properties are not a requirement.

The use of vegetal fibers avoids an inappropriate disposition which can lead to forest burns destroying kilometers of green area in high speed, to natural habitat destruction, an increase of carbon dioxide in the atmosphere, and soil erosion [8–10].

The montmorillonite clay has been largely used for improving polymer properties such as mechanical resistance, water barrier, and fire resistance. However, it should be modified by quaternary salt addition before use in order to enhance the compatibility with polar polymer and improve the dispersion and intercalation between molecules chains of the polymer [11].

The propose of this work was to study the incorporation into the recycled polymer of babassu fiber waste, without the application of any treatment in the waste, aiming at a low-cost production, since it is a recycled polymeric matrix.

Materials and Methods

Materials

The materials used in this study were recycled LDPE (r-LDPE) (MFI = 0.13 g/10 min at 190 °C, 2.16 kg) from discarded pure water sachets, recycled EVA (r-EVA) (MFI = 20.14 g/10 min at 190 °C, 2.16 kg) from packaging industry waste, natural light green clay from Cubati, Paraiba, Brazil, and babassu coconut epicarp fiber residues from babassu oil industry.

Preparation of Light Green Clay

For the process of organophilic clay modification, initially, the light green clay was dispersed in deionized water in the ratio of 4 wt% with vigorous agitation for 30 min. After that, it was added to Na_2CO_3 (50 mEq of sodium per each 100 g of the natural

green clay). Thereafter, a quarternary ammonium salt was introduced into the clay, Hexadecyl trimethylammonium chloride (70 meq of the quarternary ammonium salt) was introduced with vigorous agitation for 30 min. The organophilic light green clay (LGC) was decanted for 24 h, was dried in an air-circulating oven, and, finally, was milled to fine powder.

Preparation of Babassu Coconut Epicarp Residues

The babassu coconut epicarp fiber (BF) were washed with water to remove impurities that can be aggregated to the fibers, in sequence, it was done an immersion of the fibers in deionized water for 24 h to have a deeper cleaning and after were dried at 60 °C for 24 h in an air-circulating oven. The dry residues were reduced to fine powder, with particle sizes equal or smaller than 150 μm, by using ball mills.

Preparation of Blend and Composites

The recycled LDPE/EVA blend (r-LDPE/EVA) (50/50 wt%) and its composite were processed by melt extrusion using a twin-screw extruder Haake Rheomix with 16 mm and L/D = 25 rate from Thermo Scientific. The temperature profile was 125/130/135/140/145/150. Screw speed was 30 rpm. The extrudates coming out of the extruder were cooled down for a better dimensional stability, pelletized by a pelletizer, and fed into a flat die single screw extruder Haake Rheomex P332, Thermo Scientific. The temperature profile used during processing was 140/145/150/155/160/165 °C for and the screw' rotation was 25 rpm. The Compositions of the blend and its composite are presented in Table 1.

Table 1 Compositions of the r-LDPE/EVA Blend and its composite

Materials	r-LDPE/EVA (%wt)	Babassu coconut epicarp fiber (%wt)	Organophilic light green clay (LGC) (%wt)
r-LDPE/EVA blend	50/50	–	–
r-LDPE/EVA/BF/LGC1	98	1	1
r-LDPE/EVA/BF/LGC3	96	3	1

Characterization Methods

Mechanical Tests

Tensile tests were performed using EMIC universal testing machine according to ASTM D 882-91 at room temperature and loading rates of 500 mm/min.

X-Ray Diffraction (XRD)

The XRD analysis of the blend and its composites were carried out using a Rigaku DMAX 2200 diffractometer, operated at 40 kV and 40 mA with a CuK_{α} radiation and 15.4 Å as wave length (λ).

Field Emission Scanning Electron Microscopy (FE-SEM)

Surfaces of cryofractured samples examined using a JEOL-JSM-7401 F, FE-SEM.

Results and Discussion

Characterization of the LGC

Figure 1 shows the XRD patterns of light green clay, the spectrums show three peaks with bigger intensity, its represents the montmorillonite peak ($2\theta = 5.5°$), kaolinite peak ($2\theta = 12.3°$) and quartz peak ($2\theta = 26.6°$). After the clay modification, it can be seen a displacement to the left from $2\theta = 5.5°$ to $2\theta = 4.6°$, which correspond to the increased distances between layers from 1.6 to 1.92 nm, which confirms the intercalation of the quaternary ammonium salt between the lamellar space of light green clay.

Characterization of the BF

The XRD spectrum for babassu coconut epicarp fiber is shown in Fig. 2. It can be seen three characteristic peaks of vegetal fibers. The principal peak in 22.96° corresponds to cellulose diffraction, in which we also have peaks around 16.21° and 34.14° that is also characteristic of the cellulose presence.

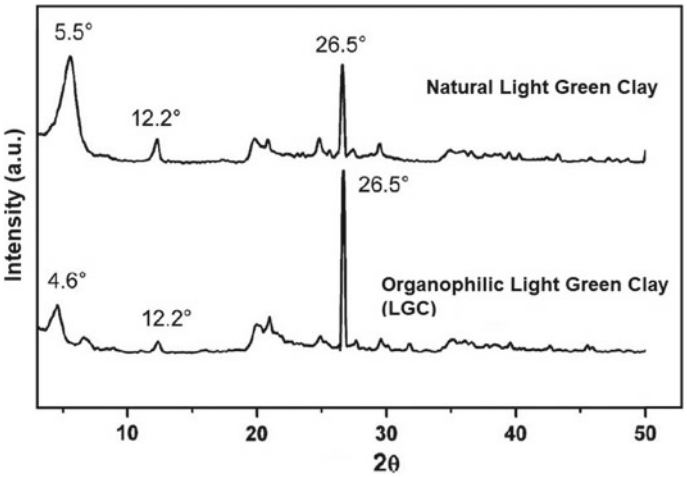

Fig. 1 XRD patterns of natural clay and organophilic clay

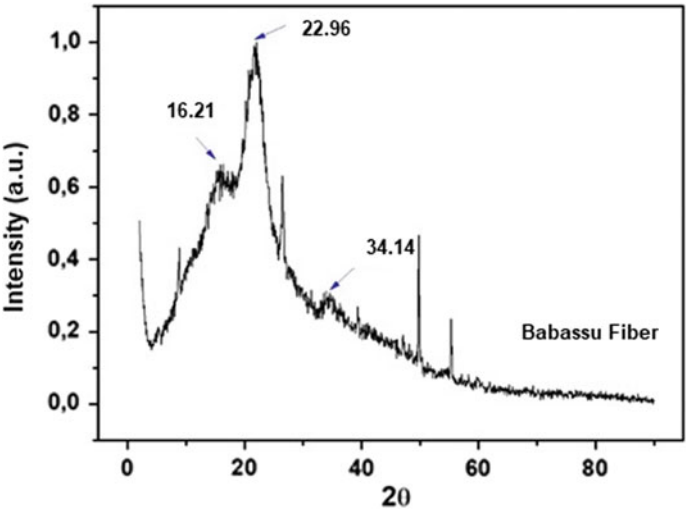

Fig. 2 XRD patterns of babassu coconut epicarp fiber

Characterization of the r-LDPE/EVA Blend and its Composites

Figure 3 shows the XRD spectrum for r-LDPE/EVA blend and its composites with the characteristic peaks of the composition. It can be seen that there is a reduction in the XRD spectrum intensity of r-LDPE/EVA blend with the increase of babassu coconut epicarp fiber incorporation.

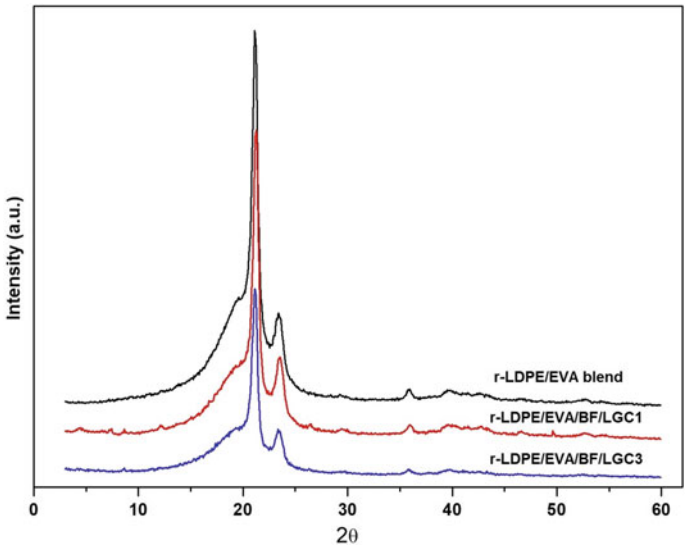

Fig. 3 XRD diffraction patterns for the r-LDPE/EVA blend and its composites

It also measured the incorporation of the reinforcement using the FEG-SEM technique. Figure 4 shows the micrography of cryofractured surface images of the composite with higher fiber percentage. It was seen that there was no good interaction between the materials, and there was a gap found between the reinforcement phase and the matrix phase.

For the final characterization, the tensile tests were carried out. The diagram stress × strain for tensile tests are shown in Fig. 5. Figure 5 shows medium values calculated from the data obtained in the test for eight samples. It can be seen that the blend required more tension to deform compared to its composites. Besides that, when the fiber percentage is higher, lower is the tension to the deformation.

The tensile strength at break, elongation at break (%), and Young's modulus are presented in Table 2. It can be seen that there was a decrease in tensile strength at break and Young's modulus with the fiber incorporation. These results are according to FE-SEM image results that show the non-homogeneous distribution of fiber in the matrix, presence of fiber agglomerates, and poor surface adhesion between fiber and r-LDPE/EVA blend.

Conclusions

The results showed losses in tensile properties due to babassu fiber residues and light green clay incorporation. SEM examination showed that there was not a good interaction between the r-LDPE/EVA blend/babassu fiber interface. However, it is necessary

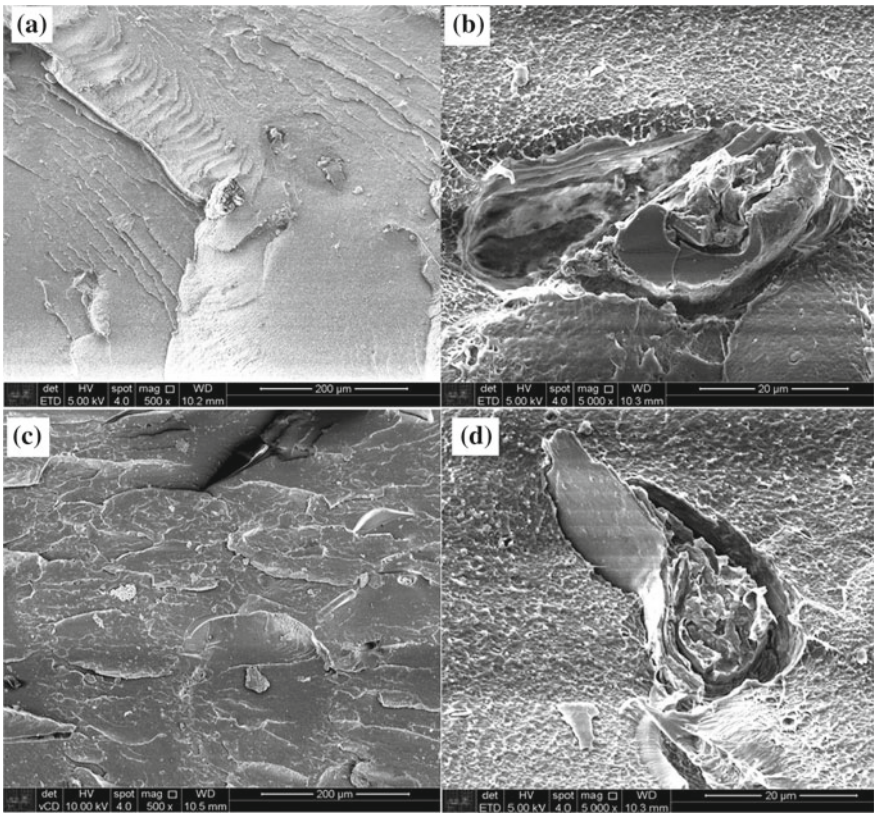

Fig. 4 SEM images of the composite containing 3 wt% of babassu fiber: **a** (500 ×), **b** (5.000 ×), **c** (500 ×), and **d** (5.000 ×)

to investigate new methods to the incorporation of babassu fiber residues in the polymer matrix, for instance, carry out preview treatment in babassu fiber residues, by some of the different methods already described in the literature, such as mercerization, in order to improve the compatibility between these wastes and the polymer matrix, in order to obtain a composite material with improved mechanical properties compared to the recycled blend. On the other hand, a study about the addition of a compatibilizer agent that will contribute to a better interface between fiber/polymer can be also one another possibility to enhance the mechanical properties of the final composites.

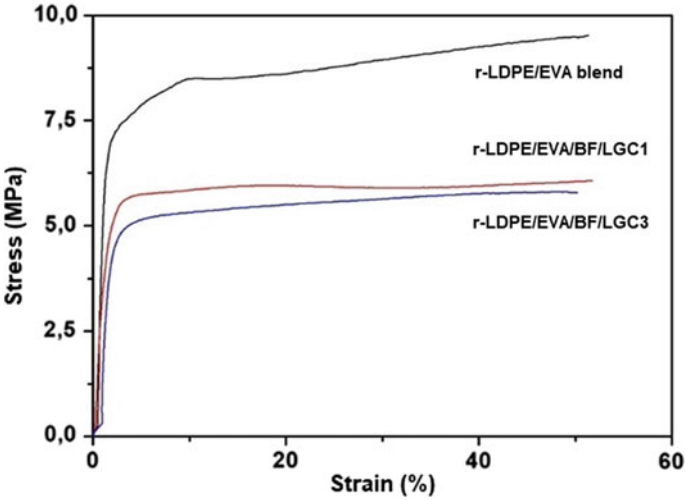

Fig. 5 Diagram stress (MPa) × strain (%) for tensile tests of the blend and its composites

Table 2 Tensile test results for r-LDPE/EVA blend and its composites

Materials	Tensile strength at break (MPa)	Elongation at break (%)	Young's modulus (GPa)
r-LDPE/EVA blend	10.12 ± 0.9	99.78 ± 2.5	0.72 ± 0.2
r-LDPE/EVA/BF/LGC1	8.66 ± 1.5	111.48 ± 9.3	0.46 ± 0.2
r-LDPE/EVA/BF/LGC3	5.96 ± 0.2	49.98 ± 9.9	0.42 ± 0.1

Acknowledgements The authors wish to thank IIAEA-CRP# 17760 RO, FAPESP, and CNPq to provide support for this work.

References

1. Dicker MPM, Duckworth PF, Baker AB, Francois G, Hazzard MK, Weaver PM (2014) Green composites: a review of material attributes and complementary applications. Compos Part A Appl Sci Manuf 56:280–289
2. La Mantia FP, Morreale M (2011) Green composites: a brief review. Compos Part A Appl Sci Manuf 42:579–588
3. Abdul Khalil HPS, Bhat AH, Ireana Yusra AF (2012) Green composites from sustainable cellulose nanofibrils: a review. Carbohydr Polym 87:963–979
4. Najafi SK (2013) Use of recycled plastics in wood plastic composites—a review. Waste Manag 33:1898–1905
5. Azwa ZN, Yousif BF, Manalo AC, Karunasena W (2013) A review on the degradability of polymeric composites based on natural fibres. Mater Des 47:424–442

6. Ammala A, Bateman S, Deana K, Petinakis E, Sangwan P, Wong S, Yuan Q, Yu L, Patrick C, Leong KH (2011) An overview of degradable and biodegradable polyolefins. Prog Polym Sci 36:1015–1049
7. Scott G (2000) Green' polymers. Polym Degrad Stab 68:1–7
8. Ardanuy M, Antunes M, Velasco JI (2012) Vegetable fibres from agricultural residues as thermo-mechanical reinforcement in recycled polypropylene-based green foams. Waste Manag 32:256–263
9. Sahari J, Sapuan SM (2011) Natural fibre reinforced biodegradable polymer composites. Rev Adv Mater Sci 30:166–174
10. Yan L, Chouw N, Jayaraman K (2014) Flax fibre and its composites—a review. Composites: Part B 56:296–317
11. GOMES LVR (2016) Preparação e caracterização de nanocompósitos de polipropileno reforçados com argila verde lodo e fibra de castanha-do-brasil. Doutor em Engenharia Metalúrgica e de Materiais. Tese, Escola Politécnica da Universidade de São Paulo

Preparation of Lithium Ion Battery Anode Materials from Precipitation Flotation Product

Huanhuan Miao, Wenjuan Wang, Yanfang Huang and Guihong Han

Abstract The anode materials for lithium ion battery can be prepared from the heavy metal ion flotation product in the metal-containing wastewater. Porous Cu–Fe–metal organic frameworks (MOFs) were pyrolyzed and synthesized from precipitation flotation product in this study. When treated as a self-template by pyrolysis of Cu–Fe–MOFs at 750 °C for 1.0 h in an air atmosphere, the porous composite oxides containing $CuFe_2O_4$ and Fe_2O_3 were prepared and tested as anode materials for lithium ion batteries (LIBs). The electrochemical measurements demonstrated that the composite oxides released an initial discharge capacity of 1453.4 mAh g^{-1} at the current density of 100 mA g^{-1} and remain reversible capacity of 519.5 mAh g^{-1} after 50 cycles, together with superior cyclic stability and unique structure. The composite oxides can be seen as to be a promising anode material for LIBs. This work can realize the effective utilization of heavy metal resources from wastewater recycling.

Keywords Precipitation flotation · Anode material · Composite oxides · Metal ions

Introduction

Heavy metal waste residue is usually disposed in a stacked manner, which can cause serious pollution to the environment, so the resource utilization of waste residue after heavy metal wastewater treatment is an urgent problem to be solved today [1]. In the former work, we studied the precipitation flotation removal of Cu(II) with humic precipitant from wastewater simulants [2]. And the waste residue was the porous metal organic frameworks (MOFs) which were obtained by precipitation flotation experiments. Based on the highly flexible in nature, MOFs can be designed and constructed the materials with large specific surface and suitable aperture distribution

H. Miao · W. Wang · Y. Huang · G. Han (✉)
School of Chemical Engineering and Energy,
Zhengzhou University, Zhengzhou 450001, People's Republic of China
e-mail: hanguihong@zzu.edu.cn

J. Li et al. (eds.), *Characterization of Minerals, Metals, and Materials 2020*,
The Minerals, Metals & Materials Series,
https://doi.org/10.1007/978-3-030-36628-5_66

[3–5]. Considering that the performance of lithium ion battery electrode materials is deeply affected by the specific surface area, pore size distribution, crystallinity, etc., this kind of MOFs can be used as both a precursor and a self-sacrificing template for the material preparation [6–8]. In order to obtain the electrode materials with excellent electrochemical performance, the structure and morphology of the materials can be controlled by appropriate pyrolysis treatment [9].

Researchers have proposed that porous structures can provide space for the intercalation and extrusion of lithium ion. It can be concluded that the electrochemical properties of the electrode materials prepared by porous MOF-based materials are optimal [10, 11].

In this paper, for the resource utilization of waste residue, the preparation of anode materials for lithium ion batteries with MOFs was studied. The system included the synthesis of MOFs and the preparation of materials with porous structure. In addition, the structures and morphologies and the electrochemical properties of the anode materials prepared for LIBs were investigated under different pyrolysis conditions.

Experiments

Synthesis and Processing of MOFs

First of all, the humic acid (HA) is purified by acid extraction, and heavy metal wastewater is simulated with Cu^{2+} solution. Then, the precipitation flotation experiment is carried out. In the Cu^{2+} wastewater, HA precipitant is added to carry out the chelation reaction for 30 min, then the flocculent $FeCl_3$ is added and the solution is stirred stably for 10 min. When the stable flocculation is formed, the cationic surfactant CTAB is added, and the solution is transferred to the microbubble flotation column after 3 min reaction for waste residue and purified water collection. Finally, in the air atmosphere, the foam obtained by the precipitation flotation is heated to 200, 500, and 750 °C at a heating rate of 5 °C min^{-1}, which are pyrolyzed at this temperature for 1.0 h to obtain the active materials.

Physical Characteristics

X-ray diffraction (XRD) measurements were carried out using D8 ADVANCE diffractometer with Cu–K α-radiation ($\lambda = 0.15406$ nm), and 2θ was in the range of 10°–80° at a scanning rate of 0.3°s^{-1}. The particle morphologies were observed at 5.0 kV by a field emission scanning electron microscope which was equipped with analysis software.

Electrochemical Measurements

For the preparation of LIBs anode materials, the active material (80 wt%), conductive agent acetylene black (10 wt%), and special binder PVDF (10 wt%) were dispersed in N-methyl-2-pyrrolidone. For the assembly of LIBs, the resulting slurry was applied to the copper coil substrate, and then dried in vacuum overnight at 60 °C, and the electrode was pressed into a disk having a diameter of 8 mm, wherein the active material loading on each electrode was about 1–3 mg. The electrodes were assembled into coin-like battery (CR2032) in glove box filled with argon, wherein the oxygen and water vapor pressures less than 0.1 ppm in the glove box.

The constant current charge/discharge test was tested at the LAND-CT2001A battery test system. The measurements were obtained in the potential range of 0.1–1.5 V relative to Li/Li^+. Cyclic voltammetry (CV) and electrochemical impedance spectroscopy (EIS) measurements were performed at the Autolab PGSTAT204 (Holland) electrochemical workstation. CV measurements were made between 0.05 and 3.0 V at a scanning rate of 0.3 mV s^{-1}. EIS measurements were obtained by applying the AC amplitude of 5 mV in the frequency range of 10^{-2}–10^5 Hz.

Results and Discussion

Characterization of Active Materials

The XRD diffractograms of the active materials are shown in Fig. 1. The material with calcination temperature of 200 °C has a taro peak around $2\theta = 25°$, which is consistent with the characteristics of organic matter. As the calcination temperature increases, the characteristic peaks of the material with calcination temperature of 500 °C correspond to composite oxide which includes with CuO, Fe_3O_4, and $CuFe_5O_8$. The characteristic peaks of the material with calcination temperature of 750 °C correspond to composite oxide containing $CuFe_2O_4$ and Fe_2O_3.

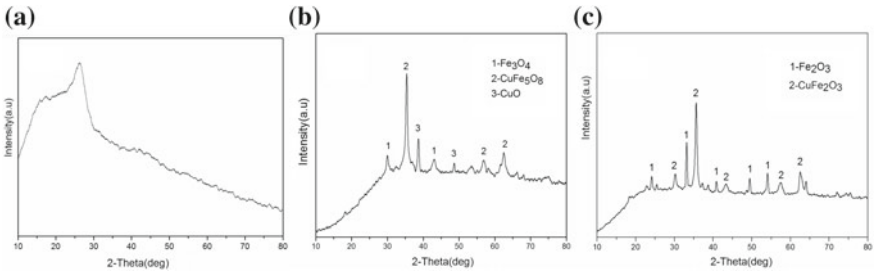

Fig. 1 XRD diffractograms of the active materials which were obtained by calcination temperature of **a** 200 °C, **b** 500 °C, and **c** 750 °C

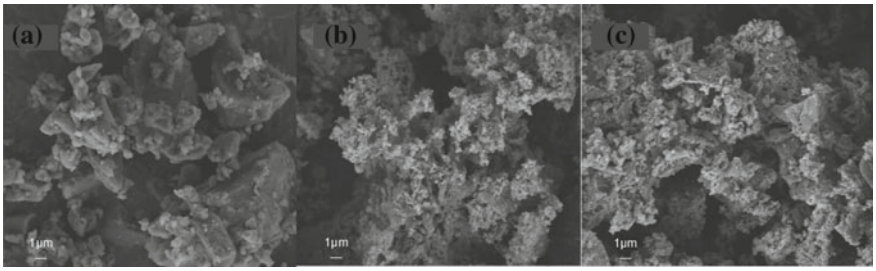

Fig. 2 SEM micrographs of the active materials which were obtained by calcination temperature of **a** 200 °C, **b** 500 °C, and **c** 750 °C

SEM micrographs of active materials are shown in Fig. 2. When the calcination temperature is 200 °C, the active material of the block structure which has small number of pores on the surface is depicted in Fig. 2a. When the calcination temperature is 500 °C, the active material has remarkable pore structure. Further, as shown in Fig. 2c, when the calcination temperature is 750 °C, the active material has porous structure.

Cu–Fe–MOFs are obtained by precipitation flotation and then subjected to a pyrolysis operation. As the calcination temperature increases, the molecular chain of the chelate can release some small molecular substances, such as CO_2 and CO. After that, the pore structure is increased, and porous structure is formed.

The Electrochemical Performances

The active materials are fabricated as anodes, and the constant current charge and discharge curve of the electrodes are shown in Fig. 3. The first discharge specific capacities of the three electrodes are 911.1 mAh g^{-1}, 1094.5 mAh g^{-1}, and 1453.4 mAh g^{-1}, respectively. The second discharge specific capacities of the three electrodes are 264.9 mAh g^{-1}, 705.5 mAh g^{-1}, and 984.3 mAh g^{-1}, respectively. The

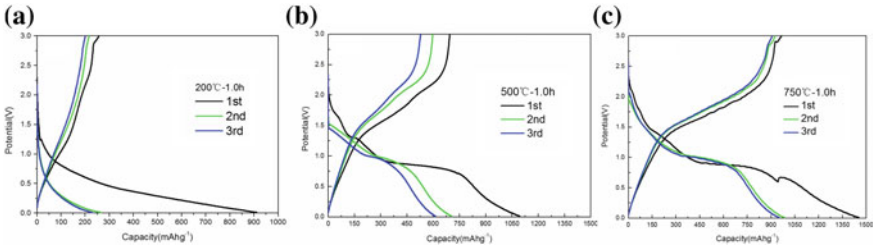

Fig. 3 Charge/discharge curve of active materials which were obtained by calcination temperature of **a** 200 °C, **b** 500 °C, and **c** 750 °C at the current density of 100 mA g^{-1}

reason for the capacity decay is that some irreversible reactions occur during the first charge/discharge, including the formation of solid electrolyte interface (SEI).

The cycle performances of the three electrodes are shown in Fig. 4. It can be observed that the discharge specific capacity of the three electrodes decreases slowly with the increase in the cycle number, and the coulomb efficiencies are maintained above 96% after 50 cycles. When the calcination temperature is 200 °C, the specific capacity of the active material drops sharply after the first charge and discharge cycle, after 30 cycles, the active material is activated to improve the storage performance of lithium, thereby its specific capacity shows an upward trend. When the calcination temperature is 500 °C, the specific capacity of the active material begins to decay after the first cycle and remains stable at a lower level after about 35 cycles, and after 50 cycles, the capacity is only 182.2 mAh g^{-1}. When the calcination temperature is 750 °C, the specific capacity of the active material also shows a downward trend, but the rate of decline is slow, after 50 cycles, the specific capacity is maintained at 519.5 mAh g^{-1}.

In summary, the electrode with calcination temperature of 750 °C exhibits the best cycle stability and high capacity compared to the electrodes which are obtained by calcination at 200 and 500 °C. The porous structure of the material which is obtained by calcination at 750 °C provides a number of sites for nucleation, which ensures efficient volume expansion space for the insertion and embedding of lithium ions, so that increases the stability and specific capacity of the electrode.

Figure 5 shows the Nyquist plot of the three electrodes. The high frequency semicircle is related to the charge transfer resistance. The electrode with calcination temperature of 750 °C has the lowest charge transfer resistance, indicating that this porous material is beneficial to reduce ion diffusion resistance and improve the electron transport speed of the electrode material.

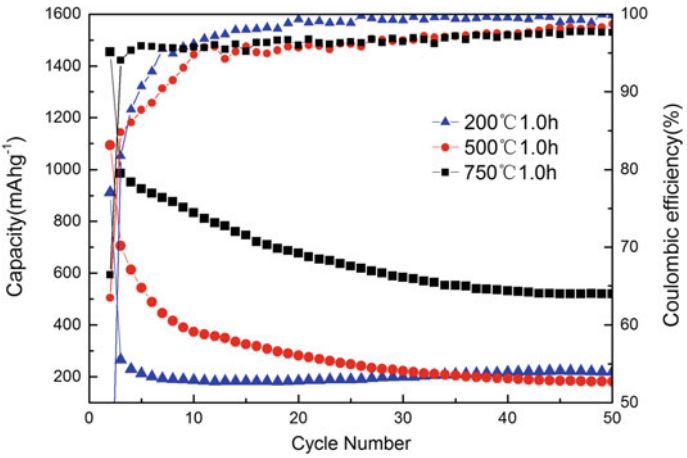

Fig. 4 Cycle performances of the active materials at the current density of 100 mA g^{-1}

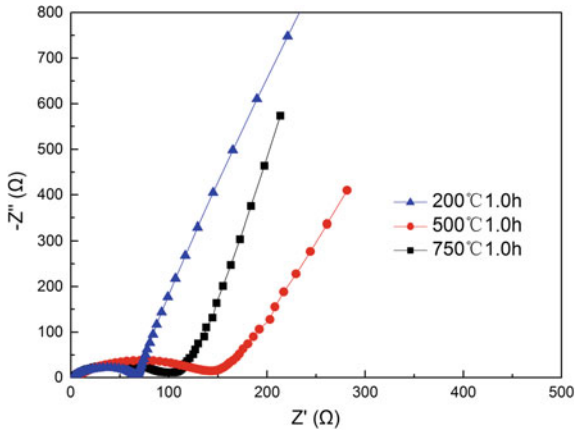

Fig. 5 Nyquist plots of the active materials

Conclusions

In this study, the porous composite is prepared by calcining Cu–Fe–MOFs in air atmosphere, wherein Cu–Fe–MOFs were obtained by precipitation flotation treatment of heavy metal wastewater. XRD and SEM results show that the synthesized materials have pore structure. The electrochemical performances show that when the calcination temperature is 750 °C, the reversible capacity of the prepared electrode can be maintained at 519.5 mAh g^{-1} after 50 cycles at the current density of 100 mA g^{-1}, and the electrode has the highest cycle stability and minimal charge transfer resistance, so the electrochemical performances are superior to the electrochemical performance of the electrode prepared at a calcination temperature of 200 and 500 °C. This study provides a possible direction for the development of high capacity for MOF-based anode materials.

Acknowledgements The authors acknowledge the financial support from the National Science Fund of China (No. 51674225 and No. 51774252), the Innovative Talents Foundation in Universities in Henan Province (No. 18HASTITO11), the Educational Commission of Henan Province of China (No. 17A450001, 18A450001), and the China Postdoctoral Science Foundation (No. 2017M622375).

References

1. Wang JL, Chen C (2015) The current status of heavy metal pollution and treatment technology development in China. Environ Technol Rev 4:39–53
2. Wu HY, Wang WJ, Huang YF (2019) Comprehensive evaluation on a prospective precipitation-flotation process for metal-ions removal from wastewater simulants. J Hazard Mater 371:592–602
3. Mohadeseh S, Mohammad MF, Nasser E, Shohreh J, Ali O, Mehrdad K (2019) A review on metal-organic frameworks: synthesis and applications. Trac-Trends Anal Chem 118:401–425

4. Yap MH, Fow KL, Chen GZ (2017) Synthesis and applications of MOF-derived porous nanostructures. Green Energy Environ Sci 2:218–245
5. Zhong M, Kong LJ, Li N (2019) Synthesis of MOF-derived nanostructures and their applications as anodes in lithium and sodium ion batteries. Coord Chem Rev 388:172–201
6. Han Y, Zhao ML, Dong L (2015) MOF-derived porous hollow Co_3O_4 parallelepipeds for building high-performance Li-ion batteries. J Mater Chem A 3:22542–22546
7. Zhang JJ, Yu AS (2015) Nanostructured transition metal oxides as advanced anodes for lithium-ion batteries. Sci Bull 9:823–838
8. Peng HJ, Hao GX, Chu ZH, He CL (2017) Mesoporous spindle-like hollow CuO/C fabricated from a Cu-based metal-organic framework as anodes for high-performance lithium storage. J Alloy Compd 727:1020–1026
9. Ke F, Qiu LG, Yuan YP (2012) Fe_3O_4@MOF core–shell magnetic microspheres with a designable metal-organic framework shell. J Mater Chem 22:94–97
10. Yin YH, Yu XX, Li QW, Cao ML (2017) Hollow porous CuO/C composite microcubes derived from metal-organic framework templates for highly reversible lithium-ion batteries. J Alloy Compd 706:97–102
11. Song YH, Chen YQ, Wu JF, Fu YY (2017) Hollow metal organic frameworks-derived porous ZnO/C nanocages as anode materials for lithium-ion batteries. J Alloy Compd 694:1246–1253

Processing and Characterization of Polyethylene-AgNPs Films—Biocide Effect

Washington Luiz Oliani, Luiz Gustavo Hiroki Komatsu, Ademar Benevolo Lugao, Vijaya Kumar Rangari and Duclerc Fernandes Parra

Abstract Low-density-polyethylene (LDPE) and Linear-low-density-polyethylene (LLDPE) nanocomposites films containing silver nitrate ($AgNO_3$) and surfactant oleic acid (AO) were manufactured via extrusion and subsequently characterised. The films were evaluated by scanning electron microscopy (SEM), energy dispersive spectroscopy (EDX), differential scanning calorimetry (DSC), transmission electron microscopy (TEM), and infrared spectroscopy (FTIR). Further, the antibacterial properties of the films were investigated against *Escherichia coli* (Gram-negative) and *Staphylococcus aureus* (Gram-positive) bacteria. The results indicated that LDPE nanocomposite films containing AgNPs have the potential to be used in antimicrobial packaging for food applications.

Keywords Polyethylene · Silver nitrate · Oleic acid · Nanocomposite · Biocide

Introduction

In recent years, there was an increased demand in the polymer industry for producing packaging films that are more efficient barrier and stronger materials than those already in the market. PE shows a wide spectrum of commercial applications potential in the packaging industry due to their well-known good mechanical properties, specifically good processability, high stiffness in molded parts, high resistance to tearing, as well as relative low price [1, 2]. Antibacterial packaging is the packaging system, which is able to kill or inhibit the growth rate of microorganisms that contaminate foods [3].

The growing interest in polymer nanocomposites that are advanced functional materials composed of nanoparticles dispersed in a polymeric matrix. An important

W. L. Oliani (✉) · L. G. H. Komatsu · A. B. Lugao · D. F. Parra
Nuclear and Energy Research Institute, IPEN, CNEN/SP, Av. Prof. Lineu Prestes, 2242 – Cidade Universitária – CEP, São Paulo 05508-000, Brazil
e-mail: washoliani@usp.br

V. K. Rangari
Department of Materials Science and Engineering, Tuskegee University, Tuskegee, USA

J. Li et al. (eds.), *Characterization of Minerals, Metals, and Materials 2020*,
The Minerals, Metals & Materials Series,
https://doi.org/10.1007/978-3-030-36628-5_67

application of polymer nanocomposites is in antimicrobial materials. They are not only used in medical applications such as catheters and prostheses, but also in food packaging [4, 5].

The incorporation of AgNPs in polymers such as plastics [e.g., polyethylene (PE) [6], polypropylene (PP) [7], polystyrene (PS) [8], polyurethane (PU) [9], thermoplastic elastomer (TPE) [10], and polyvinyl chloride (PVC) [11]] to form nanocomposites is always interesting because of their possible antibacterial activity in combination with the mechanical properties of conventional plastics.

Recently, safe biocompatible inorganic antibacterial nanoparticles with high stability under processing conditions, such as metals and metal oxides, have been preferred to organic antibiotics due to microbial resistance to the continuous use of organic products [12].

Several polymeric materials with different molecular weight such as polyethylene glycol (PEG), polyvinyl alcohol (PVA), poly(N-vinyl-2-pyrrolidone) (PVP), and others, mainly water soluble, have been used as coatings of silver nanoparticles to enable particle dispersion [13], and silver nanoparticles stabilized with oleic acid (AO) [14, 15] showed clear advantages in antibacterial activity, penetration bacteria cells, cytotoxicity, time effectiveness, efficiency, and stability against light [16].

The antimicrobial activity of these nanoparticles of silver maybe related to several mechanisms including, induction of oxidative stress due to generation of reactive oxygen species (ROS) which may cause the degradation of the membrane structure of cell and release of ions from the surface of nanoparticles that has been reported to cause bacterial death due to binding to cell membrane [17].

This respective research, the LDPE/LLDPE, has been employed as polymeric matrix for nanocomposites films. The compounds have been altered by the addition of silver nitrate and oleic acid with the use of ultrasound, and polyethylene nanocomposite (PENC). Such materials can be very valuable in films for biocide activity applications.

Materials and Methods

Materials

LDPE with a melt flow index—MFI (190/2.16) of 0.27 dg min^{-1} and density 0.92 g mL^{-1}, LLDPE with a melt flow index—MFI (190/2.16) of 0.80 dg min^{-1} and density 0.92 g mL^{-1}, Braskem (Brazil) were provided in the form of pellets. The silver nitrate ($AgNO_3$) and oleic acid (AO) were supplied by Labsynth. The commercial clay Cloisite 20 was provided by BYK Additives Company, and antioxidant (BASF Irganox B 225 ED) was added in small quantities, 2.0 wt%, to prevent the polyethylene from oxidizing and thermally cross-linking at elevated temperatures. The compatibilizer agent, polyethylene-grafted maleic anhydride (PE-g-MA), was supplied by Addivant (Polybond 3029). Three different formulations containing the LDPE/LLDPE were prepared and are represented in Table 1.

Table 1 Composition of constituents of polyethylene nanocomposites (wt%)

Samples	Matrix	Irganox	Cloisite (clay-MMT)	PE-g-MA	$AgNO_3$
PE	LDPE/LLDPE	2	–	–	–
PENC1	LDPE/LLDPE	2	1	2	1
PENC2	LDPE/LLDPE	2	–	2	1

The ultrasound equipment model USC-1400, with a working frequency of 40 kHz and maximum intensity output of 135 W RMS, was used to synthesis silver nanoparticles in oleic acid solution. The silver nitrate with AO solution was sonicated for approximately 30 min.

Preparation of the Nanocomposites

The LDPE/LLDPE (90/10) pellets were mixed with Irganox B 215 ED in a rotary mixer and maintained under this condition for 24 h. Then, the mixture was processed with the addition of clay (MMT 1% by weight), silver nitrate ($AgNO_3$ 1% by weight), and oleic acid in a twin-screw extruder Haake co-rotating, model Rheomex PTW 16/25, with the following processing conditions: The temperature profile (feed to die) was 145–170 °C, with a speed of 100 rpm. After processed, the nanocomposites were granulated in a granulator Primotécnica W-702-3. The PE films were produced in planar sheet extruder, and the material was placed directly into the hopper of the extruder with a temperature profile (feed to die) of 150–175 °C, screw speed of 50 rpm and torque of 33–45 N m. The films were produced with a thickness of ~0.05 mm.

Characterization

Scanning Electron Microscopy and Energy Dispersive X-Ray

Specimens were examined with a Hitachi TM3000 Table-top SEM coupled with a Bruker QUANTAX 70 for the collection of EDX data. SEM coupled with backscattered electron detector (BSE) and energy dispersive X-ray spectroscopy (EDX). Sample sections for the EDX analysis were taken at Analy Mode, and the acquisition period was 120 s.

Differential Scanning Calorimetry

Thermal properties of specimens were analyzed using a differential scanning calorimeter DSC 822, Mettler Toledo. The thermal behavior of films was obtained by: (1) heating from −50 to 280 °C at a heating rate of 10 °C min^{-1} under nitrogen atmosphere; (2) holding for 5 min at 280 °C; and (3) cooling to −50 °C and reheating to 280 °C at 10 °C min^{-1}. The crystallinity was calculated according to the equation:

$$X_C = P \cdot \frac{\Delta H_f \cdot 100}{\Delta H_0}$$

where ΔH_f is melting enthalpy of the sample, ΔH^0 is melting enthalpy of the 100% crystalline PE which is assumed to be 280 kJ kg^{-1} [18, 19], and P was the fraction content of PE in the sample.

Transmission Electron Microscopy

The morphology of the samples was examined with a JEOL JEM-2100 transmission electron microscope operating at voltage of 80 kV. Ultrathin sections (80 nm) were prepared with a Leica EM FC6 ultramicrotome with a diamond knife.

Infrared Spectroscopy

Infrared spectroscopy attenuated total reflection (FTIR-ATR) spectra of dried pristine and modified polyethylene films, in the wavelength range 4000–600 cm^{-1}, were analyzed using a PerkinElmer Spectrum 100 spectrometer (PerkinElmer Cetus Instruments, Norwalk, CT) with 64 scans.

Antibacterial Activity

The adapted standard JIS Z 2801 [20] was used for the tests. The cell suspension for the inoculum was 900×10^6 mL^{-1} CFU for each tested step. The following procedure was performed separately for each microorganism: Samples of the films of PE–AgNPs were placed in a sterile Petri dish and inoculated on the surface of 50 mL of suspension of each organism in an area of 40×40 mm^2. All of them were incubated for 24 h at 37 °C.

Results and Discussion

Scanning Electron Microscopy and Energy Dispersive X-Ray

The degree of dispersion of nanoparticles plays an important role in the properties of the nanocomposites. EDS combined with SEM was used to analyze the elemental composition comprising the films. Carbon, silicon, and silver, Fig. 1, and carbon and silver, Fig. 2, were found on the surface of the PE–AgNPs in polyethylene nanocomposite (PENC) matrix.

Figure 1 shows the good dispersion and distribution of silver and also silicon, and other clay constituents, such as aluminum and iron. In Fig. 2, in addition to the excellent distribution of silver particles, silver clusters can be observed on the film surface.

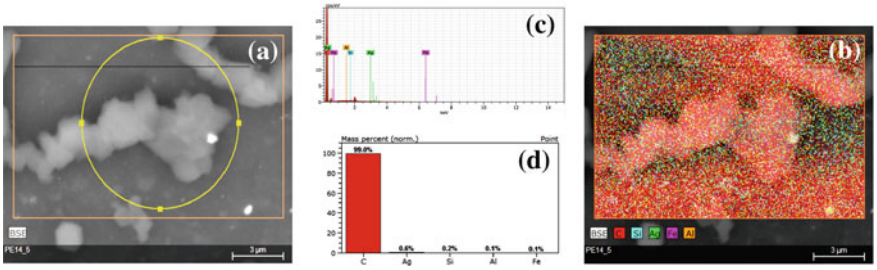

Fig. 1 SEM images and EDX mapping of AgNPs dispersed in the film of polyethylene. **a** SEM film PENC1, scale bar 3 μm; **b** mapping of the film with silver and silicon; **c** EDX data showed silver and silicon; and **d** semi-quantitative analysis of silver and silicon

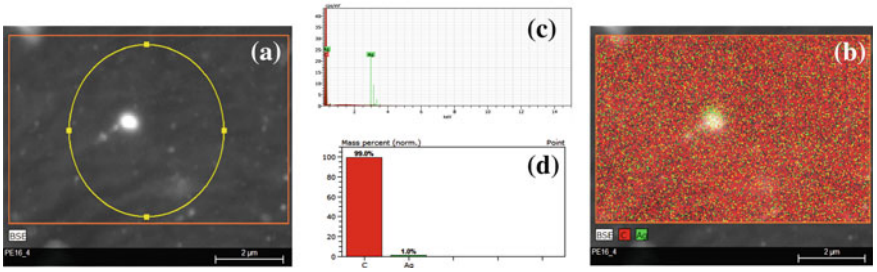

Fig. 2 SEM images and EDX mapping of AgNPs dispersed in the film of polyethylene. **a** SEM film PENC2, scale bar 2 μm; **b** mapping of the film with silver; **c** EDX data showed silver; and **d** semi-quantitative analysis of silver

Table 2 DSC data of PENC films during the second run of melting

Samples	Melting peak temperature, T_{m2}/°C (±0.1%)	Degree of crystallinity, X_C/% (±0.5%)
PE	112.1	32.0
PENC1	110.4	38.4
PENC2	111.0	32.8

Differential Scanning Calorimetry

The DSC results are shown in Table 2.

The incorporation of the MMT–AgNPs increased the degree of crystallinity (%) of PE from 32.0 to 38.4% in sample PENC1. This fact suggests that the AgNPs impart a high efficiency to the heterogeneous nucleation of PE, even at a very low AgNPs content (1.0 wt%). A research work which corroborates with the idea of this work was published by Benchacine et al. [21], and the silver incorporation in MMT plays an important role in the crystallinity degree X_C of PE that increases when Ag–MMT is added.

Transmission Electron Microscopy

The size and morphology of the nanofillers with a spherical format, synthesized with surfactant (oleic acid), were investigated with TEM, Fig. 3.

TEM microphotographs of PENC2–Ag compounds with oleic acid (OA) coated AgNPs are useful for determining particle dispersion. Oleic acid is also inexpensive,

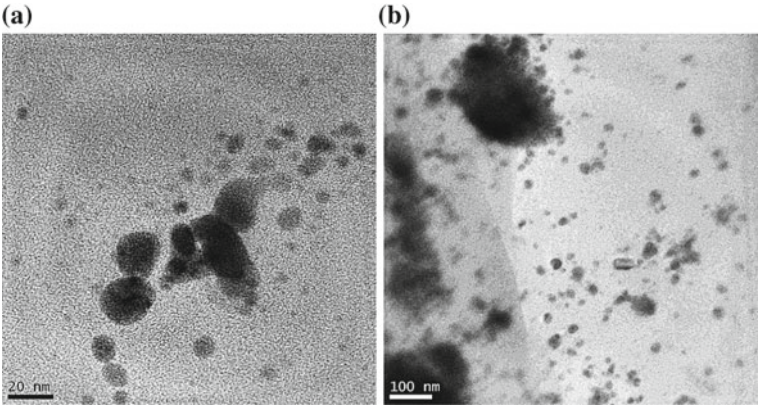

Fig. 3 TEM images of AgNPs dispersed in the film of polyethylene, PENC2. **a** TEM film PENC2, scale bar 20 nm, **b** TEM film PENC2, scale bar 100 nm

easy to use, and harmless to environment materials. As observed in Fig. 3a, the oleic acid-stabilized AgNPs are well-formed and nearly uniformly dispersed, while most of the AgNPs are discrete with moderate degrees of polydispersion.

We can clearly observe, Fig. 3b, the presence of aggregates of 150, 200 nm in size although some individual particles of about 10–30 nm in size can be distinguished. AgNPs dispersion is not complete but particles and aggregates remain in the nanoscale range.

Silver particles have a great tendency to form micro-aggregates, and the presence of a surfactant enhances better dispersion (at a nanoscale range) despite it is difficult to achieve total dispersion of individual particles even when using shear forces in the extrusion process [15].

Infrared Spectroscopy

In order to observe the presence of the oleic acid on the silver nanoparticles, infrared spectra of polyethylene films are shown in Fig. 4.

The band characteristic of oleic acid is that at 1746 cm^{-1} due to C = O stretching band of the carboxyl group (–COOH), indicating the monolayer surfactant-capped structure of the synthesized AgNPs, the O atom in the (–COOH) group of oleic acid offers an isolated electron to the silver atom and coordinates with the silver atom, corroborated by [22–24].

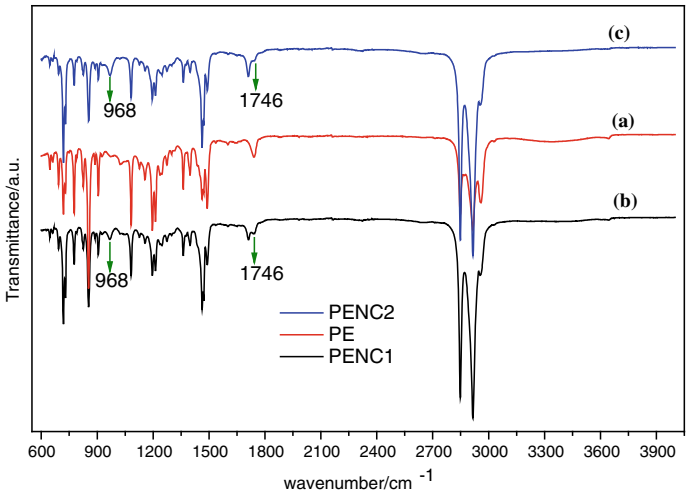

Fig. 4 FTIR-ATR spectra, **a** PE, **b** PENC1, and **c** PENC2

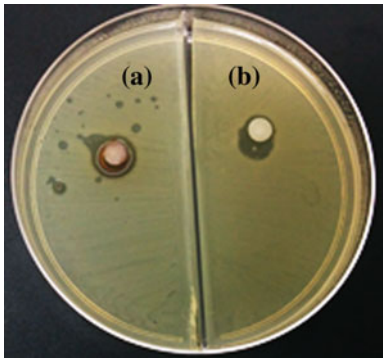

Fig. 5 Antibacterial activity of prepared samples against *E. coli* (**a**) and *S. aureus* (**b**)

Antibacterial Activity

The antibacterial activity of the prepared films was investigated using *S. aureus* and *E. coli* as model Gram-positive and Gram-negative bacteria. The antibacterial effects are shown in Fig. 5.

The results show that good dispersion and antimicrobial properties were obtained with AO as a surfactant against *S. aureus* and *E. coli*. The addition of coated $AgNO_3$ to the PE matrix represented an interesting solution for increasing protection against *S. aureus* and *E. coli*. The percentage reduction for the CFU assay showed positive 100% biocidal results for *S. aureus* and *E. coli* in film PE–AgNPs.

The inhibition zone diameters were greater for *E. coli* compared to *S. aureus*, demonstrating that the electrostatic attraction between positively charged silver ions and negatively charged bacterial cells was crucial for antibacterial activity. The antibacterial activity of PENC2 could be attributed to changes in the structure and morphology of bacterial cells by metallic silver and silver ions that were released from the films.

Conclusions

AgNPs stabilized with oleic acid were successfully synthesized. It was also presented that oleic acid-stabilized AgNPs had high levels of antibacterial activity against the Gram-positive human pathogen *S. aureus* and Gram-negative bacteria *E. coli*.

The addition of coated $AgNO_3$ to a PE matrix during the extrusion process represents an interesting solution for increasing the protection against *S. aureus* and *E. coli*. Silver in PE film properly hindered the bacterial activity in the bulk, furthermore, with the use of AO surfactant, indicates a better dispersion of AgNPs in the PE film and biocidal properties.

The modifier (oleic acid) used for silver nanoparticles improves adhesion between the nanoparticles and the PE matrix, shown in the good distribution of the silver nanoparticles in the PE as it was observed by TEM.

Acknowledgements The authors acknowledge financial support for this work from CNEN/IPEN, CAPES-Process: CSF-PVE's—88887.115684/2016-00, Centre of Science and Technology of Materials—CCTM/IPEN, for microscopy analysis (SEM and TEM), and the technicians Mr. Eleosmar Gasparin, Nelson R. Bueno, for technical support and ControlBio by testing for efficacy and antimicrobial activity.

References

1. Passador FR, Ruvolo-Filho A, Pessan LA (2016) Structural, thermal, and gas transport properties of HDPE/LLDPE blend-based nanocomposites using mixture of HDPE-g-MA and LLDPE-g-MA as compatibilizer. Polym Eng Sci 56(7):765–775
2. Liang JZ, Tan LC, Wang KJ, Li FJ, Zhang SD (2015) Melt elongation flow behaviour of LDPE/LLDPE blend. Polym Test 41:133–139
3. Dehnavi AS, Aroujalian A, Raisi A, Fazel S (2013) Preparation and characterization of polyethylene/silver nanocomposite films with antibacterial activity. J Appl Polym Sci 127(2):1180–1190
4. Pavoski G, Kalikoski R, Souza G, Brum LFW, Santos C, Marked AA, Santos JHZ, Font X, Erba I, Galland GB (2018) Synthesis of polyethylene/silica-silver nanocomposites with antibacterial properties by in situ polymerization. Eur Polym J 106:92–101
5. Deshmukha SP, Patila SM, Mullania SB, Delekara SD (2019) Silver nanoparticles as an effective disinfectant: a review. Mater Sci Eng C 97:954–965
6. Anh DH, Dumri K, Anh NT, Punyodom W, Rachtanapun P (2016) Facile fabrication of polyethylene/silver nanoparticle nanocomposites with silver nanoparticles traps and holds early antibacterial effect. J Appl Polym Sci 133:17, 43331, 1–8
7. Oliani WL, Parra DF, Komatsu LGH, Lincopan N, Rangari VK, Lugao AB (2017) Fabrication of polypropylene/silver nanocomposites for biocidal applications. Mater Sci Eng C 75:845–853
8. Deng Z, Zhu H, Peng B, Chen H, Sun Y, Gang X, Jin P, Wang J (2012) Correction to Synthesis of PS/Ag nanocomposite spheres with catalytic and antibacterial activities. J Appl Mater Interf 4(10):5625–5632
9. Madkour TM, Abdelazeem EA, Tayel A, Mustafa G, Siam R (2016) In situ polymerization of polyurethane silver nanocomposite foams with intact thermal stability, improved mechanical performance, and induced antimicrobial properties. J Appl Polym Sci 133:11, 43125, 1–9
10. Tomacheskia D, Pittol M, Simões DN, Ribeiro VF, Santana RMS (2017) Effect of natural ageing on surface of silver loaded TPE and its influence in antimicrobial efficacy. Appl Surf Sci 405(405):137
11. Braga LR, Rangel ET, Suarez PAZ, Machado F (2018) Simple synthesis of active films based on PVC incorporated with silver nanoparticles: evaluation of the thermal, structural and antimicrobial properties. Food Pack Shelf Life 15:122–129
12. Rai M, Yadav A, Gade A (2009) Silver nanoparticles as a new generation of antimicrobials. Biotech Adv 27:76–83
13. Foldbjerg R, Olesen P, Hougaard M, Dang DA, Hoffmann HJ, Autrup H (2009) PVP-coated silver nanoparticles and silver ions induce reactive oxygen species, apoptosis and necrosis in THP-1 monocytes. Toxicol Lett 28:190, 2, 156–162
14. Sarkar A, Kapoor S, Mukherjee T (2010) Oleic acid-assisted phase transfer of nanosized silver colloids. Res Chem Intermed 36:403–410

15. Fages E, Pascual J, Fenollar O, García-Sanoguera D, Balart R (2011) Study of antibacterial properties of polypropylene filled with surfactant-coated silver nanoparticles. Polym Eng Sci 51:804–811
16. Azocar MI, Tamayo L, Vejar N, Gómez G, Zhou X, Thompsom G, Cerda E, Kogan MJ, Salas E, Paez MA (2014) A systematic study of antibacterial silver nanoparticles: efficiency, enhanced permeability, and cytotoxic effects. J Nanopart Res 16(2465):1–9
17. Advances in Nanocomposite Technology (2011) Chapter 13—Applications of antimicrobial polymer nanocomposites in food packing. Published by Intech—Janeza Trdine—Croatia, pp 299–318
18. Mark JE (2007) Crystallization kinetics of polymer. In: Physical properties of polymers handbook. EUA, Springer, New York, p 636
19. Brandrup J, Immergut EH, Grulke EA (eds) (1999) Polymer handbook, vol v/13, no 1, 4th edn. Wiley-Interscience, New York, pp 445–450
20. JIS Z 2801 (2010) Japanese Industrial Standard; Antibacterial products—test for antibacterial activity and efficacy; Japanese Standards Association, Tokyo
21. Benhacine F, Hadj-Hamou AS, Habi A (2016) Development of long-term antimicrobial poly (ε-caprolactone)/silver exchanged montmorillonite nanocomposite films with silver ion release property for active packaging use. Polym Bull 73(5):1207–1227
22. Zapata PA, Tamayo L, Paez M, Cerda E, Azocar I, Rabagliati FM (2011) Nanocomposites based on polyethylene and nanosilver particles produced by metallocenic "in situ" polymerization: synthesis, characterization, and antimicrobial behavior. Eur Polym J 47:1541–1549
23. Shi YY, Sun B, Shou Z, Wu Y, Zhu M (2011) Size-controlled and large-scale of organic-soluble Ag nanocrystals in water and their formation mechanism. Prog Nat Sci Mater Inter 21:447–454
24. Chen M, Ding WH, Kong Y, Diao GW (2008) Conversion of the surface property of oleic acid stabilized silver nanoparticles from hydrophobic to hydrophilic based on host-guest binding interaction. Langmuir 24:3471–3478

Production and Characterization of PBAT Reinforced with Clay and Graphene Oxide Nanosheets—A Comparative Study

Robson S. Costa, Danielle Garcia Araujo, Marcio S. de Andrade, Rene R. Oliveira, Vijaya Rangari, Esperidiana A. B. Moura and Francisco Valenzuela Días

Abstract The poly (butylene adipate-co-terephthalate) (PBAT), a biodegradable polymer, is among the most promising materials to be considered as environmentally friendly high performance biodegradable plastics. However, the mechanical properties of PBAT are not the best for several applications. According to the literature, the properties of the biodegradable polymer can be improved by addition of a small amount of nanofillers, such as clay, silica, and graphene. The objective of this study is to compare the effect of the addition of Cloisite clay and graphene oxide (GO) on the properties of flexible films based on PBAT matrix. The composite films based on PBAT with addition of Cloisite (2.0 wt%) and PBAT composite films with addition of Cloisite and GO (0.1–0.2 wt%) were prepared by extrusion, using a twin-screw extruder and a flat die single extruder. The effects of the addition of Cloisite clay and graphene oxide on mechanical and thermal properties of films were evaluated by mechanical and water absorption tests, FE-SEM, XRD, and Raman analysis.

Keywords Nanocomposites · PBAT · Biodegradable polymer · Flexible films · Mechanical properties · Clay · Graphene oxide

R. S. Costa · D. G. Araujo · M. S. de Andrade (✉) · E. A. B. Moura
Nuclear and Energy Research Institute, Center for Chemical and Environmental Technology, 2242 Prof. Lineu Prestes Av., 05508-000 São Paulo, Brazil
e-mail: msainsonas@gmail.com

R. R. Oliveira
Nuclear and Energy Research Institute, Center for Materials Science and Technology, 2242 Prof. Lineu Prestes Av., 05508-000 São Paulo, Brazil

V. Rangari
Department of Materials Science and Engineering, Tuskegee University, Tuskegee, AL 36088, USA

F. V. Días
Metallurgical and Materials Engineering Department, Polytechnic School, University of São Paulo, Prof. Mello de Moraes, 2463, 05508-000 São Paulo, Brazil

J. Li et al. (eds.), *Characterization of Minerals, Metals, and Materials 2020*,
The Minerals, Metals & Materials Series,
https://doi.org/10.1007/978-3-030-36628-5_68

Introduction

Conventional plastics and their solid waste are an important part of the current problems that involve the maintenance of the sustainability model worldwide. The conventional plastics are generally fossil-based, non-biodegradable, and consequently are accumulated as solid wastes in the environment, which negatively affect soil and water. This problem is related to their resistance to degrade under environmental influences such as humidity and microbial attack [1–3]. Currently, with the increasing demand for environmental protection and sustainability, the packaging industry has been pushed to search for biobased and biodegradable plastics, so a solution for these environmental problems is to substitute non-biodegradable polymers by biodegradable ones [4–6].

Among various biodegradable polymers, poly (butylene adipate-co-terephthalate) (PBAT) have received enormous attention in recent years, for being a completely biodegradable aliphatic/aromatic co-polyester, which is derived from fossil resources and considered as environmentally friendly [7]. Biodegradation of PBAT depends on their chemical structure and environmental degrading conditions, mostly due to the enzymatic action of microorganisms such as bacteria, fungi, and algae present in the natural environment. Unfortunately, this polymer has low thermo-physical and mechanical resistance properties in flexible films packaging when compared with non-biodegradable polymers [1, 2].

Several studies have been performed using some fillers such as clay, carbon nanotubes, and graphene to obtain nanocomposites, so that the use has been increasing in recent years because they can improve the biodegradable polymer properties and overcome its shortcomings such as poor thermal stability and processability [7–9]. Generally, clays are used to enhance the mechanical, physical, and barrier properties of polymers matrices. The montmorillonite (MMT) is an example of clays that have been used as biodegradable polymer reinforcement fillers, due to their cost-effectiveness, availability, simple processability, and significant improvement in performance [10]. Their gallery structure allows to perform an effective modification of monolayers by cations, originated from quaternary ammonium salts. After this method, the chemical interaction between polymer and filler increases, leading to better dispersion of filler in polymer matrix [11].

Graphene consists of a bidimensional planar and hexagonal array of carbon atoms, and its complete planar exposure of the carbon atoms renders graphene a theoretical surface area of 2500 m^2/g [12, 13]. Graphene and its derivatives, such as the graphene oxide (GO), have drawn much attention due to its gas-impermeable characteristics as well as excellent mechanical and electrical properties [14]. Graphene oxide (GO) nanosheet and its highly oxidized form are characterized by the presence of oxygen-containing moieties, such as epoxy, hydroxyl, carbonyl, and carboxyl groups, on the basal plane and edges of the sheets [15–19]. This nanocomposite has gained studies, specially focusing on the improvement of the polymer, in order of its highly

exfoliated structure and homogeneous dispersion in the polymer matrix, which can be easily achieved due to the increased interfacial adhesion between GO nanosheet and polar polymer matrix [20].

In the present work, a comparative study of effects of clay and graphene oxide addition on the properties of poly (butylene adipate-co-terephthalate) (PBAT) flexible films was carried out.

Experimental

Materials

The materials used in this work to prepare the polymeric matrix were poly (butylene adipate terephtalate) (PBAT) and, as fillers, commercial Cloisite 30B Clay (C30B), and graphene oxide (GO).

Synthesis Graphene Oxide (GO)

In the present work, the graphene oxide (GO) was produced from exfoliated graphite, using the modified Hummers method. This method has been slightly modified in relation to the process times and proportions of reagents, which provide an easy protocol for manufacturing of oxidized graphene sheets. In a beaker, it was added 5 g of exfoliated graphite and 15 g of KMn04. This beaker was placed inside a 600 ml beaker containing ice and then was added 100 mL of H_2SO_4, and at this stage, there was the release of a gas under magnetic stirring for 30 min. With the sample still in the ice bath were added 400 mL of distilled water, it was possible to observe the gas release. This solution was then placed in a water bath for 1 h at 90 °C, and then, a solution of 70 mL H_2O and 30 mL H_2O_2 was prepared and added to the beaker containing the solution, where no reaction was present. For a period of 4 h (3 h on one day and the other 1 h), the solution was left under magnetic stirring and at a temperature of 50 °C. A solution was then placed in a vacuum pump with 50 mL of HCl and 450 mL of distilled water for filtration in a Büchner hopper in a vacuum system. Ultimately, the material retained on the filter was made dialysis for 5 days in a 2 L beaker, changing the water twice a day, until obtaining pH between 5 and 6. The powdered material was frozen and separated into small cups for 1 day and then lyophilized to obtain graphene oxide. The OG was placed in the 4-cycle ultrasound in a 200 mL beaker for 15 min each.

Preparation of Composites

PBAT pellets and clay were dried at 60 ± 2 °C for 4 h to reduce its moisture content to less than 2%. Polymeric composites were prepared in different compositions by weight: PBAT with addition of Cloisite (2.0 wt%) and PBAT composite films with addition of Cloisite and GO (0.1–0.2 wt%). The load was incorporated into the pure poly (butylene adipate-co-terephthalate) (PBAT) pellets in an extruder, torque rheometer coupled to twin-screw extruder Haake Rheomix with 16 mm and L/D = 25 rate from Thermo Scientific, and grinded into a knife mill to obtain the particulate material. The temperature profile was 126/130/134/135/125/120 °C. Then, were processed into extrusion blown film, single-screw machine with 25 mm diameter, and specimens test samples were obtained for mechanical and tensile tests.

Characterization

The rheological characterization of the composite after mixing can determine the level of clay dispersion and distribution of these materials, although there is still controversy regarding the type of structure formed. The viscoelastic response of the composites depends, among other factors, the degree of compatibility between the biopolymer, clay and graphene.

Analyses

Tensile Tests

The tensile tests were carried out for all samples using an INSTRON Universal Testing Machine, model 5564, according to ASTM D 638, at room temperature and loading rates of 50 mm/min.

Water Absorption Test

Pre-dried samples (were dried at 60 ± 2 °C until weight stabilized) were weighed for the dry weight and then placed in a bath with distilled water at room temperature. The samples were weighed every 30 min until weight stabilized (the samples were removed from distilled water and weighed). The water absorption capability (WAC) was calculated using the following equation: $WAC\% = [(W_{wet} - W_{dry})/W_{dry}] \times 100$, where W_{wet} represents the weight of the wet specimen, and W_{dry} is the weight of the dry specimen.

Field Emission Scanning Electron Microscopy (FE-SEM)

FE-SEM of RGO nanosheets and its composites materials with ABS were carried out using a JEOL-JSM-6701 F, microscope with an accelerating voltage of 1–30 kV, using EDS Thermo Scientific mod. Noran System Six software, in cryofractured samples under liquid nitrogen and covered with gold.

X-Ray Diffraction (XRD)

Patterns were recorded on a Bruker D8 Advance 3 kW diffractometer equipped with Cu–K alpha radiation tube and scintillation detector. The XRD analysis of the ABS and its composites materials were carried out using a Philips XPERT-MPD diffractometer with Cu–K alpha radiation ($\lambda = 1.54$ nm) operated at 40 kV and 40 mA, with 2λ varying between 2° and 90°.

Raman Spectroscopy

The Raman spectra of nanoparticles were obtained using a Raman spectrometer HORIBA Jobin Yvon, France, with a confocal microscope equipped with a solid state laser crystal ($\lambda = 532$ nm) as the excitation source. The spectra obtained were adjusted by the image acquisition software (LabSpec 5.1; HORIBA Jobin Yvon) supplied with the instrument.

Results and Discussion

Tensile Tests Results

Figure 1 shows the diagram stress (MPa) × strain (%) for PBAT matrix polymer and its composites, PBAT/C30B 2%, PBAT/C30B/GO 0.1%, and PBAT/C30B/GO 0.2%. From Fig. 1, it is possible observe that the stress increases linearly with strain, due to graphene oxide (GO) 0.2% addition. The addition of Cloisite 30B 2% and GO 0.1% in PBAT matrix polymer initially causes an increase in strength followed by a pronounced reduction, as well as a reduction in strain properties.

Table 1 presents the results of tensile tests of PBAT matrix polymer and its composites. The results presented shows the average values calculated from the data obtained in tests for five test specimens. From Table 1, it can be seen the increase in the tensile strength at break, elongation at break and Young modulus properties of PBAT matrix polymer due to C30B 2% and C30B/GO 0.2% addition. The addition of PBAT/C30B 2% and PBAT/C30B/GO 0.1% in PBAT matrix showed low increase compared to the composite PBAT/C30B/GO 0.2% of its tensile properties.

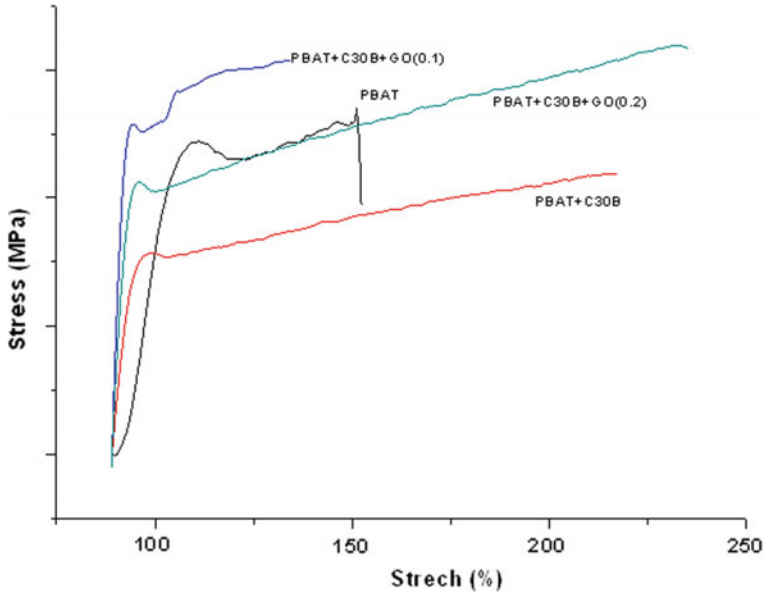

Fig. 1 Diagram stress (MPa) × strain (%) for PBAT matrix polymer and its composites

Table 1 Tensile test results of PBAT matrix polymer and its composites

Sample	Tensile strength at break (MPa)	Elongation at break (%)	Young's modulus (MPa)
PBAT	236.5 ± 26.3	89.3 ± 0.7	35.7 ± 4.0
PBAT/C30B 2%	4.5 ± 1.3	797.6 ± 95.8	11.1 ± 2.2
PBAT/C30B/GO 0.1%	31.4 ± 51.2	557.0 ± 441.2	20.2 ± 4.0
PBAT/C30B/GO 0.2%	6.8 ± 1.4	1096.2 ± 212.6	17.0 ± 3.2

X-Ray Diffraction (XRD) Analysis Results

Figure 2 shows the XRD patterns of PBAT matrix and its composites. It is possible to observe three prominent angles approximately in 2θ (°) = 5°, 7°, and 15°. The result of XRD at 5° corresponds to the C30B, and the clay was dispersed in the PBAT matrix, as shown in Fig. 2. This result is very similar to what reported in [21], also, it was possible to notice the presence of GO at 6° and 15°, according to [22], is due to the presence of oxygen-functional groups and water molecules into the carbon layer structure. The small peak observed at $2\theta = 7°$ which indicates that graphene oxide is not fully interconnected with oxygen atoms [22].

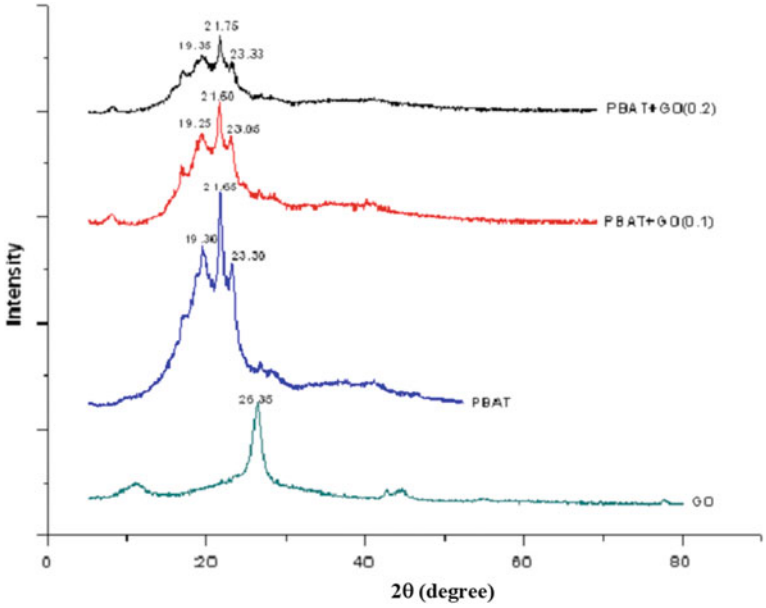

Fig. 2 XRD patterns of PBAT matrix and its composites

Water Absorption Test Results

Table 2 presents the results of water absorption test of PBAT matrix polymer and its composites. The results presented shows significant changes with the addition of C30B clay 2% and graphene oxide (GO) 0.1 and 0.2%. The WAC of nanocomposite films changed significantly depending on the type of nanofillers used and the percentage of it. The water absorption of composite PBAT/C30B 2% tends to decrease with the clay fraction. The C30B clay is organically modified clay, and this result is mainly attributed to the hydrophobicity of this modified clay [23], so as shown in Table 2, the C30B addition decreased the water solubility of films because the layers of MMT act as a barrier against the diffusion of the water to films [24]. Although, when this result is compared with the addition of Cloisite 30B and GO, the WAC increases. These results could be described by GO's poor barrier properties, and

Table 2 Water absorption test results of PBAT matrix polymer and its composites

Sample	Water absorption capability—WAC (%)
PBAT	0 ± 3,0
PBAT/Clay	0.80 ± 0,1
PBAT/Clay/GO 0.1%	1.10 ± 0,05
PBAT/Clay/GO 0.2%	1.73 ± 14,51

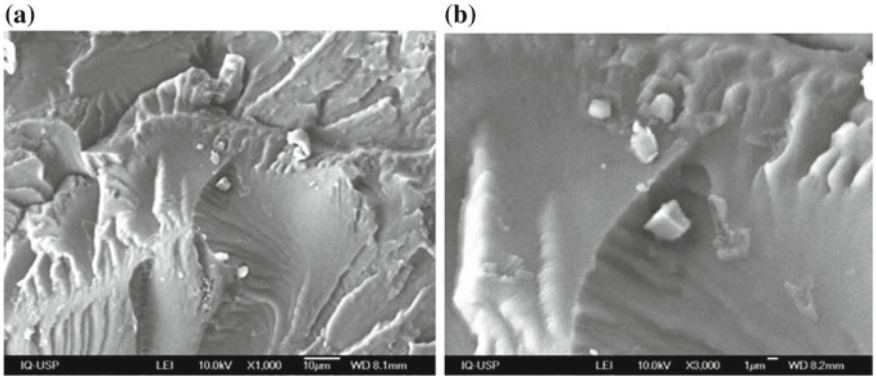

Fig. 3 FE-SEM micrographs of composite PBAT/GO 0.2% (1.000×) (**a**), and PBAT/GO 0.2% (3.000×) (**b**)

that is related to their exfoliation, uniform dispersion and alignment into the PBAT matrix and the interfacial interactions between GO and PBAT matrix [25, 26]. After 24 h, the water absorption capability property was decreased due to the PBAT matrix sample deterioration during the submersion into water (see Table 2).

Field Emission Scanning Electron Microscopy (FE-SEM) Analysis Results

FE-SEM micrographs of cryofractured surfaces of the PBAT matrix and composite specimens were studied to understand the failure mechanisms and also study possible interaction between different components. FE-SEM micrographs of PBAT matrix and its composites in different magnifications are shown in Fig. 3. Micrographs surface of PBAT/GO 0.2% with 1.000× and 3.000× of magnifications are shown in Fig. 3a and b, respectively.

Raman Spectroscopy Results

Figure 4 shows the Raman spectrum of PBAT, PBAT/C30B, PBAT/C30B/GO 0.1%, and PBAT/C30B/GO 0.2%. The characteristics D (disorder band) and G (in phase vibrations band) of GO are present, respectively, the D band is located at 1291.03 cm^{-1} and the G band at 1608.23 cm^{-1}. This result is very similar to what is reported in [27]. The bands of C30B are present and located approximately at 1450 cm^{-1}, and this result is similar to this literature [28].

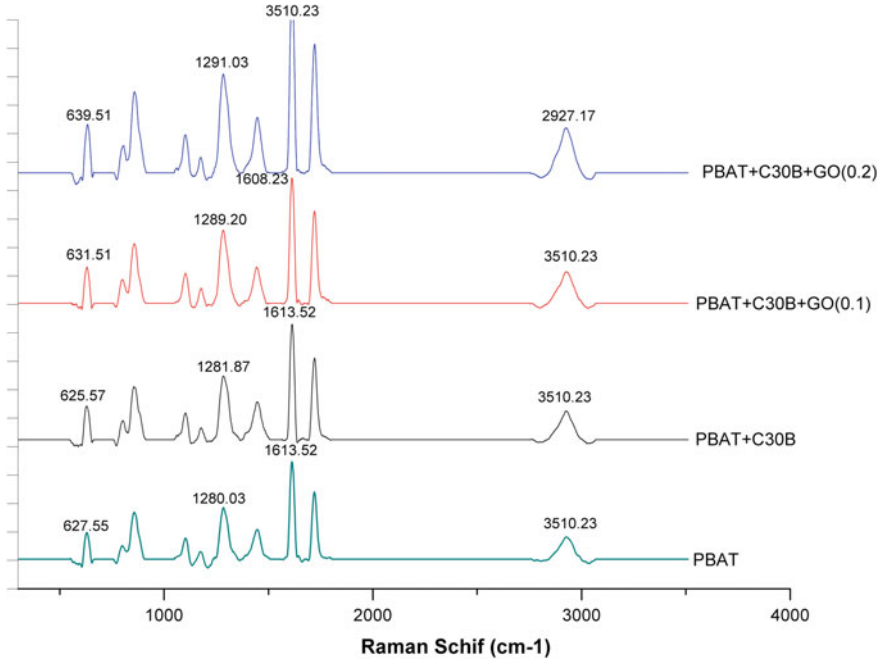

Fig. 4 Raman spectroscopy of PBAT matrix and its composites

Conclusion

In this work, the results showed a better increase related to elastic deformation using graphene oxide (GO) 0.2% and compared to the graphene oxide (GO) 0.1% and Cloisite 30B (C30B), but concerning the plastic deformation, the sample with GO 0.1% showed superior results. The sample containing only Cloisite 30B (C30B) had poor mechanical performance compared to the samples with oxide graphene (GO) addition, and even the pure PBAT. The gains as water barrier for the Cloisite 30B (C30B) addition were reduced by the graphene oxide (GO) concentration increasing. The balance between graphene oxide (GO) and Cloisite 30B (C30B) shows itself a very important parameter, since the PBAT with no additions degraded in water presence.

Acknowledgements The authors wish to thank IIAEA-CRP # 17760 RO, FAPESP, and CNPq to provide support for this work.

References

1. Ferreira FV, Cividanes LS, Gouveia RF, Lona LMF (2019) An overview on properties and applications of poly(butylene adipate-co-terephthalate)—PBAT based composites. Polym Eng Sci. https://doi.org/10.1002/pen.24770
2. Thakur MK, Thakur VK, Gupta RK, Pappu A (2016) Synthesis and applications of biodegradable soy based graft copolymers: a review. ACS Sustain Chem Eng. https://doi.org/10.1021/acssuschemeng.5b01327
3. Lebreton LCM, Van der Zwet J, Damsteeg JW, Slat B, Andrady A, Reisser J (2017) River plastic emissions to the world's oceans. Nat Commun. https://doi.org/10.1038/ncomms15611
4. Hu H et al (2019) Toward biobased, biodegradable, and smart barrier packaging material: modification of poly (neopentyl glycol 2,5-furandicarboxylate) with succinic acid. ACS Sustain Chem Eng. https://doi.org/10.1021/acssuschemeng.8b05990
5. Schneiderman DK, Hillmyer MA (2017) 50th anniversary perspective: there is a great future in sustainable polymers. Macromolecules. https://doi.org/10.1021/acs.macromol.7b00293
6. Pellis A, Acero EH, Gardossi L, Ferrario V, Guebitz GM (2016) Renewable building blocks for sustainable polyesters: new biotechnological routes for greener plastics. Polym Int. https://doi.org/10.1002/pi.5087
7. García-Quiles L, Cuello ÀF, Castell P (2019) Sustainable materials with enhanced mechanical properties based on industrial polyhydroxyalkanoates reinforced with organomodified sepiolite and montmorillonite. Polymers. https://doi.org/10.3390/polym11040696
8. Kashi S, Gupta RK, Kao N, Bhattacharya SN (2016) Viscoelastic properties and physical gelation of poly(butylene adipate-co-terephthalate)/graphene nanoplatelet nanocomposites at elevated temperatures. Polymer. https://doi.org/10.1016/j.polymer.2016.08.097
9. Kashi S, Gupta RK, Bhattacharya SN (2016) Electrical, thermal, and viscoelastic properties of graphene nanoplatelet/poly(butylene adipate-co-terephthalate) biodegradable nanocomposites. J Appl Polym Sci. https://doi.org/10.1002/app.43620
10. Tagegaonkar S, Sharman H, Pandey S, Mishra PK, Wimmer R (2017) Bionanocomposites: smart biodegradable packaging material for food preservation. In: Grumezescu AM (ed.), Food packaging. Org. Academic Press. https://doi.org/10.1016/b978-0-12-804302-8.00003-0
11. Anyszka R, Bieliński DM, Pedzich Z, Szumera M (2015) Influence of surface-modified montmorillonites on properties of silicone rubber-based ceramizable composites. J Therm Anal Calorim. https://doi.org/10.1007/s10973-014-4156-x
12. Lalwani G, D'Agati M, Khan AM, Sitharaman B (2016) Toxicology of graphene-based nanomaterials. Adv Drug Deliv Rev. https://doi.org/10.1016/j.addr.2016.04.028
13. Singh Z (2016) Applications and toxicity of graphene family nanomaterials and their composites. Nanotechnol Sci Appl. https://doi.org/10.2147/nsa.s101818
14. Kim SW, Choi HM (2015) Enhancement of thermal, mechanical, and barrier properties of ethylene vinyl alcohol copolymer by incorporation of graphene nanosheets: effect of functionalization of graphene oxide. High Perform Polym. https://doi.org/10.1177/0954008314557051
15. De Luna LAV et al (2016) Comparative in vitro toxicity of a graphene oxide-silver nanocomposite and the pristine counterparts toward macrophages. J Nanobiotechnol. https://doi.org/10.1186/s12951-016-0165-1
16. Kim H, Abdala A, Macosko C (2010) Graphene/polymer nanocomposites. Macromolecules. https://doi.org/10.1021/ma100572e
17. Adrar S, Habi A, Grohens Y (2017) Combined effect of epoxy functionalized graphene and organomontmorillonites on the morphology, rheological and thermal properties of poly (butylenes adipate-co-terephtalate) with or without a compatibilizer. Appl Clay Sci. https://doi.org/10.1016/j.clay.2017.06.009
18. Yang F, Qiu Z (2011) Preparation, crystallization, and properties of biodegradable poly(butylene adipate-co-terephthalate)/organomodified montmorillonite nanocomposites. J Appl Polym Sci. https://doi.org/10.1002/app.32619
19. Tapeli Y, Anik U (2016) Preparation, characterization and electrochemical application of graphene-metallic nanocomposites. Electroanalysis. https://doi.org/10.1002/elan.201600369

20. Miculescu M, Thakur VM, Voicu SI (2016) Graphene-based polymer nanocomposite membranes: a review. Polym Adv Technol. https://doi.org/10.1002/pat.3751
21. Yan H, Singh G, Raghavan D, Al-Enizi AM, Elzatahry A, Karim A (2014) Dispersion morphology and correlation to moduli using buckling metrology in clay–biopolymer nanocomposite thin films. ACS App Mater Interf. https://doi.org/10.1021/am5026819
22. Siburian R, Raja SL, Supeno M, Simanjuntak C (2017) New route to synthesize of graphene nano sheets. Orient J Chem. https://doi.org/10.13005/ojc/340120
23. Rhim JW, Hong SI, Ha CS (2009) Tensile, water vapor barrier and antimicrobial properties of PLA/nanoclay composite films. LWT Food Sci Technol. https://doi.org/10.1016/j.lwt.2008.02.015
24. Taghizadeh MT, Sabouri N (2013) Biodegradation behaviors and water adsorption of poly(vinyl alcohol)/starch/carboxymethyl cellulose/clay nanocomposites, Springer. https://doi.org/10.1186/2228-5326-3-51
25. Tan B, Thomas NL (2016) A review of the water barrier properties of polymer/clay and polymer/graphene nanocomposites. J Membr Sci. https://doi.org/10.1016/j.memsci.2016.05.026
26. Xu L, Teng J, Li L, Huang HD, Xu JZ, Li Y, Ren PG, Zhong GJ, Li ZM (2019) Hydrophobic graphene oxide as a promising barrier of water vapor for regenerated cellulose nanocomposite films. ACS Omega. https://doi.org/10.1021/acsomega.8b02866
27. Mend X, Geng D, Liu J, Banis MN, Zhang Y, Li R, Sun X (2010) Non-aqueous approach to synthesize amorphous/crystalline metal oxide-graphene nanosheet hybrid composites. J Phys Chem C. https://doi.org/10.1021/jp105852h
28. Valthem PV, Ballout W, Dumont D, Daoust D, Sclavons M, Cordenier F, Pardoen J, Devaux J, Bailly C (2015) Phenoxy nanocomposite carriers for delivery of nanofillers in epoxy matrix for resin transfer molding (RTM)-manufactured composites. Comp Part A Appl Sci Manuf. https://doi.org/10.1016/j.compositesa.2015.05.008

Study of Styrene Effect on Non-radiation Grafting of Vinyl Benzyl Chloride on to Polyethylene-Based Anion Exchange Membrane

Di Huang, Jiann-Yang Hwang and Zhichao Chen

Abstract A non-radiation polyethylene-based anion exchange membrane (AEM) was synthesized by chemically grafting 4-vinylbenzyl chloride (VBC) onto it. The resulting AME with a 10% styrene addition has peak IEC value, 57% higher than the non-styrene AEM. Water uptake and mechanical properties were slightly enhanced with the presence of styrene. The addition of styrene improves the compatibility between VBC and low-density polyethylene due to the formation of compatibilizer of poly(styrene-co-VBC). These were evidenced by elemental analysis, infrared spectroscopy, [1] H NMR, and Field Emission-SEM.

Keywords Anion exchange membrane · Non-radiation grafting · Styrene effect

Introduction

There are renewed interests in researching and developing high-performance ion exchange membranes which play an important role in various industrial applications. These include water treatment, desalination, and electrochemical devices [1–3]. Typically, IEM is composed of inert polymers such as polyethylene and polyvinylidene fluoride [4], as well as reactive polymers such as polystyrene that can be functionalized with ionic groups [5]. The IEM used were paired up cation exchange membranes (CEM) and anion exchanged membranes (AEM) [6]. A typical AEM contains positively charged groups, such as $–NH_3+$, $–NRH_2+$, $–PR_3+$, and $–SR_2+$ [6], fixed to the membrane backbone, and allows the passage of anions but rejects cations.

Polyolefin films such as polyethylene and polypropylene have been proven to be an attractive inert polymer material to produce IEM since they have properties of high mechanical, good chemical, and thermal stabilities [1]. 4-Vinylbenzyl Chloride,

D. Huang (✉) · J.-Y. Hwang
Department of Materials Science and Engineering, Michigan Technological University, Houghton, MI, USA
e-mail: dih@mtu.edu

J.-Y. Hwang · Z. Chen
Futianbao Environmental Technology Inc, Xian, China

J. Li et al. (eds.), *Characterization of Minerals, Metals, and Materials 2020*,
The Minerals, Metals & Materials Series,
https://doi.org/10.1007/978-3-030-36628-5_69

which contains chloromethyl groups in its structure, was reported to be an alternative reactive polymer to replace chloromethyl methyl ether (CMME) reagents to avoid a harmful chloromethylation reaction [7].

Radiation-induced graft polymerization is an option to graft reactive polymeric material on the matrix material. Richard Espiritu exploited this using gamma radiation to fabricate polyethylene-based alkaline anion exchange membranes [8]. Mi-Lim Hwang's work showed the desired PVBC-grafted PEEK film can be prepared using a simultaneous irradiation grafting method [9]. However, the radiation-induced process usually results in very complicated molecular structures, making it hard to obtain the desired properties which can be implemented in specific situation.

In this study, 4-vinylbenzyl chloride is successfully grafted on the low-density polyethylene (LDPE) inert polymer via non-radiation polymerization by using styrene as a comonomer. The wide range of PE-g-VBC anion exchange membranes has been studied. However, using a non-radiation grafting method and with the presence of styrene has not been widely reported. The introduction of styrene could not bring any contribution to functional groups grafted, but it can be copolymerized with divinylbenzene to be regarded as compatibilizer.

Experiment

Material

Low density polyethylene (LDPE) with 0.1 mm thickness was purchased from Uline Co. Ltd. Styrene (99.9% purity), 4-vinylbenzyl chloride (90% purity), 4-Divinylbenzene (DVB 80% purity), and benzyl peroxide (BPO) were purchased from Sigma Aldrich Co, Ltd. Trimethylamine (TMA), 30% solution, was purchased from Acros Organics, used as amination agent.

Membrane Preparation

Grafted Copolymerization

2.5 g low-density polyethylene films were dissolved in the around bottom flask composed with toluene and xylene at a temperature of 90 °C for 1–2 h. Styrene and 4-vinylbenzyl chloride were added into the solution as monomers. Table 1 shows the PE-St-VBC copolymerization condition with a different monomer ratio. The DVB was added with monomers as cross-linkage agent. The whole copolymerization reaction was conducted in a nitrogen atmosphere at 90 °C for 6 h.

Table 1 A preliminary study of copolymerization condition

Composition	LDPE (g)	Styrene (g) : VBC (g)	DVB (g)	BPO (g)
1	2.5	0 : 2	0.15	0.02
2	2.5	0.2 : 1.8	0.15	0.02
3	2.5	0.4 : 1.6	0.15	0.02
4	2.5	0.6 : 1.4	0.15	0.02
5	2.5	0.8 : 1.2	0.15	0.02

Membrane Preparation and Amination

The synthesized copolymer solution was diluted and stirred with toluene at 90 °C for a half hour to obtain a homogeneous solution. After mixing, the viscous copolymer solution was casted on a preheated glassy plate. To functionalize the copolymers, the LDPE-St-VBC membranes were immersed into a 30% trimethylamine aqueous solution at 40 °C for 24 h.

Characterization of Anion Exchange Membrane

Ion Exchange Capacity (IEC)

The Mohr's method was adopted to determine the chloride ion's concentration attached on the ion exchange membranes [10]. The dried membranes were cut into small pieces and stirred with 1.0 M HCl for 24 h to make sure all the functional groups were changed to the Cl–. The small pieces of AEMs were then stirred with 0.2 M $NaNO_3$ solution three times to replace the Cl– into the solution. Finally, the 0.01 M $AgNO_3$ was used to titrate the solution with Cl– with the presence of an indicator.

$$\mathrm{IEC} = \frac{\Delta V_{\mathrm{AgNO3}} \times 0.01\,\mathrm{M}}{M_{\mathrm{dry}}}$$

$\Delta V_{\mathrm{AgNO3}}$ is the volume difference before titration and after neutralization. M_{dry} is the weight of dry AEM.

Water Uptake Measure

The AEM membranes were soaked in the 0.5 mol/l NaCl for 24 h. After soaking, the wet weight of film was measured. The dry membrane was weighted after drying in an oven at 50 °C. The water uptake of AEM is calculated using the flowing equation:

$$\Phi = \left(W_{wet} - W_{dry}\right)/W_{dry}$$

where Φ represents the water uptake percentage of the film, W_{wet} is the weight of the soaked film, and W_{dry} is the weight of its dry form.

Thermal Expansion and Swelling Measurement

The AEM was cut into 3 × 3 cm piece and immerse into deionized water with designated temperatures for 12 h. After 12 h, the chances in the sizes were measured. The dimensional changing rate of AEM swelling was calculated using the following equation:

$$\text{Thermal expansion rate at specific temperature } (\%) = \text{swelling rate } (\%) = \frac{L_{wet} - L_{dry}}{L_{drym}}$$

where L_{wet} and L_{dry} represent the average length size of wet and dry AEM piece, respectively.

Mechanical Properties Measurement

Mullen burst strength is a uniform criterion of measuring the strength and lifetime of membrane material. The Zhibang ZB-NPY burst testing machine was employed to obtain the burst strength.

Morphology Characterization

The morphological characterization of AEMs was characterized and compared by performing Field Emission Scanning Electron Microscope (FE-SEM) analysis. The Hitachi S-4700 FE-SEM was equipped with Oxford energy dispersive X-ray spectroscopy (EDS) microprobe.

FT-Infrared (FTIR) Spectroscopy Analysis

The FTIR spectra of copolymer (PE-St-VBC) and ammonized membranes were characterized by using Fourier transform spectrometer. A PerkinElmer Spectrum spectrometer with universal attenuated total reflection accessory was used to record the infrared spectrum of the copolymer products and aminated membranes.

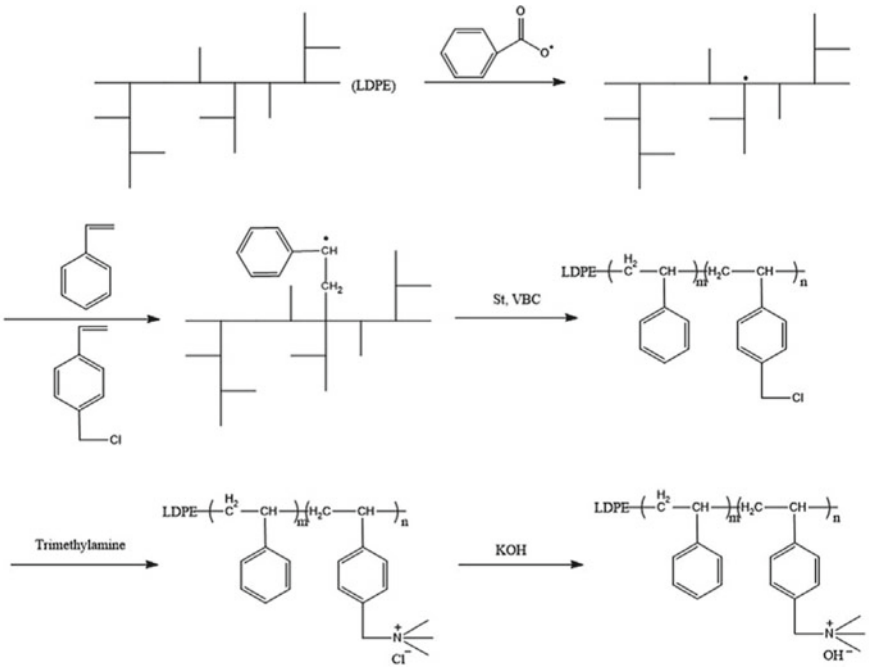

Scheme 1 Synthesis of anion exchange membranes

Results and Discussion

Preparation of PE-St-VBC AME

Scheme 1 shows the synthesis process of PE-St-VBC AME. One BPO initiator can generate two benzyloxy radicals. A copolymerization of styrene and VBC may occur if BPO radicals attack the styrene monomer. Since LDPE and VBC exhibit very low entropy of mixing, formation and coalescence of the copolymer will result upon sizable dispersed phase domains, low adhesion, and poor final properties. Adding styrene would improve the adhesion between phases through compatibilization.

Characterization of AEM by FTIR Spectroscopy Analysis

The chemical structure of the original polyethylene, copolymer PE-St-VBC with various styrene additions were analyzed and represented in Fig. 1. The 2917 cm^{-1} and 2848 cm^{-1} peaks reveal the asymmetry stretching and symmetry stretching of $–CH_2$, respectively. The $–CH_2$ deformation stretching and bending are shown at 1464 and 719 cm^{-1}. After copolymerization, some new absorption bends appear at

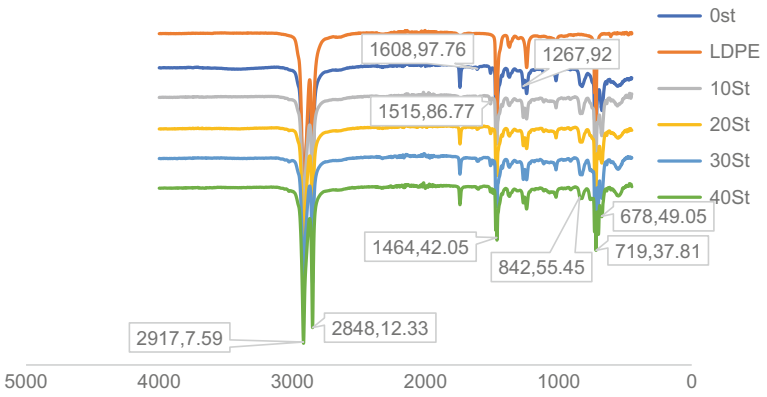

Fig. 1 FTIR spectra of the original LDPE film (top) and graft copolymers synthesized with different St : VBC ratios

1608 and 1515 cm^{-1}, corresponding the stretching of C=C aromatic double bonds [18]. The new peaks which appear at 678 cm^{-1} are assigned to C–Cl stretching, and the peak at 1267 cm^{-1} is due to $–CH_2Cl$ wagging, both resulting from the CH_2Cl group present in VBC. These can clearly indicate that the VBC monomers are successfully grafted on the PE films.

After quaternarization, the FTIR spectrum at Fig. 2 shows the C=C stretching vibration is shifted to 1632 cm^{-1}, and some characterized peaks of copolymer PE-St-VBC, such as C–Cl stretching at 678 cm^{-1} and –CH2Cl wagging peak at 1267 cm^{-1}, have disappeared from the quaternized copolymer spectrums. These absences of characterized peaks attribute to the $–CH_2Cl$ groups were aminated to the $–NR_4^+$. Some new peaks which appear at 1486 cm^{-1} and 1025 cm^{-1} correspond to asymmetric stretching vibration and bending of $–NR_4^+$ groups. These indicate that the ideal for

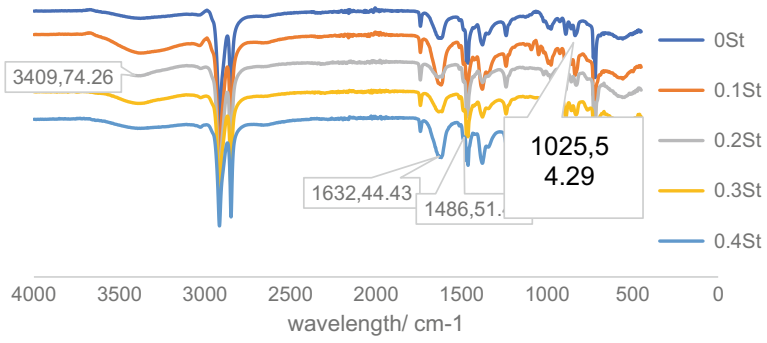

Fig. 2 FTIR spectra of aminated graft copolymers (OH– form)

adding styrene in the polymerization process is a right direction to increase the VBC grafted on the PE films.

Characterization of AEM by SEM and TEM Analysis

The FE-SEM micrography of poly (ethylene-styrene-VBC) with various styrene additions were represented on Fig. 3 (PS from 0 to 20% mass fraction). The grafted polymer polyethylene-g-VBC without styrene addition shows obvious phase separation. The irregular dimensional embossments and uneven distributional spherical particle demonstrate the low compatibility between polyethylene and VBC. The appearance of tiny pores dispersed on the matrix indicates the poor miscibility between VBC and PE. With the addition of styrene, the spherical particles with a size of less than 1 μm distributed more uniformly on the polyethylene matrix. With the increase in styrene, the surface of the PE matrix is observed to be more smooth, and dispersed phases became more continuous.

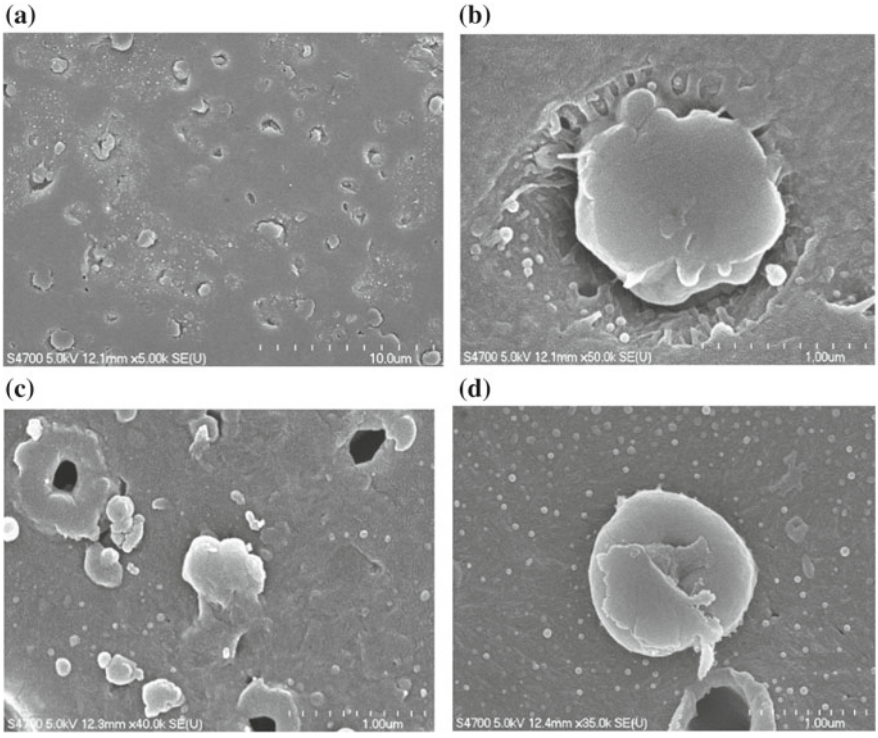

Fig. 3 SEM images of **a**, **b** PE-graft-P(VBC) and **c** PE-graft-P(St-co-VBC) (St : VBC = 10 : 90) copolymer, **d** PE-graft-P(St-co-VBC) (St : VBC = 20 : 80)

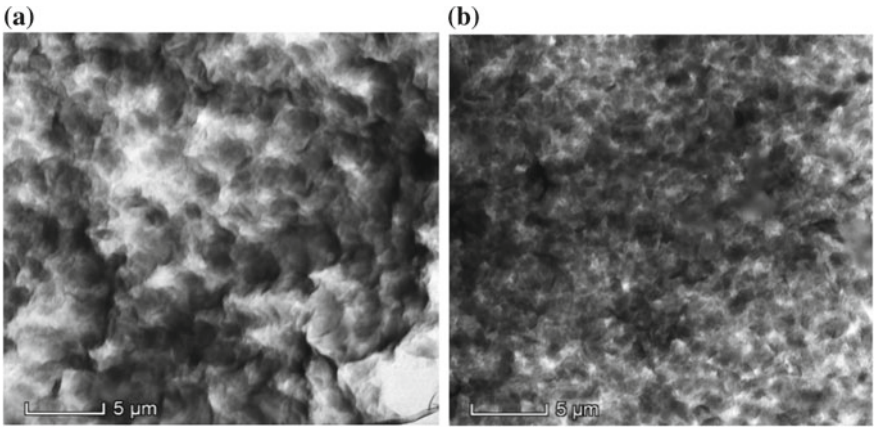

Fig. 4 TEM images of **a** PE-graft-P(VBC) and **b** PE-graft-P(St-co-VBC) (St : VBC = 10 : 90) copolymer

In Fig. 4, the sample image covered by microparticles composited with polyethylene, PE-graft-P (VBC), or PE-graft-P (St-co-VBC). The microparticles represented by bright agglomerates have less molecular weight and shorter polymer chains than the dark agglomerates. The agglomerates are generally larger in copolymer without adding styrene than those with 10% St added. Furthermore, the bright and dark agglomerates have more obvious separation in Fig. 4a than those in Fig. 4b. This indicates the addition of St improves the miscibility of PE and VBC.

Ion Exchange Capacity (IEC)

Figure 5 shows the influence of the addition of styrene to the IEC of AEM. The plot of IEC values from titration shows the presence of styrene which greatly enhances the IEC of AEM, implying that more functional groups were introduced to the PE

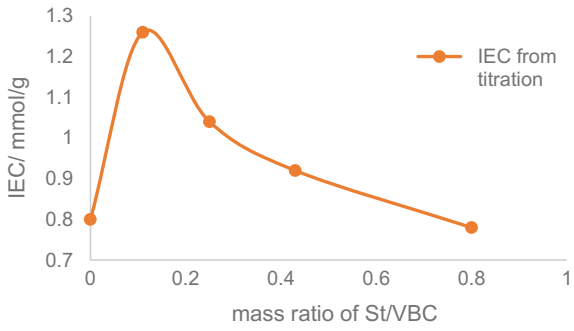

Fig. 5 Effect of St on the IEC of anion exchange membranes (OH– form)

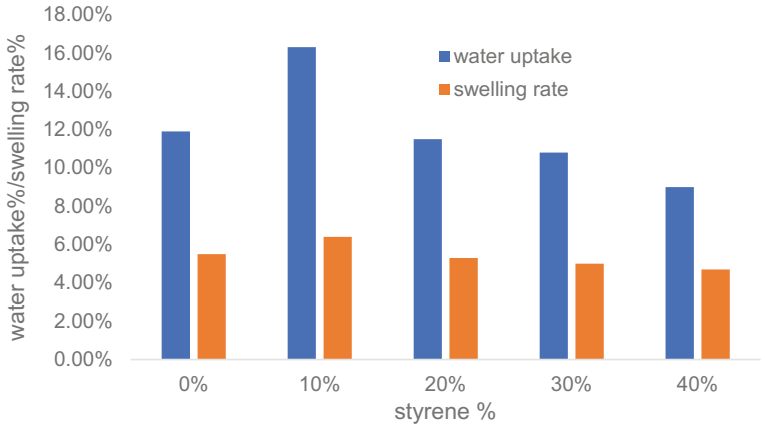

Fig. 6 Effect of styrene addition on water uptake and swelling rate of AEM

branch chains. The ion exchange capacity of 10, 20, and 30% styrene monomers addition ratios is all higher than that found with AEM without styrene addition. The peak value of IEC appears at 10% styrene added, and the value is 1.26 mmol/g, which is 57% higher than IEC of non-styrene AEM.

Water Uptake and Membrane Swelling Property

The water uptake and membrane swelling property of AEM with various styrene proportions are represented in Fig. 6. Apparently, the AEM (10% styrene proportion) with the highest IEC value uptakes the most water amount and produces the highest membrane dimensional deformation, which is in accord with the prediction. The high water uptake is mainly due to the high hydrophilic functional groups grated on the membranes which are associated with the IEC. Compared with commercial membranes, such as Nafion® 115 (~36% water uptake and 1.4 IEC value), the AEM with 10 and 20% proportion has both acceptable IEC values and water uptake rates, and the dimension variation is relatively stable.

Conclusion

Non-radiation polyethylene-based AEM was synthesized by chemically grafting VBC on it with the presence of benzoyl peroxide as the initiator and subsequent amination. The St addition has a positive effect on the final properties of the AEM. The 10% St addition dramatically improves the IEC property. The value is 1.26 mmol/g, 57% higher than IEC of non-styrene AEM. We also found that further addition of

St decreased the grafting degree of VBC since St can compete with VBC in graft polymerization. The final membrane was characterized by elemental analysis, FTIR, SEM, and TEM. Compared with the PE-g-VBC spectrum without styrene addition, the OH stretching is more obvious with styrene addition after quaternization. SEM and TEM indicated a clear phase separation between the grafting phase and the LDPE matrix on LDPE-graft-P(VBC) without St addition.

References

1. Xu T (2005) Ion exchange membranes: state of their development and perspective. J Membr Sci 263(1):1–29
2. Li X, Zhang H, Mai Z, Zhang H, Vankelecom I (2011) Ion exchange membranes for vanadium redox flow battery (VRB) applications. Energy Environ Sci 4(4):1147–1160
3. Kariduraganavar MY, Nagarale RK, Kittur AA, Kulkarni SS (2006) Ion-exchange membranes: preparative methods for electrodialysis and fuel cell applications. Desalination 197(1):225–246
4. Tran Duy T, Sawada S-I, Hasegawa S, Katsumura Y, Maekawa Y (2013) J Membr Sci 447:19–25
5. Lei QY-L, Luo Y-J, Chen F, Mei L-H (2014) Polymers 6:14–19
6. Dekel DR (2018) Review of cell performance in anion exchange membrane fuel cells. J Power Sources 375:158–169
7. Hosseini SS, Bringas E, Tan NR, Ortiz I, Ghahramani M, Shahmirzadi MA (2016) Recent progress in development of high performance polymeric membranes and materials for metal plating wastewater treatment: a review. J Water Process Eng 29(9):78–110
8. Espiritu R, MamloukMand Scott K (2016) Int J Hydrogen Energy 41:1120–1133
9. Zhao Y, Pan J, Yu H, Yang D, Li J, Zhuang L et al (2013) Int J Hydrogen Energy 38(1983–1987):12882
10. Mamlouk M, Scott K, Horsfall JA, Williams C (2011) Int J Hydrogen Energy 36:7191–7198

Study on the Separation of Zinc and Iron in Electric Arc Furnace Baghouse Dusts and Its Kinetics

Zhao-ran Wang, Cheng-Cheng Huo, Yu-hong Zha and Can-hua Li

Abstract In order to utilize the zinc–iron resources rich in the bag ash of a steel mill's electric furnace, the reaction rate and degree of zinc ferrite in the solid–solid reduction reaction are analyzed from the kinetic point of view, and the electric furnace bag is treated by the carbon-containing pellet reduction roasting method. Ash, the effect of zinc–iron separation during the reduction process, and the comprehensive utilization method of product greening were studied. The results show that in the process of reduction of zinc and iron in the bag ash of electric furnace, the weight loss rate and dezincification rate are positively correlated with the increase of reduction temperature and reduction time within a certain range. Under the condition of not considering the metallization rate, the reduction temperature of 1300 °C was determined, and the reduction rate of zinc in the electric bag ash was 98% when the reduction time was 15 min. The research on the kinetics of reductive dezincification shows that under certain process conditions, the ratio of decarburization with fixed carbon proportions is relatively fast. At this time, the dezincification rate can reach more than 90%, and the zinc removal rate is 98%.

Keywords Electric furnace cloth bag ash · Zinc extraction · Dynamics

Introduction

Electric furnace cloth bag ash is zinc-containing dust obtained by dry recovery and cloth bag collection of flue gas during electric furnace steelmaking [1]. The electric furnace cloth bag ash contains iron, zinc, chromium, lead and other elements, of which the zinc content is about 5–20% [2]. The direct discharge of electric furnace cloth bag ash not only causes serious environmental pollution and ecological damage, but also wastes metal resources such as zinc and iron. At present, the utilization methods of electric furnace cloth bag ash mainly include direct return to the sintering system, and after reprocessing and other methods [3, 4]. The most economical

Z. Wang · C.-C. Huo · Y. Zha · C. Li (✉)
School of Metallurgical Engineering, Anhui University of Technology, Ma anshan 243002, China
e-mail: licanhua1979@163.com

J. Li et al. (eds.), *Characterization of Minerals, Metals, and Materials 2020*,
The Minerals, Metals & Materials Series,
https://doi.org/10.1007/978-3-030-36628-5_70

and effective method is dezincification of the electric furnace cloth bag ash before enrichment and recycling. The resulting zinc is a valuable non-ferrous metal product, and the remaining iron is an important raw material for iron production [5]. Studying the reduction process and influencing factors of carbon-based cloth bag ash pellets, and exploring the dynamic process in dezincification are an urgent and important task in the ecological application of electric furnace cloth bag ash.

Test

Test Raw Materials

The electric furnace bag ash was taken from a company in Maanshan, and its composition was detected by X-ray fluorescence spectroscopy (XRF). The test results are shown in Table 1. The microscopic morphology was observed by field emission scanning electron microscopy (FESEM) as shown in Fig. 1. The electric furnace bag ash is mixed with 15% high-quality carbon powder and stirred uniformly, and then the gelling agent 901 glue is mixed and pressed on the ball press to form a carbon-containing pellet having a certain strength. X-ray diffraction (XRD) was used to detect the phase of the carbon-containing pellet after drying, and the results are shown in Fig. 2.

As can be seen from Fig. 1, the particle size of the electric furnace bag ash is very small, and all are less than 1 μm. From the reaction conditions, the larger surface area means a larger reaction contact area, that is, a more superior kinetic condition, which will favor carbon reduction and improve dezincification efficiency [6].

It can be seen from Table 1 that the TFe of the electric furnace bag ash has a high iron taste and the content is 56.24%. It can be seen from Fig. 2 that Fe mainly exists in the form of $ZnFe_2O_4$, Fe_3O_4, and $KFeO_2$ phases, and the impurity components are mainly CaO, MgO, and SiO_2, and the contents are 5.07%, 4.77%, and 3.29%, respectively. The content of harmful impurity elements S and P is relatively high, 1% and 0.511%, respectively. In addition, the content of valuable metal Zn in the electric furnace bag ash is 14.72%. It can be seen that the content of P, S, Zn, and Pb in the ash of the electric furnace bag is much higher than the requirement of the iron making raw material. Therefore, the content of harmful impurities must be reduced, and valuable metals can be separated to be recycled to meet the steel production requirements, and bring huge economic benefits to the company.

Test Methods

This experiment uses a method of roasting reduction. Each experiment weighed 7–10 dry carbon-containing pellets, put them into graphite crucibles, and quickly rise to

Table 1 Chemical constituents of electric furnace cloth bag ash

Constituents	TFe	Zn	CaO	Na_2O	MgO	SiO_2	MnO	Cl^-	Pbo	SO_3	P_2O_5
Content (wt%)	56.24	14.72	5.07	4.29	4.77	3.29	2.83	3.22	0.331	1.00	0.511

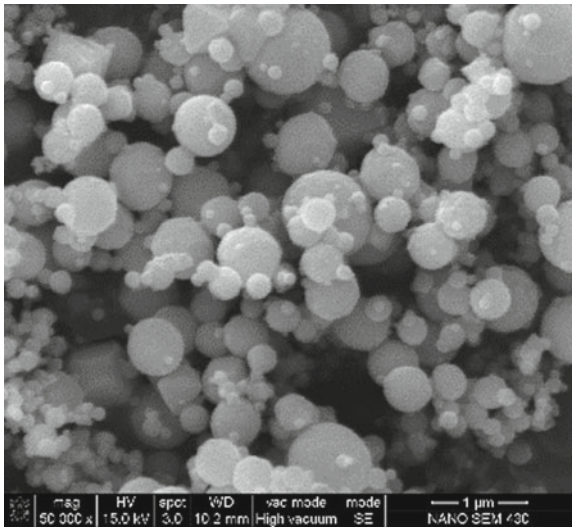

Fig. 1 Microscopic morphology of electric furnace bag

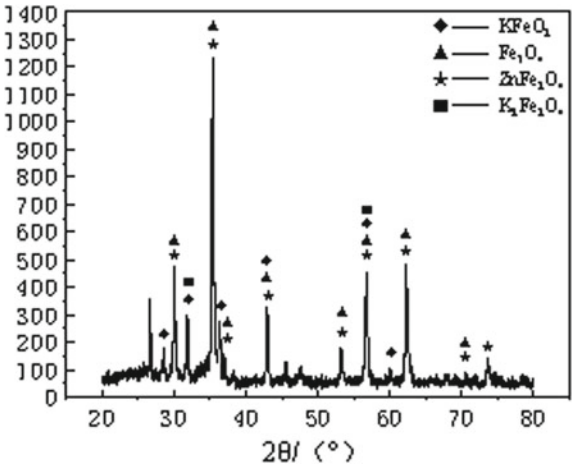

Fig. 2 Carbon-containing pellet phase after drying

the experimental temperature by high-frequency heating furnace. When the experimental temperature is reached, the timing starts. When the roasting time reaches the experimental predetermined value, it is poured. The metal phase and the slag are separated, and the mass is weighed after cooling. A soot absorption device is arranged above the heating furnace to recover the volatilized flue gas, and the reducing slag, the reducing metal, and the volatilized smoke are detected. Repeat the above experiment, mainly to investigate the weight loss rate and dezincification rate of the electric bag ash.

Weight Loss Rate

The weight loss rate is the ratio of the mass change before and after the reduction of the ash of the electric furnace in the electric furnace, see Eq. 1 [7].

$$\theta = \frac{m_0 - m}{m_0} \times 100\% \tag{1}$$

The θ is the weight loss rate/%, m_0 is the pellet mass before reduction/g, and m is the pellet mass after reduction/g.

Dezincification Rate

The dezincification rate refers to the ratio of the dezincification rate to the mass of the zinc element after reduction of the ash of the electric furnace bag and the mass of the zinc element before reduction, see Eq. 2 [8].

$$\eta = \left(1 - \frac{m \times Z}{m_0 \times Z_0}\right) \times 100\% \tag{2}$$

The η is the dezincification rate/%, Z is the mass fraction of zinc in the pellet after reduction/%, and Z_0 is the mass fraction of zinc in the pellet before reduction/%.

Results and Analysis

Weight Loss Rate

The change curve of the weight loss rate obtained after the reduction of the weight loss and after the reduction of the ash of the electric furnace bag is shown in Fig. 3.

It can be seen from Fig. 3 that when the fixed holding time is 35 min, the weight loss rate of the electric bag ash is positively correlated with the reaction temperature. When the temperature is between 900 and 1100 °C, the temperature increase has little effect on the reduction of zinc and iron. When the temperature exceeds 1100 °C, the influence of temperature on the degree of reduction increases. As can be seen from Fig. 4, when the fixed temperature is 1300 °C, the weight loss rate increases with time, 0–15 and 25–35 min. The weight loss rate changed greatly. The weight loss rate changed little when 15–25 and 35–45 min, and the overall image increased stepwise.

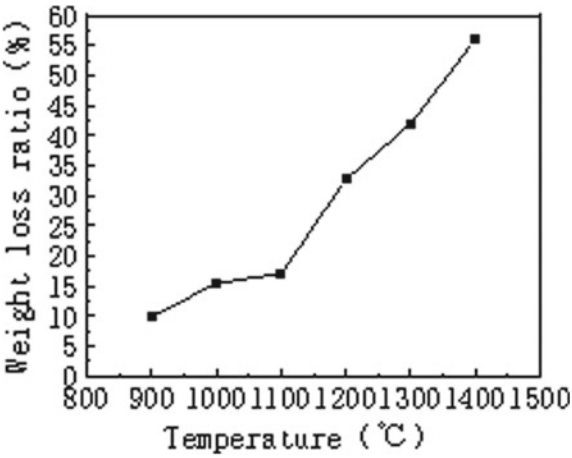

Fig. 3 Weight loss rate and temperature curve

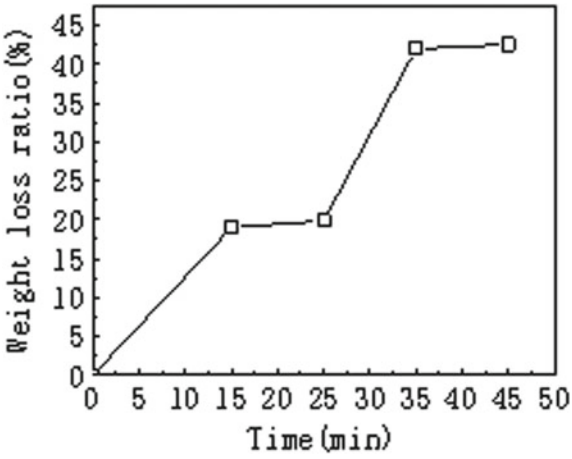

Fig. 4 Weight loss rate versus time at 1300 °C

Dezincification Rate

The content of the reduced electric furnace bag ash was measured by XRF analysis, and then the dezincification rate was calculated, and the obtained data are shown in Figs. 5 and 6.

It can be seen from Fig. 5 that the fixed holding time is 35 min, and the dezincification rate is proportional to the reduction temperature. As the reduction temperature increases, the dezincification rate also increases. When the reaction temperature is between 900 and 1100 °C, the temperature has a great influence on the dezincification rate. At 1100–1400 °C, the temperature has a weak effect on the dezincification rate. Therefore, the dezincification process can be divided into two stages, the first reduction process. At this time, the reaction mainly involves the carbon inside the

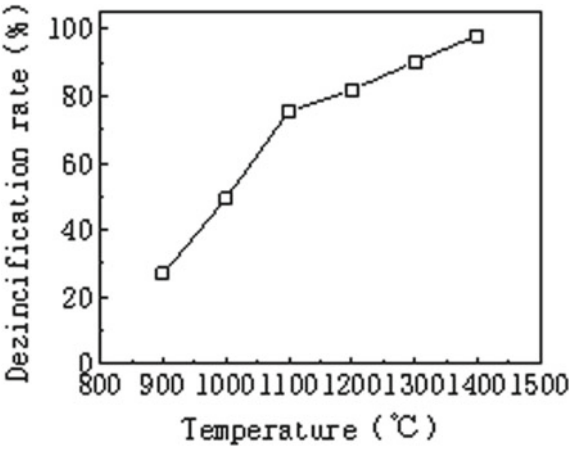

Fig. 5 Temperature and dezincification rate curve

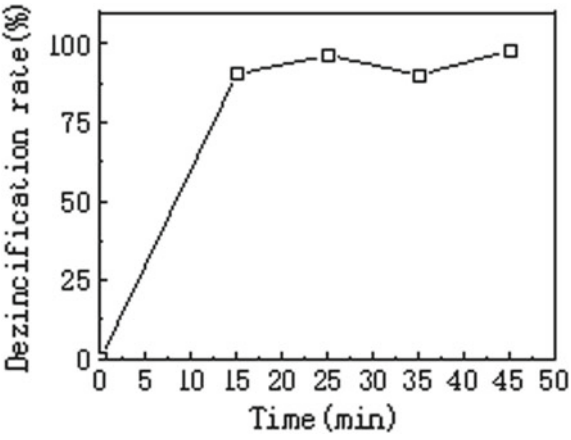

Fig. 6 Reduction time and dezincification rate curve

pellet participating in the reduction process. At this time, the dezincification rate reaches 75.44%, and the temperature reaches the temperature range of 1100–1400 °C. In the range, at this time, the second reduction process, the reduction of Zn and Fe simultaneously proceeded, and the dezincification rate reached 98.1%. At this time, a large amount of Zn and Fe were simultaneously formed, and so the dezincification rate was slightly lowered. As can be seen from Fig. 6, when the reaction temperature is 1300 °C or higher, it is only necessary to reduce the ash of the electric furnace bag for 15 min, and more than 90% of the zinc itself can be removed. When the reduction process exceeds 15 min, the zinc in the ash of the electric furnace bag is nearly completely removed.

Reduction Kinetic Analysis

Reduction Dynamics Basis

In the carbon-containing pellets, Zn is mainly present in the form of $ZnFe_2O_4$, so the following reaction will occur during the reductive dezincification process [9].

$$3ZnFe_2O_4 + C \rightarrow 2Fe_3O_4 + 3ZnO + CO \tag{3}$$

$$ZnFe_2O_4 + CO \rightarrow 2Fe + ZnO + CO_2 \tag{4}$$

$$FeO + CO \rightarrow Fe + CO_2 \tag{5}$$

$$ZnO + CO \rightarrow Zn(steam) + CO_2 \tag{6}$$

It can be seen from the chemical reaction equation that when the carbon-containing pellet is dezinced, the reduced product Zn is volatilized in the form of steam, and is again oxidized to form ZnO in the flue gas recovery device, and C is gradually reduced as a reducing agent in the reduction reaction. Therefore, in the reduction process, the particle size of the carbon-containing pellets is continuously shrinking, and the mass and size before and after the reaction are largely different, and even at a higher temperature, it is directly slag. This is a model of shrinking solid reaction kinetics in a gas–solid reaction kinetic model. The unreacted nuclear model for the entire process is a reaction nucleus that is constantly shrinking. Therefore, this experimental study determined the basis of the shrinkage unreacted nuclear model to analyze the reaction kinetics of reductive dezincification [10].

Determination of the Limiting Link of Reduction Kinetics

For the determination of the restriction link in the reactionless core-shrinking model, the chemical reaction rate constant can be compared with the diffusion coefficient. If the absolute value of K/D_e is much greater than 1, the reaction is controlled by diffusion, and conversely, the reaction is controlled by the chemical reaction interface [11]. The relationship between time and removal rate in the reactionless core-shrinking model is as follows:

$$\tau = \frac{r_0^2 \rho}{2 D_e C_0}\left[1 - 3(1-F)^{\frac{2}{3}} + 2(1-F)\right] + \frac{r_0 \rho}{K C_0}\left[1 - (1-F)^{\frac{1}{3}}\right] \tag{7}$$

τ the time required for the reduction reaction, s;
F Dezincification rate, %;
D_e diffusion coefficient, m^2/s;

K chemical reaction rate constant, m^2/s;
r_0 oxide particle radius, m;
ρ the concentration of the original oxide in the pellet, mol/L;
C_0 initial concentration of reducing gas, mol/L.

Transform Eq. (7) to get:

$$Y = aX + b \tag{8}$$

among them:
$Y = \tau/\left[1-(1-F)^{\frac{1}{3}}\right]$; $X = \left[1-3(1-F)^{\frac{2}{5}}+2(1-F)\right]/\left[1-(1-F)^{\frac{1}{3}}\right]$; $a = r_0^2\rho/(2D_eC_0)$; $b = r_0\rho/(KC_0)$; $K/D_e = 2a/br_0$.

In terms of dynamics studies, an isothermal static reduction roasting test was carried out in a vertical crucible having a diameter of 1200 mm. The test used a dry pellet having an average particle diameter of 60 mm. Table 2 shows the results of dezincification tests at different calcination times at 1300 °C in an air atmosphere.

Substituting the test results into Eq. (8) gives the regression equation (Fig. 7).

The experimental data were linearly fitted to obtain a linear regression equation $Y = 26{,}849.86761X\text{-}26{,}198.49734$, and the regression coefficient was substituted into $K/D_e = 2a/br_0$, then $K/D_e = -34.1621$. It can be seen that the rate of chemical reaction in the reduction process is much larger than the gas diffusion rate. The time used in the reduction process is mainly in the gas diffusion process, that is, the main limiting part of the dezincification process is controlled by diffusion.

Table 2 Dezincification rate at different times of static calcination at 1300 °C

Reduction time (min)	15	25	35	45
Dezincification rate (%)	90.4	93.5	97.1	97.9

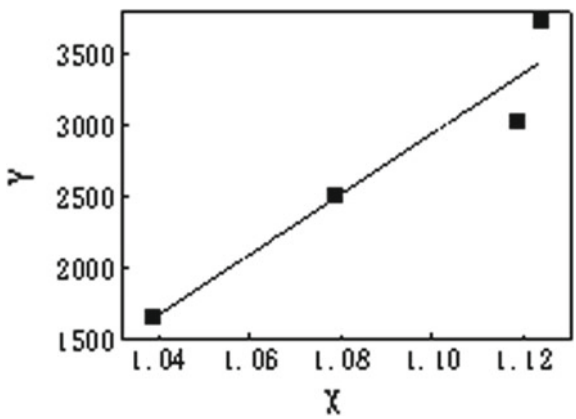

Fig. 7 Equation (7) linear regression fitting

Effect of Temperature on Dezincification

In general, the relationship between the reaction rate and the reaction temperature is determined. Because the activation energy of the reaction is much larger than the diffusion activation energy, the process is limited by chemical reactions at low temperatures and limited by mass transfer at high temperatures. Therefore, as the temperature increases, the kinetic limits disappear and the process is controlled by diffusion. The effect of the study temperature on the reduction reaction can be carried out by determining the diffusion coefficient at this temperature at the same temperature; and then calculating the activation energy according to the diffusion coefficient at different temperatures, the workload is higher [10, 11]. However, in this experimental study, it has been determined that the dezincification reaction is diffusion control, so the activation energy can be determined according to the following derivation, and the diffusion coefficient at different temperatures can be obtained. Equation (7) is simplified as follows:

$$\tau = \frac{r_0^2 \rho}{2 D_e C_0}\left[1 - 3(1-F)^{\frac{2}{3}} + 2(1-F)\right] \tag{9}$$

The effect of temperature on the diffusion coefficient D_e can be expressed by the Arrhenius formula:

$$D_e = D_0 \exp(-E/RT) \tag{10}$$

The E is the apparent activation energy (kJ/mol) of gas diffusion.

Transform Eq. (9) into the following form:

$$y = mx + n \tag{11}$$

among them:

$y = \ln\left\{\left[1 - 3(1-F)^{\frac{2}{3}} + 2(1-F)\right]T\right\}$; $x = 1/T$; $m = -E/R$; $n = \ln \frac{24.376 \tau D_0}{r_0 \rho}$.

In the reduction roasting test, the effect of temperature on the dezincification rate was investigated. The calcination time was fixed at 35 min, and the relationship between the obtained temperature and the dezincification rate in the temperature range of 900–1400 °C is shown in Table 3.

Substituting the data in Table 3 into Eq. (10) yields a linear equation (Fig. 8). The X-axis is $1/T$, the unit is $\times 10^3$ K^{-1}, and the Y-axis is $y =$

Table 3 Dezincification rate after 35 min of reduction at different temperatures

Reduction temperature (°C)	900	1000	1100	1200	1300	1400
Dezincification rate (%)	26.92	49.35	75.44	81.83	90.1	98.1

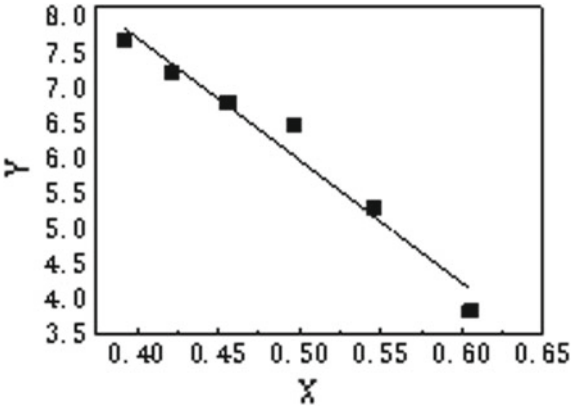

Fig. 8 Equation of the one-way regression equation described by Eq. (10)

$\ln\left\{\left[1-3(1-F)^{\frac{2}{3}}+2(1-F)\right]T\right\}$. The apparent activation energy is calculated from the regression equation:

$$E = 77.3658\,\text{kJ/mol},\ D_0 = 410930,\ De = 410930\,\exp(-77365/T).$$

Figure 8 depicts the regression equation $Y = -9.30549X + 16.6545$ of Eq. (10). It can be seen from the Fig. 8 that when the temperature is below 900 °C, there is a certain error with the curve result, and there may be a phenomenon of mixed control. When the temperature is above 900 °C, the test result is in good agreement with Eq. (7). The results show that the temperature has a great influence on the dezincification rate. When the temperature is above 1200 °C, the zinc is quickly removed.

Conclusion

(1) In the zinc and iron reduction test of the bag ash of the electric furnace, the weight loss rate and the dezincification rate are all proportional to the increase of the reduction temperature and the reduction time. Temperature has the most prominent effect on both. When the reduction reaction temperature is greater than 1300 °C and the reaction is more than 15 min, the zinc in the electric furnace bag ash is substantially removed.

(2) The study on the kinetics of dezincification removal shows that the theoretical value obtained by shrinking unreacted nuclear model is in good agreement with the experimental value, and the reduction process is controlled by diffusion, $E = 77.3658$ kJ/mol. Under certain process conditions, the reduction and dezincification processes are easier to carry out, and the dezincification rate is over 98%.

References

1. Stepin GM, Mkrtchan LS, Dovlyadov IV, Borshchevskii IK (2001) Problems related to the presence of zinc in russian blast—furnace smelting and ways of solving them. Metallurgist 10(45):39–42
2. He SM, Wang JL, Li AL et al (2016) Study on pressurized sulfuric acid leaching of steel dust from waste galvanized steel sheet. Mining Metall Eng 36(2):84–87. https://doi.org/10.3969/j.issn.0253_6099.2016.02.023
3. Romenets VA, Valavin VS, Pokhvisnev YV, Makeev S, Gimmelfarb AI (2005) Use of the innovative remelt technology to process iron-bearing wastes from mines and metallurgical plants. Metallurgist 1(54):45–49
4. Shen f M, Shi YX (1996) Gas-solid reaction kinetics in blast furnace. Metal Industry Press, Beijing
5. Chen SW, Tian C, Li J et al (2017) Separation and kinetics of blast furnace gas ash Zn-Fe. Sinter Pellets (10):39–43. https://doi.org/10.13403/j.sjqt.2017.05.060
6. Yin HT, Wu XR, Li LS et al (2013) Selective reduction of valuable elements in iron-rich metallurgical sludge. Mineral Comp Util 07(1):67–71. https://doi.org/10.3969/j.issn.1000-6532.2013.05.018
7. Dai SH (2004) Study on comprehensive utilization of dust ash in electric furnace containing zinc. Northeastern University, Liaonin
8. Xu CD (1979) Metallurgical physical chemistry of zinc. Shanghai Science and Technology Press, Shanghai
9. Chen ZL, Zhang JL, Liu ZJ et al (2017) Study on zinc removal behavior of zinc-containing dust clusters. J Central South Univ 48(7):1705–1711. https://doi.org/10.11817/j.issn.1672-7207.2017.07.003
10. Song ZQ (2001) Study on the kinetics of zinc-removal of high carbon and high zinc iron dust. Comp Util Mineral Res 10:1–5
11. Huang XH (2013) Principles of iron and steel metallurgy. Metallurgical Industry Press, Beijing

Synthesis and Characterization of $BaTiO_3$ Doped with Eu^{3+} by the Reaction Solid-State Method

J. P. Hernández-Lara, M. Pérez-Labra, F. R. Barrientos-Hernández, J. A. Romero-Serrano, A. Hernández-Ramírez, M. Reyes-Pérez, J. C. Juárez-Tapia, A. M. Teja-Ruiz, Víctor E. Reyes-Cruz and J. C. Ramírez-Castellanos

Abstract Barium Titanate ($BaTiO_3$) doped with Eu^{3+} was synthesized by the solid-state reaction method. The milling of $BaCO_3$, TiO_2 and Eu_2O_3 was carried out in an agate mortar with acetone as a control medium for 25 min and compositions of $x = 0.001, 0.007, 0.05$ and 0.1% by weight of Eu^{3+}. The precursor powders TiO_2, $BaCO_3$ and Eu_2O_3 were mixed and calcined at 800 °C for 8 h and sintered at 1200 °C for 5 h. X-ray diffraction results revealed the predominant ferroelectric tetragonal $BaTiO_3$ phase for low compositions, and secondary phases (Eu_2TiO_5) for mixtures with high concentrations of Eu^{3+}. The X-ray mapping images showed a uniform distribution of Ti, Ba and Eu in the samples. The incorporation of Eu^{3+} ions into the $BaTiO_3$ system could greatly manifest dielectric properties and can find immense scope in electronic elements including ceramic capacitors.

Keywords $BaTiO_3$ · Eu^{3+} · Doping

Introduction

Barium Titanate ($BaTiO_3$) has been widely studied during the last decades due to its excellent electrical properties. A substantial number of synthetic methods have been developed for the preparation of Barium Titanate powders [1]. Both conventional

J. P. Hernández-Lara (✉) · M. Pérez-Labra · F. R. Barrientos-Hernández · M. Reyes-Pérez · J. C. Juárez-Tapia · A. M. Teja-Ruiz · V. E. Reyes-Cruz · J. C. Ramírez-Castellanos
Academic Area of Earth Sciences and Materials, Autonomous University of the State of Hidalgo, Pachuca-Tulancingo Km 4.5, 42184 Mineral de la Reforma, Hidalgo, Mexico
e-mail: juanp_hernandezlara@hotmail.com

J. A. Romero-Serrano · A. Hernández-Ramírez
Metallurgy and Materials Department, ESIQIE-IPN, UPALM, Zacatenco, 07738 Ciudad de México, Mexico

J. Li et al. (eds.), *Characterization of Minerals, Metals, and Materials 2020*,
The Minerals, Metals & Materials Series,
https://doi.org/10.1007/978-3-030-36628-5_71

solid-state reaction methods and chemical methods such as sol-gel, coprecipitation, hydrothermal used to prepare Barium Titanate, as reported by Vigalovic et al. [2].

Barium Titanate is the first ferroelectric ceramic and a good candidate for a variety of applications due to its excellent dielectric, ferroelectric and piezoelectric properties, and it is a member of a large family of compounds with the general formula ABO3 called perovskites, it can be prepared using different methods. The synthesis method depends on the characteristics desired for the final application and has a significant influence on the structure and properties of the Barium Titanate materials [2].

In the last decade, studies have been carried out on the preparation of Barium Titanate of nanometric size, which are still carried out by several authors [3–5].

Large-scale production is often based on solid-state reactions of mixed powders $BaCO_3$ and TiO_2 at high temperatures [6]. However, this procedure can result in a ceramic with inhomogeneities of composition and formation of secondary phases that damage the electrical properties of $BaTiO_3$ [7–10].

The classic method of synthesizing $BaTiO_3$ ceramic powder, which consists of mixing and calcining barium carbonate ($BaCO_3$) and titanium oxide (TiO_2), involves a series of stages that prevent reaching the degree of purity and homogeneity required by many of the applications current. It consists of the solid-state reaction between barium carbonate and titanium oxide. The mechanism of formation of $BaTiO_3$ has been widely discussed in the literature and can be summarized in three basic steps [11–13].

1. Decomposition of $BaCO_3$ and diffusion of Ba^{2+} into TiO_2 particles.

$$BaCO_3 + TiO_2 \rightarrow BaTiO_3 + CO_2 \tag{1}$$

2. The formation of $BaTiO_3$ hinders the diffusion of Ba^{2+} ions and favors the appearance of a second phase.

$$BaCO_3 + BaTiO_3 \rightarrow Ba_2TiO_4 \tag{2}$$

3. Final formation of $BaTiO_3$.

$$Ba_2TiO_4 + TiO_2 \rightarrow 2BaTiO_3 \tag{3}$$

The use of CO_2 or N_2 atmospheres at 1100 °C can suppress the formation of the intermediate phase Ba_2TiO_4. Barium carbonate is a very stable compound and its thermal decomposition, in the presence of TiO_2, begins at temperatures of the order of 700 °C [14]. Similarly, the fact that the reaction occurs by diffusion of Ba^{2+} implies high temperatures (above 1000 °C) and long reaction times, indicating a tendency to the appearance of second remaining phases.

The present study reports the results of X-ray diffraction where the tetragonal ferroelectric $BaTiO_3$ phase predominates for low and secondary phases (Eu_2TiO_5)

for mixtures with high concentrations of Eu^{3+}, as well as elementary distribution mappings where the images showed a uniform distribution of Ti, Ba and Eu in the samples.

Experimental Methodology

Barium Titanate ($BaTiO_3$) doped with Eu^{3+} was synthesized using solid-state reaction synthesis. The grinding of $BaCO_3$, TiO_2 and Eu_2O_3 was carried out in an agate mortar with acetone as a control medium for 25 min and x-compositions = 0.001, 0.007, 0.05 and 0.1% by weight of Eu^{3+}. The precursor powders ($BaCO_3$, TiO_2 and Eu_2O_3) were dried at 300 °C in a LINDBERG Muffle. The powder mixture is placed in an alumina crucible and calcined at 800 °C for 8 h. Subsequently, they are synthesized in an alumina crucible at 1200 °C for 5 h in a FURNACE THERMOLYNE model 46200 oven.

The results of X-ray diffraction revealed the predominant phase of ferroelectric tetragonal $BaTiO_3$ for low compositions and secondary phases (Eu_2TiO_5) for mixtures with high concentrations of Eu^{3+}. X-ray mapping images showed a uniform distribution of Ti, Ba and Eu in the samples. The incorporation of Eu^{3+} ions into the $BaTiO_3$ system could greatly manifest dielectric properties and can find immense reach in electronic elements, including ceramic capacitors.

Results and Discussion

Figure 1 shows the spectra corresponding to sintered powders at 1300 °C. It can be observed that at this temperature, there is no presence of the species corresponding to precursor powders. On the contrary, there is a consolidation of tetragonal BaTiO3 (JCPDS 05-0626) in the potions $2\theta \approx 21.94°$, 31.49°, 38.81°, 45.20°, 50.93°, 56.17°, 65.83°, 70.42°, 75.16°, 79.43°, 83.68° which highlights the peak of greatest intensity at $2\theta \approx 31.49°$, as well as the identification of the secondary phases Eu_2TiO_5 (JCPDS 22-1100) at position $2\theta \approx 29.88°$ for compositions $x = 0.05, 0.1$. Mrazek et al. and Orihashi et al. found that lanthanide titanium oxides that crystallize in a pyrochloric type structure with general formula Re_2TiO_5 and $Re_2Ti_2O_7$ (Re = Rare Earths) have been extensively investigated in recent years for their interesting properties of photoluminescence [15, 16].

Figure 2 shows the images obtained by SEM of $BaTiO_3$ doped with Eu^{3+} sintered at 1300 °C for 5 h with a heating and cooling rate of 7 °C/min at different magnifications for the composition $x = 0.10$. In this figure, you can see rounded and sub-rounded particles Fig. 2a, b which present the characteristic necks of a sintering process, as well as a homogeneous distribution of the sintered particles, the grains appear to have a large distribution and the formation of the necks can be observed in more detail Fig. 2c, d.

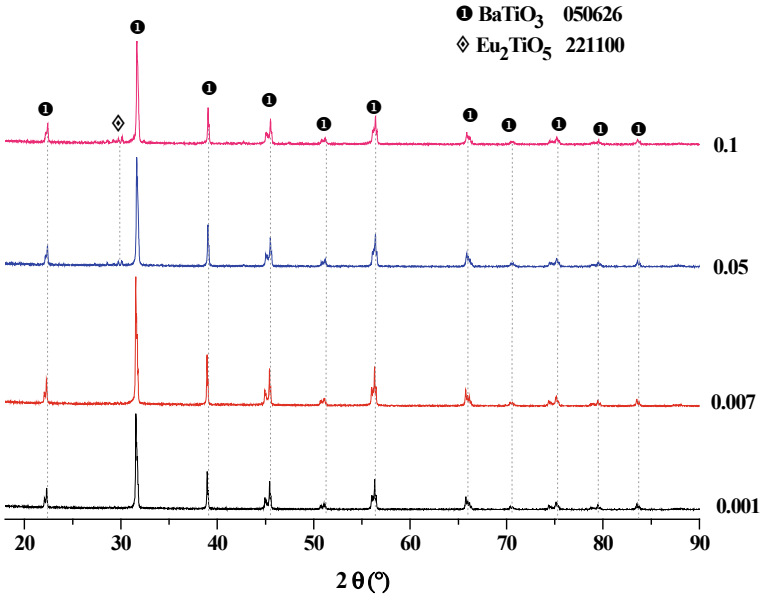

Fig. 1 X-ray diffraction spectra of $BaTiO_3$ doped with Eu^{3+}. $0.001 \leq x \geq 0.1$

Figure 3 shows the elemental distribution mappings of oxygen, titanium, and barium for the composition $x = 0.007$. In the images, a high contrast is observed due to the concentration gradient of each corresponding element, the brightest areas correspond to areas rich in oxygen, titanium and barium, on the contrary, the dark areas correspond to poor areas in the same elements. In this sample, the concentration of the europium could not be observed because it is a low europium composition and could not be detected by the team. Similarly, the EDS results of sintered powders at 1300 °C are observed where the presence of the elements O, Ti and Ba can be observed, the europium could not be detected by EDS because it is a low concentration and the equipment cannot he could detect it.

Figure 4 shows the elementary distribution mappings for oxygen, titanium, barium and europium for the composition $x = 0.05\%$ by weight Eu^{3+}, respectively. In the images, the concentration gradient of each corresponding element is observed, the brightest areas correspond to areas rich in oxygen, titanium, barium and europium, respectively, on the contrary, the dark areas correspond to poor areas in the same elements. Similarly, a homogeneous concentration is observed in the analyzed area and showed uniform distribution. In the EDS results, the presence of the elements of the doped ceramic powders can be observed, for this sample the presence of the dopant is abundant.

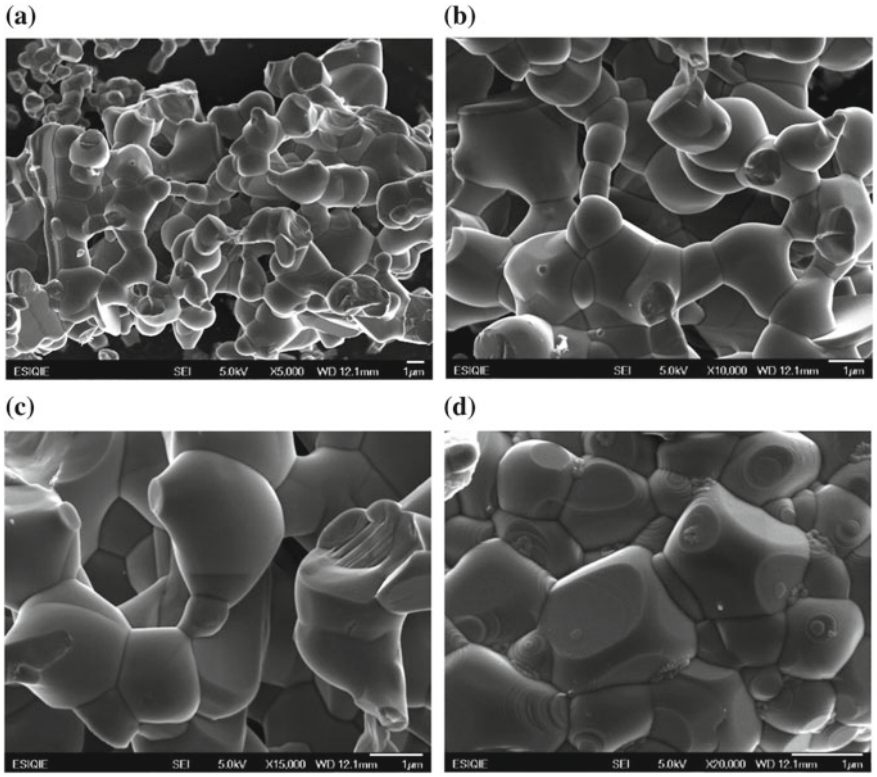

Fig. 2 Micrographs obtained by SEM of $BaTiO_3$ doped with Eu^{3+} for $x = 0.10$. **a** 5000x, **b** 10000x, **c** 15000x, **d** 20000x

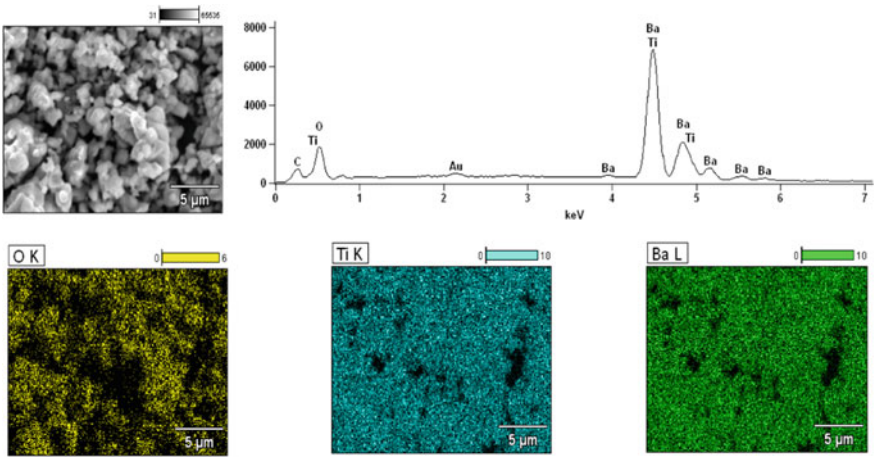

Fig. 3 Elemental distribution mapping of $BaTiO_3$ doped with Eu^{3+} for the sample $x = 0.007\%$ by weight

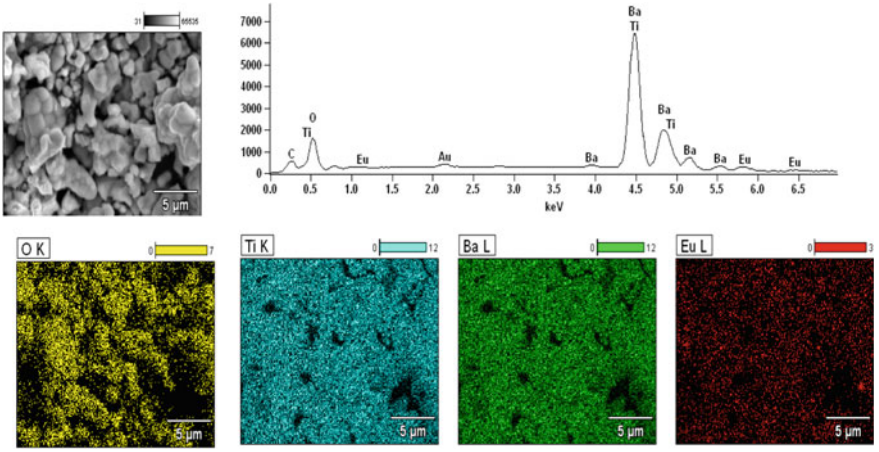

Fig. 4 Elemental distribution mapping of $BaTiO_3$ doped with Eu^{3+} for the sample $x = 0.05\%$ by weight

Conclusions

Barium Titanate doped with Eu^{3+} was synthesized using the solid-state reaction method. The X-ray diffraction spectra of sintered powders at 1300 °C confirm the formation of tetragonal $BaTiO_3$ as a consolidated phase because there is no longer any presence of Eu^{3+} remnants as well as they also show the formation of a secondary Eu_2TiO_5 phase (JCPDS 22-1100). SEM micrographs show rounded and sub-rounded particles which present the characteristic necks of a sintering process, as well as a homogeneous distribution of sintered particles, the grains appear to have a large distribution. The elementary distribution mappings show the concentration gradient of each corresponding element, the brightest areas correspond to areas rich in oxygen, titanium, barium and europium, respectively, on the contrary, the dark areas correspond to poor areas in the same elements.

References

1. Othman KI, Hassan AA, Abdelal OAA, Elshazly ES, El-Sayed Ali M, El-Raghy SM, El-Houte S (2014) Formation mechanism of barium titanate by solid-state reactions. Int J Sci Eng Res 5(7):1460–1465
2. Vigalovic MM, Bobić JD, Stojanvić BD (2008) History and challenges of barium titanate: part I. Sci Sinter 40:155–165
3. Manafi S, Rahimipour MR, Mobasherpour I, Soltanmoradi A (2012) Synthesis of nanocrystalline $BaTiO_3$ ceramics via hydrothermal condition and structural characterization by HRTEM and SAED. Int J Nano Dim 3(2):163–168. https://doi.org/10.7508/IJND.2012.02.010

4. Moon S, Lee HW, Choi C-H, Kim DK (2012) Influence of ammonia on properties of nanocrystalline barium titanate particles prepared by a hydrothermal method. J Am Ceram Soc, 1–6. https://doi.org/10.1111/j.1551-2916.201205163.x
5. Guo X (2013) Peculiar size effect in nanocrystalline $BaTiO_3$. Acta Mater 61(5):1748–1756. https://doi.org/10.1016/j.actamat.2012.11.049
6. Zheng P, Zhang L, Tan YQ, Wang CL (2012) Grain-size effects on dielectric and piezoelectric properties of poled $BaTiO_3$. Acta Mater 60(13–14):5022–5030. https://doi.org/10.1016/j.actamat.2012.06.015
7. Kong LB, Ma J, Huang H, Zhang RF, Que WX (2002) Barium titanate derived from mechanochemically activated powders. J Alloy Compd 337(1–2):226–230. https://doi.org/10.1016/S0925-8388(01)01925-9
8. Brzozowski E, Castro MS (2003) Lowering the synthesis temperature of high-purity $BaTiO_3$ powders by modifications in the processing conditions. Thermochim Acta 398(1–2):123–131
9. Berbenni V, Marini A, Bruni G (2001) Effect of mechanical milling on solid state formation of $BaTiO_3$ from $BaTiO_3$-TiO_2 (Rutile) mixtures. Thermochimi Acta 374(2):151–158. https://doi.org/10.1016/s0040-6031(01)00505-6
10. Pavlovic V, Stojanovic BD, Pavlovic VB, Marinkovic-Stanojevic Z, Zivkovic L, Ristic MM (2008) Synthesis of $BaTiO_3$ from a mechanically activated $BaCO_3$-TiO_2 system. Sci Sinter 40(1):21–26. https://doi.org/10.2298/SOS0801021P
11. Beauger A, Mutin JC, Niepce JC (1983) Synthesis reaction of metatinate $BaTiO_3$. Part 1. Effect of the gaseous atmosphere upon the thermal evolution of the system $BaCO_3$-TiO_2. J Mater Sci 18(10):3041–3046
12. Beauger A, Mutin JC, Niepce JC (1983) Synthesis reaction of metatitanate $BaTiO_3$. Part 2, study of solid-solid reaction interfaces. J Mater Sci 18:3543–3550
13. Niepce JC, Thomas G (1990) About the mechanism of the solid way synthesis of barium metatinate. Industrial consequences. Solid State Ion 43:69–76. https://doi.org/10.1016/0167-2738(90),90472-4
14. Fernandez JF, Duran P, Moure C (1991) Reaction kinetics in the $BaTiO_3$ synthesis: influence of the TiO_2 crystalline structure and morphology. In: Vicenzini P (Ed.), En ceramics today-tomorrow's ceramics, Elsevier Science Publishers, 1973–1982
15. Mrazek J, Surynek J, Bakardjieva S, Bursık J, Karsık I (2014) Synthesis and crystallization mechanism of europium-titanate $Eu_2Ti_2O_7$. J Cryst Growth 391(1):25–32
16. Orihashi T, Nakamura T, Adachi S (2016) Synthesis and unique photoluminescence properties of $Eu_2Ti_2O_7$ and Eu_2TiO_5. J Am Ceram Soc, 1–8. https://doi.org/10.1111/jace.14318

Synthesis and Characterization on Copper Oxide Anode of Lithium-Ion Battery

Xuechun Han, Shuzhen Yang, Huina Sun, Yanfang Huang and Guihong Han

Abstract Ultra-thin CuO nanomaterial was easily prepared by calcining the copper hydroxide precursor which was obtained from solution route. X-ray diffraction (XRD) and scanning electron microscope (SEM) were used to characterize the structure and morphology of annealed samples. The results demonstrate the material exists as uniform nanosheets with a nominal thickness of 5 nm. The electrochemical performances were measured and analyzed via cyclic voltammetric curves (CV), electrochemical impedance spectra (EIS), charge/discharge curves, and cycling performances. The discharge capacity of the CuO nanosheets in the first cycle can achieve 826.7 mAh g^{-1} with the coulombic efficiency of 57.45%. The first cycle has a charge specific capacity of 475 mAh g^{-1}. The charge capacity maintained 376.1 mAh g^{-1} at a current density of 100 mA g^{-1} even after 40 cycles.

Keywords Lithium-ion battery · Anode materials · Transition metal copper oxide

Introduction

Compared to other energy materials, lithium-ion batteries (LIBs) possess the characteristics of high energy density, long cycle life, high operating voltage, insignificant memory effect, and slow self-discharge. It is considered to be an ideal energy source for electric vehicles and hybrid vehicles. However, the poor cycling performance of conventional anode materials has made it impossible to meet consumer demand for high energy and high power density for lithium-ion batteries. In addition, its poor safety performance poses a significant concern. Therefore, it is necessary to explore new anode materials such as nitrides, transition metal oxides, phosphides, or fluorides to meet these requirements [1–3]. Among them, copper oxide (CuO) has been widely considered due to its high specific capacity (670 mAh g^{-1}), low cost, high safety, and facile to synthesize nano-shapes of various sizes [4]. However, its

X. Han · S. Yang · H. Sun · Y. Huang · G. Han (✉)
School of Chemical Engineering and Energy, Zhengzhou University, Zhengzhou 450001, People's Republic of China
e-mail: hanguihong@zzu.edu.cn

J. Li et al. (eds.), *Characterization of Minerals, Metals, and Materials 2020*,
The Minerals, Metals & Materials Series,
https://doi.org/10.1007/978-3-030-36628-5_72

poor conductivity and large volume change during the lithiation/delithiation process lead to a rapid decay of capacity. In order to solve this problem, some techniques for improving the performance of CuO anodes have been reported, for example, the CuO/C nanocomposite can be prepared [5–11]. The addition of carbon material not only improves the electronic conductivity but also prevents the destruction of the CuO crystal structure during the Li^+ insertion–extraction process. Nevertheless, the reversibility of CuO is reduced by the addition of carbon materials [12]. One feasible and effective way is to develop nanomaterials of CuO [12–17]. The electrochemical properties of CuO vary greatly with the morphologies. In general, uniform morphology and fine structure of the CuO nanomaterial can promote the specific capacity and cycle performance. It is meaningful to synthesize CuO nanomaterials with the uniform morphology to improve the electrochemical performance.

Herein, we focused on the synthesis of ultra-thin CuO nanosheets by a simple solution route with heat treatment. The precursor was obtained by a chemical precipitation reaction of copper sulfate pentahydrate ($CuSO_4 \cdot 5H_2O$) and sodium hydroxide (NaOH), and then calcined in air for 2 h.

Experimental Methods

Synthesis of CuO

First, 0.2 mol NaOH was dissolved in 100 mL distilled water and 1 mmol $CuSO_4 \cdot 5H_2O$ was dissolved in 10 mL distilled water. Then the $CuSO_4$ solution was dropwise added into the NaOH solution under magnetic stirring at 20 °C. After reaction for 20 min, fine grains were produced. The resulting light blue powder was collected by high-speed centrifugation and washed several times with deionized water and ethanol. The obtained blue precipitates were dried in an oven for 6 h at 60 °C. The precursor was calcined in air at 150 °C for 2 h with a heating rate of 5 °C min^{-1} to obtain a dark black powder.

Physical Characterization

The phase of the product was characterized by X-ray diffraction (XRD, Bruke D8-Advance, Cu-Kα). The morphology of CuO nanomaterials was characterized by field emission scanning electron microscopy (FESEM, HITACH S4800). The lithium-ion battery was subjected to constant current charge and discharge test and the multiple charge and discharge test using the Land 2001 A battery test system. The voltage range of constant current charge and discharge was 0.05–3 V, and the current density was 100 mA g^{-1}. Cyclic voltammetry and AC impedance testing of lithium-ion batteries were performed using the Autolab PGSTAT204 electrochemical workstation.

The cyclic voltammetry test had a voltage sweep range of 0.05–3 V at a scan rate of 0.3 mV s^{-1}, and an AC impedance test frequency range was 0.01–10^5 Hz with an AC amplitude of 5 mV.

Electrode Preparation and Battery Assembly

The working electrode (WE) was prepared by mixing an active material (CuO), a conductive agent (acetylene black), and a binder (polydiethylenedifluoride: PVDF) in the mass ratio of 8 : 1 : 1. The dispersion medium of PVDF was N-methylpyrrolidone (NMP). The obtained slurry was uniformly coated on a copper foil with a bench coater. The WE was dried in a vacuum oven at 60 °C for 12 h. Then the WE was punched into a circular electrode piece with a diameter of 14 mm using a manual punching machine.

The average mass of the electrode sheets is about 2 mg. The button cells were assembled in an argon glove box in which the contents of O_2 and H_2O are both less than 0.1 ppm. The lithium metal sheet acts as a counter electrode and a reference electrode, and the separator is polypropylene. The electrolyte is 1M $LiPF_6$, wherein the solvent composition is EC/DMC/MC with a volume ratio of 1 : 1 : 1.

Results and Discussion

XRD is mainly used to analyze the composition of synthetic samples and determine the crystal structure. The XRD pattern of the CuO sample is shown in Fig. 1. It is apparent that the sample is indexed to a monoclinic copper oxide (CuO) phase

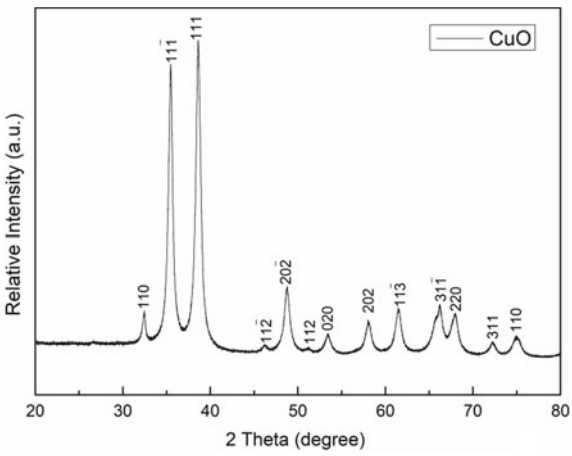

Fig. 1 XRD pattern of ultra-thin CuO nanosheets

with lattice parameters $a = 4.688$ Å, $b = 3.423$ Å, $c = 5.132$ Å (JCPDS card no. 48-1548). No characteristic peaks of $Cu(OH)_2$ and Cu_2O are observed in the XRD patterns, indicating that sample is with high purity.

Figure 2 shows SEM images of prepared CuO nanostructures, which show uniform ultra-thin nanosheets with a thickness of about 5 nm. As can be seen from Fig. 2a, the nanosheets exhibit good dispersibility.

Figure 3 shows the cyclic voltammetry curves of the 1, 2, and 3 turns of the lithium-ion battery with the CuO nanomaterial as the negative electrode in the potential range of 0.05–3.0 V and the scanning rate of 0.3 mV s^{-1}. During the reduction process, the strong reduction peak located near 0.887 V corresponds to the reduction of CuO and the formation of solid electrolyte interface (SEI) film. The reduction peak near 0.662 V corresponds to the alloying reaction between Cu and lithium ions to form a lithium intercalation compound Li_xCu. The oxidation peak near 1.603 V during the

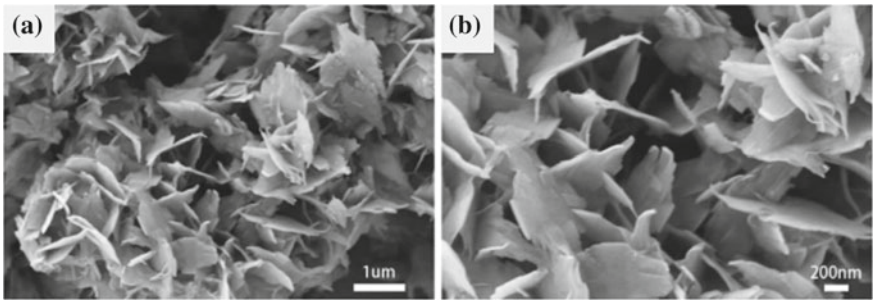

Fig. 2 **a**, **b** SEM images of ultra-thin CuO nanosheets under different magnification

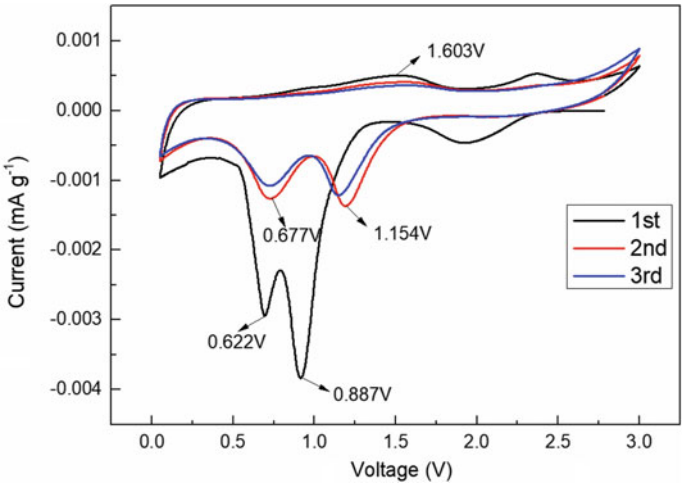

Fig. 3 CV curves of ultra-thin CuO nanosheets

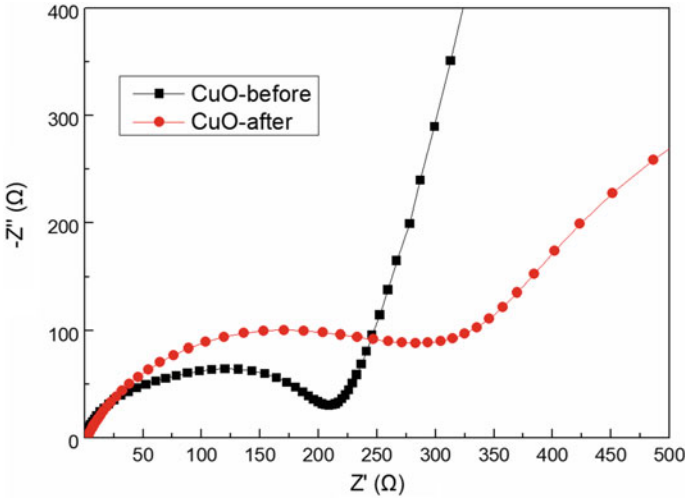

Fig. 4 EIS of the CuO electrodes

anodization corresponds to the de-alloying process of Li_xCu, which is reversible. The weaker oxidation peak at 2.4 V indicates that the reaction between Cu and Li_2O to form CuO and Li^+ is partially reversible. In the second and third circles, the weaker reduction peaks located near 0.677 V and 1.154 V are, respectively, the formation of the SEI film and the reduction of CuO, indicating that the SEI film tends to be stable in the subsequent cycles. It is observed that the second and third circles are substantially coincident, manifesting that the electrode with the CuO nanomaterial has good reversibility.

Figure 4 shows the electrochemical impedance spectroscopy (EIS) of the CuO electrode. The curve consists of a semi-circle from the high frequency to the intermediate frequency and a straight line in the low frequency region. The semi-circle is SEI impedance film, and the slope of the line is the diffusion impedance of lithium ions in the electrode active material. The larger the slope, the smaller the diffusion impedance of lithium ions [18]. Figure 4 illustrates the diffusion impedance of lithium ions increases slightly.

The cycle performance of the CuO nanosheets electrode at a current density of 100 mA g^{-1} is shown in Fig. 5a. It can be seen from the figure that the CuO nanosheets exhibit excellent cycle performance. The specific discharge capacity of the first cycle is as high as 826.7 mAh g^{-1}, which is higher than the theoretical specific capacity of CuO (670 mAh g^{-1}) [12]. The high discharge specific capacity of the first cycle is due to the reduction of the electrolyte and subsequent formation of the SEI layer on the anode material [19]. The first cycle has a charge specific capacity of 475 mAh g^{-1} with a coulombic efficiency of 57.45%. After 40 cycles, the charge capacity maintains as high as 376.1 mAh g^{-1} with a capacity retention rate of 79.2%. The high capacity retention of the CuO nanosheets is attributed to ultra-thin size and

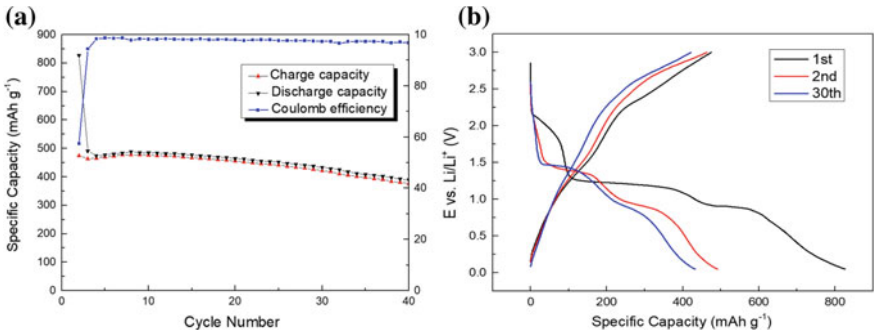

Fig. 5 **a** Cycling performance of ultra-thin CuO nanosheets, **b** the voltage–capacity curves for the first three turns of CuO

uniform dispersion, which is advantageous for adapting to volume change due to volume expansion during Li^+ reciprocating insertion and extraction.

Figure 5b displays the voltage–capacity curves for the first, second, and thirtieth cycles of ultra-thin CuO nanosheets at a current density of 100 mA g^{-1}. The first discharge cycle has three platforms, respectively, around at 2, 1.2, and 0.9 V. The platform at 1.2 V corresponds to 0.887 V in the CV figure, which indicates CuO reduction and SEI film formation. The platform at 0.9 V represents the alloying reaction between Cu and Li^+ to form Li_xCu, which corresponds to 0.622 V in the CV diagram. There are two platforms in the second and thirtieth cycles, which are around 1.3 V and 0.8 V, respectively, denoting CuO reduction and SEI membrane formation. The platform is not obvious in the charging process, which exactly coincides with the weak oxidation peak in the CV diagram.

Figure 6 illustrates the rate performance of CuO electrodes at different current densities. At 0.1C, a charge capacity of 290.9 mAh g^{-1} is obtained after 10 cycles. At 0.2C, 0.4C, 0.8C, 1.6C, the value decreased to 183.7 mAh g^{-1}, 127.1 mAh g^{-1}, 90.6 mAh g^{-1}, 56.9 mAh g^{-1}, respectively. In addition, when the current density returned to 0.1C, the charging capacity rise back to 205.7 mAh g^{-1}, demonstrating a relatively stable rate capability.

Conclusions

In this paper, ultra-thin CuO nanosheets (about 5 nm) with uniform dispersion were successfully synthesized by a simple solution route combined with heat treatment. Electrochemical tests show that the synthesized CuO nanosheets have excellent electrochemical performance. After 40 cycles, the reversible specific capacity can reach 376.61 mAh g^{-1}. Therefore, low cost, simple synthetic route, and high electrochemical performance make ultra-thin CuO nanosheets become a promising anode material for lithium-ion batteries.

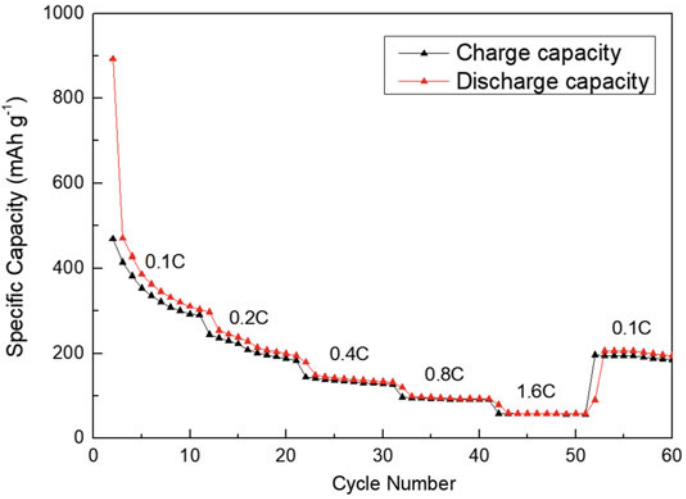

Fig. 6 Cycling performance of ultra-thin nanosheets CuO at different current densities

Acknowledgements This work was financially supported by the Natural Science Foundation of China (No. 51674225, 51974280 and 51774252), the China Postdoctoral Science Foundation (No. 2017M622375), the Educational Commission Fund of Henan Province of China (No. 17A450001, No. 18HASTIT011 and No. 18A450001).

References

1. Zhang X, Qian Y, Zhu Y et al (2014) Synthesis of Mn_2O_3 nanomaterials with controllable porosity and thickness for enhanced lithium-ion batteries performance. Nanoscale 6(3):1725–1731
2. Kiener J, Tosheva L, Parmentier J (2017) Carbide, nitride and sulfide transition metal-based macrospheres. J Eur Ceram Soc 37(3):1127–1130
3. Antipov EV, Khasanova NR, Fedotov SS (2015) Perspectives on Li and transition metal fluoride phosphates as cathode materials for a new generation of Li-ion batteries. IUCrJ 2(Pt 1):85–94
4. Pendashteh A, Mousavi MF, Rahmanifar MS (2013) Fabrication of anchored copper oxide nanoparticles on graphene oxide nanosheets via an electrostatic coprecipitation and its application as supercapacitor. Electrochim Acta 88:347–357. https://doi.org/10.1016/j.electacta.2012.10.088
5. Zheng SF, Hu JS, Zhong LS et al (2008) Introducing dual functional CNT networks into CuO nanomicrospheres toward superior electrode materials for lithium-ion batteries. Chem Mater 20:3617–3622. https://doi.org/10.1021/cm7033855
6. Wang B, Wu XL, Shu CY et al (2010) Synthesis of CuO/graphene nanocomposite as a high-performance anode material for lithium-ion batteries. Mater Chem 20:10661–10664. https://doi.org/10.1039/C0JM01941K
7. Venkatachalam S, Zhu HW, Masarapu C et al (2009) In-situ formation of sandwiched structures of nanotube/CuxOy/Cu composites for lithium battery applications. ACS Nano 3:2177–2184. https://doi.org/10.1021/nn900432u

8. Xiang JY, Tu JP, Yuan YF et al (2009) Electrochemical investigation on nanoflower-like CuO/Ni composite film as anode for lithium ion batteries. Electrochim Acta 54:1160–1165. https://doi.org/10.1016/j.electacta.2008.08.066
9. Xiang JY, Tu JP, Zhang J, Zhong J, Zhang D, Cheng JP (2010) Electrochem Commun 12:1103–1107
10. Li C, Wei W, Fang SM et al (2010) R.FIncorporation of MWCNTs into leaf-like CuO nanoplates for superior reversible Li-ion storage. Chen J Power Sources 195:2939–2944. https://doi.org/10.1016/j.elecom.2010.05.039
11. Wang HB, Pan QM, Zhao JW, Chen WT (2009) Fabrication of CuO/C films with sisal-like hierarchical microstructures and its application in lithium ion batteries. Alloys Compd 476:408–413. https://doi.org/10.1016/j.jallcom.2008.09.013
12. Wang F, Tao W, Zhao M et al (2011) Controlled synthesis of uniform ultrafine CuO nanowires as anode material for lithium-ion batteries. J Alloys Compd 509(41):9798–9803
13. Li A, Song H, Wan W et al (2014) Copper oxide nanowire arrays synthesized by in-situ thermal oxidation as an anode material for lithium-ion batteries. Electrochim Acta 132:42–48. https://doi.org/10.1016/j.electacta.2014.03.123
14. Ameri B, Davarani SSH, Roshani R et al (2017) A flexible mechanochemical route for the synthesis of copper oxide nanorods/nanoparticles/nanowires for supercapacitor applications: the effect of morphology on the charge storage ability. J Alloys Compd 695:114–123. https://doi.org/10.1016/j.jallcom.2016.10.144
15. Liu X, Cui S, Sun Z et al (2015) Copper oxide nanomaterials synthesized from simple copper salts as active catalysts for electrocatalytic water oxidation. Electrochim Acta 160:202–208. https://doi.org/10.1016/j.electacta.2015.01.123
16. Shrestha KM, Sorensen CM, Klabunde KJ (2010) Synthesis of CuO nanorods, reduction of CuO into Cu nanorods, and diffuse reflectance measurements of CuO and Cu nanomaterials in the near infrared region. J Phys Chem C 114(34):14368–14376
17. Gao P, Liu D (2015) Facile synthesis of copper oxide nanostructures and their application in non-enzymatic hydrogen peroxide sensing. Sens Actuators B Chem 208:346–354. https://doi.org/10.1016/j.snb.2014.11.051
18. An W, Fu J, Mei S et al (2017) Dual carbon layer hybridized mesoporous tin hollow spheres for fast-rechargeable and highly-stable lithium-ion battery anodes. J Mater Chem A 5(27):14422–14429
19. Debart A, Dupont L, Poizot P, Leriche JB, Tarascon JM (2001) A transmission electron microscopy study of the reactivity mechanism of tailor-made CuO particles toward lithium. J Electrochem Soc 148 A:1266. https://doi.org/10.1149/1.1409971

Author Index

J. Li et al. (eds.), *Characterization of Minerals, Metals, and Materials 2020*,
The Minerals, Metals & Materials Series,
https://doi.org/10.1007/978-3-030-36628-5

Subject Index

J. Li et al. (eds.), *Characterization of Minerals, Metals, and Materials 2020*,
The Minerals, Metals & Materials Series,
https://doi.org/10.1007/978-3-030-36628-5

N